CRANFIELD UNIVERSITY

SCHOOL OF ENGINEERING

DEPARTMENT OF AUTOMOTIVE, MECHANICAL & STRUCTURES ENGINEERING

CRASHWORTHINESS, IMPACT & STRUCTURAL MECHANICS GROUP

PHD THESIS

DEVELOPMENT OF DAMAGE DETECTION ALGORITHMS FOR STRUCTURAL SYSTEMS BASED ON STRUCTURAL DYNAMIC DATA

GIUSEPPE ZUMPANO

Academic Year 2004-05

July 2005

Supervisor: DR. MICHELE MEO

EXECUTIVE SUMMARY

Nowadays, aeronautical, civil and mechanical structures undergo expensive maintenance programs during their operative life due to safety regulations, magnitude and frequency of their operative loads, structure aging, operative conditions different from those of design etc... These maintenance programs often affect considerably the profit margins of companies, which are increasingly interested in reliable and cost effective Structural Health Monitoring or Structural Damage Identification devices capable of identifying structural faults and automating inspection programs.

Similar devices become today designable and affordable due to the availability of structural dynamic analysis systems, characterised by the extraordinary performances of sensors (sensibility, operative frequency bandwidth), signal analysers (number of channels, sampling frequencies) and actuators (forces, operative frequency bandwidths).

However, many researchers do not exploit the opportunity of an integrated design (NDT method + sensors + signal processing) of monitoring devices and often forget the final target of damage detection, the development of a fully functional SHM device. Too often, researchers developed methodologies (§6.6) employing an impracticable number of sensors, with respect to structure operative conditions, applied on numerical models

incapable of reproducing correctly the structure dynamic behaviour, because of stringent hypothesis, limited number of DoFs and etc... Therefore, in this research, a global view on the SHM was adopted, leading to damage detection processes dealing with all the phases of the SHM device design, such as data type selection, optimal sensor placement, signal processing, damage detection etc... Moreover, the differences between the several typologies of structures (civil, mechanical and aeronautical), in terms of load amplitude and frequencies, crack growth rate and etc..., and numerical considerations, such as memory and time consumption, made impossible the development of a unique damage detection methodology. Hence, two different techniques, dealing with stationary and transient structure dynamic responses, were developed: the global damage detection algorithms and a wave propagation based technique.

The global damage detection algorithms were developed mainly for large scale structures (e.g. bridges, wings) where typical damages affect relatively low frequencies (§7.2), but do not constitute an immediate threat neither to the structure health nor to its users, because of the typical structure failure modes and the nature of operative loads (e.g. low frequency).

A model updating technique was considered more suitable for this kind of structures and it was developed to meet the structural faults identification and automatic inspection requirements. This task was fulfilled by designing detection algorithms based on optimization algorithms. Two main directions were followed. The first consisted in an evolution of model updating techniques (chapter 2), aimed at the identification of structural changes by using stationary responses of the structure such as modal properties and Frequency Response Functions (FRF). The optimization algorithms were set up to minimize the differences between the undamaged and damaged structure stationary responses by changing the characteristic of a validated FE model of the undamaged structure. The second way (chapter 5) consisted in the use of an analytical function instead of a validated FE model of the structure. This produces large advantages in terms of run-time and reliability of the inverse problem solution. The structure stationary responses were acquired by use of a network of sensor deployed after a data selection process (chapter 3), which provided the selection of the data type, the target mode shape selection and, finally, the optimal sensor placement. A preliminary data processing for modal property extraction was considered for damage detection in operational conditions (chapter 4). The pre-processing was carried out by extracting free-decay signals from random ones using either the Random Decrement Technique (RDT) or the Cross-Correlation Function (CCF) based technique.

For the second group of structures (§7.2), a wave propagation based technique was designed to detect localised changes affecting mainly the high frequency of the structure and comply with the requirements of real-time detection. The methodology developed exploited the propagation of body and surface waves (chapter 7) in a medium generated by either operational loads (e.g. a coming train) or impulsive loads. The discrepancies between the damaged and the undamaged wave propagation time histories were highlighted by a time frequency algorithm, which allowed evaluating the time of flight of damage reflected waves, which was used by a specially designed ray-tracing algorithm to estimate the damage location.

CONTENTS

INDEX

Figure Index

Table Index

Appendix figure index

Appendix table index

CHAPTER 1: INTRODUCTION

1.1 Motivation for Structural Damage Identification and Health Monitoring Systems

Aeronautic, civil and mechanic structures need expensive maintenance programs during their operative life due to safety regulations, magnitude and frequency of their operative loads, structure aging, operative conditions different from those of design and etc... These maintenance programs often affect considerably the profit margins of companies, e.g. an average major airline for maintenance programs spends 12% of its annual operating costs, regional airlines up to 20% [1] and the UK railtrack administration about 20% (of which 78% is dedicated to track maintenance and renewal) [2].

Maintenance programs change from industry to industry, the most sensitive companies to this issue belong to the transport sector such as airline and railtrack companies, which are subject to the vigilance of appropriate government boards that, in some cases, issue guidelines for maintenance programs. Examples of maintenance plans are given in Table 1 (airlines), Table 2 (railtrack) and Table 3 (bridges).

Common point to every maintenance plan is the extensive employment of very specialised manpower for the identification and the quantification of structural changes. These inspections are aimed to find specific kinds of structure faults according to past experience on similar structures (e.g. airplanes) or design approaches such as damage tolerance, fail-safe.

This approach may lead to overlook some tiny fault or aspects of the structure operative life with catastrophic consequences. A blatantly example is the fracture of a main landing gear trunnion pin of a B737 in 1999 [3], triggered by corrosion due to penetration of moisture into the gap created between the bushes and lugs. The time

remaining on the trunnion pin life was about one tenth of the life calculated from the manufacturer.

At the aim to avoid accident like this, Structural Damage Identification (SDI) and Health Monitoring (HM) systems might be employed, providing, also, benefits for the operators by:

- Identifying faults that are precursors to failure and monitoring structure components using embedded sensor networks allowing the operators to schedule and anticipate the maintenance or replacement activities.
- Automating the inspection, measurements and the tests for on-condition components.

Moreover, such technologies should be able to downsize the importance of the maintenance voice in the company annual budgets and increase the safety of structures during their operative life.

When Service is Performed	Type of Service Performed	Impact on Airline Service
Prior to each flight	'Walk-around' – visual check of aircraft exterior and engines for damage, and leakage	None
Every 2-7 days	Service check (line maintenance opportunity) - service consumables (engine oils, hydraulic fluids, oxygen) and tire and brake wear	Overnight layover
Every 25-40 days	A-checks (line maintenance check) - detailed check of aircraft and engine interior, service and lubrication of systems (e.g., ignition, generators, cabin, air conditioning, hydraulics, structures, and landing gear)	Overnight layover
Every 45-75 days	B-checks (packaged A-checks) – torque tests, internal checks, and flight controls	Overnight layover
Every 12-15 months	C-checks (base maintenance visit) - detailed inspection and repair of engines and systems	Out of service 3-5 days
Every 2-5 years (depending on usage or mandatory inspection/modification requirements)	Heavy maintenance visit (or maintenance program visit) – corrosion protection and control program and structural inspections/modifications	Out of service up to 30 days

Source: Based on New Materials for Next-Generation Commercial Transports, NMAB-476, National Research Council, Washington, DC: National Academy Press (1996).

Table 1 – A Typical Airline Maintenance and Service Plan [4].

Track Category	3 (passenger)	4 (passenger)	5	6
Visual/week				
Jointed Rail	1	1	0.5	0.5
Cont. Welded Rail	0.5	0.5	0.25	0.25
Ultrasonic/annum				
Jointed Rail	0.5	0.5	0.5	0.5
Cont. Welded Rail	1	1	1	1
Track Recording Car/annum	1	1	1	1

Table 2 – Maintenance plan for different categories of railtracks [5].

Category of Inspection	Minimum Frequency for Inspection	Personnel Involved (minimum requirements)
Superficial Inspection: Impact damages, build up flood debris, erosion damage and ect.	Not more than one year	Bridge Inspector
General Inspection	2 years	Bridge Inspector
Detailed Inspection	6 years	Bridge Inspector
Special Inspections:		
Posted bridges or bridges with a known weakness or structural defect	2 years or as determined by Bridge Inspection Engineer.	Bridge Inspector
Bailey bridges	1 year	Bridge Inspector
Large or complex bridges	As agreed with the Transit Project Manager	As determined by Bridge Inspection Engineer
Earthquake. All bridges in the area seriously affected	Immediately following a significant earthquake	Bridge Inspector
Flood. Bridges over a waterway with a history of instability	Immediately following a flood	Bridge Inspector
Overload. Where a heavy overload has proceeded without the required supervision	Immediately following the event	Bridge Inspector

Table 3 – Bridge maintenance guidelines [6]

Unfortunately, SDI and HM techniques are still under development or yet not enough reliable for their application outside laboratories, although new military jets employ Health Usage Monitoring Systems (HUMS), which keep records of stress, strain and acceleration peaks of vehicle components [7-8].

In this environment still under development, the work presented in this thesis must be interpreted as an attempt to develop a SDI/HM system by using damage detection techniques in concert with an optimal sensor placement investigation and suggestion for "in operational conditions" damage detection monitoring.

1.2 Structural Health Monitoring

Structural HM allows continuous remote monitoring aimed to the detection of structural changes using Non Destructive Evaluation (NDE) systems embedded into the structure, reducing so, the structure maintenance downtime and increasing the probability of damage detection prior to catastrophic failures.

Embedded NDE systems consist in a network of sensors or probes deployed on the structure.

The sensor network has to be designed according to the fault-tolerant control system theory [10] independently by the kind of NDE methodology employed. Two level of fault-tolerance exist. The first named fail-operational guarantees the structural monitoring even if some of its components fail, while the fail-safe level cannot operate anymore after one or more components have failed.

It is clear that for HM the only fault tolerance level acceptable is the fail operational, which present three different solutions: the redundant, the parity relation and failure detection filters.

The redundant solution consists, at least, into double or triples the number of sensors to assure a fault-tolerance level. The only information available by doubling the number of sensors, in case of a component failure, is that a specific component failed without knowing which one. Using at least three times the number of sensors is possible to determine which component failed, and to keep on monitoring the structure.

Unfortunately, this solution might become impractical for HM purposes, because the number of sensors could rise too much and increase the complexity of the sensor network and its cost. For instance the number of acoustic sensors for HM on a large aircraft structure has been evaluated to be between 100 and 1000 depending on whether the entire structure is monitored or just its critical components [11].

The parity relation like the Ohm's law offers a better solution, identifying the faulted components of the control systems by comparing electric resistance of a healthy sensor with that measured during the structure operative life.

A more sophisticated fault-tolerant control system is given by failure detection filters that are derived from first-order based observers [12]. These techniques, with a proper choice of the filter feedback gain, can identify control system component failure. Moreover, using a more recent version consisting in second-order based observers, these filters can be designed to detect changes on the structure [10], (§1.4.2).

Concluding, the best solution might be given by a combination of the redundant (the double of the sensors) and either the second or the third approach proposed. The parity relation solution is easier to apply but relies on a major number of measures, while the second is more sophisticated but more complex to design. This combined solution can guarantee a constant monitoring of the structures even if sensor failures occur.

1.3 Dynamic based damage detection methods

The damage detection methods can be classified in two different branches: *vibration based methods* and *wave propagation methods.*

The vibration based approaches are based on the assumption that damage affects global structural stiffness, damping and mass properties and, therefore, structural changes can be located by analyzing the changes of the dynamic properties such as natural frequencies, mode shapes and damping. A detailed overview of vibration based damage detection can be found in Doebling [9]. The main drawback of vibration based methods is that they detect structural changes that affect mainly the global modes of the structures. Moreover, they are based on the assumption that linear elastic structures remain linear elastic after damage and their sensitivity to detect defects such as cracks is very low.

The wave propagation based methods detect structural damage by sending stress waves in the structures and measuring the changes in the received signal relative to the signal of the pristine structure [13-21]. A number of studies are under investigation by mainly using Lamb waves [19-21] to detect structural changes in aircraft structures.

A description of global and local NDE methodologies is presented in the next paragraphs.

1.4 Global NDE

Global NDE techniques exploit data that are expression of global characteristics of structures such as modal properties, displacements, accelerations, Frequency Response Function (FRF) and etc... Two main methodologies have been identified, the vibration methods and the damage detection filters, which were briefly described in the following sections.

1.4.1 Vibration methods

The vibration methods are based on the concept that changes of structure physical properties (mass, damping and stiffness) introduced by damages alter their vibration responses such as modal properties and dynamic responses. Therefore, defects can be located by acquiring those vibration properties. Vibration methods can be classified in two groups, the experimental methods and the numerical experimental methods. The numerical experimental methods define a parametric correlation between structural response characteristics predicted by a structure model (analytical or FE model) and analogous quantities derived from experimental measurements, in order to identify a structural damage [22]. The experimental methods compare the undamaged and damaged experimental response to detect any fault without using structure models.

- **Experimental vibration methods** [23-25].

  These methods identify damages by monitoring changes in the dynamic properties or response of structures, normally using response spectra or FRF. Generally, they need an excitation source such as hammer, vibro-dynamic devices or piezoelectric patches. The structure response is generally acquired by accelerometers, velocimeters, strain gauges, or piezoelectric patches. The damage is identified comparing dynamic properties or responses of structures before and after damages occur, using numerical algorithm. Advantages of these methods are:

  - The low cost of the devices employed compared to those used in other methodologies.
  - The simplicity, no particular skills are required.
  - The acquisition device can be built in the structure, without giving problem of space or weight.

  The main drawback is the resolution of the damage localisation, which depends on the sensor locations and their number.

  Therefore, those techniques are quite useful to detect the damage presence and by an apposite built metric also its severity, but are not very useful for a precise damage localisation, unless the sensors are deployed very near to the damage position.

- **Numerical Experimental vibration methods**

These methods are based on the type of measured data used, and/or the technique used to identify the damage from the measured data. In this way, the following techniques can be identified:

- **Frequency change methods**:

  These methods use frequency changes due to the damage presence to identify its location and severity.

  The frequency methods are divided in two principal classes [26]:

  - *The forward problem* consists into evaluate the frequency shifts due damage presence from a known type of damage. The damage is modelled mathematically (generally using FE model), and then, the measured frequencies are compared to the predicted frequencies to determine the damage.
  - *The inverse problem* consists in calculating damage parameters, e.g., crack length and/or location, from the frequency shifts, using mathematical or numerical models.

  This approach shows the following shortcomings [9]:

  - Low sensitivity of frequency shifts to damage.
  - The extraction of modal frequencies becomes very difficult when the structure is complex and/or at high frequencies.
  - Frequency changes cannot generally provide spatial information (e.g. position and size) on the damage, unless, are referred to high modal frequencies. Moreover, most of the times, the number of significant changes is insufficient to determine damage locations.

- **Mode shape changes**:

  In this category, the damage is detected by comparing displacements or slopes of mode shapes measured of the damage and the undamaged structure. In this way, in contrast with frequency change methods damage localisation is possible.

  A first problem of mode shape change techniques is related to the selection of the mode shapes to use in the damage identification. Some authors use the Modal Assurance Criterion (MAC) to select the most affected mode shapes by structural damages [26]. However, this approach can be used only when all typologies of damage that may occur on the structure are known; otherwise the damages not included might not be identified.

  Another approach detects the damage only by the damaged mode shapes using a laplacian operator [27].

  The main trouble of these techniques is the extraction of mode shapes that becomes very difficult with the increase of both the frequency and the complexity of the structures. Another factor very important is the resolution of the damage location that is strongly related to the sensor number, which also affects the identifiability of mode shapes (aliasing).

- **Mode shape curvature/strain mode shape changes**:

  This typology of methods is based on the concept that mode shape curvature deformations are related to strains and strain energies necessary to the structure to assume a determined mode shape [28]. So, changes in the mode shape curvature can

be assumed as indices of strain changes and consequentially as damage detectors. Some authors have found out that the evaluation of the mode shape curvature through numerical differentiation of mode shape displacements leads to unacceptable errors, which dramatically decreases by measuring directly the strain [26]. Moreover, strain mode shape changes resulted to be larger than any frequency shifts and yet measurable at a relatively large distance from the crack.

Hence, these methods are more precise of the previous seen but need a larger amount of calculations and an FE model validated to produce accurate results. As in the previously mentioned methods, the number and the positions of the sensors employed for the modal extraction have still a great influence on the damage identification quality.

- **Methods based on dynamically measured flexibility**:

  In this class of methods, the health state of the structure is estimated by analysing the static behaviour of the structure through dynamic measures of the flexibility matrix (inverse of the static stiffness matrix).

  Usually, these techniques compare the flexibility matrices of the undamaged and damaged structure, which are extracted by modal properties [29].

  Unfortunately, the number of modal properties extracted (normally few and at low frequencies) affects the damage resolution of these techniques, leading to the detection of only those damages that affects consistently the resonance properties extracted. An improvement of the flexibility matrix computation was obtained by computing the contribution of the modes outside the frequency band measured using FRF or modal data [30].

  Some researchers [26] have proved that the quality of damage identification depends on the number of experimental Degrees of Freedom (DoFs) and the reduction techniques used to fit the numerical DoFs to the experimental one. Comparing the elimination, Guyan, and indirect reduction technique, it was established that only the last two techniques give acceptable results.

- **Matrix update methods**:

  These identification methods modify structural model matrices such as mass, stiffness, and damping of a FE model of the undamaged structure (previously validated), in order to reproduce as close as possible the damaged static or dynamic responses [26]. Typically, the damage identification is obtained by comparing the structural matrices, before and after updating. These methods can be distinguished in terms of [26]:

  - *Objective functions to be minimized.*

    Usually the objective function is a measure of the differences between FE model and experimental modal properties, but sometimes the Frobenius norm or the rank of matrix perturbations ("differences" between the FE model and experimental structural matrices) have been used.

  - *Constraints placed on the problem*

    These depend on the type of algorithm, but generally they tend to preserve the characteristic of the updated matrices, such as, symmetry, sparsity and positivity.

  - *Numerical schemes used to implement the minimisation process.*

Principal numerical schemes are the Lagrange multiplier or the penalty-based optimisation algorithm. Another group of methods uses an iterative algorithm based on pseudo-inversion of the sensitivity matrix.

As the flexibility based detection techniques, these methods are affected by the same drawbacks that go from the validation of the undamaged FEM to the condensation of the FE degrees of freedom. A clear advantage with respect to the previously explored damage detection methodology is the possibility to identify a larger range of defects, because all the structural matrices are considered.

More information on matrix update techniques can be found in chapter 2.

- **Neural network-based methods** [31-32]:

  In the last years, Neural Networks (NN) based methods for damage detection purposes have been used with increasing interest. The reasons lie in the strong interpolation capacity of neural networks, allowing the identification of damages, in terms of location, extension and type, after an intensive training of the NN components. The NN training needs the analysis of a number of damaged configurations of the structure under investigation, which generally are obtained by FE models. However, the neural networks, as any interpolation "algorithm", are able to identify damage only within the training range, outside the result accuracy decrease rapidly.

1.4.2 Damage detection filters

Damage detection filters [10] follow a different approach for the damage detection problem from that of the vibration methods. These work on state estimation approach (or realization systems) fundamentally different from the system identification approach (mass, damping stiffness systems) used by the vibration methods. The filters are based on an analytical model of the structure, in contrast with the empirical models that neural networks generate internally during the training process or the FE model used by model updating techniques. Moreover, damage detection filters essentially estimate residual forces due to damage on the structure, in real-time, rather than estimating physical parameters of the structure based on experimental modal parameters as in the case of some vibration methods.

1.5 Local NDE

The local methodology requires a detailed inspection of the structure components and, most of the times, necessitates a priori knowledge of the damage location. Local NDE methods can be classified based on the physical properties exploited for damage detection. In this way, acoustic, ultrasonic, electromagnetic field, radiography, eddy-current and thermal field methods are identified.

1.5.1 Acoustic Methods

Acoustic methods, commonly known as Acoustic Emission (AE), deal with stressed structures where microscopic events release locally stored elastic energy as an expanding elastic or stress wavefront [13]. Therefore, AE monitoring consists in the analysis of acoustic bursts according to two main approaches, the direct and the indirect. The direct extracts information directly from the AE signals by measuring the arrival time of the burst and its magnitude or energy [33-35]. The indirect approach uses demodulation or convolution algorithm (as wavelets, Gabor transform and so on) to quantify and localise the damage [36].

The AE methodology is a passive class of NDE techniques because does not need external excitation, which means that does not interfere with other applications of the structures. In operative conditions, the screening between the AE and the vibration propagating within the structure due to operative loads is very complex to solve. However, it must be highlighted that the AE detection relies on the elastic energy released by defects, which is very small compared to the vibration energy due to operative loads or specific excitation loads. Therefore, in presence of a consistent noise level is more affected than the vibration techniques (§1.4.1).

Moreover, the number of sensor required for AE methods compared to that of vibration techniques is significantly lower [36].

In the last years the technologic progress provided new AE sensors with improved performances and lower costs. The cutting edge of the AE sensor technology is represented by integrated AE sensors [37], where the AE detectors are miniaturised and the wires integrated into the structures.

For a more detailed analysis of the AE methods from a wave propagation point of view refer to chapter 7.

1.5.2 Ultrasonic Method

Ultrasonic methods or Ultrasonic Testing (UT) is another common NDE technique, most often referred to as *A*, *B*, *C* scan. The *A* scan stands for a single point measurement, while *B* scan refers to multiple *A* scans measurements deployed along a line. Finally, the *C* scan is a collection of *B* scans forming a surface contour plot. Common applications are creep damage detection [13-14], hydrogen damage detection [15], corrosion detection in aircrafts [16], fatigue damage detection [17], and so on. The signal analysis involves the estimation of Time-Of-Flight Diffraction (TOFD) for the defect localization and/or signal spectra analysis for the study of the energy scattered by the flaw presence, or investigation on the attenuation effects related to signal magnitude changes.

In the past, UT sensors needed a coupling fluid to work, usually water. Nowadays, brand new contact UT sensors have been developed [18], able not only to receive ultrasonic signals but also to emit them under form of sound beams. For non-contact solutions laser scanners can be used.

The most common UT sensors are PZT patches because of their low cost, limited dimensions and large frequency band. These characteristics have made PZT the most popular UT sensors especially in aeronautic applications [19-21], where concerns related

to the weight and the space available are the most important. It must be said that the PZT excitation cannot be considered as a sound beam (compression waves) as well as for the common UT sensors, but generates an entire range of waves from P waves to Lamb waves (thin plates). This last wave type is mostly used for damage detection in thin plate-like structures [19-21]. Lamb waves are very attractive since they can propagate for long distances. This capability enables a single UT sensor to scan large sections of structures in few instant, in contrast with conventional UT techniques that need tens and tens of scans to achieve the same results. For more information about UT wave propagation applications refer to chapter 7.

A major drawback of UT is the extensive technical expertise required to UT inspectors, in order to analyse ultrasonic signals.

1.5.3 Electromagnetic field methods

Electromagnetic methods exploit electric/magnetic or electromagnetic conductivity of metallic materials or carbon fibres. This methodology is based on electric/magnetic or electromagnetic field changes due to damage presence. These changes can be caused by stress or plastic deformation, which magnitudes are very small compared to those derived from geometry variations such as dents or gauges [38].

The most recent applications are:

- Monitoring of mechanical force in steel cables by measuring changes in the magnetic permeability of the material [39].
- Corrosion damage detection in steel bridge strands using Time Domain Reflectometry (TDR) by applying a sensor wire along side the strands and then measuring the change of electromagnetic properties of the circuit constituted by the strand and the wire sensor [40].
- CFRP structure damage detection by monitoring either their electric potential [41] or their electric resistance [42].

The main drawback of this methodology is related to its inapplicability on structures made of non-conductive materials. Other shortcomings are due to electromagnetic interference of other metallic components near the structure being tested, geometric tolerances, temperature changes, humidity variations and mechanical strain or stress due to operative loads.

1.5.4 Radiography methods

Radiography methods rely on differential absorption of radiation penetrating a test object recorded as an image on film or digital systems. The damage on the test object is identified by density changes in the film compared to the surrounding material. To accentuate damaged regions often a contrasting liquid is used.

The simplicity of use and interpretation of the results of these techniques are opposed by the need of highly qualified operators, high cost equipment, special safety precautions and regulations, and accessibility of the component under inspection on both sides, resulting in a considerable limitation of their applicability.

On the other hand, radiography methods can inspect any kind of material and structures, like Ni-base gas turbine [43], helicopter main rotor blades (corrosion) [44], spent nuclear fuel [45].

1.5.5 Eddy-Current methods

Eddy currents are electrical currents generated in a conductive material by an induced alternating magnetic field. Imperfections, dimensional changes or variation in the conductivity and permeability properties of the material, can be detected by interruptions in the flow of eddy currents. Three kind of eddy-current methodologies have been used for corrosion detection in aircraft structures [46], Single Frequency Eddy-Current (SFEC), Multiple Frequency Eddy-Current (MFEC) and Pulse Eddy-Current (PEC). The first is able only to measure the first layer of multi-layer structures, because of the presence of gaps between layers filled up of sealants, adhesives, corrosion products or air, in any combination. SFEC devices cannot detect 10% material loss with a probability of detection larger than 90%. MFEC systems are able to provide more information than the SFEC but are affected by the same factors. The last techniques are still under development and, so far, have never been experimented outside of laboratories. Therefore, no information is available on real applications. Differently from the other two techniques, PEC needs contact between its probe and the structure surface. Moreover, like the SFEC is slow because requires raster scanning (a scanning pattern of parallel lines that form the display of an image projected on a cathode-ray tube of a television set or display screen).

In case of detection crack beneath rivet head [47], although eddy-current automatic equipments are able to detect crack of length up to 1mm, when it comes to real structures, the minimum crack length detectable, with false call rate less than 1%, are approximately 6mm for FastScan, 19mm for Eddyscan, 22mm for LFECA, and 17mm for GK (all commercial eddy-current scan devices). Moreover, the presence of paint affects negatively the probability of detection. Furthermore, these techniques need to centre the head of the rivets for an accurate detection, which means long scan time and very expert inspectors. Other drawbacks are the large amount of power needed and very complicate results to interpret [11].

1.5.6 Thermal field methods

Infrared (IR) thermography is based on the idea that defects on a heat-conducting medium create distortion in the heat flow lines generated by operative loads [48], constant heat flow source [49] or photographic flash devices [50]. Infrared cameras normally collect the thermal images.

Disadvantages of these techniques are:

- Initial cost of IR device.
- Calibration requirements: determination of an effective bias and gain for each of the individual detectors. Errors yield systematic noise to the pixel-to-pixel time variance between successive images.

- The lab environment, the temperature, the luminosity and so on must be controlled.

1.6 Thesis objectives and solutions pursued

Damage detection techniques can be classified according to a four level damage identification scheme [26]:

- Level 1: determination of the damage presence.
- Level 2: Level 1 and localization of the damage.
- Level 3: Level 2 and quantification of the damage severity.
- Level 4: Level 3 and prediction of the remaining service life of the structures.

By this classification, the primary objectives of the thesis was to develop level 3 damage detection algorithms, able to predict structural conditions by analysing dynamic data changes. The acquisition of the dynamic data was carried out through a network of sensors embedded on the structure. In particular, the study was focused on developing damage detection techniques capable of identifying global or local changes.

Preliminary analysis of civil, mechanical and aeronautical structures pointed out that was impractical for the time allocated to develop damage detection algorithms capable of identifying global and local changes. In particular, the complexity of the structure and the characteristics of the operative loads are so different that a common point to design an efficient and reliable HM system was not either practicable or exploitable.

Based on the above considerations, the damage detection algorithms were developed for two sets of structures, which were identified based on their structural complexity, operative load features, and critical damage sizes.

The global damage detection algorithms were developed mainly for large scale structures (e.g. bridges, wings) where typical damages affect relatively low frequencies (§7.2), but do not constitute an immediate threat neither to the structure health nor to its users, because of the typical structure failure modes and the nature of operative loads (e.g. low frequency).

The local damage detection algorithms were developed for structures where localised damage occurs, causing appreciable changes in structural dynamic responses only at high frequencies and the nature of the damage and operative loads requires quasi or real-time damage detections to prevent catastrophes.

It is clear that the first group of structures requires a HM system capable of detecting structural changes in a relatively low frequency range and does not need real time detection, since its operative loads are low frequency loads and, therefore, there is not any danger of an immediate collapse of the structure. A model updating technique was considered more suitable for this kind of structures and it was developed to meet the level 3 damage detection requirements. This task was fulfilled by designing detection algorithms based on optimization algorithms. Two main directions were followed. The first consisted in an evolution of model updating techniques (chapter 2), aimed at the identification of structural changes by using stationary responses of the structure such as modal properties and Frequency Response Functions (FRF). The optimization algorithms were set up to minimize the differences between the undamaged and damaged structure

stationary responses by changing the characteristic of a validated FE model of the undamaged structure. The second way (chapter 5) consisted in the use of an analytical function instead of a validated FE model of the structure. This produces large advantages in terms of run-time and reliability of the inverse problem solution. The structure stationary responses were acquired by use of a network of sensor deployed after a data selection process (chapter 3), which provided the selection of the data type, the target mode shape selection and, finally, the optimal sensor placement. A preliminary data processing for modal property extraction was considered for damage detection in operational conditions (chapter 4). The preprocessing was carried out by extracting free-decay signals from random ones using either the Random Decrement Technique (RDT) or the Cross-Correlation Function (CCF) based technique.

For the second group of structures (§7.2), a wave propagation based technique was designed to comply with the requirements of real-time detection and sensitivity to high frequency changes of the structure dynamic response due to damage presence. The methodology developed exploited the propagation in a medium of body and surface waves (chapter 7) generated by either operational loads (e.g. a coming train) or impulsive loads. The discrepancies between the damaged and the undamaged wave propagation time histories were highlighted by a time frequency algorithm, which allowed evaluating the time of flight of damage reflected waves, which was used by a specially designed ray-tracing algorithm to estimate the damage location.

1.7 Thesis summary

In the first chapter a brief introduction on the reasons of the need of SDI/HM techniques and an overview of existing techniques was presented. Moreover, the objectives of the thesis and the directions followed in this research were explained.

The second chapter deals with global damage detection algorithms based on model updating techniques, and an analysis of their advantages and disadvantages is given. These observations resulted into the design of the Global-Local Damage Detection Optimisation (GLDDO) approach based on a FE model of the structure under investigation, which physical properties (e.g. thicknesses and Young modules) are modified in order to reproduce the experimental response of damaged structures.

In the third chapter, techniques aimed at selecting the optimal data necessary for damage detection are presented. The data selection process was developed aimed at maximizing the information content and the noise withstanding of the acquired signals.

In chapter four, a series of methodologies aimed at the reduction of noise content in the data experimentally acquired were presented.

The fifth chapter presents a direct damage detection approach built according to the global-local procedure of the GLDDO based on an analytical model of the structure (plate-like), instead of a FE model.

Chapter 6 presents numerical damage detection results due to the application of the GLDDO.

A Wave Propagation Based Damage Detection (WPBDD) approach was presented in chapter 7.

In chapter 8, the WPBDD approach was validated on a rail structure using numerical data.

Chapter 9 highlights the drawbacks and benefits, derived from the two techniques presented, and proposes future work needed to improve them.

In appendix A, the OSP techniques introduced in chapter 3 were compared in order to highlight the best for the GLDDO approach.

Appendix B shows as a sensor network, designed according to the guidelines showed in chapter 3 and the findings of appendix A, was able to extract modal properties of a suspension bridge using ambient excitation consistently with the extraction methodologies introduced in chapter 4.

Appendix C investigates the effects on the GLDDO approach of target mode shape selection, optimal sensor placement, minimization algorithms, and residue function selection.

Finally in appendix D, the accuracy and the reliability of the damage detection technique using an analytical representation of a plate (chapter 5) were investigated.

CHAPTER 2: GLOBAL-LOCAL DAMAGE DETECTION OPTIMISATION APPROACH

2.1 Abstract

Structural Health Monitoring (SHM) is becoming a thriving research subject due to economic and social factors (§1.1). Its principal aim is giving an early warning of damage occurrence so as maintenance countermeasures can be taken, resulting into safer structures and operative cost savings. Clear objectives for a potential development in SHM were the reduction of the complexity of the NDE output (in order to cut the degree of expertise of damage inspectors), enhancement of the damage detection accuracy, and physically meaningful information on the identified damages (e.g. thickness and elastic modulus changes).

In this chapter, Non-Destructive Evaluation (NDE) techniques based on model updating are discussed and analysed to verify their capability to identify changes occurring on civil/mechanical/aeronautical structures during their operative lives.

A brief introduction on the state of art of MU techniques is presented together with an attempt to classify them for a more comprehensive understanding. Then, the MU technique developed by the author is presented and compared with the existing methods in the literature.

2.2 Model Updating history

Initially, model updating techniques were developed to enhance the reliability and accuracy of mathematical models (e.g. FE models) in order to speed up and reduce process costs for development and construction of structures. These reliability and accuracy was obtained by validating the structure FE model and, in case of discrepancies with the structures prototypes, updating it in order to reduce the differences under an accuracy level chosen according to the aim of the analysis. This methodology is based on the assumption that the error of the FE model is larger than the experimental error, which affects the acquired characteristics used to validate the FE model.

Only recently, MU techniques were considered useful tools for damage detection purposes [26], showing their great potentiality and large margin of improvement.

Therefore, this research work was poised to exploit this new methodology, in damage detection, by investigating a wide range of MU solutions to have a clear insight of the options available and a map of their advantages and drawbacks.

Then, MU advantages and drawbacks were carefully studied to support the development of an enhanced damage detection technique based on MU methodology: the Global-Local Damage Detection Optimisation (GLDDO) approach.

2.3 Model Update Techniques

The recent interest for MU techniques have been employed for NDE purposes [26], is due mainly to the improvements in the computer technology that guarantee shorter computational times and ability to handle larger FE model.

Model updating techniques consist in the solution of an inverse problem [51], which is schematically represented as follows:

$$X = H * F \tag{2.1}$$

where H is a model or an operator with an input F and an output X.

The model updating aim is to determine the model H knowing the input F and the output X, performing what is defined as an inverse problem of second kind (see Table 4).

Problem type	*Knowns*	*Unknowns*
Direct	F, H	X
Inverse first kind: Force identification	X, H	F
Inverse second kind: model updating	F, X	H

Table 4 – Summary of direct and inverse problems [51].

The MU solution exists and is unique if and only if the inverse of H exists and is continuous on X. These stringent requirements are one of the main causes for lack of consistency and success reported in many studies [52]. Another problem rises from the presence of polluted output X that cannot guarantee the determination of an updated model despite of the satisfaction of the conditions for its existence and uniqueness.

Before analysing the several MU techniques in terms of their main features, it is useful to illustrate what is called updating process, namely, the ensemble of all the steps necessary to carry out successfully an FE model updating.

2.3.1 Updating process

The updating process can be divided in 6 steps [52]:

1. Definition of the accuracy level. It is the threshold value under which the discrepancies between a FE model of the structure and its real dynamic properties can be considered negligible.
2. Model validation. This task determines whether or not the FE model needs updating. A first check can be accomplished by verifying that all the important features of the structure have been introduced in its FE model. The model validation is usually obtained using correlation functions of mode shapes (the Modal Assurance Criterion (MAC), the Coordinate Assurance criterion (COMAC)), or the FRF like the Frequency Response Assurance Criterion (FRAC).
3. Error localisation. This step is the most critical for a successful model updating. It consists in the determination of the areas, which contain errors, and then the selection of the kind and the number of model parameters (order of the problem) that need updating. The types of updating parameters used in literature were presented in next section. Previous attempts to automate this step brought to the conclusion that there is not any substitute to engineering skills for a correct error localisation [53].
4. Data selection. It involves the identification of the type of experimental data to use (e.g. modal shapes, FRF and etc.) and the selection of the sensor locations (Optimal Sensor Placements - OSP), at the aim to maximise the amount of information on the structural changes available from the real structure using a limited number of sensors.
5. Model updating. It consists in the minimisation of a measure of the discrepancies between the FE and the experimental model (real structure) by updating the parameters selected.
6. Post Processing. This task consists in the analysis of the changes carried out by the updating process.

2.3.2 Updating parameters

In the selection of the updating parameters there are not limitations [54], any data that may introduce changes in the structure response can be used. However, four types of parameters are identified:

1. Whole Matrix (WM) updating parameters. Any coefficient of the FE structural matrices can be an updating parameter, as shown:

$$[K_U]=[K_{FE}]+[\Delta K] \tag{2.2}$$

$$[M_U]=[M_{FE}]+[\Delta M] \tag{2.3}$$

where the lower indices U and FE identify, respectively, the updated and the FE model structural matrices, while Δ identifies their variations owing to the updating procedure.

Disadvantages of WM parameters are the impossibility of controlling the specific elements to update, the loss of the original connectivity of the structural matrices, which end to be dense and very difficult to handle, especially, for large FE model. A partial solution of this problem is obtained by imposing the respect of the structural matrix properties, e.g. the positive definiteness, the sparsity and so on [26, 52].

2. Spatial-type updating parameters. These parameters are coefficients that multiplied for their respective macro-element matrix identify the changes in the structural matrices as showed below:

$$[\Delta M_u] = \sum_{r=1}^{p_M} p_r [M_r^e] \tag{2.4}$$

$$[\Delta K_u] = \sum_{r=1}^{p_K} p_r [K_r^e] \tag{2.5}$$

where $[M_r^e]$ and $[K_r^e]$ are respectively the mass and stiffness matrix of the r^{th} macro-element that needs to be updated. In this way, the original connectivity is preserved as well as the matrix properties such as the sparsity, the positive definiteness and etc... A drawback of this parameter type is the limited physically meaningful explanation for their changes.

3. Design-type updating parameters. Any design input of the initial FE model falls under this definition such as finite element characteristics and material properties. Advantages of such parameter choice are the physically meaningful changes of the updating parameters, while a disadvantage is the impossibility of varying the model configuration[1] by changing them.

4. Generic elements [55], these elements generally are spring like elements that connect two degree of freedom of the structure FE model. Their mass $[M^e]$ and stiffness $[K^e]$ matrix must satisfy the following requirements:

   $[M^e]$ must be positive definite.

   $[K^e]$ must be positive semi-definite and have rigid body mode.

   $[M^e]$ and $[K^e]$ must respect the reciprocity between the two degrees of freedom, which means that changes for any couple of degrees of freedom linked by a generic element must be the same.

An example of generic element (rod) is given below [55]:

---

[1] Varying the model configuration means altering the links between the dofs in which the structure was discretized (e.g. link two dofs that in the previous configuration were not joined by any element).

$$M^e = m_0\begin{bmatrix}\frac{1}{2} & 0\\ 0 & \frac{1}{2}\end{bmatrix} \qquad K^e = k_0\begin{bmatrix}1 & -1\\ -1 & 1\end{bmatrix} \tag{2.6}$$

where:

$$m_0 = \rho AL \qquad k_0 = \frac{EA}{L} \tag{2.7}$$

By selecting this kind of parameters is possible to change the FE model configuration. In contrast, their changes cannot be easily physically interpreted.

2.4 Model updating classification

Model updating techniques are commonly divided in direct and iterative methods [26, 56-57]. The iterative can be further divided in sensitivity based and FRF based methods.

2.4.1 Direct Methods

The direct methods generally update directly the coefficients of the stiffness and mass matrices (whole matrix updating parameters), using an incomplete set of eigenvalues and eigenvectors derived from measurements. These choices determine a series of advantages like [58]:

- Certain convergence, since the techniques do not require iteration.
- Shorter computational time than the iterative methods.
- Exact reproduction of the experimental data.

On the other hand direct methods are subjected to several shortcomings:

- Very accurate experimental measurements and modal extraction are required.
- Expansion of the mode shapes to the size of the FE model.
- Loss of the original connectivity of the FE model derived from the WM updating parameters choice.
- Need of further constraints to comply with the original properties of the structural matrices.

These methodologies can be classified in Lagrange Multiplier (LM) [59-60], Matrix Mixing (MM) [58], Error Matrix (EM) [58] and Eigenstructure Assignment (EA) methods [26, 58].

Lagrange Multiplier methods minimise an objective function subjected to constraints active on the updating parameters. A first version of the LM methods goes back to late seventies [61], where the objective function was a mass matrix weighted function of the differences between the FEM and the experimental mode shapes (see equation 2.8-a).

$$J = \left\| [M_{FE}]^{\frac{1}{2}} ([\Phi_U] - [\Phi_X]) \right\| \tag{2.8-a}$$

where $\|\ \|$ is the Euclidian norm, while $[\Phi_U]$ is the matrix of the updated mode shapes and $[\Phi_X]$ is the matrix of the experimental mode shapes.

Moreover, the mass matrix had to satisfy the following orthogonality condition:

$$[\Phi_U]^T[M_{FE}][\Phi_U]=[I] \tag{2.8-b}$$

with $[I]$ is the identical matrix.

A more recent technique [62] updates simultaneously the mass and the stiffness matrices using a penalty function so structured:

$$J=\left\|[M_{FE}]^{-\frac{1}{2}}([K_U]-[K_{FE}])[M_{FE}]^{-\frac{1}{2}}\right\|+\left\|[M_{FE}]^{-\frac{1}{2}}([M_U]-[M_{FE}])[M_{FE}]^{-\frac{1}{2}}\right\| \tag{2.9}$$

As well as the orthogonality condition (2.8-b) the symmetry of the updated matrices is imposed for this late version.

Matrix mixing methods are based on the assumption that all the vibration modes are measured and mass normalized. In this case the mass and stiffness matrix can be mathematically derived from the subsequent expressions [58]:

$$[M_U]^{-1}=[\Phi_X][\Phi_X]^T \tag{2.10}$$

$$[K_U]^{-1}=[\Phi_X][\omega_X^2]^{-1}[\Phi_X]^T \tag{2.11}$$

Unfortunately, this approach is limited by two main problems [58]. First, the number of FEM Degrees of Freedom (DoFs) is far larger than the number of the modes measured. At the same time, the structure dynamic response usually can be measured only on a limited number of points of those of interest (FEM DoFs). This last drawback can be solved, at least partially, by expanding the experimental measures using the full FEM structural matrices. For the first negative aspect, many alternatives were used such as adding a number of independent vectors or adding a number of FEM mode shapes in order to square the mode shape matrix $[\Phi_X]$.

Error Matrix methods [58] use the error matrices (2.12) to evaluate the mass and stiffness matrices using only the modes measured.

$$\begin{aligned}[\Delta M]&=[M_X]-[M_{FE}]\\ [\Delta K]&=[K_X]-[K_{FE}]\end{aligned} \tag{2.12}$$

Assuming that the error matrix norms are small and, then, exploiting the expansion matrix series properties which, for the stiffness matrix, lead to the following expression [52]:

$$[K_X]^{-1}=\left([I]+[K_{FE}]^{-1}[\Delta K]\right)^{-1}[K_{FE}]^{-1} \tag{2.13}$$

Then, substituting equation (2.10), (2.11) and (2.13) into equation (2.12) the EM method is obtained [52]:

$$[\Delta K]\cong[K_{FE}]\left([\Phi_{FE}][\omega_{FE}^2]^{-1}[\Phi_{FE}]^T-[\Phi_X][\omega_X^2]^{-1}[\Phi_X]^T\right)[K_{FE}] \tag{2.14}$$

$$[\Delta M]\cong[M_{FE}]\left([\Phi_{FE}][\Phi_{FE}]^T-[\Phi_{FE}][\Phi_X]^T\right)[M_{FE}] \tag{2.15}$$

Eigenstructure assignment methods exploit control theory at the aim to reproduce exactly the mode shapes measured. The methodology consists in to evaluate a feedback control matrix using expanded mode shapes [26, 58].

2.4.2 Iterative Methods

Normally, iterative methods minimise a non-linear objective function of selected updating parameters [63]. These techniques are quite popular for the freedom in the selection of the updating parameters (e.g. whole matrix, spatial-type, design-type and generic element updating parameters) and for the applicability of the methodologies even with incomplete data [59]. These techniques can be classified in terms of the experimental data used [64], static, modal and response function methods. However, the most common classification [58] divides the iterative methods in sensitivity based and FRF based methods.

2.4.2.1 Sensitivity based techniques

Sensitivity based techniques minimise a residue function of the discrepancies between the FE model $\{\vartheta_{FE}\}$ and the experimental $\{\vartheta_X\}$ modal properties. The residue function can be assumed as square differences (2.16) or weighted least squares (2.17) [67].

$$J = \{\varepsilon\}^T \{\varepsilon\} \tag{2.16}$$

$$J = \{\varepsilon\}^T [W] \{\varepsilon\} \tag{2.17}$$

where:

- $\{\varepsilon\} = \{\vartheta_X\} - \{\vartheta_{FE}(\mathbf{p})\}$ (2.18)
- $[W]$ is a weight matrices.
- $\mathbf{p}$ is the vector of the updating parameters selected.

Since, the FE model $\{\vartheta_{FE}(\mathbf{p})\}$ is a non-linear function of the updating parameter changes, the minimisation problem is non-linear. Therefore, in the attempt to linearise the problem a Taylor series expansion truncated after the first term is used, obtaining:

$$\{\vartheta_{FE}(\mathbf{p})\} = \{\vartheta_0\} + [S_0]\{\Delta p\} \tag{2.19}$$

with:

- $\{\vartheta_0\}$ mode property vector of the initial FE model.
- $[S_0] = \left[\frac{\partial \vartheta_{FE}}{\partial \mathbf{p}}\right]$ sensitivity matrix evaluated with respect to the initial FE model parameters set $\{p\}^0$.
- $\{\Delta p\} = \{p\} - \{p\}^0$ parameter changes.

Substituting the (2.19) into the (2.18) is obtained:

$$\{\varepsilon\} = \{\vartheta_X\} - \{\vartheta_0\} - [S_0]\{\Delta p\} \tag{2.20}$$

Generally, this equation is solved by a least square algorithm [67] or by a Singular Value Decomposition SVD approach [68].

After solved equation (2.20), if the residue norm is larger than the accuracy level chosen, a new parameter configuration is evaluated using $\{\Delta p\}$ and then, a new sensitivity matrix is evaluated from the new FE model configuration, then equation (2.20) is solved again. This procedure is iterated until when the accuracy level requested is satisfied.

These techniques need to pair the numeric mode shapes with the experimental ones. A useful tool, for this task, is the Modal Assurance Criterion (MAC) [65-66]. Unfortunately, the MAC does not give an absolute guarantee that the FE and the experimental mode shapes are actually paired. A further problem is the different scaling of the experimental mode shapes from those of the FE model. This problem can be solved using the Modal Scale Factor (MSF) [58].

$$MSF_j = \frac{\{\phi_{FE}\}_j^T \{\phi_X\}_j^T}{\{\phi_{FE}\}_j^T \{\phi_{FE}\}_j^T} \tag{2.21}$$

The sensitivity matrix is evaluated either using a forward finite difference derivation scheme [69] or using particular techniques such as the simultaneous iteration scheme [70], the Fox and Kapoor algorithm [67] and etc..

The maximum number of parameters identifiable by a sensitivity based method with a least square approach was determined theoretically [71]. The findings proved that the maximum number P of parameters identifiable by a sensitivity-based method acquiring N modes on a grid of M sensors and using N_{FE} numerical mode shapes to evaluate the sensitivity matrix is:

$$P \leq \min\left\{M \cdot N, \frac{N}{2}\left[2N_{FE} - (N+1)\right]\right\} \tag{2.22}$$

Static shape deformations also have been used as data for sensitivity-based methods (least square approach) [72]. The only difference with the previous illustrated case is the evaluation of the sensitivity matrix, which involves only the stiffness matrix.

2.4.2.2 FRF based methods

The development of the FRF based methods is due to the need for the researchers to avoid some of the drawbacks of the modal based techniques. In fact, the FRF based methods offer the following advantages [52]:

- A larger amount of data available than modal data.
- Automatic inclusion of damping in the measured data.
- No pairing between numerical and experimental data is required.
- Availability of data also at high frequencies, where the mode property extraction is difficult.

These techniques are classified in terms of the objective function used [58], as the equation error penalty function and the output error objective function methods.

Equation error penalty function is derived from the motion dynamic equation in the frequency space (2.23).

$$\left(-\omega^2[M_{FE}]+i\omega[C_{FE}]+[K_{FE}]\right)\{X_{FE}(\omega)\}=\{f_{FE}(\omega)\} \tag{2.23}$$

where:

- $[C_{FE}]$ is the damping matrix of the FE model.
- $\{X_{FE}(\omega)\}$ is the Fourier transform of the FEM displacement vector.
- $\{f_{FE}(\omega)\}$ is the Fourier transform of the excitation vector.
- ω is the circular frequency.

This equation can be rewritten in terms of dynamic stiffness [Z_{FE}] matrix obtaining:

$$[Z_{FE}(\omega)]\{X_{FE}(\omega)\}=\{f_{FE}(\omega)\} \tag{2.24}$$

Finally, the equation of error penalty function is evaluated as the difference between the numerical and the experimental force $\{f_X\}$ [58]:

$$\{\varepsilon_{EE}\}=\{f_X(\omega)\}-[Z_{FE}(\omega)]\{X_{FE}(\omega)\} \tag{2.25}$$

From equation (2.25), a linear system in the unknowns (**p**'s coefficients) can be derived by assuming that all degrees of freedom (DoFs) are measured and that the dynamic matrix can be written as linear combination of the updating parameters. The system can be solved by either a least square algorithm or by a SVD approach.

The major advantage of this methodology is the linear dependence of the error by the updating parameters so that a rapid convergence can be achieved. The major drawback is the need to have measures of all the FEM degrees of freedom, although this problem can be solved by expanding the experimental measures over the FE model degrees of freedom.

The output error objective function $\{\Delta H\}$ [52] is evaluated as difference between the numerical and the experimental FRF. The updating procedure is derived from the definition of receptance (2.26) [73], as the system displacements normalised by the excitation force.

$$[H_{FE}(\omega)]=\frac{\{X_{FE}(\omega)\}}{\{f_{FE}(\omega)\}} \tag{2.26}$$

Hence, from eq. (2.24) is obtained:

$$[Z_{FE}][H_{FE}]=[I] \tag{2.27}$$

expressing the experimental dynamic stiffness matrix as into eq. (2.28):

$$[Z_X]=[Z_{FE}]+[\Delta Z] \tag{2.28}$$

and considering that eq. (2.27) is satisfied also by the experimental data, it follows that:

$$[\Delta Z][H_X]=[Z_{FE}]([H_{FE}]-[H_X]) \tag{2.29}$$

Then, pre-multiplying eq. (2.29) for the FE model receptance and applying eq. (2.27) is obtained:

$$[H_{FE}][\Delta Z][H_X]=[H_{FE}]-[H_X] \tag{2.30}$$

Finally, taking just one column of the experimental receptance matrix (j^{th}) eq. (2.30) is reduced to [63]:

$$[H_{FE}][\Delta Z]\{H_X\}_j = \{H_{FE}\}_j - \{H_X\}_j = \{\Delta H\} \tag{2.31}$$

Eq. (2.31) is the error output equation and represents the core of what is better known as the Response Function (RF) method.

The solution of this problem is obtained by linearising $[\Delta Z]$ with respect to the updating parameters as illustrated in eq. (2.32).

$$[\Delta Z] = \sum_{i=1}^{P}\left(\frac{\partial [Z]}{\partial p_i}\Delta p_i\right) \tag{2.32}$$

For a correct FE model updating, the accuracy of the experimental data was recently evaluated [51] confirming the idea that the measurement errors $[\varepsilon]$ must be much smaller than the modelling error $[\Delta Z]$ as the following inequality proves:

$$\frac{\|[\varepsilon]\|}{\|[H_X]-[\varepsilon]\|} << \frac{\|[\Delta Z]\|}{\|[Z_{FE}]+[\Delta Z]\|} \tag{2.33}$$

Due to the non-linearity of the output-error function this methodology is prone to have convergence problems and may require a considerable CPU effort [58].

2.5 Conclusions on the model updating techniques in literature

By the short review above presented is clear that direct methods are the fastest but requires a skilful hand in handling the updating variables. On the other hand, the iterative methods have a larger range of parameters to be selected, but the procedure does not guarantee the convergence and in some case the run time may become an issue. Both approaches, however, need pairing modal shapes. To avoid this problem some iterative methods use FRF with a more significant CPU effort, convergence troubles and a run-time increase. Another important aspect of both approaches presented is the linearisation of the inverse problem. A further aspect of the methodologies considered is the fact that they reproduce the experimental data without taking into account the noise pollution of these data, determining the need to have "clean" data

In light of this analysis, a further development of the model updating techniques is required for damage detection purposes in order to increase their sensibility to the updating parameters in presence of noise, to reduce the CPU effort and the run-time necessary and to enhance the efficiency and reliability of the updating procedure.

At this aim, an iterative model updating technique was developed using design-type parameters (or Design Variables, DVs) to have physically meaningful information on the nature of the damage such as thickness loss or Young modulus changes. This gives immediately interpretable results in terms of structural changes, when the updating procedure is used for damage detection purposes. Moreover, in the attempt to reduce the noise, different types of residue functions based on correlation functions, such as the MAC, Coordinate Modal Assurance criterion (COMAC) and etc., were analysed. In this way, the need of pairing numerical and experimental mode shapes was avoided. Furthermore, together with the linear approach used in literature to update the FE model,

non-linear optimisation algorithms were analysed, with the intention to increase the reliability and the efficiency of the damage detection, although liable to be more expensive in terms of run-time.

A last study was carried out to decrease the run-time of the model updating. This study compared the damage detection performances of the developed technique using a global approach with those using a global-local approach.

2.6 The Global-local optimisation approach

The Global-Local Optimisation (GLO) approach is an evolution of the iterative methods. Its main goal is to reduce the number of the updating parameters and, therefore, to reduce the run-time of the updating process. At this aim the GLO approach was structured as a two-step global-local optimisation.

Moreover, at the aim to reduce drawbacks as the need of pairing and scaling of mode shapes, the need of evaluation and derivation of the dynamic stiffness matrix and etc., several residue functions, using modal or FRF data, and minimisation procedures, using gradient or zero order approaches, were analysed.

The proposed two step methodology was structured as follows (for simplicity, the FE thicknesses have been assumed as DVs of the updating problem):

- In the first step (error localisation), the structure is divided in macro-areas, and their thicknesses are assumed as initial design variables. The selected objective function is then minimized. This process identifies the macro-area/areas, where the discrepancies between the FE model and the real structure are contained, by comparing the optimised updating parameter values with those of the initial FE model.
- In the second step, the thickness of the elements of the macro-area/areas, identified by the largest thickness changes, are chosen as new design variables. The optimisation process is performed again to find a correct set of updating parameters, for the FE model, able to reduce the initial discrepancies under the accuracy level chosen.

This approach reduces the number of updating parameters and run-time, resulting in a robust optimisation method, and normally generates a smooth distribution of the model properties, able to represent the zones in the structures investigated, where the "FEM-structure" discrepancies are concentrated.

2.7 Residue functions

In order to find a representative function of the difference between the numerical and experimental data of the structure, various residue functions (residual vectors) were considered. The characteristics sought were a reduced dependence to noise, information on the orthogonality properties of mode shapes and no need of MSF (2.21) to compare the experimental and the numerical data. All these properties have been found in the correlation functions such as MAC, COMAC, using modal properties, and Frequency Response Assurance Criterion (FRAC) using FRF data.

2.7.1 Mode shape based residue functions

An analysis of the mode shape correlation functions MAC and COMAC is necessary for the full understanding of the mode shape based residue functions developed.

Given a numerical and an experimental set of N mode shapes evaluated over a grid of M sensors, the MAC is a matrix of N by N coefficients estimated as follows [73]:

$$MAC_{ij} = \frac{\left|\left\{\phi_{FE}^{i}\right\}^{T}\left\{\phi_{X}^{j}\right\}^{*}\right|^{2}}{\left\{\phi_{FE}^{i}\right\}^{T}\left\{\phi_{FE}^{i}\right\}^{*}\left\{\phi_{X}^{j}\right\}^{T}\left\{\phi_{X}^{j}\right\}^{*}} \tag{2.34}$$

where $\left\{\phi_{FE}^{i}\right\}$ and $\left\{\phi_{X}^{i}\right\}$ are respectively i[th] numerical mode shape and j[th] experimental mode shape. A MAC value close to 1 suggests that the two modes are well correlated, while a value close to 0 means uncorrelated mode pairs.

The Coordinate Modal Assurance Criterion (COMAC) correlates experimental and numerical mode shapes at selected degrees of freedom. Thus, local information on mode shapes is obtained without averaging them on all point of structure as for the MAC.

The amount of correlation at each coordinate over the mode pairs selected is estimated as follows:

$$COMAC_{i} = \frac{\sum_{r=1}^{N}\left|\left\{\phi_{FE}^{r}\right\}_{i}\left\{\phi_{X}^{r}\right\}_{i}^{*}\right|^{2}}{\sum_{r=1}^{N}\left\{\phi_{FE}^{r}\right\}_{i}^{2}\sum_{r=1}^{N}\left\{\phi_{X}^{r}\right\}_{i}^{2}} \tag{2.35}$$

To have a good coordinate correlation the COMAC value has to be near to 1.

Both correlation functions are expression of the orthogonality properties of the selected mode shapes. Moreover, the use of these correlation functions avoids the need to pair the FE model and experimental mode shapes. The mode shapes can be processed in the same order that are extracted by the numerical and experimental analysis, allowing the developed residue functions to measure the numerical/experimental mode shape swap as a discrepancy between the FE model and the real structure. Since, the COMAC and MAC function measure the similarity (correlation) between numerical and experimental mode shapes, the need of the MSF (2.21), is not necessary.

Moreover, these correlation functions downsize the effect of the noise on the data as shown in appendix C (§C.3).

From the point of view of damage detection, the COMAC function seemed to provide a better solution because its coefficients are evaluated on the sensor locations in contrast with the MAC function, which estimates the correlation between each mode shapes averaging the local discrepancies. As mentioned before, the residue function have to measure the discrepancy between the FE model and the experimental mode shape set, therefore the i[th] component of the COMAC residue function (COMAC_ReF, eq. 2.36) is evaluated as the difference between the i[th] component of the COMAC function calculated as if the two mode shape sets are well-correlated (=1), and the i[th] component of the COMAC function calculated using the FE model and the experimental modal properties.

$$COMAC\_\mathrm{Re}F_{i} = 1 - COMAC_{i} \tag{2.36}$$

In order to impose the shapes correlation between the experimental and numerical modes, the coefficients of the principal diagonal of the MAC matrix were added to the COMAC coefficients to build a second residue function termed COMAC_MAC_ReF:

$$COMAC\_MAC\_\mathrm{Re}F = \begin{Bmatrix} 1-COMAC_1 \\ \vdots \\ 1-COMAC_M \\ 1-MAC_{11} \\ \vdots \\ 1-MAC_{NN} \end{Bmatrix} \tag{2.37}$$

The last residue function evaluated using mode shape data was an evolution of the previous presented, and based on the observation that the experimental mode frequencies are less noise polluted than mode shapes [54], therefore they were inserted into the COMAC_MAC residue function generating the COMAC_MAC_FREQ residue vector:

$$COMAC\_MAC\_FREQ\_\mathrm{Re}F = \begin{Bmatrix} 1-COMAC_1 \\ \vdots \\ 1-COMAC_M \\ 1-MAC_{11} \\ \vdots \\ 1-MAC_{NN} \\ \dfrac{\omega_X^1-\omega_{FE}^1}{\omega_X^1} \\ \vdots \\ \dfrac{\omega_X^N-\omega_{FE}^N}{\omega_X^N} \end{Bmatrix} \tag{2.38}$$

The frequency differences were normalised with respect to the experimental mode frequencies in order to have all the coefficients of the same order.

2.7.2 FRF based residue function

The residue functions, presented in the previous section, were designed to be sensitive to the structural changes that affect the mode shapes selected (target mode shapes). Therefore, in order to enhance the efficiency and the reliability of the model updating process, a preliminary analysis has to be performed at the aim to select the most sensitive mode shapes to the typology of damage under investigation (chapter 3). A way to avoid such investigation is to use data in the frequency space like the FRF obtaining, at once, three improvements with respect to the mode shape data. First, no further data elaboration is required because these data are directly acquired from the structures. Second, the updating process can be performed on a broad range of frequencies and not bounded to the modal frequencies. Last, the incidence of noise on FRF data is far less than that on the mode shape data (see Chapter 4).

Therefore a new kind of objective function was developed, the Frequency Response Assurance Criterion (FRAC) based residue functions.

The FRAC [74] is a correlation function similar to the COMAC. It measures the correlation between the experimental and the numerical FRFs, described by the expression below:

$$FRAC(j,k)=\frac{\left|\left\{{}_{A}FRF_{jk}\right\}^{T}\left\{{}_{X}FRF_{jk}\right\}^{*}\right|^{2}}{\left(\left\{{}_{A}FRF_{jk}\right\}^{T}\left\{{}_{A}FRF_{jk}\right\}^{*}\right)\left(\left\{{}_{X}FRF_{jk}\right\}^{T}\left\{{}_{X}FRF_{jk}\right\}^{*}\right)} \tag{2.39}$$

where ${}_{A}FRF_{jk}$ is the analytical FRF calculated at the j^{th} DoF, exciting at k^{th} DoF and ${}_{X}FRF_{jk}$ is the corresponding experimental FRF. The FRAC produces values between 0 and 1 for each degree of freedom. Where 1 means perfect correlation and 0 stands for two complete uncorrelated signals. It is clear that, for a grid of M sensors placed on the structure and using any one a time as exciter, the FRAC correlation function ends up to be a square matrix of order M.

Similarly to the COMAC residue function, the FRAC based functions can be built in order to highlight the inconsistency introduced in the FRF due to damage presence. The first residue function used was the FRAC matrix residue function (FRACm_ReF):

$$FRACm\_\mathrm{Re}F_{(i-1)M+j}=1-FRAC_{ij} \qquad \forall i,j\in\{1,2,\cdots,M\} \tag{2.40}$$

A major drawback of the FRACm_ReF is the need to perform as many harmonic analysis as the number of sensors employed (M), which causes a rising of the run time up to 1.5*N times the COMAC one. To avoid this, two more residue functions, FRACr_ReF, FRACc_ReF were derived by the FRACm_ReF and described by the following expressions:

$$FRACr\_\mathrm{Re}F_{i}=1-FRAC_{ij} \tag{2.41}$$

$$FRACc=1-FRAC_{ij} \tag{2.42}$$

where i is the index of the selected row and j the column index of the FRAC matrix.

The selection of the FRAC matrix row or of the FRAC coefficient was carried out by evaluating the FRAC matrix, and then, selecting the FRAC matrix row or the coefficient having the smallest norm. The norm was calculated using the following expression:

$$\min_{i}\sum_{j}FRAC_{ij} \qquad (FRACr\_ReF) \tag{2.43}$$

$$\min FRAC_{ij} \qquad (FRACc\_ReF) \tag{2.44}$$

Using these objective functions a significant run-time saving is obtained, since the number of harmonic analysis to be performed is reduced from M to 1.

2.8 Minimisation procedures

Once that the objective functions (norm of residue functions) $f(\mathbf{p})$ are defined, the last task is their minimisation by changing the updating parameters **p**.

The General Minimization Problem (GMP) consists in the minimisation of an objective function $f(\mathbf{p})$ subjected to some constraints as described below:

$$\begin{aligned} &\underset{\mathbf{p}\in\Re^P}{\text{minimize}}\ f(\mathbf{p}) \\ &\text{subjected to:}\quad \sum_i G_i\mathbf{p}=0 \qquad i=\{1,2,\cdots,C_l\} \\ &\qquad\qquad \mathrm{K}_i(\mathbf{p})\le 0 \quad i=\{C_{l+1},\cdots,C_T\} \\ &\qquad\qquad \mathbf{p}_l\le\mathbf{p}\le\mathbf{p}_u \end{aligned} \tag{2.45}$$

where:

- G_i are the coefficients of a linear constraint of the updating parameters.
- K_i are non linear constraints of the updating parameters.
- $\mathbf{p}_l$ and $\mathbf{p}_u$ are the lower and upper bound for the updating parameters.
- C_l is the number of the linear constraints.
- C_T is the total number of constraints.

The minimisation procedures investigated can be classified as linear and non-linear approaches. Linear approaches approximate the norm of the residue function, as a linear function of the selected updating parameters, updated at each step by estimating its sensitivity (Sensitivity approach). The non-linear option minimises the problem by approximating the function using a quadratic function (Subproblem Approximation Method – SAM) or using a function approximating the objective function in a region around the current minimum (Trust Region Method, Large Scale Optimisation – LSO).

2.8.1 Sensitivity approach

The sensitivity approach is used in the sensitivity based iterative methods described in section 2.4.2.1, although the solver used is slightly different due to the different kind of residue functions employed.

Independently from the residue function chosen, the norm of the residue function (ReF) is:

$$f(\mathbf{p})=\sum_{i=1}^{R}|\mathrm{ReF}_i| \tag{2.46}$$

where R is the number of the ReF components.

The minimisation process was articulated into 5 tasks, described in Figure 1, where:

- $\mathbf{p}^0$ is the updating parameter vector settled for the FE model initial configuration.
- **ExM** is the set of experimental measures acquired from the real structure.
- $\mathbf{CoF}^0$ is the correlation function vector or simply the vector obtained by the residue function evaluated using the initial FE model parameter vector and adding at each coefficient 1.
- Δ is the perturbation value used to estimates the sensitivity matrix.

- **CoF**^{i} is the correlation function vector estimated by perturbing the ith component of the parameter vector.

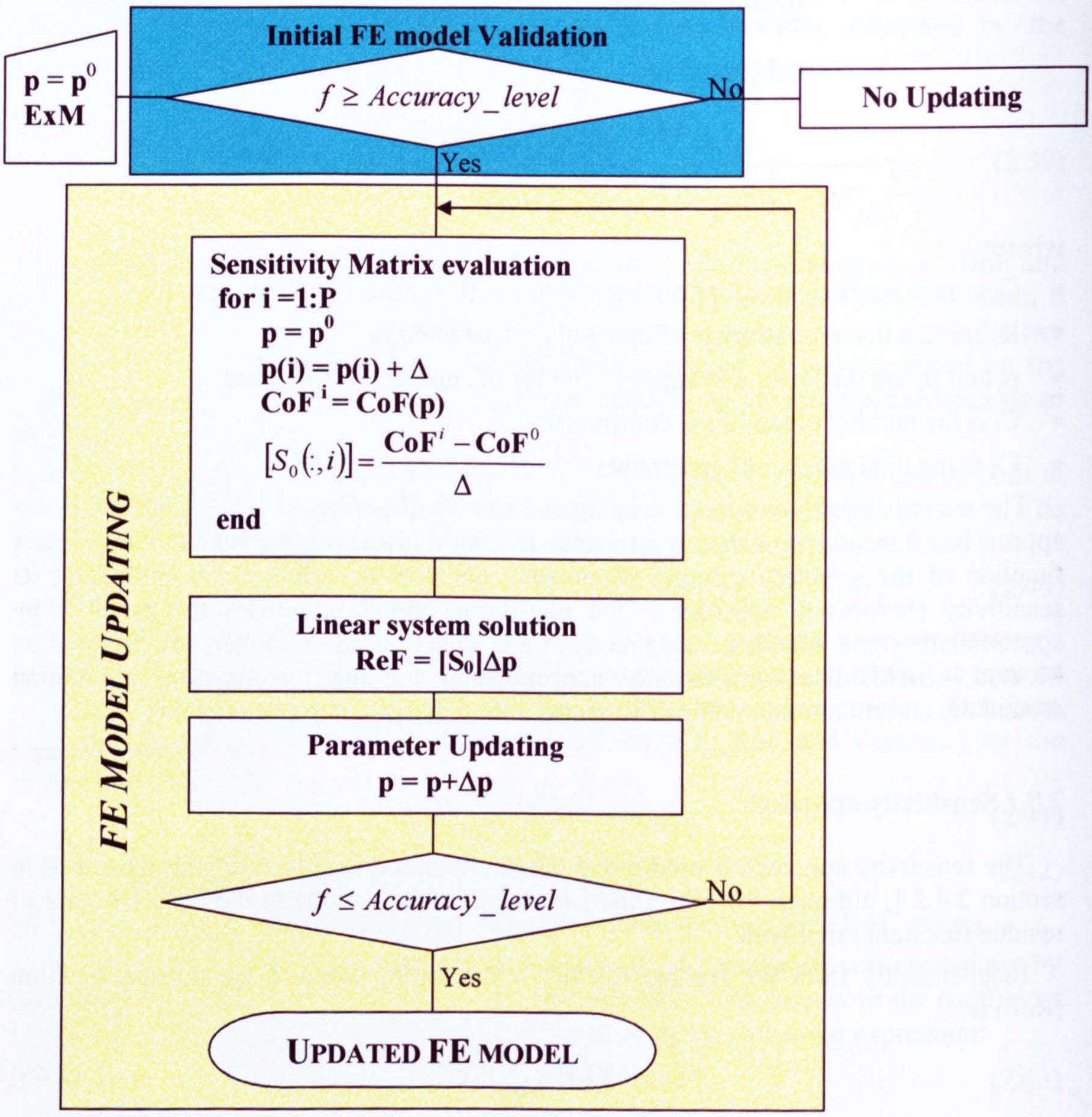

Figure 1 – Sensitivity based approach flowchart.

The first task is the initial FE Model Validation that, as mentioned in section 2.3.1, is a decisional phase of the updating process and consists in the evaluation of a norm of the residue function using the experimental data **ExM** acquired from the structure monitored. If the residue function norm value is smaller than the accuracy level fixed, the updating process stops and the FE model is considered dynamically equivalent to the real structure in the frequency range investigated and according to the accuracy level chosen.

On the other hand, if the discrepancies between the FE model and the real structure dynamic responses determine an objective function value larger than the accuracy level,

the FE model needs updating and the system starts to evaluate the sensitivity matrix (second steps) as illustrated in Figure 1. This performs as many modal or dynamic analyses as the number of the parameter vector coefficients P by perturbing them one by one, in order to evaluate the derivatives of the correlation function $\mathbf{CoF}^0$, which are carried out using a forward finite difference derivation scheme (see Figure 1, sensitivity matrix evaluation block).

Afterwards, the linear system so defined is solved. At this purpose, two approaches were investigated the Linear Least Square Optimisation (LLSO) and the Singular Value Decomposition (SVD) method.

At the aim to compute the parameter changes due to the damage presence, the LLSO algorithm solves the following problem [75]:

$$\min_{\Delta \mathbf{p}} \frac{1}{2} \left\| [S_0] \Delta \mathbf{p} - \mathbf{ReF} \right\|^2 \tag{2.47}$$

by evaluating the parameter changes $\Delta \mathbf{p}$ from the following equation:

$$g(\Delta \mathbf{p}) = \frac{1}{2} \Delta \mathbf{p}^T [C]^T [C] \Delta \mathbf{p} + \Delta \mathbf{p} [C]^T \mathbf{d} \tag{2.48}$$

where

- [C] is the sensitivity matrix after having been preconditioned using the method of Preconditioned Conjugate Gradients (PCG) [76] in order to have a well-conditioned coefficient matrix [C].
- **d** is the search direction estimated using the subspace trust region method (see section 2.8.3).

The Singular Value Decomposition (SVD) [77] technique solves the linear algebraic equation system by transforming it, in a determined system of linear independent equations.

The SVD method is based on the homonym theorem [78], which states that two orthogonal matrices [P] (m by m) and [Q] (n by n) can be evaluated at the aim to decompose a generic matrix [A] (m by n) into a diagonal matrix [D] (m by n), which its not negligible diagonal coefficients are named singular values.

$$[P]^T [A] [Q] = [D] \tag{2.49}$$

Changing [A] with [S_0] and recalling the orthogonality properties of [P] and [Q], eq. (2.49) can be written as:

$$[S_0] = [P][D][Q]^T = \begin{bmatrix} P_1 & P_2 \end{bmatrix} \begin{bmatrix} S_1 & 0 \\ 0 & S_2 \end{bmatrix} \begin{bmatrix} Q_1^T \\ Q_2^T \end{bmatrix} \tag{2.50}$$

where [P], [D] and [Q] have been partitioned according to the order of the problem P (the number of unknowns). Therefore, P_1, S_1 and Q_1 are [PxP] matrices, while the remaining matrices are of order (R-P). Moreover, the singular values are sorted out in decreasing order in the diagonal matrices S_1 and S_2, which means that the P largest singular value are S_1 coefficients.

Then, substituting eq. (2.50) inside the algebraic system (see Figure 1, linear system solution block):

$$\begin{bmatrix} P_1 & P_2 \end{bmatrix} \begin{bmatrix} S_1 & 0 \\ 0 & S_2 \end{bmatrix} \begin{bmatrix} Q_1^T \\ Q_2^T \end{bmatrix} \Delta \mathbf{p} = \mathbf{ReF} \tag{2.51}$$

Finally, solving the equation above, for $\Delta \mathbf{p}$ is obtained:

$$\Delta \mathbf{p} = Q_1 S_1^{-1} P_1^T \mathbf{ReF} \tag{2.52}$$

where S_1^{-1} is a diagonal matrix, whose coefficients are the inverse of the principal diagonal coefficients of S_1.

Both the techniques are efficient if the system is at least determined and well conditioned. This means that the number of the system independent rows must be at least equal to the number of the updating parameters (unknowns) and the Condition Number (2.53) must be as close as possible to 1.

$$CN = \frac{\lambda_{max}}{\lambda_{min}} \tag{2.53}$$

where λ_{min} and λ_{max} are, respectively, the minimum and the maximum eigenvalue of $[S_0]$, evaluated as the square roots of the minimum and the maximum eigenvalue of the matrix $[S_0]^T[S_0]$ (a [PxP] matrix).

After the evaluation of the linear system solution, the design variables **p** are updated (see Figure 1, parameter updating block, forth step), and then, once again, the objective function is evaluated (fifth step), as for the initial FE model Validation step with the only difference that this time the parameter set has been updated. At this stage, if the inequality is satisfied (see Figure 1, decisional block) the program execution ends and an updated FE model of the real structure, approximating its static and dynamic behaviour in the limits given by the accuracy level chosen, is found.

2.8.2 Subproblem Approximation Method

The Subproblem Approximation Method (SAM) [79] is the first of the non-linear approaches investigated. This method is a zero-order technique that requires only the evaluation of the dependent variables (objective and constraint functions) and not their derivatives.

The objective function minimised by this problem is the same used for the sensitivity approach (2.45), namely, the sum of the absolute values of the residue function coefficients. Moreover, as for the sensitivity approach the updating procedure starts if and only if the residue function, evaluated for the initial FE model, has a value larger than the accuracy level chosen.

The objective function is approximated as quadratic functions of the updating parameters:

$$f = a_0 + \sum_{i=1}^{P} a_i p_i + \sum_{i=1}^{P} \sum_{j=1}^{P} b_{ij} p_i p_j + err = \hat{f} + err \tag{2.54}$$

where the coefficients, a_i and b_{ij}, are evaluated using a weighted least square technique, which minimises the error norm E (2.55).

$$E^2 = \sum_{j=1}^{V} w^{(J)} \left(f^{(J)} - \hat{f}^{(J)} \right)^2 \tag{2.55}$$

with:

- $w^{(j)}$ weight associated with the j^{th} iteration that is inversely proportional to the objective function value, to the distance from the best design set (parameter set with the lowest objective function value) and to the design set feasibility (with respect to the constraints).
- $f^{(j)}$ and $\hat{f}^{(J)}$ are, respectively, the objective function and its approximation at the j^{th} iteration.
- V is the current number of iteration or objective function evaluations.

Before, the technique may be able to compute the approximations of the dependent variables, P+2 function evaluations are performed by generating as many random design sets.

Once that the approximations are made, the constrained problem is converted to an unconstrained one, using penalty functions as showed below:

$$F(\mathbf{p}, k_j) = \hat{f}(\mathbf{p}) + f(\mathbf{p}^0) k_j \left(\sum_{i=1}^{P} X(p_i) + \sum_{i=1}^{C} H(\hat{G}_i) \right) \tag{2.56}$$

where X and H are the penalty functions used to enforce respectively the updating parameters (design variables) and the dependent variable constraints (see eq. 2.45). The objective function evaluated for the initial FE model configuration is introduced in order to achieve consistent units. The function $F(\mathbf{p},k_j)$ is called response surface and k_j is its quality parameter. This unconstrained problem is solved using a Sequential unconstrained minimisation technique (SUMT), which performs subiterations increasing the quality parameters in order to enhance the accuracy of the results.

After the evaluation of the unconstrained problem minimum, the design set $\tilde{\mathbf{p}}^j$, corresponding to, is used to evaluate the design set for the subsequently iteration (j+1) according to the following expression:

$$\mathbf{p}^{j+1} = \mathbf{p}^b + C\left(\tilde{\mathbf{p}}^j - \mathbf{p}^b \right) \tag{2.57}$$

in which:

- $\mathbf{p}^b$ is the best design set.
- C is internally chosen value between 0 and 1, based on the number of the infeasible solutions.

The process is stopped when one of the following convergence controls is satisfied:

$$\left| f^{(J)} - f^{(J-1)} \right| \le \tau$$
$$\left| f^{(J)} - f^{(b)} \right| \le \tau \tag{2.58}$$
$$f \le Accuracy\_level$$

where τ is a coefficient (tolerance) chosen by the user.

2.8.3 Large scale optimisation approach

The large scale optimisation approach [75] is a subspace trust region method that minimises the general problem (2.45) in the least square sense by:

$$\min_{\mathbf{p}} \frac{1}{2}\left\|\mathrm{Re}\,F(\mathbf{p})\right\|^2 = \min_{\mathbf{p}} f(\mathbf{p}) \tag{2.59}$$

As for the sensitivity approach the updating procedure starts if and only if the residue function, evaluated for the initial FE model, has a value larger than the accuracy level chosen.

At each iteration, the algorithm approximates the objective function *f* with a simpler function q in a neighbourhood Y, termed trust region. The trial set of updating parameters is obtained minimising q in the region Y (2.60) defining what is called trust region subproblem.

$$\min_{\mathbf{p}}\{q(\mathbf{p}): \mathbf{p} \in Y\} \tag{2.60}$$

The updating of the current parameter set is acknowledged only if $f(\mathbf{p}^{i+1}) < f(\mathbf{p}^{i})$, otherwise, the current set is updated and the trust region is shrunk and the step is repeated.

In the definition of the trust region Y, the function q is assumed to be a quadratic approximation of *f*, evaluated using the first two terms of its Taylor expansion series. A further assumption is that the trust region has a spherical or ellipsoidal shape. Under this assumption the (2.60) can be rewritten as:

$$\min_{\mathbf{p}}\left\{\frac{1}{2}\mathbf{p}^T[HM]\mathbf{p} + \mathbf{p}^T\nabla\mathbf{f}: \ \ \|[L]\mathbf{p}\| \le \Delta\right\} \tag{2.61}$$

where:

- [HM] is the Hessian matrix, evaluated by BFGS [75] algorithm using only the first order derivatives of *f*.
- $\nabla\mathbf{f}$ is the gradient vector of *f*.
- [L] is a diagonal scaling matrix.
- Δ is a positive scalar.

Then, eq. (2.61) can be solved using a full eigensystem and Newton process applied to its secular equation (2.62) [75] obtained by reducing the trust region space in a two-dimensional (2D) space $V=\{v_1,v_2\}$ [75], where v_1 is the direction of the gradient vector and v_2 is either an approximate Newton direction (2.63) or a negative curvature direction (2.64) evaluated by the PCG method.

$$\frac{1}{\Delta} - \frac{1}{\|\mathbf{v}\|} = 0 \tag{2.62}$$

$$[HM]\mathbf{v}_2 = -\nabla\mathbf{f} \tag{2.63}$$

$$\mathbf{v}_2^T[HM]\mathbf{v}_2 \le 0 \tag{2.64}$$

In this way the minimisation process is speeded up because the problem is only 2D.

2.9 Damage detection

The damage detection process looks for structural changes in the structure that may occur during its operative life, by comparing the experimental data acquired during the structure service life with data of a numerical model or experimental data of the undamaged structures. This means that two models or sets of data of the structure are required, the undamaged and the in-service model. It is fundamental that the structural changes identified must be physically meaningful, which means that the parameters used to identify them must be related to the characteristics of the real damages. Moreover, if areas prone to be damaged, during the operative life, are not known, the entire structure must be considered liable to damage, leading to an increase of the CPU memory consumption and significant run-times. The number of updating areas might be reduced by a wise use of the error localisation step but this needs a great deal of engineering skill.

A partial solution at this problem is given by the two step GLO approach, in which the first step identifies the most damaged structure macro-areas. The second step redefines the updating parameters in the damaged macro-areas, before minimising the objective function. In this way the first step works as a sort of automated error localisation step, limiting so the intervention of the user.

The Damage Detection Process (DDP) derived from the use of the GLO approach has been named Global-Local Damage Detection Optimisation (GLDDO) approach and divided in two phases (Figure 2), the Damage Detection Set-up (DDS) and the Damage Detection (DD).

2.9.1 Damage Detection Set-up

The DDS consists in four steps (see Figure 2): the Undamaged Structure (US) FE model design and validation, the error localisation, the data and accuracy level selection.. The DDS is the only phase of the DDP that requires engineering skills and, therefore, the most critical. On the other hand, this step has to be carried out only once for every structure to monitor.

This phase consists in the construction and updating of the US model, which can be performed using the updating algorithm described in section 2.4.2, as well as the GLO approach.

The remaining sub-tasks (the error localisation, the data and accuracy level selection, see Figure 2) to perform depend on the damage to be identified.

In the error localisation step (the second, see Figure 2), once the damages to be monitored is/are identified, the physical parameters that most are able to identify the changes occurring on the structure due to the presence of the damage (for instance, thickness of finite elements or assemble of them for corrosion damages) are chosen as updating parameters for the DD step. If a priori data on the possible damage locations are available (e.g. maintenance records of similar structures, damage tolerance evaluation and etc.), the US model parameterisation for the damage detection can be restricted to only these regions, otherwise, is extended to the entire structure.

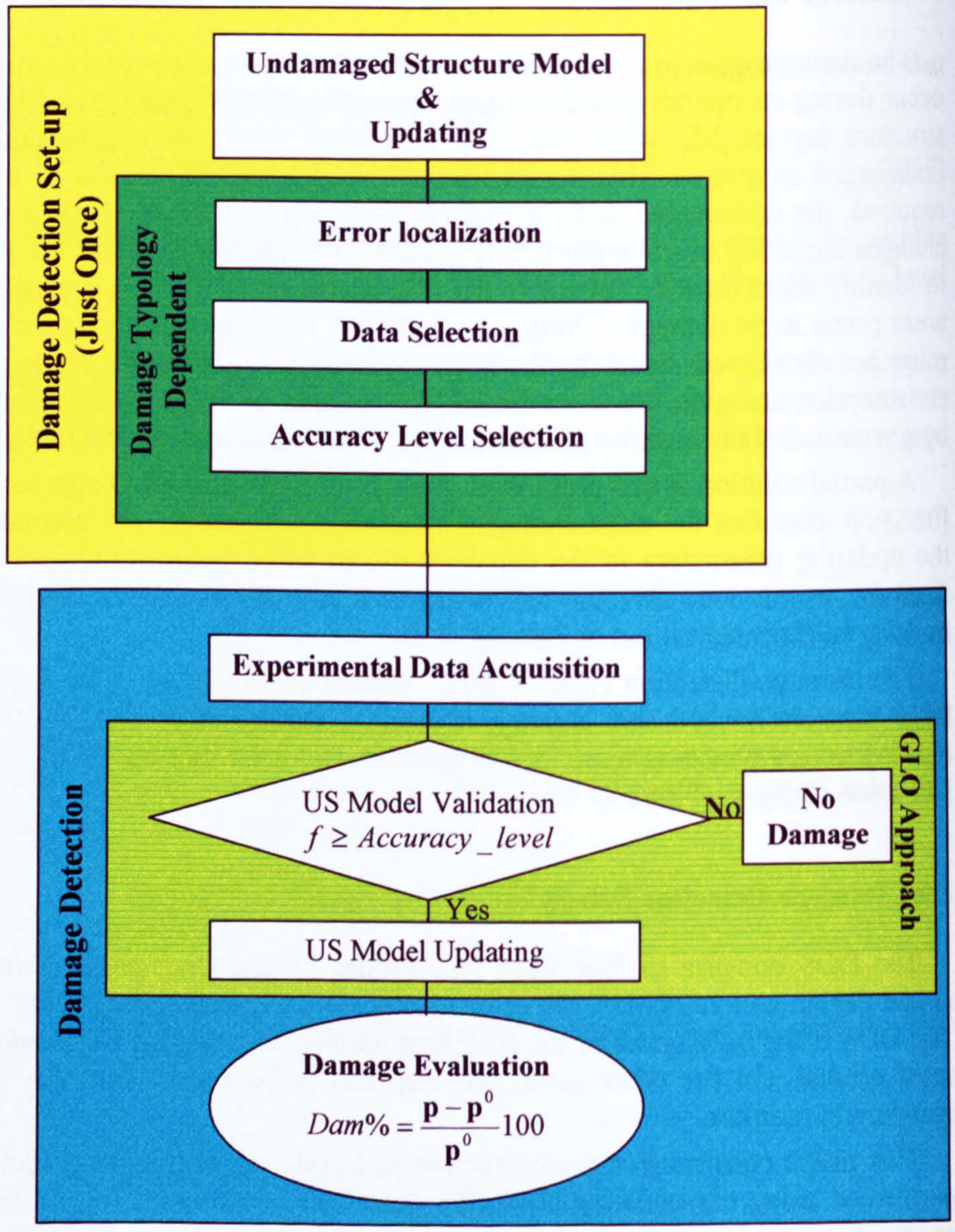

Figure 2 – Damage Detection Process.

For the data selection step (the third, see Figure 2), the first problem is the selection of the data type to acquire, modal properties or FRF. From a point of view of the quality and the acquisition speed of data, FRFs are far better than modal properties, because they are directly acquired from structures and do not need further processing. On the other hand, the FRF to be evaluated need the control of the excitation force (§4.2). This requirement prevents the FRF use in operative conditions, where mostly the load history is unknown. In such circumstances, when the in-service loads can be considered randomly distributed, the modal properties can be extracted using various techniques (see chapter 4).

Hence, when the excitation force control is not known, the data type choice falls on the modal properties.

However in both cases, because of economic and practical reasons, the number of sensors is limited. Therefore, there is the need to select the locations that are the most sensitive to structural changes (see chapter 3).

To finish, the selection of the accuracy level (the forth step, see Figure 2) is subjected to the precision requested for the damage accuracy and the time limitation. A less stringent accuracy level choice leads to a smaller number of iteration of the GLO approach than a more restrictive, resulting in run-time savings, but also, in less accurate damage estimation.

2.9.2 Damage Detection Step

The DD step as showed in Figure 2 involves four tasks: experimental data acquisition, US model validation, US model updating and the damage evaluation. The first involves the acquisition of the experimental data from sensors and than their processing at the aim to evaluate FRFs or mode shapes of the structure (see chapter 4).

Once the experimental data have been acquired and processed the GLO approach is used to validate the US model and if necessary to update it (Figure 2). The US model is validated by evaluating the residue function and checking if this is smaller or larger than the accuracy level selected. If the real structure behaves as the FE model, in the limit of the accuracy level chosen and the frequency range analysed, the structure is considered to be undamaged (see Figure 2). If the real structure has a certain amount of discrepancies with the US model, the structure is judged to be damaged and the US model updating is carried out at the aim to localise and quantify the structural changes occurred.

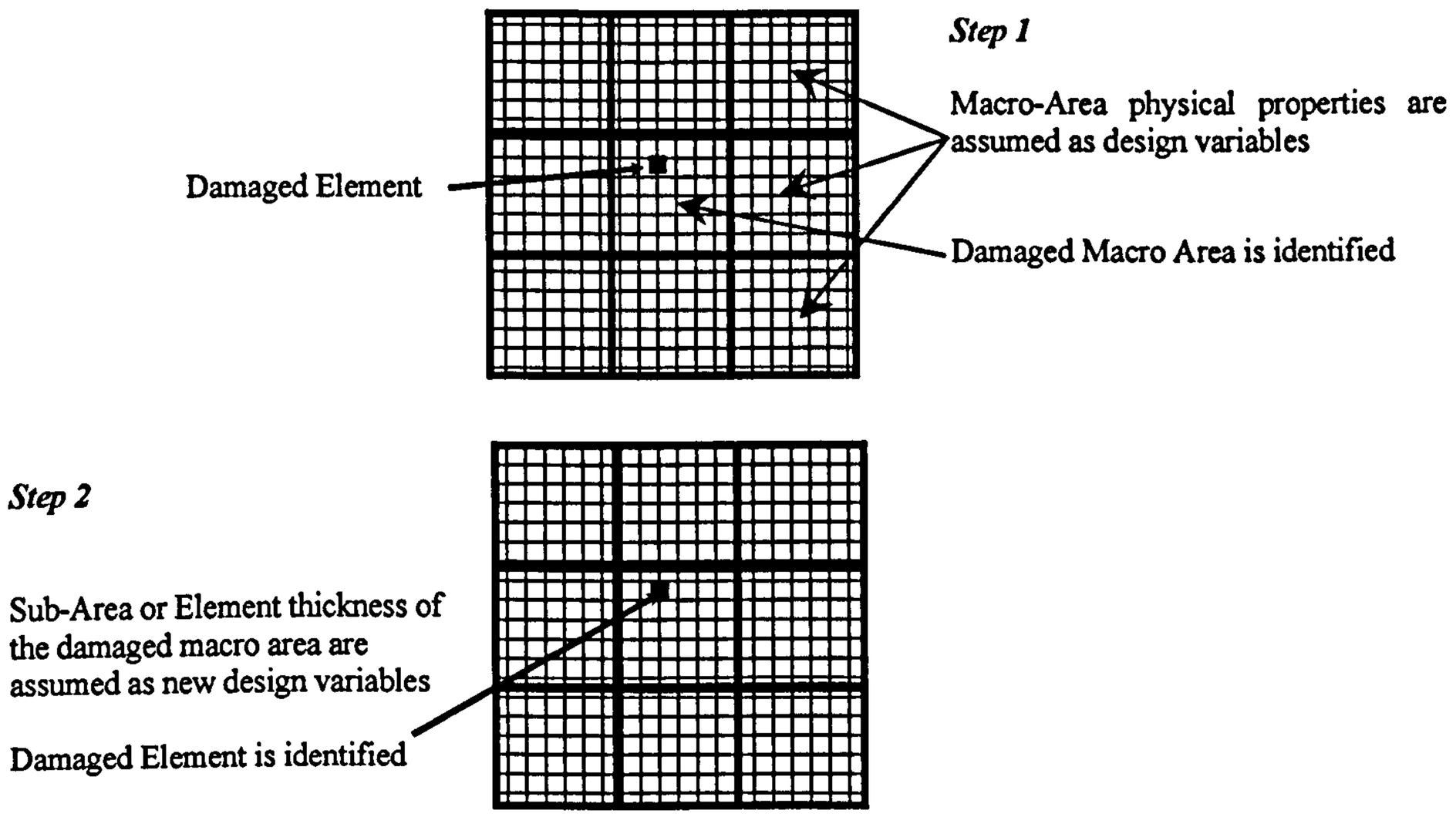

Figure 3 - Global–Local Optimisation Approach.

As described in paragraph 2.6 the US updating step is articulated in two stages (see Figure 3). At the first stage, the structure is divided in macro-areas, and their spatial-type parameters, identified in the DDS, are assumed as initial design variables. The selected objective function is then minimized. This process identifies damaged macro-area/areas by comparing the optimisation results with the initial values of the undamaged macro-areas. For the second stage, the thickness of the elements of the damaged macro-area/areas, identified by the largest thickness change, are chosen as new design variables. The optimisation process is performed again to find the damage location and severity by comparing the damaged and the undamaged updating parameter sets (see the forth step of the DD step of the DDP described in Figure 2).

As mentioned before (§2.6), the use of the GLO approach reduces the number of updating parameters and run-time, resulting in a robust optimisation method, and a smooth distribution of the model properties, able to represent the damaged zones in the structure investigated as showed in Figure 3.

2.10 GLDDO approach applicability

The GLDDO approach as well as all the damage detection techniques based on MU methodology need a validated FE model of the undamaged structure, which accuracy and resolutions has to be correlated with the minimum damage size to detect and its signature in terms of changes of the structure stationary properties (modal properties and FRFs). Moreover, the more accurate the model the larger the damage detection run-time. These drawbacks together with the rising difficulty of modal property extraction with the increase of frequency made this GLDDO approach suitable for those structures, which do not need a real-time detection. Moreover, in order to avoid difficulties in the modal properties extractions (since most of the time controlled excitation is not possible) the minimum damage size signature should affect relatively low frequencies (as for the bridge showed in §7.2), but should not constitute an immediate threat neither to the structure health nor to its users. These kind requisites are fulfilled by civil structures as buildings industrial plants and bridges, because their typical failure modes and their operative loads (e.g. low frequency) are not associated with fast crack growth, as for mechanical and aeronautical structures.

The methodology developed was tested numerically on a cantilever beam (appendix A) and on a plate-like structure (appendix C) and the results are discussed in chapter 6.

2.11 Conclusions

The chapter main objective was to introduce the MU damage detection technique developed by the author. Its development process started with a careful analysis of MU advantages and drawbacks, at the aim to identify the right specifications that could determine an enhancement of damage detection processes based on MU.

The developed MU based damaged detection process was named Global-Local Damage Detection Optimisation (GLDDO).

The global-local approach (see §2.4-§2.6) was adopted to reduce the number of variables (updating parameters) involved in the damage detection process, so as to obtain a reduction of the run-time and an increase of the precision in the identification of the location and severity of the damage compared to those of single step model updating methods, as proved in §6.5.1. The increase of resolution is due to the fact that the global-local approach can exploit the maximum number of variables, allowed for the acquired data [71] (see equation 2.22), twice. The first time in the first step and, then, again in the second step but only in the regions were structural changes are identified. This means that the smallest region that can be inspected by global-local process is "twice" smaller than that investigated by a single step approach (§6.5.1).

In some extent the first step of the global-local process works as an error localisation phase of the model updating procedure, automating so one of its most critical points.

The optimisation was meant to reduce more efficiently the discrepancies between a FE model of the structure and its real dynamic properties by changing FE model characteristics (updating parameters). This solution is very effective, especially, in presence of strongly nonlinear structure responses due to either geometric or material nonlinearities compared to iterative approaches. Because, these use a pure gradient driven minimisation process (e.g. the sensitivity matrix, see section 2.4.2) for the residue function, with no control on the extension of the region on which such linearization is valid and no possible way to check if the minimum is a local or the global one. On the contrary, the large scale optimisation algorithm controls the validity of the gradient evaluated by investigating the residue function through the trust region. A more efficient way to get the global minimum of the residue function investigated is given by the subproblem approximation method which does not evaluate any gradient but builds a quadratic surface which minimum should be located in proximity of the global minimum. Its efficiency compared to the linear and the nonlinear approach was confirmed by the investigation results analysed in §6.5.

Furthermore, the technique developed is an iterative model updating technique. This means larger computational times and convergence troubles with respect to direct methods. On the other hand, it was possible to design a model updating approach that can use any type of updating parameter (variables of the optimisation process) and incomplete data.

Hence, for a better understanding of the proposed method, physical quantities of structure regions, such as thicknesses, Young modules and etc., were used as FE model (updating) parameters. This assumption gave the possibility to evaluate:

- The damage severity as differences between the parameters of the updated FE model of the damaged and undamaged structure and, therefore, can be expressed in terms of percentage of the undamaged structure thickness or elastic modulus and so on.
- The damage location as the location of the parameter/parameters, which values have changed after the FE updating.

As mentioned in paragraph 2.4, direct and iterative methods have to pair and scale the data experimentally acquired, this was avoided by using correlation functions (§2.7.1) to measure the discrepancies between the mathematical and the experimental model of the

structures. Additionally, the adoption of correlation functions provides a noise reduction as reported in appendix C (§C.3).

Moreover, in the evaluation of the residue function using correlation function, no expansion of the experimental data, from the degree of freedoms of the experimental model to those of the FE model, is needed. Thus, the smearing of the structural changes on the structure is avoided [52].

Numerical comparisons between these algorithms were reported in appendix (A and C) and discussed in chapter 6.

CHAPTER 3: OPTIMAL DATA SELECTION AND SENSOR PLACEMENT

3.1 Abstract

An issue generally neglected by Model Updating (MU)/MU Damage Detection (DD) technique developers is data selection (modal properties, Frequency Response Function – FRF), which can guarantee a successful MU process. The influence of data selection over MU outcomes is due to the information content of experimentally acquired data. The importance of an appropriated data selection on MU efficiency must be found in its economic and practical aspects. For instance, to acquire experimental data from every FEM DoFs is impossible because devices to measure rotational DoFs behaviour do not exist. Moreover, to measure every displacement DoFs is not practical because the time necessary would be huge. In addition, all this is uneconomic because of the enormous number of sensors and expertise needed for such operation.

Consequently, a successful MU/DD is strongly dependent on the optimal data selection so, in the design of the GLO approach (§2.6-2.9), data selection issues were taken into account and tackled with a preliminary analysis step in the GLO approach damage detection set-up phase (§2.9.1) targeted to the selection of the data type.

The first task was to study possible data to be acquired (§3.2), which involves an analysis of the data acquisition conditions and of MU/DD targets (e.g. smallest damage to be detected). After the data type selection, a TMS Selection (TMSS - §3.3) is required

when modal properties are selected as data type for the MU/DD process. Finally, the OPS (§3.4) aimed at the maximisation of the information content of the acquired signals were analysed. These three phases were explored separately by analysing different methodologies present in literature and some developments were proposed by the author and, then, tested on the GLO approach on different structure typologies as illustrated in chapter 6.

3.2 Data type selection

Data type selection is the first phase devised to tackle practical and economic issues related to data acquisition. These concerns introduce limitations on the possible number of sensors to deploy, on their locations (since not all locations are always accessible), on the data type acquirable and etc... Therefore, an accurate analysis on the impact that these limitations have on the information content of the acquired data is compulsory. Moreover, this analysis should deal also with the maximisation of the experimental data information content and of the Signal Noise Ratio under the structure operative conditions, since the acquired data should be sensitive to structure features (changes). At this aim, a data selection process was designed within the GLO approach. The first phase is an accurate analysis of the structure and its operative conditions targeted to establish which type of experimental data would be the most suitable. Further, in this investigation, an important role is played by the smallest structure feature (e.g. smallest damage, smallest structure geometry particular) to be captured by the updated FE model. Therefore, a broad frequency range of investigation is advisable, since the data sensitivity to structural changes (or feature size) increases with the frequency [23]. Accordingly with the GLO technique (§2.6-2.9), two typologies of data, mode shapes and FRFs, can be used. The mode shapes needs post-processing and is difficult to evaluate at high frequencies. On the other hand, mode shapes can be evaluated in service conditions, in contrast with the FRFs that need an excitation source control and more run-time and computational resources (chapter 4), in the MU/DD process. Moreover, the FRFs guarantee information at every frequency scanned (not only at the modal ones) and do not need further elaboration. However, the problem of the extraction of mode shapes at high frequencies can be solved by extracting only those of interest, named Target Mode Shapes (TMS), using a wavelet based extraction technique (see chapter 4) that helps to separate coupled modes.

Therefore, in line with the issues highlighted above, the data type selection was articulated in three steps:

- Structure analysis.
- Definition of the frequency range of the investigation.
- Actual data type selection.
- TMS selection

Following, data selection process the Optimal Sensor Placement (OSP) was investigated in §3.4-3.7.

3.3Target mode shape selection

Target Mode Shape Selection (TMSS), consists in the identification of those mode shapes that best characterize the structure behaviour in a given frequency range. These modes are, first, used for the identification of the optimal sensor placements and, then, exploited as data for the GLO approach in the damage detection process. As mentioned before, the TMSS is unnecessary for damage detection processes employing FRF data, where the selection of the target mode shapes is a lot simpler, because once selected the frequency range of interest, all the mode shapes in that range are the target mode shapes used for the OSP. However, when the number of sensors (M) is smaller than the number of TMSs (N), some OSP methods may require a TMSS (§3.5.1-§3.5.3).

On the other hand, for damage detection process that uses mode shape data, the selection of the target mode shapes is crucial for successful damage detections.

In literature, many TMSS methods are present and used mainly for testing aerospace structures [80-81]. TMSS techniques can be divided in two main branches, the energetic and control theory based methods. Here, only the first, energetic techniques, were explored because the control theory based methods such as the balanced singular technique [82] or modal cost technique [83-84] need a fully characterised structure not only in terms of mass and stiffness but also in term of damping, which characteristics are not easy to reproduce.

The energetic TMSS techniques investigated were the Root-Sum-Square displacement (RSS) method, the Modal Kinetic Energy (MKE) approach and the Maximum Strain Energy (MSE) criterion.

A fourth TMSS technique was analysed, the Minimum Modal Frequency (MMF) criterion, because together with the MSE was the only one used for damage detection purposes [86].

3.3.1 Minimum Modal Frequency criterion

The Minimum Modal Frequency (MMF) criterion selects the first few modes of the structure. The MMF method is the most used between the TMSS techniques analysed, since the extraction of the first modes is very easy and more accurate than higher frequency modes. Moreover, the first modes retain the bulk of the structure characteristics and, therefore, their contribution to the structure dynamics is predominant. This feature may reduce their sensitivity to local structure changes but is balanced by the fact that they absorb the most of the excitation energy and, consequently, global changes are easier to detect.

3.3.2 Root-Sum-Square displacement method

The Root-Sum-Square displacement (RSS) method was initially used in TMSS for ground vibration test of the X33 vehicle [80]. This technique selects the mode shapes that have the highest overall motion energy for a set of FEM nodes [85]. The methodology estimates the resultant modal displacements (3.1), for each mode shape investigated, and then selects those with the highest values.

$$RSS\_resultant\_value_j = \sum_{i=1}^{node\_N} \left[\{\phi^j\}_{xi} + \{\phi^j\}_{yi} + \{\phi^j\}_{zi} \right]^2 \quad (3.1)$$

where:

- j identifies the j^{th} mode shape investigated.
- i identifies the i^{th} node between the set selected.
- node_N number of node selected.

For the selection of the set of nodes used for TMSS many issues, such as accessibility of the node locations, space issues for sensors placement and etc..., must be taken into account.

3.3.3 Modal Kinetic Energy approach

The Modal Kinetic Energy (MKE) approach selects [80] mode shapes with the highest kinetic energy content using the mass matrix of a structure FE model. In this case, differently from the RSS method there is no need of node pre-selection, although, in some application was found out that this technique tended to select non-interesting modes, even though rarely missed a global one [80].

The selection consists in the evaluation of the modal kinetic energy content (3.2) of each eigenvector and selecting those with the highest values.

$$\{KE\} = diag\left([\Phi_{FE}]^T [M_{FE}] [\Phi_{FE}] \right) \quad (3.2)$$

3.3.4 Maximum Strain Energy criterion

The Maximum Strain Energy (MSE) criterion together with the minimum modal frequency criterion is the only used for DD purposes [86]. The technique selects the mode shapes that have the highest energy contents, generally located at the highest frequencies analysed. The modal strain energy expression is derived from the general definition of the strain energy using the FE model stiffness matrix as showed below:

$$U = \frac{1}{2} \{x\}^T [K_{FE}] \{x\} \quad (3.3)$$

where {x} is the structure displacement vector.

Therefore, the modal strain energy associated to the j^{th} mode shape is the strain energy stored in the structure by deflecting it in accordance with its shape.

$$MSE_j = \frac{1}{2} \{\phi^j\}^T [K_{FE}] \{\phi^j\} \quad (3.4)$$

If mass normalised mode shapes are used, eq. (3.4) can be exemplified by recalling eq. (2.11) in:

$$MSE_j = \frac{1}{2} \{\phi^j\}^T \left([\Phi_{FE}]^T [\omega_{FE}^2] [\Phi_{FE}] \right)^{-1} \{\phi^j\} \quad (3.5)$$

In the case that damage locations are a priori known, the mode shapes to be used at that point can be the damaged ones instead of those undamaged. This choice seemed improving the quality of damage detection [87].

3.4 Optimal Sensor Placements

After the optimum data selection, there was the need to study Optimal Sensor Placement (OPS). OSP is a common problem encountered in many engineering applications. Sensor placement is a critical issue in the construction and implementation of an effective health monitoring system. An optimal configuration can minimise the number of sensors required, increase accuracy and provide a robust system. Moreover, OSP is important in cases where the properties of a system, described in terms of continuous functions, need to be identified using discrete information.

This, in turn, implies that a minimum number of sensors must be judiciously placed on the structure under assessment, in order to provide a clear "image" of the structural behaviour, highlighting as much as possible structural changes that may occur due to faults presence. Hence, OSP critical issues are how many and which degrees of freedom should be taken in the damage identification process. In solving this problem due account has to be taken of economic and practical factors, which may require sensors being placed at accessible locations of the real structure.

In literature, a number of different OSP methods have been investigated, some based on intuitive placement or heuristic approaches, others employing systematic optimisation methods. All can be classified in three different branches:

- The statistic OSP methods. These maximise a measure of the data independence, such as the Fisher Information matrix [87-88] or the data variance [89].
- The energetic techniques. These are based on the maximisation of the experimental signal energy content [98-99].
- The control theory based approaches. These maximise the observability of the system under investigation [101].

3.5 Statistic approach

Statistic methods select optimal sensor locations by maximising a measure of data independence and strength such as the Fisher Information Matrix [87-88] or the data variance [89].

For the Fisher Information Matrix based techniques, the following methods were investigated:

- The Effective Independence method (EFI) developed for in-orbit modal identification of large space structures [90], was also used for a range of different applications e.g. the reconstruction of acoustic field around a vibrating surface [91].
- The EFI-DPR [54] is a compromise between the EFI technique and an energetic approach named Driving Point Residue [92] (§3.6.2). It was used on large mechanical structures such as an engine case and nozzle [54].

- The Kinetic energy method (KEM) is an evolution of EFI, where the Information matrix is weighted by the mass matrix and was mainly employed in structural health monitoring of large bridges [93].

For the variance based techniques, the following methods were studied:

- The Principal Components Analysis (PCA) [94]. It is mainly a reduction technique widely utilised for data compression, for instance, in image recognition [95] or process control [96]. The technique was converted by the author to OSP proposes.
- The Most Informative Subset (MIS) [97]. It was developed to reduce the data amount, at the aim to study their dependences and characteristics. The MIS method was used for optimal design of experiments in meteorology and economic studies.
- The Variance based method (VrM) (developed by the author). It is founded on a physical interpretation of the covariance matrix coefficients [89].
- The Gradient based Method (GrM) developed by the author. It consists in a statistic analysis of the mode shape sensitive functions evaluated with respect to the damaged locations.

3.5.1 Effective independence method

The Effective Independence (EFI) sensor placement method [90-91] places M sensors on a structure by maximising both the spatial independence and the signal strength of N target mode shapes. The sensor placement selection is carried out by an iterative algorithm, which maximises the Fisher information matrix determinant as explained below.

The measured structural response vector $\{y_s\}$ can be estimated as a combination of N mode shapes as follows:

$$\{y_s\} = [\Phi_{FE}]\{q\} + \{w\} = \sum_{i=1}^{N} q_i \{\phi^i\} + \{w\} \tag{3.6}$$

where:

- $[\Phi_{FE}]$ is a [nxN] matrix having the N FEM target mode shapes as columns and the n candidate sensor locations as rows;
- $\{q\}$ is the coefficient response vector;
- $\{w\}$ is a sensor noise vector, assumed to be randomly distributed with zero mean.

This representation of structural responses is based on the concept [73] that, the response in any point of an elastic structure can be obtained in time or frequency domain as a linear combination of mode shape values.

Evaluating the coefficient response vector using an efficient unbiased estimator [90] and then, computing its covariance matrix is obtained:

$$J = \mathrm{cov}(\mathbf{q}) = \left[\frac{1}{\sigma^2}[\Phi_{FE}]^T[\Phi_{FE}]\right]^{-1} = [Q]^{-1} \tag{3.7}$$

where [Q] is the Fisher information matrix [87].

$$[G]^T = \frac{\partial \mathbf{y}_s^T(\mathbf{q})}{\partial \mathbf{q}} \qquad Q(\mathbf{q}) = \frac{1}{\sigma^2}[G]^T[G] \tag{3.8}$$

with [G] sensitive matrix and σ error standard deviation.

Hence, the best estimation of q occurs when Q is maximised, which means that the sensitivity to the response vector coefficients is maximised at the same time. Therefore, choosing the Fisher information matrix determinant as a measure of the information content of the Fisher information matrix, the best M sensor placements are those that maximise this measure.

The maximisation procedure is an iterative algorithm [90], which at any iteration computes the candidate sensor location contributions to the [Q] determinant using the Effective Independence Distribution (EID) vector:

$$\{EID\} = \left\langle \left[\Phi_{FE}\right]\left[\Psi\right]\right\rangle^2 [\lambda]^{-1}\{1\}_k \tag{3.9}$$

where:

- $[\psi]$ is the eigenvector matrix of [Q].
- $[\lambda]$ is [Q] eigenvalue matrix.
- $\{1\}_k$ is the sum of all coefficients belonging to the k^{th} row
- $\langle\ \rangle^2$ is the square of any single element of the matrix product.

In order to ensure the maximisation of [Q] determinant, the sensor position having the smallest EID coefficient is eliminated, from the initial set of candidate sensors. This process is iterated until the number of candidate sensor n equals M.

The EFI major drawback, common to all OSP methodologies based on the Fisher Information matrix, is that in order to have a non-singular Fisher Information matrix the sensor number must be bigger or equal than the target mode shape number N.

3.5.2 EFI-DPR method

The EFI-DPR method [54] was developed in order to avoid the selection of low energy sensor locations from the EFI algorithm with a consequent loss of information. The EFI-DPR (Driving-Point Residue [92]) overcomes the drawback above mentioned by multiplying the candidate sensor contribution to [Q] determinant (EID coefficient) for the corresponding Driving Point Residue (DPR) coefficient, as follows:

$$\{EID\} = \left\langle \left[\Phi_{FE}\right]\left[\Psi\right]\right\rangle^2 [\lambda]^{-1}\{1\}_k \{DPR\} \tag{3.10}$$

where the Driving Point Residue (DPR) evaluated for the i^{th} candidate sensor location is given by [92]:

$$DPR_i = \sum_{j=1}^{N} \frac{\{\phi^j\}_i}{\omega_j^2} \tag{3.11}$$

with ω_j is the j^{th} target mode frequency.

3.5.3 Kinetic energy method

The Kinetic Energy Method (KEM) [93] uses the same algorithm of the EFI method, the main difference lies on the evaluation of the Fisher Information matrix [Q]. This is

evaluated (see eq. 3.12) as a mass normalised product of the target mode shape matrix $[\Phi_{FE}]$ for its transpose.

$$[Kem]=[\Phi_{FE}]^T[M_{FE}][\Phi_{FE}]=[Q] \tag{3.12}$$

At the aim to evaluate the EID vector coefficients a Cholesky factorization of the Fisher information matrix [Kem] was performed (see eq. 3.13) so that the EID components could be evaluated as described by eq. (3.14)

$$[Q]=[\Gamma]^T[\Gamma] \tag{3.13}$$

$$\{EID\}=\left\langle[\Gamma][\Psi]\right\rangle^2[\lambda]^{-1}\{1\}_k \tag{3.14}$$

By use of the [Kem], the EFI iteration algorithm selects M sensor locations with the highest kinetic energy content among all possible combination of M candidate locations. In this way, the occurrence of the selection of low energy sensor locations from the EFI algorithm is avoided without damaging the maximisation of both the spatial independence and signal strength.

3.5.4 Principal Components Analysis

The Principal Components Analysis (PCA) is mainly a reduction technique widely utilised for data compression. The main intent of the PCA [95-96] is the reduction of a multivariate problem to a set of principal components so that the error between the two representation of the phenomenon is negligible or, at least, smaller than an established tolerance.

For OSP purposes, the PCA aim is the selection of M candidate sensor positions that give the largest contribution to the principal components selected, which can be interpreted as the directions having the most significant amount of energy [94].

In the case studied, the multivariate problem is defined by the matrix $[\Phi_{FE}]$, whose rows represent the problem variables (the sensor candidate positions) and the corresponding values on the column their samples (the mode shape values).

Calculating the covariance matrix [C] of $[\Phi_{FE}]$ and, then, evaluating its eigenvectors and eigenvalues sorted out from the largest to the smallest. The space on which to project the data analysed in order to reduce their dimension is constituted by M eigenvectors (principal components) associated with the largest M eigenvalues. In this way, the created space is an ordered orthogonal base, whose directions lie according to the largest variances of the data. Naming [A] the matrix having as columns the selected eigenvectors, the new compressed data {y} are given by:

$$\{y\}=[A]^T\left(\{\phi^j\}-\mu_j\right) \tag{3.15}$$

where μ_j is the mean of the j^{th} row of $[\Phi_{FE}]$.

The measure of the candidate sensor position contribution to the compressed data could be calculated by the below expression:

$$E_D=abs([C][A])\{1\}_k \tag{3.16}$$

where the vector E_D is equivalent to the effective independence distribution vector utilised in the EFI algorithm (§3.5.1), given by the sum of the contributions of the candidate sensor locations to the principal components.

The selection algorithm consisted in picking up only the M candidate sensor locations having the largest values of the distribution vector E_D.

3.5.5 The most informative subset technique

The Most Informative Subset (MIS) technique [97] is a statistics method that relies on a covariance analysis approach. This method was developed for problems related to evaluation and approximation of a phenomenon by a finite number of observations.

For OSP purposes, the phenomenon investigated by the MIS technique is the evaluation of the mode shapes in non-instrumented points of the structure.

Therefore, supposing that each TMS is evaluated (observed) in M $y_M=\{y_1, y_2, \ldots, y_M\}$ of the possible n locations, the mode shapes need to be estimated in the remaining n-M positions $y_p=\{y_{M+1}, y_{M+2}, \ldots, y_{M+p}\}$(n=M+p). This problem can be solved using, the best linear unbiased estimator of y_p [97] given by the following equation:

$$\hat{y}_p = C_{pp} C_{MM}^{-1} y_M \tag{3.17}$$

where if the matrix Y is assumed equal to $\{y_M, y_p\}=[\Phi_{FE}]^T$, the matrices C_{pp} and C_{MM} are the diagonal matrices of its covariance matrix [97]:

$$\mathrm{cov}(Y)=\begin{bmatrix} C_{MM} & C_{Mp} \\ C_{pM} & C_{pp} \end{bmatrix}=\begin{bmatrix} \mathrm{cov}(y_M) & C_{Mp} \\ C_{pM} & \mathrm{cov}(y_p) \end{bmatrix} \tag{3.18}$$

Evaluating the covariance of the estimation error as follows [97]:

$$D_{pp} = \mathrm{cov}(\hat{y}_p - y_p) = C_{pp} - C_{pM} C_{MM}^{-1} C_{Mp} \tag{3.19}$$

Then, any kind of monotonous function $Q(D_{PP})$ could be used to measure the efficiency of the estimator by measuring the dynamic response in the location x_i for i from 1 to M.

Taking as efficient measure of the estimation, the D_{pp} determinant (D-criterion), the best M sensor positions will be those that minimise the D_{pp} determinant.

Therefore, considering the below algebraic rule [97]:

$$\mathrm{cov}(Y)=\begin{vmatrix} C_{MM} & C_{Mp} \\ C_{pM} & C_{pp} \end{vmatrix}=\left|C_{MM}\right|\left|C_{pp} C_{pM} C_{MM}^{-1} C_{Mp}\right|=\left|C_{MM}\right|\left|D_{pp}\right| \tag{3.20}$$

The minimisation of the D_{pp} determinant is equivalent to the maximisation of the C_{MM} determinant. Hence, the OSP is reduced to the maximisation of the determinant of the $[\Phi_{FE}]^T$ covariance matrix for a set of M sensor positions:

$$\max_{M \; sel} \left|\mathrm{cov}\left([\Phi_{FE}]^T\right)\right| \tag{3.21}$$

3.5.6 The variance based method

The variance method (VM) is an evolution of the Most Informative Subset (MIS) technique [97] according to physical and mathematical considerations on the coefficients of the covariance matrix [C] [89]. The MIS technique selects the OSPs by maximizing the determinant of cov($[\Phi_{FE}]^T$) (eq. 3.21), this guarantees that the rank of the target mode shape matrix Φ restricted to the M selected locations is equal to N, but it does not ensure that the signal strength is maximised. Therefore, taking into account the following properties of the covariance matrix coefficients c_{ij} [89]:

- For $i \neq j$ if $c_{ij}=0$, the i^{th} and the j^{th} row of $[\Phi_{FE}]$ are independent.
- For $i=j$ $c_{ij=}\sigma_i^2$ that is the vector $\{\Phi_{FE}\}^i$ variance. Consequently, the diagonal coefficients can be considered as a measure of the signal strength acquired by the i^{th} candidate sensor.

The simultaneously satisfaction of the maximisation of the determinant of C_{MM} and the maximisation of the signal strength can be met for a C_{MM} matrix, which off-diagonal coefficients tend to zero, while its diagonal terms tend to 1 (the maximum for the standard deviation is 1 - constant distribution). This is equivalent to the maximisation of the function Vr:

$$Vr = \sum_{i=1}^{M} \frac{c_{ii}}{Dep_i} \qquad Dep_i = \sum_{i \neq j} c_{ij} \tag{3.22}$$

For this reason is sufficient to select M sensor locations (k) having the highest ratio between the diagonal covariance coefficient c_{kk} and the sum of its off-diagonal terms Dep_k. However, this way to maximise the function Vr, common to most of the energetic OSP techniques (EVP, NODP), leads to a concentration of the sensor locations selected in few regions of the structure under investigation. The problem was solved by selecting the local maxima of the function Vr sorted in decreasing order. This solution has the advantage to:

- Distribute the sensors selected throughout the structure, assuring an improved capture of the vibration mode shapes.
- Suggest the number of sensors employable through the number of local maxima. This point is an important breakthrough for OSP, since none of the techniques described in literature gives any information about the optimal number of sensors to use.
- Consistently reduce the computation time of the MIS, since the evaluation of the determinant of the C_{MM} is avoided.

3.5.7 Gradient based method

The Gradient based method (GrM) is a statistical method that uses, as data, sensitive functions (gradients) of the mode shapes with respect to the design variables. Sensitive functions were selected in order to have a sensor location algorithm that was sensible to the damage locations and capable of maximising the acquired signal strength by selecting the sensor locations associated with the largest gradients. The methodology consisted in a statistical analysis of the sensitive functions in order to select the candidate sensor positions having the maximum averaged variance. The procedure followed was divided in four steps:

- Evaluation of the sensitive function. This task may be performed, using the ANSYS gradient tool that evaluates automatically the derivatives requested by a forward finite differences expression [79].
- Variance and mean evaluation. At this step, the variance and the mean of the gradients for a single candidate sensor position and mode shape investigated were evaluated. In this way, the dimension of the problem was reduced from three (design variables, candidate sensor positions and mode shapes) to two variables (candidate sensor positions and mode shapes).
- Averaged variance estimation. In order to normalise the variance estimated and to avoid the major scattering of the low order with respect to high order mode shapes, the variance previously calculated was weighted by the gradient average for any mode shape. Then, the contributions of any mode shape was added, so that a weighted variance distribution vector (WVD) was obtained:

$$WVD_i = \sum_{j=1}^{N} \left(\frac{Variance_{ij}}{Average_{ij}} \right) \tag{3.23}$$

- Selection of the M sensor positions. Two sensor selection algorithms were proposed. The first (Gr1) selected the M location having the largest WVD values, since the weighted variance measures the strength of the sensitivity to damage in a determined sensor position. The second selection algorithm (Gr2) chose the locations of the M largest peaks of WVD, obtaining so a well-distributed sensor network together with the maximisation of the associated variance.

3.6 Energetic approach

Energetic based methods maximise the energy content of the acquired signals for M sensor locations between the n candidates.

Five energetic techniques were studied:

- The Eigenvalue vector product (EVP) extensively used for both large mechanical [98] and space structures [99].
- The Driving Point Residue (DPR) or averaged DPR used by the Leuven Measurement Systems [92] for large scale modal testing on space frame structures.
- The Non-Optimal Driving Point (NODP) [54] utilised for exciter placement on large mechanical structures.
- The Condition Number method (CNM) [100] exploited for the evaluation of elastic constant of composite materials.
- The Guyan reduction based method (GRM) was used in modal testing of large aeronautic structures [81].

3.6.1 Eigenvalue vector product

The Eigenvalue Vector Product (EVP) is an energetic-based technique [98-99] consisting in the evaluation of a participation vector EVP:

$$EVP_i = \prod_{j=1}^{N} \left| \{\phi^j\}_i \right| \tag{3.24}$$

Then, in order to prevent the placement of sensors on nodal lines and to maximise their vibration energy, optimal sensor locations are those with the M largest EVP coefficients.

3.6.2 Driving point residue

The Driving-Point Residue [92] (DPR) or modal participation factor method (as previously described in section 3.4.2) is an energetic based technique that selects the sensor locations having the maximum average response over all the target mode shapes, as described by the following expression:

$$DPR_i = \sum_{j=1}^{N} \frac{\{\phi^j\}_i}{\omega_j^2} \tag{3.25}$$

A clear drawback of this method is the major importance given to the low order mode shapes compared with the high order due to the weighting of the eigenvector displacements with their respective mode frequencies. This could seriously affect the success of damage detections, because high order modes are the most sensitive to damage presence [86].

3.6.3 Non-optimal driving point

The Non-Optimal Drive Point (NODP) [54] is an energetic based method, generally used to select optimal excitation points. The NODP principle is based on the concept that the amount of vibration energy of any mode shape depends on the relative positions of the excitation source and the mode shape nodal lines. Therefore, the amount of the vibration energy measured, by sensors, is function of the relative positions of the sensors and the mode shape nodal lines. Hence, the NODP based method can be used to identify the optimal sensor placements.

The methodology consists in the evaluation of the NODP vector (3.26) and, then, in the selection of M sensor candidate locations having the M largest NODP vector coefficients.

$$NODP_i = \min_j \left| \Phi_{ij} \right| \tag{3.26}$$

3.6.4 Condition number method

The condition number (CNM) [100] is a numerical technique that selects a sensor set, which mode shape values constitute a base for the vectorial space defined by the mode shape matrix $[\Phi_{FE}]$. In order to discriminate between the infinite possible bases, the independence and the conditioning of the bases were measured using their condition number. Because the smaller the condition number value the more independent and well

conditioned the base [78], the selection criterion consisted in choosing the base with the smallest condition number.

The selection of the sensor locations by the minimisation of the condition number is obtained using an iterative algorithm articulated in two steps:

- Selection of the first sensor position. Differently from the original version of the algorithm [100] that gives no indication for the selection of the first point, the author proposed to select the candidate location having the largest EVP value (3.24), in order to avoid the selection of a base characterised by low energy content.
- Selection of the second sensor position. This task consists in the selection of the candidate sensor location that maximises the rank of the matrix $[A]_i$ and minimises its condition number, that is:

$$[A]_i = \begin{bmatrix} \{\phi^F\}_1 & \{\phi^i\}_1 \\ \{\phi^F\}_2 & \{\phi^i\}_2 \\ \vdots & \vdots \\ \{\phi^F\}_N & \{\phi^i\}_N \end{bmatrix}^T \qquad CN_i = \frac{\lambda^i_{max}}{\lambda^i_{min}} \in [1,+\infty[\tag{3.27}$$

where F is the index of the first sensor selected, while the coefficients λ_{min}^i and λ_{max}^i are the minimum and the maximum eigenvalue of the matrix $[A]_i^T[A]_i$.

The selection of the rest of the sensor positions up to the requested M is obtained by adding to the matrix A_i a new column and repeating the step 2 operations.

3.6.5 Guyan reduction based method

The objective of the Guyan reduction based method (GRM) [81-92] is to maximise the mass/stiffness ratios in order to select as sensor positions, the candidates having high inertia and low stiffness and so high vibrational energy. Therefore, the optimal sensor placements for this method are the M sensor locations that have the Maximum Ratios (MR) mass/stiffness as showed below:

$$MR_i = \max_M \frac{diag([M_{FE}])_i}{diag([K_{FE}])_i} \tag{3.28}$$

3.7 Control theory approach

The control theory approach deals with the applicability of robust observability criteria, developed for process monitoring tubular reactors for partial oxidation of Benzene to Maleic Anhydride [101].

These criteria are based on the observability concept, which defines the capability of discerning state variables using the output acquired. A problem related to this definition of observability is its binary nature: a system is simply observable or not. In the years, many researchers studied the problem [101-102] and defined measures of observability, allowing the comparison of different observable sensor configurations monitoring the same problem. Before starting the description of robust observability criteria, it is useful to give some insights into linear time invariant systems and the related control theory.

3.7.1 Linear Time invariant system from FE model

A state-space representation of a Linear Time Invariant (LTI) system is described below [103]:

$$\{\dot{x}(t)\} = [A]\{x(t)\} + [B]\{u(t)\} \quad t \geq t_0 \quad \{x(t_0)\} = \{x_0\} \tag{3.29}$$

$$\{y(t)\} = [C]\{x(t)\} \tag{3.30}$$

where the vector x, y and u are, respectively, the state variables, the measured output and the excitation vector, while the matrix [A], [B] and [C] are related to the structural matrices of the system FE model. These relationships can be evaluated by exploring the dynamic representation of the problem under investigation using the FEM approach as described below.

Considering the equation of motion:

$$[M]\{\ddot{d}\} + [L]\{\dot{d}\} + [K]\{d\} = \{F\} \tag{3.31}$$

where:

- [M], [L] and [K] are respectively, the mass the damping and the stiffness matrices of the structure FE model.
- $\{d\}, \{\dot{d}\}$ and $\{\ddot{d}\}$ are the displacement vector and its first and second time derivatives.
- {F} is the excitation force vector.

Then, assuming for example the presence of a hysteric damping, the damping matrix [L] can be rewritten as:

$$[L] = \alpha [K] \tag{3.32}$$

with α hysteric damping coefficient.

And finally, assuming the displacements d as state variables x_1 and their time derivatives $\dot{d}$ as state variables x_2, the dynamic problem described by eq. (3.31) can be written as a LTI system:

$$\{\dot{x}\} = \begin{Bmatrix} \{\dot{x}_1\} \\ \{\dot{x}_2\} \end{Bmatrix} = \begin{bmatrix} [0] & [I] \\ -\dfrac{[K]}{[M]} & -\alpha\dfrac{[K]}{[M]} \end{bmatrix} \begin{Bmatrix} \{x_1\} \\ \{x_2\} \end{Bmatrix} + \begin{bmatrix} [0] \\ \dfrac{1}{[M]} \end{bmatrix} \{F\} \tag{3.33}$$

$$y = [I \quad 0] \begin{Bmatrix} x_1 \\ x_2 \end{Bmatrix} \tag{3.34}$$

This equation system is built in the hypothesis that the outputs are only the displacements d. A further simplification may be obtained by assuming only one excitation point. This reduces the matrix B to one of its columns that corresponds to the degree of freedom excited. At the same time, the vector u(t) (the vector F) becomes a scalar.

3.7.2 Robust observability criteria based method

The robust observability criteria based methods [101-102] are founded on the control theory concept of observability [103]. From the control theory point of view, the HM

problem is an observability problem because deals with the identification of the design variables (that are function of the displacements x) through the dynamic response y(t) of the structure analysed.

Because of the binary nature of the observability, there is need to find a way to measure this system property in order to compare two observable LTI systems describing the same phenomenon.

To facilitate the explanation of the observability criteria genesis, a more deepen analysis of observable system properties is necessary.

A complete solution of LTI system, as represented by the equations (3.29-30), is given by the following expressions [103]:

$$\{y(t)\} = [C]\Psi(t,t_0)\{x_0\} + [C]\int_{t_0}^{t}\Psi(t,\tau)[B]\{u(t)\}d(\tau) \qquad t \geq t_0 \tag{3.35}$$

$$\Psi(t-t_0) = e^{[A](t-t_0)} \tag{3.36}$$

where the function $\Psi(t\text{-}t_0)$ is called state-transition matrix.

The observability concept concerns the estimation of the initial state x_0 of the LTI system with an excitation u(t) over the time range $[t_0, t]$ by means of the output y(t).

The control theory states [103] that an LTI system is completely observable on the time interval $[t_0, t]$, if and only if, the columns of the matrix $[C]\Psi(t\text{-}t_0)$ are linearly independent over $[t_0, t]$ or equivalently, its Grammian W (see eq. 3.37) is non-singular. This can be easily understood by equation (3.38), where the initial state x_0 is given as the product of the Grammian inverse and an integration term. Moreover, by this expression can be understood that the more is well conditioned the Grammian W the more the LTI system is observable [103]. In other words, it is possible to assume a measure of the Grammian non-singularity as degree of observability in order to compare different configurations of the same system.

$$W(t,t_0) = \int_{t_0}^{t}\Psi^T(t,t_0)[C]^T[C]\Psi(t,t_0)dt \tag{3.37}$$

$$x_0 = W^{-1}(t,t_0)\int_{t_0}^{t}\Psi^T(t,t_0)[C]^T y(t)dt \tag{3.38}$$

The estimation of the Grammian for the LTI system is performed by the solution of the Lyapunov equation (3.39) using a solver implemented in the commercial software MATLAB:

$$[A]^T W + W[A] + [C]^T[C] = 0 \tag{3.39}$$

A last consideration is on the physical interpretation of the Grammian coefficients. If the excitation force is supposed to be impulsive the solution y(t) of the LTI system is simplified to $[C]\Psi(t\text{-}t_0)\{x_0\}$. Hence, the Grammian diagonal coefficient W_{ii} can be interpreted as the energy content of a scaled signal (scaled because is missing the contribution of x_0), while the off-diagonal elements W_{ij} represent a degree of dependence between the two scaled signals acquired in the locations i and j.

The criteria studied in this research were based on the following three principles:

- The maximisation of the Grammian matrix trace [101].
- The Grammian determinant maximisation (proposed by the author).
- The minimisation of the condition number of the Grammian Matrix [102].

In the next sub-sections the observability criteria mentioned above are discussed.

3.7.3 Grammian trace maximisation

The Grammian trace maximisation method [101] is based on the maximisation of the observability Grammian trace to reduce the system state dimension (candidate sensor number) that for the physical interpretation of Grammians means maximising the energy measured by the sensor network.

By analysing equation (3.29) and the energy explanation for the Grammian observability, it is possible to relate the Grammian diagonal terms, associated with the displacements, to the elastic energy of the structure, and those associated with the velocity, to the kinetic energy of the structure.

Therefore, there are several possible ways to maximise the Grammian trace based on the maximisation of the elastic and/or the kinetic energy. Moreover, the interpretation of the off-diagonal coefficients could be used to maximise the energy content together with the orthogonality of the acquired signals.

Hence, five different degrees of observability based on Grammian trace criteria were explored:

- Elastic energy maximisation (Gm1, developed by the author). This criterion consists in the maximisation of the Grammian trace part related to the displacements. The selection algorithm (3.40) picks up the M candidate sensor positions associated with the M largest values of the indicated diagonal part.

$$\max_{M}[diag(W(x_1))] \tag{3.40}$$

  where $W(x_1)$ represent the partition of the observability Grammian associated with the displacements x_1.
- Kinetic energy maximisation (Gm2) [101]. It is a specular approach of the previous one with the difference that, in this case, the Kinetic energy is maximised.
- System energy maximisation (Gm3, developed by the author). This observability criterion is based on the maximisation of the system energy, in other words, the elastic plus the kinetic energy. This task was performed by adding the dimensionless contributions of the elastic (D_EE) and the kinetic energy (D_KE), and then, selecting the M candidate sensors having the largest energy contributions. The dimensionless coefficients were evaluated as follows:

$$D\_EE_i = \left(\frac{diag[W(x_1)] - \min(diag[W(x_1)])}{\max(diag[W(x_1)]) - \min(diag[W(x_1)])} \right)_i \tag{3.41}$$

$$D\_KE_i = \left(\frac{diag[W(x_2)] - \min(diag[W(x_2)])}{\max(diag[W(x_2)]) - \min(diag[W(x_2)])} \right)_i \tag{3.42}$$

- Independent elastic energy maximisation (Gm4, developed by the author). In this criterion the procedure followed was the same of the elastic energy maximisation with the only difference that the diagonal coefficients are weighted with the sum of the off-diagonal terms. In this way, by selecting the M largest weighted values (Wed_i, see eq. 3.43), the elastic energy maximisation and the independence of the measured signals should be guaranteed.

$$WEd_i = \frac{diag[W(x_1)]}{\sum_{j,i \neq j} W(x_1)_{ij}} \tag{3.43}$$

- Independent Kinetic energy maximisation (Gm5, developed by the author). It is identical to the previous selection technique, but the partition of the observability Grammian is $W(x_2)$. Therefore, the kinetic energy content is maximised together with the independence of the signals acquired.

3.7.4 The Grammian determinant maximisation

The Grammian determinant maximisation (GDM) criterion consists in the assumption of the Grammian determinant as a measure of the $[C]\Psi(t-t_0)$ columns independence.

The selection of the optimal sensor locations using this criterion was carried out by an iterative algorithm, which unselects from the candidate sensor set, the location having the smallest contribution to the Grammian determinant. The elimination of the candidate sensor identified is performed by erasing the corresponding row and column in the stiffness and mass matrices. The algorithm converges when the sensor number is downsized to the established M.

The contribution of each candidate sensor to the Grammian determinant is estimated as the sum of the projection of the Grammian rows on its eigenvector space (Ψ), as showed by the below expression:

$$CsC = \langle W\Psi \rangle^2 \tag{3.44}$$

3.7.5 The Grammian condition number criterion

The Grammian condition number criterion (GCN) [101] is based on the minimisation of the condition number of the Grammian matrix in the attempt to increase the system observability.

The procedure consists in building a matrix with the minimum condition number, whose rows are selected between the rows of the Grammian matrix.

The algorithm can be divided in three steps. The first step selects, as first row of the new matrix, a row corresponding to the candidate sensor having the largest energy content. This is identified as the first location chosen by the system energy maximisation (Gm3), trace criterion (§3.7.3).

In the second step, the algorithm picks up a second row from the Grammian matrix that minimises the condition number (3.27-b) of the matrix A_i (3.45) constituted by the row selected in the first step and another one of the Grammian matrix.

$$A_i = \begin{bmatrix} W_{F1} & \cdots & W_{i1} \\ \vdots & \ddots & \vdots \\ W_{F,2xn} & \cdots & W_{F,2xn} \end{bmatrix}^T \tag{3.45}$$

where F is the index of the first sensor selected and n is the number of the candidate sensor positions.

The last step is the iteration of the second algorithm phase until the number of candidate sensor equals the established one M.

3.8 Optimal data selection and optimal sensor placement investigation

Since, there is no presence in literature of the possible influence of optimal data selection and OSP techniques on MU based damaged detection methods, extensive investigations on their influence were carried out. A first investigation, consisting in screening among the OSP methods examined, was carried out using a cantilever beam (appendix A) and comparing the results according to three criteria. The first criterion measured the capability of each OSP technique to capture target mode property shapes. The second criterion studied the effects of the damage locations on the optimal sensor placements selected by the different methodologies investigated. The last criterion analysed the reliability and efficiency of the information provided by the OSP techniques for damage detection on the cantilever beam using the GLDDO approach.

An application to a real structure is presented in appendix B, where the OSP problem was analysed on a bridge structure for the design of a GPS sensor network aimed at the extraction of modal properties from ambient vibration. Finally, the combined influence of the optimal data selection and the OSP techniques were studied on a plate-like structure (Appendix C).

3.9 Conclusion

In this chapter, data selection methods relative to experimental data selection and OSP were explored.

In particular, experimental acquisition issues, such as technologic, economic and practical limits, were pointed out as a source of concern for the DD/MU process, since these limits were curbing down the amount of information that could be retrieved by acquired data. Therefore, the need of a clever and accurate selection of data aimed at maximising the information content and the SNR of the acquired data.

For this purpose, a procedure was developed and it was structured in three steps: the data type selection, the TMS selection and the OSP.

The data type selection involves an accurate analysis of the structure and the definition of an investigation frequency range, in order to choose the data typology to acquire. As first task, MU/DD process designers should look after structure component accessibility, sensor features (e.g. sizes, power supply), sensor-structure interactions and etc..., in order

to evaluate the technologic, economic and practical restrictions that the data monitoring faces. Then, the investigation of monitoring conditions, like environmental noise, operative conditions and etc..., helps to further define the experimental factors that concur, together with the MU/DD targets, to the evaluation of the frequency range of investigation and, finally, to the actual data type selection. An example of such procedure was showed in Appendix B for a suspension bridge.

Once, a data type is selected between modal properties and FRFs, the data type selection process is focused on the TMSS, which task is to select those TMS that best characterise the dynamic behaviour of the structures in the frequency range defined in the data type selection phase. The TMSS criteria investigated were based on the maximisation of motion (RSS), kinetic (MKE) and strain (MSE) energy of the TMS selected. A forth TMSS technique (MMF) was based on the observation that low frequency mode shapes are easier to excite, absorb the great part of the excitation energy (so their changes are easier to detect), and easier to extract than high frequency mode shapes. A comprehensive investigation of the TMSS influence on DD using the GLDDO approach, for plate-like structure, was reported in appendix C and discussed in chapter 6, where the MSE TMSS technique resulted the best, confirming its tendency (§3.3.4) to select high frequency mode shapes (at the top end of the frequency range of investigation) and their larger sensitivity to structure changes (damages) than low frequency modal properties.

After the TMSS, the identification of the optimal locations for the network sensors is the final task for the maximisation of the acquired signal information content targeted to increase the sensitivity of the MU/DD process to structural features, such as damages, tiny particular of the structure geometry and etc... Three main classes of approaches were analysed (the statistic, the energetic and the control theory approach) and, in some cases, further developed by the author. Common ground of those approaches was the maximisation of a particular measure of the strength and the independence of sensor acquired signals. The most reliable measure seemed to be the Fisher Information Matrix determinant, according to investigation results reported in appendices A, B and C, and the relative discussion in chapter 6.

CHAPTER 4: EXPERIMENTAL MODAL DATA EXTRACTION

4.1 Abstract

In recent years, technologic advancements have contributed to increase the accuracy of measurements and reduce their associated costs. However, nonetheless the huge improvements, experimental data acquisition still deals with environmental noise (on the structure and sensors), electrical noise (from the equipment), technical problems (e.g. extraction of high frequency modal properties) and etc... These issues were target of a number of publications that too often are neglected in the development of Model Updating/Damage Detection (MU/DD) techniques. Instead, in this research a global view of MU processes was considered, bringing into light the strong dependence of these procedures on data selection and acquisition. The first, data selection, extensively analysed in the previous chapter, consisted in the selection of the data type to acquire and in the design of the acquisition sensor network. This process maximised the signal information content and their SNR. However, a further improvement is needed to extract meaningful dynamic data from experimental acquired data.

In this chapter, numerical techniques were analysed and developed to extract modal properties from experimentally acquired data. Particular attention was devoted to numerical techniques capable of dealing with the presence of noise in the acquired signal.

A particular effort was put on developing techniques able to extract modal properties from ambient excitation loads.

4.2 Noise in data acquisition

Several ambient factors, such as temperature, humidity, wind, ground vibration and etc..., may introduce a certain level of uncertainty in the evaluation of the structural properties. This uncertainty can severely undermine the capability of a damage detection process to correctly identify defects or particular features of the structure. Moreover, the uncertainty in measuring FRFs and modal properties increases with the variability of ambient factors. An index widely used to measure the signal pollution derived by those factors is the Signal Noise Ratio (SNR):

$$SNR = 20\log\left(\frac{A_S}{A_N}\right) \tag{4.1}$$

where A_S and A_N are, respectively, the amplitude of the time signal and of the noise.

It is clear from eq. (4.1) that the smaller SNR the larger the noise.

In literature, there are many techniques aimed at reducing the noise effects on the measurements and, consequently, decreasing their negative influence on the DD/MU procedure. Here, only those related with FRFs and modal extraction were investigated. These techniques are mainly based on statistic evidences such as:

1. The ambient noise has a random distribution and, therefore, its average on long time periods should be zero.
2. The noise is uncorrelated with the structural dynamic response.

These properties were exploited in different ways from different researchers. However, the two main ways are:

a. To reduce the noise content in the signals through averaging. This is the only solution available for the FRFs (see §4.3). However, under a certain margin (e.g. structural integrity, exciter power limits and so on) an increase of the magnitude of the controlled excitation can reduce the effect of the noise.
b. To assume ambient excitation as random load distribution with zero mean. In this case, a structure impulsive response can be extracted using statistical based methods (see §4.4. and followings). Moreover, this choice overrules the use of FRFs and can be the right solution for the modal extraction.

These two approaches were analysed in the following paragraphs.

4.3 Frequency Response Function experimental evaluation

The Frequency Response Function (FRF) of a Multi-Degree of Freedom (MDoF) system (structure) fully defines its dynamic behaviour under external forces in the frequency space. The FRF for an MDoF system can be easily derived by the equation of motion for harmonic excitation:

$$[M]\{\ddot{d}\}+[L]\{\dot{d}\}+[K]\{d\}=\{f\}e^{i\omega t} \tag{4.2}$$

where ω identifies the excitation frequency.

Assuming that the solution of the equation of motion (4.2) is:

$$\{d\}e^{i\omega t} \tag{4.3}$$

Then, substituting eq. (4.3) into eq. (4.2) is obtained:

$$\left([K]+i\omega[L]-\omega^2[M]\right)\{d\}e^{i\omega t}=\{f\}e^{i\omega t} \tag{4.4}$$

$$\{d\}=\left([K]+i\omega[L]-\omega^2[M]\right)^{-1}\{f\} \tag{4.5}$$

Finally, extracting from eq. (4.4) the displacement vector {d} (eq. 4.5) is possible to define the FRF for displacements, named compliance, as follows:

$$[H(\omega)]=\frac{\{d\}}{\{f\}}=\left([K]+i\omega[L]-\omega^2[M]\right)^{-1} \tag{4.6}$$

The FRF for the velocity and the acceleration are called Mobility and Accelerance, respectively.

According to eq. (4.6) the FRF measured in the DoF j exciting in the DoF k is given by the ratio between the spectrum of the displacement time-history acquired in j (X_j) and the spectrum of the excitation force (F_k), as showed below:

$$H_{jk}=\frac{X_j}{F_k} \tag{4.7}$$

Ideally, a compliance measure in line with eq. (4.7) involves exciting the structure with a measurable force, acquiring the dynamic response in time and, finally, computing the ratio between the response and the force spectra. In practice, there are a number of problems to cope with, such as:

- Mechanical noise in the structures, including non-linear behaviour.
- Electrical noise in the instrumentation.
- Limited analysis resolution (related to the spectra evaluation [105]).

In order to minimise the impact of these drawbacks on the FRF measures, a statistical approach is needed. There are two different approaches according to when the noise is reckoned to be either in the structure dynamic response measurements (output) or in the actuation (input).

In the first case, the force time history is recorded by a force transducer directly connected at the point where the excitation is provided. Therefore, apart from an inevitable very low level electric noise in the instrumentation, the true actuation can be measured.

External/internal dynamic process (machines, wind, footsteps, joints etc.) may generate added vibration to the test object. Therefore, the response signal not only contains the response due to the measured excitation, but also the response due to the ambient vibration. These conditions define a typical measurement having noise in the measured output signal.

The solution found to minimise the noise at the output is based on the principle of least squares that allows defining the best FRF estimator as [106]:

$$H(\omega)=\frac{\sum F^{*}X}{\sum F^{*}F} \tag{4.8}$$

where F and F^{*} are, respectively, the excitation force spectrum and its conjugate, while X identifies the structure response spectrum.

This estimator is called H_1 and can be seen as the ratio between the response and the force cross spectrum (G_{FX}) and the autospectrum of the force (G_{FF}) [105]:

$$H_1(\omega) = \frac{\sum G_{FX}}{\sum G_{FF}} \tag{4.9}$$

The best estimator H_1 is capable of removing the random noise through the averaging process, eq. (4.9), and converging to the true FRF (H) with the increase of the number of averages.

When actuator natural frequencies are among those excited, the actuator cannot drive the structure at its natural frequencies. In this case the SNR may drop significantly at those frequencies making the FRF meaningless. This situation describes one of the possible sources of noise in the input measures. Using once again the least square approach, the best estimator for such conditions is given by the ratio of the autospectra of the response G_{XX} and the force and response cross spectrum G_{XF} [106]:

$$H_2 = \frac{\sum G_{XX}}{\sum G_{XF}} \tag{4.10}$$

As for H_1, H_2 converges to the true FRF with the increase of the number of averages. When the noise is present in both the input and the output, H_1 and H_2 generally form a confidence interval for the true FRF (H) [106]:

$$H_1 \leq H \leq H_2 \tag{4.11}$$

In this situation, the selection of the most suitable FRF estimator depends on the FRF itself and its applications. For example, in presence of random excitation, H_2 is the best estimator because cancels the noise at the input. For impact excitation both the estimators are equal at the resonances, while at the antiresonances H_1 is the best, since the dominant problem is in the output.

4.4 Experimental modal extraction

Whenever structure environmental excitations cannot be neglected or excitation control is not possible, the characterization of structure dynamic behaviour is left to the acquisition of modal properties using environmental excitation. This is essential for HM of large civil structures such as bridges, offshore platforms and etc..., enabling the use of MU/DD techniques, as the GLDDO approach, otherwise useless.

In literature, there is a large branch of modal extraction techniques that deals with ambient excitation. Common point in all approaches developed is the assumption that for structures under their natural working conditions, excitations cannot be measured. They are usually non-stationary and of complex nature. Examples are offshore structures subject to the turbulent action of the swell, which depends on wind and weather conditions; aircraft structures subject to strength, varying with flight conditions; bridges subject to wind, traffic, etc...

For the techniques reviewed, the nature of the ambient excitation is assumed to be an unobserved white noise. This hypothesis was proved true by many experimental

applications provided on: pre-stressed concrete tower [107-109], steel transmitter mast [110], large concrete bridges [111-113] and on aircrafts [114].

Two main approaches are available in literature. The first procedure splits the modal extraction in two steps [107-109, 113, 115]:

1. Computation of free-decay signals out of the ambient excited dynamic response. This task is carried out exploiting the properties of the white noise signals, which describes the ambient excitation.
2. Modal properties extraction. This can be performed using any kind of modal extraction techniques able to work either with the free-decay signals or their spectra. A comprehensive survey of these methods can be found in [116].

The second approach extracts the modal properties in one step using different stochastic solutions that are listed below:

- Reference-based stochastic subspace identification method [110]. Basically this methodology avoid the computation of the output (ambient structure response) covariance matrix through a cleverly designed projection of the row space of the future outputs into the row space of past reference outputs.
- Matrix block Hankel stochastic realisation method [117]. This technique is based on the Hankel matrix of a state-space system, representing the structure under investigation.
- Multivariate AR model [111]. The method is based on the equivalence between the correlation function matrix for the responses of a linear system subject to white noise input and the deterministic free-vibration response of the system. This assures a correct evaluation of the coefficient of the ARV model through the use of a least square approach.

The main difference between the two main approaches lies on the fact that in many cases with the stochastic based methods some of the entities extracted may have no physical meaning, therefore, a post-processing interpretation of the output is necessary. Moreover, the modal properties are not sorted out in crescent order with the frequency. Therefore, it may be difficult to adjust the variables involved in order to end up with the number and the modal properties requested. Finally, since there is not any reference on the physical sense of the characteristic extracted, there is no way to understand if a natural frequency extracted is coupled with another that has not been yet computed. This is a big problem especially with high modal density structures (for example aeronautic structures), where coupled natural resonances are common.

This lack of control on the output of the modal property extraction undermines the possibility of automating the health monitoring process. Moreover, a very expert user is needed to sort out the uncertainty of the data extracted.

In order to avoid this drawback, the current research was focused on the two step approach, which can guarantee a better control on the output of the modal process, since the actual extraction is performed using conventional techniques [116].

The modal extraction procedure investigated in this work was organised in two parts:

1. Ambient response pre-processing. For this task two techniques were analysed, the Random decrement techniques (RDT) and the Cross-Correlation Function based (CCF) technique.

2. Modal property extraction. This assignment was investigated through two different techniques, the Eigensystem Realisation Algorithm (ERA) and the Wavelet Based Modal Extraction (WBME) technique. The first was selected for its large noise withstanding capabilities (§4.6.1), while the second (§4.6.2) was considered for its capability of extracting a specific vibration mode and for its physically interpretable outputs.

4.5 Ambient response pre-processing

Ambient response pre-processing is based on the concept that the ambient responses are composed by two components: the structural and the random constituent. The structural component is a free-decay signal (Figure 4) containing all the resonance characteristics of the structure stimulated by the ambient excitation. The second component is characterised by a random distribution that is modelled as a white noise distribution [107-117].

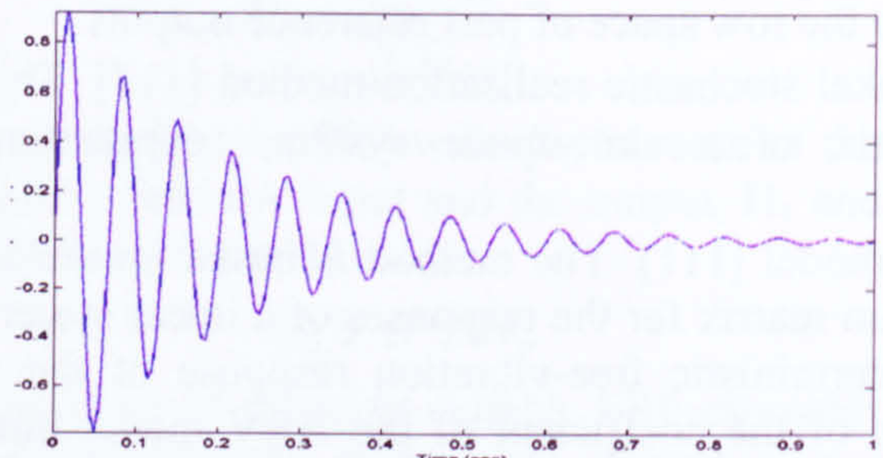

Figure 4 – Free-decay signal

The separation procedure of the two components consists in stochastic algorithm based on the white noise properties. According to those properties [118] a random process f (t) is said to be white if it has zero mean (4.12) and the (auto-)correlation function (4.13) proportional to an impulse (Figure 5).

$$m_f(t) = E[f(t)] = \lim_{T\to\infty} \frac{1}{2T} \int_{-T}^{+T} f(t)dt = 0 \tag{4.12}$$

$$R_{ff}(\tau) = E[f(t)f(t+\tau)] = \lim_{T\to\infty} \frac{1}{2T} \int_{-T}^{+T} f(t)f(t+\tau)dt = \frac{N_0}{2}\delta(\tau) \tag{4.13}$$

where δ is the Dirac delta function [118].

The Fourier transformation of eq. (4.13) (see eq. 4.14, [118]) is constant at every frequency and is equal to the amplitude of the impulse (Dirac delta function, see third term eq. 4.13), termed spectral height.

$$S_f(\omega) = \int_{-\infty}^{+\infty} R_{ff}(\tau)e^{-i\omega\tau}d\tau = \int_{-\infty}^{+\infty} \frac{N_0}{2}\delta(\tau)e^{-i\omega\tau} = \frac{N_0}{2} \tag{4.14}$$

A constant spectrum throughout the frequency space is not realistic, since ambient excitation is associated with natural phenomena, which generally is quite limited and changes with the characteristics of structures (e.g. wind-structure interaction and

turbulence derived from) and their operative conditions (e.g. traffic for civil structures). However, the constant amplitude excitation at low frequencies can be considered true [118] and, therefore, the white-noise assumption correct.

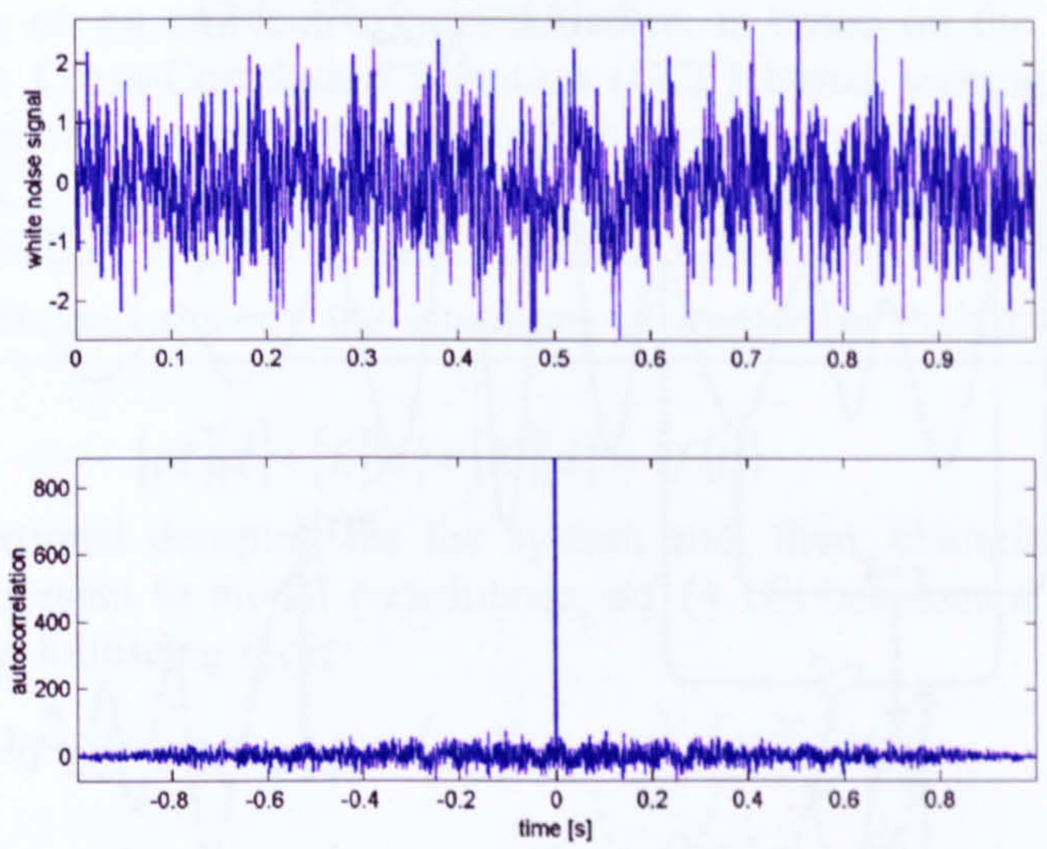

Figure 5 - White noise signal: (a) time history; (b) autocorrelation.

Two methodologies exploiting the white noise properties were investigated, the Random decrement technique (RDT) and the Cross-Correlation Function based (CCF) technique.

4.5.1 Random decrement technique

The Random Decrement Technique (RDT) [107-109, 115] is the most used methodology to separate the free-decay signal from the random component of the ambient response.

The dynamic response of a structure under ambient excitation at the instant $t+t_0$ is given by the combination of three contributions [108, 116]:

- The step response due to the initial displacement at the time $t=t_0$.
- The Impulse Response Function (IRF) caused by the initial velocity at the time t_0.
- The random response due to the random excitation applied to the structure in the time interval $[t_0, t+t_0]$.

The RDT procedure is divided in two steps, the ambient response segmenting and the averaging.

The ambient response segmenting consists in extracting signal segments of constant time length $[t, t + \tau]$ from the ambient dynamic response of the structure *s(t)*, every time that the triggering condition is satisfied (e.g. when the signal amplitude reaches a certain value x_0 as showed in Figure 6). For the full list of triggering condition refer to [108].

These segments are then averaged (averaging step, see Figure 7 and eq. 4.15), so as that the IRF and the random contribution are even out, leaving only a free-decay signal named randomdec signature. The IRF component of the signal is averaged out, since the initial velocity sign appears alternatively (Figure 7), while the random component is

assumed to have zero mean (white noise assumption). This hypothesis is valid [108, 116] for long acquisition times.

$$\delta_N(\tau) = \frac{1}{N}\sum_{r=1}^{N} s(t_r + \tau) \tag{4.15}$$

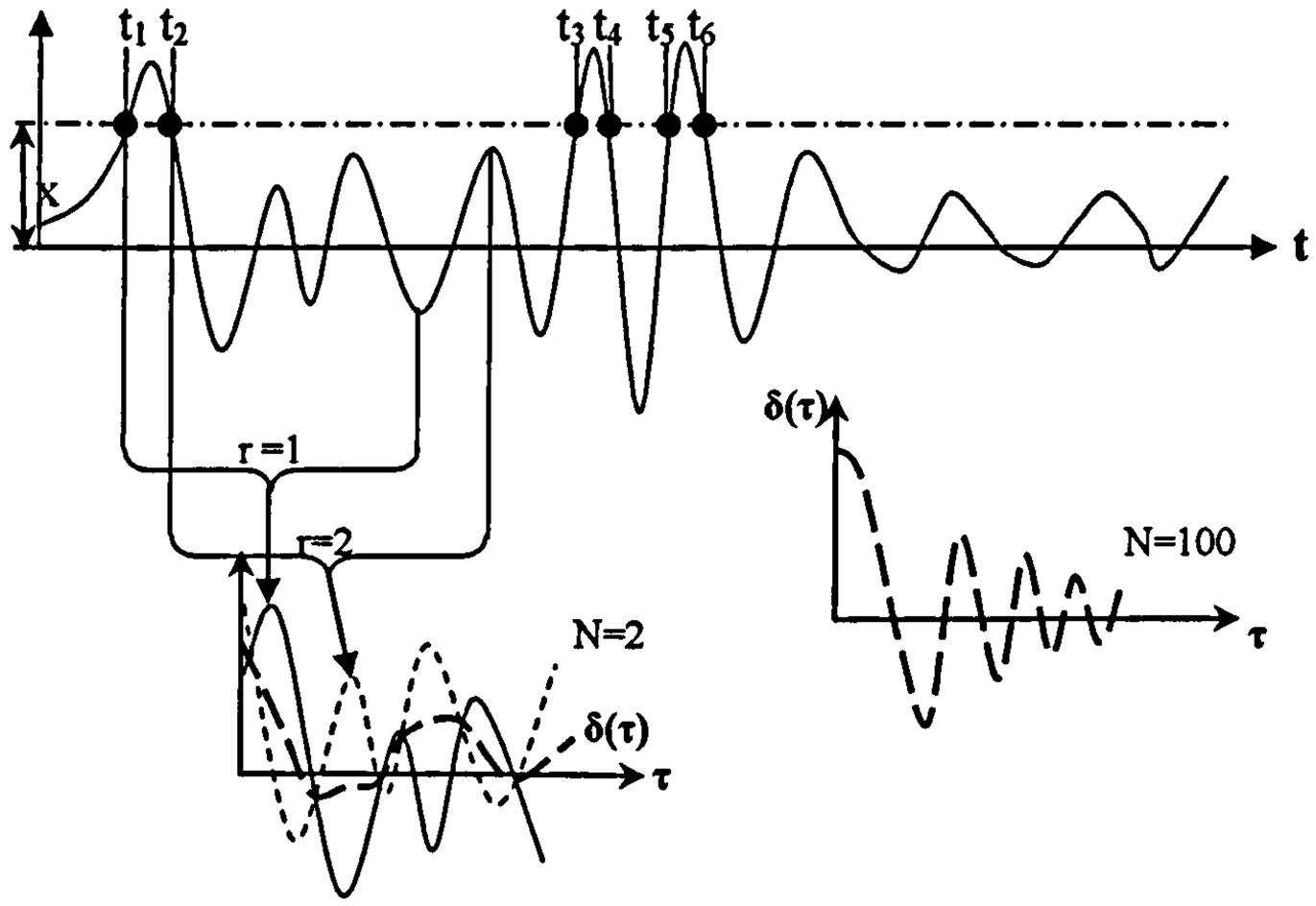

Figure 6 – Time segment selection.

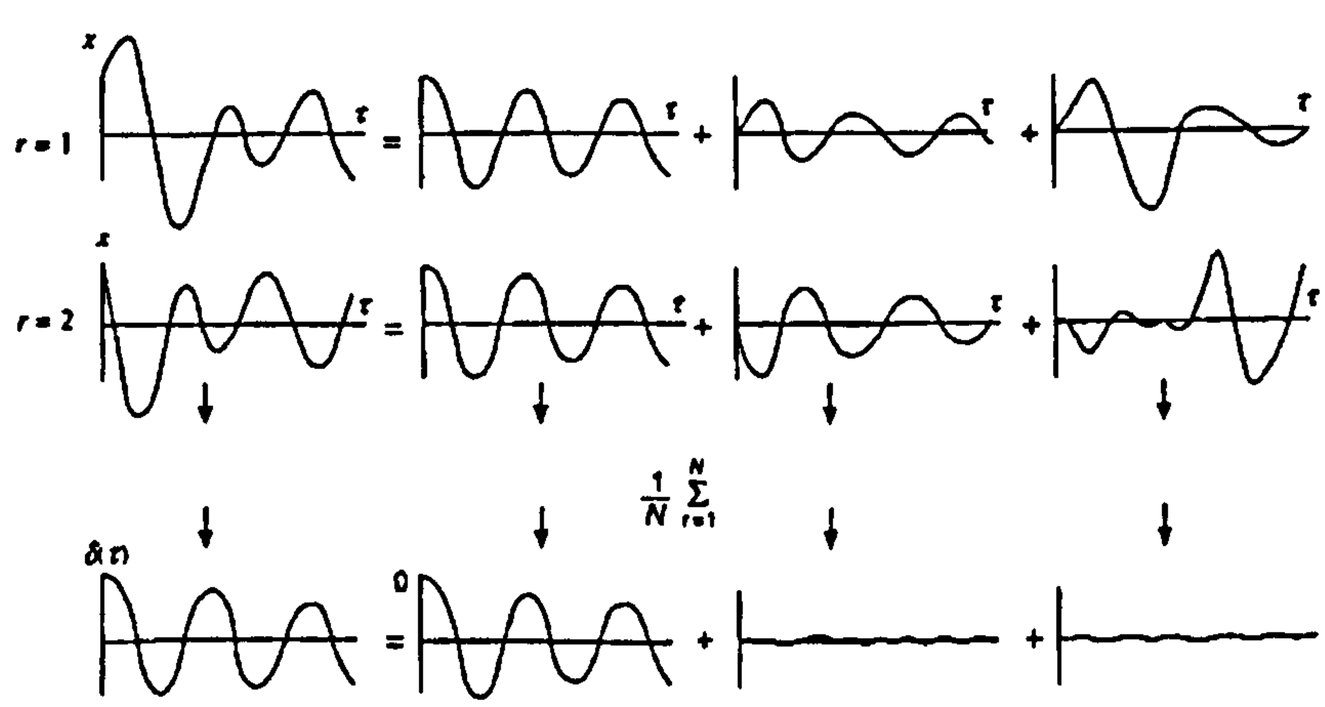

Figure 7 –Time segment averaging [116].

For multi-DoF systems, the same procedure is extended to each DoF. However, because the measurement at every DoF are synchronised, the ambient response segmenting has to be performed just for only one degree of freedom and, then, applied to all the remaining system DoFs.

4.5.2 Cross-Correlation Function based technique

The second technique investigated to evaluate a system impulse function from measurements made on an ambient excited structure, is based on the cross-correlation function [113]. The Cross-Correlation Function (CCF) based technique evaluates the CCF between the ambient responses measured on the structure using one as reference. The output of the CCF is a free-decay signal having the same characteristics as a system impulse response function. A proof of such outcome is given below [113].

For an n DoFs damped system, the equations of motion in their matrix formulation appear as:

$$[M]\{\ddot{d}\}+[L]\{\dot{d}\}+[K]\{d\}=\{f(t)\} \tag{4.16}$$

Assuming proportional damping for the system and, then, changing the coordinate system from the Cartesian to modal coordinates, eq. (4.16) becomes a set of uncoupled scalar equations with following form:

$$\ddot{q}^r+2\zeta^r\omega_n^r\dot{q}^r+(\omega_n^r)^2q^r=\frac{1}{m^r}\{\phi^r\}^T\{f(t)\} \tag{4.17}$$

where the superscript r denotes values associated with the r^{th} mode, q represents the displacement in modal coordinates, ϕ is the mode shape vector, ω_n is the natural frequency, and m is the modal mass.

Applying the convolution integral using a general forcing function and zero initial condition, the solution of eq. (4.17) is obtained. Then, it is back-transformed into the original coordinates:

$$\{d\}=\sum_{r=1}^{n}\{\phi^r\}^T\int_{-\infty}^{t}\{\phi^r\}^T\{f(\tau)\}g^r(t-\tau)d(\tau) \tag{4.18}$$

where $g^r(t)=\left(\frac{1}{m^r\omega_d^r}\right)e^{\zeta\omega_n^r t}\sin(\omega_d^r t)$ the impulse response function associated with the mode r, ω_d^r is the rth damped natural frequency.

Hence, the dynamic response for the DoF i due to the excitation $f_k(t)$ in the location k according to eq. (4.18) is given by:

$$d_{ik}=\sum_{r=1}^{n}\phi_i^r\phi_k^r\int_{-\infty}^{t}f_k(\tau)g^r(t-\tau)d\tau \tag{4.19}$$

If $f(\tau)$ is a Dirac delta function at $\tau=0$, eq. (4.19) becomes:

$$d_{ik}=\sum_{r=1}^{n}\left(\frac{\phi_i^r\phi_k^r}{m^r\omega_d^r}\right)e^{\zeta\omega_n^r t}\sin(\omega_d^r t) \tag{4.20}$$

According to the cross-correlation function definition given in [118], the cross-correlation function R_{ijk} relative to two dynamic responses measured at locations i and j generated by a white noise random excitation in k is:

$$R_{ijk}(T)=E\{x_{ik}(t+T)x_{jk}(t)\} \tag{4.21}$$

Taking into account eq. (4.20), the CCF (4.21) between two dynamic signals acquired respectively in *i* and *j* for a white noise excitation in k becomes:

$$R_{ijk} = \sum_{r=1}^{n}\sum_{s=1}^{n}\phi_i^r\phi_k^r\phi_i^s\phi_k^s \int_{-\infty}^{t}\int_{-\infty}^{t+T} g^r(t+T-\sigma)g^s(t-\tau)E\{f_k(\sigma)f_k(\tau)\}d\sigma d\tau \qquad (4.22)$$

Recalling that the auto-correlation function of white noise *f(t)* is impulsive (see eq. 4.13) and, then, renaming the spectral height as α_k and considering λ=t-τ, eq. (4.22) becomes:

$$R_{ijk} = \sum_{r=1}^{n}\sum_{s=1}^{n}\alpha_k\phi_i^r\phi_k^r\phi_i^s\phi_k^s \int_{-\infty}^{t+T} g^r(\lambda+T)g^s(\lambda)d\lambda \qquad (4.23)$$

From the g^r definition and the trigonometric identity for the sine of a sum, eq. (4.23) is simplified out as:

$$R_{ijk}(T) = \sum_{r=1}^{n} G_{ijk}^r\left[e^{-\zeta^r\omega_n^r T}\cos(\omega_d^r T)\right] + H_{ijk}^r\left[e^{-\zeta^r\omega_n^r T}\sin(\omega_d^r T)\right] \qquad (4.24)$$

where

$$\begin{Bmatrix} G_{ijk}^r \\ H_{ijk}^r \end{Bmatrix} = \sum_{s=1}^{n}\frac{\alpha_k\phi_i^r\phi_k^r\phi_i^s\phi_k^s}{m^r\omega_d^r m^s\omega_d^s}\int_0^{+\infty} e^{(-\zeta^r\omega_n^r-\zeta^s\omega_n^s)\lambda}\sin(\omega_d^r\lambda)\begin{Bmatrix}\sin(\omega_d^r\lambda)\\ \cos(\omega_d^r\lambda)\end{Bmatrix}d\lambda \qquad (4.25)$$

The last two equations (4.24) and (4.25) describe a decaying behaviour of the CCF R_{ijk} as sum of decaying sinusoids having the characteristics of a system impulse response function.

Therefore, the eigenvalues (natural frequencies) and eigenvectors (mode shapes) extracted by the CCFs coincide with those of the structures under environmental loads.

4.6 Modal property extraction

Comprehensive surveys on modal extraction methodologies can be found in [73, 116].

Between the several existing techniques, the attention was focused on those methods that were prone to be automated, capable of withstanding large level of noise and screening between coupled natural frequencies. These characteristics seemed to identify a brand new technique, the Wavelet Based Modal Extraction (WBME) technique [109, 112 and 115], which recently is becoming very popular due to its singular analysis approach. For comparison reason together with this technique a second technique was investigated the Eigensystem Realisation Algorithm (ERA) [119-120]. The ERA is a well known technique and very reliable in presence of noise [120] and high modal density [121-122], and easy to automate.

4.6.1 Eigensystem Realisation Algorithm

The Eigensystem Realization algorithm [119-120] is an evolution of the Ho-Kalman approach [123] for time-domain (state-space) problems. This work introduced the concept of minimum realization, which allows the identification of a model with the

smallest state dimension that has the same input-output relations of the real system within a specified degree of accuracy. Moreover, it was showed that the minimum realization problem is equivalent to a problem described by a sequence of real matrices known as Markov parameters (impulse response functions).

The ERA advantages lie in its capability of minimizing the distortion of the state-space parameters caused by noise. This is accomplished by introducing in the minimum-order realization identification, the Singular Value Decomposition (SVD) approach [78], which is widely recognized as being very effective and numerically stable in presence of noise.

The ERA is based on a state-space representation of the equation of motion (4.16) as already described in section 3.7.1 by the following equations:

$$\{\dot{x}(t)\} = [A]\{x(t)\} + [B]\{u(t)\} \quad t \geq t_0 \quad \{x(t_0)\} = \{x_0\} \tag{3.29}$$

$$\{y(t)\} = [C]\{x(t)\} \tag{3.30}$$

The LTI matrices [A], [B] and [C] are function of the mass, damping and stiffness matrix as showed by the equation 3.33 and 3.34.

The continuum solution of the equations above described was reported in section 3.6.2 (equations 3.35 and 3.36). This can be easily converted in a discrete solution for a constant time sampling Δt as follows [124]:

$$x(k+1) = \Psi x(k) + Gu(k) \quad G = [g_1, g_2, \cdots, g_m] \tag{4.27}$$

$$y(k) = Cx(k) \quad C^T = [c_1^T, c_2^T, \ldots, c_p^T] \tag{4.28}$$

where

- $\Psi(t - t_0) = e^{[A]\Delta t}$ is the state-transition matrix.
- $G = \int_0^{\Delta t} \Psi B d(\tau) = (\Psi - I)A^{-1}B$.
- x is a n-dimensional state vector.
- u is a m-directional input or control vector.
- y is an p-dimensional output or measurement vector.
- k is the sample indicator.

The system described by the equations (4.27) and (4.28) admits two special solutions, known as Markov parameters. The first solution is for an impulsive excitation:

$$y_{ji}(k) = c_j \Psi^{k-1} g_i \quad i = \{1,2,\cdots,m\} \quad j = \{1,2,\cdots,p\} \quad k = \{1,2,\cdots\} \tag{4.29a}$$

that in matrix form becomes:

$$Y(k) = C\Psi^{k-1}G \tag{4.29b}$$

While the second solution for an initial state response, identified by the vector of the initial condition $[x_1(0), x_2(0), \ldots, x_m(0)]$, is:

$$Y(k) = C\Psi^k [x_1(0), x_2(0), \cdots, x_m(0)] \tag{4.30}$$

The ERA aim is to solve a realization problem consisting in the evaluation of the characteristics of a system in its state variable form (Ψ, G, C), by using its output defined by the equations (4.29) and (4.30).

The first step toward the solution of the realization problem, mentioned above, is the construction of an r x s (r by s) block matrix $H_{rs}(k-1)$ known as generalized Hankel matrix:

$$H_{rs}(k-1)=\begin{bmatrix} Y(k) & Y(k+t_1) & \cdots & Y(k+t_{s-1}) \\ Y(j_1+k) & Y(j_1+k+t_1) & \cdots & Y(j_1+k+t_{s-1}) \\ \vdots & \vdots & \ddots & \vdots \\ Y(j_{r-1}+k) & Y(j_{r-1}+k+t_1) & \cdots & Y(j_{r-1}+k+t_{s-1}) \end{bmatrix} \tag{4.31}$$

where $j_i=\{1, 2, \ldots, r\text{-}1\}$ and $t_i=\{1, 2, \ldots, s\text{-}1\}$ are arbitrary integers.

Recalling eq. (4.29b) and the definition of observability and controllability matrices [103] the Hankel matrix for the state k, $H_{rs}(k)$, can be written as:

$$H_{rs}(k)=\begin{bmatrix} C \\ C\Psi^{j_1} \\ \vdots \\ C\Psi^{j_{r-1}} \end{bmatrix}\Psi^k\begin{bmatrix} G & A^{t_1}G & \cdots & A^{t_{s-1}}G \end{bmatrix}=V_r\Psi^k W_s \tag{4.32}$$

where the observability matrix V_r is a rp x n rectangular matrix, while the controllability matrix W_s is a n x ms rectangular matrix.

In order to proceed to the extraction of the matrices Ψ, G and C defining the system under investigation from the Hankel matrix is necessary evaluate a matrix $H^{\#}$ satisfying the following relation:

$$W_s H^{\#} V_r = I_n \tag{4.33}$$

The matrix $H^{\#}$ is the pseudo-inverse of the matrix $H_{rs}(0)$ as the following identities prove:

$$H_{rs}(0)H^{\#}H_{rs}(0)=V_rW_sH^{\#}V_rW_s=V_rW_s=H_{rs}(0) \tag{4.34}$$

The $H_{rs}(0)$ pseudo-inverse computation can be easily carried out by using the SVD theorem [78]. According to the SVD theorem, $H_{rs}(0)$ can be decomposed into three matrices (see eq. 4.35), P (rp x n) and Q (ms x n), which are orthogonal matrices [78] and a diagonal matrix D with positive elements $[d_1, d_2, \ldots, d_n]$.

$$H_{rs}(0)=PDQ^T \tag{4.35}$$

Equation (4.32) for k=0 gives eq. (4.35) as showed below:

$$H_{rs}(0)=P_dQ^T=V_rW_s \tag{4.36}$$

Pre-multiplying eq. (4.36) for P_d^T and then solving it for Q^T yields:

$$TW_s=\left(P_d^TP_d\right)^{-1}P_d^TV_rW_s=Q^T \tag{4.37}$$

The matrix T is non singular because there is a matrix U:

$$U=W_sQ\left(Q^TQ\right)^{-1}=W_sQ \tag{4.38}$$

such that $TU=I$ by eq. (4.37). Therefore, if $TU=I$ also $UT=I$ and, finally, by eq. (4.37):

$$UT=W_sQ\left(P_d^TP_d\right)^{-1}P_d^TV_r=I_n \tag{4.39}$$

By comparing eq. (4.33) to eq. (4.39) results that the pseudo-inverse of $H_{rs}(0)$ is equal to:

$$H^{\#} = Q\left(P_d^T P_d\right)^{-1} P_d^T = Q\left(DP^T PD\right)^{-1} DP^T = QD^{-1}P^T = QP_d^{\#} \tag{4.40}$$

Finally, the Markov parameter Y(k+1) can be derived from the equations (4.31) and (4.32) as follows:

$$Y(k+1) = E_p^T H_{rs}(k) E_m \tag{4.41}$$

where $E_p^T=\{I_p, 0_p, \ldots, 0_p\}$ (p x pr) and $E_m^T=\{I_m, 0_m, \ldots, 0_m\}$ (m x ms) with I and 0 respectively identity and null matrices of order p or m.

To finish, rearranging equation (4.41) according to eq. (4.32), (4.33) and (4.40), the Markov parameters can be estimated as:

$$Y(k+1) = E_p^T PD^{1/2}\left[D^{-1/2}P^T H_{rs}(1)QD^{-1/2}\right]D^{1/2}Q^T E_m \tag{4.42}$$

Then comparing eq. (4.42) and eq. (4.29b), the matrices Ψ, G and C can be estimated as:

$$\Psi = D^{-1/2}P^T H_{rs}(1)QD^{-1/2} \tag{4.43}$$

$$G = D^{1/2}Q^T E_m \tag{4.44}$$

$$C = E_p^T PD^{1/2} \tag{4.45}$$

Once, the matrices, Ψ, G and C, are evaluated, the realization problem is solved. The only remaining task is the computation of the modal properties (circular frequency ω_i, modal damping ζ_i and mode shape ϕ_i), which are related to the eigenvectors (Ξ) and eigenvalues (μ) of the state-transition matrix Ψ [124-125] according to the following expressions:

$$\omega_i = \frac{1}{\Delta t}\sqrt{\left[\ln\left(\mu_i \mu_i^*\right)\right]^2 + 4\left[\cos^{-1}\left(\frac{\mu_i + \mu_i^*}{2\sqrt{\mu_i \mu_i^*}}\right)\right]^2} \tag{4.46}$$

$$\zeta_i = \frac{\left[\ln\left(\mu_i \mu_i^*\right)\right]^2}{\sqrt{\left[\ln\left(\mu_i \mu_i^*\right)\right]^2 + 4\left[\cos^{-1}\left(\frac{\mu_i + \mu_i^*}{2\sqrt{\mu_i \mu_i^*}}\right)\right]^2}} \tag{4.47}$$

$$\Phi = \{\phi_1, \phi_2, \cdots, \phi_n\} C\Xi \tag{4.48}$$

In brief the modal extraction process using the ERA algorithm consists in the following steps:

1. Construction of the Hankel matrices for k={0, 1} according to equation (4.31) using the free-decaying dynamic responses of the structure.
2. Singular Value Decomposition of the $H_{rs}(0)$ (SxS). This operation provides n singular values if n ($<S$) is the rank of $H_{rs}(0)$. Unfortunately, because of the noise presence in the real data, the SVD generally can give up to S singular values. Hence, in order to reduce the effect of the noise an empirical threshold χ is settled to discard those

singular values smaller than it. The χ value is based on information about the acquisition error, the noise level, previous experiences on the same structure or environment and etc...

3. Evaluation of the sub-matrices of P, D and Q derived at the step 2. If n singular values result larger than χ, only the restriction of the matrices P, D, and Q relative to these n singular values are used for the computation of the realization problem. This approach reduces the noise impact on the system identification.
4. Evaluation of the system matrices: Ψ, G and C. This task is carried out using equations (4.43-4.45).
5. Estimation of the system modal properties out of the system realization (the matrices Ψ, G and C) using equations (4.46-4.48).

4.6.2 Wavelet Based Modal Extraction method

The Wavelet Based Modal Extraction (WBME) method is a new technique that exploits the capability of wavelets to decompose a signal in the time-frequency space [126]. More information about the wavelet properties and their behaviour in decomposing a time-signal in the time frequency field are given in chapter 6.

In this chapter only the wavelet properties that are utilized for modal extraction are analysed. At the aim to have an organic understanding of the wavelet characteristics employed for the modal extraction, this section was divided in 3 subsections:

1. Wavelet governing relationships.
2. Wavelet resolution.
3. Wavelet system identification algorithm.

4.6.2.1 Wavelet governing relationships

The wavelet transform is a linear decomposition of an arbitrary signal $s(\tau)$ on basis functions that are simply dilations and translations of the parent wavelet $g(\tau)$ through the convolution function [115]:

$$W(a,t)=\frac{1}{\sqrt{a}}\int_{-\infty}^{\infty}s(\tau)g^{*}\left(\frac{\tau-t}{a}\right)d\tau \tag{4.49}$$

where a is the dilation parameter and t is the translation parameter.

Equation (4.49) appears in the frequency space as:

$$W(a,t)=\frac{1}{2\pi\sqrt{a}}\int_{-\infty}^{\infty}S(\omega')G^{*}\left(\frac{\omega'}{a}\right)e^{-j\omega' t} \tag{4.50}$$

where S and G are the Fourier transform of $s(\tau)$ and $g(\tau)$.

According to equations (4.49-4.50), time-frequency localisation is possible using wavelets since parent wavelet acts as window functions. The wavelet coefficients, $W(a, t)$, represent a measure of the similitude between the dilated/shifted parent wavelet and the signal at that time t and scale (frequency) a. According to this interpretation is simple to draw the following conclusions [127]:

- The resolution along the time axis increases with the frequency (decrease of the dilation parameter, eq. 4.49).
- Along the frequency axis, the resolution is inversely proportional to the dilation parameter *a*.

These two observations describe the multi-resolution property of the wavelet transform (Figure 8).

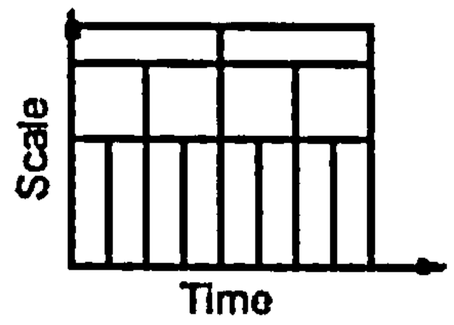

Figure 8 - CWT Resolution.

The relation between the dilation coefficient and a (pseudo) frequency is given by [128]:

$$F_a = \frac{F_c}{a\Delta t} \tag{4.51}$$

where F_c is the central frequency of the parent wavelet.

Nonetheless, the countless number of existing parent wavelets used for the most various applications, when it comes to system identification [109, 112, 115 and 129] only one kind of wavelet is used, the complex Morlet wavelet, through the Continuous Wavelet Transform (CWT).

The reasons for this choice can be found in the analogies between the Morlet wavelets and the Fourier transforms expressed by the following equation [115]:

$$g(t) = e^{-\frac{t^2}{2}}\left(\cos(\omega_0 t) + i\sin(\omega_0 t)\right) \tag{4.52}$$

Mainly, the Morlet wavelets are a Gaussian-windowed Fourier transform (Figure 9), with a central frequency $f_0=\omega_0/2\pi$.

By maximising eq. (4.52) in the frequency domain (eq. 4.54, [115]) a unique relation between the dilation parameter *a* and the frequency *f* is obtained [115]:

$$f = \frac{a}{f_0} \tag{4.53}$$

$$G(af) = \sqrt{2\pi}\, e^{-2\pi^2(af-f_0)^2} \tag{4.54}$$

The wavelet coefficients evaluated by a CWT of a time signal are generally analysed in terms of their square modulus $|W(a,t)|^2$, termed scalogram [115], and are plotted in the time-frequency space as shown in Figure 10. In the scalogram, the coefficients achieve their maximum value at the instantaneous frequency (Figure 10), corresponding to the dominant frequency in the signal analysed at each instant in time. The instantaneous frequencies varying in the time build up the ridges (Figure 10), whose coefficients define the skeleton. The skeleton has a real and imaginary part, which represents the signal and its Hilbert transform at the ridge frequency.

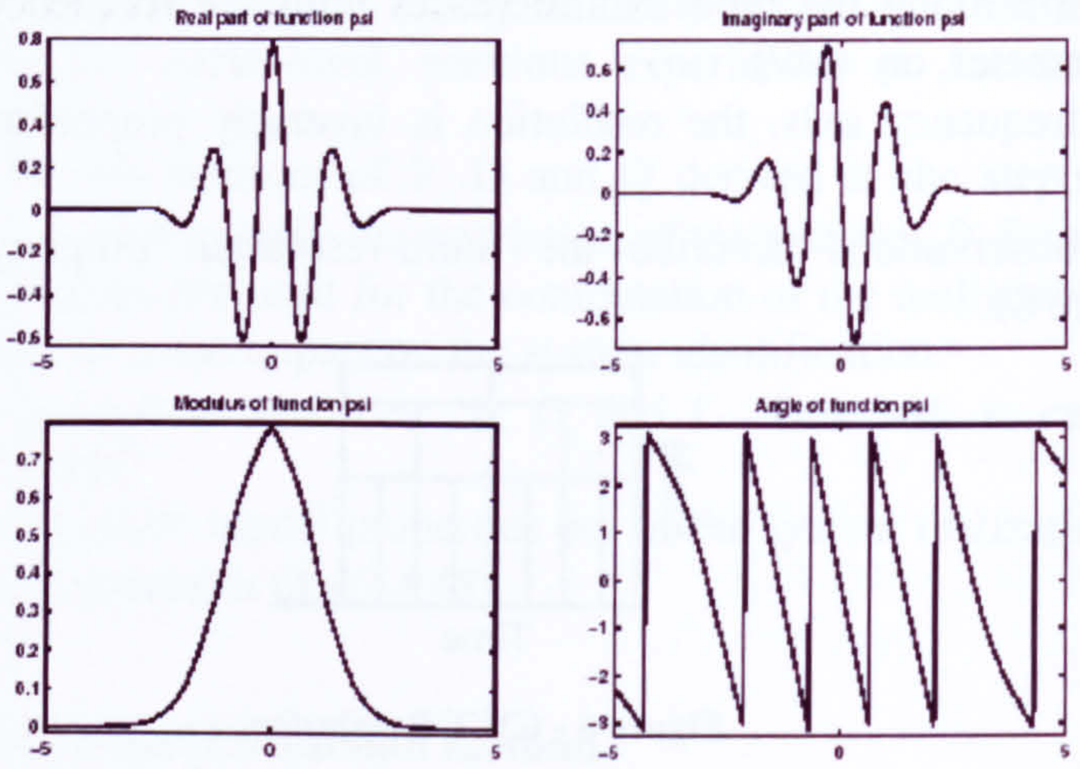

Figure 9 - Morlet Wavelet.

At each time instant of the phenomenon analysed an instantaneous spectrum can be estimated as a slice of the scalogram at a given time (Figure 10).

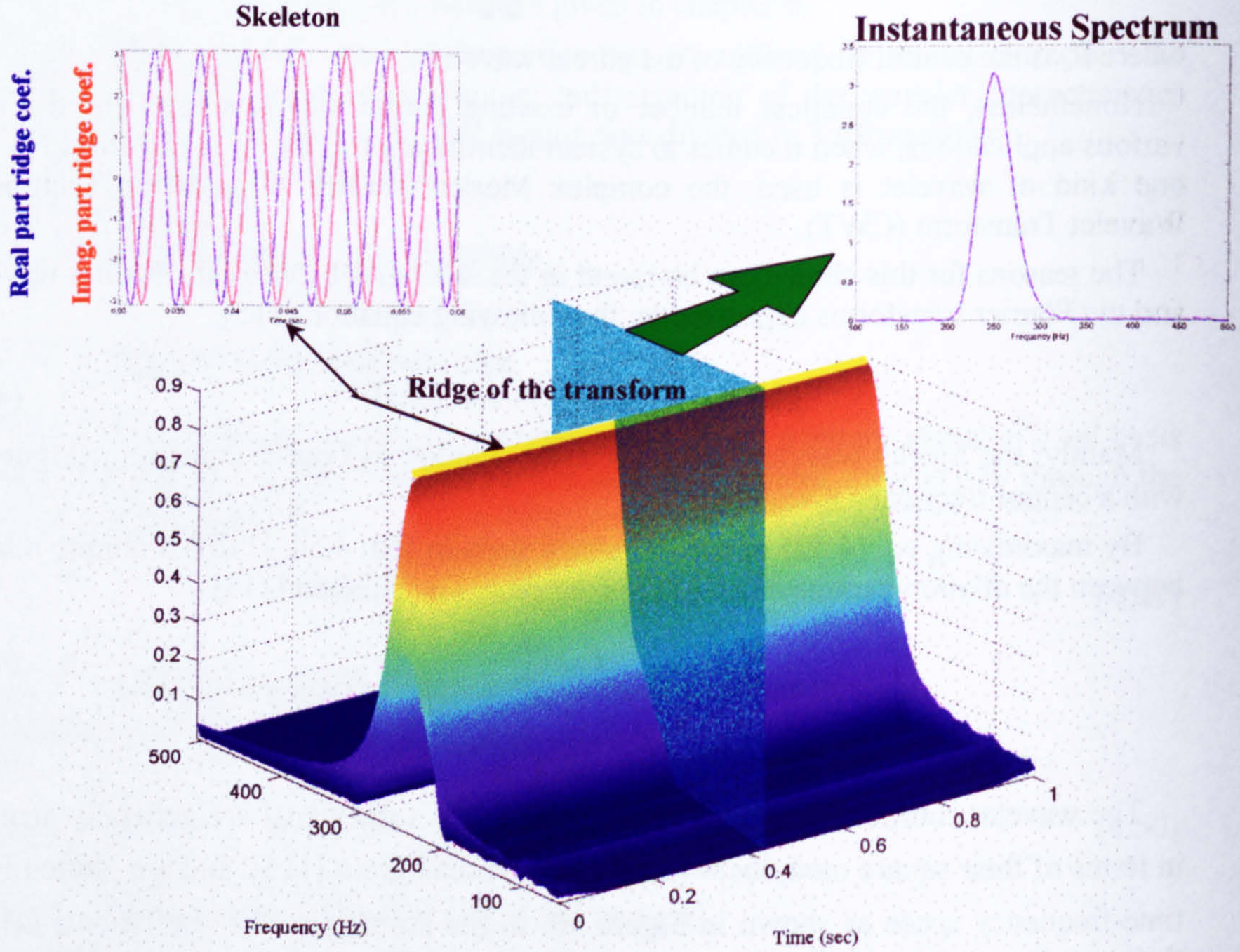

Figure 10 – Wavelet scalogram properties.

The time and frequency resolution are essential for correct system identifications. Moreover, according to Figure 8 the resolution for the CWT changes with the frequency and the time.

These characteristics and many more are discussed in the following section.

4.6.2.2 Wavelet resolution

In this section together with the time frequency resolution also the end effects in the CWT were discussed.

The time-frequency resolution is critical for effective and reliable system identifications. A major concern in a modal extraction analysis is the frequency resolution, since this allows discriminating between two close modal resonances. For the Morlet wavelet, the frequency resolution Δf_i evaluated as the root mean square of the frequency bandwidth at the frequency f_i is given by [115] (for more information see chapter 6):

$$\Delta f_i = \frac{f_i}{2\pi\sqrt{2} f_0} \tag{4.55}$$

The equation (4.55) proves that the frequency resolution decreases for high frequencies, see Figure 8. Moreover, the resolutions can be carefully adjusted by choosing the central frequency f_0.

By simple calculation, it can be seen that in the range $[f-\Delta f_i, f+\Delta f_i]$ only the 68% of the frequency Gaussian window area defined by the equation (4.54) is accounted for (Figure 11). This can be a problem when the goal is to separate two near resonances, since the two frequency windows defined by the Morlet wavelet overlap, making almost impossible their separation, see Figure 12 for α=1.

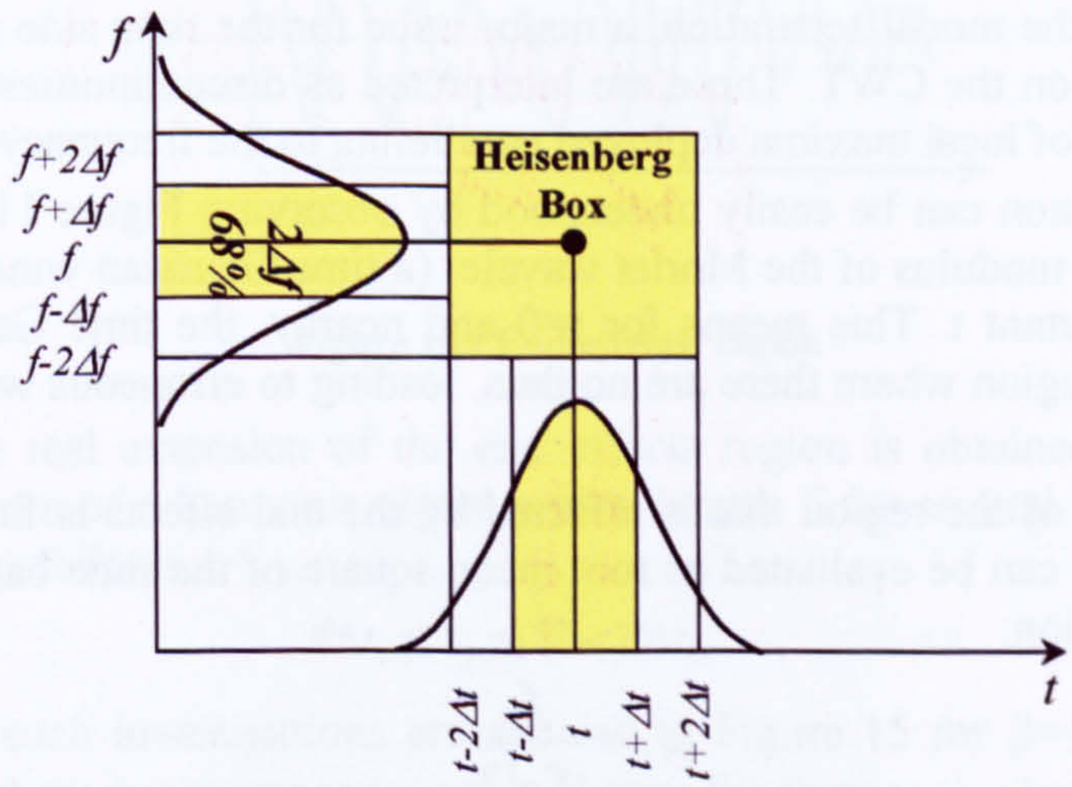

Figure 11 - Time and frequency resolution.

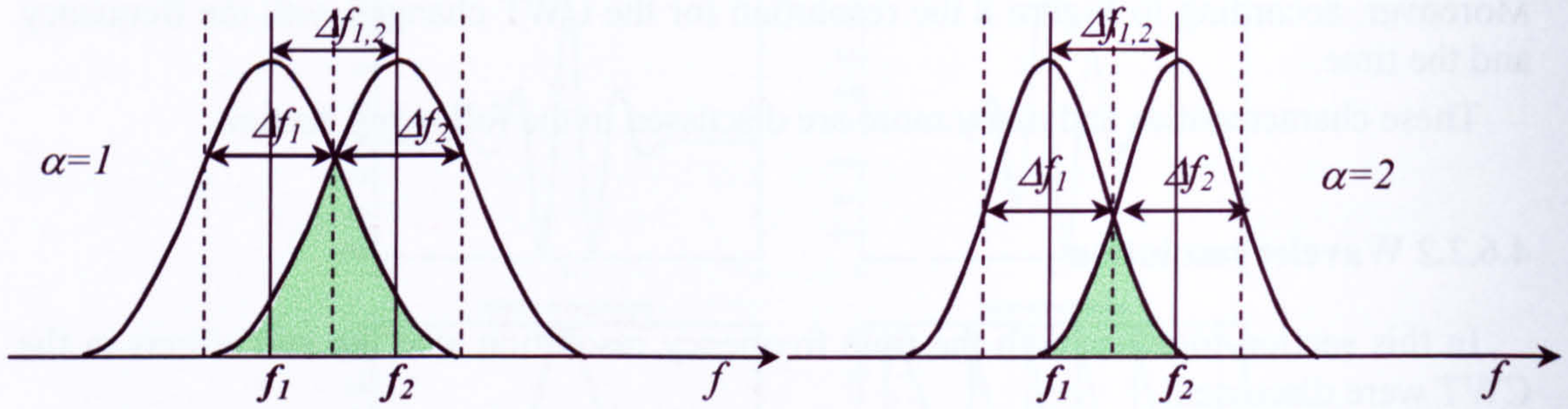

Figure 12 - Modal separation

Observing eq. (4.55), a possible way to solve this problem is modulating the Morlet central frequency accordingly with the $\Delta f_{1,2}$ necessary for the modal separation. Therefore, the Morlet frequency Gaussian window shrinks around the Morlet central frequency f_0, so as a larger percentage of its area is not anymore overlapped, see Figure 12 for α=2. Hence, accordingly equation (4.55), the minimum central frequency f_0 necessary to separate two very close frequencies f_1 and f_2 is given by:

$$f_0 = 2\alpha \frac{\left(\frac{f_1 + f_2}{2}\right)}{2\pi\sqrt{2}(f_2 - f_1)} \tag{4.56}$$

where α defines the amount of overlap between two adjacent Morlet frequency Gaussian windows (Figure 12). As Figure 12 shows with α=1 the overlap area is about the 40% of Morlet frequency Gaussian windows, while for α=2 the overlap areas is reduced to about the 25%. Typically, it is sufficient to assign α=2 although for very close modal resonances the best choice is α=3 with just the 5% of overlap.

If on the frequency side of the time-frequency representation given by the CWT, the main concern is the modal separation, a major issue for the time side is the effect of the time-signal ends on the CWT. These are interpreted as discontinuities in the signal and, therefore, source of local maxima deployed paralleling to the frequency axis (Figure 13).

This phenomenon can be easily understood by observing Figure 11 on the time side. This presents the modulus of the Morlet wavelet (a time Gaussian window, see Figure 9) centred at the instant t. This means for t=0 and nearby, the time Gaussian window is extended into a region where there are no data, leading to erroneous wavelet coefficients (Figure 14).

The extension of the region that is affected by the end effects is function of the time resolution, which can be evaluated as root mean square of the time bandwidth as for the frequency resolution:

$$\Delta t_i = \frac{f_0}{f_i\sqrt{2}} \tag{4.57}$$

As expected the time resolution is function of the frequency, precisely inversely proportional, as equation (4.57) and Figure 8 show.

Similarly to the frequency field, the time resolution Δt_i refers to only the 68% of the Morlet time Gaussian window (Figure 11), which means that in reality the length of the Morlet time window is much larger and, therefore, the region concerned to the end effects is also much larger.

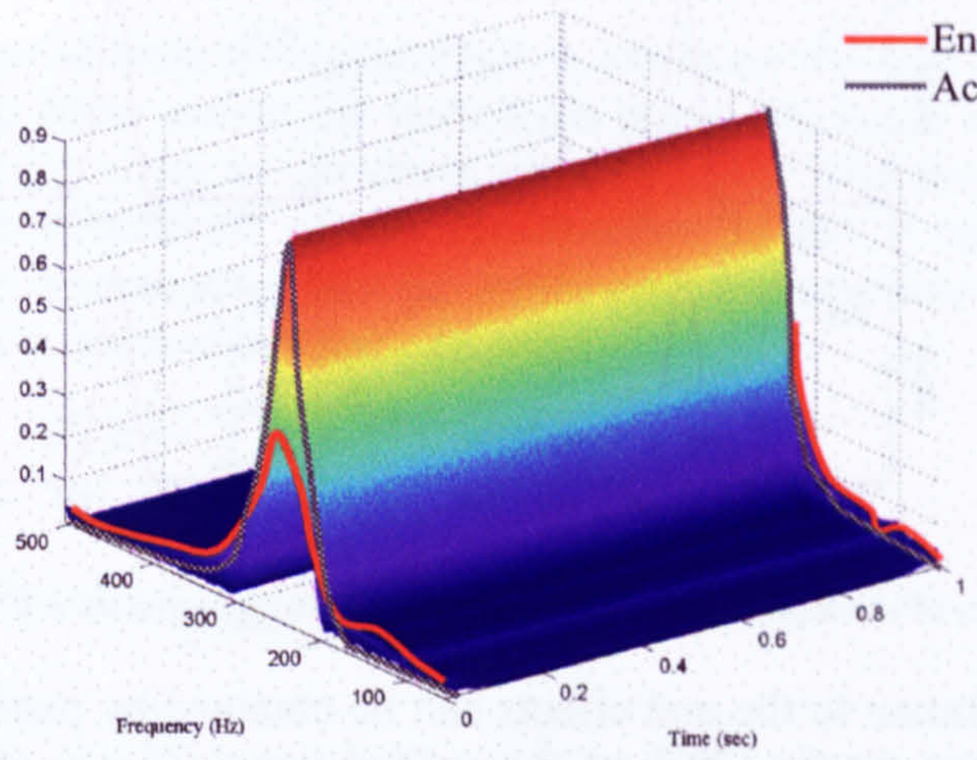

Figure 13 - End Effects

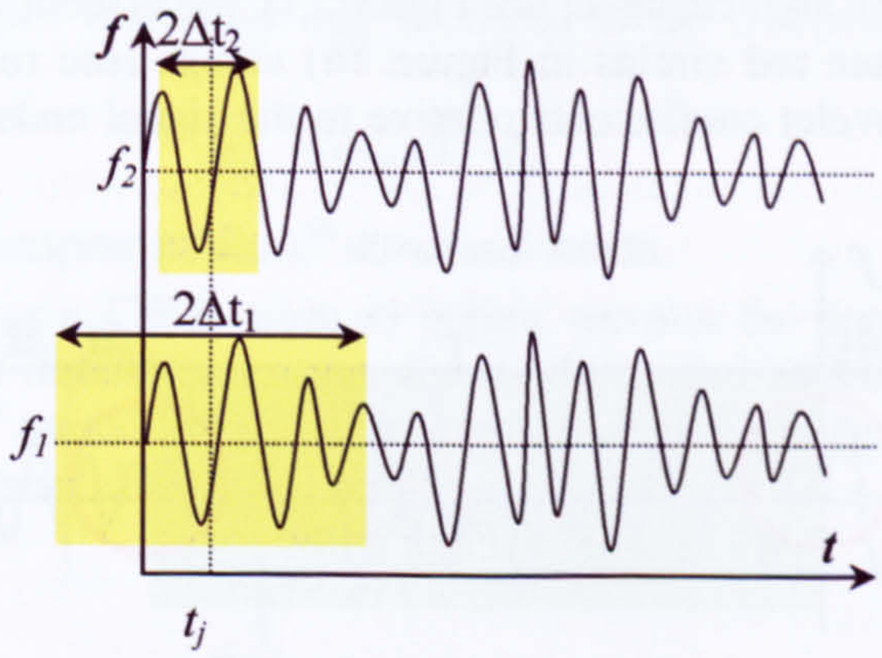

Figure 14 - End effects' region

A proof of the real extension of the end effects region is obtained by plotting the instantaneous spectra of a harmonic signal with a length T for several time instants t_j in intervals defined as follows:

$$\beta\Delta t_i \le t_j \le T - \beta\Delta t_i \tag{4.58}$$

The results of such investigations are showed in Figure 15 for $\beta=\{1, 2, \ldots,6\}$. It is clear that for $\beta>3$ there is not any appreciable change for frequencies larger than 100 Hz.

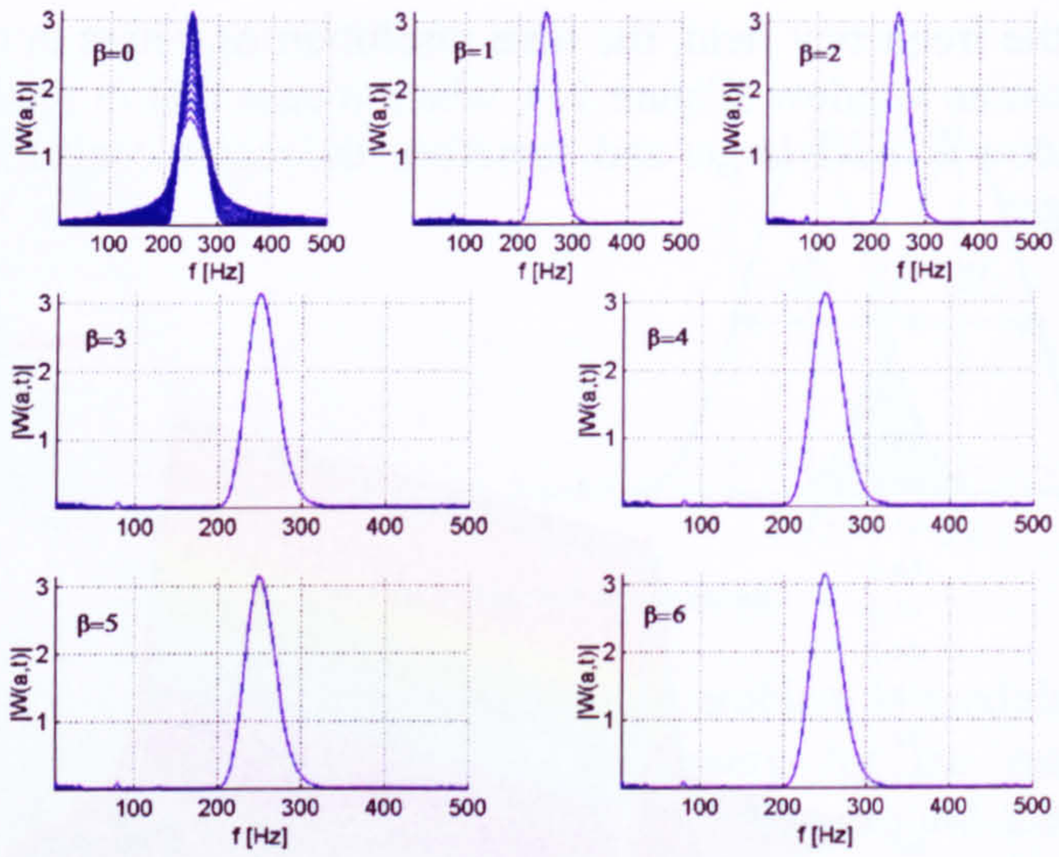

Figure 15 - Effects of the signal ends on the instantaneous spectra on a CWT of a 250 Hz sinusoid.

Therefore, a solution to the end effects can be obtained by padding the time signal at its ends and carrying out the CWT on the padded signal (Figure 16). The signal padding is obtained by reflecting a portion of the signal about its beginning and end [115]. However, the author observed that if the signal portions taken are added at the signal ends more carefully (e.g. the sign changed, see Figure 17), the discontinuities in the new signal due to the padding (see red circles in Figure 16) vanish (see red circles in Figure 17). Consequently, the wavelet coefficients relative to the signal ends are not conditioned by those discontinuities.

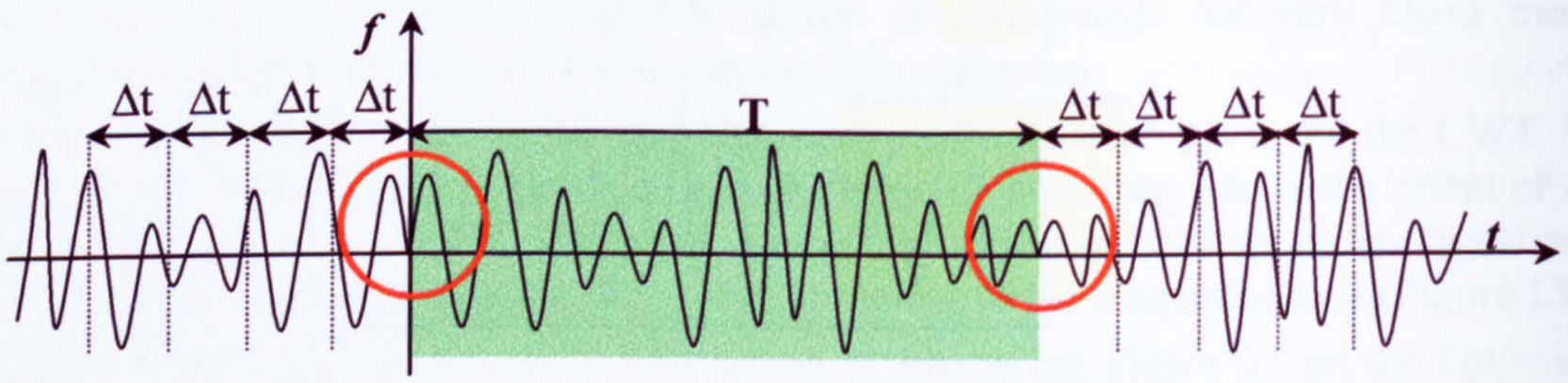

Figure 16 - Time signal padding

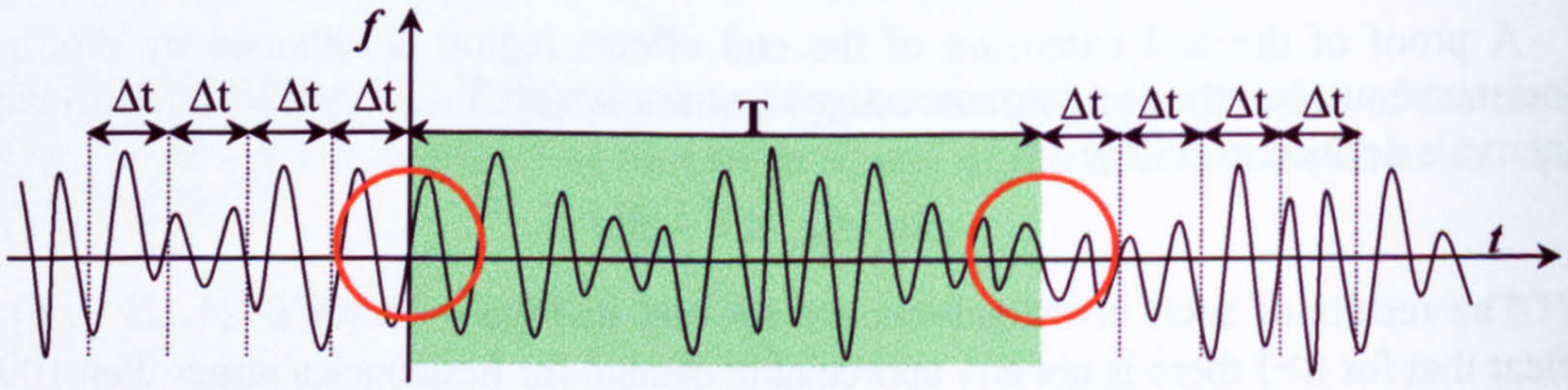

Figure 17 – Author's suggested signal padding

Finally, the length of the padding is $\beta\Delta t$ (with $\beta>3$), where Δt is the largest time resolution in the frequency range of interest. This corresponds to the resolution evaluated

for the smallest frequency of interest, since the time resolution Δt_i decreases with the frequency f_i.

4.6.2.3 Wavelet system identification algorithm

The wavelet system identification algorithm is based on the CWT of the free-decay signal evaluated using either one of the techniques above discussed for ambient excited structures or measuring it using an impulsive excitation. The free-decay signal $\delta_N(\tau)$ can be considered as a superposition of the contributions of the P mode shapes in the frequency range under investigation (see eq. 4.59), and its continuous wavelet transform in the frequency domain is described in eq. (4.60).

$$\delta_N(\tau) = \sum_{k=1}^{P} B_k e^{-\xi_k \omega_{nk} \tau} \cos(\omega_{dk} \tau + \varphi_{0k}) \tag{4.59}$$

$$W(a,t) = \frac{\sqrt{a}}{2} \sum B_k e^{\xi_k \omega_{nk} t} G^*(a\omega_{dk}) e^{j(\omega_{dk} t + \varphi_{0k})} \tag{4.60}$$

where:

- B_k is the amplitude of the k^{th} mode shape contribution to the free-decay $\delta_N(\tau)$.
- φ_k initial phase of the k^{th} mode shape contribution.

The circular undamped frequency ω_{nk} is related to the damped ω_{dk} according to the following expression:

$$\omega_{dk} = \omega_{nk} \sqrt{1 - \xi_k^2} \tag{4.61}$$

where ξ_k is the modal damping of the k^{th} structural mode.

Therefore, performing a CWT using as parent wavelet the complex Morlet wavelet and selecting the right central frequency f_0 and the signal padding as showed in the previous section, the k^{th} modal frequency will appear, in the scalogram, as a ridge parallel to the time axis (see Figure 10 and Figure 18).

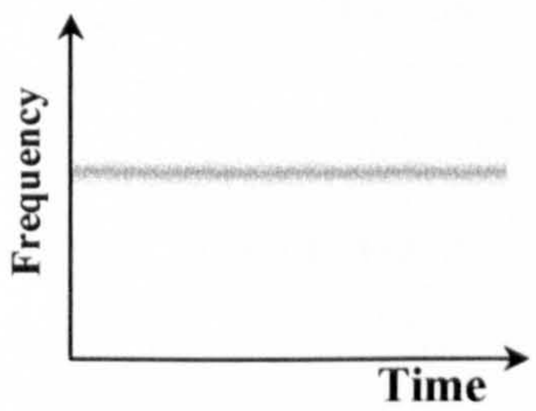

Figure 18 - Modal properties in the scalogram.

By analysing the skeleton (4.62) amplitude and phase components, it is possible to extract the modal characteristics of the vibration mode at which the skeleton corresponds.

$$W(a_k,t) = \frac{\sqrt{a}}{2} B_k e^{\xi_k \omega_{nk} t} G^*(a\omega_{dk}) e^{j(\omega_{dk} t + \varphi_{0k})} \tag{4.62}$$

In fact, by observing the skeleton amplitude, it is clear that the modal damping of the vibration mode investigated can be evaluated by simply computing its natural logarithm, as the following equation:

$$\ln\left|W(a_k,t)\right| = -\xi_k \omega_{nk} t + \ln\left(\frac{\sqrt{a_k}}{2} B_k \left|G^*(a_k \omega_{dk})\right|\right) \tag{4.63}$$

Equation (4.63) describes a line of slope $-\xi_k\omega_{nk}$ in the time space t, which means that, in the hypothesis of lightly damped structures $\xi<<1$ and $\omega_d \approx \omega_n$ (damped structure resonates at the damped natural frequency ω_d), the damping of the k^{th} mode is given by:

$$\xi_k \cong \frac{\dfrac{d\left(\ln\left|W(a_k,t)\right|\right)}{dt}}{IF_k} \tag{4.64}$$

On the other hand, the skeleton phase allows the estimation of the damped natural frequency as from the following expression.

$$Arg\left(W(a_k,t)\right) = \omega_{dk} t + \varphi_{0k} \Rightarrow \frac{d\left(Arg\left(W(a_k,t)\right)\right)}{dt} = \omega_{dk} \tag{4.65}$$

Finally, using the skeleton in its complex form is possible to estimate the shapes of the k^{th} modal property. In fact, the j^{th} component (j^{th} sensor) of the k^{th} modal property referred to the r^{th} sensor (ψ_{ij}) is derived as follows:

$$\left(\phi^k\right)_j = \frac{W^j(a_k,t)}{W^r(a_k,t)} \tag{4.66}$$

However, when real data are used, $(\phi^k)_j$ is not constant throughout the time length of the free-decay and, therefore, the real mode shapes is different from that evaluated. In order to minimize the error between those two, a best estimate of the k^{th} mode shape according to the least mean square approach can be evaluated as follows [112]:

$$\left(\phi^k\right)_j = r_{kj} + \sqrt{-1}\, s_{kj} \tag{4.67}$$

$$r_{kj} = \frac{\sum_{i=1}^{n} q_j(t_i,a_k) q_r(t_i,a_k)}{\sum_{i=1}^{n} [q_r(t_i,a_k)]^2} \qquad s_{kj} = \frac{\sum_{i=1}^{n} q_j(t_i,a_k) p_r(t_i,a_k)}{\sum_{i=1}^{n} [q_r(t_i,a_k)]^2} \tag{4.68}$$

where $q_j(t_i, a_k)=\mathrm{Re}[W^j(t_i, a_k)]$, $p_k(t_i, a_k)=\mathrm{Im}[W^j(t_i, a_k)]$ and n is the number of time samples used.

4.7 Experimental modal data extraction application

Extraction of modal properties in operative conditions is a very complicated task. A solution to this problem is offered by statistic based methodologies that extracts, from ambient excited structure responses, structure free decays enabling modal property extraction. This approach was used for the extraction of the modal properties of the Nottingham suspension bridge using a network of GPS sensors designed by the author.

The procedure and the results of this investigation are reported in appendix B and discussed in chapter 6.

4.8 Conclusions

In this chapter numerical techniques able to extract meaningful dynamic data from experimental acquired data were investigated. In particular, careful attention was devoted to numerical techniques capable of dealing with the presence of noise in the acquired signal. The analysed techniques assume the noise as a randomly distributed time function with zero mean.

For the estimate of FRFs in noisy environments, a practicable solution was offered by a least square approach exploiting the zero mean property of the noise model (§4.3).

When dealing with large scale structures only ambient vibration can be used to extract modal data. The noise in the ambient response can be eliminated by separating the free-decay structural response from the random constituent (§4.5). Two techniques (RDT and CCF) were analysed. Once the structure free-decays are evaluated, the extraction of the structure modal properties can be carried out by using two approaches: the ERA and the wavelet based method. The ERA is a very established realization technique, which was designed to be capable of extracting modal properties in presence of noise using the SVD algorithm. Although, this technique is very efficient with polluted data, is affected by the same drawbacks of other realization/statistic based technique, such as the impossibility to extract a determined mode shape or every mode shape in a determined frequency range, the necessity of a post processing for the eigen-properties evaluated and etc...

A solution at these issues is offered by the wavelet based extraction technique, which works in the time-frequency space and is capable of identifying real mode shapes, and separate coupled modal properties by simply changing the central frequency of the Morlet wavelet. Moreover, this approach offers the possibility of extracting only the mode shapes of choice in a desired frequency range. This huge operative flexibility makes the wavelet based approach particularly suitable for modal updating aimed to damage detection based on modal extraction. Both techniques were used to extract modal properties from a suspension bridge (§B.5), proving their reliability and efficiency as observed in §6.3.2.

CHAPTER 5: DIRECT APPROACH - AN ANALYTICAL APPROACH FOR PLATE STRUCTURAL DAMAGE IDENTIFICATION: FREQUENCY RESPONSE FUNCTION BASED

5.1 Abstract

A clear limit of MU technique lies in the FE model, which is a discrete representation of a structure and, therefore, unable to fully reproduce its dynamic behaviour. However, the FEM discrete representation most of the time is suitable to reproduce the structure dynamic behaviour in the limit of an accuracy level within a certain frequency range. On the other hand, in certain cases, where the frequency range requested is very large, the complexity of the FEM and its dimensions (e.g. number of elements, nodes and etc...) make MU almost impracticable, because of huge computational times and memory consumption. A solution to this problem is available for structures whose behaviour can be described by analytical functions. In order to exploit these advantages, a Direct Approach based on analytical representation of plate-like structures was developed.

The idea of such approach was derived by a similar methodology applied on beam structures [130, 131]. Therefore, all along this chapter, references and comparisons with the analogue approach, above mentioned, were added. The methodology was developed

for plate-like structures, but is liable to be extended to any kind of structures that can be represented by an analytic function.

5.2 Direct approach

A practicable alternative to FE models, for plate-like structures, is offered by analytical functions capable of providing continuous dynamic responses of the excited structures. Therefore, issues such as structure discritization, dimensions of FE model, time and memory consumption, and very skilled user, can be solved by the adoption of an analytical representation of the structure. Unfortunately, very few structures can be represented by an analytical function, such as beams and plate-like structures. In order to show the potentiality of a similar approach for damage detection purposes, a damage detection technique for plate like structure based on their analytical functions was investigated. This methodology was modelled on a similar technique developed for beams [130]. The methodology was based on the Classical Plate Theory (CPT- §5.3), which was modified to take into account the damage presence (§5.4) by introducing a damage influence matrix (§5.5). This matrix was used for the construction of a linear algebraic equation system in the frequency space (§5.6), which unknowns are the severities of flaws dislocated in different areas of the structure. Then, the algebraic system can be solved by using one of the three methods proposed (§5.6).

5.3 Dynamics of an undamaged plate

For a comprehensive understanding of the direct approach, the analysis of the analytical representation of a plate, according to the Classical Plate Theory (CPT) [132], is necessary. The CPT is based on the following assumptions:

- Small deformations (<< h).
- The mid plate plane is a neutral surface (no membrane forces are induced on it, when the plate is deformed).
- Straight material lines orthogonal to the neutral surface remain straight and normal to, in the deformed state.
- Three dimensional linearly elastic medium, with Young coefficient E, Poisson ratio ν and density ρ.

Therefore, considering a plate as pictured in Figure 19, its dynamic behaviour is defined by the following equation:

$$\rho h\ddot{w} + \nabla^2\left(D\nabla^2 w\right) = p(x,y,t) \tag{5.1}$$

where:

$$\nabla^4 = \frac{\partial^4}{\partial^4 x} + 2\frac{\partial^4}{\partial^2 x \partial^2 y} + \frac{\partial^4}{\partial^4 y} \tag{5.2}$$

- p is the excitation force orthogonal to the plane.
- D is the plate flexural rigidity:

$$D = \frac{Eh^3}{12(1-\nu^2)} \tag{5.3}$$

Then, assuming the plate flexural rigidity constant all over the plate, eq. (5.1) becomes:

$$\rho h\ddot{w} + D\nabla^4 w = p(x,y,t) \tag{5.4}$$

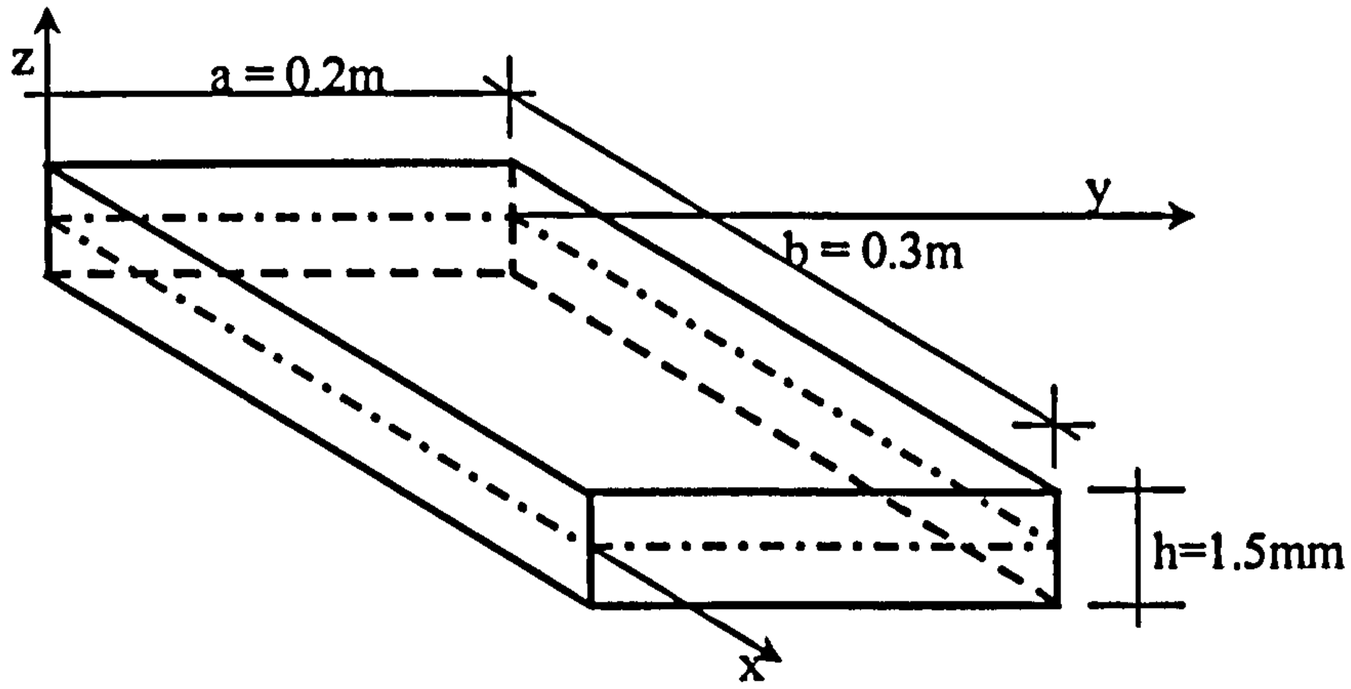

Figure 19 – Plate schematisation.

Supposing that the plate is simply supported all along its edges as described by the boundary conditions of eq. (5.5), its i^{th} mode shape W^i is expressed by equation (5.6).

$$\begin{aligned} W^i(x,0) &= M^i_{yy}(x,0) = 0 \\ W^i(x,a) &= M^i_{yy}(x,b) = 0 \\ W^i(0,y) &= M^i_{xx}(0,y) = 0 \\ W^i(a,y) &= M^i_{xx}(a,y) = 0 \end{aligned} \tag{5.5}$$

$$W^i(x,y) = A_{mn} \sin\left(\frac{m\pi y}{a}\right)\sin\left(\frac{n\pi x}{b}\right) \tag{5.6}$$

where m and n ={1, 2, 3, ...} indicate the dome number respectively along **a** and **b** (Figure 19), while A_{mn} is a constant evaluated as follows:

$$A_{mn} = \frac{2}{\sqrt{ab\rho h}} \tag{5.7}$$

The natural pulses (circular frequencies) Ω_i of the plate are calculated by the equation (5.8).

$$\Omega_i = \Omega_{mn} = \left(\frac{D}{\rho h}\right)^{\frac{1}{2}}\left[\left(\frac{m\pi}{a}\right)^2 + \left(\frac{n\pi}{b}\right)^2\right] \tag{5.8}$$

where the correspondence between the integers i, m and n is established by ordering the natural frequencies in increasing way $\Omega_1 \leq \Omega_2 \leq \Omega_3 \leq \ldots$

Finally, the plate forced vibration response can be derived as superposition of N vibration modes:

$$w = \sum_{m=1}^{N} W^m(x,y) q_m(t) \tag{5.9}$$

with $q_m(t)$ generalised coordinate of the dynamic response in the modal space.

Substituting equation (5.9) in the plate dynamic equation (5.4), for the free vibration case (p=0), the eigenvalue problem equation (5.10) can be derived. The eigenvector solutions W^1 satisfy the orthogonality properties illustrated by equations (5.11-5.12).

$$D\nabla^4 W^m - \rho h \Omega_m^2 W^m = 0 \qquad m = \{1,2,3,\ldots,N\} \tag{5.10}$$

$$\int_A \rho h W^m W^n dA = \delta_{mn} \tag{5.11}$$

$$\int_A D\nabla^4 (W^m) W^n dA = \Omega_m^2 \delta_{mn} \tag{5.12}$$

where δ_{mn} is the Kronecker delta symbol that for m=n is equal to 1 and nil for m≠n.

At the aim to evaluate the generalised coordinate $q_m(t)$, the derivation order of eq. (5.12) is reduced by applying twice the Green's theorem:

$$\int_A f\nabla^2 g dA + \int_A \left(\frac{\partial g}{\partial x}\frac{\partial f}{\partial x} + \frac{\partial g}{\partial y}\frac{\partial f}{\partial y} \right) dA = \oint_C f \frac{dg}{d\mathbf{n}} ds \tag{5.13}$$

where:

- C is the intersection curve between the neutral plane and the plate cylindrical surface.
- **n** is the outwards normal of C laying on the plane xy.
- A is the plane region enclosed in C termed the plate area.

Obtaining so, a second order derivation equation as follows:

$$D \int_A \left[\frac{\partial^2 W^m}{\partial x^2}\frac{\partial^2 W^n}{\partial x^2} + 2\frac{\partial^2 W^m}{\partial x \partial y}\frac{\partial^2 W^n}{\partial x \partial y} + \frac{\partial^2 W^m}{\partial y^2}\frac{\partial^2 W^n}{\partial y^2} \right] dA = \Omega_m^2 \delta_{mn} \tag{5.14}$$

Applying the orthogonality properties (5.11, 5.14) to the plate dynamic equation (5.4), after having substituted the equation (5.9) in, and then rearranging, a second order differential ordinary equation system (5.15), in the independent variable t of the modal coordinate q_m, is obtained.

$$\ddot{q}_m + \Omega_m^2 q_m = p_m(t) \qquad m = \{1,2,\cdots,N\} \tag{5.15}$$

where p_m is the m^{th} modal component of the excitation force p(x,y,t) as represented below:

$$p_m(t) = \int_A p(x,y,t) W^m dA \tag{5.16}$$

Supposing to excite the plate using a harmonic force concentrated in the plate point $F_0=\{x_{Fo}, y_{Fo}\}$ and expressing the excitation force as in eq. (5.17), the solution of the modal system is illustrated by eq. (5.18)

$$p_m(t) = \int_A P_0 \delta(F - F_0) e^{i\omega t} W^m = W^m(F_0) P_0 e^{i\omega t} \tag{5.17}$$

where P_0 is the excitation force amplitude and ω its (circular) frequency. In this case, δ is the delta of Dirac, whose integral, extended to the plate surface, yields 1 if $F=F_0$ otherwise is zero.

$$q_m(t) = \frac{W^m(F_0)}{\Omega_m^2 - \omega^2} P_0 e^{i\omega t} \tag{5.18}$$

5.4 Dynamic equation for a damaged plate

In order to obtain an equation that describes the dynamic behaviour of a damaged plate, it is necessary to assume damages as perturbations of the three-dimensional homogenous medium (as supposed by the CPT, §5.3) on the plate. These were introduced as variations of the plate flexural rigidity D, considered uniform through the plate thickness h, described by the function Θ:

$$\Theta = Dd(x,y) \tag{5.19}$$

where d is a function, which values are included in the interval [0,1].

Hence, recalling eq. (5.1), the plate dynamic general equation for a damaged plate can be expressed as:

$$\rho h\ddot{w} + D\nabla^4 w - \nabla^2\left(\Theta\nabla^2 w\right) = p(x,y,t) \tag{5.20}$$

The solution could be obtained as a linear combination of the undamaged vibration modes W^m weighted by the damaged modal coordinates $\bar{q}_m$:

$$w(x,y,t) = \sum_{m=1}^{N} W^m \bar{q}_m(t) \tag{5.21}$$

With the purpose of deriving a modal equation system for the plate dynamic general equation (5.20), the equation (5.2) is replaced in it, and then, recalling the orthogonality properties of the mode shapes (5.11, 5.14) and rearranging, the following second order differential ordinary equation system, in the damaged modal components, is obtained:

$$\ddot{\bar{q}}_m + \Omega_m^2 \bar{q}_m - \sum_{n=1}^{M} \lambda_{mn} \bar{q}_n = p_m(t) \qquad m = \{1,2,\cdots,N\} \tag{5.22}$$

where:

$$\lambda_{mn} = D\int_A \nabla^2\left[d(x,y)\nabla^2 W^m\right] W^n dA = DIM \tag{5.23}$$

Equation (5.23) defines the plate Damage Influence Matrix (DIM) [130], whose off-diagonal terms quantify the importance of the damage in terms of the induced coupling between two different mode shapes. Because of this property, these coefficients were named Damage-Induced Modal Coupling (DIMC) coefficients. While the diagonal elements of the DIM quantify the importance of the damage induced on the relative vibration mode. In [131], the DIMC were supposed negligible, making the DIM diagonal. Although, this hypothesis simplified the nature of the problem investigated and also introduced a critical approximation, which might harm the accuracy of the DA.

The circular frequencies of the damaged plate can be estimated solving the eigenvalue problem:

$$\det\left|\left(\Omega_m^2-\overline{\Omega}_m^2\right)\delta_{mn}-\lambda_{mn}\right|=0 \tag{5.24}$$

In the hypothesis that the damaged induced variations are small, it is possible to consider the solution of system (5.22) as a perturbation of the intact plate solution, as in eq. (5.25).

$$\overline{q}_m(t)=q_m(t)+\Delta q_m(t) \tag{5.25}$$

Therefore, by the small perturbation hypothesis, the equation system (5.22) turns in:

$$\Delta\ddot{q}_m+\Omega_m^2\Delta q_m-\sum_{n=1}^{N}\lambda_{mn}\Delta q_n=\sum_{n=1}^{N}\lambda_{mn}q_n \qquad m=\{1,2,\cdots,N\} \tag{5.26}$$

admitting as solution:

$$\Delta q_m(t)=\sum_{n=1}^{N}\sum_{l=1}^{N}\left[\left(\Omega_m^2-\omega^2\right)\delta_{ml}-\lambda_{ml}\right]^{-1}\lambda_{mn}\frac{W^m(F_0)}{\Omega_m^2-\omega^2}P_0e^{i\omega t} \tag{5.27}$$

A further simplification, due to the small perturbation assumption, was obtained considering the third term of eq. (5.26) negligible. Hence, the solution becomes:

$$\Delta q_m(t)=\sum_{n=1}^{N}\frac{\lambda_{mn}}{\Omega_m^2-\omega^2}\frac{W^n(F_0)}{\Omega_n^2-\omega^2}P_0e^{i\omega t} \tag{5.28}$$

Resuming, taking into account equations (5.18, 5.25 and 5.28), the small-perturbed solution of the damaged plate dynamic equation is:

$$w(x,y,t)=\left[\sum_{m=1}^{N}\frac{W^m(x,y)W^m(F_0)}{\Omega_m^2-\omega^2}+\sum_{m=1}^{N}\sum_{n=1}^{N}\lambda_{mn}\frac{W^m(x,y)}{\Omega_m^2-\omega^2}\frac{W^n(F_0)}{\Omega_n^2-\omega^2}\right]P_0e^{i\omega t} \tag{5.29}$$

In the next paragraph, the types of damages introduced in the plate as well as the evaluation of the DIM are discussed.

5.5 Plate damage introduction and damage influence matrix evaluation

As previously mentioned, the damage was considered as a perturbation added to the uniformly distributed plate properties. This disturbance was represented by the function Θ (5.19) that appears in the solution through the DI matrix (5.29).

The choice of perturbing the plate flexural rigidity D revealed to be a better solution than the perturbation of the elastic modulus E [131], bringing to a simpler formulation of the DIM.

The function d (see eq. 5.19) was considered as a two dimensional Heviside's function (5.30) with a constant magnitude $\bar{d}$ over a limited rectangular surface $\bar{A}$ of the plate, built it around the point $F_D=\{x_D, y_D\}$ with a half extension $\bar{x}$ along x and $\bar{y}$ along y (Figure 20).

$$d(x,y)=\begin{cases}\bar{d}\,if & F\subseteq\bar{A}\\ 0\,if & F\not\subset\bar{A}\end{cases} \tag{5.31}$$

This assumption determined the simplification of the damage induced matrix expression to:

$$\lambda_{mn} = D\left(\int_A \nabla^4\left(W^m\right)W^n dA\right)\bar{d} \equiv k_{mn}\bar{d} \tag{5.32}$$

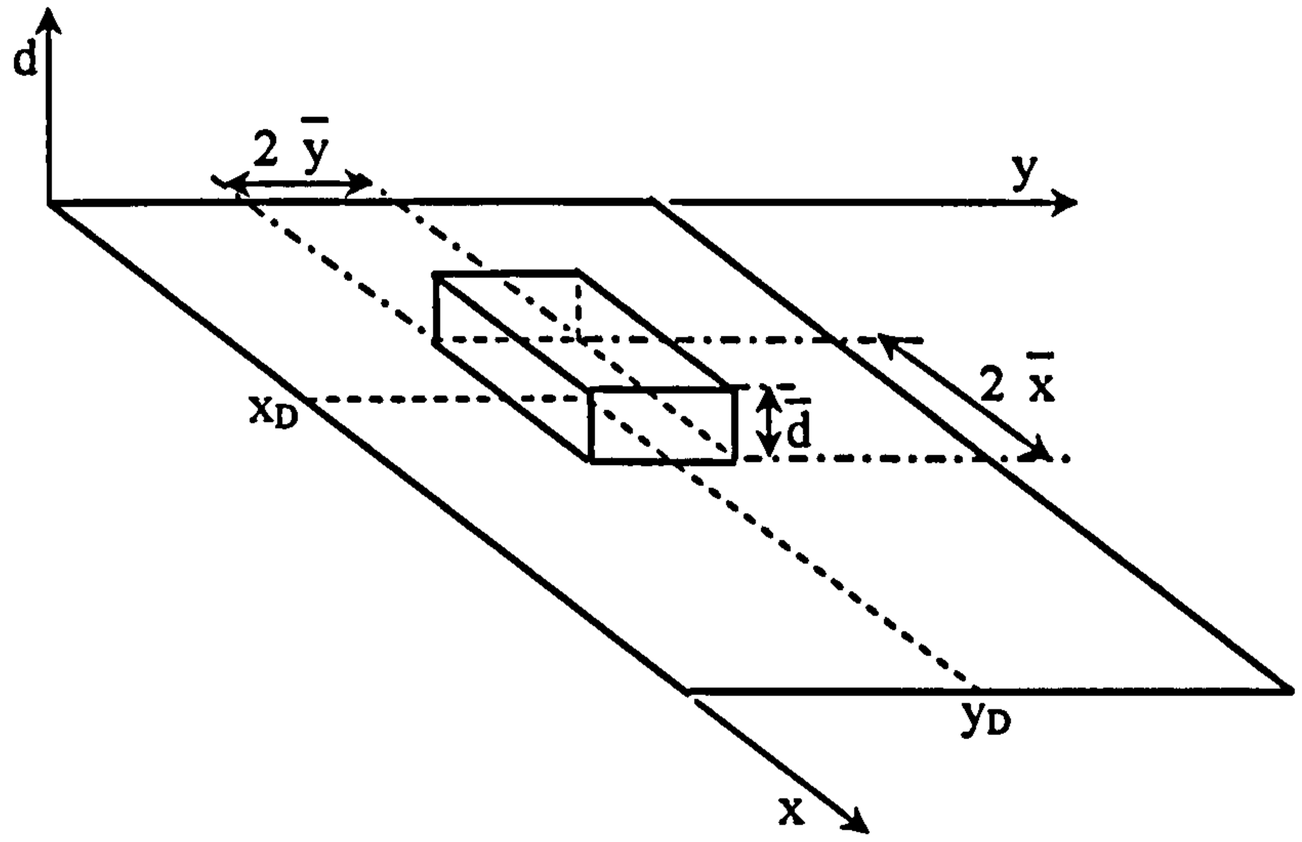

Figure 20 – Two-dimensional Heviside's function.

Hence, the DIM for multi site damages is given by:

$$\lambda_{mn} = \sum_{j=1}^{L} D\left(\int_A \nabla^4\left(W^m\right)W^n dA\right)\bar{d}_j \equiv \sum_{j=1}^{L} k_{mn}^j \bar{d}_j \tag{5.31}$$

with L number of damaged locations.

Both equations (5.31-5.32) can be simplified by using eq. (5.14), which makes possible the evaluation of the DIM by only derivatives of second order, instead of the fourth. This simplification determines not only run-time savings, but also an enhancement of the accuracy in the DIM computation.

In next section, using the above representation of the DI matrix, an algebraic system, in the unknown $\bar{d}_j$, is built to identify damage in terms of its location and severity.

5.6 Damage detection technique

The previous paragraph showed as the DIM can be evaluated by a linear superposition of single damage contributions. This property was used to assess damage magnitudes and locations by changes in the distribution of the plate flexural rigidity D. The starting point of the detection process was the partitioning of the plate in L areas liable to be damaged. In this perspective the dynamic response of the plate is governed by the equation (5.33) derived from equations (5.29, 5.32).

$$w(F,t) = \left[\sum_{m=1}^{N} \frac{W^m(F)W^m(F_0)}{\Omega_m^2 - \omega^2} + \sum_{j=1}^{L}\left(\sum_{m=1}^{N}\sum_{n=1}^{N} k_{mn}^j \frac{W^m(F)}{\Omega_m^2 - \omega^2}\frac{W^n(F_0)}{\Omega_n^2 - \omega^2}\right)\bar{d}_j\right] P_0 e^{i\omega t} \tag{5.33}$$

where the $\bar{d}_j$ values identify the damage severity of the j^{th} area.

The above equation can be simplified in an algebraic one using the FRF (receptance) of the signal described in equation (5.33), see below equation:

$$A(F,\omega)=\sum_{m=1}^{N}\frac{W^m(F)W^m(F_0)}{\Omega_m^2-\omega^2}+\sum_{j=1}^{L}\left(\sum_{m=1}^{N}\sum_{n=1}^{N}k_{mn}^{j}\frac{W^m(F)}{\Omega_m^2-\omega^2}\frac{W^n(F_0)}{\Omega_n^2-\omega^2}\right)\bar{d}_j \quad (5.34)$$

The receptance or the inertance (FRF for the acceleration) can be measured easily experimentally without any further elaboration as for the vibration modes of the structure.

Providing the FRF measures in several locations and at different frequencies, and then, supposing that the vibration modes of the undamaged plate are available (measured before the damage occurrence), it is possible to write a linear system having as unknowns the flexural rigidities of the plate areas prone to be damaged, as described below:

$$[X_{ij}]\{\bar{d}_j\}=\{Y_i\} \qquad j=\{1,2,\cdots,L\} \quad (5.35)$$

where:

- $$X_{ij}=\left\{\frac{W^m(F_i)}{\Omega_m^2-\omega_i^2}\right\}^T k_{mn}^{j}\left\{\frac{W^n(F_{0i})}{\Omega_m^2-\omega_i^2}\right\} \qquad m,n=\{1,2,\cdots,N\} \quad (5.36)$$
- $$Y_i=A(F_i,\omega_i)-\sum_{m=1}^{N}\frac{W^m(F_i)W^m(F_{0i})}{\Omega_m^2-\omega_i^2} \quad (5.37)$$
- F_i, F_{0i} and ω_i are, respectively, the sensor, the exciter and excitation frequency relative to the i^{th} row of the system (5.35).

Thus, a simple damage detection technique that needs only the inversion of an algebraic system is built. For its evaluation, the following experimental data are required:

1. The natural frequencies of the undamaged structure.
2. The mode shapes of the undamaged structure.
3. The FRFs of the damaged structure.

Differently from many other techniques, this does not need the acquisition of damaged modal characteristics that is surely an advantage. Anyway, a drawback is due to the spatial resolution of the vibration modes, which is requested for the evaluation of the DI matrix.

Another problem is the correct selection of the system rows and its influence on the reliability and efficiency of the methodology developed. This aspect of the damage detection was investigated in next section.

5.6.1 System Evaluation

In contrast with the analogue approach present in literature [131], the author proposed some solutions for the selection of sensor and exciter locations, together with some solver aimed at enhancing the quality of the detection and reducing the negative effects of the noise.

The evaluation of the structural changes from experimental data, as in the previous chapters was highlighted, is affected by many factors such as:

1. The selection of the sensor locations.
2. The selection of the exciter positions.

3. The excitation frequency choice.

However, other factors dependent on the detection algorithm characteristics need to be considered, such as the efficiency of the inversion of the algebraic equation system and the numerical method used to solve it.

All the points above listed are strongly connected each other and are not easy to separate. The first three are due to numerical-physical factors relying on the need to maximise the information collected by experimental tests on the structural changes.

This maximisation of the information content is mainly obtained by an opportune selection of the sensors and exciters locations, of the target mode shapes, and of the frequency range.

A full range of solutions on the selection of the sensor positions, as well as, the methodologies for a correct selection of the target mode shapes were explored in chapter 3. The possible excitation locations can be assumed coincident with the sensor locations. In this way, all the target mode shapes are surely excited, since the sensor location selected will not be on their nodal line. Moreover, the frequency range to analyse can be included in the frequency interval between the smallest and the largest target mode shape frequency. The number of sensors can be fixed to be the minimum number of locations able to identify univocally all the target mode shapes considered. This means that the sensors number is equal to the target mode shape number.

As far as it concerns the numerical-mathematical aspect of algebraic systems, the main requirement involves the uniqueness of the solution. Which according to the Rouche-Capelli theorem [133] needs the equality of the ranks of the coefficient matrix [Xij] and of the complete matrix [Xc] (5.38) to the number of the unknowns L.

$$[X_c]=\left[\ [X_{ij}]\{Y_i\}\ \right] \tag{5.38}$$

The efficiency of the numeric inversion of the equation system relies on the coefficient matrix conditioning. In other words, if the coefficient matrix [Xij] is hill conditioned (high condition number) the results are inevitably affected and not reliable.

Three solutions were identified in the attempt to solve this problem:

- Use of regularization methodologies that solve the hill conditioned system.
- Build a coefficient matrix well conditioned.
- Limit the number of operations connected with the matrix inversion, for example working with diagonal matrices.

Hence, three different ways to solve the algebraic system (5.35) were considered:

1. The construction of an Over-Determined System (ODS) and estimate of its solution by a Least Square Optimisation algorithm (LSO, §2.8.1), which provides a correction of the matrix conditioning through the PCG method.
2. The construction of a Determined System (DS) by selecting L rows from the ODS that minimise the DS coefficient matrix condition number.
3. The solution of the ODS defined at point 1 using a Singular Value Decomposition solver (SVD, §2.8.1).

5.6.2 Over-determined system

For Over-Determined System (ODS) is meant a system having the number of equations larger than the number of unknowns. Therefore, a surplus of information regarding the system (structure) is available and can be used to increase the noise withstanding of the solution together with the efficiency and reliability of the detection method. In the studied case, an ODS is obtained by simply using a combined number of excitation frequencies, sensors and actuation locations that is larger than the number of unknowns (possible damaged locations L). Hence, the solution is computed using a least square optimisation algorithm (§2.8.1).

5.6.3 Determined system

A Determined System (DS) is a system of equations, which number is equal to their unknown number. Once excitation frequencies, sensors and actuation locations are selected a number of DS can be selected, therefore, an iterative algorithm was devised to select the rows of the DS by maximising its information content, reliability, and noise withstanding. The rows selected were picked up by the over-determined system described in the previous section following the procedure explained below:

1. Selection of the first row. This task is critical because can lead to the selection of a set of rows that correspond to an exciter-sensor-frequency set characterised by a low energy content and probably with a low sensitivity to structural changes. In order to avoid this problem, the first row has to be characterised by an exciter-sensor-frequency set with the largest energy content possible. This was obtained by selecting the row having as:
   - Exciter, the location with the largest Eigenvector Vector Product value (§3.6.1) evaluated between the OSP chosen locations. This selection guarantees that any mode shape within the frequency range of interest receives the largest vibration energy rate possible.
   - Sensor, the position with the largest Driving Point Residue value (§3.6.2) among those selected by the OSP method except for the one identified as excitation location. This ensures that the energy content of the acquired signal is the largest between the locations investigated.
   - Frequency, the one corresponding to the largest FRF amplitude acquired using the exciter and sensor above defined.
2. Selection of the second row: this is selected as the one that maximises the rank of the matrix A_i and minimises its condition number, that is:

$$A_i = \begin{bmatrix} X_{F1} & X_{i1} \\ X_{F2} & X_{i2} \\ \vdots & \vdots \\ X_{FN} & X_{iN} \end{bmatrix}^T \qquad condition\_number_i = \frac{\lambda^i_{max}}{\lambda^i_{min}} \qquad (5.39)$$

where F is the index of the first row selected, while the coefficients λ_{min}^{i} and λ_{max}^{i} are the minimum and the maximum eigenvalue of the matrix $A_i^T A_i$.

3. The selection of the rest of the system's rows, up to the requested L, is obtained adding to the matrix A_i a new column and repeating step 2 operations.

Once that the coefficient matrix is calculated, the system can be solved inverting the coefficient matrix as follows:

$$\{\bar{d}_j\}=[X_{ij}]^{-1}\{Y_i\} \tag{5.40}$$

A further and more reliable solution might be estimated using the LSO algorithm, especially in presence of noisy FRFs.

5.6.4 Singular Value Decomposition

The application of Singular Value Decomposition (SVD) to solve the linear algebraic equation system (5.35) reduces the computational time of the ODS (§5.6.2) and increase its robustness from a numerical point of view.

As explained in section 2.7.1, the SVD method is based on a well-known theorem [130]. Therefore, recalling eq. (2.53) and changing the sensitivity matrix with the coefficient matrix [Xij] evaluated as described in (§5.6.2), is obtained:

$$[X_{ij}]=[P][D][Q]^T=[P_1 \quad P_2]\begin{bmatrix}S_1 & 0\\ 0 & S_2\end{bmatrix}\begin{bmatrix}Q_1^T\\ Q_2^T\end{bmatrix} \tag{5.41}$$

where the matrices P_1, S_1 and Q_1^T are L by L matrices (L number of the unknowns).

Then, substituting eq. (5.41) inside eq. (5.35), the algebraic system assumes the following aspect:

$$[P_1 \quad P_2]\begin{bmatrix}S_1 & 0\\ 0 & S_2\end{bmatrix}\begin{bmatrix}Q_1^T\\ Q_2^T\end{bmatrix}\{\bar{d}_j\}=\{Y_i\} \tag{5.42}$$

Finally, solving the equation above for $\{\bar{d}_j\}$:

$$\{\bar{d}_j\}=Q_1S_1^{-1}P_1^T\{Y_i\} \tag{5.43}$$

where S_1^{-1} is a diagonal matrix, whose coefficients are the inverse of the principal diagonal coefficients of S_1.

Once again, a more efficient solution of eq. (5.42) system might be obtained using the LSO algorithm, which should provide a more robust convergence in presence of noisy FRFs.

5.7 Direct approach application

A numerical validation of the direct approach using polluted data according to a zero mean gaussian distribution was carried out on a plate like structure identical to that used for the numerical validation of the GLDDO approach (appendix D). The results were discussed in §6.8 and compared in terms of accuracy and reliability of detection with the results of an analogous technique present in literature.

5.8 Conclusion

In this chapter, a damage detection technique, the Direct Approach, based on an analytical representation of the structure under investigation (plate-like structures) was analysed. The DA consisted in the solution of an algebraic equation system, built using natural frequency and mode shapes of the undamaged structure and FRFs of the damaged structure, and exploiting the Classical Plate Theory (CPT).

The use of an analytical representation of the structural behaviour is source for two concerns. First, the extension of the DA to a more complex structure relies on the existence of an analytical solution of its dynamic behaviour.

Second, even if an analytical solution for a complex structure exists, a technical problem is due to the acquisition of the undamaged vibration mode with a very large spatial resolution (needed to evaluate the DIM matrix) that is really time expensive and surely strongly affected by experimental noise and numerical error due to their extraction. However, once the undamaged vibration modes are extracted no more modal acquisitions are required, because the damaged structural changes are evaluated using the FRFs that do no need any further particular elaboration. This compared to many other damage detection methods, present in literature, is a clear advantage (see chapter 1 and 2), although many of them (e.g. GLDDO approach) do not need the same accuracy.

The methodology developed is without any doubt almost identical to that developed by Lee and Shin [131], both were derived by the same paper of the same authors, applied on a beam [130], and both the works used the CPT. However, differences can be identified. In the current study, the plate flexural rigidity was decreased to simulate the damage presence, instead of the Young modulus as in [131].

Moreover, in the evaluation of the DIM matrix, the damage-induced coupling between modal coordinates was not considered negligible as in [131]. This decision was based on the assumption that the damage introduced into the plate would have altered the orthogonality of the undamaged mode shapes and determined non zero non diagonal coefficients in the DIM matrix, as confirmed later by numerical simulations (appendix D). This assumption brought to the definition of an equation system that was not diagonal as that built by Lee and Shin [131], and needing so to be inverted. However, this disadvantage was compensated by a major precision in the localisation and the severity quantification of the damage as highlighted by comparing the results of the author's DA and the SDIM [131] (§6.8).

CHAPTER 6: MODEL UPDATING DAMAGE DETECTION RESULT DISCUSSION

6.1 Abstract

In the recent years, an increasing interest on damage detection technology is driving the research community into the development of new non destructive techniques. As mentioned in chapter 1, a number of approach were considered, among these two methodologies (MU, and wave propagation) seemed responding to the requirements set up by the author for an efficient reliable and economically affordable HM device (§1.6). The first was comprehensively investigated and further developed in chapters 2-5, appeared to be very reliable and quite affordable for large civil structures. In this chapter, the MU based damage detection methodology (the Global-Local Damage Detection Optimised – GLDDO – approach), developed by the author, was investigated. Since, an efficient and reliable Damage Detection (DD) technique cannot be independent from the data selection (chapter 3) and the data acquisition (chapter 4), an organic study, on the effects of these issues on damage detection, was carried out using three different structures, a cantilever beam, a suspension bridge and a plate-like structure. The first task performed dealt with the selection of the optimal design for a sensor network. This was carried out comparing the Optimal Sensor Placement (OSP) techniques, analysed in chapter 3, in terms of the their ability to capture the vibration mode shape, to maximise the acquired energy and signal information content (§6.2-6.4).

Second task was the analysis of DD investigations performed using the GLDDO approach on a plate-like structure. At this aim three single-site damages and a multi-site damage, randomly picked, were introduced on the structure and, then, identified in terms of location and severity of the defects (§6.5). The analysis outcomes showed, the capability of the methodology developed to detect damage characteristics correctly and better than other similar methodologies present in literature (§6.6-6.7).

Finally, a Direct Approach (DA – see chapter 5) exploiting an analytical representation of a plate-like structure, was explored (§6.8). The results showed that the methodology developed was clearly a quasi-real time (30-120 sec) and better performing than a similar methodology present in literature. However, the unavailability of analytical representations of real structures makes of the DA approach just an academic investigation, especially if, compared to the GLDDO approach, which design makes real applications not unthinkable in a near future.

The full details of the structures and the analysis performed are in appendix A, B, C and D.

6.2 Cantilever beam

The importance of Optimal Sensor Placement (OSP) has being highlighted in chapter 3, where several methodologies were presented. In order to size down the number of OSP techniques, a first investigation on their capabilities was carried out using three terms of comparison (Appendix A).

The first criterion estimated the Mean Square Error (MSE) between the undamaged FE model and cubic spline interpolated mode shapes. The second comparison criterion explored the effects of damage locations on the optimal sensor placements. The last criterion explored the ability of OSP techniques to design a sensor network capable of supplying sufficient information, on structural changes due to damage, to detect the location and the severity of the defect. This analysis was carried out by introducing three damages on a cantilever beam and detecting their presence, location and severity using the GLDDO approach fitted with the COMAC_MAC residue function (§2.7).

Although, these three comparison principles are very different, a certain convergence of results was remarked. First of all, the MSE comparison criterion (Figure 21) was in good agreement with the Damage Detection (DD) results (Table 5-Table 7). In fact, by cross-checking the two criterion results, it is clear that the OSP techniques having the smallest mean square error values, mostly coincided with those OSP techniques that scored the best damage detection performances. Examples are EFI and KE methods for the Fisher Information matrix methods, the NODP method for the variance based techniques and the Gm2 for the control theory based methods. In contrast, the EVP method performed far better than the fellow class method (NODP), nonetheless its MSE was two size units larger.

Statistic OSP Techniques		Sub-Class	*Fisher Inf. Mat. Methods*			*Variance based Methods*				
		Method	***EFI***	***EFI-DPR***	***KEM***	***PCA***	***MIS***	***VrM***	***Gr1***	***Gr2***
Damaged Configurations	***1st El. 9***	***Localised***	*Next Element (10)*	*Next Element (10)*	*YES*	*Next Element (10)*	*Next Element (10)*	*Next Element (10)*	*NO*	*Next Macro-section (El. 11)*
		Severity %	5.22	2.94	3.87	3.5	3.5	3.5	1.65	1.05
		Error %	47.8	70.6	61.3	65	65	65	83.5	89.5
	2nd El. 63	***Localised***	*YES*	*YES*	*YES*	*YES*	*YES*	*YES*	*YES*	*YES*
		Severity %	4.95	4.76	4.42	3.25	3.25	3.25	5.5	4.25
		Error %	50.5	52.4	55.8	67.5	67.5	67.5	45	57.5
	3rd El. 90	**Localised**	*YES*	*NO*	*YES*	*NO*	*NO*	*NO*	*NO*	*NO*
		Severity %	5.79	0.96	8.75	0.4	0.4	0.4	0.35	0.3
		Error %	42.1	90.4	12.5	96	96	96	96.5	97

Table 5 – Statistic OSP techniques: damage detection results.

Energetic OSP Methods		Method	***EVP***	***DPR***	***NODP***	***CNM***	***GRM***
Damaged Configurations	***1st El. 9***	***Localised***	*Next Element (10)*	*Next Element (10)*	*Next Macro-section (El. 11)*	*Next Macro-section (El. 11)*	*NO*
		Severity %	1.21	3.52	0.81	1.39	1.42
		Error %	87.9	64.8	91.9	86.1	85.8
	2nd El. 63	***Localised***	*YES*	*YES*	*Next element (64)*	*Previous Element (62)*	*YES*
		Severity %	5.21	3.25	4.25	3.9	5.65
		Error %	47.9	67.5	57.5	61	43.5
	3rd El. 90	**Localised**	*YES*	*NO*	*YES*	*NO*	*NO*
		Severity %	4.49	0.4	5.5	1.65	4.12
		Error %	55.1	96	45	83.5	58.8

Table 6 – Energetic OSP techniques: damage detection results.

CTB OSP Techniques		Sub-Class	*Grammian Trace Matrix Methods*					***GDM***	***GCN***
		Method	***Gm1***	***Gm2***	***Gm3***	***Gm4***	***Gm5***		
Damaged Configurations	***1st El. 9***	***Localised***	*Next Element (10)*	*YES*	*Next Element (10)*	*NO*	*YES*	*Macro-section (El.7)*	*Previous Element (8)*
		Severity %	4.72	4.56	4.72	1.62	5.99	0.8	2.42
		Error %	52.8	54.4	52.8	83.8	40.1	92	75.8
	2nd El. 63	***Localised***	*YES*	*YES*	*YES*	*Next Element (64)*	*Next Element (64)*	*YES*	*YES*
		Severity %	4.22	4.41	4.22	4.95	4.75	1.78	1.56
		Error %	57.8	55.9	57.8	50.5	52.5	82.2	84.4
	3rd El. 90	**Localised**	*NO*	*NO*	*NO*	*NO*	*NO*	*NO*	*NO*
		Severity %	1.04	0.41	1.04	0.7	1.74	0.72	1.23
		Error %	89.6	95.9	89.6	93	82.6	92.8	87.7

Table 7 – Control Theory Based OSP techniques: damage detection results.

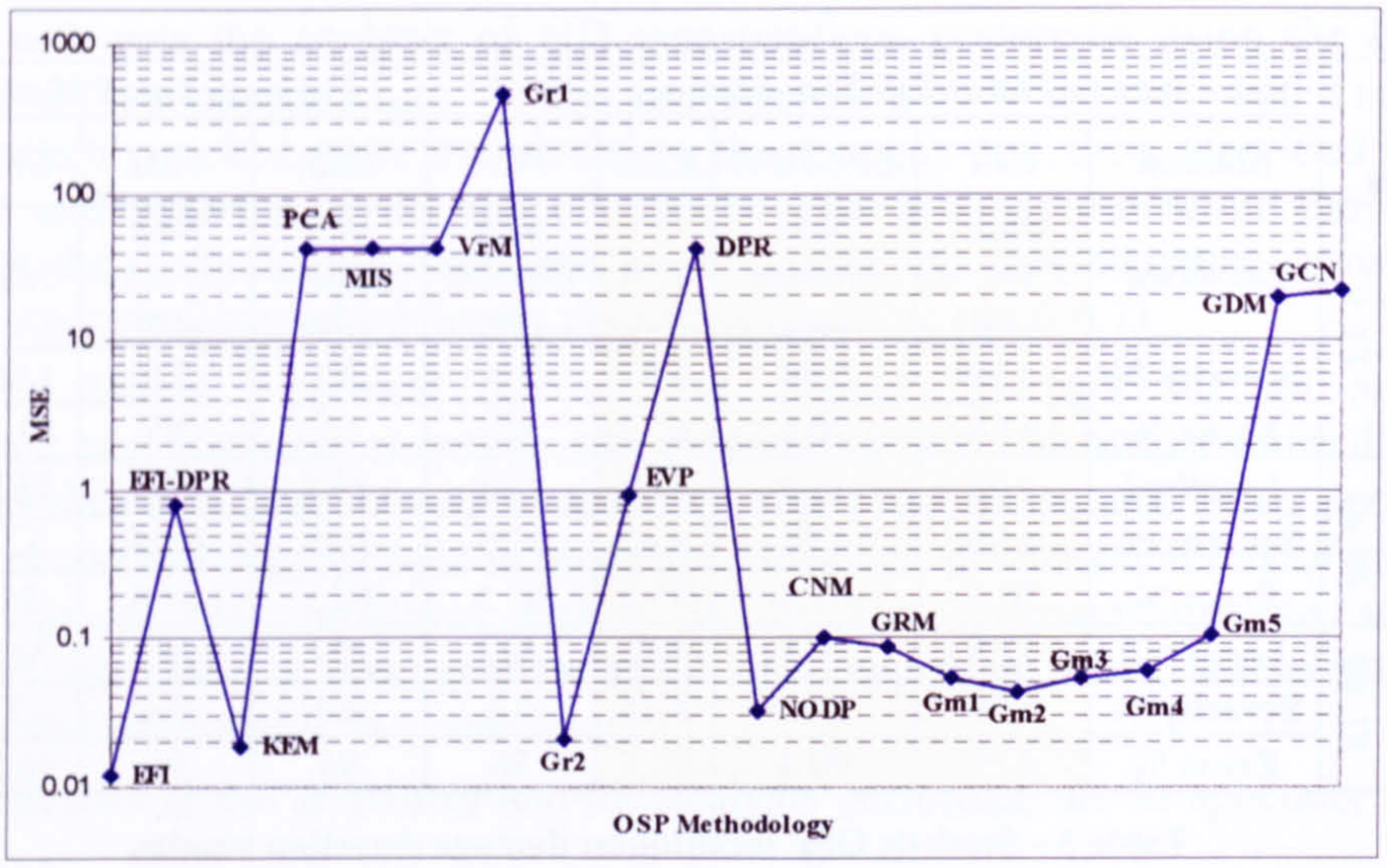

Figure 21 - OPS techniques: MSE comparison criterion

A further incongruence with the behaviour highlighted is given by the Gr2 technique, which had a MSE value three times smaller than PCA, MIS and Vr method, but had far worse damage detection performances.

A further crosschecking, involving the second comparison criterion, highlighted that those OSP techniques, having small MSE values as well as small changes due to damage location and severity variations, provided the best damage detections (see appendix section A.3), see for EFI and KEM in Figure 22.

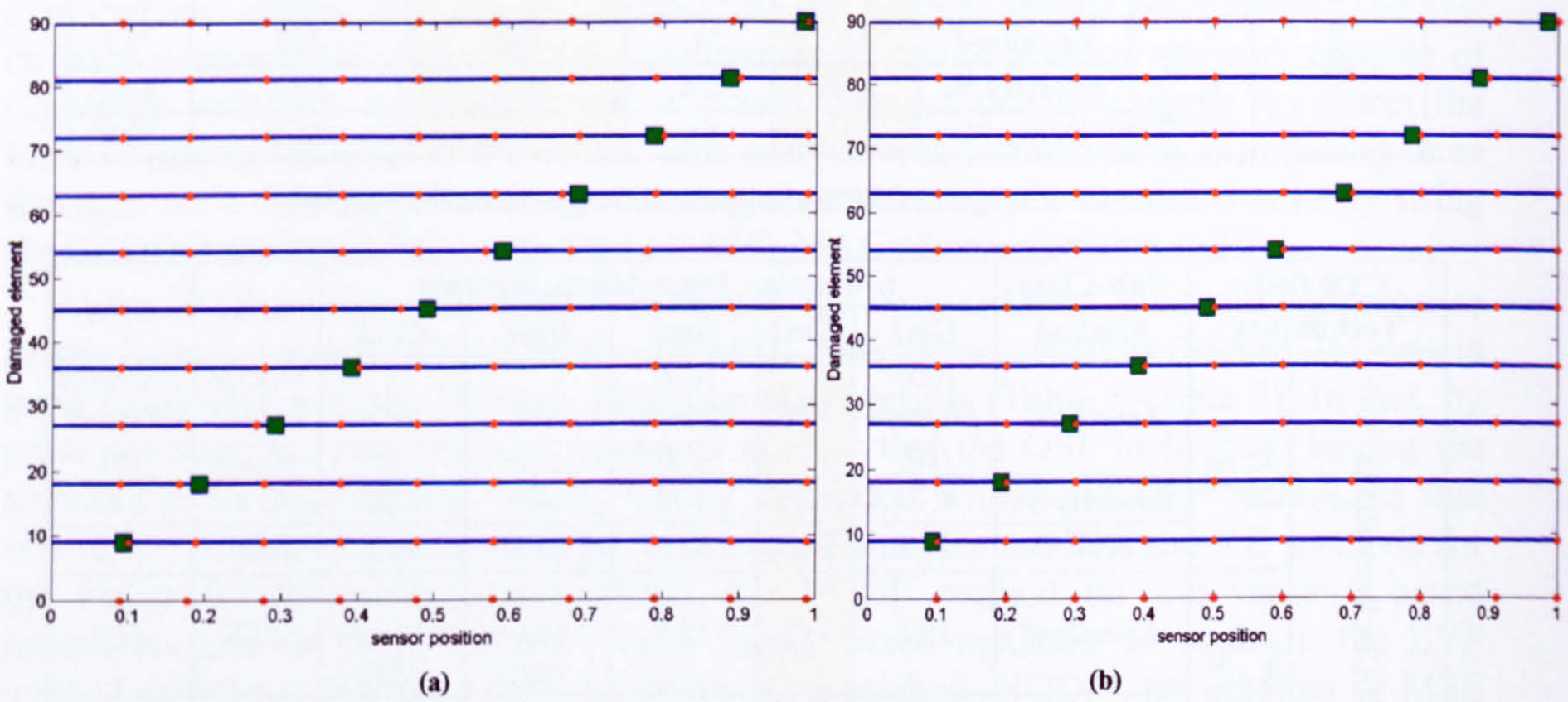

Figure 22 - Damage location effect on OSP: (a) KEM; (b) EFI.

Furthermore, the concentration of the sensor locations on the free edge of the cantilever beam (Figure 24), as designed by PCA, MIS, VrM and DPR methods, was capable of supplying sufficient information for the correct detection of damages placed in

elements 9 and 63 (Figure 23), while failed, unexpectedly, to identify the damage introduced in element 90 (Table 5-Table 7).

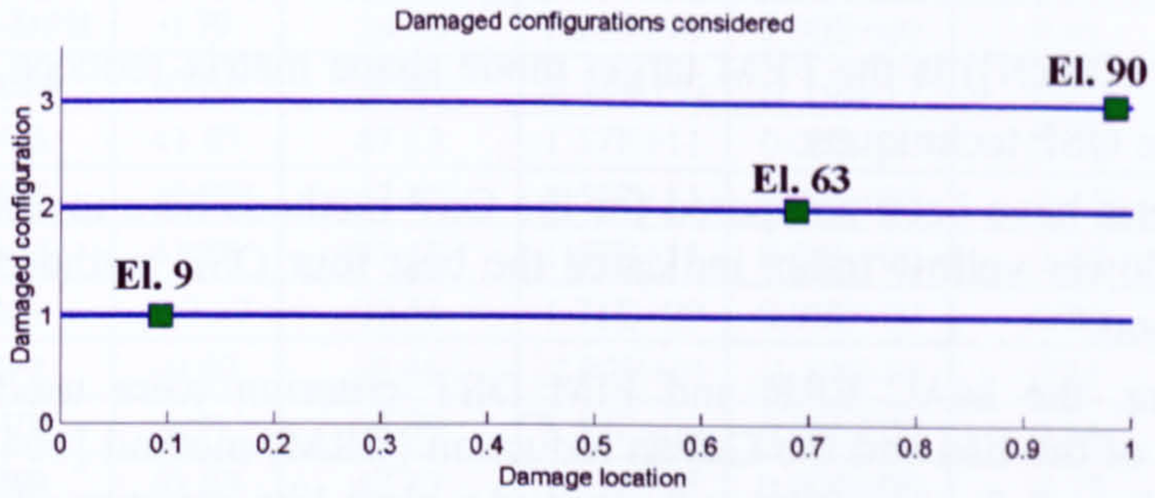

Figure 23 - – Damaged configuration investigated.

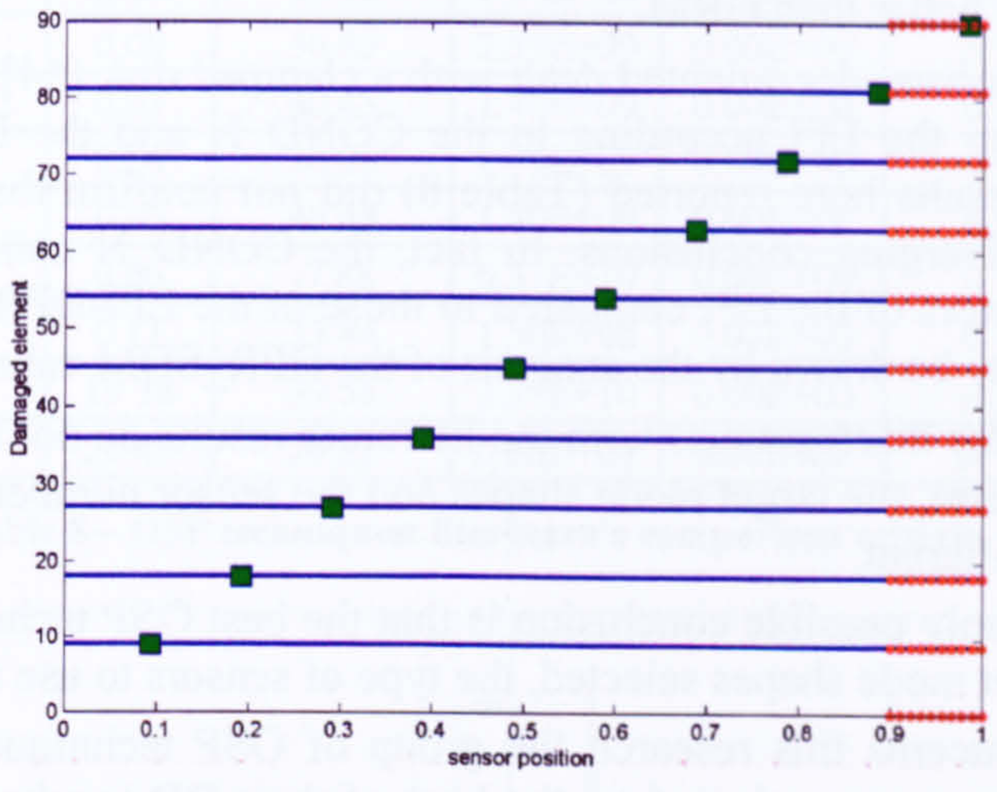

Figure 24 - Damage location effect on OSP: PCA method.

Based on the convergence between the results of the selected comparison criteria the use of the EFI and KEM as selecting criteria of the best optimal sensor set for damage detection purposes seems more appropriate.

Of course, there is not a perfect rule for the selection of the best set of sensor locations, in literature, many comparison criteria have been used, such as the MAC error [104] (MAC_ERR, eq. 3.47), the condition number [54] (COND_N, eq. 3.48), the Fisher Information matrix determinant [93,104] (FIM_DET, eq. (3.49) and the sum of DPR coefficients [54] (DPR_SUM, eq. 3.50).

$$MAC\_ERR = \left(\sum_{i=1}^{N} \sum_{j=1}^{N} MAC\left(\left[\Phi_{OSP} \right] \right)_{ij} \right) - N \tag{6.1}$$

$$COND\_N = \frac{\lambda_{\max}\left(\left[\Phi_{OSP} \right] \right)}{\lambda_{\min}\left(\left[\Phi_{OSP} \right] \right)} \tag{6.2}$$

$$FIM\_DET = \left| \left[\Phi_{OSP} \right]^T \left[\Phi_{OSP} \right] \right| \tag{6.3}$$

$$DPR\_SUM = \sum_{i=1}^{M} DPR([\Phi_{OSP}])_i \tag{6.4}$$

where $[\Phi_{OSP}]$ ([MxN]) is the FEM target mode shape matrix reduced to only the DoFs selected by the OSP techniques.

These criteria have been compared for the OSP methods here investigated, see Table 8, where the lower yellow index indicated the best four OSP methods according to the column criterion.

In literature, the MAC_ERR and FIM_DET criterion were used to compare the performances of the EFI and the Guyan reduction (GRM) method [104] (6-18 sensors, 6 target mode shapes) for a cantilever beam and a plate-like structure. The results showed similar performances of the two techniques, in contrast with the results here obtained were the EFI is far better than GRM.

A second comparison documented dealt with a clamped disk [54], where the EFI-DPR resulted better than the EFI according to the COND_N and the DPR_SUM criterion. Once again, the results here reported (Table 8) did not confirm the literature outcomes and highlighted diverging conclusions. In fact, the COND_N condition confirmed the superior performances of the EFI compared to those of the EFI-DPR, in contrast with the conclusion that may be drawn by the analysis of the DPR_SUM values.

Concluding, these discrepancies with the literature results do not have a great meaning because the structures, the target mode shapes and the sensor number and many other tiny particulars were different.

Therefore, the only possible conclusion is that the best OSP technique depends on the structure, the target mode shapes selected, the type of sensors to use and etc...

As far as it concerns this research the group of OSP techniques that were used in further investigations were selected on the base of their DD results. Hence, the EFI, the KEM, the EVP, the EFI-DPR and the Gm2 techniques were selected.

A last remark has to be made on the selection of the number of sensors. Taking into account that in literature, there is no mention about it, for this investigation the number was fixed based on linear algebra considerations of the independence of the data acquired. For example, if 10 (number of target mode shapes selected, see §A.2) are the mode shapes to acquire at the aim to have 10 vectors linear independent, the number of sensors must be at least 10.

In the attempt to find a better solution at this problem and to check on the efficiency of the solution proposed, the values of the 5 comparison criteria investigated in Table 8 after having been normalised with respect to the number of sensors selected were plotted against it.

Unfortunately, by this comparison only three OSP techniques showed behaviours different from a monotonic crescent with the sensor number and only for the MAC_ERR criterion. Two (the EFI and the KE method) showed an identical conduct (see KEM plot in Figure 25), identifying a set of 19 sensors as the best solution up to 80 sensors.

	MSE	MAC_ERR	COND_N	FIM_DET	DPR_SUM
EFI	$_1$0.01	$_3$4.49	$_1$2.01E+01	$_1$2.25E-17	0.40
EFI-DPR	0.79	24.16	1.23E+10	0.00E+00	0.91
KEM	$_2$0.02	$_2$2.40	$_2$2.28E+01	$_2$1.10E-17	0.37
PCA	41.83	47.13	1.57E+11	0.00E+00	$_1$1.13
MIS	41.83	47.13	1.57E+11	0.00E+00	$_1$1.13
VrM	41.83	47.13	1.57E+11	0.00E+00	$_1$1.13
Gr1	467.27	30.51	1.71E+09	0.00E+00	0.00
Gr2	$_3$0.02	$_1$0.46	$_3$2.99E+01	$_3$1.19E-18	0.35
EVP	0.91	25.99	6.59E+08	0.00E+00	0.64
DPR	41.83	47.13	1.57E+11	0.00E+00	$_1$1.13
NODP	$_4$0.03	18.73	$_4$4.49E+03	1.47E-26	0.46
CNM	0.10	13.13	1.34E+04	$_4$1.33E-23	0.54
GRM	0.09	36.85	2.39E+09	0.00E+00	$_4$0.93
Gm1	0.05	40.43	1.40E+09	0.00E+00	0.85
Gm2	0.04	36.95	2.75E+09	0.00E+00	0.91
Gm3	0.05	40.43	1.40E+09	0.00E+00	0.85
Gm4	0.06	$_4$7.88	6.31E+10	0.00E+00	0.17
Gm5	0.11	33.84	1.50E+08	0.00E+00	0.67
GDM	19.38	39.55	3.29E+10	0.00E+00	$_2$1.08
GCN	21.42	29.21	6.68E+09	0.00E+00	$_3$0.97

Table 8 – OSP techniques: literature's comparison criteria.

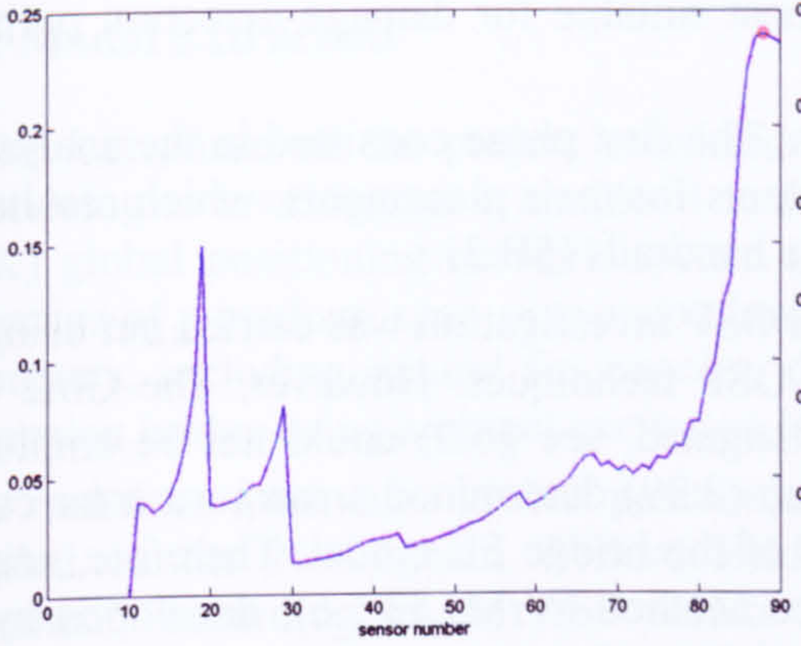

Figure 25 – KEM MAC_ERR plot.

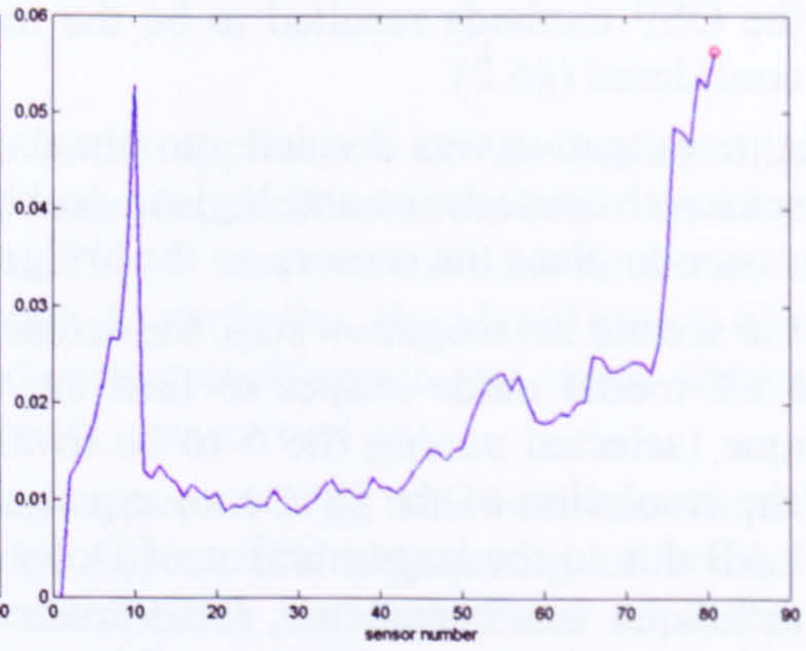

Figure 26 – CNM MAC_ERR plot.

However, the chosen sensor number (10 sensors) had better information content for each sensor than a network of 60 sensors. This finding confirms the robustness of the number selection criterion used (Figure 25).

The third OSP technique that showed a non-monotonic crescent performance with the increase of the sensor number was the CNM, which identified a network of 10 sensors as the best set up to 80 sensors (Figure 26).

These plots may be of help in the selection of the optimal sensor number.

6.3 Suspension Bridge

As mentioned before, the structure typology may affect the efficiency and the reliability of an OSP technique to design a sensor network capable of retaining sufficient information for a damage detection investigation. In order to verify this issue, a complex structure, as a suspension bridge, was used as a further test case for an OSP enquire, which results were experimentally verified by extracting the bridge mode shapes.

This investigation was part of a broader research project [180-181] aimed at undertaking the research required to set up a basic remote health monitoring system, using GPS sensors placed on an operational bridge (the Nottingham Wilford Bridge), linked to a new finite element/optimisation based health assessment software.

The research was structured in three tasks. In the first task carried out by Cranfield University, all the data on the bridge structure and geometry were analysed and used to build a bridge FE model, in order to design the best sensor network using OSP techniques. The second phase required the placement of the GPS sensors in the locations indicated by Cranfield and the acquisition of the data necessary (Nottingham University) for the extraction of the bridge modal properties (third task - Cranfield University).

6.3.1 OSP investigation

Considered the complexity of the structure and the considerable computational effort necessary for the evaluation of each OSP technique investigated in the previous section, only the OSP methods resulted to be the most suitable for damage detection purposes were considered (§6.2).

The investigation was divided into phases. The first phase consisted in the analysis of GPS sensor characteristics and logistic problems for their placements, which resulted in the decision to place the sensors on the bridge handrails (§B.3).

In the second investigation step, the actual OSP investigation was carried out using the bridge FE model mode shapes to feed the OSP techniques. However, The Gm2 OSP technique (selected among the 5 to be investigated, see §6.2) could not be employed, since the resolution of the Lyapunov equation (3.39) determined a memory error call in MATLAB due to the large number of DoFs of the bridge FE model. Therefore, another OSP technique was considered, the Variance Method (VrM, §3.5.6), developed by the author from the Most Informative Subset (MIS, §3.5.5) technique, which was also considered for comparison.

Differently from the application of the VrM method employed on the cantilever beam investigation, which used a selection algorithm analogous to that used by the EVP and other traditional energetic based techniques, in this investigation the VrM algorithm placed the sensors on the locations of local maxima of the function Vr (see eq. 3.22) sorted in decreasing order (§3.5.6). A further, OSP technique investigated was NODP, which in the first OSP investigation, performed on a cantilever beam, had the second best performance between the energetic OSP approaches, after the EVP method.

Therefore, for the OSP investigation task, seven different optimal sensor placement techniques were analysed, three based on the maximisation of the Fisher information

matrix (EFI, EFI-DPR and KEM), two on statistics (MIS and VrM) and two on the energetic approach (EVP and NODP).

FEM mode shape displacements were taken as "measured" data set and two comparison criteria were employed. The first criterion was based on the mean square error between the FE model and the cubic spline interpolated mode shapes. The second criterion measured the information content of each sensor location to investigate the strength of the acquired signals and their ability to withstand the noise pollution keeping intact the information content relative to the structure properties.

The comparison criteria results (appendix B) showed a better performance of the EFI based techniques compared to the KEM, VrM and energetic approach based methods. More specifically, the Effective Independence Driving-Point Residue (EFI-DPR) method designed the best sensor network for the identification of low frequency vibration characteristics of the studied bridge, because of its small MSE, large signal strength and its capability of respecting the bridge symmetry (§B.4).

The OSP technique developed by the author resulted very close to the EFI-DPR technique, in terms of the capability to capture the vibration mode shape and in terms of signal strength. However, the VrM presented a unique characteristic in the world of the OSP techniques, which is the indication of the Optimal Number of Sensors (ONS). This characteristic was not exploited since the ONS resulted larger than the number of GPS sensors available. However, the author is confident on the efficiency and the reliability of this new feature (ONS) introduced by the VrM, for future applications.

6.3.2 Modal Extraction

The last phase of the project consisted in the application of the modal extraction methodologies investigated in chapter 4 to test the capabilities of the real-time kinematic (RTK) global positioning network system (GPS) to measure the low frequency modal properties of a medium span suspension bridge. In particular, the identification of modal parameters, including natural frequencies, damping coefficients and mode shapes of a suspension bridge using ambient excitation loads, was carried out.

A real-time kinematic global positioning system (GPS) has been developed and installed on the Nottingham Wilford Bridge for on-line monitoring of bridge deck movements according to the OSP results obtained in the first phase of the project. Displacements responses of this structural system were fed to wavelet transforms to identify its dynamic characteristics. The modal properties were extracted using a two-step methodology. In the first step, the random decrement method was used to transform random signals in free vibration responses. Finally, the Eigensystem Realization Algorithm (ERA) and wavelet based techniques were used to extract natural frequencies and to determine the first bending mode shapes of the structure. This work showed the potential of using GPS sensors to monitor and measure the vibration properties of a medium span suspension bridge in a low frequency range.

As shown in appendix B paragraph B.5, only the first global frequency mode was extracted from the data collected. No other modes were extracted. This was expected to depend on in-service loads (i.e. wind, people passing on the bridge), incapable of exciting other vibration modes, on the low frequency resolution of the GPS used (<10Hz), and on

the failure in meeting the requirement of in-service loads randomly distributed with zero mean.

The comparison between the experimental data and the FE model showed that the first natural frequency was computed with an error of 20% (Table 9). This difference is justified by the fact that many uncertainty and unknown variables were present when building the FE model. In particular, accurate material properties (aging effect) and section geometry of beams placed under the wood deck of the bridge were not available. However, it must be pointed out that the main objectives of building the FE model was to provide indications on the optimal sensor location and maximum frequency that could be measured with the GPS, which were successfully met.

Moreover, this experimental extraction confirmed the capability of the wavelet approach to extract structure mode shapes with reliability and efficiency comparable to that of the ERA. Moreover, the separation between noise derived and actual mode shapes becomes easier with the wavelet based approach, which allows the user to select the mode shape to extract according to physic based rules (§4.6.2). So a less expert user is required with respect to the ERA method. As matter of the fact, the ERA sorted out the actual first bridge mode shape as its 7^{th}, requiring to the user to avert the mathematical mode shapes from the real modes. This was carried out by comparing the shapes of the FE mode shapes with those extracted by the ERA. Instead, for the wavelet based technique (Figure 27), only one mode complied with the requested feature (§4.6.2) in the frequency range inspected (1-5 Hz). This vibration mode was described in Figure 27 by a red line parallel to the time axis in the time-frequency space, evaluated using a wavelet transform of a free-decay signal derived by a GPS acquired time signal employing the Random Decrement Technique (RDT, §B.5.2). The remaining lines parallel to the time axis (in white) were not considered because either did not last for the whole time lag investigated or had an amplitude to small compared to the free-decay signal magnitude.

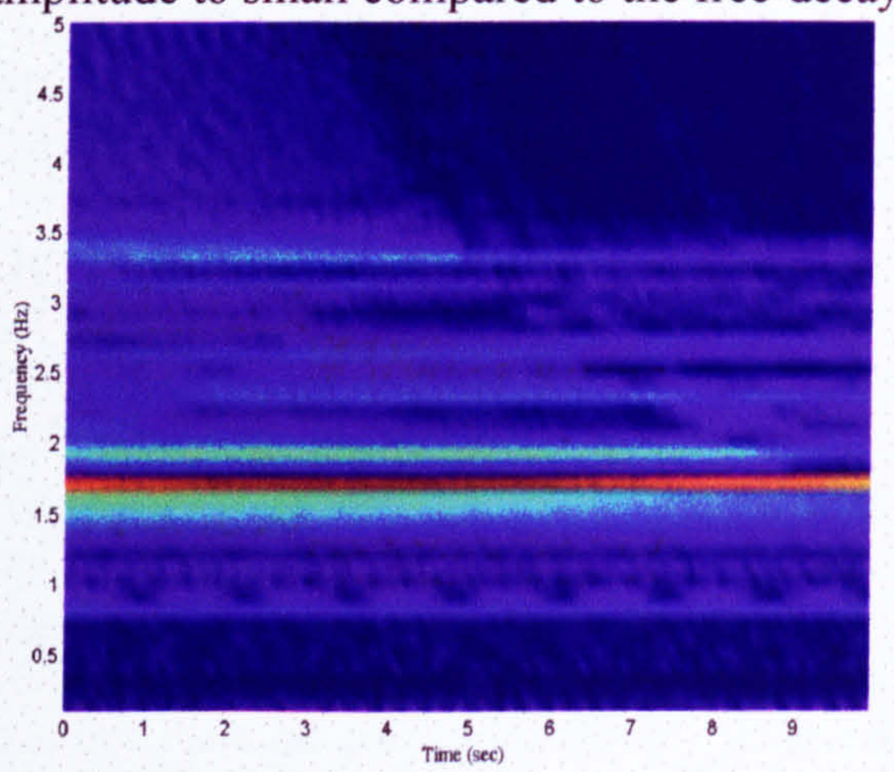

Figure 27 – Wavelet transform of a GPS signal acquired on the Wilford suspension bridge.

Extraction Technique	Frequency [H z]	Modal Damping
ERA	1.74	0.025
WME	1.72	0.019
FEM	1.44	Not estimated

Table 9 – Modal frequency comparison.

6.4 Cantilever beam vs. suspension bridge: OSP results

As mentioned in §6.2, OSP techniques have different behaviours according to the typology and geometry of the structure under investigation. This means that an OSP technique "optimal" for a beam might not be "optimal" for a bridge.

This is clear by comparing the cantilever beam and the suspension bridge using FIM_DET (sorted out in decreasing order in Table 10) and MSE (sorted out in increasing order in Table 11) comparison criteria.

At first glance, the performance fall of the KEM (yellow shadowed cells) was clear in both applications, as well as the great improvement of the EFI-DPR technique (red shadowed cells). Furthermore, a deterioration of the NODP and EVP was also evident, while the EFI kept on top behaving with the change of the structure (light blue cells). Although, the EFI was third in terms of MSE for the bridge, its difference with the VrM and the EFI-DPR method was very small (§B.4). As far as it concerns the VrM, its improvement were related to the different sensor selection algorithm employed. This picked up the location corresponding to the local maxima of the Vr function, instead of those corresponding to its highest values (§B.3) as for the VrM of the beam application.

FiM_DET order	Cantilever beam	Suspension Bridge
1	EFI	EFI
2	KEM	EFI-DPR
3	NODP	VrM
4	EVP	KEM
5	VrM	EVP
6	EFI-DPR	MIS
7	MIS	NODP

Table 10 – OSP comparison: first and second OSP investigation – FIM_DET.

MSE order	Cantilever beam	Suspension Bridge
1	EFI	EFI-DPR
2	KEM	VrM
3	NODP	EFI
4	EVP	NODP
5	VrM	KEM
6	EFI-DPR	EVP
7	MIS	MIS

Table 11 - OSP comparison: first and second OSP investigation – MSE.

By comparing the physical deployment of the sensors on the structures carried out by the OSP techniques analysed both on the cantilever beam (Figure 28) and on the suspension bridge (Figure 29), it is clear that a common feature of the best performing OSP methods, according to the comparison criteria used, is the equal spacing of the sensors on the structures, which determines a sort of regular grid of sensors on the structure. This characteristic is common to the EFI and KEM, the best OSP methods on

the cantilever beam, and also familiar to the EFI, EFI-DPR and, on a certain extent, to the VrM, the best OSP techniques for the bridge studied.

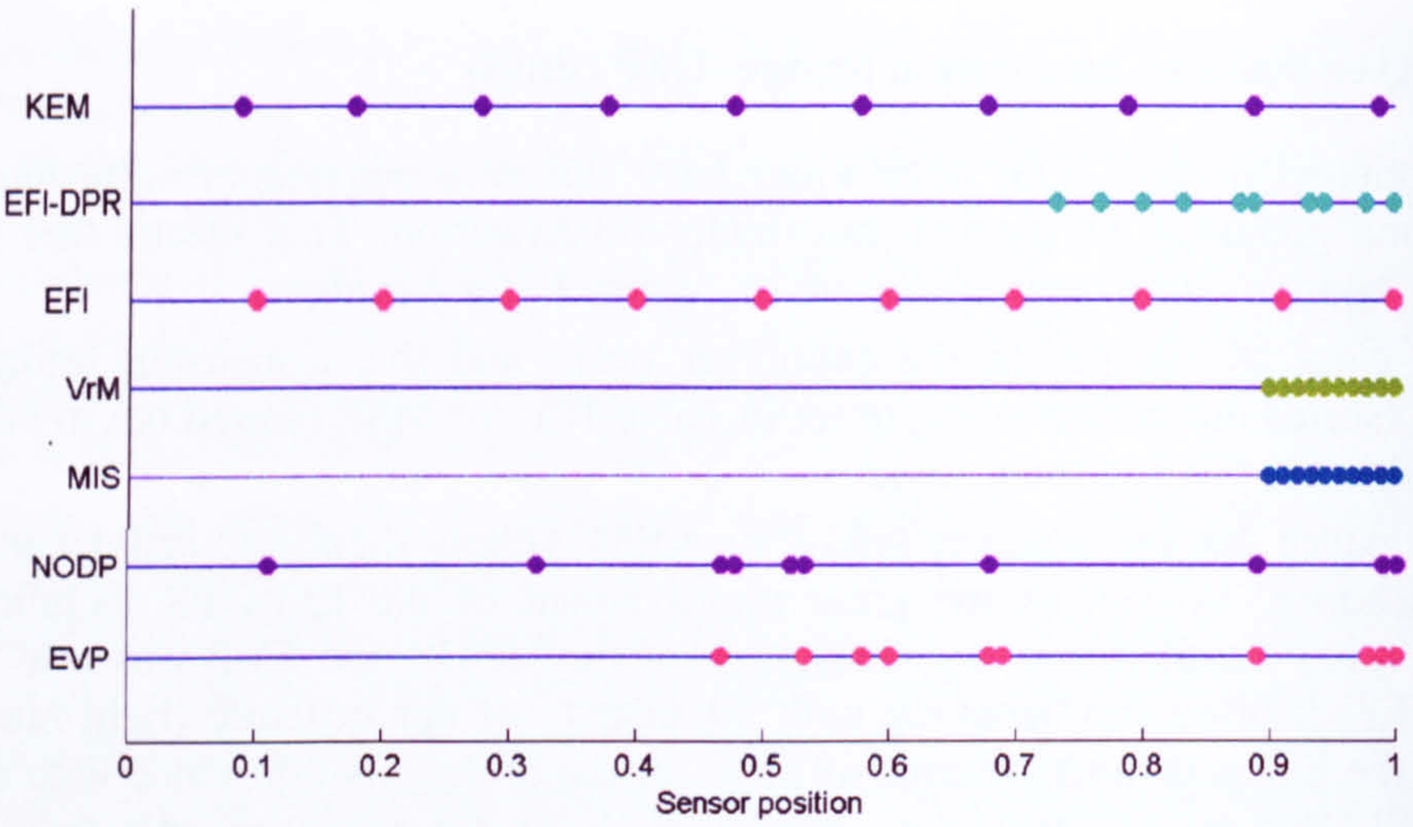

Figure 28 – OSP comparison: Cantilever beam sensor deployment.

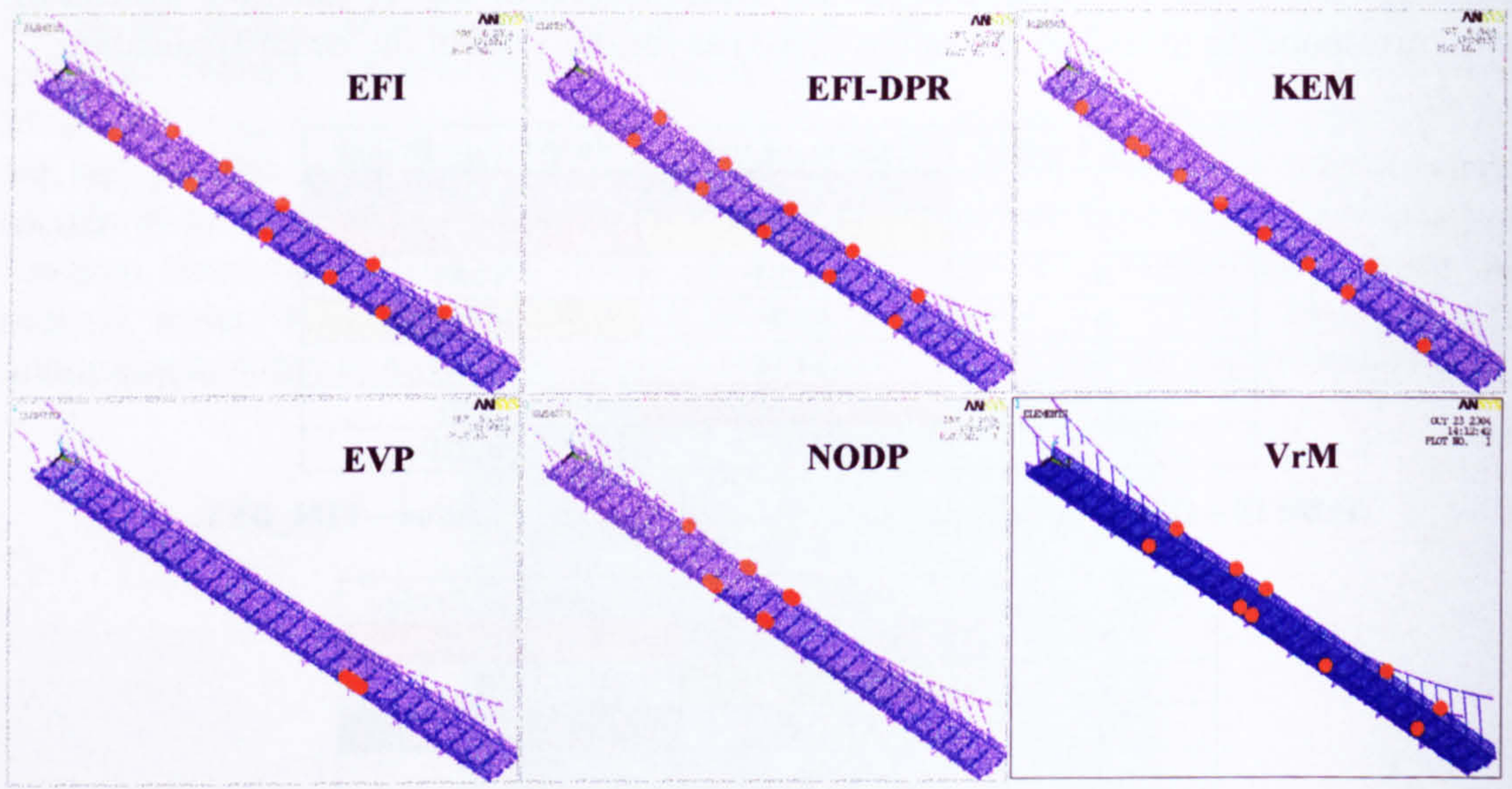

Figure 29 – OSP comparison: Suspension bridge sensor deployment.

Finally, the properties, which an optimal sensor network should respond to, can be stated:

1. The sensor deployment should capture the structure dynamic response by being capable of reproducing the structure vibration mode shapes with the smallest error possible (e.g. minimisation of the MSE).
2. The sensor deployment should maximise the information content of the acquired signal (e.g. maximisation of the FIM_DET).
3. The sensor should be deployed according to a well spaced grid enveloping the entire structure surface.

6.5 Plate-like structures: GLDDO approach

In the previous paragraphs, the OSP techniques were investigated on two different kinds of structures, in order to identify the best OSP technique and the guidelines to recognize a well deployed sensor network for damage detection purposes. No attempts were carried out to find out the effects of Target Mode Shape Selection (TMSS) techniques, residue functions and minimisation algorithms on the damage detection. At this aim a third investigation explored the consequences on damage detection of these factors on a plate-like structure, since this is the most common typology of components in aeronautic and civil structures. Moreover, the five OSP techniques resulted to be best performing on the cantilever beam (EFI, EFI-DPR, KEM, EVP and Gm2) were used to design the sensor networks on the test case selected (appendix C). Further attention was given at the influence of a global approach compared to the global-local on damage detection. A last effort was committed to a comparative analysis of the residue function designed by the author to a mode shape based residue function (MODE) used in literature (§2.4.2.1).

A detailed account of the results obtained is given in appendix C, where the six factors, mentioned above, were analysed.

6.5.1 Global-Local vs. Global approach

The first variable to be investigated was the effectiveness of a Global-Local (G-L) approach compared to the conventional Global (G) approach. The investigation was aimed at establishing the damage detection improvements deriving by the adoption of the G-L approach instead of a global one. Expected advantages were an improved convergence of residue function minimisation to solution, leading to a greater resolution and smaller errors, consistent run time savings, due to the reduction of the variables involved in the minimisation, and smaller amount of data employed (§6.6).

Because of run time issues (for some residue functions could exceed 1000 minutes), the analysis was carried out using only one OSP technique, the EFI method. The choice of the EFI was due to the reliability showed in the investigation performed on the cantilever and the bridge structure, where the EFI method was the sole to be constantly among the most performing OSP techniques.

Furthermore, the G-L vs. G investigation was also set to explore the effects of the Target Mode Shape (TMS), Residue Function (RF) and Minimisation Algorithm (MA) selection on the damage detection output. Among the RF inspected, there was also the MODE RF.

The investigation results (§C.4.3) showed that a correct identification of the defects (Figure 30-Figure 31), introduced in the three damaged configuration investigated (§C.2), was affected by the variables (TMS, RF, MA) investigated in many ways.

The most evident outcome concerned the utterly inefficiency of the G approach for damage detection using gradient based MA as LLSO or the LSO. An exception was given by the SVD MA (sensitivity approach, §2.4.2.1) using the MODE RF, which predicted correctly the damaged locations, although the flaw severities were constantly overestimated up to 20%. However, the G-L approach, gradient based MA, identified the

damages, introduced in the plate-like structures, only for TMS selected using the Maximum Strain Energy (MSE) approach. No combination of the variables considered was capable of providing a correct identification of the introduced defects for TMS selected using either Minimum Modal Frequency (MMF) or Maximum Kinetic Energy (MKE) criterion. Moreover, convergence problem were recorded for the MODE RF using the G approach when was minimised by LLSO and SVD MA (§C.4.3.1). The time savings deriving by the use of the G-L approach using gradient based MA (LLSO, SVD and LSO) were very large (Figure 31) 40 minutes (G-L) against the 200 of the global approach (MODE RF).

On the other hand, the damage detection predictions obtained using the SAM as MA (Figure 30) appeared to be in clear contrast with the previously discussed results. The RFs minimised by the SAM were:

- The COMAC_MAC RF, the only RF investigated among the MAC and COMAC based, since these RFs showed the same behaviour when minimised using gradient based (LLSO) or SVD algorithms.
- The FRAC based RFs (FRACm, FRACr and FRACc). These RFs were minimised only with SAM, because gradient based algorithms are more liable to hit local minima than the SAM, and because FRF based algorithm are prone to convergence problems (§2.4.2.2). Moreover, the sensor networks used were the same employed by the COMAC and MAC based functions.

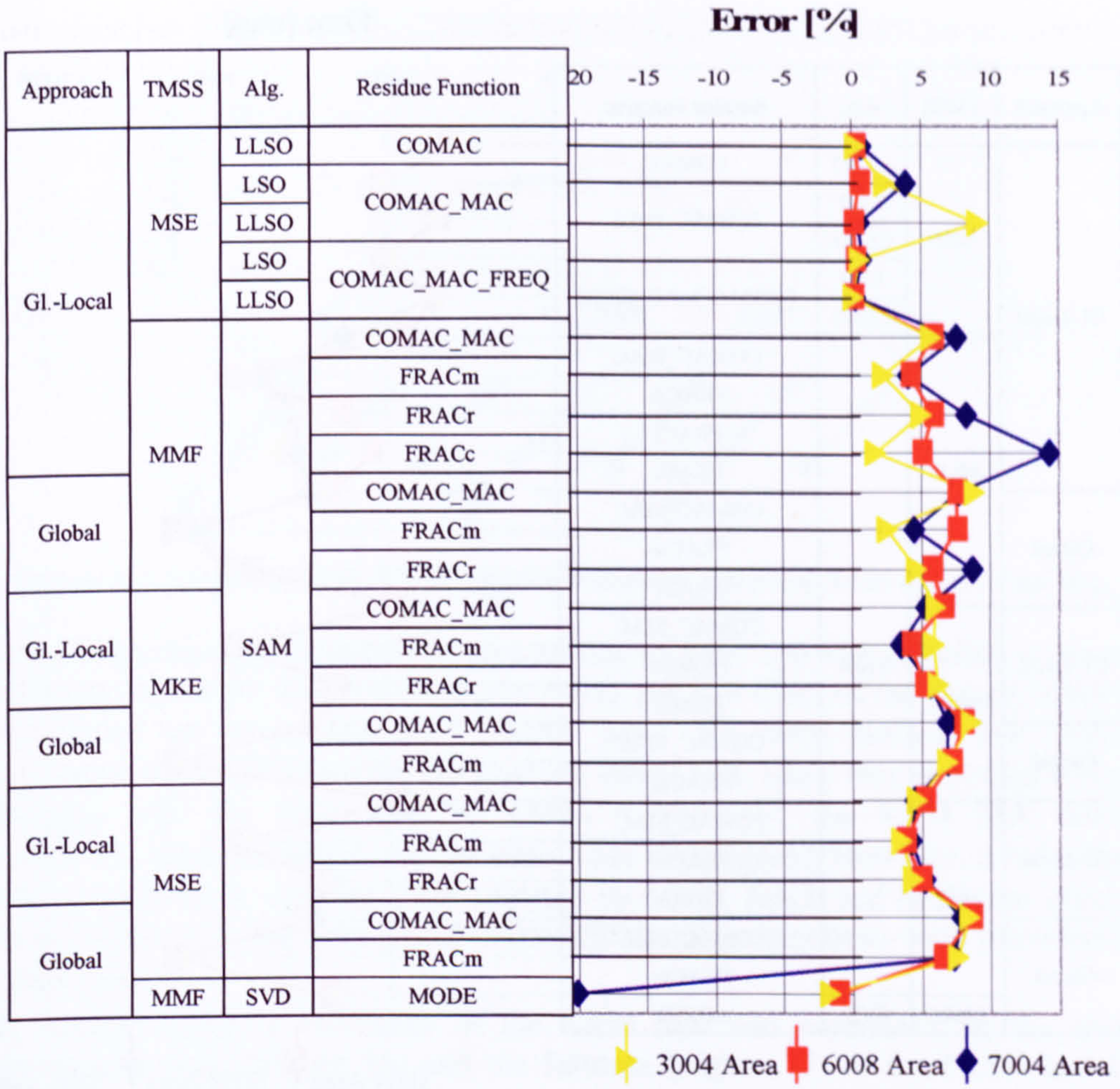

Figure 30 – Global-Local vs. Global approach damage detection: Error of the damage severity predicted.

The SAM damage detection results, showed in Figure 30 and reported in appendix C, did not record convergence problems. Furthermore, despite of some faulted detection predicted by FRACc and FRACr RFs used with MMF and MKE selected TMSs, the damage detection process resulted very successful. The G-L approach was better in predicting damage severity than the global process, reaching improvements of 50% (Figure 32). The time saving realised adopting a G-L approach, instead of the G, ranged from a minimum of 40% to a maximum of 80% (Figure 33).

Approach	TMSS	Alg.	Residue Function
Gl.-Local	MSE	LLSO	COMAC
		LSO	COMAC_MAC
		LLSO	
		LSO	COMAC_MAC_FREQ
		LLSO	
	MMF	SAM	COMAC_MAC
			FRACm
			FRACr
			FRACc
Global			COMAC_MAC
			FRACm
			FRACr
Gl.-Local	MKE		COMAC_MAC
			FRACm
			FRACr
Global			COMAC_MAC
			FRACm
Gl.-Local	MSE		COMAC_MAC
			FRACm
			FRACr
Global			COMAC_MAC
			FRACm
	MMF	SVD	MODE

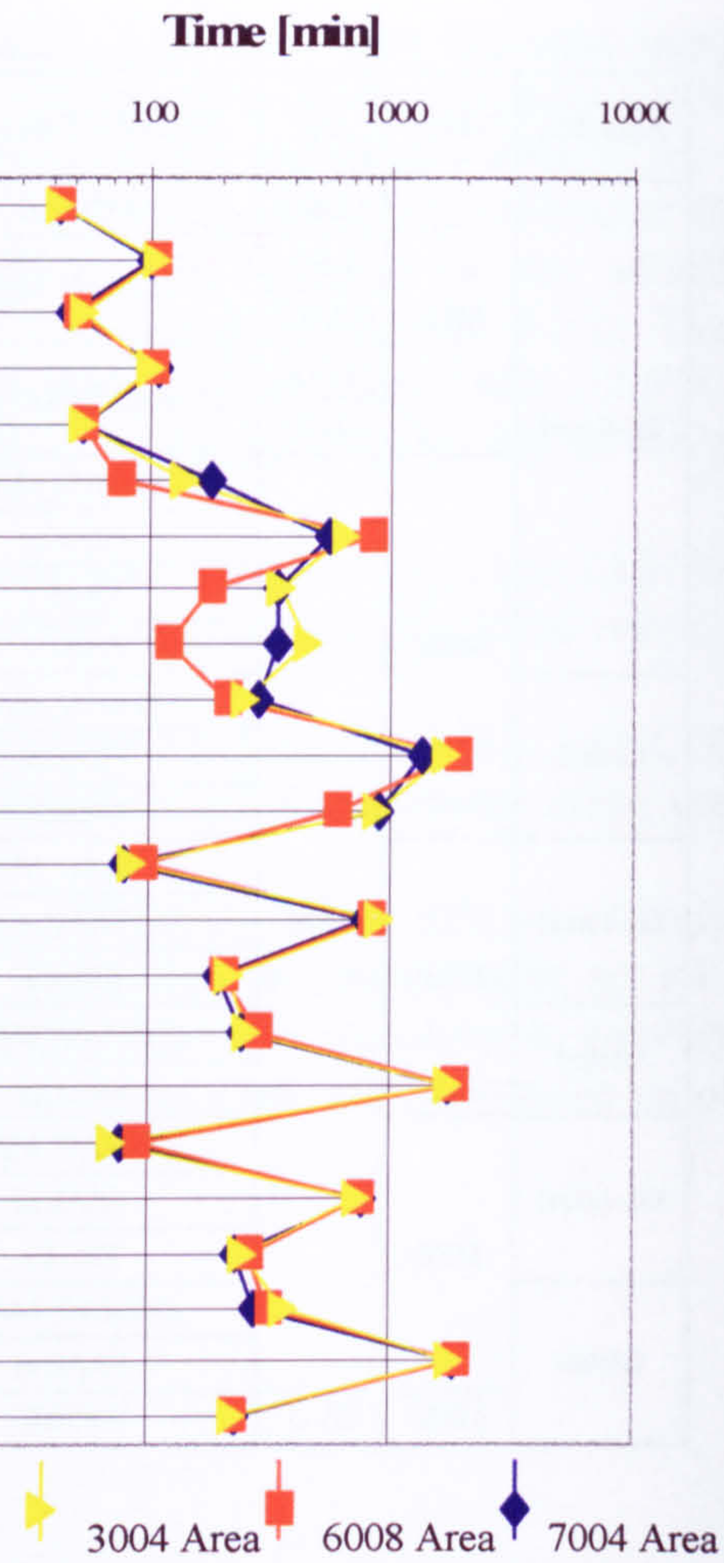

Figure 31 – Global-Local vs. Global approach damage detection: Run Time.

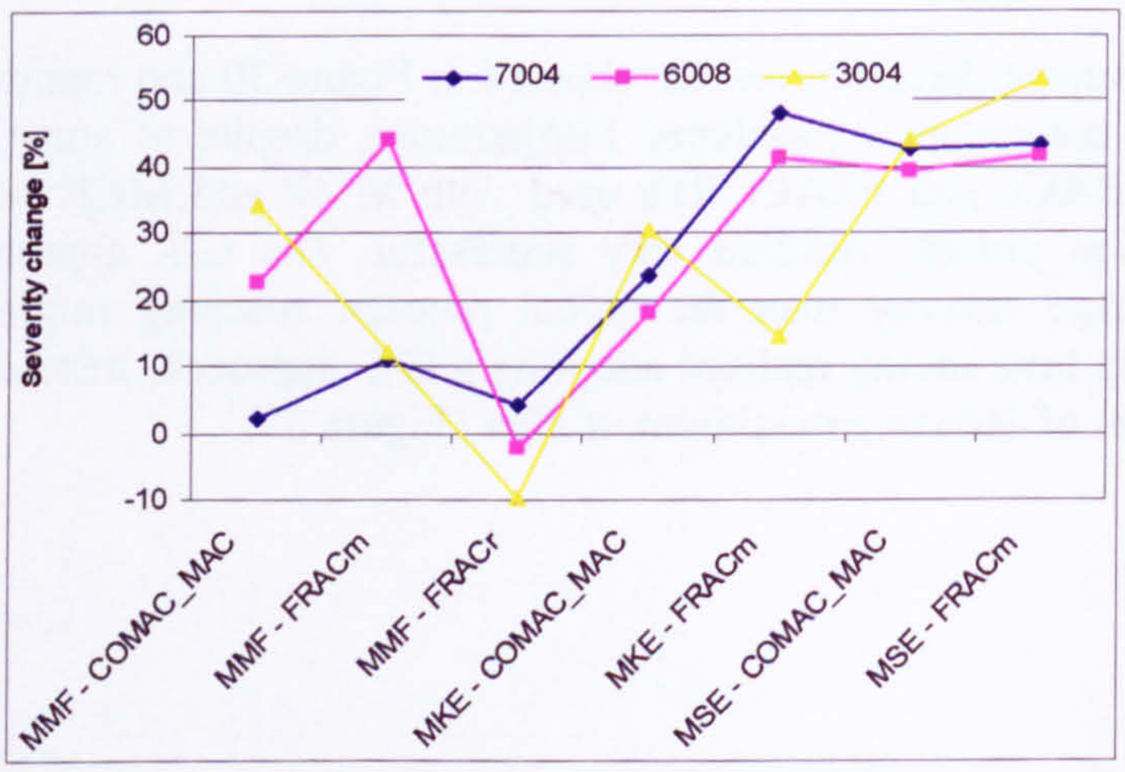

Figure 32 – Global-Local vs. Global approach damage detection: SAM severity estimation improvements.

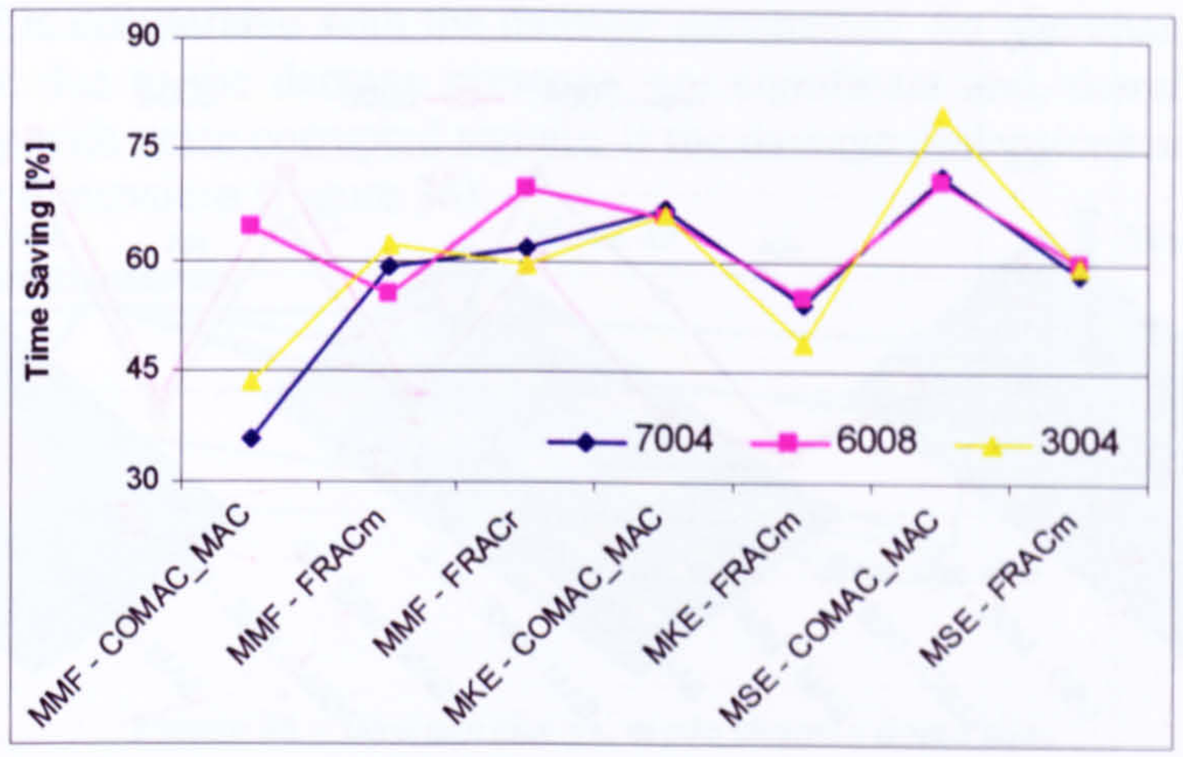

Figure 33 – Global-Local vs. Global approach damage detection: SAM run time savings.

An insight on the damage detection process due to TMS and MA selection is given by Figure 34 and Figure 35, where the severity errors and run times of the damage detection process, carried out minimising the COMAC_MAC RF, were plotted. The TMSS is clearly a major influence factor for the gradient based MA, since they provided a correct identification only for MSE selected TMSs. Conversely, the SAM MA detected successfully the damages introduced for every case investigated. However, a reduction of the SAM severity error with the TMS selected by MMF, MKE and MSE was observed (Figure 34). Moreover, the only global successful damage detections were provided by a SAM minimisation.

The damage detecting efficiency of the SAM MA was contrasted by the smaller damage severity error (Figure 34) and the fastness (Figure 35) of the LLSO and LSO algorithms.

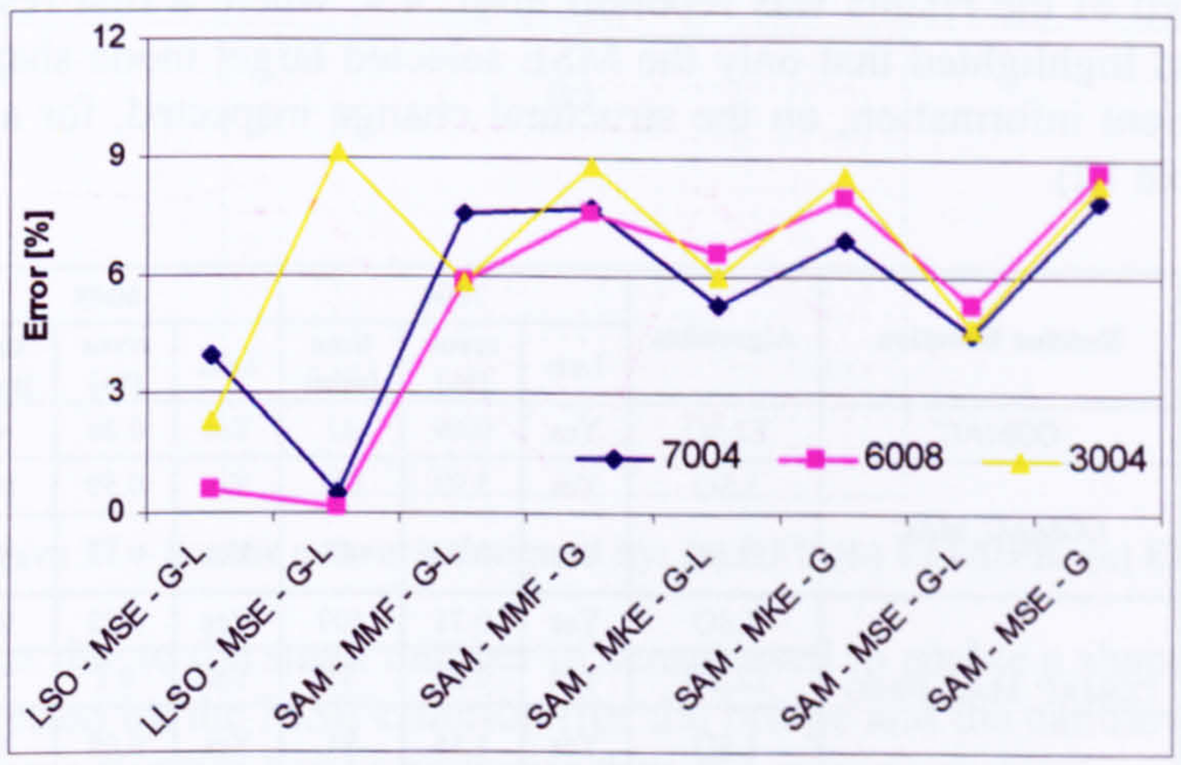

Figure 34 – Global-Local vs. Global approach damage detection: COMAC_MAC severity estimation.

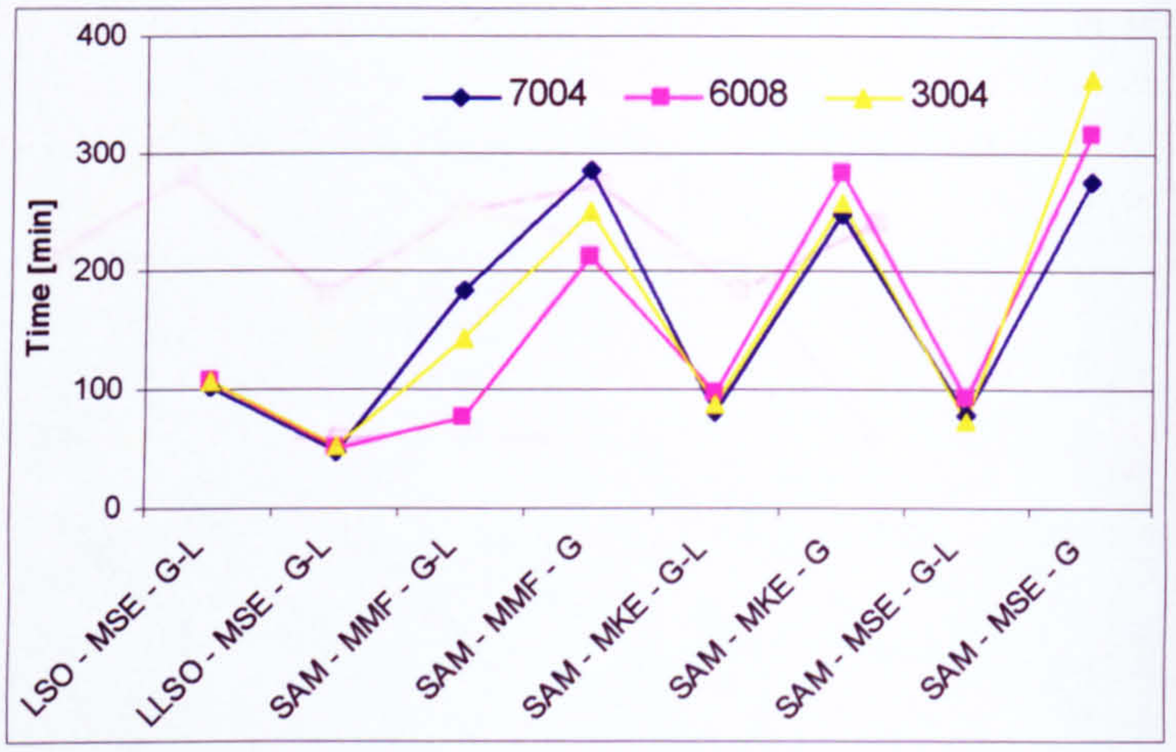

Figure 35 – Global-Local vs. Global approach damage detection: COMAC_MAC run time.

6.5.2 OSP results

The cantilever beam OSP investigation outcomes (§6.2) gave some insight on the OSP for the GLDDO approach. Then, these results were compared to a second OSP investigation on a suspension bridge, which led to the statement of three general rules (§6.4) that a sensor network should comply with. Finally, these guidelines were further tested on the same plate-like structure inspected for the G-L/G approach comparison. This last test was carried out on the 6 OSP techniques selected in §6.2, EFI, EFI-DPR, KEM, EVP and Gm2, using all COMAC and MAC based RFs and gradient based MA, and all the TMSS techniques, (investigated in §3.3, MMF, RRS, MKE, MSE). The SAM MA and FRAC based RFs were not investigated due to run time issues.

A full record of the results was reported in §C.4.4, where a first result analysis was carried out and highlighted that only the MSE selected target mode shapes were able to provide sufficient information, on the structural change inspected, for a correct damage detection (Table 12).

TMSS	OSP	Residue Function	Algorithm	7004			6008			3004		
				Loc.	error [%]	time [min]	Loc.	error [%]	time [min]	Loc.	error [%]	time [min]
MSE	EFI	COMAC	LLSO	Yes	0.69	42	Yes	0.26	42	Yes	0.3	43
		COMAC_MAC	LSO	Yes	3.93	102	Yes	0.59	106	Yes	2.32	106
			LLSO	Yes	0.50	47	Yes	0.15	49	N. A. 2006	9.15	53
		COMAC_MAC_FREQ	LSO	Yes	0.71	109	Yes	0.22	103	Yes	0.59	100
			LLSO	Yes	0.28	54	Yes	0.1	54	Yes	0.13	53
	EFI-DPR		LSO	Yes	1.35	84	Yes	0.09	89	Yes	0.76	95
	EVP	COMAC_MAC	LLSO	Yes	10.28	43	Yes	1.07	40	Yes	0.53	46

Table 12 – Plate-like structure: OSP results.

This result was not completely unexpected, since likewise to damage detection ultrasonic techniques, the damage can be detected if and only if the wavelength of the

ultrasonic signal is comparable with the damage dimensions. So, the changes occurring on mode shapes, due to the damage presence, are significant and, therefore, easier to detect, especially with noise corrupted signals, if the damage dimensions are comparable with mode dome dimensions (Figure 36).

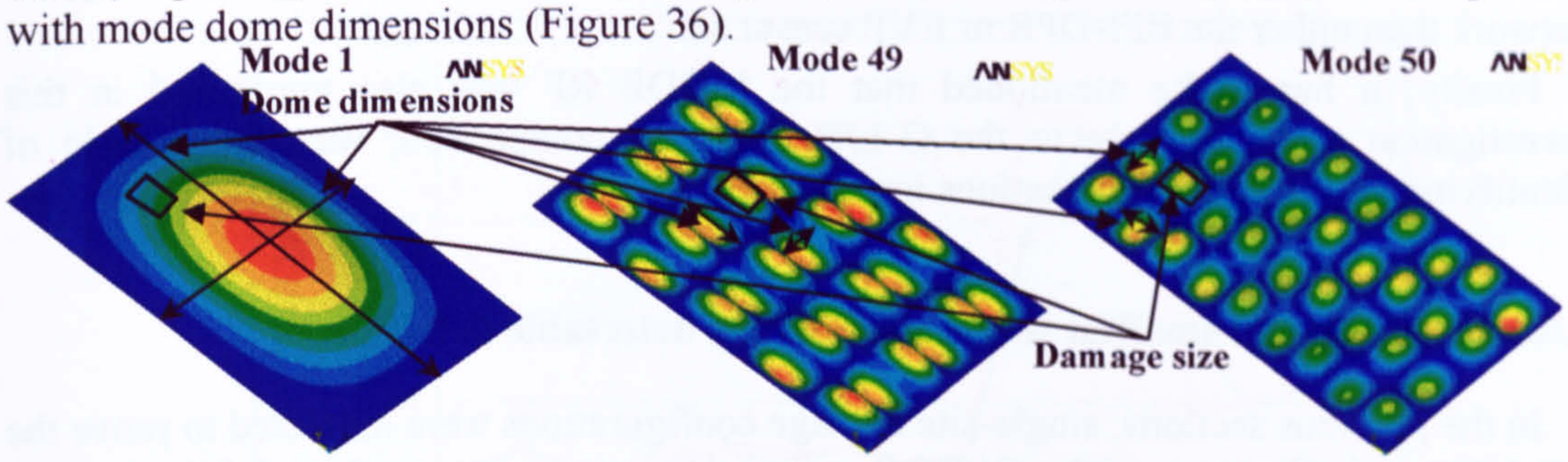

Figure 36 – Damage size vs. mode shape's dome size.

This evidence drives the TMS selection to high frequency modes, whose dome size are comparable to the size of the smallest damage to identify. Unfortunately, this trend contrasts with the high density of vibration modes at high frequencies and the increase of problems related to their extraction, SNR, mode separations, mode excitation and etc…

Furthermore, it must be mentioned that the sensor network derived using the MSE selected target mode shapes did not fulfil the guidelines traced in §6.4 (Figure 37).

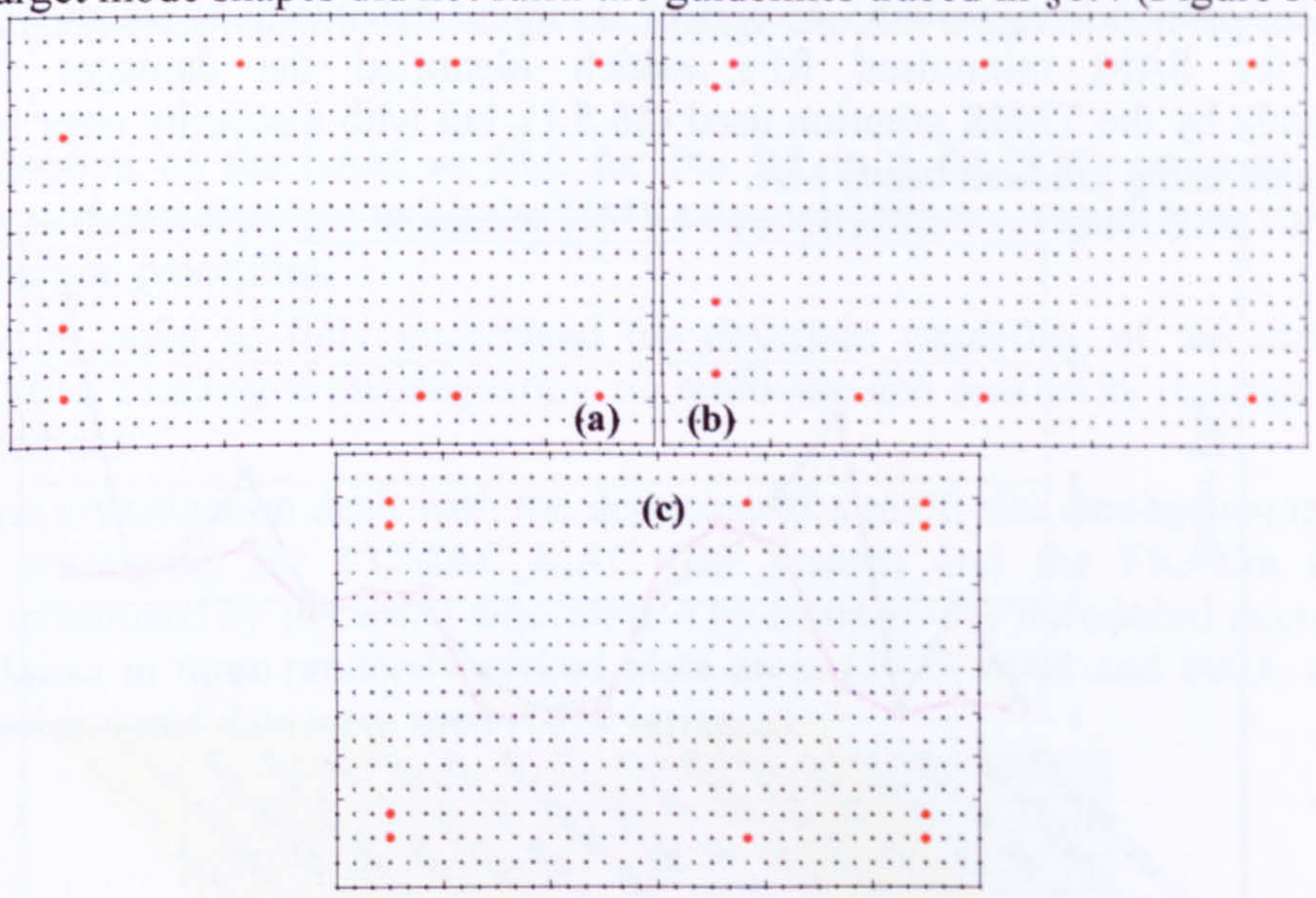

Figure 37 – Sensor network designed by: (a) EFI; (b) EFI-DPR; (c) EVP.

The reason was due to the small number of sensor used to enable a shape reproduction of the modes selected by the MSE criterion (for the bridge and the cantilever beam). For such task the sensor number has to be larger than the maximum number of mode shape domes present in the TMS investigated (e.g. for the case investigated at least 36 sensors are necessary to reproduce the 50^{th} mode shape). However, nonetheless the poor sensor networks (according to §6.4 rules), the damages introduced were detected correctly using only three sensor sets against the 16 investigated (§C.4.2). Among these sensor deployments the best resulted to be the EFI method, which was capable of supplying

enough information to the damage detection process to detect the damage inspected for all three COMAC and MAC based RFs against one for the EFI-DPR and EVP (Table 12). Moreover, the damage severity was predicted with a smaller error using an EFI sensor network than either the EFI-DPR or EVP sensor set.

Finally, it has to be mentioned that the MODE RF was also minimised in this investigation and, similarly to the G-L/G approach comparison, was not capable of identifying all the damaged locations investigated (§C.4.4).

6.5.3 Multi-site and smallest single-site damage detectable detection

In the previous sections, single-site damage configurations were inspected to prove the reliability and efficiency of the GLDDO approach in comparison with a global approach and a mode shape based RF (MODE). At the same time, the influence of OSP, TMSS and MA was investigated. These investigations highlighted the large improvements in terms of damage severity error and run time savings due to the adoption of G-L approach (§6.5.1) and the reliability of an EFI designed sensor network (§6.5.1-6.5.2). Furthermore, the importance of the TMS selection was also brought to attention by analysing the OSP results (§6.5.1), which underlined the strong link between a correct damage detection and a MSE selected TMS set for gradient based RF minimisation (LLSO, LSO and SVD algorithm). Moreover, a similar behaviour, although weaker, was observed for SAM minimised RFs, which identified the damages introduced independently by the TMSS criterion used (§6.5.1), but with a severity error larger than that evaluated using gradient based MA.

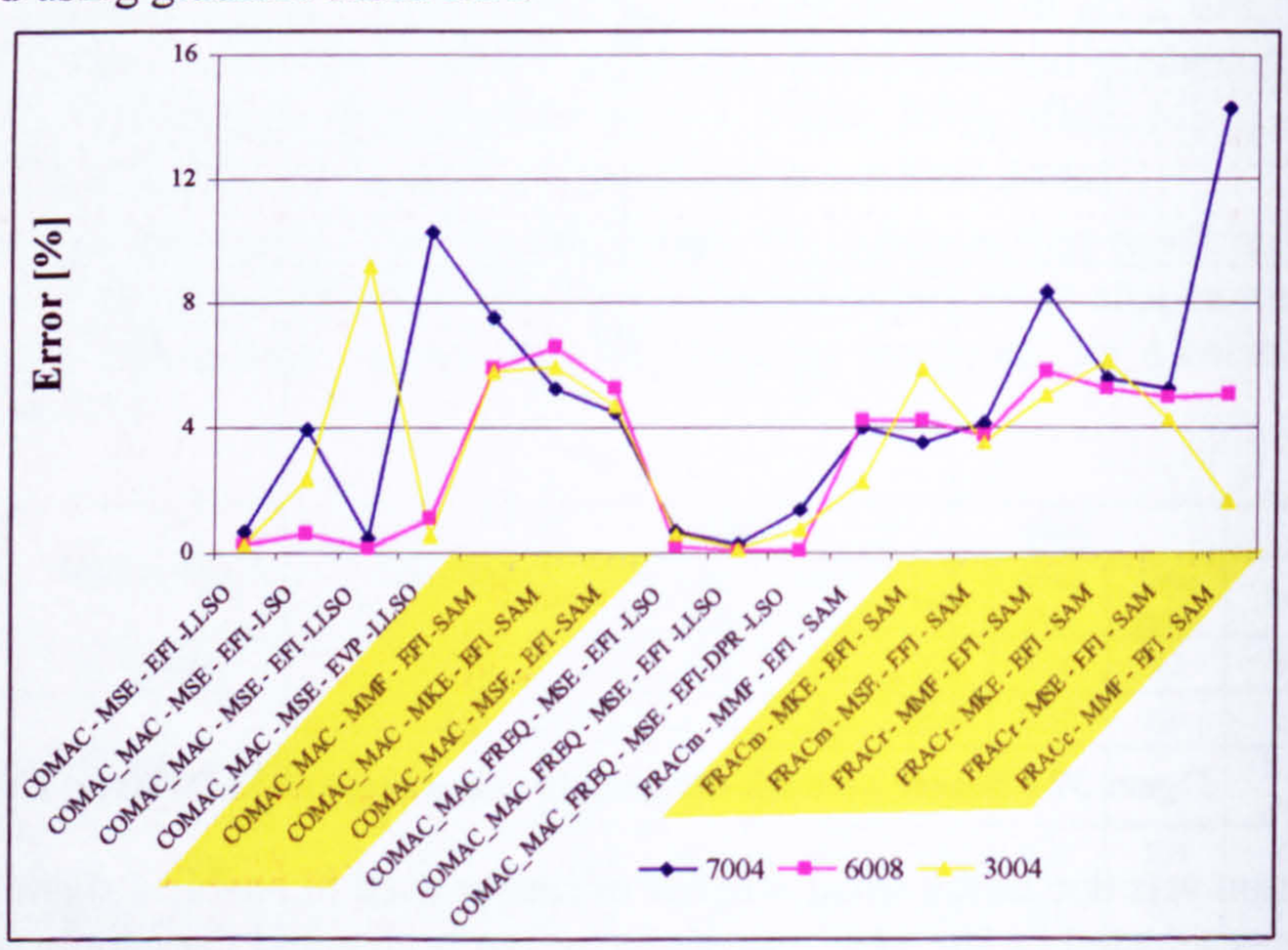

Figure 38 – Plate-like structure: single site damage detection using GLDDO approach – severity error.

Therefore, taking into account the problems related to the high frequency mode extractions (§6.5.2), the detection reliability, the SAM minimisation algorithm was considered to be the best among those investigated.

Among the four RFs minimised by the SAM, the FRACm resulted the best in terms of severity prediction, while the COMAC_MAC RF was the fastest, and the run times were comparable with those of the gradient based techniques (Figure 39).

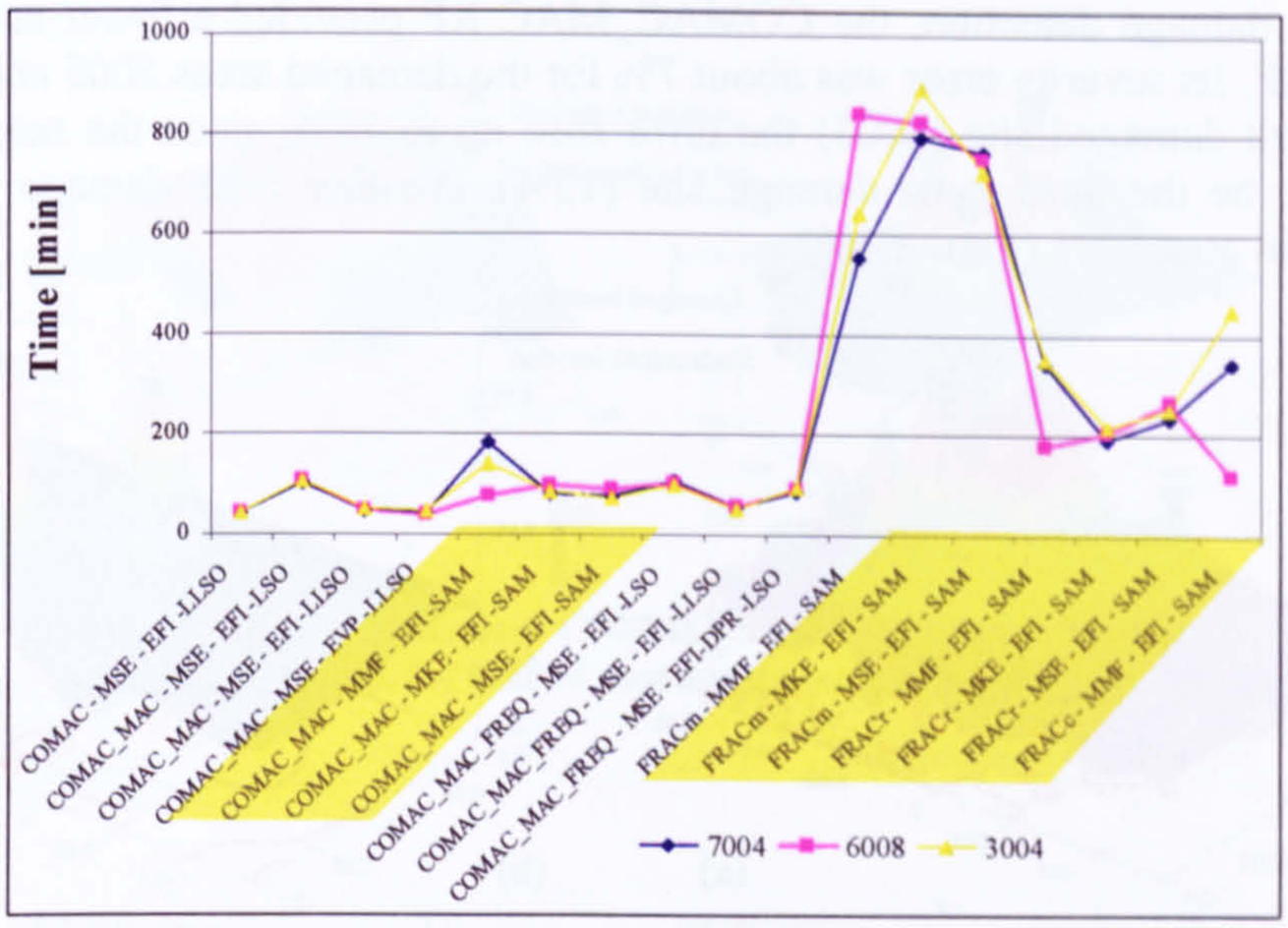

Figure 39 – Plate-like structure: single site damage detection using GLDDO approach – run times.

The adoption of the SAM as MA for the RF in a GLDDO approach gives the possibility to detect damages using the MMF selection criterion, simplifying the vibration mode extraction procedure.

Finally, in order to fully understand the detection capability of the methodology developed two conclusive investigations, on multi-site and sensitivity damage detection, were carried out.

The first investigation dealt with the detection of a multi-site damage using GLDDO approach employing the COMAC_MAC (the fastest) and the FRACm (the most accurate) minimised by the SAM algorithm. The damage was introduced decreasing the plate thickness in three randomly picked plate areas (5005, 6008 and 8003, see Figure 40). Noise corrupted data were used (10% variance).

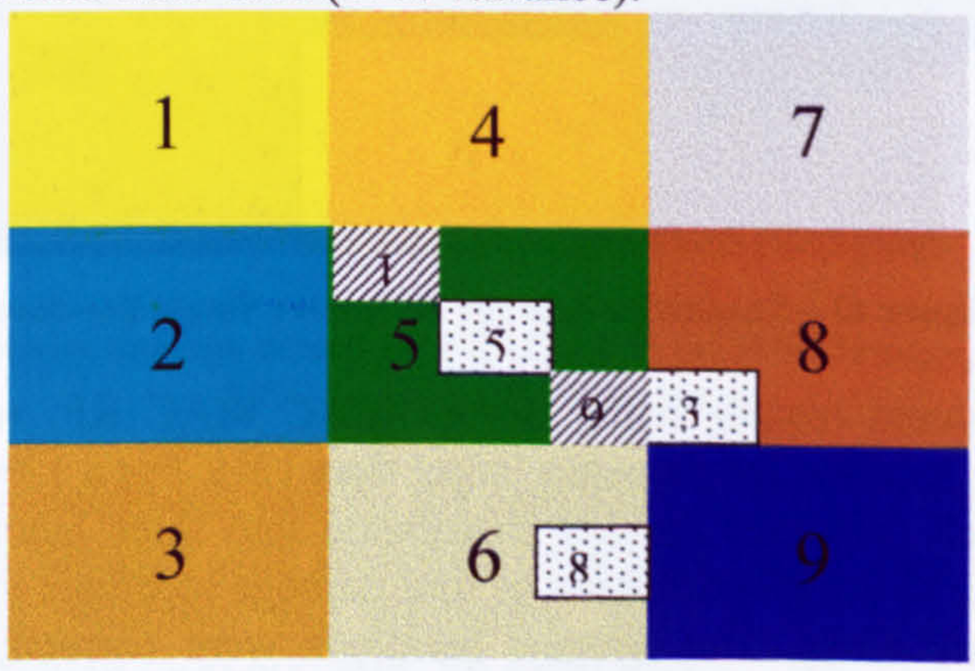

Figure 40 – Multi-site damage.

The damage estimations (Figure 41) showed that the FRACm residue function was able to detect the multi-site damage with a maximum error of 5%, although three false damages were detected with a damage severity estimated smaller than 5%. As for the single-site damage detection, the COMAC_MAC RF provided a lower accuracy of the FRACm RF. Its severity error was about 7% for the damaged areas 5005 and 6008, while for the third damaged site (8003) the error rose up to 15%, since the next area (5009) resulted to be the third most damage site (15%). Another false damage site was also identified in area 5001 (Figure 40).

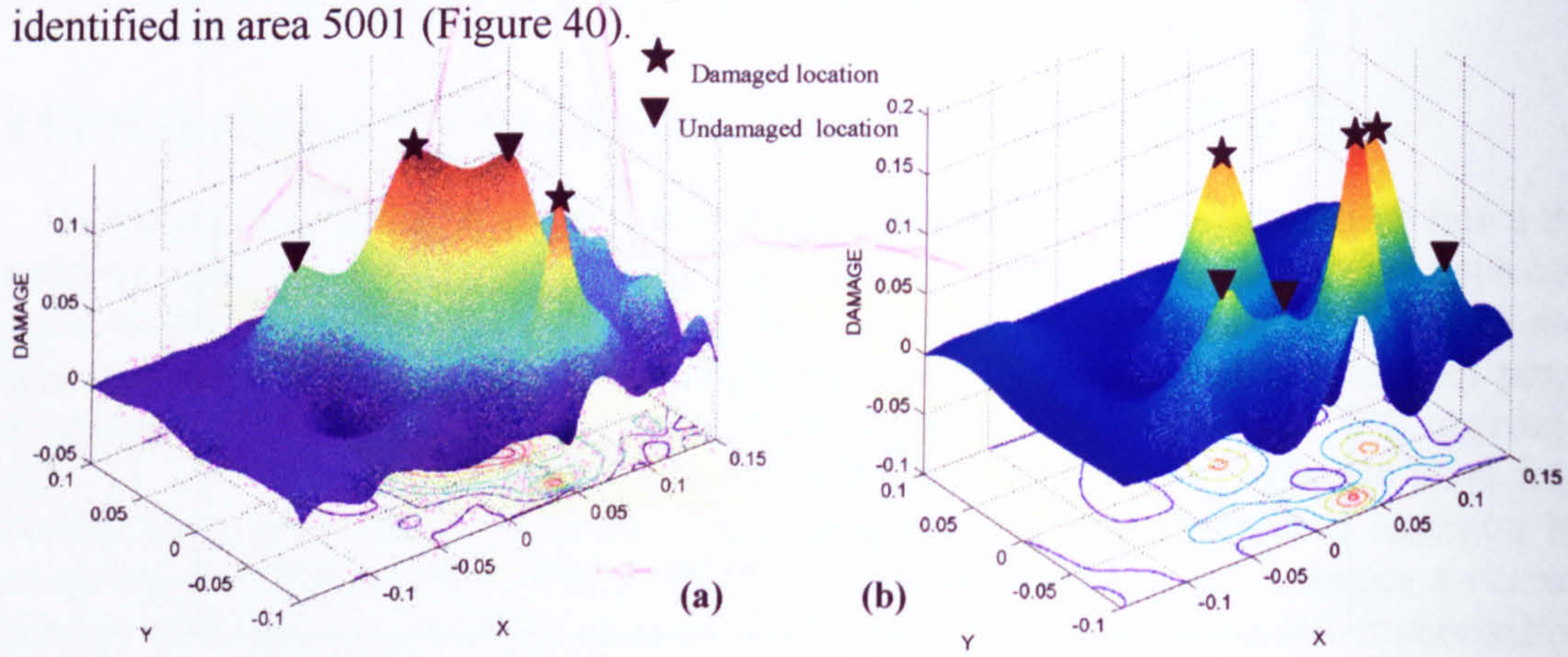

Figure 41 – Multi-site damage estimates: (a) COMAC_MAC; (b) FRACm .

The sensitivity damage detection case analysed the smallest damage detectable with the GLODD approach set-up as for the single and multi-site damage detection investigations reported above. At this aim the damage introduced in area 2009 (randomly picked, Figure 42) was progressively decreased in severity from 20% to 7% of the plate thickness.

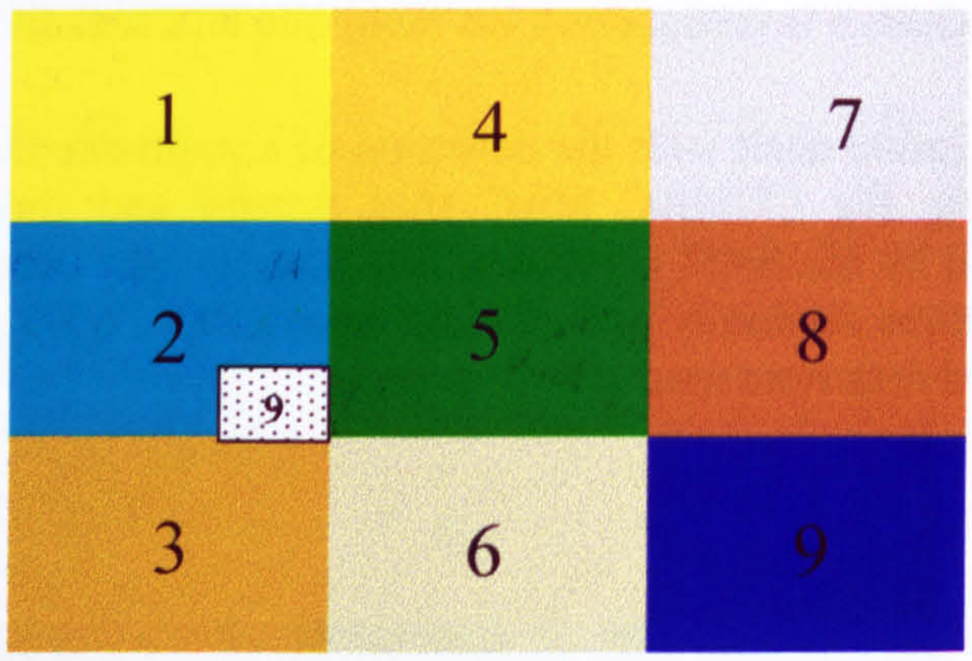

Figure 42 – Sensitivity damage detection: Single site-damage.

The detection process results, using the COMAC_MAC RF, were able to predict correctly the damage location for damages larger than 13%. For a 13% thickness decrease the GLDDO approach predicted damage distributed into three macro-areas, 2, 3 and 5 (Figure 43-a), leading to the identification of four damage locations in the second damage detection step (Figure 43-b). The damage locations were correctly predicted and the severity was underestimated by 10%. Considerable improvements were obtained using

the FRACm RF, the damage in area 2009 was identified correctly with decreasing damage severity till 7%, where three damage locations were identified. Among these, the actual damaged area resulted the least damaged with an error in the severity prediction of 4.68%.

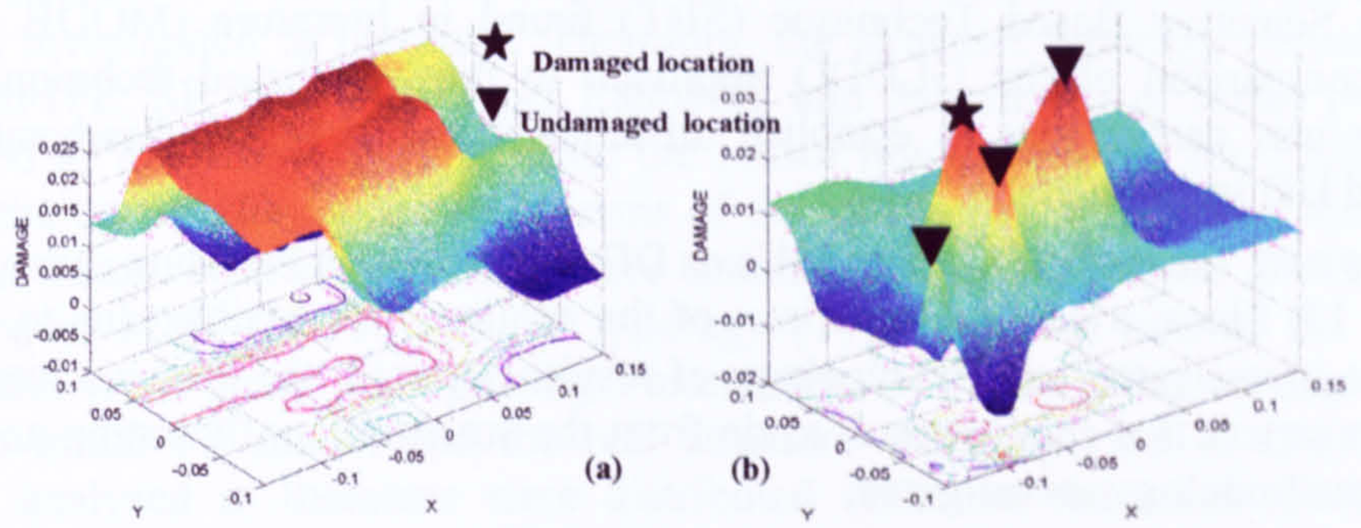

Figure 43 – Sensitivity damage detection: COMAC_MAC RF (13% damage). (a) First damage detection step. (b) Second damage detection technique.

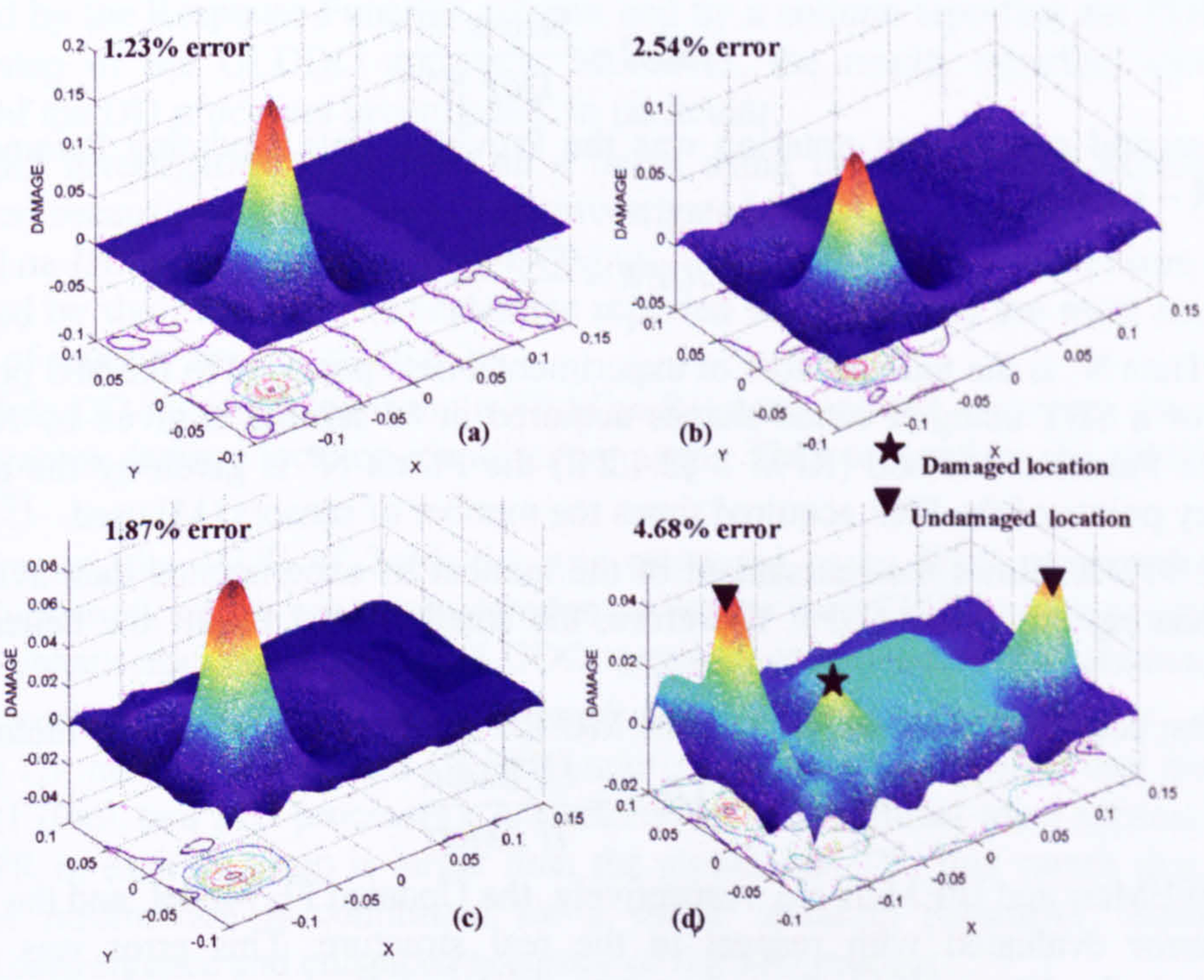

Figure 44 – Sensitivity damage detection: FRACm RF. (a) 20% damage. (b) 13% damage. (c) 10% damage. (d) 7% damage.

These last two investigations proved the capability of the GLDDO approach to detect single and multi-site damages with severities detectable larger than 7%. In contrast with the proved detection reliability and efficiency, there is the large computational time needed for such prediction (500-600 min, FRACm RF).

6.6 GLDDO approach vs. MU based damage detection approaches in literature

In the previous paragraphs, Damage Detections (DDs) using the GLDDO approach (on plate and beam structures) were carried out along side to DDs using the most common Sensitive Based Technique (SBT) found in literature (MODE §2.4.2.1). A further comparison of the GLDDO approach to the MU based technique present in literature was carried out to establish advantages and eventual disadvantages of the presented DD technique.

At this aim, the results of either MUs or DDs, presented in literature, were summarised in Table 13. Since, a direct comparison of the results is impossible, due to the different structures investigated and the typology of results reported, the analysis was focused on three parameters that should result aside from the structure configuration and depend on the MU methodology investigated.

The first comparison parameter was the Sensor Degrees of freedom Ratio (SDR – eq. 6.5). This was aimed at identifying the degree of information supplied to the MU process. A SDR smaller than 1 means a lack of information, hence, the smaller is SDR the more effective and reliable must be the MU Technique (MUT) employed, for a successful updating.

$$SDR = \frac{Sensor\ N^{\bullet}}{\text{DoF } N^{\bullet}} \tag{6.5}$$

The second comparison criterion was the Provided Data Updating Parameter Ratio (PDUPR – eq. 6.6).

$$PDUPR = \frac{PData\ N^{\bullet}}{\text{UP } N^{\bullet}} \tag{6.6}$$

where PData N° is the total number of experimental data provided to the MU process that in case of a SBT using N mode shapes acquired in M sensors is given by NM. For a Response Function Method (RFM - §2.4.2.2) the PData N° is given by the number of frequency points of the FRF acquired times the number of sensors (M) used.

The UPPDR allows the assessment of the number of experimental data available for each Updating Parameter (UP). Therefore, the smaller the UPPDR the better the MU process.

The last comparison parameter was the MU Efficiency (MUE – eq. 6.7) factor.

$$MUE = \frac{UFEMerr}{IFEMerr} \tag{6.7}$$

where UFEMerr and IFEMerr are, respectively, the Updated FE Model, and the Initial FE Model error evaluated with respect to the real structure. This error was evaluated according to the data available from the papers analysed. So there were:

- Target Mode Shape Based (TMSB) errors, which were evaluated by estimating the MAC (§2.7.1, see eq. 2.34) between the FEM and the real structure TMSs.
- Modal Frequency (MF) errors that were estimated by evaluating the averaged MF discrepancy between the FEM and the structure.
- Design-type UP (DUP) error, which was computed as the average of the difference of FEM and the real structure Design-type UP values.

The MUE factor gives the enhancement of the initial FE model obtained through MU with respect to the IFEMerr. Therefore, the smaller MUE factor the better the MU process.

Further information is reported in Table 13 in order to have a comprehensive view of the problem investigated in literature. Therefore, the structure typology (structure), the FE type used (FE, SE stands for Super Element), and the number of nodes (Nodes N) were reported as FE Model DATA, while the sensor number (Sens), the TMS number (TMS) and the data pollution (given in terms of the variance of a Gaussian distribution, for EXP was meant experimental data) were assembled as Experimental DATA. At the end, the type of MUT (MUT), the UP typology (Type) and the aim of the updating process (AIM) were group as Updating Parameters, while the kind of discrepancies between the initial FE model and the real structure were reported in Changes. The discrepancy analysed in literature were distributed thickness reduction (thick), Truss Removal (TR), localised elastic module reduction (E), localised reduction of the product inertia times elastic module (EI), Distributed UP Changes (DUPC).

A similar table to that used to survey the literature MUT results was used to report the DD results obtained using the GLDDO approach (Table 14). The only difference is represented by the elimination of the Ref, MUT and AIM columns which were substituted by the Response Function column and by a column reporting the PDUPR for a single step of the GLDDO approach. Moreover, the results reported were just a selection of the DD processes investigated. In particular:

- The DD investigation performed on a beam using the KEM OSP technique was reported because the best among those investigated (§6.2).
- The plate DD investigation using a COMAC_MAC_FREQ RF with sensors location selected by the EFI OSP technique was reported since resulted the most accurate in terms of severity predicted (§6.5.2).
- The plate DD investigation using a FRACm RF was reported since was the only one to guarantee damage location identification using TMS selected by the MMF method (§6.5.3).

Furthermore, the MUE of Table 14 was estimated using DUP errors (changes of element thickness), which were considered more proper then TMSB errors to identify the FE model enhancement because the GLDDO approach used design-type parameters.

A last consideration has to be addressed on the "Updating Parameters" columns, where the UP number is for each GLDDO approach step, which means that the overall UPs are 81 (9x9, two MU processes). A direct effect of the global-local approach is that the PDUPR in each DD step is larger than the global PDUPR, this means that a larger content of information is committed for a single updating parameter, leading to a improved convergence and enhanced accuracy of the MU process.

From an overall comparison of the data reported in Table 13 and Table 14, the SDR values for the GLDDO DDs resulted to be the lowest except for the MU of a C-Duct [54], which presented a value comparable (0.09) to that of the plate investigated (0.08). On the other hand, C-Duct MU process presented a larger PDUPR value than the plate GLDDO approach due to its smaller number of UPs (6) and its larger number of sensors (90) compared to those reported in Table 14. Nevertheless, the actual GLDDO PDUPR (per step) is larger than the C-Duct one, when the FRACm RF is used. Moreover, the C-Duct

MU process efficiency (13 MF), according to the MUE factor, is comparable to that obtained using the FRACm RF (11-20 DUP). However, it has to be mentioned that for FRACm RF function a reliable but not so accurate minimisation algorithm was used (SAM), when more accurate minimisation process are employed like the LLSO for the COMAC_MAC_FREQ RF, the MUE factor falls under 1% (Table 14).

Ref.	FE Model DATA			Experimental DATA				Updating Parameters (UPs)					Changes	MUE [%]
	Structure	FE	Nodes N.	Sens	TMS	SDR [%]	Pollution	MUT	Type	N.	PDUPR	AIM		
[54]	C-Duct	shell	15333	90	9	0.09	EXP	SBT	Spatial-type	6	135	MU	DUPC	13 (MF) 98 (TMSB)
[58]	plate	shell	16	16	6	33.33	1% FRF	RFM	Gen. Element	21	4.57	MU	DUPC	10.0 (TMSB)
[58]	plate	shell	60	60	15	33.33	0%	RFM	Design-type	180	5.00	MU	DUPC	3.5 (TMSB)
[58]	plate	shell	48	48	18	33.33	EXP	RFM	Design-type	140	6.17	MU	DUPC	57.8 (TMSB)
[58]	plate	shell	48	72	19	50.00	EXP	RFM	Design-type	140	9.77	MU	DUPC	39.5 (TMSB)
[63]	Beam	beam	32	29	7	32.22	2%	RFM	Design-type	30	6.77	MU	14% thick[1]	0.92 (TMSB)
[63]	Beam	beam	32	29	7	32.22	0.2% MF 2% MS	SBT	Design-type	30	6.77	MU	14% thick[1]	12.8 (TMSB)
[63]	Beam	beam	32	15	7	16.67	2%	RFM	Design-type	30	3.50	MU	14% thick[1]	0.60 (TMSB)
[63]	Beam	beam	32	15	7	16.67	0.2% MF 2% MS	SBT	Design-type	30	3.50	MU	14% thick[1]	11.9 (TMSB)
[67]	Aircraft	SE	282	413	19	24.41	EXP	SBT	Whole Matrix	18	435.94	MU	DUPC	43.5 (TMSB)
[69]	Mock Aircr.	beam	136	24	9	5.88	EXP	SBT	Design-type	10	21.60	MU	DUPC	35.65 (TMSB)
[86]	truss	beam	50	111	5	74.00	EXP	SBT	Design-type	50	11.10	DD	TR	0.08 (DUP)
[86]	truss	beam	50	111	5	74.00	EXP	SBT	Design-type	50	11.10	DD	TR	2.68 (DUP)
[86]	truss	beam	50	111	5	74.00	EXP	SBT	Design-type	50	11.10	DD	TR	2.87 (DUP)
[182]	Ass. plates	SE	245	63	11	25.71	EXP	RFM	Design-type	23	30.13	MU	DUPC	10.0 (TMSB)
[183]	Conc. bridge	beam	126	297	5	39.29	EXP	SBT	Design-type	16	92.81	DD	DUPC	32.0 (TMSB)
[184]	Conc. beam	beam	31	62	4	33.33	EXP	SBT	Design-type	8	31.00	DD	DUPC	6.34 (TMSB)
[185]	truss	SE	30	80	16	33.33	EXP	SBT	Gen. Element	40	32.00	MU	DUPC	76.0 (TMSB)
[186]	Conc. frame	beam	32	30	6	15.63	0.5% MF 1% MS	SBT	Design-type	32	5.63	DD	15.5% EI[1]	21.4 (TMSB)
[187]	TV Tower	beam	17	10	4	29.41	EXP	SBT	Design-type	17	2.35	MU	DUPC	No data
[188]	tail-plane	beam	32	29	4	15.10	EXP	SBT	Spatial-type	19	8.9	MU	DUPC	71.3 (TMSB)
[189]	Bridge	SE	99	211	12	100.0	0%	SBT	Gen. Element	369	6.86	MU	DUPC	56.8 (TMSB)
[189]	Bridge	SE	99	96	12	45.50	0%	SBT	Gen. Element	369	3.12	MU	DUPC	61.0 (TMSB)
[189]	Bridge	SE	99	60-EFI	12	28.44	0%	SBT	Gen. Element	369	1.95	MU	DUPC	55.2 (TMSB)
[189]	Bridge	SE	99	60-EFI	12	28.44	1% MF 5% MS	SBT	Gen. Element	369	1.95	MU	DUPC	65.0 (TMSB)
[189]	Bridge	SE	99	60-EFI	12	28.44	0%	SBT	Gen. Element	369	1.95	DD	20% E	57.0 (TMSB)

Table 13 – MUT results in literature.

Likewise to the C-Duct MU, the aircraft Super Element (SE) model updating ([67], Table 13) showed a high PDUPR due to the large number of sensors and TMS used but yet an MUE factor smaller than those reported in Table 14. In defence of the C-Duct and the aircraft SE model updating, there are the high complexity of the structures and the use of experimental data. However, the level of pollution used for the GLDDO approach investigations is considered to be in line with the experimental evidences on the data

[1] Value averaged on all beam elements.

variation, which claim errors within 10% for TMS [190], 1/10th of the TMS error for the MF [63], while the FRF errors are believed to be smaller than the TMS error due to the controlled excitation force and noise reduction techniques used (§4.3). In confirmation of the FRF accuracy, a plate model updating [58] performed using both numerical and experimental data showed an increase of the MUE factor from 3.5 (for no noise) to 57.8 (for experimental FRF), but via 10 (for 1% variance noise). This means that even assuming a linear behaviour of the MUE factor with the noise variance, for the 10% variance employed for the GLDDO approach investigation, a MUE factor of 100 would be obtained, worse than that obtained using experimental FRFs. Therefore, it is clear that the level of noise pollution (Table 14), adopted in this work, is in line with experimental noise.

Response Function	FE Model DATA			Experimental DATA				Updating Parameters			Changes	MUE [%]
	structure	FE	Nodes N	Sens	TMS	SDR [%]	Pollution	N (step)	PDUPR for step	PDUPR		
COMAC_MAC	beam	beam	91	10	10	1.83	10% MS & MF	9	11.11	1.23	Elem 9 10% thick	61.30
COMAC_MAC	beam	beam	91	10	10	1.83	10% MS & MF	9	11.11	1.23	Elem 63 10% thick	55.80
COMAC_MAC	beam	beam	91	10	10	1.83	10% MS & MF	9	11.11	1.23	Elem 90 10% thick	12.50
COMAC_MAC_FREQ	plate	shell	1990	10	10	0.08	10% MS & MF	9	11.11	1.23	Area 7004 20 thick	1.40
COMAC_MAC_FREQ	plate	shell	1990	10	10	0.08	10% MS & MF	9	11.11	1.23	Area 6008 20 thick	0.50
COMAC_MAC_FREQ	plate	shell	1990	10	10	0.08	10% MS & MF	9	11.11	1.23	Area 3004 20 thick	0.65
FRACm	plate	shell	1990	10	10	0.08	10% FRF	9	444.4	1.23	Area 7004 20 thick	20.10
FRACm	plate	shell	1990	10	10	0.08	10% FRF	9	444.4	49.38	Area 6008 20 thick	21.10
FRACm	plate	shell	1990	10	10	0.08	10% FRF	9	444.4	49.38	Area 3004 20 thick	11.30
FRACm	plate	shell	1990	10	10	0.08	10% FRF	9	444.4	49.38	Area 2009 13 thick	19.54
FRACm	plate	shell	1990	10	10	0.08	10% FRF	9	444.4	49.38	Area 2009 10 thick	28.70

Table 14 – GLDDO approach survey results.

The comparison between different RFM plate updating processes [58] (Table 13) was possible, because their SDR were constant (33%) and their PDUPR were almost constant (between 4 and 6) despite of different node, sensor and UP numbers.

Although, the experimental data variance was simulated through Gaussian distributed noise pollution of the numerical data employed for the GLODDO approach damage detections, the complexity of the C-duct [54] and aircraft [67] structures undermines the comparison. Therefore, in order to clear also this last issue, the two structures investigated (beam and plate) were compared, respectively, to beam and plate MU results.

In the case of the beam, the closest MU example, found in literature (Table 13), to that studied in this work is given by a 32 node beam model [63] updated using either a RFM or a SBT method and numerically polluted data. In the literature reported beam MU results [63], a rather peculiar outcome is highlighted, for a fall from 32% to 17% of the SDR a slightly improvement of the MU process accuracy was observed for both the MU methodologies used. This seemed being in contrast with the concept the more sensors the better, as supported by a bridge SE model updating [189], where a SDR fall from 100 to

45% corresponded to a reduction of the updating process accuracy (rising MUE factor, from 56.8 to 61%). However, by selecting sensor locations according to the EFI method, the MU accuracy increased (MUE =55.2), nonetheless a reduction of the SDR (down to 28%), so a further support to the importance of OSP, claimed along this entire thesis work, was given. In the light of this analysis, the discrepancy, highlighted previously on the enhancement of the MU accuracy even though the SDR was reduced [63], should be seen with regards to optimal sensor placements, an indication of it, it is the placement of the sensors according to a regular spaced grid in agreement with one of the three properties that a sensor network should comply with (§6.4). Completing the analysis of this 32 node beam model [63] updating, its PDUPR (3.5-6.8) is smaller than that estimated for the GLDDO approach (11.11 PDUPR step, Table 14), yet the MUE factor indicated a closer match of the updated model of the literature beam to the "experimental model" than the GLDDO processed model. This poor accuracy of the methodology studied is ascribable to higher noise pollution of the "experimental data" (10% vs. 2%) and a smaller structural change introduced on the beam (10% on a beam element against an average of 14%). Another beam MU, to score a better accuracy than that of the GLDDO approach, was a concrete beam MU [184] using experimentally polluted data. In this case, the reason for such outcome is due to larger values of the SDR and PDUPR and to a smaller TMS number (the first 4 MS are easier to match than the first 10 MS) than those of the GLDDO updated beam.

Finally, a completion of the GLODD approach and literature MU processes comparison, the plate DD investigated, in paragraph 6.5 and summarized in Table 14, was analysed against a plate FE model [58] updated by a RFM using either numerical or experimental data (Table 13). As expected a comparison of the GLDDO approach results, using the FRACm RF, with the literature numerical polluted plate MU results showed a better performance of the latter (see MUE factors in Table 13 and Table 14), this is mainly due to the low level of numerical noise pollution used in the literature plate MU (1% against 10%). However, as previously mentioned, a more likely comparable noise level to that adopted in these work investigations (10%) is the experimental noise present in the last two plate MU reported in Table 13. In this case, the MUE factor indicated that the FRF based RF (FRACm) minimised in the GLDDO approach over performed the literature reported RFM based plate MU [58]. This result pointed out once more the efficiency of the MU and DD technique developed by the author.

Concluding, the above performed comparison pointed out the existence of a big difference between the majority of the research community and the author approach to the DD/MU problem. First of all, the great part of the literature works is lacking of an organic look to the subject investigated. Many researchers focused only on the updating processing, neglecting the importance of a harmonisation of a series of factors, such as UP selection, OSP, experimental data manipulation, that clearly strongly affect the overall result as this work has highlighted many times. Second, researchers tends to propose numerical and experimental investigations to validate their works that involve a so large number of sensors on relative small and simple structures that the simple transfer of such methodologies on real structures becomes almost, practically and economically, impossible. This practice is utterly in contrast with the applications investigated in this thesis, where the sensor number was related with the TMS number and the DD accuracy and, therefore, independent from the structure complexity and dimensions.

6.7 GLDDO approach: result analysis for future works

As observed in the previous paragraphs, GLDDO damage detection processes using FRF based RF, resulted to be considerably less accurate than equivalent processes using mode shape based RF, in contrast with the well known major FRF accuracy (§4.3) and larger PDUPR values (Table 14) of the first against the second. Although, the greater accuracy of gradient based minimisation processes (LLSO - §2.8.1, LSO - §2.8.3) than SAM (used to minimize the FRF based RFs) can justify a less accurate damage severity estimation, it cannot explain the convergence FRACm residue value being between 60 and 90 in contrast with convergence values around 0 of the mode shape based RFs obtained using either gradient based or zero-order (SAM) minimization algorithms (see eq. 2.40).

In confirmation of the above remarks, the FRAC coefficient (eq. 2.39) estimated between the plate undamaged and the single-site damaged (explored for the sensitivity damage detection -20% introduced damage - §6.5.3) configuration, showed a fast step decrement behaviour with the frequency (Figure 45). These sudden changes were localised at the resonance frequency, where the configuration investigated had the largest differences (Figure 46). Moreover, the amplitude of the FRAC coefficient step changes decreased with the frequency to vanish over 2500 Hz. A first reason is the decrease of the FRF amplitude with the frequency. A second reason is hidden in the FRAC expression itself, which is a sort of weight average. This means that large FRF amplitude (generally located at low frequencies), associated with small FRF amplitude changes between the damaged and undamaged structure configuration, have larger weight than small FRF amplitude (generally located at high frequencies), even if associated with large FRF amplitude changes between the damaged and undamaged structure configuration.

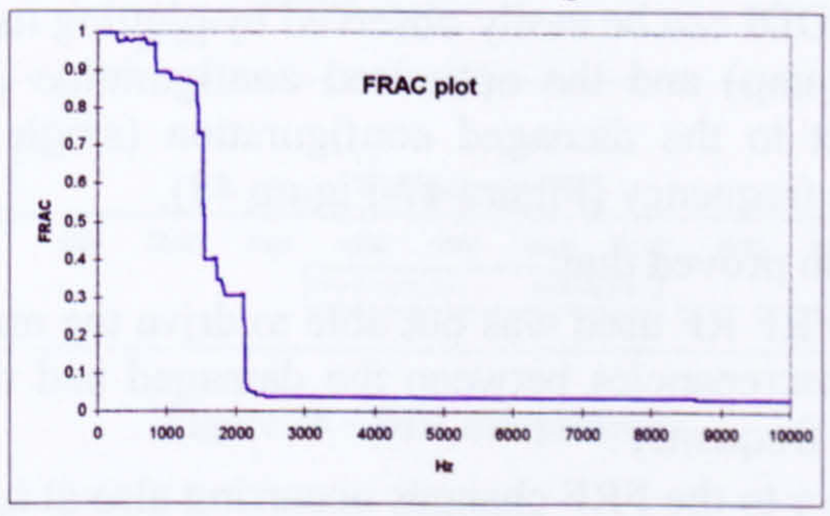

Figure 45 – FRAC plot

Consequently, an improvement of the FRF based RF developed in this work is needed. At this aim two main lines should be followed. The first investigation line should pursue a segmentation of the FRF frequency range in smaller ranges having comparable FRF peak amplitudes, so as their contribution to FRAC coefficients is equivalent. The new FRAC based RF will be defined as the sum of the old RF defined in each identified frequency range. In this way, high frequency FRF discrepancies will have the same weight in the GLDDO minimisation process of the low frequencies FRF changes.

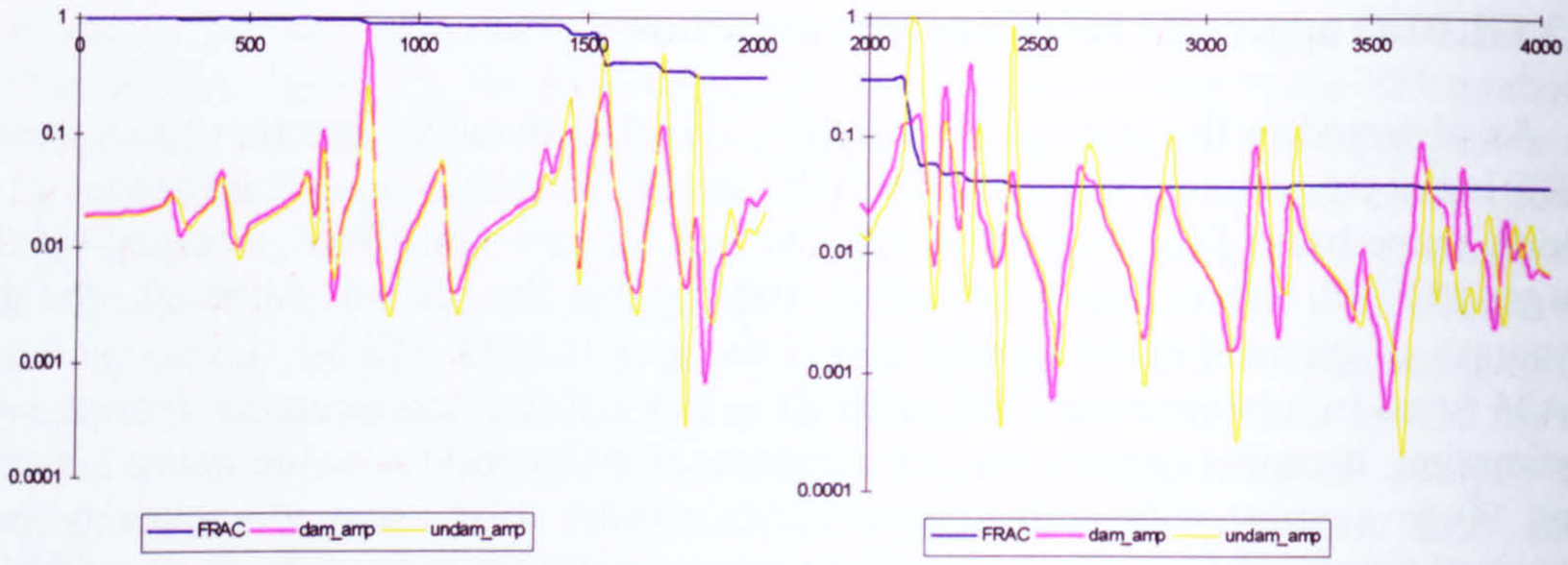

Figure 46 –FRF comparison between the damaged und the undamaged configuration.

The second development direction should explore a new class of RF based on normalised errors. These RFs should be sensible, in equal measure, to low and high frequency discrepancies. Such feature is present in an experimental Damage Detection Index (DDI) previously investigated by the author [23], see equation below:

$$DDI = \frac{\sum_{i=1}^{N}\left(\frac{\left|FD_i - Fopt_i\right|}{FD_i}\right)}{N} \tag{6.8}$$

where:

- FD_i and $Fopt_i$ are the FRF magnitudes respectively of damaged and optimised configuration.
- N is the number of frequency points.

The efficacy of the DDI can be easily observed by plotting its behaviour, computed for the undamaged (und_amp) and the optimised configuration (by GLDDO approach – opt_amp) with respect to the damaged configuration (single site damage - §6.5.3 – dam_amp), against the frequency (Figure 47-Figure 48).

The DDI comparison proved that:

- The FRAC based FRF RF used was not able to drive the minimisation process to the reduction of the discrepancies between the damaged and the updated configuration with the rise of the frequency.
- The DDI is sensitive to the FRF changes occurring also at high frequencies, since the DDI values (Figure 48) increased with the frequency according to the damaged and undamaged/optimised FRF differences (Figure 47)

However, it is useful to remind that the frequency range used for the DD was between 0 and 5000Hz.

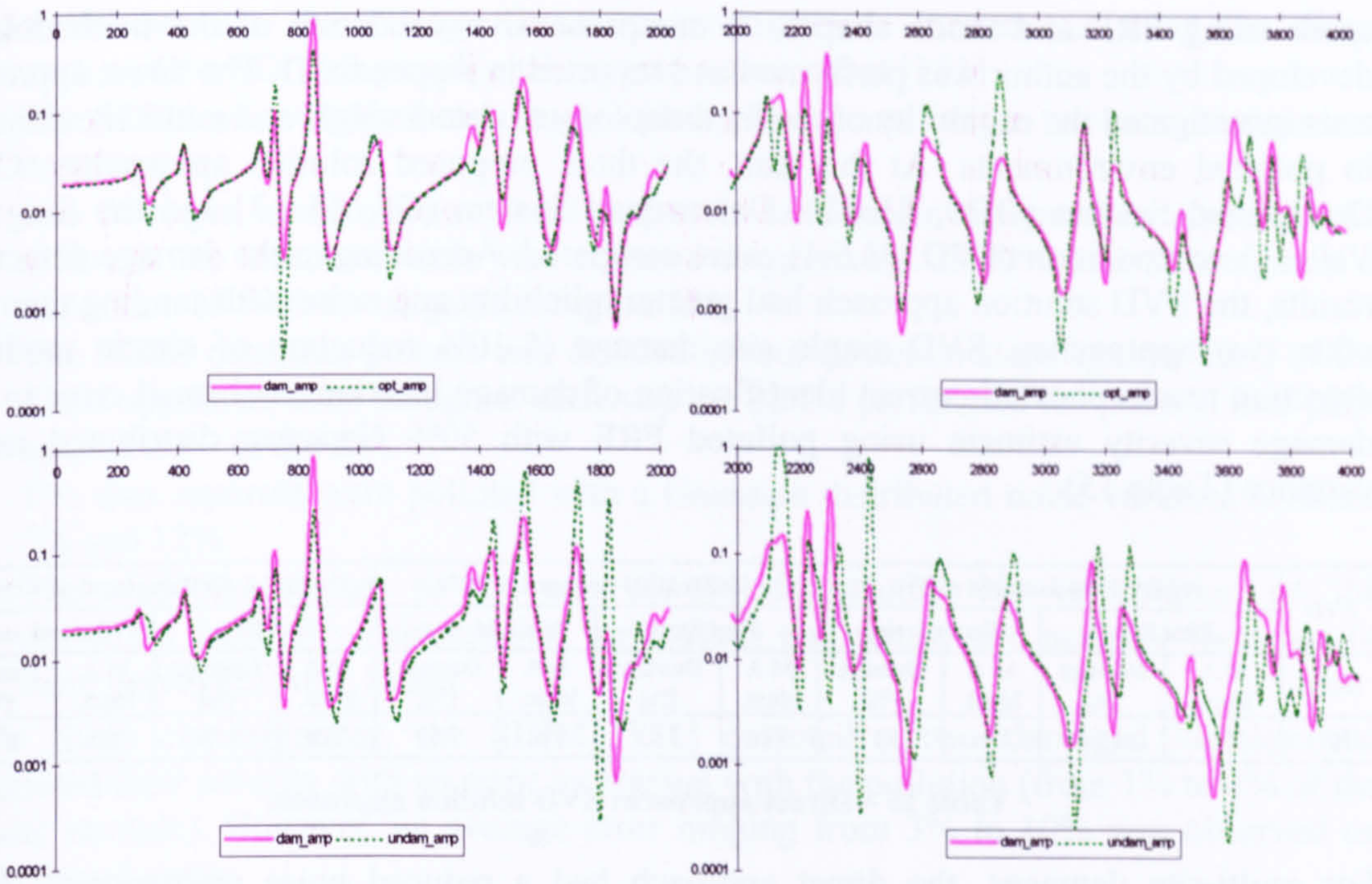

Figure 47 – Comparison among the damaged-optimised FRFs and damaged-undamaged FRFs.

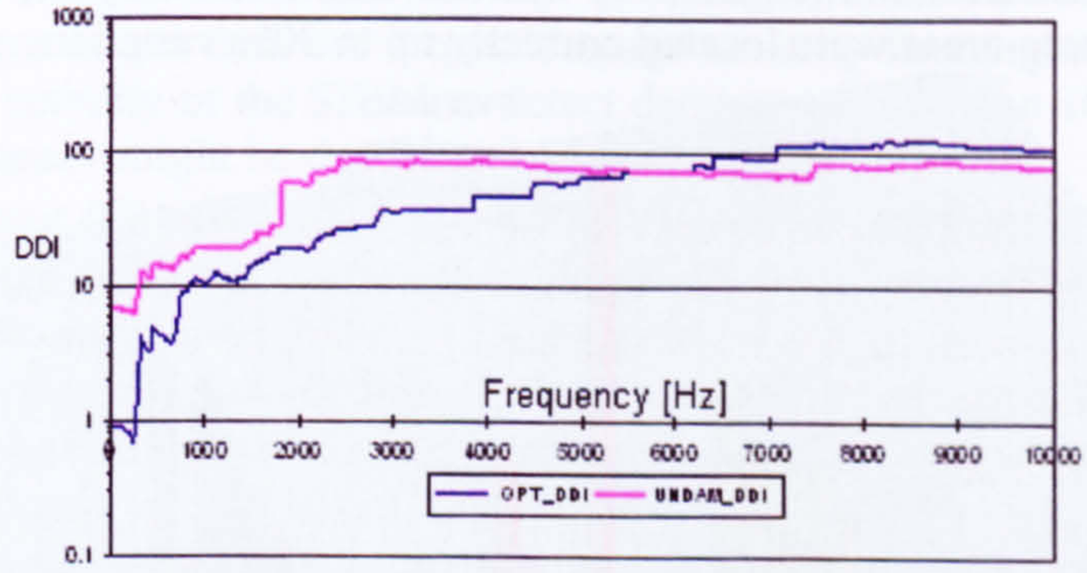

Figure 48 – DDI comparison.

6.8 Plate-like structures: direct approach

In the previous paragraphs, the GLDDO DD results were analysed and discussed in the light of DD and MU results present in literature. A common point of all the results analysed was the FE model of the structure under investigation. This structure model gives a discrete representation of the structure properties within a certain approximation, with a consequence loss of information unless very fine meshes are employed. Thus, large computational times are required in order to carry out damage detections or model updating. A solution is offered by the adoption of an analytical model of the structure investigated, when available. This is the case of the Direct Approach (DA) presented in chapter 5 for plate-like structures. The DA detects the locations and the severity of damages by inverting an analytical equation of plate-like structures in the frequency

space using FRF and mode shapes. A comprehensive validation of the methodology developed by the author was performed and reported in Appendix D. The direct approach tests investigated the capability of the methodology to detect single and multi site damage in polluted environments. At this aim, the three proposed solution approaches, Over Determined System (ODS, §5.6.2), Determined System (DS, §5.6.3) and the Singular Value Decomposition (SVD, §5.6.4), were compared. According to the damage detection results, the SVD solution approach had greater reliability and noise withstanding than the other two approaches. SVD single site damage (5-10% reduction of elastic module) detection results showed correct identification of damage locations and small error in the damage severity estimate using polluted FRF with 50% Gaussian distributed noise variance (Table 15).

SVD	AREA 3004 damaged of 5%				AREA 3004 damaged of 10%				AREA 6008 damaged of 10%			
	First Step		Second step		First Step		Second step		First Step		Second step	
Noise	M A Ident.	Damage [%]	M A Ident.	Damage [%]	M A Ident.	Damage [%]	M A Ident.	Damage [%]	M A Ident.	Damage [%]	M A Ident.	Damage [%]
50%	Yes	1.24	Yes	3.17	Yes	3.92	Yes	7.69	Yes	1.29	Yes	8.20

Table 15 – Direct approach: SVD solution approach.

For multi-site damages, the direct approach had a reduced noise resistance (<10%) compared to that showed for single site damage detections. More precisely, the direct approach for noise over 5% (Figure 49) was not able to identify the damage. However, the damaged macro-areas were located correctly up to 30% variation.

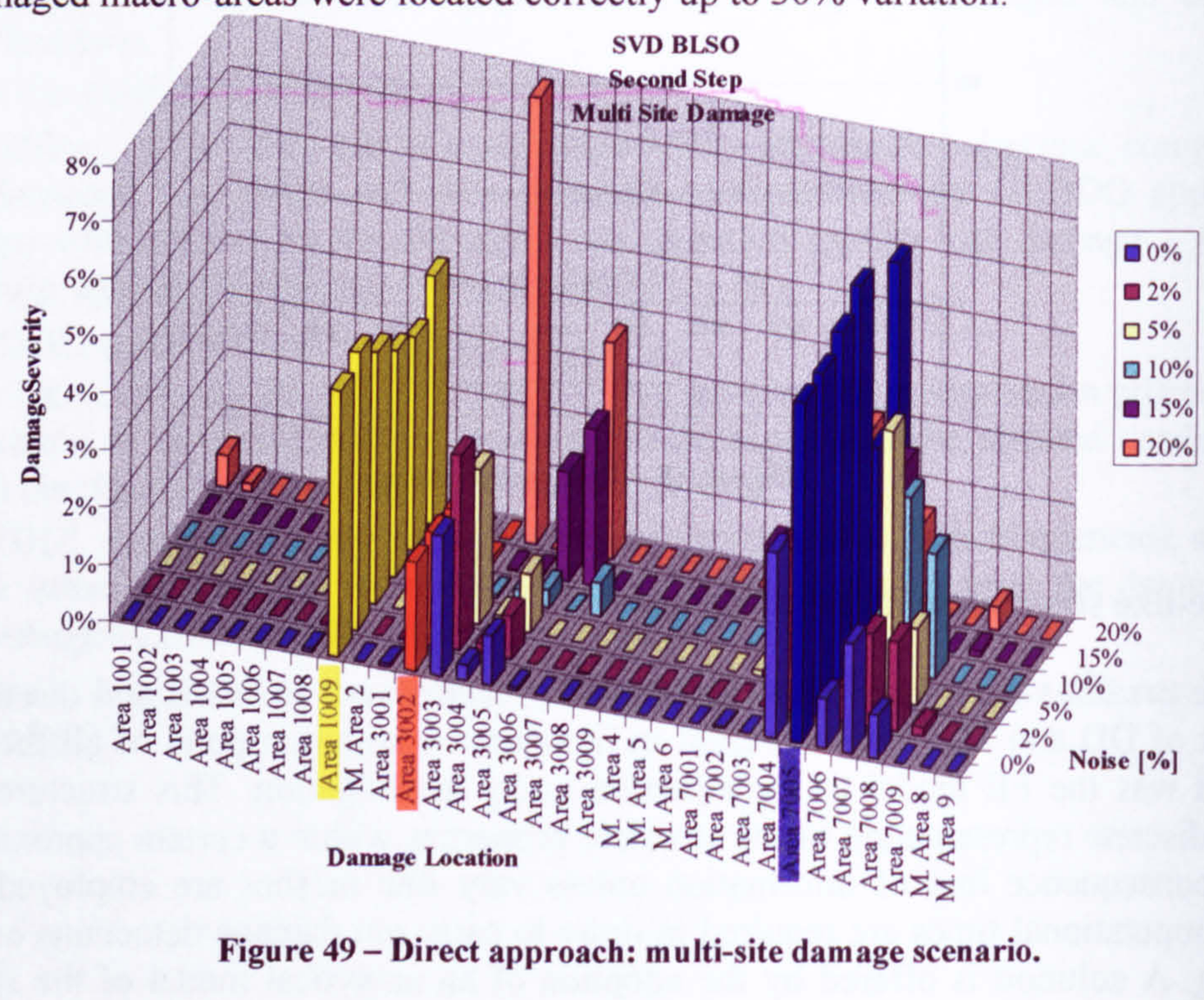

Figure 49 – Direct approach: multi-site damage scenario.

As mentioned in chapter 5, the direct method is identical, apart from few differences highlighted in chapter 5, to the Structural Damage Identification Method (SDIM, [131]).

A parallel between the damage detection investigations carried out using the direct approach and the SDIM is possible taking into account that [131]:

- The SDIM was validated on a square plate (32cm) and only a two-site damage was investigated.
- The damaged area size was about a quarter of those investigated in Appendix D, although the elastic module was reduced respectively of 40% and 50% against a maximum of 10% investigated using the DA.
- The SDIM detection process was divided in four detection steps against the 2 of the direct approach, even though at each step the SDIM partitioned the plate in four parts against the 9 of the DA.
- The data reported were polluted with a Gaussian distributed noise variance between 5% and 12%.
- The algebraic system solved was always determined. No information on the excitation frequency selected (64 were used) and sensor and actuator locations (4 were deployed) were found.

In these circumstances, the SDIM [131] detected a two damaged location and estimated their severity with an error increasing with the pollution (from 1% to 4% of the elastic module). However, an average error ranging from 3% to 10% was observed on undamaged areas.

By comparing the above reported SDIM results with the DA results, summed up in Figure 49, the DA showed a stronger stability to noise pollution than the SDIM, which had an average error larger than the largest damage severity investigated with the DA. This indicated the inability of the SDIM to detect damage smaller than 10% if not larger. The DA larger accuracy might be due to many factors:

- Damage Influence (DI) matrix (§5.4) coefficients outside the principal diagonal were assumed not negligible, in contrast with the SDIM. This increased the sensitivity of the DA to the damage severity.
- SVD noise withstanding. This feature, well known in literature as mentioned in section 4.6.1, allowed the damage detection of flaws with severity smaller than 10% of the elastic module in presence of large pollution (up to 50%).
- OSP. This increases the SNR and, therefore, reduces the noise influence on the damage detection process.

However, nonetheless the outstanding results above analysed, the DA application is strongly limited by the availability of analytical representation of real structures. This shortcoming makes the DA approach an academic exercise until further development of mathematics will provide continuum representation of real structures.

6.9. Conclusions

In this chapter, the reliability and the efficiency of the GLDDO approach into damage detection of single and multi-site damages were investigated along side the effects of TMSS, OSP, MA and RF. This extensive investigation proved the interconnection of the above mentioned variables with successful damage identification, and outlined the need of a global look of the detection process, involving the damage identification process as much as issues as OSP, TMS, MA and RF selection. This point of view appeared in open

contrast with the general modus operandi of other researchers, who focused only on the MU technique development aspect, neglecting a series of factors (e.g. noise, economic and practical limits), which may undermine or make completely unutilisable these works in practical situations. Instead, in this research, the applicability of the proposed methodology was considered since the starting (§1.6, 2.6, 2.9) by setting very clear targets in this direction. This brought to the design of procedures involving the selection of the data type to acquire, the deployment of sensors, the selection of minimization algorithm and residual functions. Moreover, this detection process proved to be efficient and reliable in the identification of damages randomly introduced in the test cases investigated. The comparison with literature approaches further demonstrated the success of the approach followed and, therefore, the benefit of the novelties (e.g. use of correlation functions as RFs, the Global-Local approach, integrated data selection process, and etc...) introduced in the MU process.

CHAPTER 7: WAVE PROPAGATION

7.1 Abstract

In the last years, increasing attention was given to the study of wave propagation phenomena in structures, because of their huge potential for structural characterization and damage detection. The principal reason was the capability of a wave to travel through a structure with great speed and so to supply information on damage presence, location, and severity, and complete an inspection in few seconds. These characteristics constitute a rather large enhancement of current ultrasonic inspections, which are quite time consuming because require meticulous through-the thickness C-scans over large areas of the structure.

Therefore, a second damage detection technique capable of exploiting wave propagation phenomena (P, S, Rayleigh and guided wave velocities) was developed. The proposed damage detection was devised to identify discrepancies, due to damage presence, in the dynamic behaviour of the structure. The uncorrelations are generated by waves reflected back to the sensor locations by the flaw surfaces. The peculiarity of the presented approach is the use of a time frequency coherence function for the identification of the arrivals of guided waves reflected back to the sensors by the damage surfaces.

The damage detection methodology developed was divided in three steps. In the first step, the presence of the damage on the structure was assessed. In the second step, the arrival time of the reflected wave (or echo) was estimated using the continuous wavelet

transform. Then, the detection algorithm was able, through a ray-tracing algorithm, to estimate the location of damage.

Further work is needed to establish the damage severity by relating the magnitude of the changes of the time frequency coherence to reflection and attenuation coefficients of each guided wave used and on the selection of the best range of frequency according to the type of damage to be identified.

7.2 Why wave propagation?

Damage detection techniques based on FE model or analytical model capable of reproducing dynamic responses of structure generally need large computational time to locate faults and estimate their severity. Moreover, the construction and the validation of the structure models, although necessary only for the undamaged state, need a remarkable experience and effort. Additionally, because two structures (e.g. two airplanes or two cars) coming out from the same assembling line, according to the same specifics, may present different dynamic features (different designs, different mass locations etc...), which reproduction might lead to the generation and validation of two different FE models.

Therefore, despite of the reliability and the resolution in detecting damages, model based techniques for massive and repetitive structures (rail track, pipelines) are quite time consuming because of the high mesh density required to detect the smallest damage demanded by safety regulations. Consequently, in many cases where a real time investigation is requested those methods are not applicable.

Conversely, MU techniques are the best solution for global monitoring conditions of large civil structures such as bridges and buildings, where occurring damages might affect relatively low frequencies (Figure 50), but do not constitute an immediate threat neither to the structure health nor to its users, because of the structure typology and the nature of operative loads (e.g. low frequency).

However, when there is a need to monitor localized damage the global methods are not applicable. In this case, critical damage sizes cause appreciable changes in structure dynamic responses only at high frequencies. For this task, wave propagation techniques resulted suitable, since are able to detect very small damages by modulating the scanning frequency and provide real-time detections in few seconds with relative cheap equipment.

Hence, to exploit the new enhancements in UT technology, the author developed a second damage detection technique based on wave propagation. Its working principle is based on the propagation of a perturbation (wave) through the structure under investigation (see §7.9.1). If damage is present the wave is partially reflected (echoes are generated) towards the sensor locations. The measure of the Time of Flight (ToF or echo arrival time, which is the time that a wave needs to travel from its source to impinge on the damage surface and to be reflected back to the sensor location - see §7.9.2) enables a ray-tracing algorithm to locate the damage (see §7.9.3). The analysis of the echo magnitude of the damage echoes gives an estimate of the extension of the structure fault.

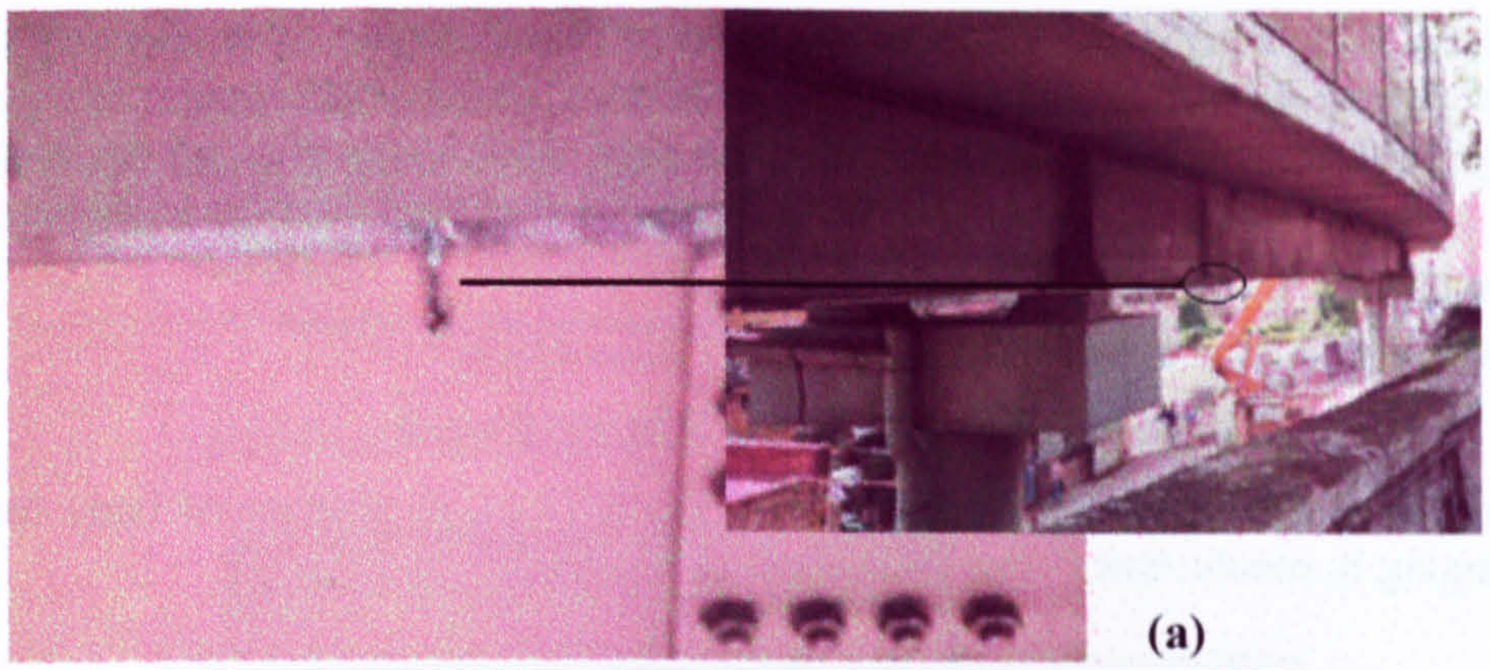

(a)

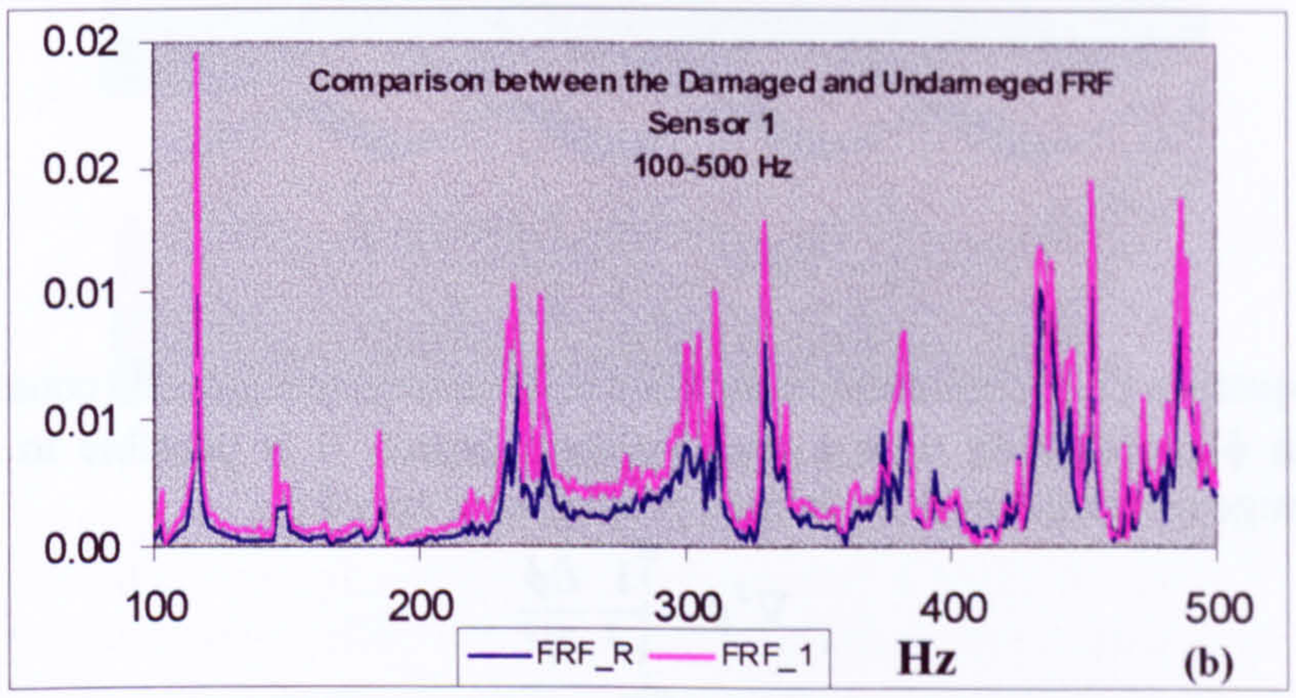

Figure 50 – Civil structure [134]: (a) severe damage; (b) comparison between damaged (FRF_1) and undamaged (FRF_R) FRF.

At the aim to clear out any issue related to the methodology developed and the wave propagation phenomena, in this chapter the wave propagation theory (§7.3) is presented with its existing applications (§7.4). Then, an accurate analysis on the signal analysis techniques (§7.5-7.6) in the time-frequency space was carried out for damage detection purposes. Finally, the developed damage detection methodology is illustrated (§7.9).

7.3 Wave propagation theory

The complex phenomenon of wave propagation can be described in an infinite media by the Navier's differential equations [135]:

$$(\lambda+\mu)\left(\frac{\partial^2 u}{\partial^2 x^2}+\frac{\partial^2 v}{\partial x\partial y}+\frac{\partial^2 w}{\partial x\partial z}\right)+\mu\nabla^2 u+\rho f_x=\rho\frac{\partial^2 u}{\partial t^2}$$

$$(\lambda+\mu)\left(\frac{\partial^2 u}{\partial y\partial x}+\frac{\partial^2 v}{\partial^2 y^2}+\frac{\partial^2 w}{\partial y\partial z}\right)+\mu\nabla^2 v+\rho f_y=\rho\frac{\partial^2 v}{\partial t^2} \qquad (7.1)$$

$$(\lambda+\mu)\left(\frac{\partial^2 u}{\partial z\partial x}+\frac{\partial^2 v}{\partial z\partial y}+\frac{\partial^2 w}{\partial^2 z^2}\right)+\mu\nabla^2 w+\rho f_z=\rho\frac{\partial^2 w}{\partial t^2}$$

where:

- u, v and w are the particle displacements in the x, y and z directions.
- f_x, f_y and f_z represent the component of the body force in the x, y and z directions.
- λ, μ are the Lame's constants.
- ρ material density.

The vector equivalent form of eq. (7.1) is:

$$(\lambda+\mu)\nabla\nabla\cdot\mathbf{u}+\nabla^2\mathbf{u}+\rho\,\mathbf{f}+\rho\,\ddot{\mathbf{u}} \tag{7.2}$$

Performing the operation of divergence on eq. (7.1), in absence of body forces, and rearranging it, results that:

$$\nabla^2\Delta=\frac{1}{c_1^2}\frac{\partial\Delta}{\partial t^2} \tag{7.3}$$

where:

$$\Delta=\nabla\mathbf{u} \qquad c_1=\left(\frac{\lambda+2\mu}{\rho}\right)^{\frac{1}{2}} \tag{7.4}$$

In the equation (7.3), the wave equation can be easily recognised (equation 7.5, for a perturbation ϕ propagating with a speed c) and, hence, it is possible to state that the volume change (dilatational disturbance) propagate at speed c_1.

$$\nabla^2\phi=\frac{1}{c^2}\frac{\partial\phi}{\partial t^2} \tag{7.5}$$

Appling the curl operator ($\nabla\times$) to equation (7.2) and taking into account that $\nabla\times\nabla\phi=0$ results:

$$\nabla^2\boldsymbol{\omega}=\frac{1}{c_2^2}\frac{\partial^2\boldsymbol{\omega}}{\partial t^2} \qquad c_2=\sqrt{\frac{\mu}{\rho}} \tag{7.6}$$

with $\boldsymbol{\omega}=\frac{1}{2}\nabla\times\mathbf{u}$ the displacement rotation vector.

Once again, the wave equation is obtained (eq. 7.5) but, in this case, rules the rotational or distortional disturbance, propagating with a velocity c_2.

In other words, two basic types of wave, dilatational and distortional, can propagate in infinite media with specific characteristic speeds, c_1 and c_2.

A variety of terminologies exists for the two wave types. Dilatational waves are also called irrotational and primary (P) waves. The rotational waves are also named equi-voluminal, distortional and secondary (S) waves. In seismology the P and S waves can be named also 'push' and 'shake' waves. A last definition for the P and S waves can be understood assuming the wave propagation front plane and normal to the propagating direction (Figure 51), in this case appears immediate why the P waves are termed longitudinal waves and the S waves, shear waves.

When an elastic wave encounters a boundary between two media, its energy is divided between the reflected and the refracted wave. The same laws such as the Fermat's principle and the Snell's law drive the phenomenon not differently from the analogue

problems in acoustics or optics. To differ from the acoustic and optic phenomena is the mode conversion associated with the incident P waves on a free surface. For example, the impinging P wave is reflected with an angle different from the incident since, at the same time, a shear wave called SV wave is generated [135] (Figure 52).

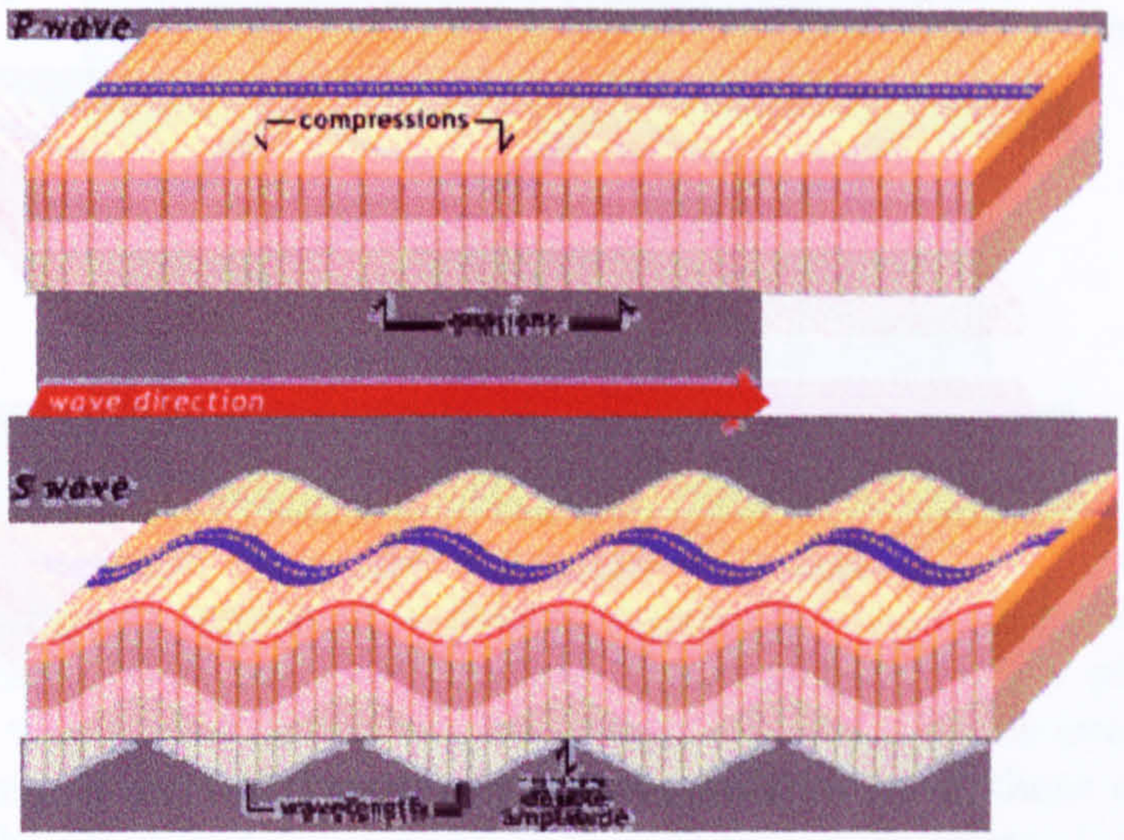

Figure 51- Body waves [136]

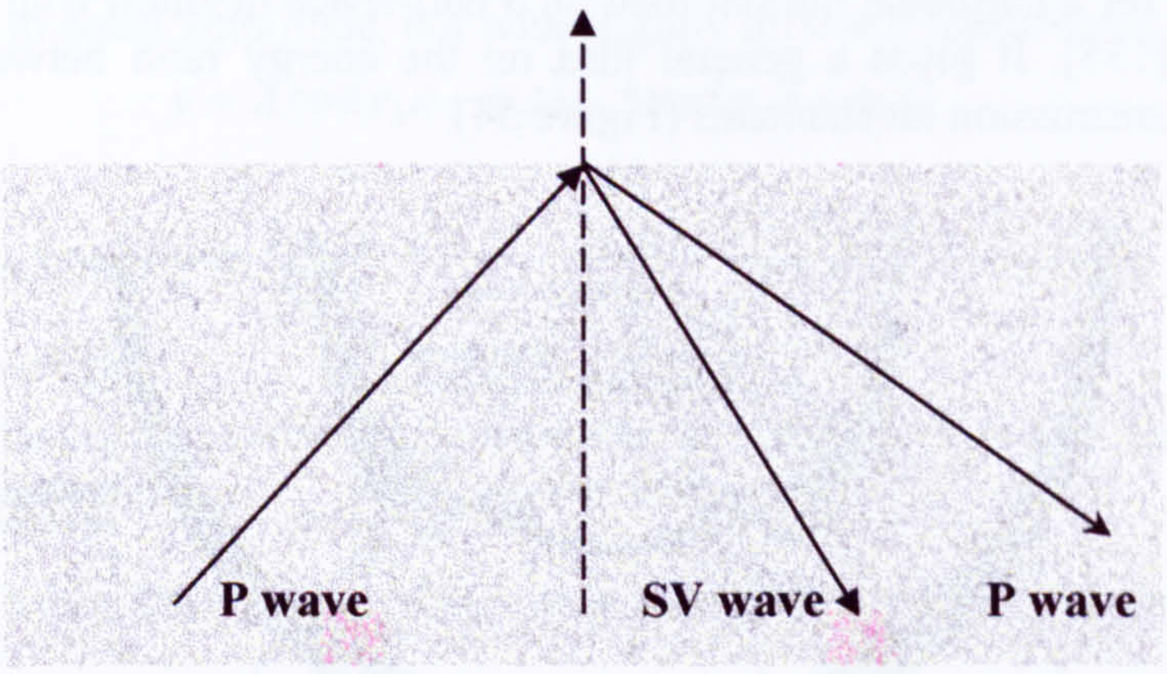

Figure 52 – Conversion mode of an impinging P wave.

Another aspect, associated with the presence of free boundaries, is the existence of additional wave types. Those waves are named surface waves at the aim to differentiate them from the P and S waves defined as body waves.

The surface waves are connected with particle movements close to the free boundaries of a medium surface. Rayleigh was the first to notice the presence of a particular surface wave named after him. A main characteristic of this type of waves is the rapid decrease of their magnitude with depth, which makes them almost imperceptible at depths larger than the double of their wavelength. These waves are characteristic of seismic phenomena, where are defined as ground roll waves due to the particle motion confined in the vertical plane containing the direction of propagation and retrogrades elliptically (Figure 53). The propagation speed of such waves is close to that of the S waves ($c_R/c_2 \cong (0.87+1.12\nu)/(1+\nu)$ [24, 135]).

A second type of surface wave, Love's waves named after its discoverer, travels by a transverse and horizontal motion of the particles (Figure 53). These waves are similar to S waves and occur when the S waves speed increase with the depth (layered media). Moreover, their propagation speed depends on the frequency and approaches the shear wave speed in the substrate material for frequencies tending to zero.

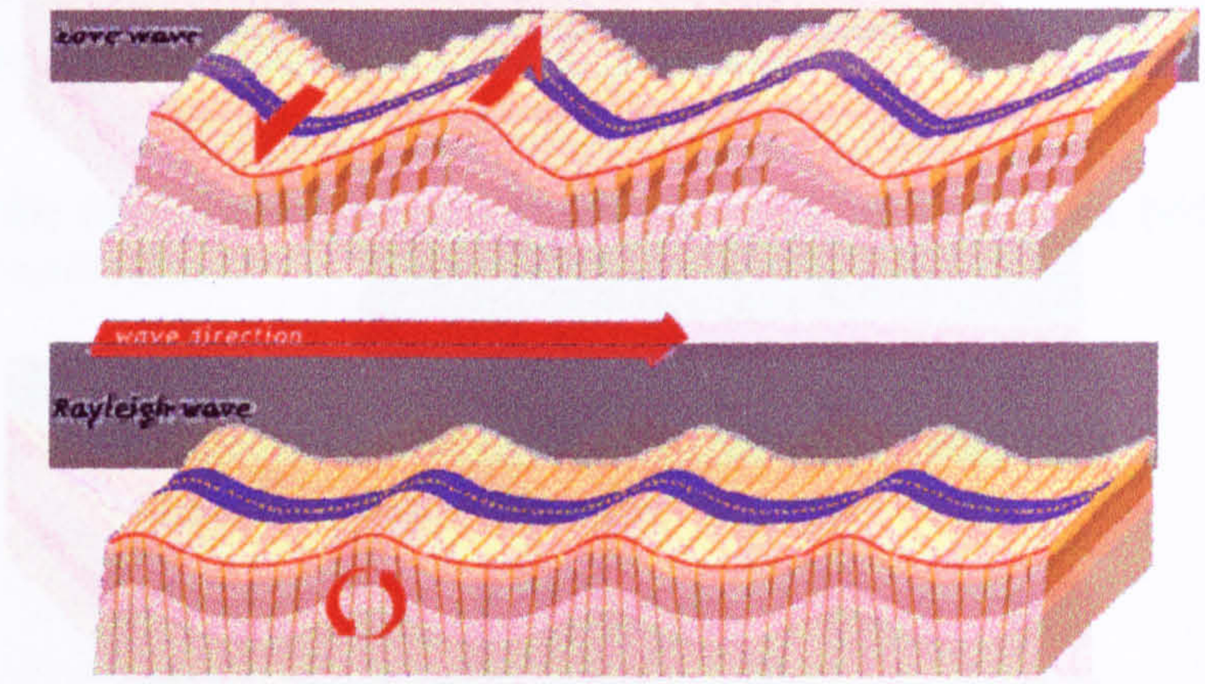

Figure 53 - Surface waves [136]

An example of distribution of displacements and energy in dilatational, shear and surface waves for a harmonic normal load on a half-space medium with $\nu = 1/4$ is shown in Figure 54 [135]. It gives a general idea on the energy ratio between the different perturbation transmission mechanisms (Figure 54).

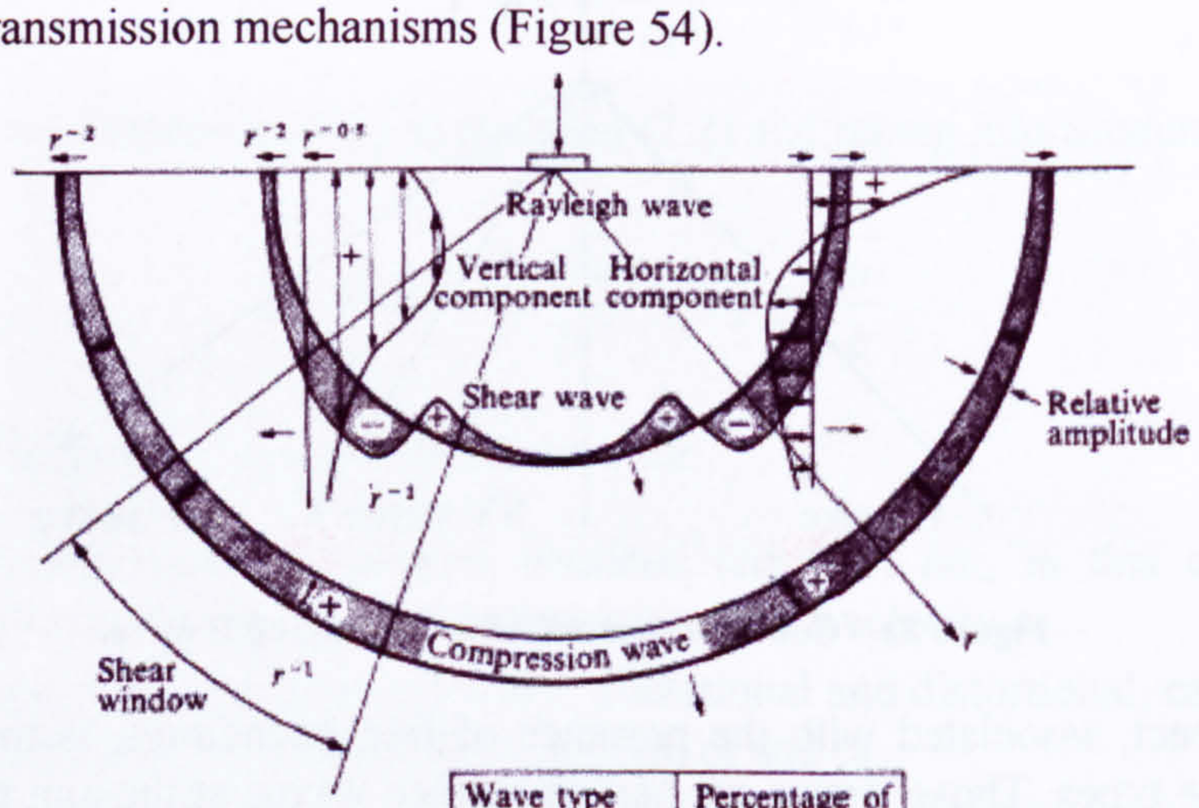

Wave type	Percentage of total energy
Rayleigh	67
Shear	26
Compression	7

Figure 54 – Displacement and energy distribution due to harmonic loads [135].

Another wave type extensively used for damage detection goals is the Lamb wave, which is an elastic perturbation propagating in thin plates of finite thickness with free surfaces. The particle motion occurs both in the wave propagation direction and through the plane of the plate (Figure 55).

For Lamb waves the velocity of sound depends not only on the material elastic constants, but also on the plate thickness and on the frequency [137-138].

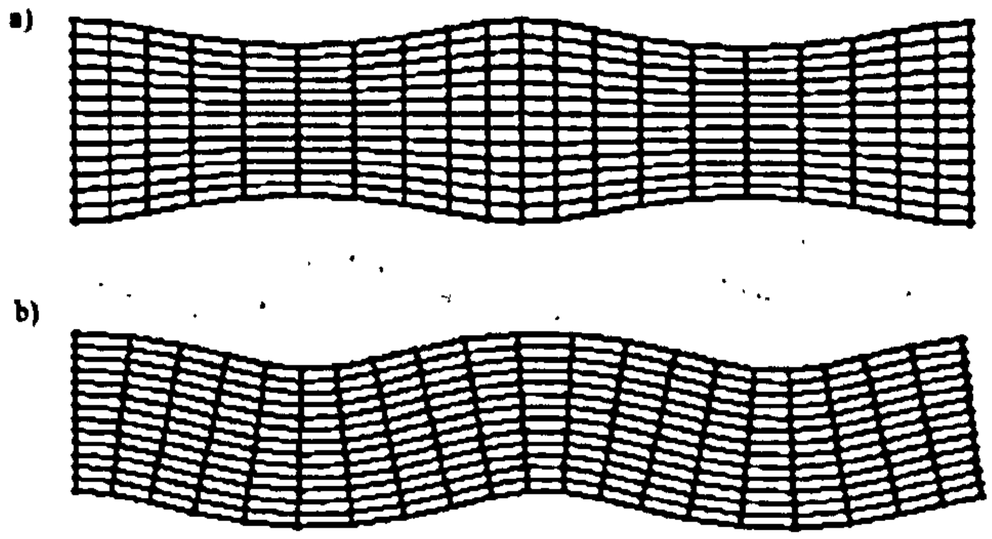

Figure 55 – Lowest order symmetric (a) and asymmetric (b) Lamb waves in a plate [137]

A further phenomenon connected to the propagation of waves with close frequencies is the Group Velocity (GV) concept. The first observation of the GV phenomena goes back to Rayleigh, who remarked that when a group of waves advance into still water, the velocity of the group is less than that of any of its individual wave; these waves appear to advance through the group and dying away as they approach its interior limit [139].

The GV concept can be easily analytically explained by considering two propagating harmonic waves of equal amplitude, but with slightly different frequency ω_1 and ω_2:

$$y = A\cos(\gamma_1 x + \omega_1 t) + A\cos(\gamma_2 x + \omega_2 t) \tag{7.7}$$

where:

- γ is the wavenumber $\gamma = \frac{2\pi}{\lambda}$;
- λ is the wave length

Substituting the cosine double angle formulae in equation (7.7) and then rearranging, eq. (7.7) can be rewritten as:

$$y = 2A\cos\left(\frac{1}{2}(\gamma_2 - \gamma_1)x - \frac{1}{2}(\omega_2 - \omega_1)t\right)\cos\left(\frac{1}{2}(\gamma_2 + \gamma_1)x - \frac{1}{2}(\omega_2 + \omega_1)t\right) \tag{7.8}$$

Since the frequencies are slightly different also the wavenumbers are slightly different. Therefore, assuming:

$$\Delta\omega = \omega_2 - \omega_1 \quad \Delta\gamma = \gamma_2 - \gamma_1 \tag{7.9}$$

$$\omega = \frac{1}{2}(\omega_1 + \omega_2) \quad \gamma = \frac{1}{2}(\gamma_1 + \gamma_2) \tag{7.10}$$

and defining as average phase velocity c, the ratio ω/γ, equation (7.8) can be rewritten as:

$$y = 2A\cos\left(\frac{1}{2}\Delta\gamma x - \frac{1}{2}\Delta\omega t\right)\cos(\gamma x - \omega t) \tag{7.11}$$

Equation (7.11) describes (see Figure 56) a high frequency wave (ω second term of eq. 7.11) propagating with a (phase) velocity c modulated by a low frequency wave ($\Delta\omega$ first term of eq. 7.11) propagating with a velocity c_g:

$$c_g = \frac{\Delta\omega}{\Delta\gamma} \tag{7.12}$$

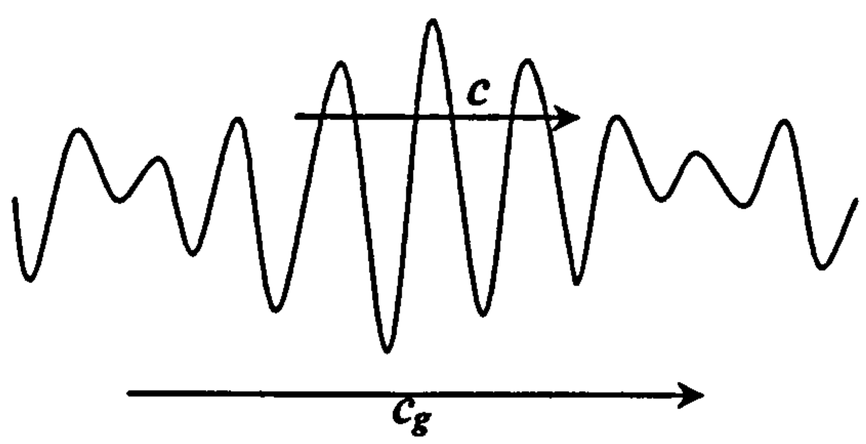

Figure 56 – Wave group formed by two waves with close frequency.

The velocity c_g is called group velocity.

In the past, the application of the wave propagation concepts through Acoustic Emissions (AE) and Ultrasonic Testing (UT) was limited by the high cost and fragility of acquisition devices that confined their use in non-harsh environment.

Nowadays, the technology progress wiped out those limitations supplying cheaper and more efficient acquisition systems fitted by sensors capable of withstanding harsh environments, giving a new boost to wave propagation studies and applications as next paragraph explained.

7.4 Wave propagation applications

The wave propagation phenomena have been applied over the years in the most different fields, like Acoustic Emission (AE), Ultrasonic testing (UT), Seismic Applications (SA), reservoir exploration, and so on. Some of the most common application (AE, UT and SA) are discussed in the following sections.

7.4.1 Acoustic Emission

Acoustic Emissions are high frequency, transient sound waves (P-waves) emitted when rapid stress redistributions occur in a material. This is why most of the time the AE recording requires constant loading of the specimen, even though its magnitude may also vary (i.e. cyclic loads, general loading condition). The stress redistributions are normally caused by generation of structural changes within the material. The emission analysis characterizes the signals according to intensity and frequency content, and, also, is entailed to locate the release mechanisms by comparing the time signals [140].

An advanced AE technique requires the recording of the acoustic emission activity and its waveforms during the loading of a specimen. An example is given by the analysis of the damaged zone behaviour in fibre reinforced concrete [141], where the radiation pattern of acoustic emission sources and the seismic moment as well as the type and orientation of the cracks have been determined using moment tensor inversion methods

based on a complex arrival time picking algorithm (based on statistic evidences) to discriminate between noise and echoes.

A different localisation approach was used for the analysis of waves due to acoustic bursts propagating in composite laminates [142]. A Time-Frequency Representation (TFR) of dispersive plate waves was used, proving that peaks of the TFR magnitude evaluated using Gabor wavelets are related to the echo arrival time of Lamb waves. Moreover, a triangulation method provides accurate results of damage location in anisotropic laminates, as well.

A contrasting damage detection with those presented above [143] consisted in a localisation algorithm that minimises the run-time differences between experimental and theoretical signal travel time (p-waves). The theoretical wave propagation path was assumed straight and the p-wave velocity was evaluated by ultrasound pulse measurements.

AE are also used to characterise material fatigue behaviour when classical fracture mechanics approaches fail as for micro-cracks generated inside materials, before visible failure. In this case, brand new algorithms have been used to manipulate the data strongly affected by noise. Those algorithms were based on Floating threshold, spatial filtering, linear guard sensors and wavelets transform [144, 145].

For low-velocity impact damages on laminated composite [146], AE proved to be very effective due to its capability of detecting defects hidden inside the composite structures. However, conventional AE analysis methods in time or frequency resulted unsuitable, because different Lamb's wave types and damage severities are undistinguishable in acoustic emissions generated by impact loads. In this case a profitable way to analyze the signal resulted to be its decomposition by wavelet transform in the time-frequency space.

7.4.2 Ultrasonic testing

Ultrasonic testing (UT) is one of the most widely used NDT techniques for discontinuity detection and material characterization in many engineering fields. Advantages of UT compared to other metal tests techniques are higher penetration, higher sensitivity and greater accuracy. A major drawback of UT is the extensive technical expertise required to UT inspectors [147]. UT consists in an ultrasonic pulse that propagates in the structures tested, which behaviour is acquired by apposite sensors, deciphered and correlated to discontinuities or other indications on the specimen.

UT has been used as non-invasive method for thin thickness measurements of multi-layer structures [148]. In this case, A-scan approach (§1.5.2) in concert with wavelets tools showed their reliability for the detection of partially overlapped echoes in a noisy environment as the ophthalmic and microelectronic technologic field can be.

For detection of damage in rails [149], elastic guided waves propagating through the rail were used. The detection has been made possible by exploiting the energy propagating from the train wheel in contact with the rail. Essentially, the detection technique is based on the following two concepts. If there is not damage between two sensors the signals received by both sensors are approximately the same. On the other hand, if a defect occurs between the two sensors, the output at the nearest sensors to the coming train would increase in magnitude significantly being the result of the sum of the

impinging elastic wave energy and the elastic wave energy reflected from the broken rail. On the other hand, the output of the second sensor is reduced.

For a better comprehension of the wave propagation phenomenology within rails in presence of vertical crack, experimental data [150] were compared to numerical data evaluated using the Elastodynamic Finite Integration Technique (EFIT) [151]. This comparison helped to clear up the complex evolution of the front wave propagation leading to a correct interpretation of the acquired signals.

Ultrasonic flaw detection has been observed in many other studies where the structures investigated were plate or plate-like. The approaches used can be resumed in two main branches. The first concerns classic ultrasonic damage detection methods consisting in locating the damage and estimating its characteristics using echo arrival times and group velocity. The application range goes from the detection of disbond in adhesive joints [152] to corrosion detection [153].

The second class of methods [154-158] uses time-frequency approaches to screen the experimental data. Those procedures involve the use of Short Time Fourier Transform (STFT), pseudo Wigner-Ville distribution and Wavelet Transform (WT) in both forms, discrete and continue with an improved resolution in the signal representation, in the detection of damage presence, location and size estimation.

7.4.3 Seismic application and Reservoir exploration

Wave propagation phenomena are at the heart of seismology, helping the scientists to locate earthquake epicentres and being a useful tool for geophysical investigations. A very profitable application of geophysical outcomes is reservoir exploration, which exploits wave propagation phenomena to locate oilfields. Both seismic and reservoir explorations work on half space media. This hypothesis reduces to the minimum the problem to screen among reflected waves by boundaries and those reflected by other surface of discontinuity (target). The main concerns for such applications are the characterisation of the Earth, which is thought to be subdivided into a finite number of layers of effectively uniform acoustic impedance [159], assumption valid for low frequency range.

On these bases, the Earthquakes source is found by the evaluation of the time difference between the arrival of the P and S waves at the same station [160, 161].

7.5 Time-Frequency Representation

In the above overview, a global picture of the application fields for wave propagating phenomena has been given, with particular emphasis on all the aspects connected to localisation and exploration of discontinuities within structure boundaries. The different techniques, used to analyse AE and UT signals, were stressed, at the aim to give a first glimpse of the variety of approaches developed.

The first techniques used to analyse ultrasonic signals were developed in either the time or frequency domain. Unfortunately, their performances decrease consistently in

presence of echo overlap, attenuation phenomena at high frequencies and critical sampling [148].

Those limitations were overcome by the introduction of Time Frequency Representations (TFR), which adoption increased the accuracy of the measures, reduced the attenuation phenomena and allowed to screen between overlapped echoes.

Between the several TFRs existing [127] only two of them have been analysed, the Short Time Fourier Transformation (STFT) and the Continuous Wavelet Transformation (CWT), which are reviewed in the following sections.

7.5.1 Short Time Fourier Transformation

STFT is the most standard approach to analyse a time signal $s(t)$, in the time-frequency space. This splits the time domain signal into many windows termed short time windows, and then, makes the Fourier transform of each segment. The whole operation can be synthesised as [127]:

$$STFT(t,\omega)=\int s(t')w(t'-\tau)e^{-j\omega t'}dt' \tag{7.7}$$

The STFT differs from the Fourier transform only by the presence of the window function $w(t)$.

Alternatively, the STFT can be interpreted from eq. (7.7) as the projection of the signal $s(t')$ onto a set of bases $w^*(t'-\tau)exp(j\omega t')$ parameterised in τ and ω (* stands for complex conjugated), which are, respectively, the time and circular frequency. Since, those bases last a finite extent in time, the signal frequencies can be monitored as a function of time.

The definition of the STFT can be given also in terms of frequency [127]:

$$STFT(t,\omega)=\frac{1}{2\pi}e^{-j\omega t}\int S(\omega')W(\omega'-\omega)e^{-j\omega' t}d\omega' \tag{7.8}$$

where $S(\omega)$ and $W(\omega)$ are the Fourier transform of $s(t)$ and $w(t)$. Observing the expressions (7.7) and (7.8), the following observations can be made:

- Phenomena lasting shorter than the time window duration tend to be smeared out.
- The width of the frequency window $W(\omega)$ limits the resolution in the frequency domain.
- The time and frequency domain resolution is inversely correlated by the uncertainty principle [162]
- The resolution across the entire time-frequency plane is fixed by the windows width (see Figure 57).

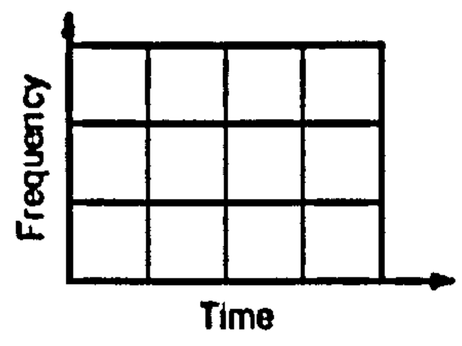

Figure 57 – STFT resolution.

7.5.2 Continuous Wavelet Transform

A natural evolution of the STFT are the wavelets [126], which linearly decompose an arbitrary signal *s(t)* by projecting it on functions that are simply dilations and translations of a parent (or mother) wavelet *g(t)* via the convolution of the signal and the scaled/shifted parent wavelet [126]:

$$CWT(a,t)=\frac{1}{\sqrt{a}}\int_{-\infty}^{\infty}s(\tau)g^{*}\left(\frac{t-\tau}{a}\right)d\tau \tag{7.9}$$

where a is the dilation parameter and τ is the translation parameter.

Analysing eq. (7.9) is clear that the wavelets basis functions have variable width according to a and τ (see Figure 8).

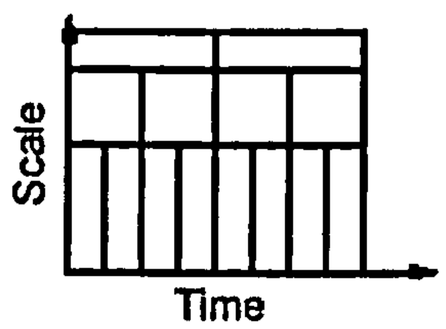

Figure 58 - CWT Resolution.

More information about the wavelet transform can be found in section 4.7.2.

In the next paragraph, the motivations for the choice of the CWT have been illustrated through consideration regarding resolution and noise issues.

7.6 Choice of the TFR

The time frequency representation choice was based on two comparison criteria: the resolution and the sensitivity to random noise.

7.6.1 Resolution

The resolution of the TFR is critical to differentiate different echoes when these are very close.

Because both the TFRs under analysis use particular window functions, a comparison can be done only in terms of Root Mean Square (RMS) of their duration and bandwidth.

The RMS duration can be evaluated as [148]:

$$\Delta t=\frac{1}{\|w\|_2^2}\sqrt{\int_{-\infty}^{\infty}(t-t_{\bullet})^2|w(t)|^2\,dt} \tag{7.12}$$

where:

- $t_{\bullet}$ is the temporal centre of the window function:

$$t_* = \frac{1}{\|w\|_2^2} \int_{-\infty}^{\infty} t|w(t)|^2 dt \tag{7.13}$$

- $\|w\|_2^2$ is the Euclidean norm of the time window *w(t)* evaluated as:

$$\|w\|_2^2 = \int_{-\infty}^{\infty} |w(t)|^2 dt \tag{7.14}$$

Similarly operating in the frequency domain, the RMS bandwidth can be obtained [148]:

$$\Delta f = \frac{1}{\|W\|_2^2} \sqrt{\int_{-\infty}^{\infty} (f - f_*)^2 |W(f)|^2 df} \tag{7.15}$$

where:

$$f_* = \frac{1}{\|W\|_2^2} \int_{-\infty}^{\infty} f|W(f)|^2 df \tag{7.16}$$

$$\|W\|_2^2 = \int_{-\infty}^{\infty} |W(f)|^2 df \tag{7.17}$$

Together the duration and the bandwidth RMS measure the time-frequency localisation (resolution) of the TFRs.

In eq. (7.7) is possible to identify $w(t'-\tau)e^{-j2\pi ft}$ ($\omega=2\pi f$) as a time-shifted and modulated version of the window function w(t).

By analysing $w(t'-\tau)e^{-j2\pi ft}$, it is possible to prove for any time-frequency point (f_0, τ_0) that its time centre is $t_*' = t_* + \tau_0$ and its RMS duration $\Delta t' = \Delta t$. Therefore, the time localisation interval is given by $[t_* + \tau_0 - \Delta t, t_* + \tau_0 + \Delta t]$ with a time resolution of $2\Delta t$. Similarly, for the frequency domain the centre frequency of $w(t'-\tau)e^{-j2\pi ft}$ is $f_*' = f_* + f_0$ with RMS bandwidth $\Delta f' = \Delta f$. Accordingly, the frequency resolution is $2\Delta f$. Then, the time-frequency resolution for any point (f_0, τ_0) is a rectangle whose width is the time resolution $2\Delta t$ and height is the frequency resolution $2\Delta f$, with area $4\Delta t\Delta f$ (fig.34-a). Moreover, the possibility of having high resolution in both the domains, time and frequency, is limited by the uncertainty principle, which bound the rectangle area to be $4\Delta t\Delta f \geq 1/\pi$ [148].

In contrast with the constant resolution of the STFT is the already mentioned multi-resolution of the CWT. As matter of the fact, the time localisation (see eq. 7.8) is given by $[a^{-1}(t_* + \tau_0 - \Delta t), a^{-1}(t_* + \tau_0 + \Delta t)]$ for a time resolution of $2a^{-1}\Delta t$. In an analogous manner, the frequency resolution can be estimated equal to $2a\Delta t$. Hence, the time-frequency resolution for any time-frequency point is a rectangle of width $2a^{-1}\Delta t$ and of length $2a\Delta t$ with a constant area along the time-frequency domain of $4\Delta t\Delta f$, as the STFT. However, the time resolution increases with the frequency, while the frequency resolution decreases to keep up the constant area (Figure 59-b).

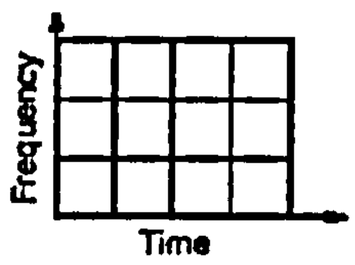

(a)

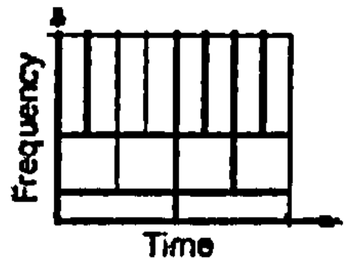

(b)

Figure 59 – Comparison between the STFT (a) and wavelet (b) transformation resolution.

Concluding, The Wavelet Transform (WT) allows the screening of the echo start times with more resolution if measured at high frequencies.

7.6.2 Noise sensitivity

The noise sensitivity of any TFR is of great importance because significant noise sensitivity could lead to faulted measurements. For classic TFRs such as STFT, the noise tends to be uniformly distributed over the time-frequency domain [148].

Conversely, the noise effect on the WT is concentrated into the high frequencies [148]. In this way, it is possible to measure the echo start times (instant in which the echo arrives at the sensor location) from a region of the time-frequency plane where the Signal Noise Ratio (SNR- §4.2) is acceptable.

Hence, choosing the CWT is possible to enhance the time resolution with consistent improvements in the localisation of the echo start time, and at the same time to reduce the sensitivity to the noise of the time-frequency analysis.

In order to have enough elements for the interpretation of the TFRs in case of echo presence, their behaviour for the most common scattering mechanisms is described in the next paragraph.

7.7 Interpretation of the TFRs

A correct interpretation of the TFRs can lead the user to a deeper understanding of the wave propagation phenomenon. At this aim the most common scattering mechanism were analysed [127].

Scattering of structure surfaces or edges [164-166], (Figure 60-a) appears as a discrete time event, identified on the time-frequency plane as a vertical line, since it occurs at a particular instant but for the whole frequency range.

When in the TFR images a horizontal line is observed [164,166] (Figure 60-b), the scattering event observed is a resonance of the structure, since the scattering mechanism can be observed over all the time of acquisition but becomes prominent only at determined frequencies.

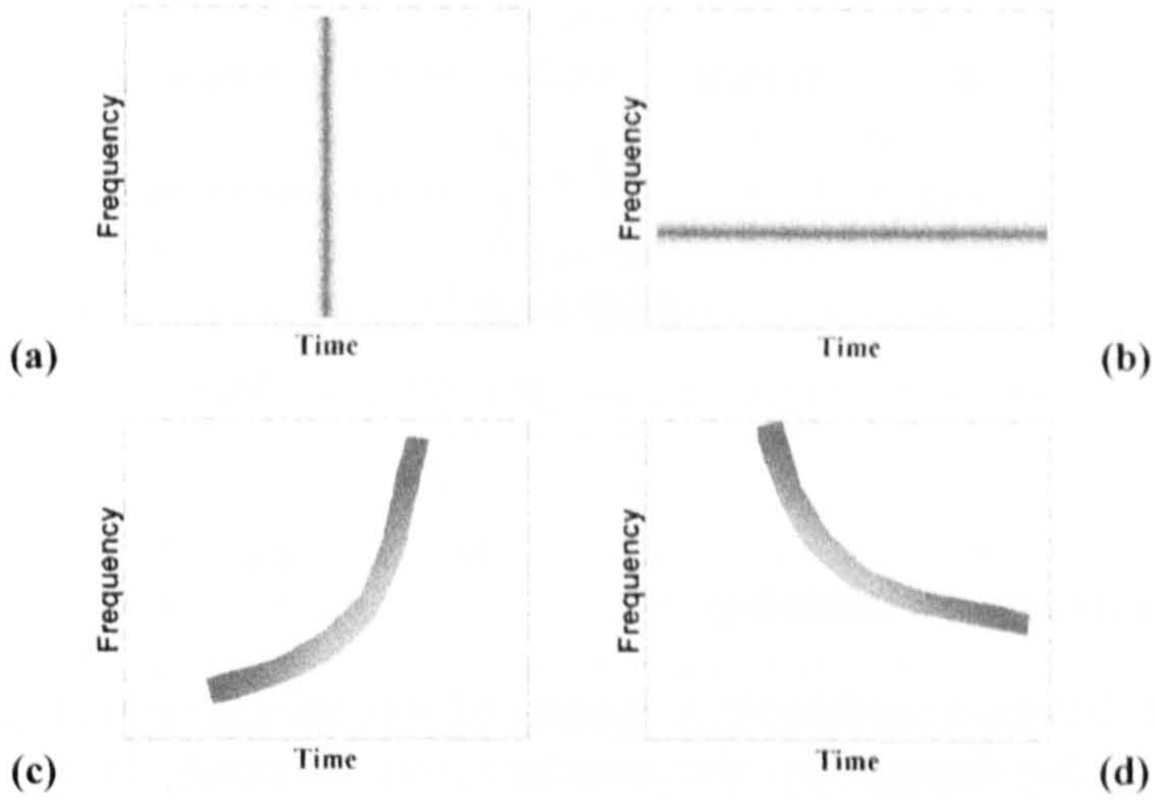

Figure 60 – Most common scattering mechanisms [127].

Dispersive phenomena are identified on the time-frequency plane by slanted lines (Figure 60-c and –d). For material dispersion [167] the curve has a positive slope (Figure 60-c), while if the slope is negative, the scattering mechanism is related to waveguide structures[1] (Figure 60-d) [164-166, 168].

In the next paragraph, the choice of the parent wavelet between the countless existing was discussed.

7.8 Parent wavelet selection

The number of parent wavelets (or mother wavelet) present in literature are countless and their application the most various. For example, in ultrasonic NDE of composite material [154] the Coifman wavelet was used for multiscale characterisation of pitting corrosion [169], while for crack damage detection on composite panels [170], the Daubechies family was exploited. However, most of the times to analyse time signal coming from structures, the complex Morlet wavelet [154,126, 171-173] was used, because of its particularity of giving magnitude and phase information, very useful to visualise possible discontinuities. Moreover, this wavelet becomes very attractive for harmonic analysis, due to its analogies with the Fourier transforms expressed by its equation [174]:

$$g(t)=\frac{1}{\sqrt{\pi\gamma}}e^{-\frac{t^2}{\gamma}}\left(\cos(\omega_0 t)+i\sin(\omega_0 t)\right) \tag{7.18}$$

A Morlet wavelet is a Gaussian-windowed Fourier transform, with a central frequency $f_0=\omega_0/2\pi$, but differently from the Morlet wavelet illustrated in chapter 4, the width of the Gauss' curve (the wavelet frequency band) γ is also parameterised. As for chapter 4

[1] For waveguide structure is meant a structure that guides stress waves along its length. Typical waveguide structures are pipes, rods, rails and etc...

wavelet, by maximising the eq. (7.18) in the frequency domain (eq. 7.20, [174]) a unique relation between the dilation parameter a and frequency f is obtained:

$$f = \frac{a}{f_0} \tag{7.19}$$

$$G(af) = e^{-\pi^2 \gamma (af - f_0)} \tag{7.20}$$

Hence, because of these unique features the complex Morlet wavelet was chosen as parent wavelet.

7.9 Damage Detection Methodology

The damage detection methodology developed was split in three steps. In the first step the presence of the damage on the structure was assessed. In the second step the extraction arrival time of the reflected wave (or echo) was estimated, and in the third step the damage location through a simplified Ray-Tracing algorithm was detected.

7.9.1 Damage presence detection

As described in section 7.7, structural changes (e.g. cracks, plasticization and corrosion) appear in the TFR as either vertical lines or slanted lines. A similar behaviour is expected from perturbation waves reflected back by the structure boundaries. This explains why conventional UT needs skilled inspectors to discriminate the reflected waves due to structural changes from those due to structure boundaries. Therefore, at the aim to simplify the interpretation of the ultrasonic signals a brand new approach was developed. This was based on the idea that damage introduces, in the wave propagation phenomenon of the undamaged structure, an uncorrelated time signal due to the presence of waves reflected by the defect surface. Hence, in order to highlight the time discrepancy between the damaged and undamaged signal a Coherence Function Based Algorithm (CFBA) was used. The method was structured into two parts. The first involved the evaluation of a time-frequency coherence function, while the second phase identifies the presence of damages by discriminating between the time-frequency coherence changes due to noise and damage reflected wave arrivals.

In the first phase of the CFBA, the Time Frequency Coherence (TFC) function, between the undamaged $s_u(t)$ and the damaged $s_d(t)$ signals, is evaluated as the ratio of the wavelet cross-spectrum S_{ud} and the product of the wavelet auto-spectra of the two time signals (S_{uu}, S_{dd}) [163]:

$$TFC(f,t) = \sqrt{\frac{|S_{ud}(f,t)|^2}{S_{uu}(f,t) S_{dd}(f,t)^*}} \tag{7.21}$$

where the power spectra S_{uu}, S_{dd} and S_{ud} are given by:

$$S_{ij}(f,t) = \int_0^t w_i^*(f,\tau) w_j(f,\tau) d\tau \tag{7.22}$$

with i, j ={u, d}.

The integration time window [0, t] in eq. (7.22) was selected in the attempt to reduce the noise effects, which should be mitigated on a long time range. Unfortunately, this process, together with the noise, averages out, also, the changes in the coherence due to the arrival of the waves reflected by the damage surfaces. Therefore, a shorter time windows [t-Δt, t+Δt] was also used to evaluate the power spectra:

$$S_{ij}(f,t) = \int_{t-\Delta t}^{t+\Delta t} w_i^*(f,\tau) w_j(f,\tau) d\tau \tag{7.23}$$

In both cases, the time discrepancies caused by noise appear as peaks randomly distributed in contrast with those due to defect reflected wave arrivals, which are characterised by sudden changes of the coherence along a wide frequency range. For the first time window chosen, the coherence change will extend in time and present rapid variation in coincidence of the arrivals of the wave reflected by the damage surface (P, S, Rayleigh wave, group velocity, see Figure 61-a). For the second time window considered [t-Δt, t+Δt] the sudden coherence changes decrease shortly after to zero (see Figure 61-b).

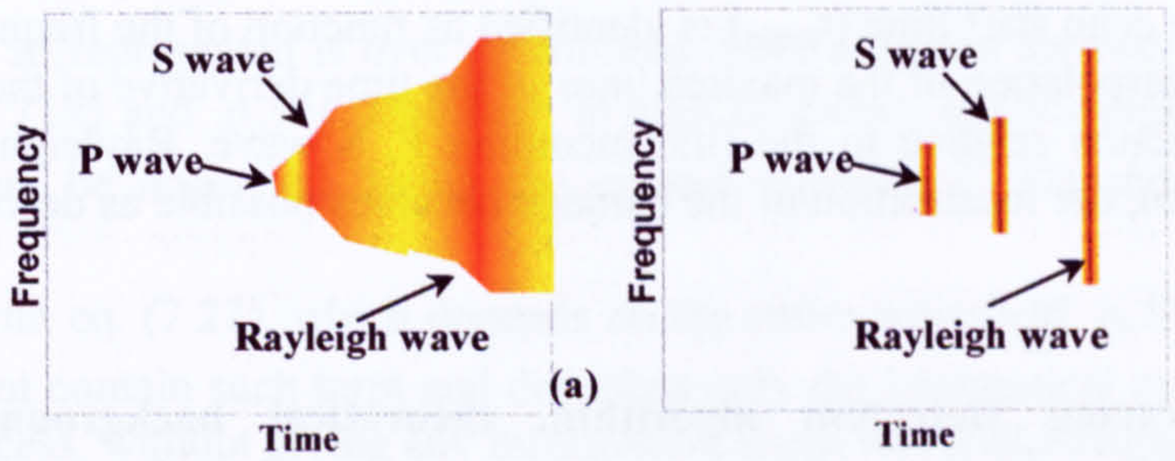

Figure 61 – Time-frequency coherence changes due to damage reflected waves

Once, the damage presence is certain by recognising the behaviour described above, it is possible to proceed to the extraction of the echo start time as next section illustrates.

7.9.2 Echo Start Time Extraction Algorithm (ESTE)

The detection of the arrival times of the echoes is very important, because, the precision of the damage locations is strongly dependent on its correct estimation. At this extent the Echo Start Time Extraction (ESTE) algorithm was developed. This consists in a two stage process. In the first stage, a pass-band noise filter reduces the noise effects and, then, the echo start time is identified by the evaluation of maxima lines.

The pass-band noise filter effectiveness depends on two factors, the CWT tendency to concentrate the noise into high frequencies and the poor SNR at low frequencies due to the high frequency content of the signal discrepancy generated by the damage occurrence. In this way, two frequencies (f_1, f_2) are identified, which values rely on the SNR level respectively at low and high frequencies.

At this point, the echo start time (echo arrival time) could be extracted by simply identifying, at each frequency, either the times at which the coherence has the most rapid change (for a time window [0,t]) or the time of coherence local maxima (for the second

time window used). In both case the results will appear as a series of lines almost parallel to the frequency axis (Figure 62, see black lines). Unfortunately, the noise presence makes very difficult the extraction of the ridges and in many cases ends up in winding lines (red line in Figure 62). Therefore, in order to minimise the noise effect on the time of flight extraction, the time frequency coherence was derived with respect to time. This highlights the wave arrivals as local maxima lines and reduces the winding behaviour showed in Figure 62. Furthermore, a least square polynomial interpolation of the maxima lines identified can be used to improve the localisation of the wave arrivals.

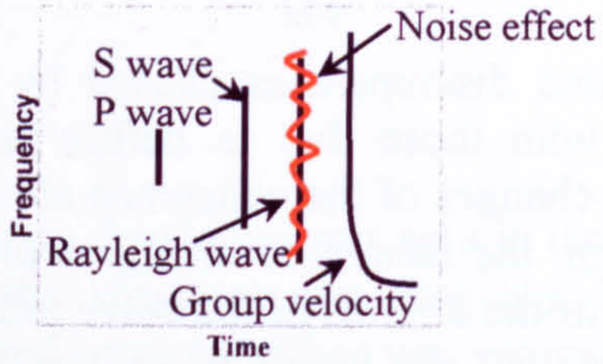

Figure 62 - Echo-start times

Finally, the echo start time (t_{target}) is identified as function of the frequencies through a polynomial interpolation of the maxima lines of the time derivative of the time frequency coherence function relative to the first incoming P, S wave, Rayleigh wave or group velocities. Then, the localisation of the damage becomes possible as described in the next two sections.

7.9.3 Ray-Tracing Detection algorithm, theoretical background and set-up considerations

Many laws or principles rule wave propagation within media, such as: the Huygen's principle, the Fermat's principle and the Snell laws regulating the reflection and refraction phenomena [135].

For the Huygen's principle [135] each point on a wavefront can be considered as a generation point for succeeding spherical waves. This means that, assuming the perturbation source so small to be reduced to a point, the wavefront generated are spherical with a radius equal to the product between the wave travelling speed (considered to be constant) and the travelling time. Moreover, for the principle of the least time (Fermat's), waves travel the fastest possible path between two points. Therefore, in uniform media, waves travel in space in straight lines, which can be easily proved for P wave propagation by use of the Eikonal equation [173].

The P wave can be assumed as a pressure disturbance propagating in a isotropic medium (7.24):

$$p(\vec{x},t) = p_0(\vec{x}) f[t - T(\vec{x})] \tag{7.24}$$

where:

- $T(\vec{x})$ represents the propagating wavefront.
- $p_0(\vec{x})$ is the initial wavefield.
- $\vec{x}$ is a 3D location.

- f is an arbitrary smooth function.
  The scalar (acoustic) equation in 3D, for medium with constant density, reads:

$$\nabla^2 p(\vec{x},t)=\frac{1}{c_1^2}\frac{\partial^2 p(\vec{x},t)}{\partial t^2} \tag{7.25}$$

Inserting eq. (7.24) into eq. (7.25) is obtained:

$$f''p_0\left[(\nabla T)^2-\frac{1}{c_1^2}\right]-f'\left(2\nabla p_0\cdot\nabla T+p_0\nabla^2 T\right)+f\nabla^2 p=0 \tag{7.26}$$

To satisfy eq. (7.26) for every function f, its three terms must vanish separately, resulting in the following three equations:

$$(\nabla T)^2-\frac{1}{c_1^2}=0 \tag{7.27}$$

$$2\nabla p_0\cdot\nabla T+p_0\nabla^2 T=0 \tag{7.28}$$

$$\nabla^2 p=0 \tag{7.29}$$

The problem so represented is over determined, three equation for two unknowns the scalar functions $T(\vec{x})$ and $p_0(\vec{x})$. However, in high frequency applications the terms in f of eq. (7.26) can be neglected, living the eikonal equation (7.27) and the transport equation (7.28).

In contrast with eq. (7.27), which depends on the entire wavefield $p_0(\vec{x})$, the eikonal equation does not contain such term and describes only the kinematical properties of the propagation process, without giving any information about wavefield magnitudes.

In a homogeneous medium (the pressure perturbation speed is constant), so as the solution of the eikonal equation coincides with the Huygens' wave representation (7.30) with concentric spherical wavefronts centred in the source point $\vec{x}_0$.

$$T(\vec{x})=t_0+\frac{|\vec{x}-\vec{x}_0|}{c_1^2} \tag{7.30}$$

This means that the wave propagates along straight lines from the source point $\vec{x}_0$ to a generic point $\vec{x}$ on the spherical wave front (see eq. 7.30 term $|\vec{x}-\vec{x}_0|$).

For media with boundaries, the wave propagation phenomenon is still governed by the same principles and laws, but for complex domain like rails, the wave travel path is not necessarily straight. In some cases, a further complication in the set-up of the defect localisation process rises from the impossibility to have the sensor location coincident with the excitation area as for rails, where the excitation is provided by the train through the rail rolling surface. This means that a different location for the sensors must be chosen.

For this selection, two factors must be taken into consideration. The first is related to the damage to be identified, for example, rolling contact fatigue damages on rails. In other words, defects bounded on the railhead, which is a simple connected domain. The second factor is the sensitivity to structural changes of the sensor location, whose max

value is located on the most flexible part of the structure, i.e. the rail web (since structural flexibility is inversely proportional to the structure thickness [175]).

Therefore a solution of compromise can be placing the sensor on the railhead but opposite to its rolling surface. This implies that the wave path is composed by two straight lines, the impinging line (from the excitation point up to the defect surface) and the reflected line ending in the sensor place (see Figure 63).

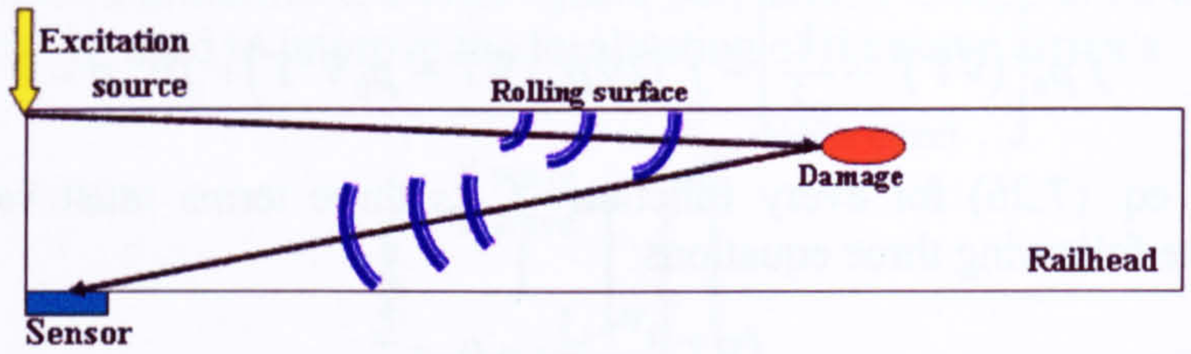

Figure 63 - Wave echo path.

The sensor number is determined by analysing the localisation problem from a mathematical point of view. Defining the domain $\Omega(x, y, z) \subset \Re^3$ (the structure) and $d\Omega(x, y, z)$ its surface, the probable damage position $\vec{x}_D$ is univocally identified by its three coordinates (unknowns). Therefore, three independent equations must be written in the three unknowns. In a 3D domain, a point is univocally located as the vertex of a tetrahedron (Figure 64), if and only if the locations of the other three vertices and the length of its edges are known.

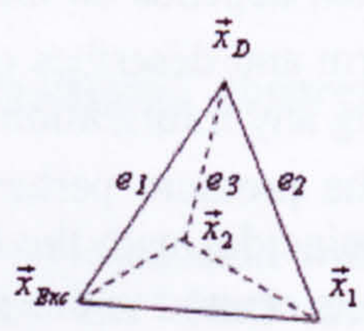

Figure 64 – Tetrahedron of localisation.

Hence, considering a tetrahedron having as vertices: $\vec{x}_D$, the excitation point $\vec{x}_{Exc}$ and two sensor locations, $\vec{x}_1$ and $\vec{x}_2$, the edge lengths between $\vec{x}_{Exc}$, $\vec{x}_1$, $\vec{x}_2$ and $\vec{x}_D$ are unknown. The only known parameters are the wave path lengths from $\vec{x}_{Exc}$ to the two sensors ($\vec{x}_1$ and $\vec{x}_2$). Hence, only two independent equations can be identified (7.31), while for a well-posed problem three equations are needed.

$$\begin{aligned} e_1 + e_2 &= \ell_1 = t_{target\,1}\, c \\ e_1 + e_3 &= \ell_2 = t_{target\,2}\, c \end{aligned} \tag{7.31}$$

where c is the speed of the waves (P, S, Rayleigh wave and group velocity) used to extract the t_{target}.

Each one of the equations (7.31) defines the locus of the points [176] $\Gamma \subset \Re^3$ described by the vertex $\vec{x}_D$ of the triangle $\vec{x}_{Exc}\ \vec{x}_1\ \vec{x}_D$ ($\vec{x}_{Exc}\ \vec{x}_2\ \vec{x}_D$) whose distances e_1 and e_2 (e_3) from the two fixed points $\vec{x}_{Exc}$ and $\vec{x}_1$ (or $\vec{x}_2$, the foci) gives a constant sum equal to the

wave path length ($\ell=\{\ell_1, \ell_2\}$) from $\vec{x}_{Exc}$ to the first (second) sensor. Therefore, Γ is the surface of a revolution ellipsoid (Figure 65) along the $\vec{x}_{Exc}\,\vec{x}_1$ ($\vec{x}_{Exc}\,\vec{x}_2$) direction. The ellipsoid equation in the canonical Cartesian coordinate system $X_cY_cZ_c$, with the axis Y_c parallel to the direction of wave propagation Z and its origin (x_0, y_0, z_0) coincident with the mid point of the tetrahedron side $\vec{x}_{Exc}\,\vec{x}_1$ ($\vec{x}_{Exc}\,\vec{x}_2$), is

$$\frac{x_c^2}{a^2}+\frac{y_c^2}{b^2}+\frac{z_c^2}{c^2}=1 \tag{7.32}$$

with the semi-axes lengths

$$a=\frac{\ell}{2} \qquad b=c=\frac{\ell}{2}\sin\theta \qquad \theta=\operatorname{acos}\left(\frac{d\left(\vec{x}_{Exc},\vec{x}_i\right)}{\ell}\right) \tag{7.33}$$

and i={1, 2}.

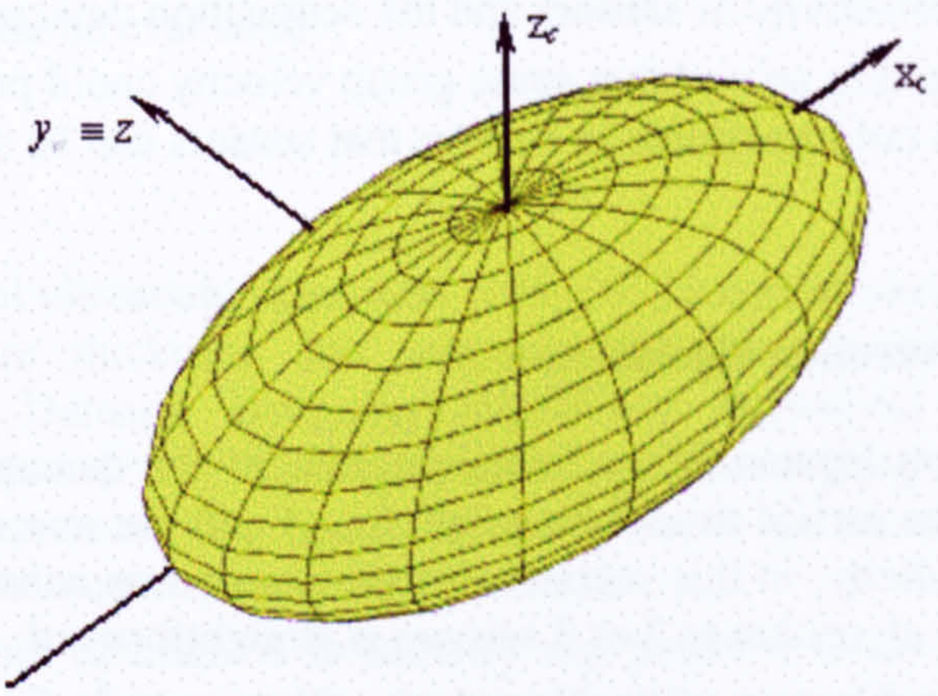

Figure 65 – Ellipsoid of the probable damage locations.

The simultaneous satisfaction of equations (7.31) results in an ellipse intersection of the two ellipsoids described by the equation (7.32). This confirms that a third equation is needed. Two possible solutions were considered:

1. If a third point (sensor) is selected $\vec{x}_3$ and, consequently, a third ellipsoid is defined, the equation system, constituted by either the three ellipsoid equations (7.33) in the global coordinate system or, equivalently, in the form of the equations (7.31), admits a unique solution if only if its Hessian is a positive definite matrix. Therefore, the locations of the sensors must be adjusted in order to fulfil this requirement for every $\vec{x}_D \in \Omega(x, y, z)$.

$$\begin{cases} a_1x^2+b_1y^2+c_1z^2+2f_1yz+2g_1zx+2h_1xy+2p_1x+2q_1y+2r_1z+d_1=0 \\ a_2x^2+b_2y^2+c_2z^2+2f_2yz+2g_2zx+2h_2xy+2p_2x+2q_2y+2r_1z+d_2=0 \\ a_3x^2+b_3y^2+c_3z^2+2f_33yz+2g_3zx+2h_3xy+2p_3x+2q_3y+2r_3z+d_3=0 \end{cases} \tag{7.33}$$

2. If damages are located only on the surface or next to it, the structure surface equation can be used as the third independent equation:

$$d\Omega(x,y,z)=0 \tag{7.34}$$

It is clear that the result of the geometric intersections, in most of the cases, yields two points. However, only one point will be in the direction of propagation. Therefore, this point will identify the damage location.

For structures that behave as waveguides (e.g. rails, aircraft spars and stringers), an approximated solution can be obtained using only one sensor (one ellipsoid). This means that only the structure cross section location of the damaged area, normal to the wave propagation direction, can be computed.

The single sensor approach is considered as an appropriate solution for damage detection in waveguide structures. This reduces to the minimum the number of sensors and, therefore, the installation and the related maintenance expenses.

The distance between two sensors deployed along the rail depends on the attenuation that the magnitude of the wave perturbations undergoes during the propagation phenomenon, the size of the minimum damage to identify, the range of frequencies investigated and the sensitivity of sensors and the acquisition devices.

However, recent studies proved that some group velocity could propagate up to 2134m [177]. Therefore, it is not impossible to believe that sensors can be spaced every 300-600 meters.

7.9.4 Ray-Tracing Detection algorithm

The RTD algorithm locates the probable position of the damage by minimising the difference between the arrival times measured (t_{target}) and the numeric wave travel time (Figure 63). For simplicity, in this section a single sensor was considered. However, the extension of the RDT algorithm to 2 or 3 sensors is straightforward.

Since, the t_{target} is a function of the frequency, either a single frequency or a range of frequencies can be used to evaluate the damage location. In the last case, a least square optimisation algorithm can be used. Here, for simplicity a single frequency was used. The main difference is that, in the case of a single frequency, t_{target} is a scalar instead of a vector (a coefficient for each frequency used) when a range of frequencies is used.

The wave travel time (7.35) is computed measuring, and summing up the Euclidean distances $d(\vec{x}_1, \vec{x}_2)$ between the probable damage position $\vec{x}_D$ and, respectively, the excitation location $\vec{x}_{Exc}$ and the sensor position $\vec{x}_{Sens}$, and then dividing for the wave speed c.

$$t(\vec{x}_D) = \frac{d(\vec{x}_D, \vec{x}_{Exc}) + d(\vec{x}_D, \vec{x}_{Sens})}{c} \tag{7.35}$$

The minimisation of the Wave Travel Time Difference (WTTD, (7.35)) is carried out by an optimisation algorithm based on the Quasi-Newton method [75].

$$WTTD(\vec{x}_D) = \left| t_{target} - t(\vec{x}_D) \right| \tag{7.36}$$

The optimisation process formulates, at each iteration, a quadratic model problem (7.37) through curvature information.

$$\min_{\vec{x}_D} \frac{1}{2} \vec{x}_D^T H \vec{x}_D + e^T \vec{x}_D + b \tag{7.37}$$

where H is the Hessian matrix of WTTD, e and b are respectively a constant vector and a constant. The optimal solution of the quadratic model problem occurs when its partial derivatives of $\vec{x}_D$ tend to zero:

$$\nabla WTTD(\vec{x}_D) = H\vec{x}_D + e = 0 \tag{7.38}$$

Therefore, the optimal solution (the most probable damage position) was evaluated by:

$$\vec{x}_D = -H^{-1}e \tag{7.39}$$

The Hessian matrix evaluation in the Quasi-Newton approach is performed by using the observed behaviour of WTTD and its gradient, in contrast with the pure Newton-type method, which calculates the Hessian matrix numerically involving a large amount of computation. In this case, the Hessian matrix has been approximated by use of the BFGS formula [75].

After the t_{target} is evaluated, the damage localisation with the developed damage detection algorithm can be evaluated.

7.10 Conclusions

While convectional ultrasonic inspection [149, 177] uses ultrasonic beams propagating through the structure thickness, the proposed damage detection approach (Wave Propagation Based Damage Detection (WPBDD) algorithm) exploits the wave propagation phenomena (P, S, Rayleigh waves and wave group velocities [135]) by identifying the discrepancies, due to damage presence, in the dynamic behaviour of the structure using a time-frequency coherence function.

The purpose of this function is to identify any possible uncorrelation (discrepancy) present between two time histories. The first time history is used as reference and must be acquired when the structure is in pristine conditions, while the second time signal is used to monitor the health state of structures, acquiring it every time a trigger condition (based on a minimum level of excitation, signal shape, noise conditions and so on) is satisfied.

Physically, the discrepancies are generated by waves (P, S, Rayleigh waves and wave group velocities) reflected back to the sensor locations by the flaw surfaces, which in its absence would not exist (as confirmed in §8.4.2.1 for wave propagation in rails). Because the coherence function is defined in the time-frequency space, the arrivals of the perturbation waves, generated by the damage presence, are function of the frequency (§8.4.2.1). By calculating the arrival time of the waves interacting with the defect surfaces, the detection algorithm is able, through a ray-tracing algorithm, to estimate the location of damage.

This methodology is also capable of identifying multi-site damages by analysing the signatures of their reflected waves in the time frequency representation of the coherence function, where different damages will appear as different uncorrelated bursts as that described in Figure 61. However, further developments aimed at the automatic recognition of these bursts from the ESTE algorithm have to be carried out.

Differently from similar techniques, the main advantages of the proposed methodology is that there is no need to the control the excitation force nor an expert

ultrasonic testing inspector to discriminate between boundary and damage reflected waves [147, 149, 137, 177-179].

Moreover, since a vibration wave can propagate within a medium on large distances with a very little amplitude loss, a single sensor can inspect large portion of the structures in few instants (as showed in §8.4.2.3), in contrast with conventional ultrasonic techniques, which to inspect the same area need a number of scans, using very expensive devices named B and C scan.

The present methodology was numerically validated on the detection of rolling contact fatigue defects occurring on rail structures. The results are presented and discussed in chapter 8.

CHAPTER 8: WAVE PROPAGATION ON RAILS

8.1 Abstract

The capability of the proposed Wave Propagation Based Damage Detection (WPBDD) technique to establish the presence and location of damage was tested on a rail structure. The rolling contact fatigue defects were selected, because resulted the most severe between those occurring on rail according to a brief review on the subject.

The damage detection was preceded by an analysis of the wave propagation phenomena within a rail, with or without damage. The analysis outcomes pointed out that a detection of the damage presence would not be possible by a simple comparison between the damaged and undamaged time histories, since no difference could be spotted. Moreover, it was observed that the Time Frequency Coherence (TFC – §7.9.1) function (devised by the author) was capable of highlighting the damage presence and by its maxima lines using the Echo Start Time Extraction (ESTE - §7.9.2) algorithm to estimate the time of flight of the damage reflected wave.

Then, a numerical investigation of two single damages was carried out. The damage was introduced on the railhead surface to simulate rolling contact fatigue defects. The results showed that the proposed methodology can be successfully used in localising the damage location, however, as expected, the localisation is strongly affected by the frequency range used. The results suggested that the separation and the characterisation of single modes are crucial for the identification of different types of rail defects. Further work is needed to establish the damage severity by relating the magnitude of the changes

of the time frequency coherence to reflection and attenuation coefficients of each wave group velocity used and on the selection of the best range of frequency according to the type of damage to be identified.

8.2 Rail defects

Since the earliest days of railroading, maintenance was a main concern. However, nowadays, maintenance issues are becoming overwhelming because of the increase of operating loads, traffic, and high-speed trains. Therefore, today, maintenance means prevention of catastrophic rail failure to avert loss of rolling material as well as of lives. The figures involved are staggering, only in the EU the cost related to rail failure is around € 2 billion per year [194]. The number of derailments in the United States for the 2001 was 290 according to Federal Railroad Administration for a total cost of € 97 million [194]. However, these estimates are only approximations of the real data, since national railways are reluctant to ascribe specific causes to accidents. Nonetheless, the stakes are so huge that the International Union of Railways (UIC) made of the Rail Defect Management (RDM) its fist World Joint Research Project [195]. RDM is the process that controls the formation and the propagation of defects on the rails through regular inspection and the implementation of prescribed actions when these are found.

Rail defects have been classified in many ways. By classifying rail defects based on their origins [194], three broad families are usually identified:

- Rail manufacturing defects.
- Improper use or handling rail defects.
- Rail wear and fatigue.

Rail manufacturing defects are generally due to inclusions of non-metallic origin or wrong local mixing of the rail steel components that, under operative loads, generate local concentration of stresses, which trigger the rail failure process [196]. A convenient classification of this class of rail defects is based on the direction of propagation of the flaws under operative loads. Two types of damages are classified [197-198]:

- Transverse defects: any progressive fracture that occurs in the head of rails with a transverse direction (Figure 66). This type of defect account for the 29% of train derailments in the U.S.A. between 1992 and 1995 [198] (the total number of derailments in this period was 554 for a cost of $ 70 million).
- Longitudinal defects: any internal progressive fracture that propagates longitudinally in the rails. There are two longitudinal defects, the vertical split heads, and the horizontal split head (Figure 67). According to the Federal Railroad Administration this type of damage is the cause of the 43% of derailments between the 1992 and 1995 [198].

Defects deriving from improper use or handling of the rails are generally due to spinning of the train wheels on the rails or sudden train brakes. An example of this type of damage is the wheelburn defect showed in Figure 68.

The last class of defects is due to wearing mechanisms of the rolling surface and/or to fatigue. In this flaw typology, three defects are the most frequent:

- Corrugation.
- Rolling Contact Fatigue (RCF) damage.

- Bolt-hole cracks.

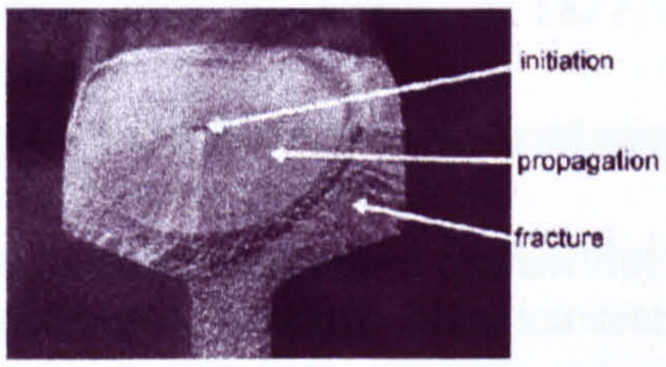

Figure 66 - Large transverse fracture [194].

Figure 67 - Horizontal split head [198].

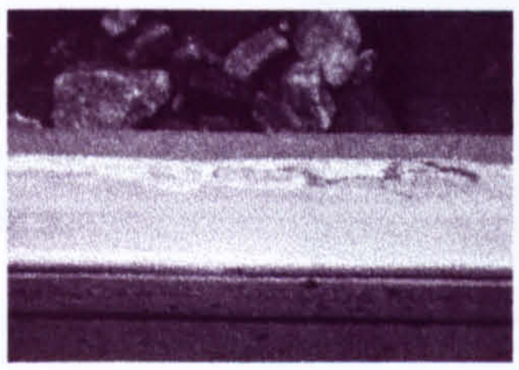

Figure 68 - Wheelburn defect [194].

Corrugation is an event strictly correlated to the wearing of the railhead, generated by a wavelength-fixing mechanism related to train speed, distance between the sleepers [199], friction [200] and so on. Six types of corrugation can be identified [201]: heavy haul corrugation, light rail corrugation, corrugation on resiliently booted sleepers, contact fatigue corrugation in curves, rutting and roaring rails or short-pitch corrugation.

The corrugation does not compromise rolling safety, but has an adverse effect on track elements and rolling stocks by increasing noise emissions, loading and reducing their fatigue life [202]. An example of corrugated profiles of a rail is given in Figure 69, where the magnitude of the corrugation phenomenon (1mm) can be extrapolated and the relation between the corrugation severity and the sleepers distance is proved.

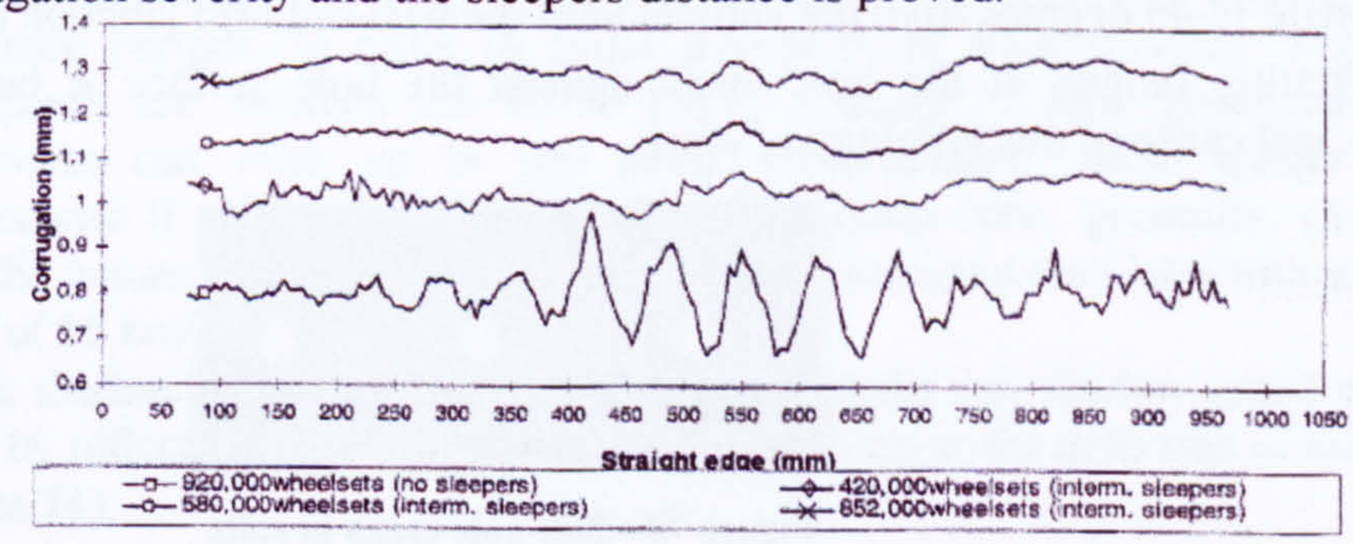

Figure 69 - Comparison of corrugation profiles for normally spaced (no sleepers) sleepers and for half spaced sleepers (interm. sleepers) [199].

In this last damage typology, the RCF damage is the most severe from the point of view of the structure integrity [194, 203, 204]. The fatigue crack initiates on or very close to the rail rolling surface, and it is not related to any material defect [203]. Its occurrence is increasing on high speed passenger lines, mixed and heavy haul railways and can lead to:

1. Expensive rail grinding in the attempt to remove it.
2. Premature removal of the rails.
3. Complete rail failure.

The rolling contact fatigue damage on rails can be divided in headchecks (Figure 70), squats (Figure 71) and spalling (Figure 72).

RCF damages incidence can be reduced by lubricating the rolling surfaces, although, fluid entrapment in the metal is one of the most common causes for speeding up the surface initiated crack growth [194].

Figure 70 – Distributed spalling and headchecks [204].

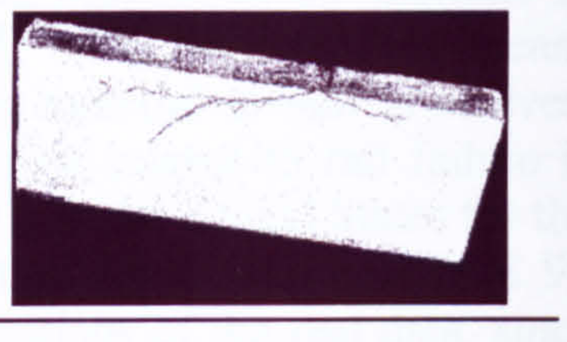

Traffic Direction

Figure 71 – Longitudinal/vertical section through a squat [203].

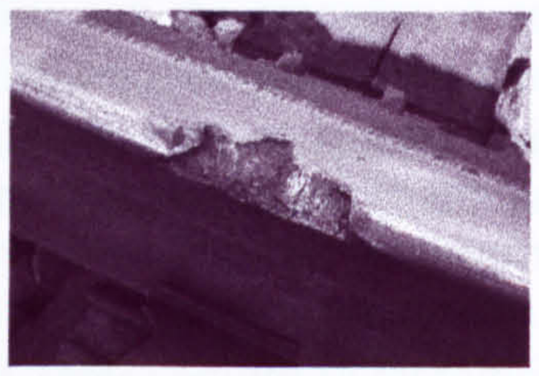

Figure 72 – Severe localised spalling [204].

Bolt-hole cracks account for about the 50% of the rail defects in joined tracks [205]. These cracks originate on the closest bolt-hole surface to the rail end and propagate with an angle +/-45 degrees from the vertical until the web-railhead junction (Figure 73).

Fretting fatigue of the bolt shank against the hole surface is believed to be the principal cause of this typology of crack.

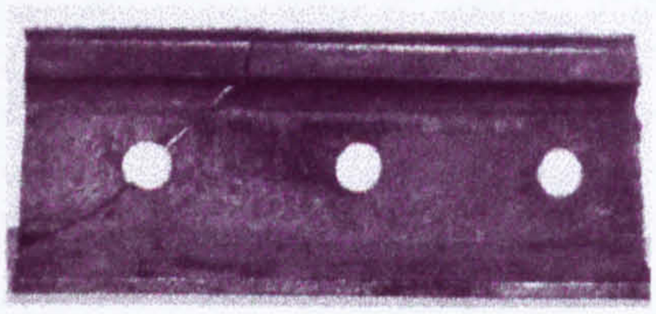

Figure 73 - Bolt-hole crack in rails

8.3 Inspection techniques

The first type of inspection ever used was the visual inspection. A sands mirror inspector was capable to inspect one mile of rail per day. Unfortunately, many external and internal defects were overlooked in this way.

Since 1923 with the invention of the rail flaw detector car, based on the induction method developed by Herring in 1877, it has been the most common way to inspect railroads [197].

In the 1960s, the induction detector was integrated with ultrasonic sensors, becoming standard for inspection cars [206].

The induction technique exploits electromagnetic phenomena. Basically, the rail becomes part of a circuit, where an ampere generator through brushes, in contact with the rail surface, injects high currents, which in presence of a defect are distorted. This distortion of the current flux in the rail generates discrepancies, in the associated magnetic field, detected by a special designed group of sensors placed on the inspection car [206].

Recently, a non-contact induction technique based on eddy currents was developed [207]. This method does not employ brushes to close the circuit with the rail, but uses, instead, a magnetic core to induce eddy currents in the rail, which losses are correlated to the damage presence.

However, although this technology allows using bogies of a standard railway car or coach at the standard speed of the line, only damages on the surface, or close to it, can be monitored. This is a common problem of induction techniques, which are not capable of penetrating in depth the railhead.

This is why, as mentioned previously, in the 1960s ultrasonic inspection [194, 198, 205-209] was introduced and used together with or in alternative at the induction inspection. Ultrasonic techniques scan railhead through ultrasonic beams and detect the return of reflected or scattered energy using ultrasonic transducers. The amplitude of the reflections and their arrival times indicate the presence, the location and the severity of the damage [206]. Although, ultrasonic testing is capable of inspecting the whole railhead [208], it has several drawbacks such as:

- Limited ultrasonic inspection car speeds [194]. These are generally much slower than the line speed, compelling the inspection operation to be carried out outside the commercial track periods, in order to avoid disruption of train services. Typical operational speeds are between the 40-70 km/h, although, a new generation of ultrasonic devices can work up to 100 km/h. Unfortunately, these speeds are theoretical, because if a damage is detected the inspection crew, generally, checks immediately the nature and the severity of the damage, reducing the inspection speed to an average of 15 km/h.
- Shallow crack shadowing [194, 198]. Small shallow cracks can shadow much more severe cracks by reflecting the ultrasonic beams, preventing so the detection of deeper defects (Figure 74).

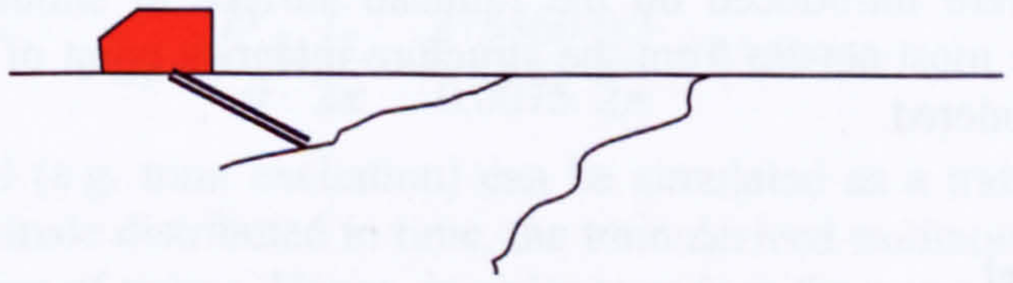

Figure 74 - Shallow crack shadowing

- False defect detection [198]. Current data reports that from 70 to 80% of the defect detections reveal to be false during the hand test verification. This contributes to a further slowing down of the inspection operations.

In the last decade other inspection techniques were developed and investigated for rail inspection application. Some of them are reported below:

- A photothermal method [210]. This consists in a laser beam modulated at certain frequencies that hits the investigated surface and being diffused in thermal-waves, which are captured by a thermal detector. Because of the heavy dumped nature of the thermal-waves, this technique is suitable only for detecting superficial flaws.
- Corrugation detection techniques based on either image processing through Gabor filtering [211] or Barkhaunes-noise correlation [212].
- Elastic guided waves propagating through the rail. The technique exploits the capability of some guided wave modes to travel for great distance, e.g. 2130m, allowing also the possibility to check for the damage throughout the rail cross section [149, 177].
- The wave propagation approach is also exploited by the G-scan rail testing instrument developed by Imperial College in a joint project with National Rail [218]. This G-scan employs a set of independent ultrasonic transmitter/receiver sensors placed along the rail cross section through a clamp mechanism which setting need about 30 sec and other 10 to remove it. Each transmitter/receiver sensor excites and acquires the structure response (A-scan - §1.5.2), which is processed and reflection coefficient maps are extracted from and compared with those of the undamaged structure, any difference identifies damage. This technique has been tailored to inspect alumino-thermic welds.
- The resonant method [217] based on the magnitude loss of a resonance frequency excited by a transmitter and acquired by a receiver located on opposite side with respect to the rail and as much as possible parallel to the damage orientation.
- Acoustic Emission (AE). The technique has been applied on a scaled test rig. The results did not show the hoped AE activity of the surface damages, although changes in the vibration activity of the test rig due to seeded surface damages were recorded [213].

8.4 Validation of the Wave Propagation Based Damage Detection algorithm

In order to test the developed Wave Propagation Based Damage Detection (WPBDD) algorithm (chapter 6), numerical simulations of wave propagation phenomena on a rail sample, in pristine and damaged conditions, were carried out.

The damages were introduced on the railhead surface to simulate rolling contact fatigue defects (the most severe from the structure integrity point of view). Two single damages were considered.

8.4.1 Rail FE model

In this study, a particular rail was under investigation the 113A rail section (provided by CORUS GROUP, see Figure 75). The rail material stress-strain curve (Grade 220 rail

steel) is shown in Figure 76. The density was 7850 kg/m^3 and the Poisson modulus was 0.33.

The test sample was 650mm long (typical distance between two sleepers), whose foot was constrained at both its ends for 10mm (half width of a sleeper). A FE model of the test case structure using the commercial FE code ANSYS was built.

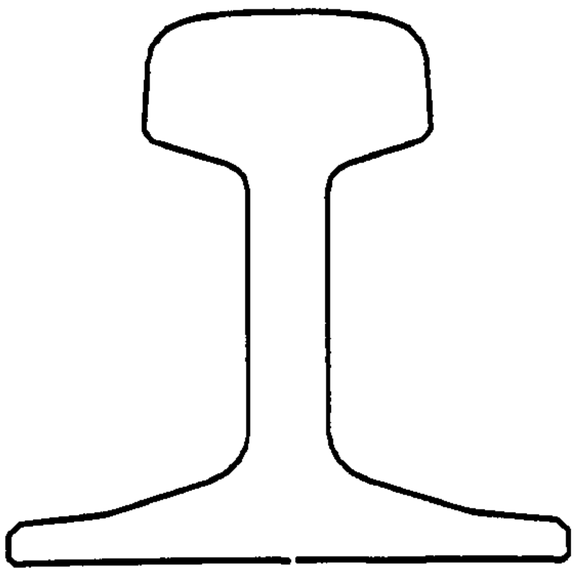

Figure 75 – Rail section 113A.

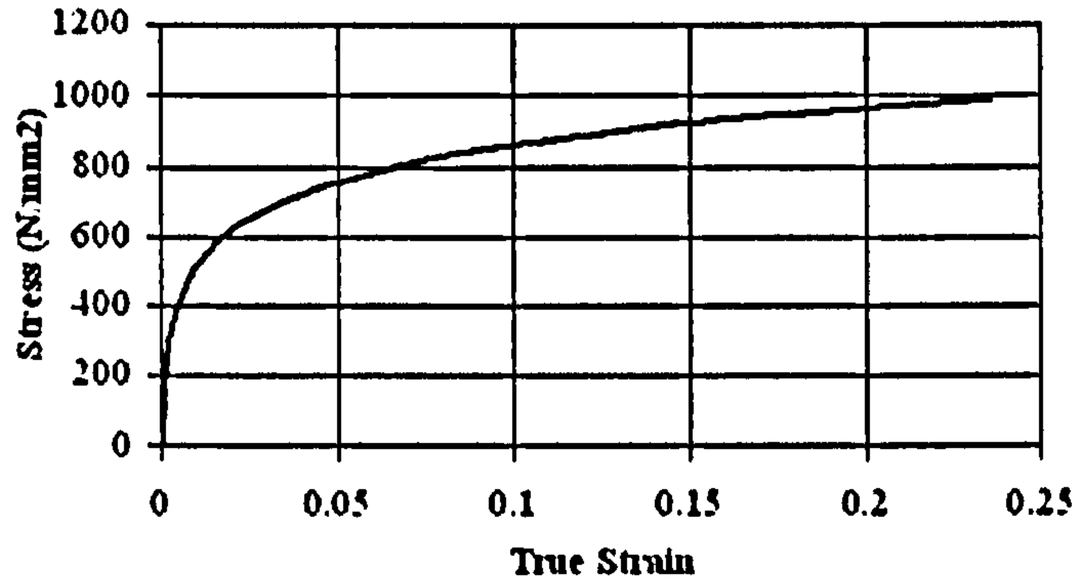

Figure 76 – Stress-strain curve for Grade 220 Rail Steel (CORUS GROUP).

To capture correctly the wave propagation and avoid space aliasing, the mesh size was based on an approach defined in [214], used for finite difference analysis and method of characteristics that leads to an appropriate design of the mesh density and to the computation of the integration time step.

To describe with a sufficient resolution the phenomenon under investigation, it is necessary to define the size of the smallest characteristic of interest, termed critical wavelength (Lw). In the case studied, Lw was assumed equal to the size of the smallest damage to be detected along the wave propagation direction, along the rail axis. According to CORUS GROUP a typical (critical) rolling contact fatigue defect is 15mm long, 5mm large and 2mm deep. In line with the critical damage size, the transient analysis was carried out using a sampling time t_i (integration time – eq. 8.1 [214]) of 1.14μs and finite element length (g) of 7.5mm (half of the critical damage length [214]).

$$t_i = \frac{g}{V_P} \tag{8.1}$$

with V_P P wave speed (§7.3)

According to Cook [215] and Bathe [214] the maximum frequency is related to the P wave speed V_P and the FE length g (see eq. 8.2). However, taking into account numerical errors and the approximation of the equation (8.2) a safe factor (f_S) was considered.

$$f_{\max} = \frac{2V_P}{g}\frac{f_S}{2\pi} = \frac{2 \cdot 6560}{0.0075}\frac{0.3}{2\pi} \cong 83500Hz \tag{8.2}$$

Since any signal (e.g. train excitation) can be simulated as a train (series) of pulses with different amplitude distributed in time, the train derived excitation on the rail can be considered as a series of pulses. Hence, in order to reduce the computational time, only a single pulse was considered (a step pulse lasting 1.14μs) and applied on the railhead (Figure 77). Two single site damaged scenarios were (Figure 77) introduced at the middle

and at ¾ of the rail length from the excitation point. This type of damage was simulated by deleting two finite elements at the coordinates displayed in Table 16 and Table 17. The damage size for both the damage cases was identical with a volume of 150 mm^3 and a weight of 1.2 grams against a global weight of 36.6 kg of the rail portion investigated.

Only one sensor was used (§7.9.2) and placed opposed to both the rail-wheel contact surface and to the rail side where the damages were introduced (Figure 77).

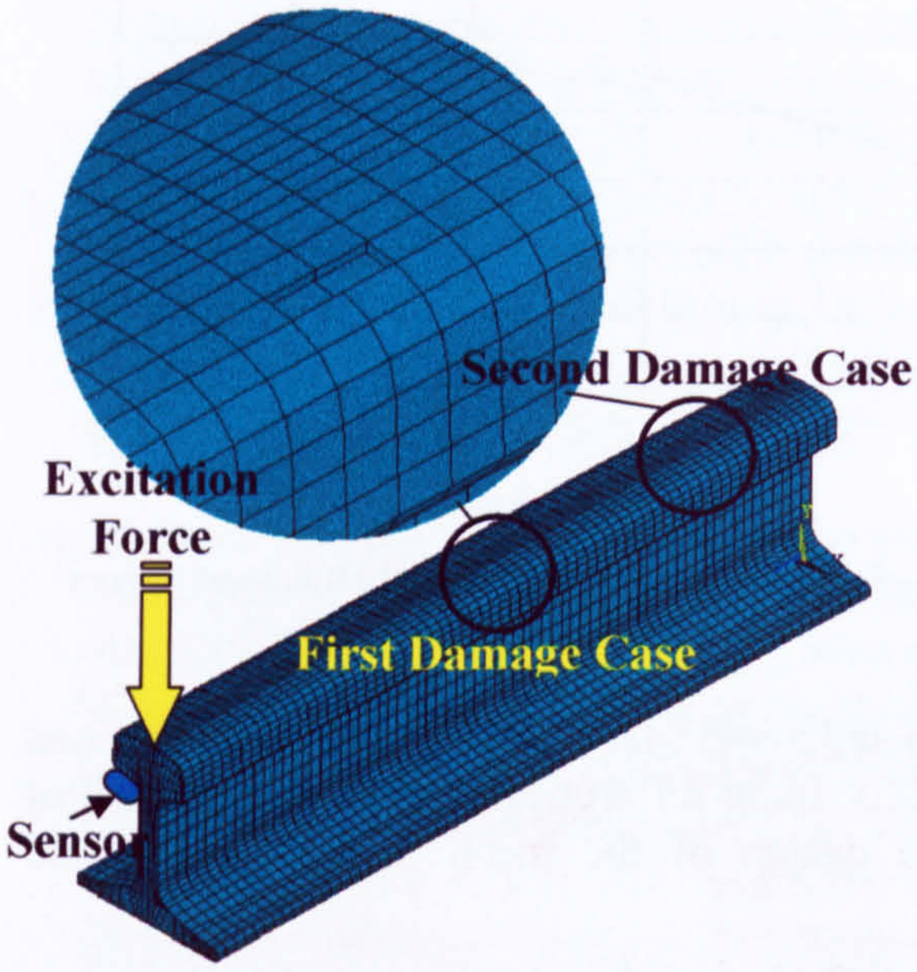

Figure 77 – Set-up configuration.

Damage coordinates			
	X [mm]	Y [mm]	Z [mm]
min	19.642	154.61	315.44
max	25.117	157.58	330.56
Δ(max-min)	5.475	2.97	15.12

Table 16 – First damaged scenario coordinates

Damage coordinates			
	X [mm]	Y [mm]	Z [mm]
Min	19.642	154.61	150.94
Max	25.117	157.58	165.06
Δ(max-min)	5.475	2.97	15.12

Table 17 – Second damaged scenario coordinates

The ANSYS' transient solver used, for the analysis described above, was an implicit solver using the Newmark approach. Moreover, a structural damping was added through a logarithm decay parameter (0.05 – ANSYS default value) [79].

8.4.2 Results

The numerical data obtained by the FE analysis in form of displacements were converted into accelerations through a numeric derivation according to the finite differences approach [224]. The data analysis was targeted to the surface of the rail, since is the only accessible rail part. Therefore, only the surface displacements were saved by the ANSYS process and, then, uploaded by MATLAB scripts, which made possible the following analysis and the damage localisation. It must be pointed out that the only intervention of the user was the selection of the group velocity speed to use for the detection of the damage locations.

8.4.2.1 Analysis of the propagation phenomenon

The presence of structure boundaries alters the shape of the propagation wave fronts. However, according to Huygen's principle, their shapes tend to be spherical like as it can be observed in Figure 78, where the displacements where pictured using a colour scale from blue to red according to their magnitude.

The damage presence introduces only visible changes in the rail dynamic response next to the damage location as pictured in Figure 79-a and b. The damage occurrence can be highlighted by calculating the difference between the dynamic response of the damaged and the undamaged configuration as shown in Figure 79-c. Using this approach, the propagation of the perturbation introduced by the damage presence is magnified (Figure 80), and shows similarities to the impulsive propagation path showed in Figure 78. The intensity of the discrepancy due to the damage introduction increases with time because of the arrival of wave group velocities, with higher energy content. Moreover, the changes introduced by the damage presence propagate with larger magnitudes downstream the damage location rather than upstream (Figure 80).

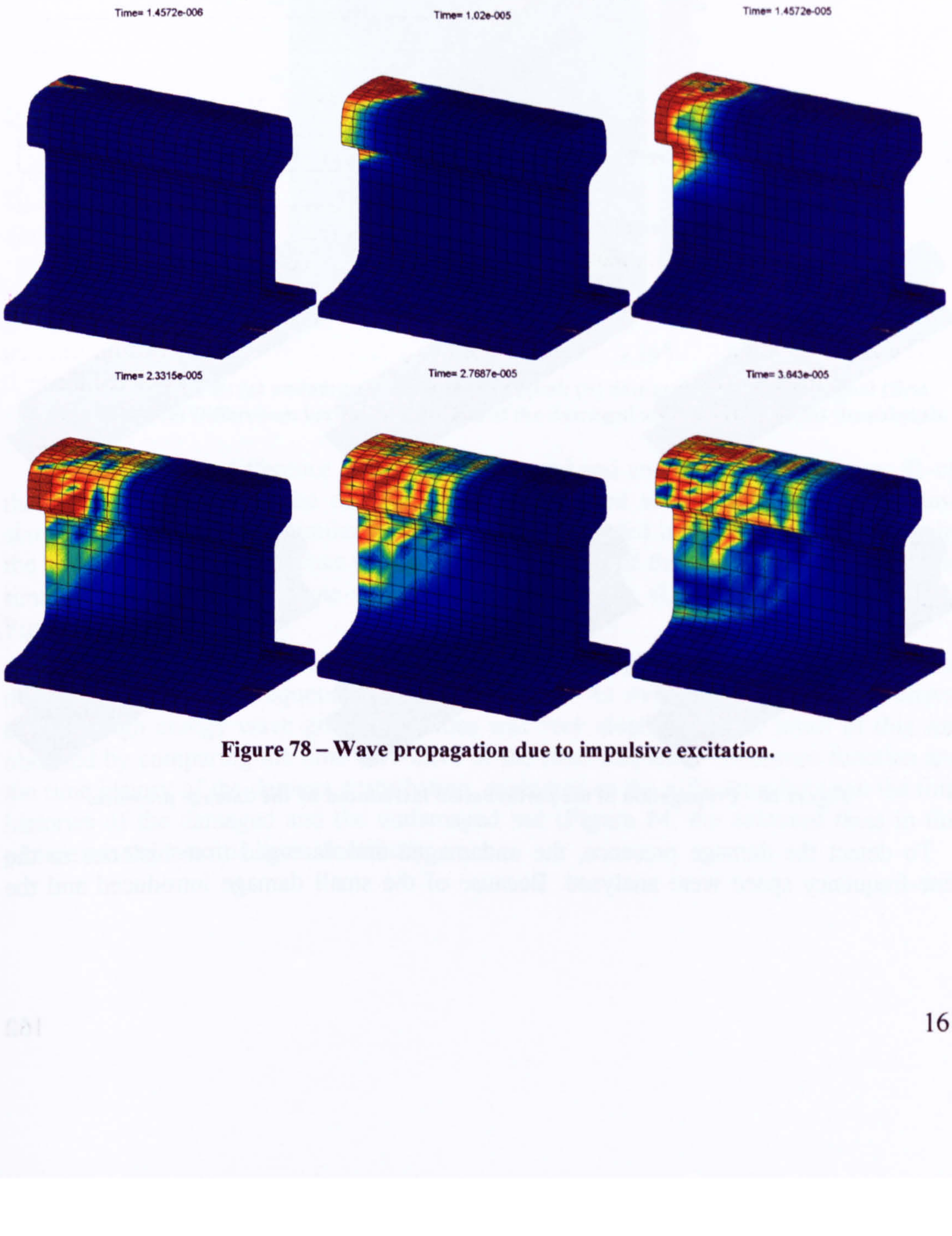

Figure 78 – Wave propagation due to impulsive excitation.

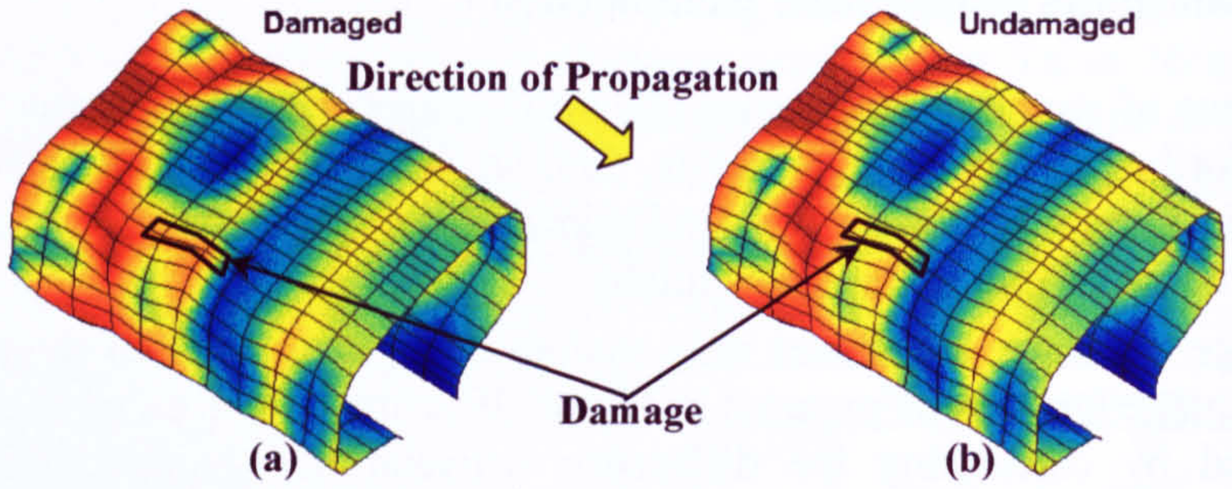

Figure 79 - Damage effect on the wave propagation.

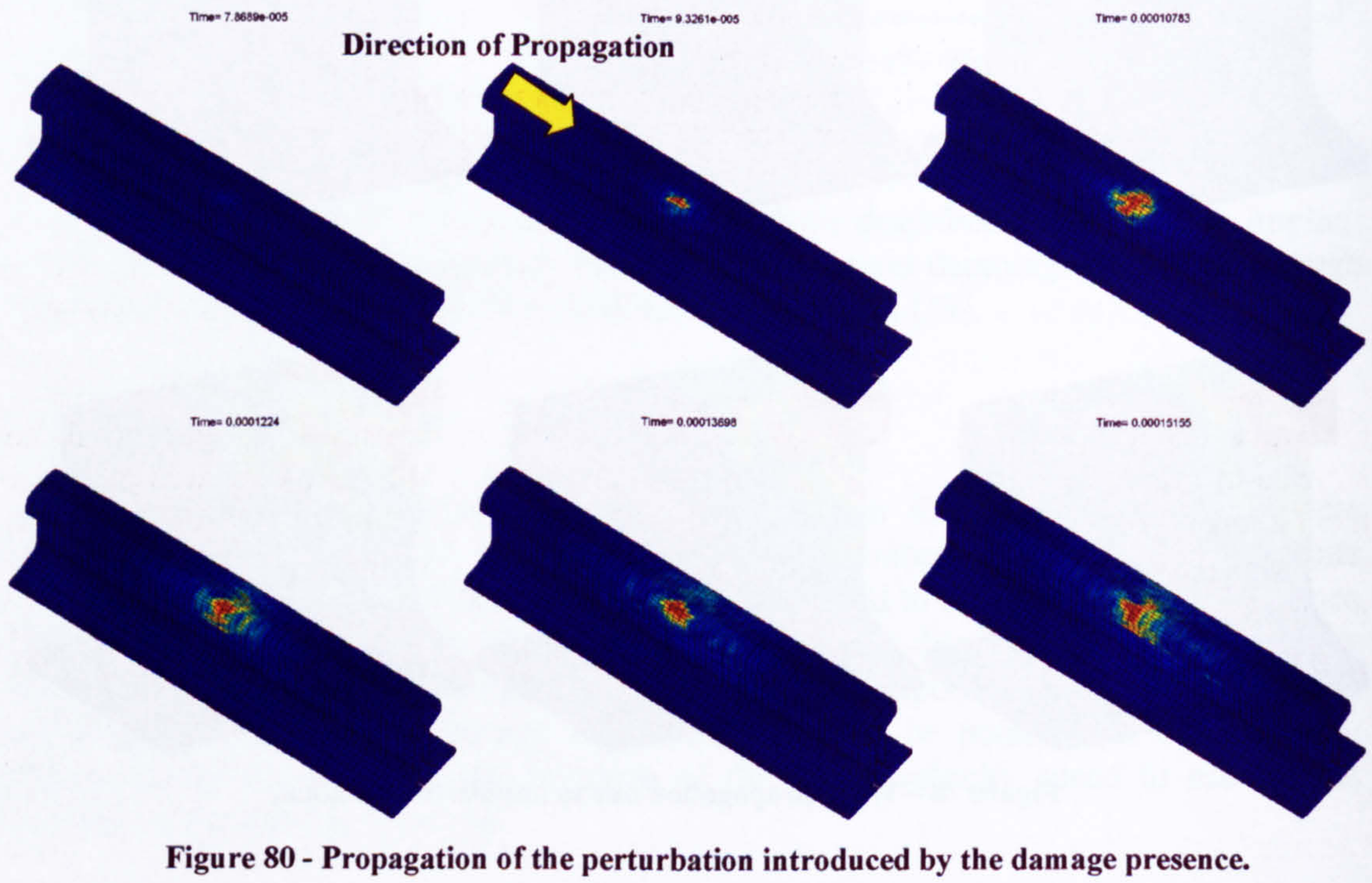

Figure 80 - Propagation of the perturbation introduced by the damage presence.

To detect the damage presence, the undamaged and damaged time histories in the time-frequency space were analysed. Because of the small damage introduced and the

impulsive excitation provided, there were not visible changes between Time-Frequency Representations (TFRs) of the undamaged and damaged time signals (Figure 81-a, b).

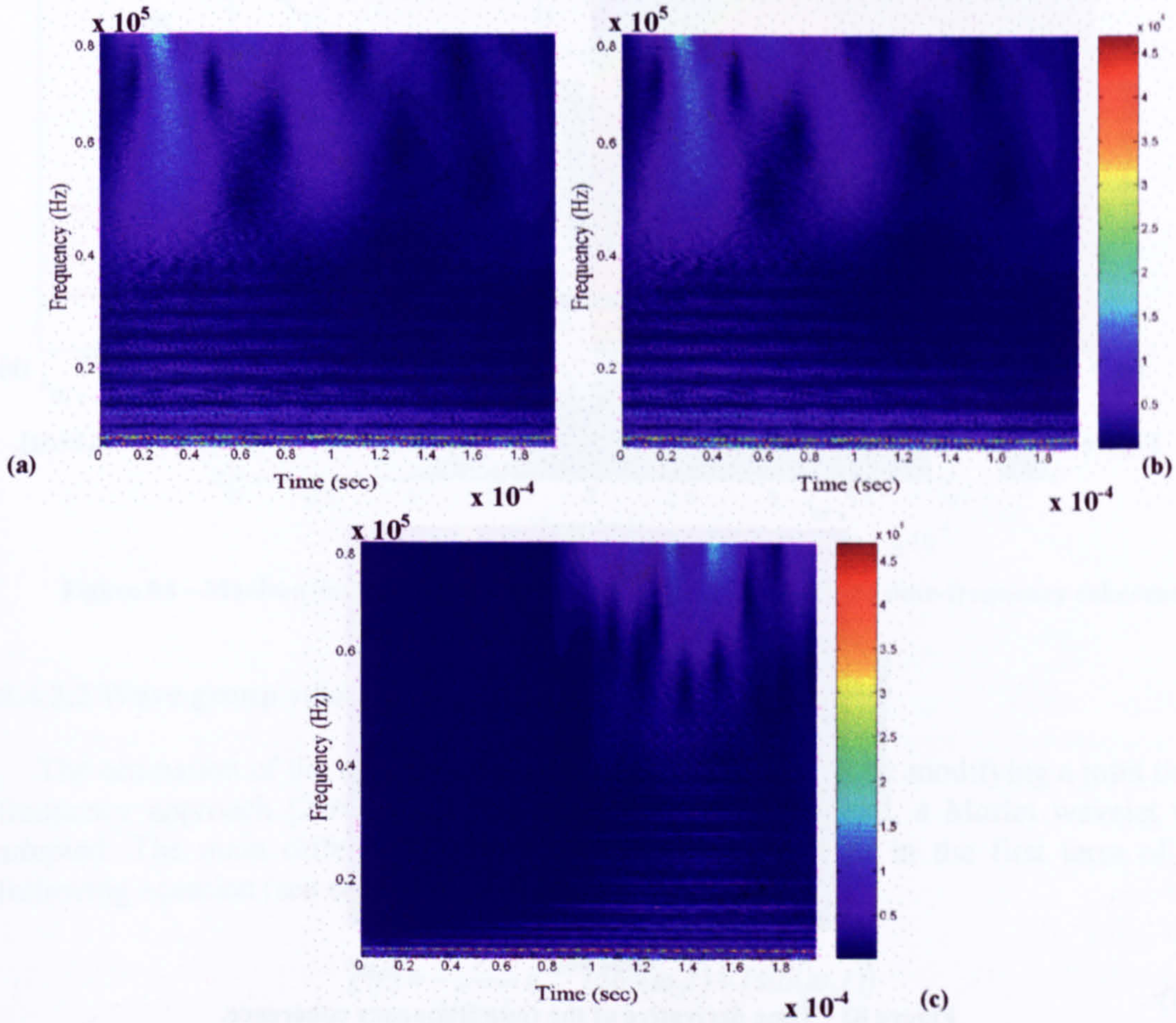

Figure 81 – TFR: (a) undamaged acceleration signal; (b) damaged acceleration signal (first damaged case) (c) Differences between the CWTs of the damaged and the undamaged time signals.

By analysing the difference between the damaged and undamaged TFR (Figure 81-c), the wave echoes due to the damage presence appeared shifted with respect to those showed in Figure 81-a. A similar behaviour to that recorded in Figure 81-b was given by the Time-Frequency Coherence (TFC - §7.9.1) function of the undamaged and damaged time signals for both the time windows investigated ([0, t], [t-Δt, t+Δt]) as shown in Figure 82.

The wave propagation arrival times can be highlighted by evaluating the time derivative of the time-frequency coherence function. As shown in Figure 83, the arrival of three high energy wave group velocities was very clear. A further proof of this was obtained by comparing the time derivative of the time-frequency coherence function and the time history of the damage perturbation, evaluated as the difference between the time histories of the damaged and the undamaged rail (Figure 84, the coloured lines in this picture are the maxima lines identified).

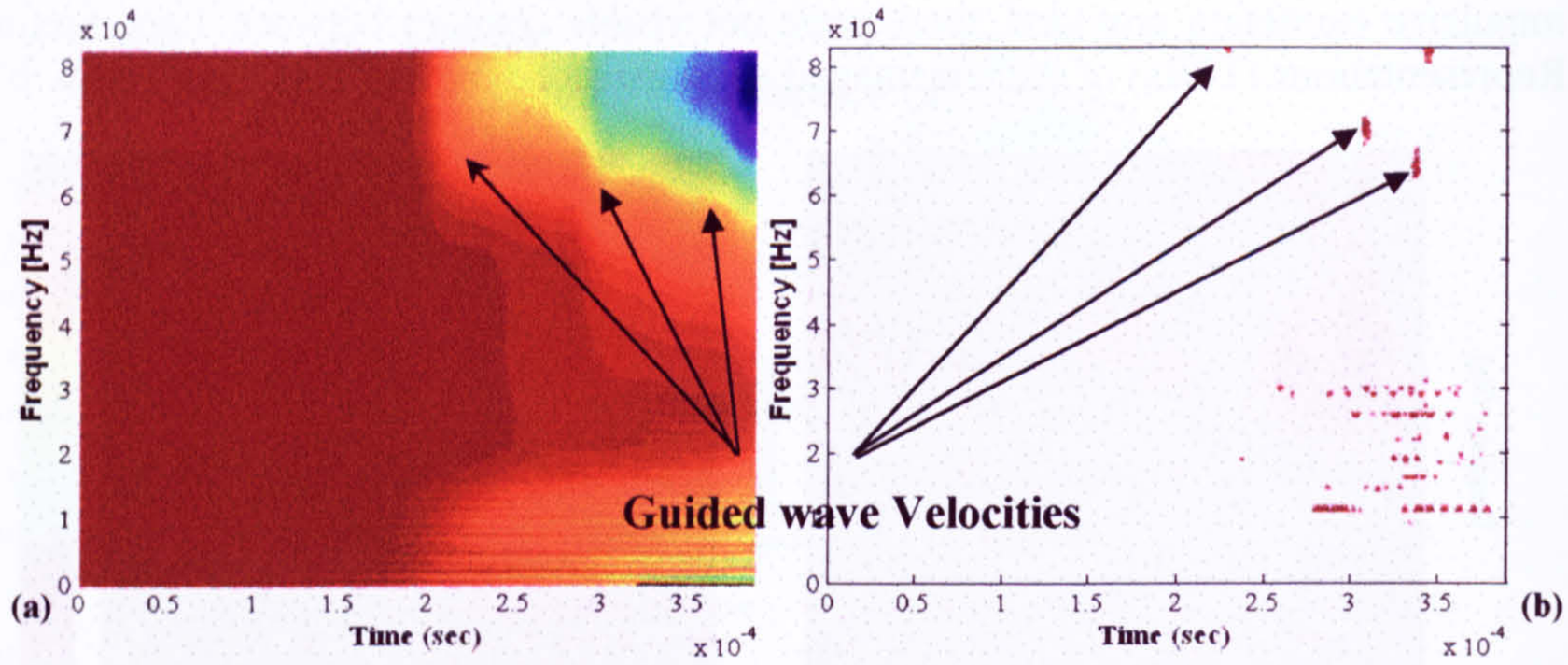

Figure 82 - Time frequency coherence (first single site damaged case): (a) [0, t]; (b) [t-Δt, t+Δt].

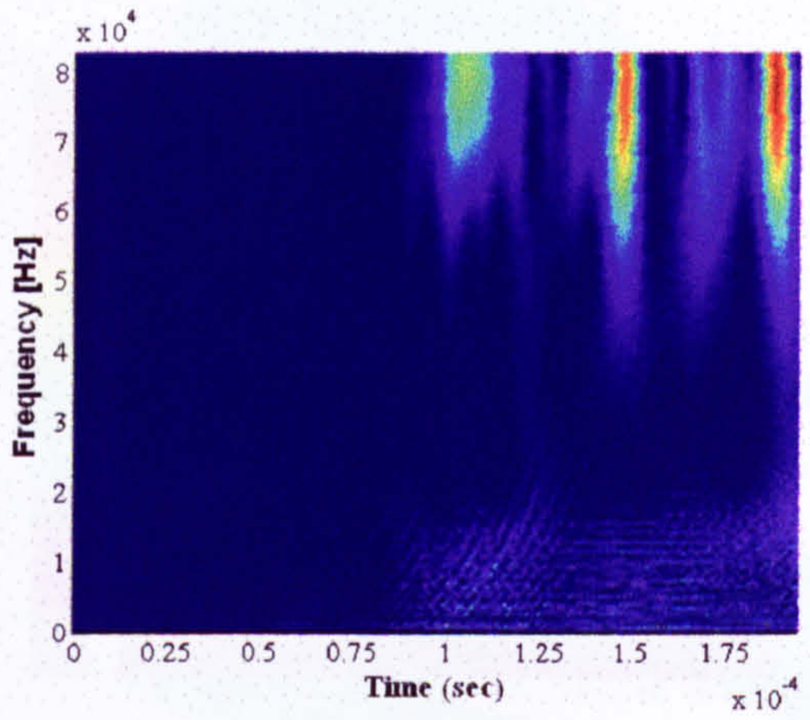

Figure 83 - Time derivative of the time-frequency coherence.

A first group of guided waves identified by the maxima line labelled 1, then, a second group with smaller amplitude referenced by the maxima line 2, were clearly identified (Figure 84). Finally, a large group of waves was present (maxima lines from 3 to 8), but its shapes did not resemble a unique group of waves, since the space travelled was very short. Because of this uncertainty in the identification of the wave group velocities only the first wave group was used for the damage identification.

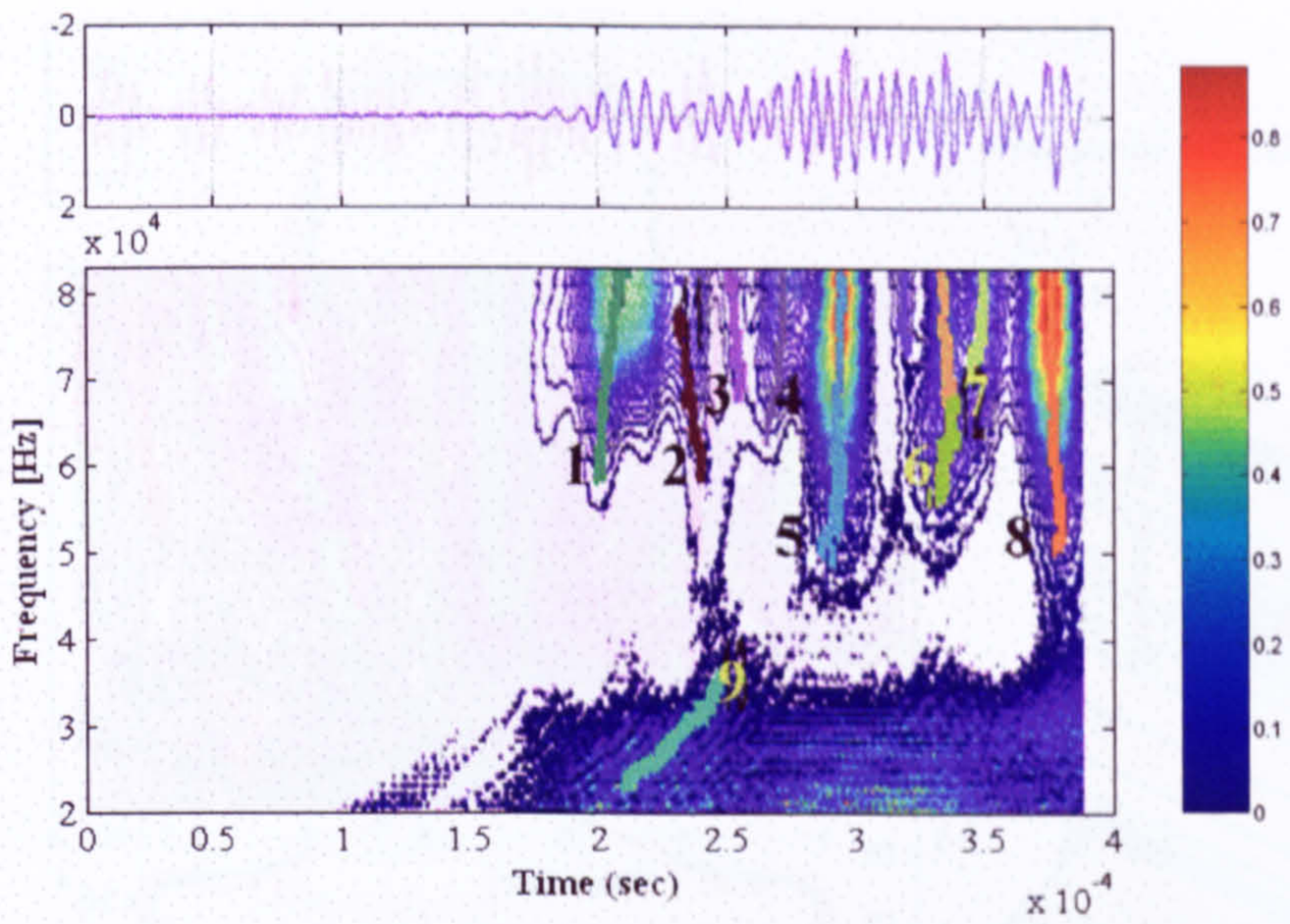

Figure 84 – Maxima lines extraction from the time derivative of the time-frequency coherence.

8.4.2.2 Wave group velocity evaluation

The estimation of the wave group velocities was carried out by modifying a joint time-frequency approach [216]. Instead of using the Gabor wavelet, a Morlet wavelet was adopted. The main difference between the two wavelets lies in the first term of the following equation (see eq. 7.18):

$$g(t)=\frac{1}{\sqrt[4]{\pi\gamma^2}}e^{\frac{t^2}{\gamma^2}}\left(\cos(\omega_0 t)+i\sin(\omega_0 t)\right) \tag{8.3}$$

In order to satisfy a requirement for the Morlet wavelet ($\gamma\omega_0^2>>1$) [174], the two parameters, γ and f_0, were assumed equal to 0.25 and 10, for a $\gamma(2\pi f_0)^2=987$, well above 1.

The wave group velocities were estimated as the ratio of the distance between two sections (50mm, the first section distant 325 mm from the excitation source and the second section located 50mm from the fist in the wave propagation direction) and the time Δt needed to a selected wave group velocity to travel it. The time Δt was evaluated as the difference between the two maxima lines identifying the arrival times of the selected group velocity at the sections selected (Figure 85-Figure 86).

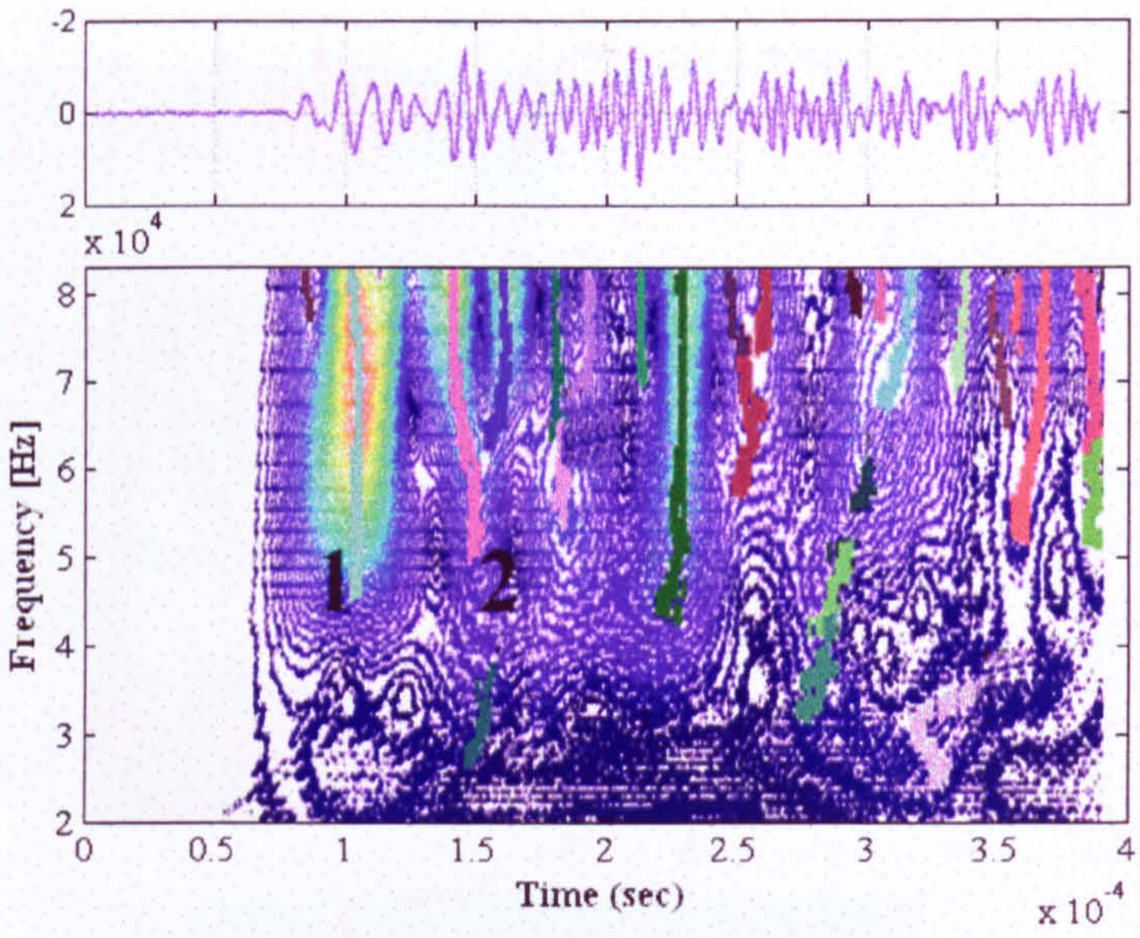

Figure 85 – First section.

By both the CWT representations showed above, it is clear that only the first group velocity is clearly identifiable. It was also possible to identify the shape of the wave propagation mode corresponding to the first maxima line of Figure 85-Figure 86 (see Figure 87). The shape of the propagation mode identified is clearly connected to the excitation source as suggested by the large compression region at the middle of the headrail top.

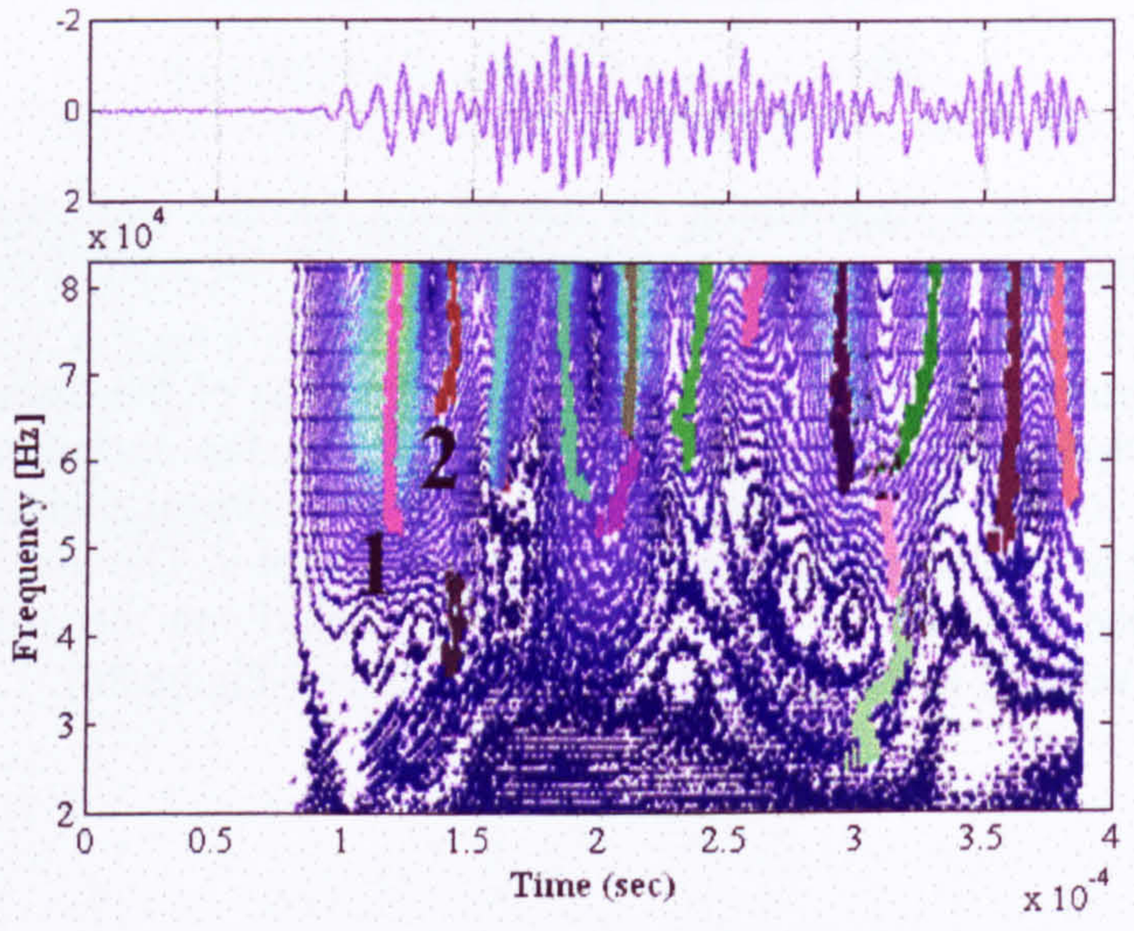

Figure 86 – Second section.

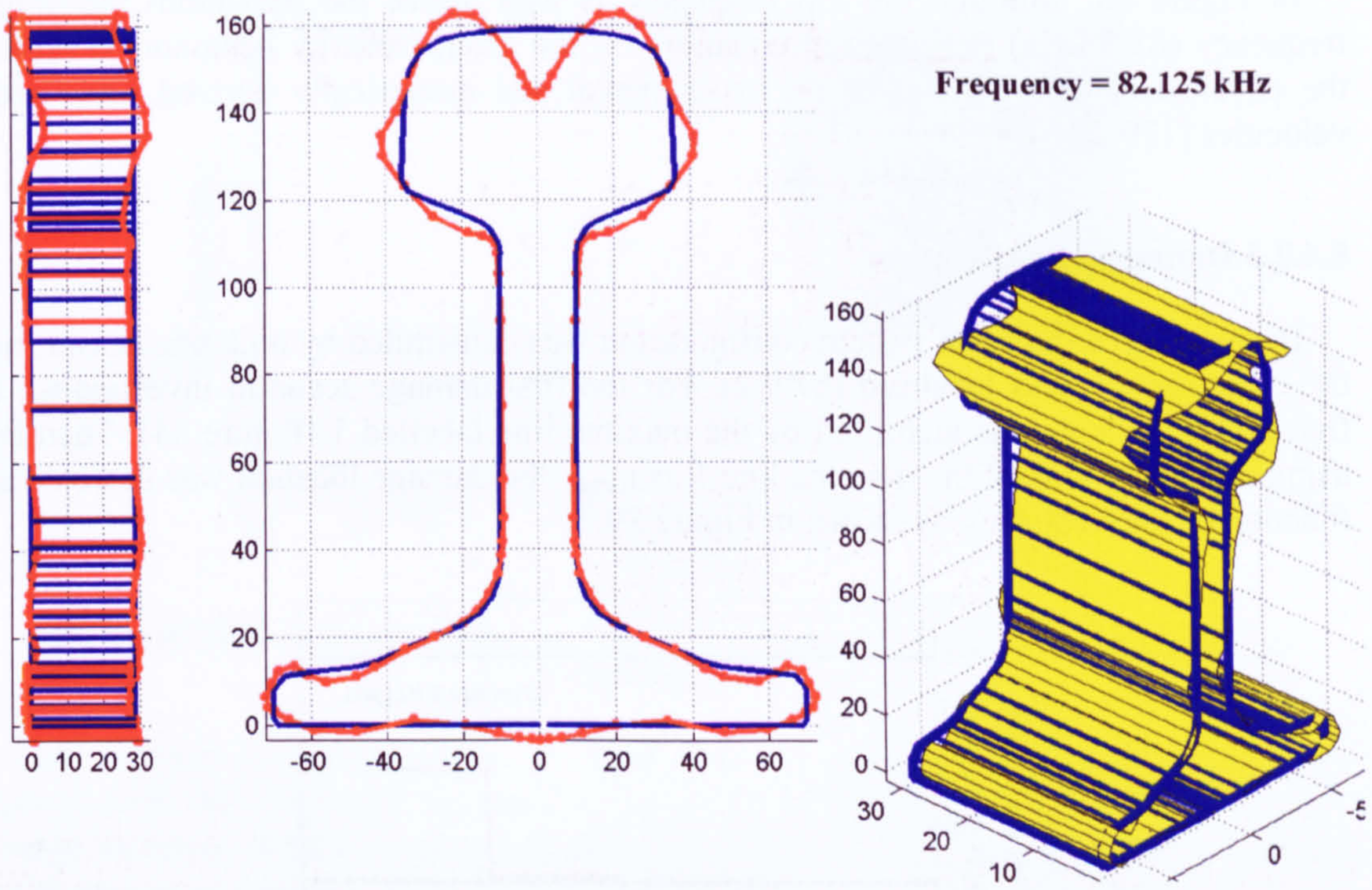

Figure 87 – Shape of the wave propagation mode identified by the maxima line 1 at 82.125 kHz.

The speed of the wave group velocity was plotted against the frequency in Figure 88. The wave group velocity showed a non dissipative behaviour with the increase of the frequency as for the group velocities showed in [216]. Unfortunately, a direct comparison with the values found in literature [216] could not be made, since the maximum frequency at which the group velocity evaluated in literature (8000Hz) is well below the minimum frequency investigated in this work.

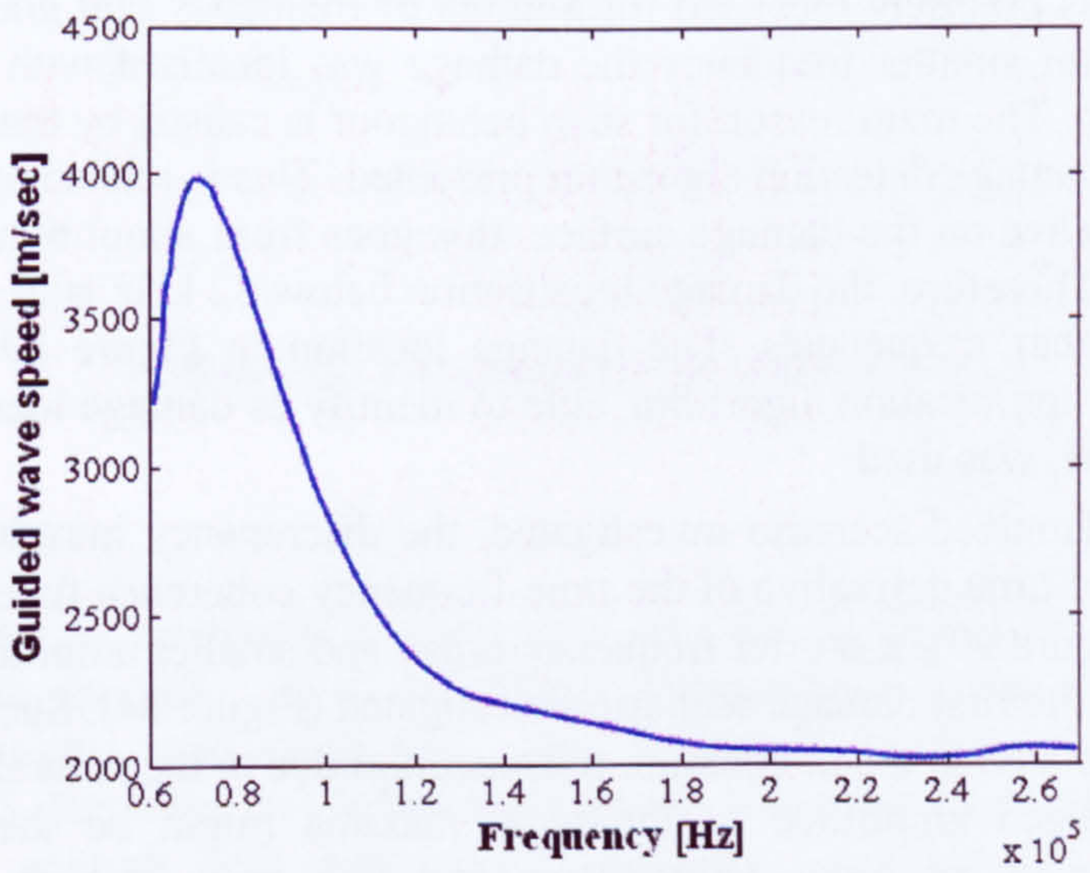

Figure 88 - Wave group velocity extracted.

In Figure 88, although the top frequency is well above the maximum meaningful frequency (83.5 kHz) evaluated in equation 19, the group velocity behaviour resembles the physical conduct of studies on experimental and numerically derived wave group velocities [179, 216].

8.4.2.3 Damage identification

Because the acquisition system configuration was constituted by only one sensor, only the cross section was localised (§7.9.2). For the first damage scenario investigated, the first group velocity was identified by the maxima line labelled 1 (Figure 84). Therefore, using the time points of the maxima line 1 as t_{target}, the damage location was detected as a function of the frequency as shown in Figure 89.

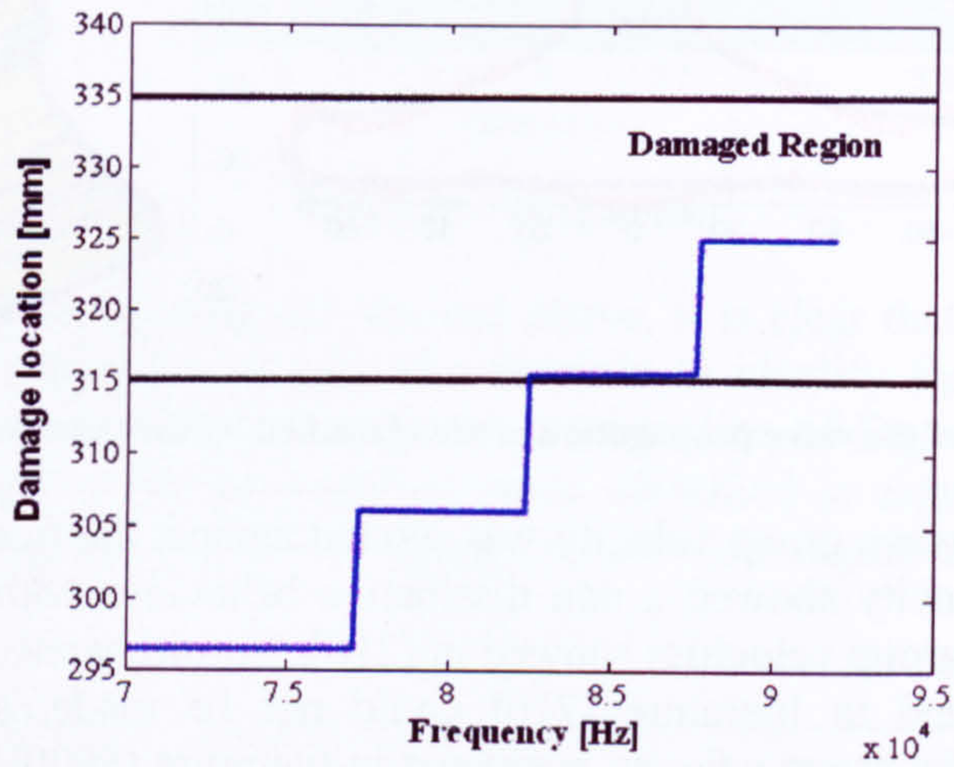

Figure 89 - First damage scenario.

The damage was precisely localised for a range of frequency that goes from 82 to 92 kHz. In contrast, for smaller frequency the damage was localised with a variable error smaller than 20mm. The main reason for such behaviour is caused by the different spatial resolutions of the damage detection algorithm presented. This is related to the wavelength of the impinging wave on the damage surface, this goes from about 60mm at 70 kHz to 40mm at 90 kHz. Therefore, the damage localisation below 82 kHz is in accordance with those given at higher frequencies. The damage location in Figure 89 varies in steps because a discrete optimisation algorithm, able to identify as damage location only nodes of the rail FE model, was used.

In the second damaged scenario investigated, the discrepancy introduced by damage presence has, in the time derivative of the time-frequency coherence function for the first group velocity (Figure 90), a shorter frequency range and smaller amplitude compared to that introduced by the first damage scenario investigated (Figure 84). Such amplitude and frequency loss is related to the attenuation phenomenon due to the natural damping of the material. The reduced amplitude of the local maxima might be the reason for an erroneous selection of the group velocity maxima line, since at high frequencies the maxima can become comparable to numerical errors generated by the FE code and the numerical derivation carried out to convert displacements into accelerations.

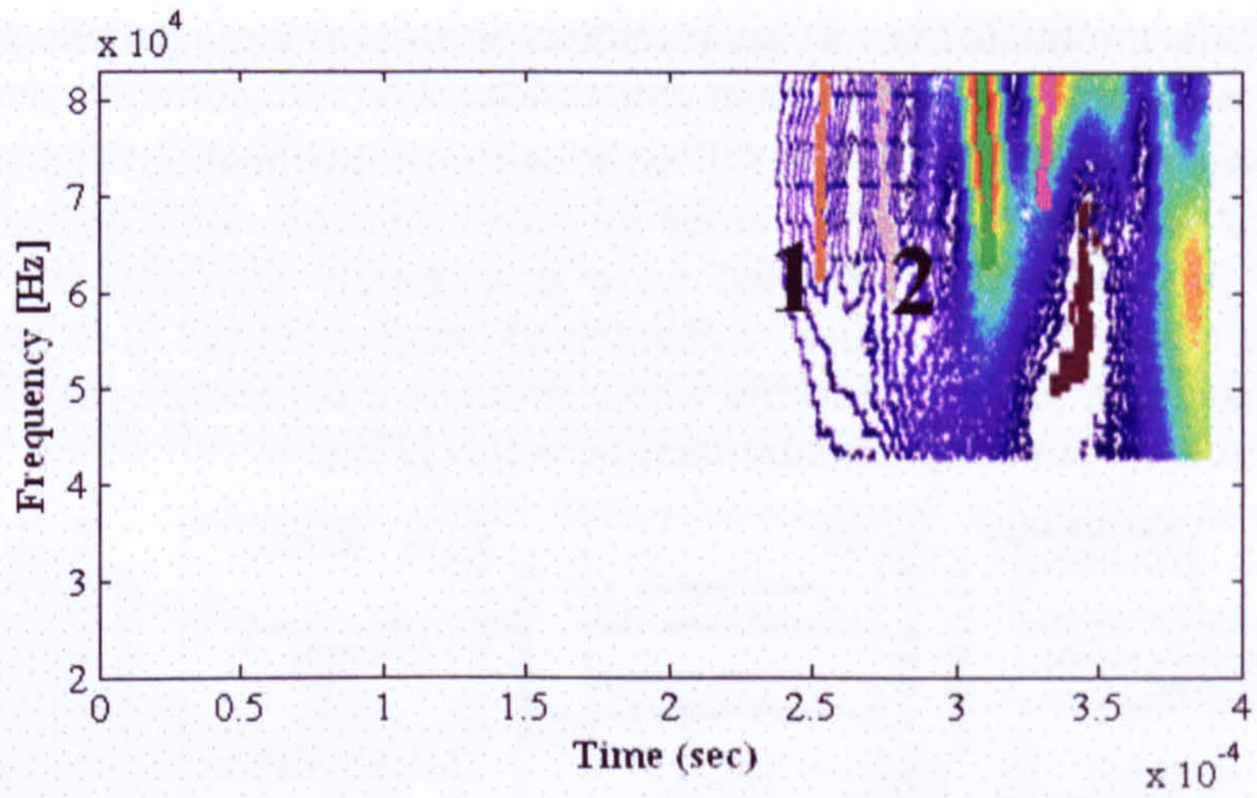

Figure 90 - Time derivative of the time-frequency coherence function for the second damage investigated.

This concern is confirmed by the behaviour of the identification of the damage location with the frequency showed in Figure 91. The error in the identification of the damage location increases with the frequency, although it is in any case smaller than the spatial resolution (smaller than 40mm), evaluated before.

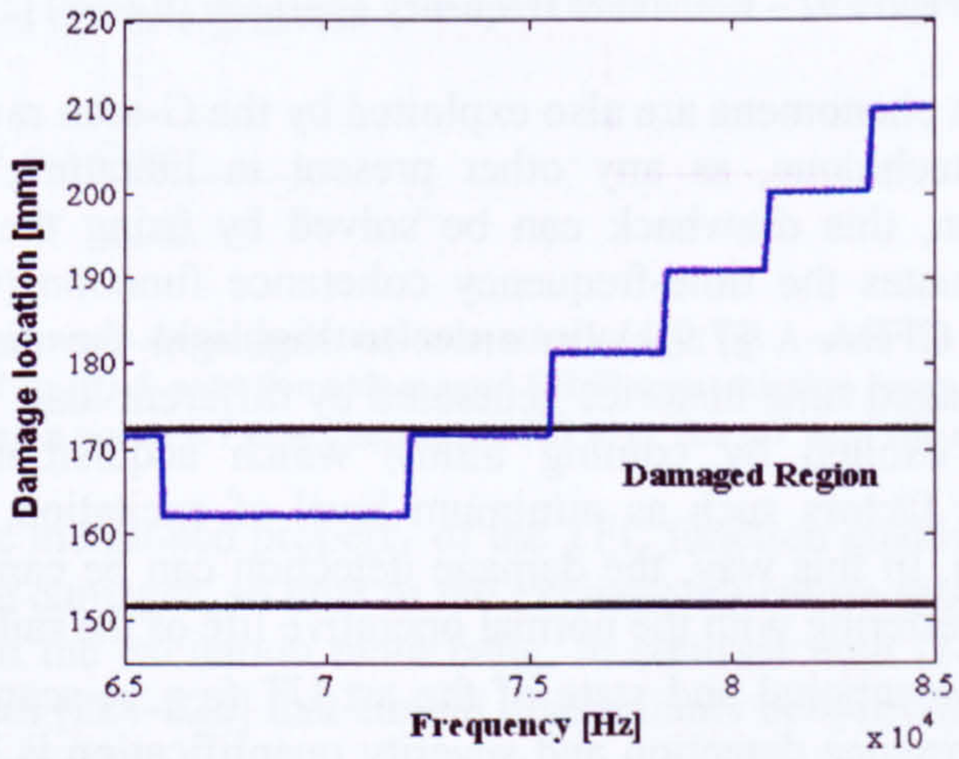

Figure 91 - Second damage scenario localisation.

8.5 Discussion

In this chapter, a numerical investigation of damage detection of rolling contact fatigue damages on rail, using the Wave Propagation Based Damage Detection (WPBDD) technique was presented. This technique exploited wave propagation phenomena (P, S, Rayleigh waves and wave group velocities [135]) propagating through the structure in contrast with convectional ultrasonic inspections [194, 198, 205-209] (§1.5.2), which use ultrasonic beams propagating through the structure thickness. Therefore, because a vibration wave can propagate within a medium on large distances

with a very little amplitude loss, a single sensor can inspect large portion of structures in few instants, with higher resolution than convectional UT.

Current state of the art, such as B, C scan and resonant methods (§8.3), to be really effective need to rotate sensors in order to detect damages with different orientation (Figure 92). In contrast the proposed wave propagation approach, can inspect large portion of the structure investigated, without shadowing effect (§8.3) or sensor rotations, since the propagation mode interest the whole structure cross section (e.g. Figure 87) and is capable of fully penetrating alumino-thermic welds [218].

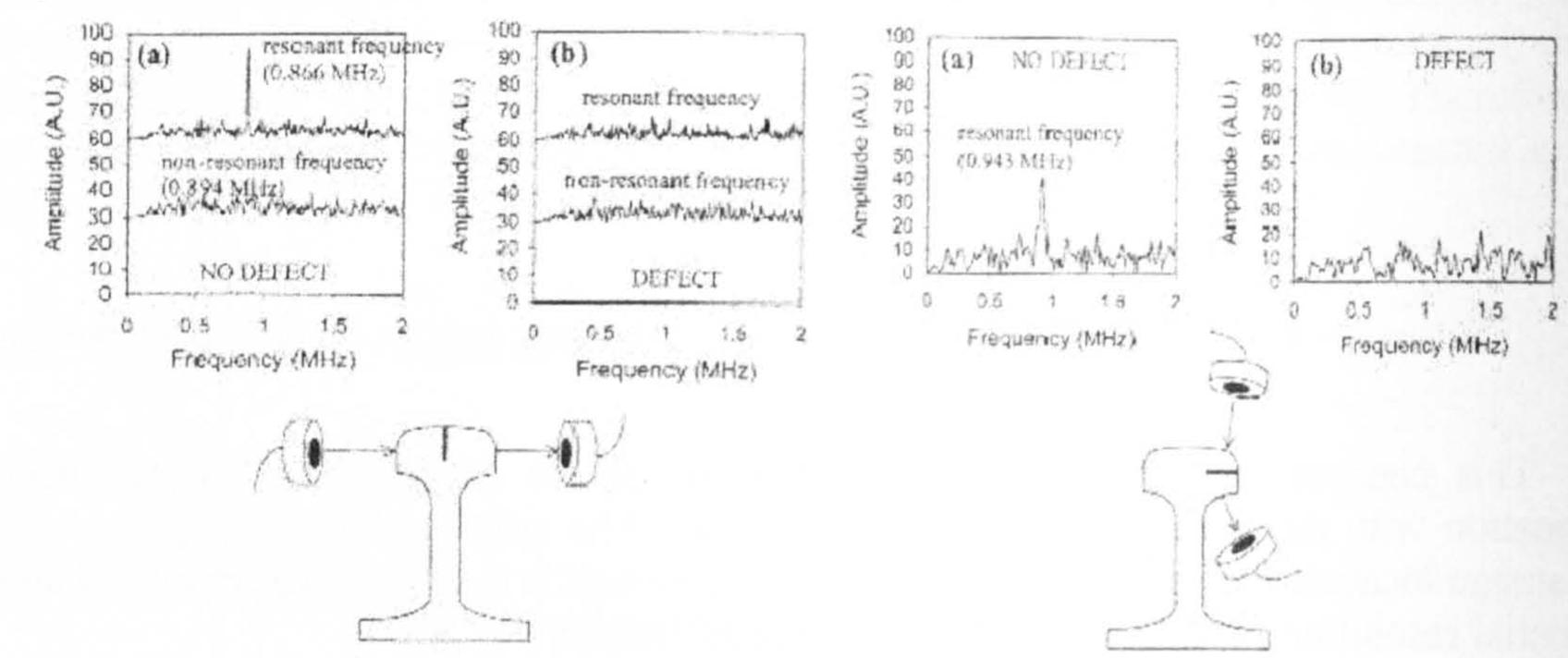

Figure 92 – Resonance frequency approach (B-scan) [217].

Wave propagation phenomena are also exploited by the G-scan rail testing instruments [218] (§8.3). This technique, as any other present in literature, needs a controlled excitation. As shown, this drawback can be solved by using the proposed WPBDD method, which evaluates the time-frequency coherence function (Coherence Function Based Algorithm – CFBA - §7.9.1), in order to highlight the discrepancies between undamaged and damaged time histories generated by different load. The CFBA uses rail dynamic responses excited by coming trains, which acquisition can be triggered according to several factors such as minimum level of excitation, signal shape, noise conditions and so on. In this way, the damage detection can be carried out in operative condition without interfering with the normal operative life of the rail network.

Moreover, for conventional and state of the art UT (e.g. A-scan, G-scan and etc..., §8.3), the damage presence detection and severity quantification is based on the loss of edge echoes (Figure 93-a and b) or of reflection coefficients dependent on the echoes energy loss. Further, the damage location identification is based on the recognition of wave groups reflected by the damage surface (Figure 93-b) and the measure of the Time of Flight (ToF). Analyzing Figure 93, it is clear that the energy loss based detection criterion to identify the presence of damage is not reliable if the damage is located near the edge gate (the structure backwall) in contrast with the reflection coefficient based approach (G-scan), which presents asymmetries in the reflection maps of the wave modes. However, all the above mentioned techniques are not capable of locating or detecting the damage if the defect reflected waves (notch, Figure 93-c) have amplitude not comparable to the backwall reflection. These drawbacks were resolved, in the WPBDD method, by exploiting the Time-Frequency Coherence (TFC) function property

of highlighting the uncorrelation between the damaged and the undamaged time history. As a result, only experimental noise and waves reflected by the damage surface (§7.9.1-7.9.2) appear in the time-frequency representation as proved in section 8.4.2.1 (Figure 83-Figure 84). Moreover, the noise contribution is easily filterable out, since wavelets tend to relegate it at high frequencies (§7.6.2). Consequently, the echoes as those showed in Figure 93-c can be detected, as proved for the numerical damage detection, where the difference between the damaged and the undamaged time history might induce the UT inspector to overlook the reflected wave presence (Figure 79, Figure 81).

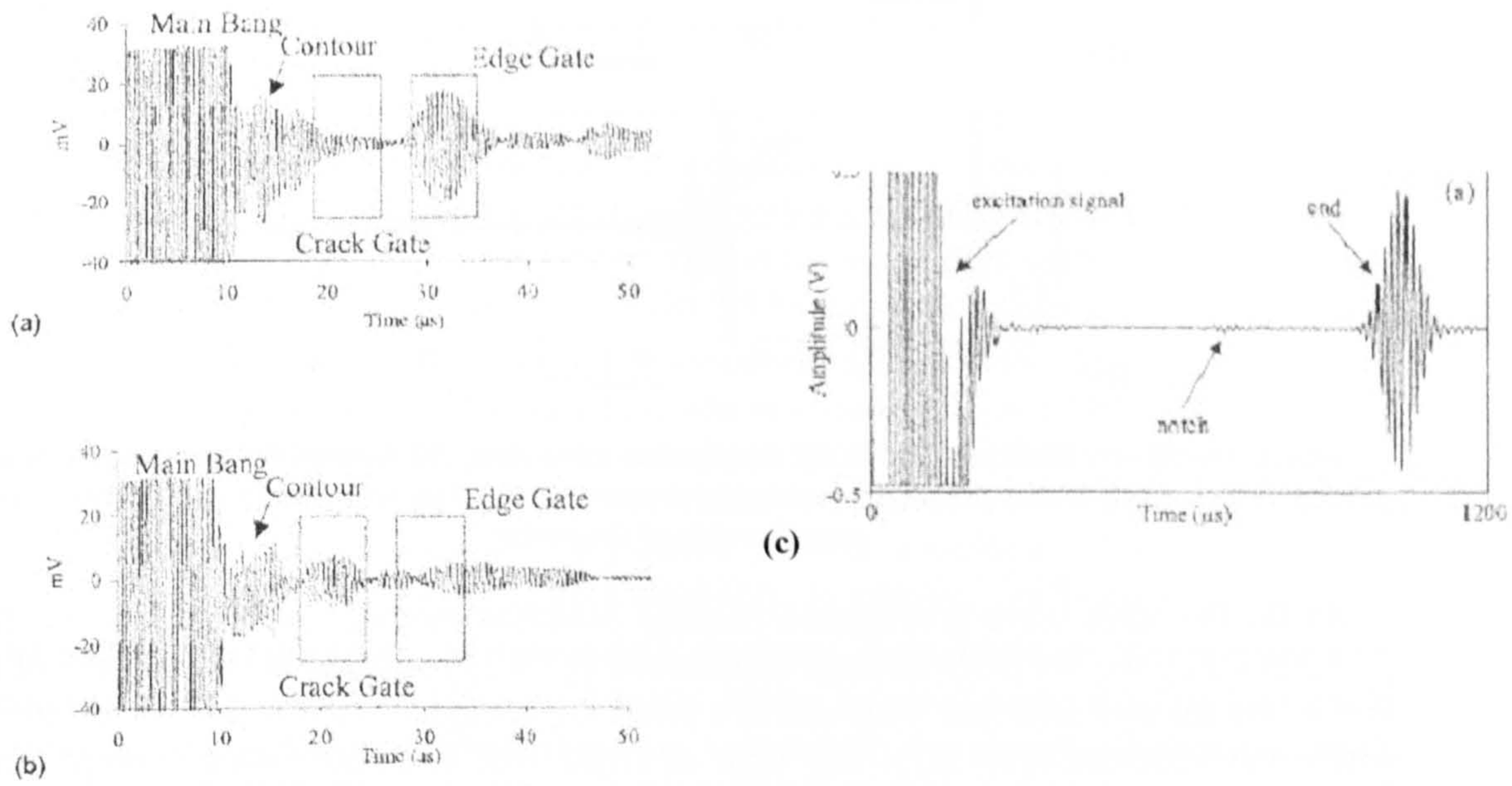

Figure 93 – Guided wave damage detection methodology: (a) A-scan for an undamaged SH68 transmission beam [178]; (b) A-scan for a damaged SH68 transmission beam [178]; (c) A-scan for a damaged pipe having a notch 2.7 mm deep extended over the 6.7% of the circumference [219].

Further, the above mentioned property of the TFC function enables the CFBA (§7.9.1) to identify and locate damages, so near to the excitation location that its echoes (reflected waves) are hidden in the excitation main bang, in contrast with G-scan approach [218] and similar techniques [221-222] that cannot discriminate between the main bang and the damage echoes (Figure 93).

In addition, all the methodologies reported in literature (§1.5.1-1.5.2, 7.4, 8.3) need an expert user able to discriminate between reflected waves of structure features (e.g. welds, elbow and etc…) and those reflected by damages (e.g. see Figure 94). This stringent requirement is not necessary for the WPBDD method, since reflected waves of structure features are presented in the undamaged and, therefore, if damage is not present, no uncorrelation is detected by the CFBA (§7.9.1). Consequently, WPBDD method is also capable of detecting damages occurring on these structural discontinuities (e.g. joints, welds, cross section changes and etc…) that otherwise would need an accurate analysis of the reflected signal.

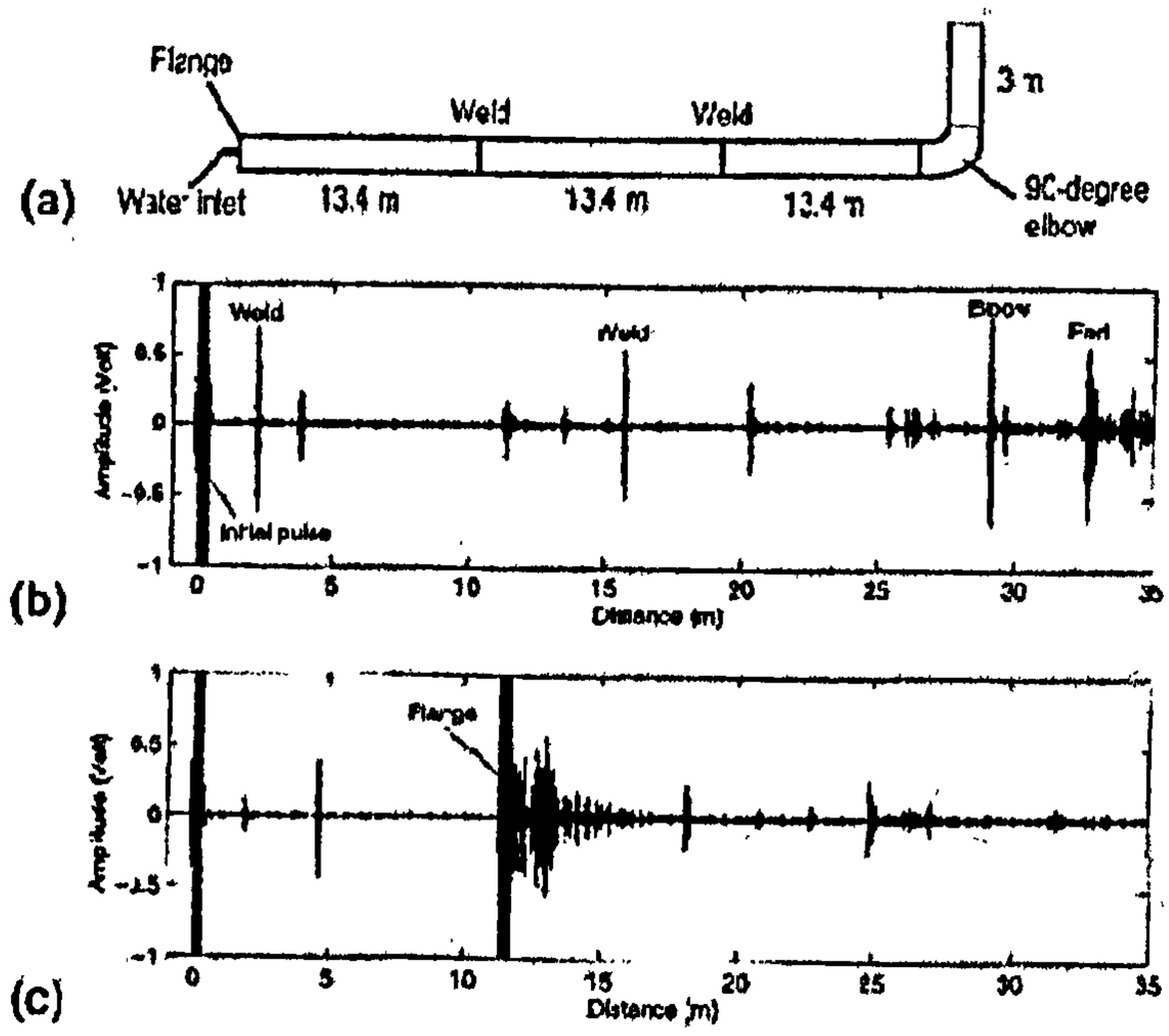

Figure 94 – Water filled pipeline [220]: (a) pipeline schematic; (b) A-scan obtained by launching a guided wave to the positive side of the sensor; (c) A-scan obtained by launching a guided wave to the negative side of the sensor

As for the other wave propagation damage detection methods presented in literature [218,221-222], the WPBDD damage localisation (§7.9.2) consisted in the measure of the ToF of the damage reflected wave and in a priori knowledge of the wave speed behaviour within the structure (§8.4.2.2). The time of flight was evaluated using maxima lines, which reduce the noise effect, since are evaluated on the largest values of the damage reflected wave amplitudes (§7.9.2) [157]. In contrast with common techniques that use threshold based algorithm [223], leading to a large scattering of the ToF.

The WPBDD damage location is provided by the Ray Tracing Detection (RTD - §7.9.3-7.9.4) algorithm, which uses, in wave guide structure as the rail, only one sensor to identify the damaged rail cross section (§7.9.3). The RTD architecture is based on the concept that the loci of the damage are described by an ellipsoid surface, whose foci are the source and the sensor locations, assumed not coincident, since the first is assumed to be on the rolling contact surface. This configuration is similar to that used in conventional UT, the only difference lies in the fact that the transmission and the reflection angle are known, since the transmitter and the receiver are able to operate at just a fix angle, generally, 45 or 70 degrees.

In the particular case that the source and the sensor locations are coincident the ellipsoid surface becomes a spherical surface and the RTD algorithm becomes identical to many others described in literature [218-221].

For damage severity estimation, various methods are available like quantification of the energy loss of the end echo [178], amplitude of the reflection coefficient map changes [218], difference between the energy of incident field (power produced by the transmitter) and the energy acquired by the receiver according to Auld's formula [221], loss of the resonant amplitude frequency [217] and etc... Accordingly with these

techniques, the WPBDD method could be fitted with algorithms capable of evaluating the damage severity. An immediate estimate can be given by measuring the amplitude of the time frequency coherence function maxima lines at a reference frequency, the larger the amplitude the larger the damage severity. Further analysis can be carried out to establish a correlation between the damage severity and the magnitudes of maxima lines.

Moreover, the time frequency representation can be source of further information related to the damage size, since its dimensions are somehow related to the smallest frequency at which an uncorrelation caused by damage presence is identified. Supplementary studies have to be performed to corroborate this relationship.

8.6 Conclusion

This chapter presents a numerical investigation on a partial rail of the wave propagation based fault detection technique illustrated in chapter 7. The proposed method is based on the idea that the damage introduces, in the wave propagation, an uncorrelated time signal due to the presence of waves reflected by the defect surface.

The damage detection methodology developed was split in three steps. In the first step the presence of the damage on the structure was assessed. The time discrepancy between the damaged and undamaged signal was calculated by using a Coherence Function Based Algorithm (CFBA). In the second step the extraction arrival time of the reflected wave (or echo) was estimated using the continuous wavelet transform. Then, the detection algorithm was able, through a ray-tracing algorithm, to estimate the location of damage.

Numerical investigations of two single damages were studied. The damage was introduced on the railhead surface to simulate rolling contact fatigue defects. The results showed that the proposed methodology can successfully localise the damage location, however, as expected, the localisation is strongly affected by the frequency range used. The results also showed that the separation and the characterisation of single modes will be crucial for the identification of different types of rail defects. Further work is needed to establish damage severity by relating the magnitude of the changes of the time frequency coherence to the reflection and the attenuation coefficients of each wave group velocity used and on the selection of the best range of frequency according to the type of damage to be identified.

Additionally, the independence of the damage localisation, above presented, to the magnitude of the excitation makes possible the use of the structure excitation provided by a passing train. It is clear that in such event, the nature of the excitation is slightly different from the point shape here simulated and, therefore, the type of the wave propagation mode excited will be different. Consequently, also the group velocity generated by the train transit will be different.

The author is aware of the fact that an extensive numerical and experimental campaign focused on the identification and the recording of the wave group velocity properties and behaviour, with more typologies of damages, is needed. However, the positive results presented show that the approach is promising and a good margin of improvement can be achieved on longer samples, where the wave group velocities with larger energy contents are sufficiently separated from each other.

The separation and the characterisation of single modes will be crucial for the identification of different types of rail defects. The damage severity can be also assessed by relating the magnitude of the changes of the time frequency coherence to the reflection and the attenuation coefficients of each wave group velocity used.

Further studies should be carried out on the selection of the best range of frequency to use according to the type of damage to be identified. These investigations will be dominated by two main contrasting factors, the spatial resolution and the attenuation phenomenon. Both increase with the frequency. Consequently, if high spatial resolutions are required, shorter portion of rail can be scanned and more sensors will be necessary. Therefore, it is clear that a compromise between these two opposite driving requirements must be found.

CHAPTER 9: CONCLUSIONS

9.1 Introduction

The high complexity and costs of conventional health monitoring systems, combined with high operational reliability and safety requirements of structural systems, have brought to an increasing interest in new approaches for structural health monitoring and damage analysis from both industrial and academic world. Classic non-destructive damage analysis techniques (NDT) already used in many industrial fields satisfy only part of the requirements of an ideal NDT. Commonly the main disadvantages of these approaches are:

- Applicability to small objects.
- Need for accessibility of the monitored components.
- Need for disassembling the structural system.

On the contrary new requirements for NDT include:

- Integration of the system within the structure.
- Possibility of monitoring the structure during in-use conditions.
- Low complexity of data analysis algorithms.

Availability of structural dynamic analysis systems, characterised by extraordinary performances of sensors (sensibility, operative frequency bandwidth), signal analysers (number of channels, sampling frequencies) and actuators (forces, operative frequency bandwidths) employed in high-tech research fields, allows today to develop more effective and reliable NDE techniques for monitoring structural health.

However, many researchers do not exploit the opportunity of an integrated design (NDT method + sensors + signal processing) of monitoring devices and often forget the final target of damage detection, the development of a fully functional SHM device. Too often, researchers developed methodologies (§6.6) employing an impracticable number of sensors, with very small noise pollution, with respect to structure operative conditions, applied on numerical models incapable of reproducing correctly the structure dynamic behaviour, because of stringent hypothesis, limited number of DoFs and etc... Therefore, in this research, a global view on the SHM was adopted, leading to damage detection processes dealing with all the phases of the SHM device design, such as data type selection, optimal sensor placement, signal processing and damage detection. Moreover, the differences between the several typologies of structures (civil, mechanical and aeronautical), in terms of load amplitude and frequencies, crack growth rate and etc..., and numerical considerations, such as memory and time consumption, made impossible the development of a unique damage detection methodology. Hence, two different techniques, dealing with stationary and transient structure dynamic responses, were developed. The first (the GLDDO method), exploiting stationary structure dynamic response properties, was conceived to detect global changes on those structures were real-time damage detection is not needed (bridges, buildings), since even severe damages do not constitute an immediate threat neither to the structure health nor to its users, because of the structure typology and the nature of operative loads.

On the contrary, aircraft or mechanical structures, due to the high frequency content of the operational loads, can be subjected to fast growing defects, and therefore there is the need of using local damage detection. At this aim a wave propagation based damage detection methodology (the WPBDD method) was developed.

9.2 Global-Local Damage Detection Optimization approach

The GLDDO approach was developed by modifying existing Model Updating methodologies. The enhancements carried out on MU methodology for damage detection purposes were aimed at memory and computational time reduction, noise withstanding increase, elimination of experimental and numerical data coupling (e.g. use of MSF), simple interpretation of the detection results in terms of location and severity, clarification of the data selection process, smooth convergence of the updating convergence and reduced expert user intervention.

The reduction of the memory and time consumption were achieved by introducing a global-local approach, which redistributed the FE model updating on two steps and reduced the number of updating parameters. Issues as noise withstanding increase, elimination of experimental and numerical data coupling were solved by adopting, as residue functions, a manipulation of correlation functions such as MAC, COMAC and FRAC. These new RFs considered damages as sources of discrepancies in the stationary

structure dynamic response properties and evaluated as such, also, modal property swap. The simple interpretation of the detection results in terms of location and severity was obtained using as updating parameters design-type parameters like FE thickness, elastic modules and etc... The development of the data selection process involving the data type, target mode shape and optimal sensor selection brought a further insight on the importance of such activity on the damage detection process as was extensively proved in §6.2-6.6.

The smooth convergence of the updating convergence was due to concurring factors such as the Global-Local approach, which made well conditioned sensitivity matrices, the adoption of improved minimization algorithms (e.g. SAM, LLSO and LSO), the introduction of correlation based residue functions, which reduced the noise pollution in the minimization process, the optimal sensor placements, target mode shape selection and etc...

Expert users' intervention was confined in the set-up phase, where the structure FE model has to be built and the accuracy level and the data type have to be selected (only once per each structure). The remaining phases of the detection process were automated: the modal extraction and the error localization process. The error localization process is sorted out by the global-local process, which automatically identifies the most damaged areas (first step) and, then, increases the updating parameters only in these.

The error localization process automation is a considerable improvement with respect to the methods reported in literature, where some author stated [53] that there was no substituted to engineer skills for a correct error localization.

As results of these improvements:

- Time savings ranging from 30 to 90% were achieved.
- No convergence problems were recorded using the residue functions developed by the author in contrast with the MODE RF found in literature.
- Increased accuracy was obtained. Since the most common RF present in literature (MODE RF), the only time that accurately predicted the damage locations, overestimated of 100% the introduced damage severities. Comparison with literature results (using the MUE factor, §6.6) showed the extreme enhancement provided by the developed technique.
- No guessing on the optimal sensor placement.
- Reduction of noise influence on acquired data through OSP and TMSS.
- Smaller defects can be detected. The GLDDO approach can commit the maximum theoretical number of updating parameters twice, thanks to the global-local approach using the same experimental data of literature reported techniques.

Moreover, the GLDDO approach was tested in polluted virtual environments showing the capability of detecting single-site damages and multi-site damages.

Finally, the extreme sensitivity to damage showed by the COMAC_MAC and FRACm RFs minimized using SAM algorithm with a sensor network designed by the EFI OSP techniques employing target mode shape selected by the MMF approach, made of the GLDDO approach an ideal SHM solution for large civil structure, where the extraction of low frequency mode shapes can be easily carried out even with ambient excitation.

9.3 Wave Propagation Based Damage Detection algorithm

As previously mentioned, for local damage detections, a second approach based on wave propagation was developed. Differently from conventional ultrasonic inspections that employ ultrasonic beam propagating through the structure thickness, the WPBDD algorithm developed by the author exploits waves propagating through the structure, making inspections faster and economically affordable, because there is no need of raster scanning, since a network of sensors can be built in on structures and, detect changes in wave propagation phenomena due to damage presence. In this way, the probability of detection is also increased, since UT problems like shadowing effects and damage orientation do not constitute a source of concern, because wave propagation phenomena like Lamb, guided waves interest the whole structure cross section.

Furthermore, some WPBDD algorithm features, such as no need of controlled excitation, no boundary reflected waves, no main bang shadowing of the damage reflected waves, damage detection in structural discontinuities (e.g. lap-joints, structure bends) and no need of expert users, constitute novelties in the world of the state of art of wave propagation inspection methodologies. All these novelties can be referred to the introduction of the time-frequency coherence function (Coherence Function Based Algorithm – CFBA - §7.9.1), which highlights the discrepancies between undamaged and damaged time histories generated by different load amplitudes as far as their shape is the same. So, wave propagation sources can be operational loads, which activate the SHM device any time an amplitude threshold is overcome. Moreover, since the CFBA highlights only the discrepancies, between a reference (undamaged structure) and a monitoring signal, and then, averaging and filtering out noise contributions through numerical and physical considerations, the CFBA output presents only damage reflected wave arrivals. Therefore, no boundary and main bang shadowing is possible. Furthermore, the absence of boundary reflected waves allows also the detection of defects hidden within structure boundaries.

As global results of these features, the application of the WPBDD algorithm on real structures becomes very simple, since it does not need any expert user capable of discriminate between damage and boundary echoes. Furthermore, the sensitivity of the methodology to damage presence is very high, because numerical polluted investigations carried out on a rail provided reliable damage detection and localisation of very small rolling contact fatigue defects.

9.3 Future Works

In the last two chapters, several improvements or further investigations were proposed for both the methodologies developed. However, both methodologies need to be experimentally validated.

In particular the GLDDO approach will be object of an extensive experimental campaign aimed at the identification of changes in the dynamic responses of the Nottingham Bridge, where the GPS network designed by the author will be upgraded by a new generation of GPSs with an improved sampling frequency of 100Hz, allowing the extraction of at least the first 10 mode shapes.

Moreover, numerical investigations need to be carried out in order to test the residue functions proposed in §6.7 in order to improve the accuracy of the GLDDO approach using FRF data.

For the WPBDD algorithm the experimental validation need to involve also anisotropic structures as composite structures, at this aim the ray tracing algorithm need to support a wave propagation speed changing with propagation directions. Moreover, the WPBDD algorithm needs to be fitted with a severity estimation system that can be based on the amplitude and the frequency extension of the discrepancy measured by the CFBA. Finally accurate studies on the attenuation phenomena of the propagating perturbation are essential for a correct deployment of sensors.

9.4 Publication activities

The Ph. D. research was supported by an intensive publication campaign aimed at validate through publications on refereed journal papers and presentations in front audiences of world expects in sensor networks, signal processing and damage detection. In this way useful information on the progress made and on the subject to analyse was gathered. Therefore, the OSP investigations on the Nottingham suspension bridge were target of a journal and a conference paper:

1. M. Meo, G. Zumpano, **On the optimal sensor placement techniques for a bridge structure,** in press on *Engineering structures*, 2005.
2. M. Meo, G. Zumpano, **Optimal Sensor Placement on a large scale civil structure,** *Smart Structures and Materials 2004*, SPIE, San Diego – California.

The same line was followed for the modal extraction investigations operated on the Nottingham suspension bridge, where the experimental acquisition was carried out by Nottingham University for a EPSRC's funded project (A Remote Bridge Health Monitoring System Using Computational Simulation and GPS Sensor Data):

3. M. Meo , G Zumpano, Xiaolin Meng , Gethin Roberts, Emily Cosser, Alan Dodson, **Measurements of dynamic properties of a medium span suspension bridge by using the wavelet transforms,** in press on *Mechanical Systems and Signal Processing*, 2005.
4. M. Meo, G. Zumpano, X. Meng, G. Roberts, E. Cosser, A. Dodson, **Identification of Nottingham Wilford Bridge modal parameters using wavelet transforms,** Smart *Structures and Materials 2004*, SPIE, San Diego – California.

The Global-Local Damage Detection Optimisation was also object of two publications, one conference and one journal paper (under reviewing):

5. M. Meo, G. Zumpano, **Damage Assessment on Plate-Like Structures Using a Global-Local Optimisation Approach,** submitted to *Optimization and Engineering*, 2005.
6. G. Zumpano, M. Meo, **Corrosion Damage Identification on Plate by Optimisation Algorithm**. In: Proc. of the *First European Workshop - Structural Health Monitoring*, pp. 137-144, 2002.

Other two papers (one conference, one journal) were published on rail damage detection using the Wave Propagation Based Damage Detection algorithm:

7. G. Zumpano, M. Meo, **A new damage detection technique based on wave propagation for rails**, in press on *International Journal of Solids and Structures*, 2005.
8. G. Zumpano, M. Meo, **A New Damage Detection Technique for Rails base on Wave Propagation**, *Smart Structures and Materials 2004*, SPIE, San Diego - California.

Moreover, the know how matured on the wave propagations was applied on impact localisations on composite plates using an upgraded version of the ray tracing algorithm here presented that took into account the change of wave propagation speed with the direction. On the subject two publications were made:

9. M. Meo, G Zumpano, **Impact Identification on a Sandwich Plate from Wave Propagation Responses** submitted to *Composite Structures Journal*, 2005.
10. M. Meo, G Zumpano, M Piggott and G Marengo, **Identification of the impact location of a sandwich plate from wave propagation responses**, *ICCST/5 Conference*, February 1-3, 2005 - Sharjah, United Arab Emirates.

Furthermore, the wave propagation expertise was additionally exploited for the development of a non classical non linear wave propagation code (in FORTRAN) within the European founded project AeroNEWS, which was object of two publications:

11. M. Meo, G. Zumpano, U. Polimeno, **Numerical investigation of wave propagation phenomena in composite beams using a hysteretic damage model**, *ICCM-15*, Durban, South Africa, 24 June – 01 July 2005.
12. M. Meo, G. Zumpano, **Corrosion identification on aluminium plate-like structure by monitoring the wave propagation phenomena**, *First World Conference on Corrosion in the Military*, Sorrento – Italy, 6-8 June 2005.

Finally, the combined signal processing and wave propagation skills, expanded during this research, were exploited for Nonlinear Elastic Wave Spectroscopy (NEWS) for AeroNEWS experimental activities on composite plate-like structures. These activities were object of two AeroNEWS reports and 5 conference papers:

13. M. Meo, G. Zumpano, **Nonlinear Elastic Wave Spectroscopy identification of Impact Damage on a sandwich plate**, submitted to *Composite Structures Journal*, 2005.
14. M. Meo, G. Zumpano, **Impact Damage monitoring in a sandwich panel through nonlinear elastic wave spectroscopy**, *12th International Congress on Sound Vibration*, ICSV12, Lisbon - Portugal, 11-14 July 2005.
15. G. Zumpano, M. Meo, **Damage detection in an aircraft foam sandwich panel using nonlinear elastic wave spectroscopy**, *2nd ECCOMAS Thematic Conference on Smart Structures and Materials*, Lisbon, Portugal, July 18-21, 2005.
16. M. Meo, G. Zumpano, **Identification of impact damage on a sandwich plate through non linear elastic wave spectroscopy (NEWS) using wavelet analysis**, *ICCM-15*, Durban, South Africa, 24 June – 01 July 2005
17. M. Meo and G. Zumpano, **Impact damage identification on sandwich plates through non linear elastic wave spectroscopy**, *ICCST/5 Conference*, February 1-3, 2005 - Sharjah, United Arab Emirates.
18. M. Meo, G. Zumpano, et al. **AERONEWS - 6 month report**, *EU 6th Framework Program, Aeronautic and Space*, September 2004.

19. M. Meo, G. Zumpano, et al. **AERONEWS – 1st year report**, *EU 6th Framework Program, Aeronautic and Space*, March 2005.

Therefore, it is clear that the work developed all over the Ph. D. program was object of constant critical review of world experts in the studied sectors. Moreover, the tools developed and expertise acquired resulted to be useful devices for investigations carried out in other fields like novel FE codes, impact localization and NEWS.

REFERENCES

1. S. Low, Jane's All the World's Aircrafts, 2001.
2. A. N/A, **Review of railtrack's work on usage costs**, *Office of the Rail Regulator*, R/00202, 1999. www.rail-reg.gov.uk/filestore/consultants/bah-cost_caus_cont.htm.
3. A. N/A, **Report on accident in Melbourne airport occurred 4th April 1999**. www.basi.gov.au/occurs/ob199901455.html.
4. T. E. Munns, R. E. Beard, A. M. Culp, D. A. Murphy, R. M. Kent, **Analysis of Regulatory Guidance for Health Monitoring**, NASA/CR-2000-210643, 2000, http://library01.gsfc.nasa.gov/NewDocs/NewDocs.htm.
5. A. N/A, **Appendix 3: maintenance costs on freight-only lines**, *Europe Economics / Brown & Root Consulting*, 2003, www.rail-reg.gov.uk/filestore/consultants/ee-appendix3.pdf.
6. A. N/A, **Bridge Inspection Policy**, *Transit New Zealand*, TNZS6: 2000, 2000, www.transit.govt.nz/technical_information/content_files/Specification80_pdfFile.pdf.
7. M. Neumair, **Requirements on Future Structural Health Monitoring Systems**, *Proceedings of the 7th RTO Meetings*, May 1998. ftp://ftp.rta.nato.int/pubfulltext/rto/mp/rto-mp-007/$mp-007-01.pdf.
8. S. R. Hunt, I. G. Hedben, **Eurofighter 2000 structural health and usage monitoring: an integrated approach**, *The second Joint NASA/FAA/DoD Conference on Aging Aircraft*, NASA/CP-1999-208982/part1, January 1999.

9. S. W. Doebling, C. R. Farrar, M. B. Prime, **A Summary Review of Vibration-Based Damage Identification Methods**, *The Shock and Vibration Digest*, Vol. 30, No. 2, pp. 91-105. 1998. www.lanl.gov/projects/ncsd/pubs/doebling_svd.pdf.

10. S. J. Kranock, **Real-Time Damage Detection Using Model-Based Observers**, *College of Engineering, Colorado University*, Ph. D. Dissertation, CU-CAS-00-05, 2000. http://sdcl.colorado.edu/Publications/2000/CAS_Reports/CU-CAS-00-05.pdf.

11. S. S. Kessler, **Piezoelectric-based In-Situ Damage Detection of Composite Materials for Structural Health Monitoring Systems**, MIT, 2002.

12. D. G. Luenberger, **An Introduction to Observers**, *IEEE Transactions on Automatic Control*, Volume AC-16, No 6, pages 596-602, December 1971.

13. R. Martinez-Ona, M. C. Perez, **Research on creep damage detection in reformer tubes by Ultrasonic Testing**, *15th WCNDT Roma*, 2000. www.ndt.net/wcndt00/papers/idn238/idn238.htm.

14. L. H. Bisbee, H. E. Queen, R. K. Bezzant, **Ultrasonic Testing Metric for Creep Damage Assessment**, *Structural Integrity Associates Inc.*, 1999 www.structint.com/tekbrefs/t99014r0.pdf.

15. S. E. Kruger, J. M. A. Rebello, P. C. de Camargo, **Hydrogen damage detection by ultrasonic spectral analysis**, *NDT&E International*, vol. 32, pp. 275-281, 1999.

16. N. Shehl, W. Hoppe, A. Berens, R. Ko, **Evaluation of an Intergranular Corrosion Detection Method on the Structural Repair of Aging Aircraft Program**, *The 5th Joint NASA/FAA/DoD Conference on Aging Aircraft, September 2001*, www.agingaircraft2001.com/papers/IndexPDFs/6B_4.pdf.

17. T. Tanaka, Y. Izawa, **Detection Method of Fatigue Damage in Carbon Steel Using Laser Ultrasonics**, *Journal of Nuclear Science and Technology*, Vol. 39, No. 5, pp. 514-519, May 2002. http://wwwsoc.nii.ac.jp/aesj/publication/JNST2002/No.5/39_514-519.pdf.

18. A. N/A, **Ultrasonic Transducers catalogue**, *General Electrics Power Systems*, 2003, www.gepower.com/dhtml/panametrics/en_us/index.jsp.

19. C. A. Paget, S. Grondel, K. Levin, C. Delebarre, **Damage Detection in Composites by a Wavelet-Coefficient Technique**, *Proceedings of the First European Workshop – Structural Health Monitoring*, 2002.

20. P. Guy, T. Monnier, J.C. Baboux, Y. Jayet, **Simultaneous Monitoring of Ageing and Damage in Large Plate-Like Composite Structures Using Integrated Piezoelectric Sensors**, *Proceedings of the First European Workshop – Structural Health Monitoring*, 2002.

21. K. Diamanti, J. M. Hodgkinson, C. Soutis, **Damage Detection of composite Laminates Using PZT Generated Lamb Waves**, *Proceedings of the First European Workshop – Structural Health Monitoring*, 2002.

22. E. Atkan, J. Beck, P. Cornwell, A. Helmicki, E. Safak, J. Yao, **The State of the Art in Structural Identification of Constructed Facilities**, *A Report by the ASCE Committee on Structural Identification of Constructed Facilities*, Draft, 28 June 1999.

23. G. Zumpano, M. Viscardi, L. Lecce, **Structural Damage Analysis On A Typical Aeronautical Structure Using Piezoelectric Devices**, 42nd AIAA/ASME/ ASCE/AHS/ASC Structures, Structural Dynamics and Materials Conference, 16-19 April 2001, Seattle, WA., U.S.A.

24. V. Giurgiutiu, C. A. Rogers, **Electro-Mechanical (E/M) impendence method for structural health monitoring and non-destructive evaluation**, *International Workshop on Structural Health Monitoring,* Stanford University, CA, September 18-20,1997.

25. D. M. Peairs, G. Park, D. J. Inman, **Low Cost Impedance Monitoring Using Smart Materials**, *Proceedings of the First European Workshop – Structural Health Monitoring*, 2002.

26. S. W. Doebling, C. R. Farrar, M. B. Prime, D. W. Shevitz, **Damage Identification and Health Monitoring of Structural and Mechanical System from Change in Their Vibration Characteristic: A Literature Review**, *Los Alamos National Laboratory report*, LA-13070-MS, May 1996, www.lanl.gov/projects/ncsd/pubs/lit_review.pdf.

27. C. P. Ratcliffe, **Damage detection using a modified laplacian operator on mode shape data**, *Journal of Sound and Vibration*, vol. 204, No. 3, pp. 505-517, 1997.

28. A. K. Pandey, M. Biswas, **Damage detection from changes in curvature mode shapes**, *Journal of Sound and Vibration*, vol. 145, No. 2, pp. 321-332, 1991.

29. Y. Gao, B. F. Spencer Jr., **Damage localisation under ambient vibration using changes in flexibility**, *Journal of Earthquake Engineering and Earthquake Vibration,* vol. 1, No 1, pp. 136-144, 2002. http://cee.uiuc.edu/sstl/papers/EEEV_2002.pdf.

30. S. W. Doebling, L. D. Peterson, K. F. Alvin, **Estimation of reciprocal residual flexibility from experimental modal data**, *AIAA Journal*, Vol. 34, No. 8, pp. 1678-1685, 1996.

31. K. Worden, **Structural fault detection using a novelty measure**, *Journal of Sound and Vibration*, vol. 201, No. 1, pp. 85-101, 1997.

32. I. Trendafilove, W. Heylen, P. Sas, **Damage localisation in structures. A pattern recognition perspective**, ISMA 23, September 1998, www.isma-isaac.be/publications/PMA_MOD_publications/ISMA23/p99p106.pdf.

33. T. Holroyd, H. Meisuria, D. Lin, N. Randall, **Development of a Practical Acoustic Emission Based Structural Monitoring System**, *Proceedings of the First European Workshop – Structural Health Monitoring*, 2002.

34. O. O. Oladopo, M. J. Shulz, **Acoustic Emission Detection on Large Structures**, *Paper draft,* http://qemnetwork.qem.org/Sharp%20Plus%202000%20Abstracts/Oladapo.pdf.

35. P. T. Coverley, W. J. Staszewski, **Impact Damage Location in Composite Structures Using Genetic Algorithm**, *Proceedings of the First European Workshop – Structural Health Monitoring*, 2002.

36. G. T. Zheng, **Non Destructive Structural Health Monitoring with Acoustic Emission Signal Processing**, *Proceedings of the First European Workshop – Structural Health Monitoring*, 2002.

37. J. Saniger, J.-P. Dupuis, **Composite Damage Localisation Using Integrated Acoustic Emission Technology**, *Proceedings of the First European Workshop – Structural Health Monitoring*, 2002.

38. G. L. Burkhardt, **Technology status assessment for development of nonlinear harmonic sensors for detection of mechanical damage**, *Technical Assessment Report – U.S. Department of Energy*, 2002. www.netl.doe.gov/scng/publications/t&d/tsa/MechDamageTech.PDF.

39. R. Sam, M. Y. Choi, **Development of an Electromagnetic Based Sensor for Measurement of Mechanical Force in Pre-Stressed Steel Cables and Tendons.** *Proceedings of the First European Workshop – Structural Health Monitoring*, 2002.

40. W. Liu, R. Hunsperger, M. Chajes, E. Kunz, **An Overview of Corrosion Damage Detection in Steel Bridge Strands Using TDR**, Proc. of the 2nd International *Symposium on TDR for Innovative Applications, Evanston, Illinois,* 2001, www.ee.udel.edu/~hunsperg/corrosion/Evanston2001.pdf.

41. N. Khemiri, N. Angelidis, P. E. Irving, **Experimental and finite element study of the electrical potential technique for damage detection in CFRP laminates**, Conference of Smart Structures & Demonstrators, December 2001.

42. A. Todoroki, Y. Tanaka, Y. Shimamura, **Electric Resistance Change Method for Monitoring of Embedded Delaminations of Quasi-Isotropic CFRP Laminated Plates**, **Proceedings** *of the First European Workshop – Structural Health Monitoring*, 2002.

43. H. Aygun, E. Selcuk, **A new approach for reliable inspection in radiography of turbine blades**, *Proceedings of the 7th RTO Meetings*, May 1998. ftp://ftp.rta.nato.int/pubfulltext/rto/mp/rto-mp-007/$mp-007-01.pdf.

44. M. M. D. Coetzer, **An Evaluation of Shearography and Neutron Radiography for the Non-Destructive Inspection of Helicopter Main Rotor Blades**, Defence Aeronautics Programme Defencetek, 1999, www.arofe.army.mil/Conferences/NDE-workshop/Coetzer.pdf.

45. E. H. Lehmann, P. Vontobel, L. Weizel, **The investigation of highly activated samples by neutron radiography at the spallation source SINQ**, *Proc. 6th World Conf. On Neutron Radiography,* 1999, http://neutra.web.psi.ch/publication/WC-6_paper2.pdf.

46. J. P. Komorowski, D. S. Forsyth, D. L. Simpson, R. W. Gould, **Probability of detection of corrosion in aircraft in aircraft structures**, *Proceedings of the 7th RTO Meetings*, May 1998. ftp://ftp.rta.nato.int/pubfulltext/rto/mp/rto-mp-007/$mp-007-01.pdf.

47. F. W. Spencer, **Detection reliability for small cracks beneath rivet heads using eddy-current nondestructive inspection techniques**, *Final Report* December 1998, http://aar400.tc.faa.gov/acc/accompdocs/97-73.pdf.

48. G. A. Hartman, J. M. Larsen, **Infrared Damage Detection Systems (IDDS)**, *Web Journal of Advanced Measurement* Methods, 2003, www.sem.org/SEMNanoMat/HartmanLarsen.pdf.

49. J. K. C. Shih, M. Hsin, R. Delpak, C. W. Hu, P. Plassmann, **Application of Infrared Thermography for Damage Detection in Structural Concrete – a Preliminary Report**, *NDT.net* Vol. 5, No 2, 2000, www.ndt.net/article/v05n02/shih/shih.htm.

50. Y. A. Plotnikov, W. P. Winfree, **Visualization of subsurface defects in composites using a focal plane array infrared camera**, *Proc. SPIE*, Vol.3700, 1999, pp.26-31.

51. S. Ziaei-Rad, M. Imregun, **On the accuracy required of experimental data for finite element model updating**, *Journal of Sound and Vibration*, Vol. 196, No. 3, pp. 323-336, 1996.

52. D. J. Ewins, **Adjustments or updating model**, *Sadhana,* (printed in India), Vol. 25, Part 3, pp 235-245, June 2000, www.ias.ac.in/sadhana/Pdf2000June/Pe873.pdf.

53. A. Calvi, **Finite element model updating in structural dynamics using design sensitivity and optimisation**, *College of Aeronautics – Cranfield University*, Ph. D Thesis, 1998.

54. N. Imamovic, **Model validation of large finite element models using test data**, *Imperial College, Technology & Medicine*, London, 1998.

55. H. Ahmadian, G. M. L. Gladwell, F. Ismail, **Parameter selection strategies in finite element model updating**, *Journal of Vibration and Acoustics*, Vol. 119, No. 1, pp. 37-45, 1997.

56. M. Imregun W. J. Visser, **A review of model updating techniques**, *The Shock and Vibration Digest*, Vol. 23, No. 1, pp. 9-20, 1991.

57. J. E. Mottershead, M. I. Friswell, **Model updating in structural dynamics: A survey**, *Journal of Sound and Vibration*, Vol. 167, No. 2, pp. 347-375, 1993.

58. S. Z. Rad, **Methods for updating numerical models in structural dynamics**, *Imperial College of Science, Technology and Medicine,* Ph. D. Thesis, June 1997, www.me.ic.ac.uk/dynamics/publication/thesis/phd97ziaeirad.pdf.

59. S. V. Modak. T. K. Kundra, B. C. Nakra, **Prediction of dynamic characteristics using updated finite element models**, *Journal of Sound Vibration*, Vol. 254, No. 3, pp. 447-467, 2002.

60. Y. Halevi, I. Bucher, **Model updating via weighted reference basic with connectivity constraints**, *Journal of Sound Vibration*, Vol. 265, No. 3, pp. 451-481, 2003.

61. M. Baruch, Y. Bar Itzhac, **Optimisation weighted orthogonalisation of measured modes**, *AIAA Journal*, Vol. 16, No. 4, pp. 346-351, 1978.

62. F. S. Wei, **Structural dynamic model improvement using vibration test data**, *AIAA Journal*, Vol. 28, No. 1, pp. 1686-1688, 1990.

63. S. V. Modak, T. K. Kundra, B. C. Nakra, **Comparative study of model updating methods using simulated experimental data**, *Computers and Structures*, Vol. 80, pp. 437-447, 2002.

64. K. K. Denoyer, **Structural model update using dynamically measured static flexibility matrices**, *University of Colorado*, Ph. D thesis, 1996, http://sdcl.colorado.edu/Publications/1996/CAS_Reports/CU-CAS-96-27.pdf.

65. J. K. Sinha, M. I. Friswell, **The use of model updating for reliable finite element modelling and fault diagnosis of structural components used in nuclear plans**, *Nuclear Engineering and Design*, Vol. 233, pp. 11-23, 2003.

66. S. V. Modak, T. K. Kundra, B. C. Nakra, **Model updating using constrained optimisation**, *Mechanics Research Communications*, Vol. 27, No. 5, pp. 543-551, 2000.

67. D. Goge, **Automatic updating of large aircraft models using experimental data from ground vibration testing**, *Aerospace Science and Technology*, Vol. 7, pp. 33-45, 2003.

68. Y. X. Wu, J. Zhong, C. Conti, P. Dehombreux, **Quasi-mode shape based dynamic finite element model updating method**, *Journal of Materials Processing Technology*, Vol. 138, pp. 518-521, 2003.

69. D. Goge, M. Link, **Assessment of computational model updating procedures with regard to model variation**, *Aerospace Science and Technology*, Vol. 7, pp. 47-61, 2003.

70. C. E. Roger, A. L. Andrew, **Computing derivatives of eigenvalues and eigenvectors by simultaneous iteration**, *IMA Journal of Numerical Analysis*, Vol. 9, pp. 111-122, 1989.

71. M. M. Gola, A. Soma, D. Botto, **On theoretical limits of dynamics model updating using a sensitivity-based approach**, *Journal of Sound and Vibration*, Vol. 244, No. 4, 2001.

72. A. Shonrock, E. Dascotte, K. H. Dufour, **Validation of an aeroengine carcass finite element model by means of computational model updating based on static stiffness testing**, *FEMtool Report*, 1999. www.femtools.com/download/docs/epf99.pdf.

73. D. J. Ewins, **Modal testing: theory and practice**, *Research Studies Press LTD*, 2001.

74. D. Fotsch, D. J. Ewins, **Applications of MAC in the Frequency Domain**, *Proc. of the 18th International Modal Analysis Conference*, pp. 1225, 2000.

75. T. Coleman, M. A. Branch, A. Grace, **Optimisation Toolbox. User's Guide, Version 2**, *The Math Works Inc*, 1999.

76. D. Bindel, **Parallel conjugate assignment**, *Berkeley University*, Course Notes, 2003 www.cs.berkeley.edu/~dbindel/cs267ta/cgnotes.pdf.

77. A. N/A, **Solution of linear algebraic equations**, *efunda – Engineering fundamentals*, 2003, www.efunda.com/math/num_linearalgebra/num_linearalgebra.cfm#SV.
78. C. Meola, G. De Felice, **Fondamenti lineari per la fluidodinamica numerica**, *Ed. Ateneo s.a.s*, Napoli, 1996.
79. P. Konhke, **ANSYS Inc. Theory manual – Twelfth Edition**, *SAS IP Inc.*, 2001.
80. H. Bedrossian, M. L. Tinker, H. Hidalgo, **Ground vibration test planning and pre-test analysis for the X-33 Vehicle**, *AIAA Journal*, AIAA-2000-1586, 2000.
81. T. Van Langenhove, M. Brughmans, **Using MSC/NASTRAN and LMS/PRETEST to find an optimal sensor placement for modal identification and correlation of aerospace structures**, MSC 1999 Aerospace Users' Conference Proceedings, 1999, www.mscsoftware.com/support/library/conf/auc99/p06099.pdf.
82. C. Z. Gregory Jr., **Reduction of large flexible spacecraft models using internal balancing theory**, *Journal of Guidance*, Vol. 7, No. 6, pp. 725-732, Nov.- Dec., 1984.
83. R. E. Skelton, P. C. Hughes, **Modal cost analysis for linear matrix second-order systems**, *Journal of Dynamics Systems, Measurements, and Control*, Vol. 102, pp 151-158, Sept. 1980.
84. W. Gawronski, T. Williams, **Model reduction for flexible space structures**, *Journal of Guidance*, Vol. 14, No. 1, pp. 68-76, 1990.
85. H. Hidalgo Jr., **An innovative structural mode selection methodology: application for the X-33 launch vehicle finite element model**, *41st AIAA/ASME/AHS/ASC/ Structures, Structural Dynamics, and Materials Conference and Exhibit*, AIAA-2000-1587, pp. 83-102, 3-6 April 2000.
86. S. W. Doebling, F. M. Hemez, L. D. Peterson, C. Farhat, **Improved damage location accuracy using strain energy-based mode selection criteria**, AIAA Journal, Vol. 35, No. 4, pp. 693-699, 1997, www.lanl.gov/projects/ncsd/pubs/mode_selection_paper.rev2.pdf.
87. E. Dowski, **Fisher Information and Cramer-Rao bound**, *Colorado University - Department of Electrical Engineering*, Web page, 1995 www.colorado.edu/isl/papers/info/node2.html.
88. D. Middlenton, **An introduction to statistical communication theory**, *McGraw-Hill*, 1960.
89. R. O. Duda, **Covariance**, *Department of Electrical Engineering San Jose State University*, 1997, www.engr.sjsu.edu/~knapp/HCIRODPR/PR_Mahal/cov.htm.
90. D. C. Kammer, **Sensor Placement for On Orbit Modal Identification and Correlation of Large Space Structures**, *AIAA Journal of Guidance, Control and Dynamics*, AIAA-94-1730-CP, Vol. 14, No. 2, pp. 251-259, 1992.
91. B.-K. Kim, J. G. Ih, **On the reconstruction of a vibro-acoustic filed over the surface enclosing an interior space using the boundary element method**, *Journal of the Acoustical Society of America*, Vol. 100, No. 50, 1996.
92. K. Worden, A.P. Burrows, **Optimal sensor placement for fault detection**, *Engineering Structures*, Vol. 23, pp. 885-901, 2001.

93. G. Heo, M. L. Wang, D. Satpathi, **Optimal transducer placement for health monitoring of long span bridge**, *Soil Dynamics and Earthquake Engineering*, Vol. 16, pp 495-502, 1997.
94. J. Hollmen, **Principal component analysis**, *Helsinki University*, 1997, www.cis.hut.fi/~jhollmen/dippa/node30.html.
95. L. Paletta, A. Pinz, **Active objective recognition by view integration and reinforcement learning**, *Robotics and Autonomous Systems*, Vol. 31, pp. 71-86, 2000.
96. R. A. Eek, O. H. Bosgra, **Controllability of particulate processes in relation to the sensor characteristics**, *Powder Technology*, Vol. 108, pp 137-146, 2000.
97. V. Fedorov, P. Hackl, **Optimal experimental design: spatial sampling**, *Calcutta Statistical Association Bulletin*, Vol. 44, March & June, pp. 173-174, 1994.
98. S. W. Doebling, **Measurement of structural flexibility matrices for experiments with incomplete reciprocity**, *Colorado University*, PhD dissertation, 1996, http://sdcl.colorado.edu/Publications/1995/Theses/Doebling_PhD.pdf.
99. C. B. Larson, D. C. Zimmerman, E.L. Marek, **A comparison of modal test planning techniques: excitation and sensor placement using the NASA 8-bay truss**, *Proceedings of the 12th International Modal Analysis Conference, Honolulu, HA*, pp. 205-211, 1994.
100. J. Cunha, J. Piranda, **Application of model updating techniques in dynamics for the identification of elastic constants of composite materials**, *Composites: Part B*, Vol. 30, pp. 79-85, 1999.
101. F. W. J. van den Berg, H. C. J. Hoefsloot, H. F. M. Boelens, A. K. Smilde, **Selection of optimal sensor position in a tubular reactor using robust degree of observability criteria**, *Chemical Engineering Science*, Vol. 55, pp. 827-837, 2000.
102. D. Dochain, N. Tali-Maanar, J. P. Babary, **On modelling, monitoring and control of fixed bed bioreactors**, *Computers and Chemical Engineering*, Vol. 21, pp. 1255-1266, 1997.
103. M. Jamshidi, M. Malek-Zavarei, **Linear control systems – A computer-aided approach**, *Pergamon Press*, 1986.
104. J. E. T. Penny, M. I. Friswell, S. D. Garvey, **Automatic choice of measurement location for dynamic testing**, *AIAA Journal*, Vol. 32, No. 2, February 1994.
105. A. V. Oppenheim, R. W. Schafer, **Digital signal processing**, *Englewood Cliffs, N.J: Prentice-Hall*, 1975.
106. O. Dossing, **Structural Testing. Part 1: Mechanical Mobility Measurement**, *Bruel & Kjaer*, April 1988.
107. M.Q. Feng, J.-M. Kim, **Identification of a dynamic system using ambient vibration measurements**, *Journal of Applied Mechanics – Transactions of ASME*, Vol. 65, December 1998, pp 1010-1021.
108. J. C. Asmussen, **Modal analysis based on the random decrement technique. Application to civil engineering structures**, *University of Aalborg – Denmark*, Ph. D. dissertation, 1997, http://www.aub.auc.dk/phd/department06/text/asmussen-john.pdf.
109. J. Lardies, S. Gouttebroze, **Identification of modal parameters using the wavelet transform**, *International Journal of Mechanical Sciences*, Vol. 44, pp 2263-2283, 2002.

110. B. Peeters, G. de Roeck, **Reference-based stochastic subspace identification for output-only modal analysis,** *Mechanical Systems and Signal Processing*, Vol. 13(6), pp 855-878, 1999.
111. C. S. Huang, **Structural identification from ambient vibration measurement using the multivariate AR model,** *Journal of Sound and Vibration*, Vol. 241(3), pp 337-359, 2001.
112. B. A. D. Piombo, A. Fasana, S. Marchesiello, M. Ruzzene, **Modelling and identification of the dynamic response of a supported bridge,** *Mechanical Systems and Signal Processing*, Vol. 14(1), pp 75-89, 2000.
113. C. R. Farrar, G. H. James III, **System identification from ambient vibration measurements on a bridge,** *Journal of Sound and Vibration*, Vol. 205(1), pp 1-18, 1997.
114. M. Abdelghani, M. Goursat, T. Biolchini, **On-line modal monitoring of aircraft structures under unknown excitation,** *Mechanical Systems and Signal Processing*, Vol. 13(6), pp 839-853, 1999.
115. T. Kijecwski, A. Kareem, **Wavelet transforms for systems identification in civil engineering,** *Computer-Aided Civil and Infrastructure Engineering*, Vol. 18, pp 339-355, 2003.
116. H. Jemin, Z.-F. Fu, **Modal Analysis,** *Oxford: Butterworth Heinemann*, 2001.
117. J. Lardies, **State-space identification of vibrating systems from multi-output measurements,** *Mechanical Systems and Signal Processing*, Vol. 12(4), pp 5435-558, 1998.
118. J. S. Bendat, **Principles and application of random noise theory,** *John Wiley & Sons, Inc.*, 1958.
119. J.-N. Juang, R.S. Pappa, **An eigensystem realization algorithm for modal parameter identification and model reduction,** *Journal of Guidance, Control, and Dynamics*, Vol. 8(5), pp 620-627, 1985.
120. J.-N. Juang, R.S. Pappa, **Effects of noise on modal parameters identified by the eigensystem realization algorithm,** *Journal of Guidance, Control, and Dynamics*, Vol. 9(3), pp 294-303, 1986.
121. R.S. Pappa, **Independent Analysis of the Space Station Node Modal Test Data,** *NASA/TM-97-206262*, December 1997.
122. J. Pritchard, R. Buehrle, R. Pappa, F. Grosveld, **Comparison of modal analysis methods applied to a vibro-acoustic test article,** *Proceedings of the IMAC-XX Conference and Exposition on Structural Dynamics*, Los Angeles, California, February 4-7, 2002.
123. B.L. Ho, R.E. Kalman, **Effective Construction of Linear State-Variable Models from Input/Output Data,** *3rd Annual Allerton Conference on Circuit and System Theory*, pp. 449-459, 1965.
124. J. Lardies, **Modal parameter identification from output only measurements,** *Mechanic Research Communications*, Vol. 24(5), pp521-528, 1997.
125. N. C. Mickleborough, L. Pi, **Modal parameter identification using z-transforms,** *International Journal for Numerical Methods in Engineering*, Vol. 28(10) pp 2307-2321, 1989.
126. S. Mallat, **A wavelet tour of signal processing,** *Academic Press*, 1998.

127. V. C. Chen, H. Ling, **Time-Frequency Transformation for Radar Imaging and Signal Analysis**, *Artech House, Boston, London*, 2002.
128. M. Misiti, Y. Misiti, G. Oppenheim, J-M Poggi, **Wavelet Toolbox: User Guide, Version 2**, *The MathWorks*, 2002.
129. W. J. Staszewki, **Identification of damping in MDOF systems usinf time-scale decomposition**, *Journal of Sound and Vibration*, Vol. 2035(2), pp 283-305, 1997.
130. U. Lee, J. Shin, **A frequency response function-based structural damage identification method**, *Computers & Structures*, Vol. 80, No. 2, pp. 117-132, 2002.
131. U. Lee, J. Shin, **A structural damage identification method for plate structures**, *Engineering Structures*, Vol. 24, No. 9, Pages 1177-1188, 2002.
132. H. Reismann, **Elastic plates: theory and application**, *John Wiley & Sons*, 1988.
133. M. Castellano, **Elements of linear algebra**, *Liguori Editore*, 1988.
134. E. Monaco, G. Zumpano, L. Lecce, **Experimental damage detection on a partial bridge using MADAVIC Heavy Magnetostrictive Actuator (HMSA)**, DPA Internal Report, Naples University, 2001.
135. K. F. Graff, **Wave motion in elastic solids**, *Clarendon Press*, Oxford, 1975.
136. N. Wanner, **Why the earth shakes: Seismic Science**, *The exploratorium*, 1999, www.exploratorium.edu/faultline/earthquakescience/index.html.
137. I. A. Viktorov, **Raleigh and Lamb waves: physical theory and application**, *Plenum Press: New York*, 1967.
138. J. and H. Krautkramer, **Ultrasonic testing of materials. Third revised edition**, *Springer-Verlag*, Berlin Heidelberg New York, 1983.
139. J. L. Rose, **Ultrasonic Waves in solid Media**, *Cambridge University Press*, 1999.
140. A. N. A., **AEA – Acoustic Emission Analysis. Detecting and evaluating faults**, *Vallen-Systeme GmbH*, 2003, www.vallen.de/ae/index.html.
141. C. U. Grosse, B. Weiler, H. W. Reinhartdt, **Bond behaviour of fiber and formation of a damage zone in fibre reinforced concrete**, *NDT.net*, Vol. 5, No. 2, February 2000, www.ndt.net/article/v05n02/grosse/grosse.htm.
142. H. Jeong, Y.-S. Jang, **Wavelet analysis of plate propagation in composite laminates**, *Composite Structures*, 49, pg. 443, 2000.
143. S. Aicher, L. Hofflin, G. Dill-Langer, **Damage evolution and acoustic emission of wood at tension perpendicular to fiber**, *Holz als Roh – und Werkstoff*, Springer-Verlag, 59, pg. 104, 2001.
144. A Berkovits, D. Fang, **Study of fatigue crack characteristics by acoustic emission**, *Engineering Fracture Mechanics*, 51, pg. 401, 1995
145. E. T. Ng, G. Qi, **Material fatigue behaviour characterization using the wavelet-based AE technique – a case study of acrylic bone cement**, *Engineering Fracture Mechanics*, 68, pg. 1477, 2001.
146. D.-U. Sung, C.-G. Kim, C.-S. Hong, **Monitoring of impact damages in composite laminates using wavelets transform**, *Composite. Part B: engineering*, 33, pg. 35, 2002.
147. R. Franklin, U. B. Halabe, B. Gopalakrishnan, **NDT Solution – Knowledge based assistant for ultrasonic testing methodology of materials**, *American Society for Nondestructive Testing*, December 2001, www.asnt.org/publications/materialseval/solution/dec01solution/dec01sol.htm.

148. L. Angrisani, P. Daponte, **Thin thickness measurements by means of a wavelets transform-based method**, *Measurement*, 20 (4), pg. 227, 1997.
149. J. L. Rose, **Elastic wave analysis for broken rail detection**, *15th WCNDT – Rome*, 2000, www.ndt.net/article/wcndt00/papers/idn270/idn270.htm.
150. F. Schubert, B. Koehler, O. Sacharova, **Ultrasonic testing of rails with vertical crack – Numerical modelling and experimental results**, *NDT.net*, 3 (6), June 1998, www.ndt.net/article/0698/schub/schub.htm.
151. P. Fellinger, R. Marlein, K.J. Langnberg, S. Klaholz, **Numerical modelling of elastic wave propagation and scattering with EFIT – Elastodynamic Finite Integration Technique**, *Wave Motion*, 21, pg. 47, 1995.
152. V. Mustafa, A. Chahbaz, D. R. Hay, M. Brassard, S. Dubois, **Imaging of disbond in adhesive joint with lamb waves**, *NDT.net*, 2 (3), March 1997, www.ndt.net/article/tektren2/tektren2.htm.
153. A. Chahbaz, V. Mustafa, D. R. Hay, **Corrosion detection in aircraft structures using guided lamb waves**, *NDT.net*, 1 (11), November 1997, www.ndt.net/article/tektrend/tektrend.htm.
154. S. Legendre, J. Goyette, D. Massicotte, **Ultrasonic NDE of composite material structures using wavelets coefficients**, *NDT&E International*, 34, pg 31, 2001.
155. M. Z. Silva, R. Gouyon, F. Lepoutre, **Hidden corrosion detection in aircraft aluminium structures using laser ultrasonic and wavelets transform signal analysis**, *Ultrasonics*, article in press, (2003).
156. M. Castillo, E. Moreno, O. Sanchez, M. Gonzales, M. Rodrigues, **Ultrasonic flaw detection in cast iron using a multi-resolution analysis**, *Instrumentation and Development*, 3 (10), pg. 27, 1998.
157. L. Angrisani, L. Bechou, D. Dallet, P. Daponte, Y. Ousten, **Detection and location of detects in electronic devices by means of scanning ultrasonic microscopy and the wavelet transform**, *Measurement*, 31, pp. 77-91, 2002.
158. S. Hurlebaus, M. Neithammer, L. J. Jacobs, C. Valle, **Automated methodology to locate notches with Lamb waves**, *Acoustic Research Letters Online*, Acoustical Society of America, June 2001, www.ce.gatech.edu/~ljacobs/stef_ARLO.pdf.
159. N. Anderson, **Overview of the shallow seismic reflection techniques**, *Geophysics 2000*, St. Louis, Missouri, 2000, www.modot.state.mo.us/g2000/.
160. Author not Available, **How are Earthquakes located?**, *Education & Outreach Series No. 6*, IRIS consortium, 2003, www.iris.edu/edu/onepagers/no6.pdf.
161. T. A. de Perez, F. D'Alvano, O. Sucre, M. Abonado, A. Viloria, **P and S waves detection using Time-Frequency Representation**, *Geophysical- ICSPAT*, 1997, www.icspat.com/papers/250mfi.pdf.
162. P. J. Loughlin, L. Cohen, **The uncertainty principle: global, local, or both?**, *IEEE Transaction on Signal Processing*, Vol. 52(5), May 2004.
163. A. Kareem, T. Kijewski, **Time-frequency analysis of wind effects on structures**, *Journal of Wind Engineering and Industrial Aerodynamics*, Vol. 90, pg. 1435, 2002.
164. H. Kim, H. Ling, **Wavelet Analysis of Radar Echo from Finite-size Target**, *IEEE Transactions on antennas and propagation*, Vol. 41(2), 1993.

165. L. C. Trintinalia, H. Ling, **Interpretation of Scattering Phenomenology in Slotted Waveguide Structures via Time-Frequency Processing**, *IEEE Transactions on antennas and propagation*, Vol. 43(11), 1995.
166. J. Moore, H. Ling, **Super-Resolved Time-Frequency Analysis of Wideband Backscattered Data**, *IEEE Transactions on antennas and propagation*, Vol. 43(6), 1995.
167. H. Ling, J. Moore, D. Bouche, V. Saavedra, **Time-Frequency Analysis of Backscattered Data from a Coated Strip with a Gap**, *IEEE Transactions on antennas and propagation*, Vol. 41(8), 1993.
168. L. Carin, L. B. Felsen, D. R. Kralj, H. S. Oh, S. Unnikrishna Pillai, **Wave-Oriented Signal Processing Of Dispersive Time-Domain Scattering Data**, *IEEE Transactions on antennas and propagation*, Vol. 45(4), 1997.
169. G. N. Frantziskonis, L. B. Simmon, J. Woo, T. E. Matikas, **Miltiscale characterisation of pitting corrosion and application to an aluminium alloy**, Eur. Journal of mechanics A/Solids, Vol. 19, pg. 309, 2000.
170. Y. J. Yan, L.H. Yam, **Online detection of crack damage in composite plates using embedded piezoelectric actuators/sensors and wavelets analysis**, *Composite strctures*, Vol. 58, pg. 29, 2002.
171. X. Gilliam, J. Dunyak, A. Doggett, D. Smith, **Coherent structure detection using wavelet analysis in long time-series**, *J. of Wind Engineering and Industrial Aerodynamics*, Vol. 88, pg. 183, 2000.,
172. W. J. Staszwski, **Identification of damping in MDOF systems using time-scale decomposition**, *J. of Sound and Vibration*, Vol. 203(2), pg. 283, 1997.
173. Jurgen Mann, **Derivation and implementation of a seismic image wave theory and its application to seismic reflection data**, *University of Karlsruhe- Geophysical Institute*, Diploma thesis (English version), March 1998, www-gpi.physik.uni-karlsruhe.de/pub/jmann/MScThesis/newdipeng.pdf.
174. A. Teolis, **Computational signal processing with wavelets**, *Birkhauser: Boston*, 1998.
175. J. M. Gere, S. P. Timishenko, **Mechanics of Materials – 3rd Edition**, *PWS-KENT Publishing Company – Boston*, 1990.
176. E. W. Weisstein, **Ellipse**, *Wolfram Research Inc.* 2003, www.mathworld.wolfram.com/Ellipse.html.
177. J. L. Rose, M. J. Avioli, P. Mudge, R. Sanderson, **Guided wave inspection potential of defects in rail**, *NDT&E International*, Vol. 37, pp. 153-161, 2004.
178. T. R. Hay, J. L. Rose, **Guided wave testing optimization**, *Material Evaluation – American Society for Nondestructive Testing*, Vol. 60(10), pp. 1239-1252, 2002.
179. P. Cawley, M. J. S. Lowe, D. N. Alleyne, B. Pavlakovic, P. Wilcox, **Practical long range guided wave testing: applications for pipes and rail**, *Material Evaluation – American Society for Nondestructive Testing*, Vol. 61(1), pp. 66-74, 2002.
180. G. W. Roberts, X. Meng, E. Cosser, A. H. Dodson, A. Morris, M. Meo, **A remote bridge health monitoring system using computational simulation and single frequency GPS data**, *Proceedings of the 16th International Technical Meeting of the Satellite Division of the Institute of Navigation*, Portland, Oregon, USA, September 2003.

181. G. W. Roberts, X. Meng, E. Cosser, A. H. Dodson, A. Morris, M. Meo, **A Remote Bridge Health Monitoring System Using Computational Simulation and GPS Sensor Data. Presented at the Deformation Measurements and Analysis**, 11th International *Symposium on Deformation Measurements, International Federation of Surveyors (FIG), Commission 6 - Engineering Surveys, Working Group 6.1*, Santorini, Greece, May 2003.
182. H. Grafe, **Model Updating of Large Structural Dynamics Models Using Measured Response Functions**, *Imperial College of Science, Technology and Medecine*, Ph. D Dissertation, 1998.
183. A. Teughels, G. De Roeck, **Structural damage identification of the highway bridge Z24 by FE model updating**, *Journal of Sound and Vibration*, Vol. 278, pp. 589-610, 2004.
184. A. Teughels, J. Maeck, G. De Roeck, **Damage assessment by FE model updating using damage functions**, *Computers and Structures*, Vol. 80, pp. 1869-1979, 2002.
185. S. S. Law, T. H. T. Chan, D. Wu, **Super-Element With Semi-Rigid Joints In Model Updating**, *Journal of Sound and Vibration*, Vol. 239(1), pp. 19-39, 2001.
186. Y. Xia, H. Hao, **Measurement selection for vibration-based structural damage identification**, *Journal of Sound and Vibration*, Vol. 236(1), pp. 89-104, 2000.
187. J. R. Wu, Q. S. Li, **Finite element model updating for a high-rise structure based on ambient vibration measurements**, *Engineering Structures*, Vol. 26, pp. 979-990, 2004.
188. S. J. Guo, **Improvement of a tail-plane structural model using vibration test data**, *Journal of Sound and Vibration*, Vol. 256(4), pp. 647-663, 2002.
189. S. S. Law, T. H. T. Chan, D. Wu, **Efficient numerical model for the damage detection of large scale structures**, *Engineering Structures*, Vol. 23, pp. 436-451, 2001.
190. K. Jones, J. Turcotte, **Finite element model updating using antiresonant frequencies**, *Journal of Sound and Vibration*, Vol. 252(4), pp. 717-727, 2002.
194. D. F. Cannon, K. –O. Edel, S. L. Grassie, K. Sawley, **Rail defects: an Overview**, *Fatigue & Fracture of Engineering Materials & Structures*, Vol. 26, pp. 865-887, 2003.
195. J. R. Lundgren, D. F. Cannon, P. Zuber, **An international cooperative research approach for rail defect risk management**, *7th International Heavy Haul Association Conference*, Brisbane, Australia, 2001.
196. V. V. Murav'ev, E. V. Boyarkin, **Nondestructive Testing of the Structural-Mechanical State of Currently Produced Rails on the Basis of the Ultrasonic Wave Velocity**, *Russian Journal of Nondestructive Testing*, Vol. 39(3), pp. 24-33, 2003.
197. K. Abbaszadeh, M. Rahimian, H. A. Toliyat, L. E. Olson, **Rails defect diagnosis using wavelet packet decomposition**, *Industry Applications, IEEE Transactions on*, Vol. 39(5), Sept.-Oct. 2003.
198. B. D. Jeffrey, M. L. Peterson, **Assessment of rail flaw inspection data**, *Mountain-Plains Consortium*, Report N. MPC-99-106, August 1999, www.ndsu.nodak.edu/ndsu/ugpti/MPC_Pubs/pdf/MPC99-106.pdf.
199. E. G. Vadillo, J. A. Tarrago, G. G. Zubiaurre. C. A. Duque, **Effect of sleeper distance on rail corrugation**, *Wear*, 217, pp. 140-146, 1998.

200. D. T. Eadie, J. Kalousek, K. C. Chiddick, **The role of high positive friction (HPF) modifier in the control of short pitch corrugation and related phenomena**, *Contact Mechanics 2000 Conference*, in Tokyo, July 2000, http://www.kelsan.com/007_publications.html.
201. S. Mueller, **A linear wheel-rail model to investigate stability and corrugation on straight track**, *Wear*, 243, pp. 122-132, 2000.
202. A. Bohmer, T. Klimpel, **Plastic deformation of corrugated rails – a numerical approach using material data of rail steel**, *Wear*, Vol. 253, pp. 150-161, 2002.
203. D. F. Cannon, H. Pradier, **Rail rolling contact fatigue research by the European Rail Research Institute**, *Wear*, 191, pp. 1-13, 1996.
204. S. Grassie, P. Nilsson, K. Bjurstrom, A. Frick, L. G. Hansson, **Alleviation of rolling contact fatigue on Sweden's heavy haul railway**, *Wear*, Vol. 253, pp. 42-53, 2002.
205. D. Y. Jeong, **Progress in rail integrity research**, *Federal Railroad administration – Department of Transportation*, Report DOT/FRA/ORD-01/18, Oct. 2001.
206. R. Clark, **Rail flaw detection: overview and need for future developments**, *NDT&E International*, Vol. 37, pp. 111-118, 2004.
207. L. Oukhellou, P. Aknin, J.-P. Perrin, **Dedicated sensor and classifier of rail head defects**, *Control Engineering Practice*, Vol. 7, pp. 57-61, 1999.
208. J. J. Marais, K. C. Mistry, **Rail integrity management by means of ultrasonic testing**, *Fatigue & Fracture of Engineering Materials & Structures*, Vol. 26, pp. 931-938, 2003.
209. A. A. Markov, D. A. Shpagin, M. N. Shilov, **Ultrasonic multichannel flaw detector for testing rails with signal recording**, *Russian Journal of Nondestructive Testing*, Vol. 39(2), pp. 105-114, 2003.
210. A. Mandelis, M. Munidasa, L. Nicolaides, **Laser infrared photothermal radiometric depth profilometry of steel and its potential in rail track evaluation**, *NDT&E International*, Vol. 32, pp. 437-443, 1999.
211. C. Mandriota, E. Stella, M. Nitti, N. Ancona, A. Distante, **Rail corrugation detection by Gabor filtering**, *Image Processing*, International Conference on, IEEE, Vol. 2, pp. 626 - 628, 7-10 Oct. 2001.
212. N. Takacs, G. Y. Posgay, L. Harasztosi, D. L. Beke, **Correlation between Barkhausen-noise and corrugation of railway rails**, *Journal of Material Science*, Vol. 37, pp. 3599-3601, 2002.
213. K. Bruzelius, D. Mba, **An initial investigation on the potential applicability of Acoustic Emission to rail track fault detection**, *NDT&E International*, article in press, 2004.
214. K.-J. Bathe, **Finite element procedures in engineering analysis**, *Prentice-Hall Inc.*, 1982.
215. R. D. Cook, D. S. Malkus, M. E. Plesha, **Concepts and applications of finite element analysis – 3rd Edition**, *John Wiley & Sons*, 1989.
216. F. Lanza di Scalea, J. McNamara, **Measuring high-frequency wave propagation in railroad tracks by joint time-frequency analysis**, *Journal of Sound and Vibration*, Vol. 273(3), pp. 637-651, 2004.

217. F. Lanza di Scalea, J. McNamara, **Ultrasonics NDE of railroad tracks: air-coupled cross-sectional inspection and long-range inspection,** *Insight*, Vol. 45(6), 2003.
218. P. Wilcox, M. Evans, B. Pavlskovic, D. Alleyne, K. Vine, P. Cawley, M. Lowe, **Guided wave testing of rail,** *Insight*, Vol. 45(6), 2003.
219. D. N. Alleyne, M. J. S. Lowe, P. Cawley, **The reflection of guided waves from circumferential notches in pipes,** *Journal of Applied Mechanics*, ASME, Vol. 65, September 1998.
220. H. Kwun, S. Y. Kim, G. M. Light, **The magnitostrictive sensor technology for long range guided wave testing and monitoring of structures,** *Material Evaluation*, January 2003.
221. J. Qu, L. J. Jacobs, **Guided circumferential waves and their applications in the characterizing cracks in annular components,** *Material Evaluation*, January 2003.
222. W-J Song, J. L. Rose, H. Whitesel, **An ultrasonic guided wave technique for damage testing in a ship hull,** *Material Evaluation*, January 2003.
223. Y. Ding, R. L. Reuben, J. A. Steel, **A new method for waveform analysis for estimating AE wave arrival times using wavelet decomposition,** *NDT&E International*, in press, 2004.
224. M. R. Spiegel, **Theory and problems of calculus of finite differences and difference equations,** *Schaum's Outline Series, McGraw-Hill*, 1971.
225. A.J. Morris, R. Vignjevic, **Consistent Finite Element Structural Analysis and Error Control,** *Computer Methods in Applied Mechanics and Engineering*, 140(1-2):87-108, 1997.
226. R. J. Guyan, **Reduction of stiffness and mass matrices,** *American Institute of Aeronautics and Astronautics Journal*, Vol. 3(2), pp 380, 1965.
227. X. Meng, G W Roberts, A H Dodson, M Andreotti, E Cosser, M Meo, **Development of a Prototype Remote Structural Heath Monitoring System (RSHMS),** *1st FIG International Symposium on Engineering Survey for Construction Works and Structural Engineering*, 28 June – 1 July 2004, the University of Nottingham.

APPENDIX A: CANTILEVER BEAM

A.1 Introduction

To compare the efficiency and the reliability of the OSP techniques illustrated in chapter 3 for structural HM, three criteria were used. The first criterion was based on the measure of the mean square error between the undamaged FE model and cubic spline interpolated mode shapes. The second analyses the effects of the damage locations on the optimal sensor placements selected by the different methodologies investigated. The last criterion placed sensor in locations in such a way that they provide reliable and sensitive information on the potential damage to the structural system. In other words, the OSP methodologies explored were used for a damage detection analysis and the results were compared, in order to identify which technique provided the best information to the Damage Detection (DD) algorithm used.

A comprehensive comparative analysis would involve the exploration of the OSP criteria, above mentioned, over a bunch of different types of structures using different target mode shape selection criteria and different residue functions. Unfortunately, such analysis was not carried out due to the significant run-time. Therefore, several reductions on the initial plan were carried out:

- The type of structure analyzed was a cantilever beam (see Figure A. 1).
- As target mode shape selection method, the minimum modal frequency criterion was used, resulting in the selection of the first 10 mode shapes of the cantilever beam.
- The number of sensor was fixed to 10.

- The DD residue function used was the COMAC_MAC_ReF minimised by the Large-Scale Optimisation (LSO) algorithm. This DD approach was selected because was believed to be the fastest between those developed.

Although the above restrictions, the comparison analysis showed efficiency in providing information on damage presence of the OSP methods studied. This allowed a first screening of the OSP techniques that, successively, were compared using real (suspended bridge, APPENDIX B) and/or more complex structures (plate like structures, APPENDIX C).

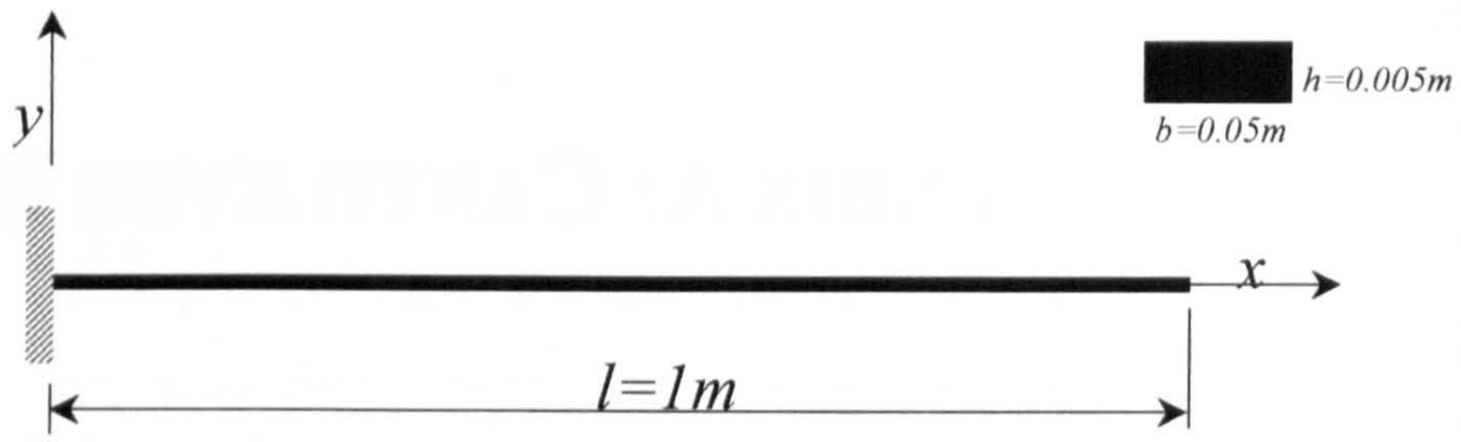

Figure A. 1 – Beam geometry and section properties

The FE mode shapes, necessary for this analysis, have been evaluated using a 90 finite elements model of the beam, built using the commercial FE code ANSYS.

A.2 Mode shape matching

The mode shape matching criterion assesses the capability of each OSP technique to capture the dynamic response of a structure by measuring the Mean Square Error (MSE) between the FE model mode shape (FE) and the mode shape obtained by a cubic spline interpolation (CS) of the displacements measured at the sensor locations selected. The MSE of each vibration mode i^{th} was normalised to its standard deviation σ_i to evaluate the Total MSE (TMSE, eq. A.1) given by the following expression:

$$MSE = \sum_{i=1}^{N} \frac{\frac{1}{\sigma_i^{\,2}} \sum_{j=1}^{n} \left(\left\{ {}_{CS}\phi^{\,i} \right\}_j - \left\{ {}_{FE}\phi^{\,i} \right\}_j \right)^2}{n} \tag{A.1}$$

The use of σ_i ensured that the contribution of every mode shapes has the same weight in the MSE computation.

A.2.1 Statistic OSP techniques

As mentioned above, the statistic OSP methods were divided into two different sub-classes, the Fisher information matrix and the variance based techniques.

As expected, the first sub-class presented well-spaced sensor locations (see Figure A. 2, EFI and KEM) than those selected by the variance based techniques (Figure A. 3).

The reasons of these differences lay on the design principles of the two approaches, the Fisher based techniques maximise simultaneously the independence and the strength of the signals acquired, while the later maximise only the signal strength. This is why the identified sensor locations are concentrated near the beam free edge. This last characteristic can be observed, although with less intensity, for the EFI-DPR technique (Figure A. 3), since the DPR correction to the EFI algorithm privileges high energy locations, undermining the independence of the acquired signals.

The Gr2 technique presented a set of well-spaced sensor locations due to its selection algorithm that does not pick up locations with the largest weighted variance distribution vector coefficients (as the Gr1), but those corresponding to local maxima (Figure A. 4).

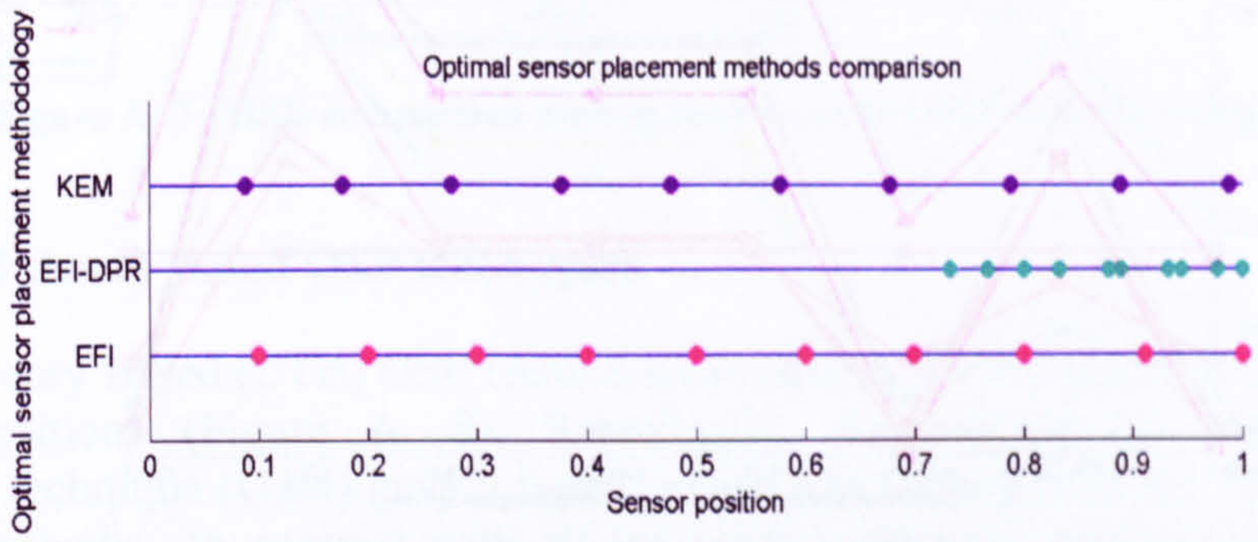

Figure A. 2– Comparison of the sensor locations selected from Fisher information matrix based OSP techniques.

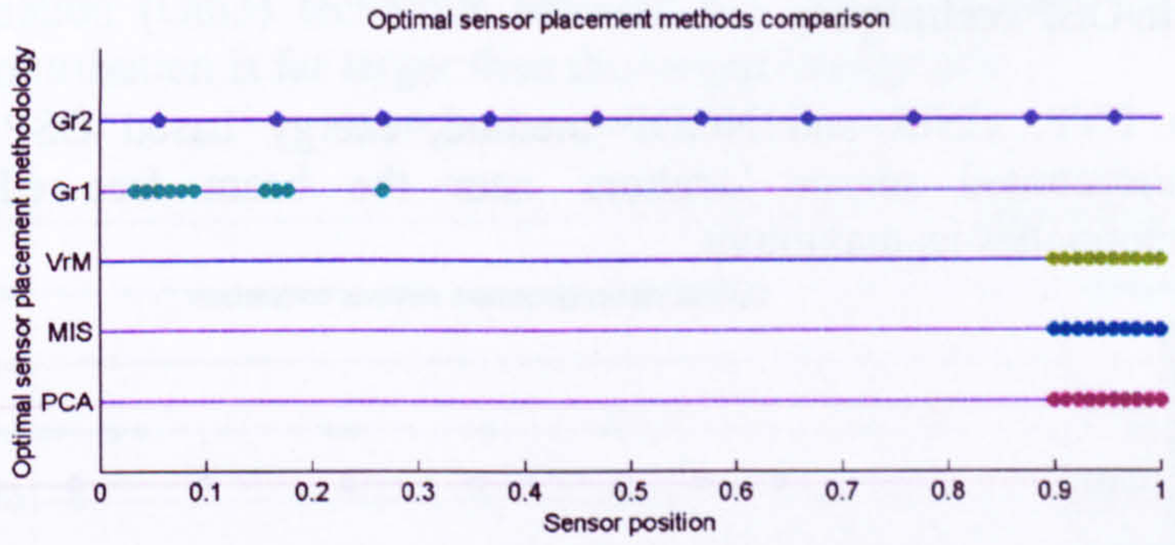

Figure A. 3 – Comparison of the sensor locations selected from variance based OSP techniques.

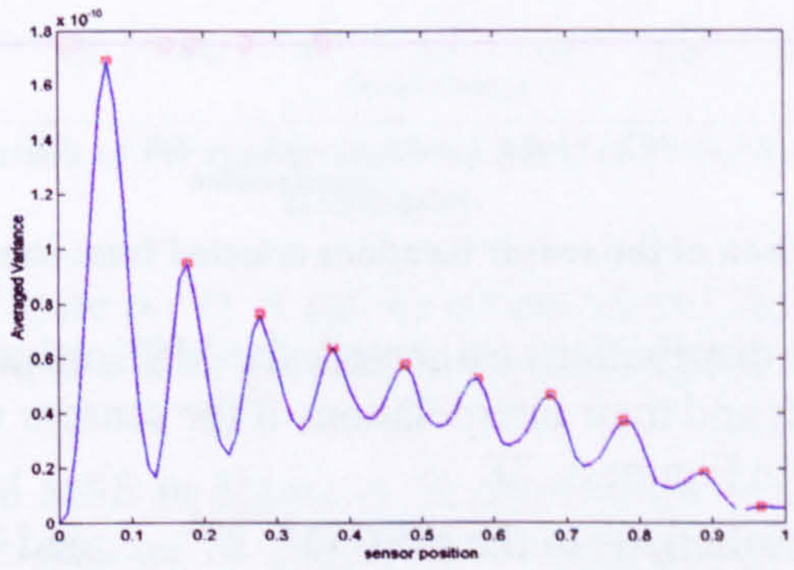

Figure A. 4 – Weighted Variance Distribution – Gr2

The contributions of the ten target mode shapes to the MSE, displayed in Figure A. 5, clearly indicate that the most important was the 10th, except for the EFI where the 1st MoS contribution was the largest. Moreover, the EFI method had the best matching of the target mode shapes selected (smallest value of MSE), after it, the KEM and Gr2 had values slightly larger.

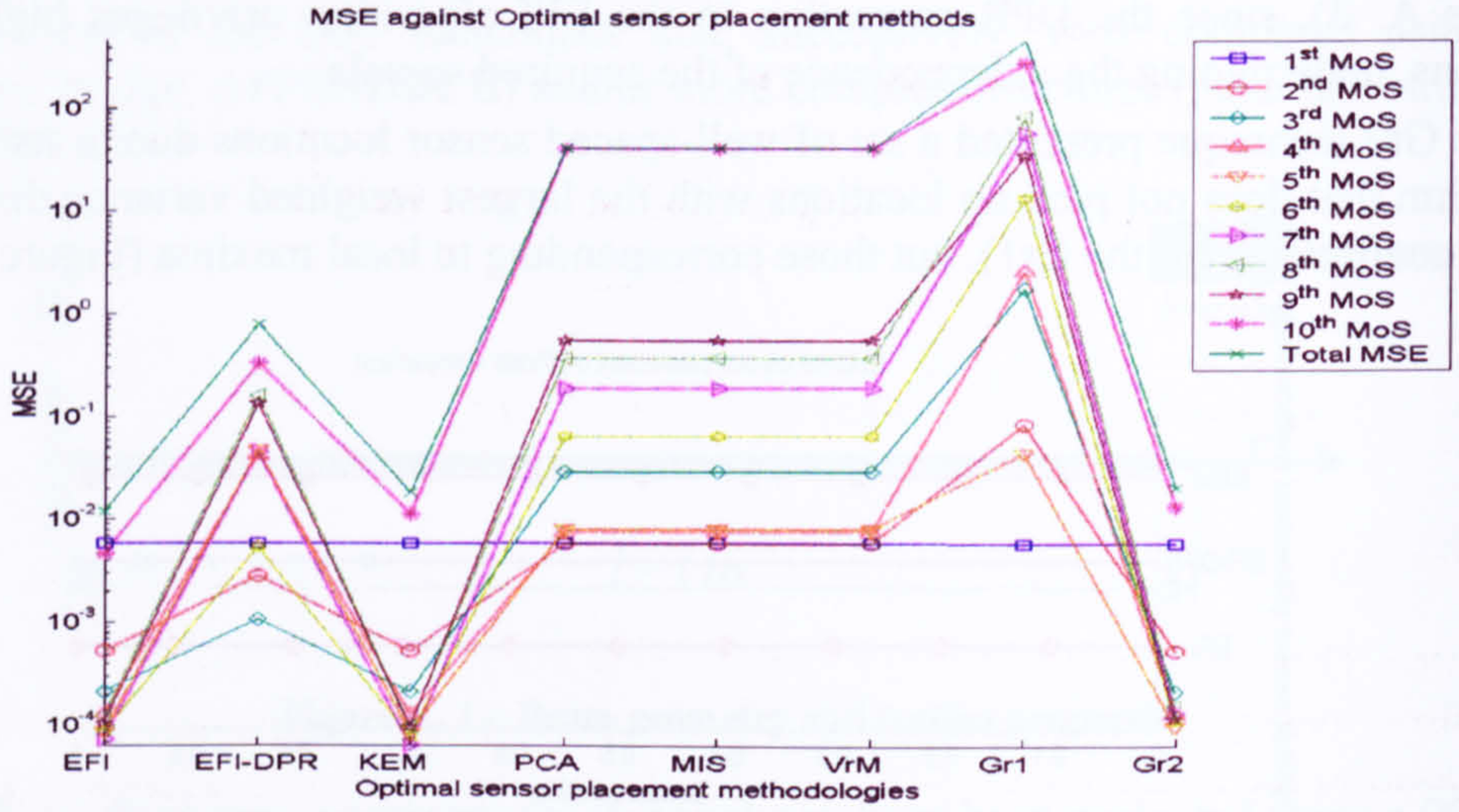

Figure A. 5 – MSE comparison among the statistic OSP methods studied.

A.2.2 Energetic OSP techniques

Apart from EVP, CNM and NODP method, energy based OSP (Figure A. 6) techniques concentrated sensor locations near the beam free edge, where the displacement energy has its maximum.

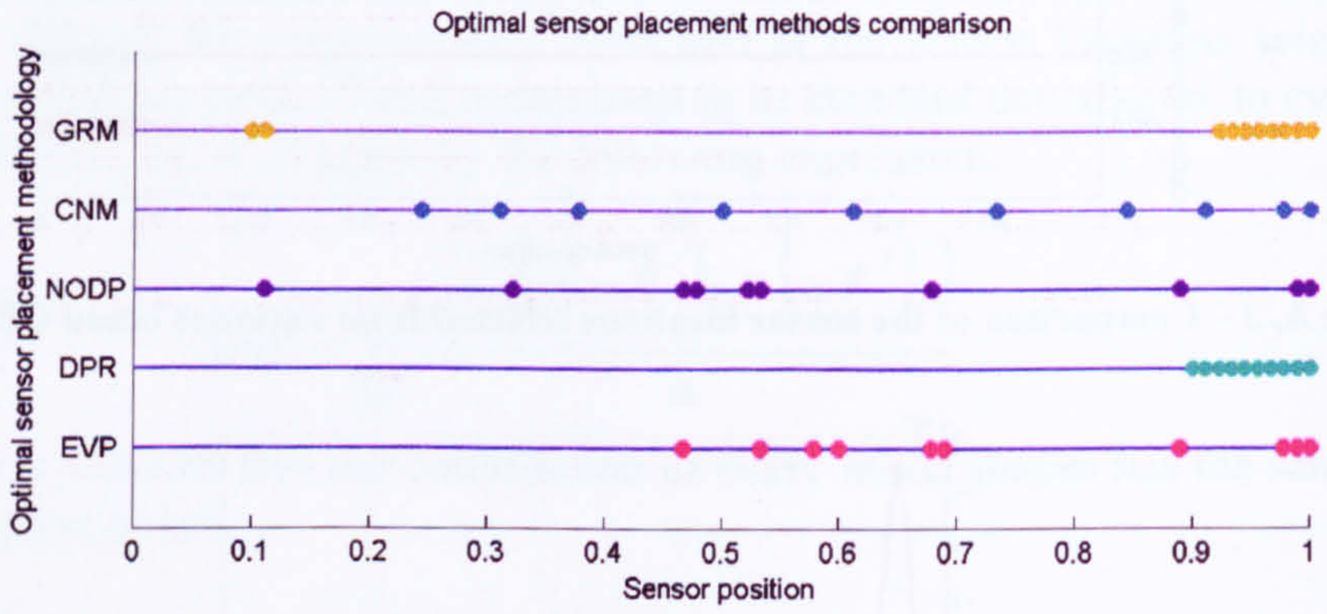

Figure A. 6 - Comparison of the sensor locations selected from energy based OSP techniques.

Observing the sensor distributions estimated, the MSE values indicated a good match between the mode shapes and their interpolations if the sensors were placed by the NODP method (see Total MSE in Figure A. 7).

Moreover, by the contributions to the MSE (1st, 2nd , … and 10th MoS, in fig. 9) of the single mode shapes is possible to see as the 10th mode shape had the largest contribution to MSE, as expected.

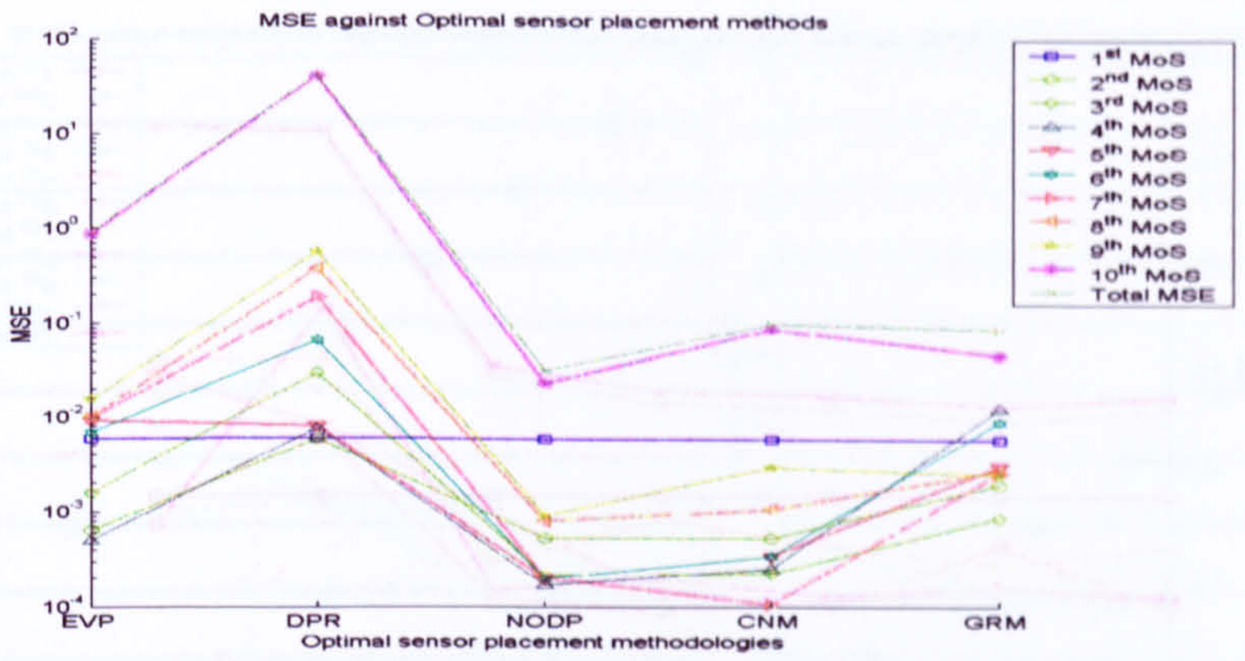

Figure A. 7– MSE comparison among the energetic OSP methods studied.

A.2.3 Control theory based OSP techniques

Control Theory Based (CTB) OSP techniques presented several possible combinations of sensor positions (Figure A. 8). Specifically, the independent elastic energy maximisation technique (Gm4) gave a better sensor distribution over the beam than the other CTB methods. In contrast with all the other techniques studied, privileged the positions in proximity of the clamped edge of the beam (Figure A. 1). Moreover, it must be observed (Figure A. 8) that the elastic energy maximisation (Gm1) and the system energy maximisation (Gm3) technique selected the same locations showing that the elastic energy contribution is far larger than the kinetic energy one.

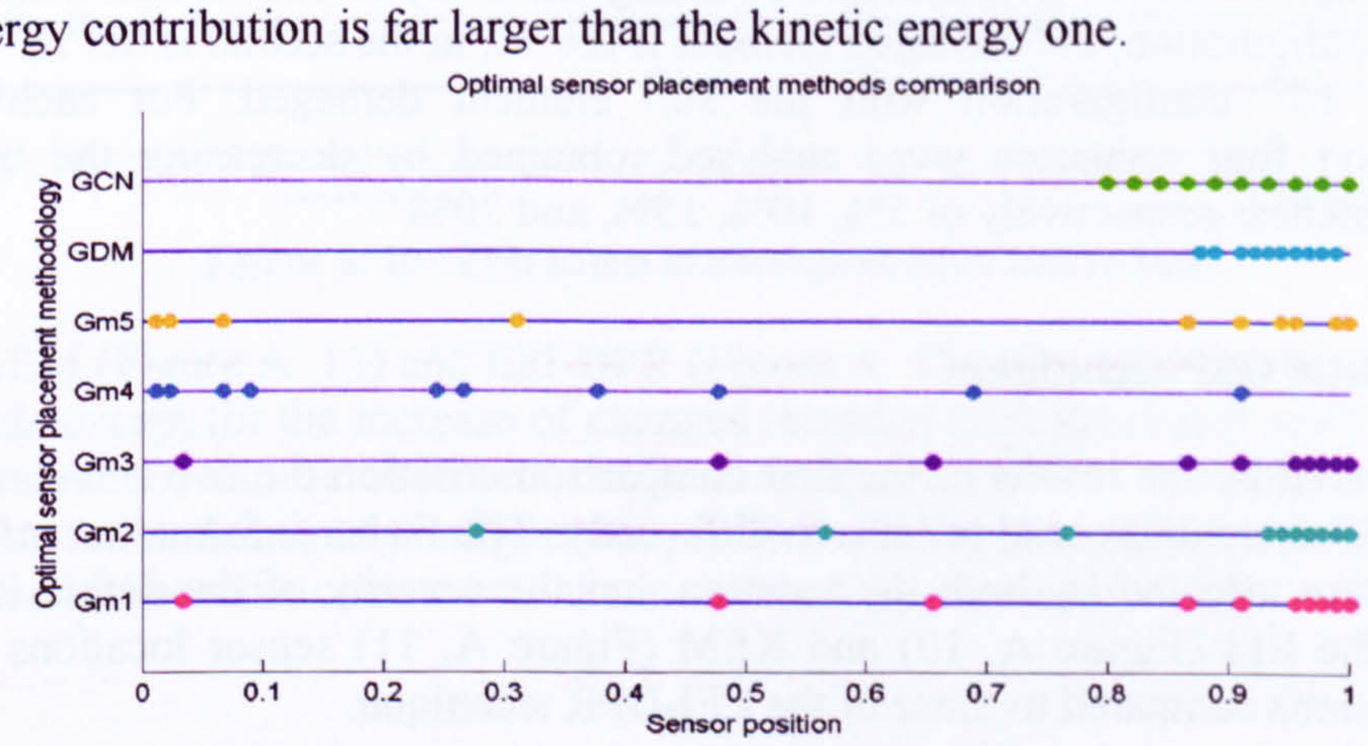

Figure A. 8 - Comparison of the sensor locations selected from control theory based OSP techniques.

Analysing the MSE (Figure A. 9), it can be observed that the contribution of the 10th mode shape to the mean square error resulted to be, once again, the largest, since had the most complex shape.

The global MSE (Total MSE in Figure A. 9) showed that the best matching occurred using the sensor locations selected by the kinetic energy maximisation approach (Gm2), although the differences with the other Grammian trace algorithm were not very large.

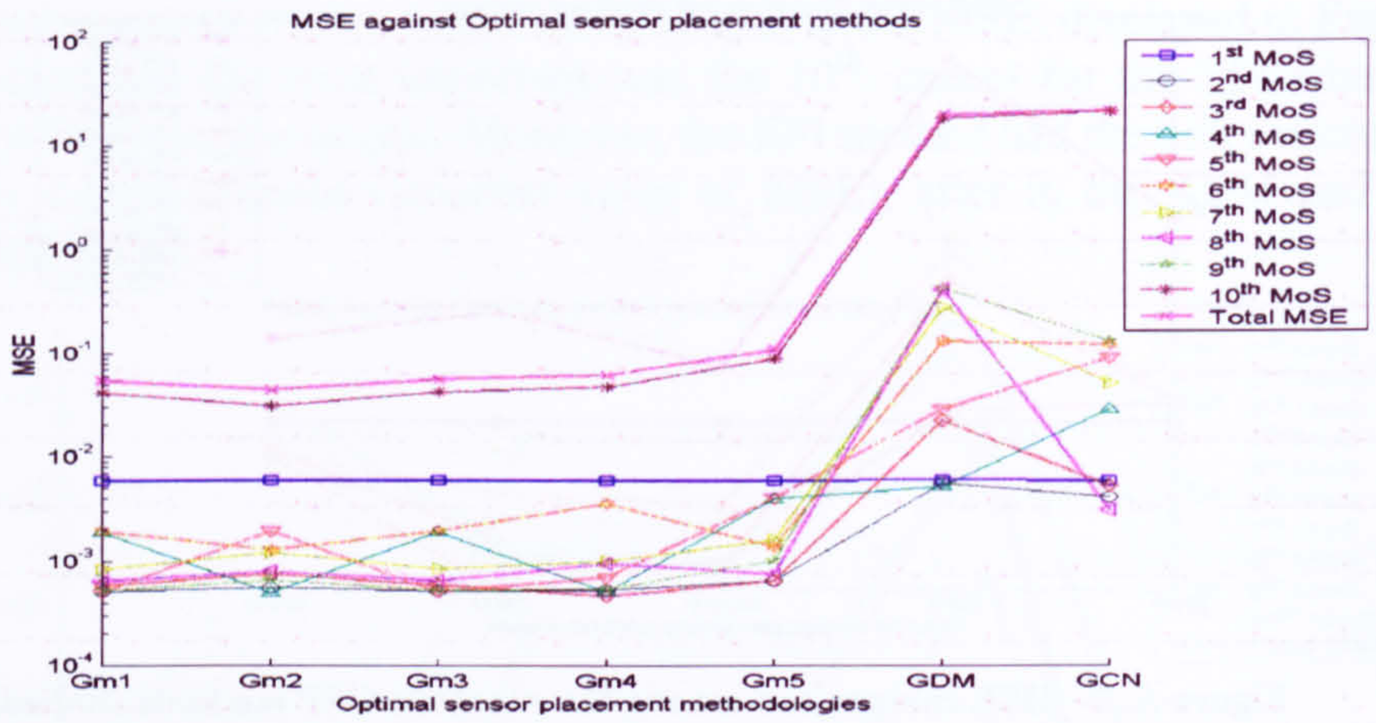

Figure A. 9 – MSE comparison among the CTB OSP methods studied.

A.3 Damage location effects on OSP techniques

At the aim to establish if the selection of the optimal sensor locations, using the techniques investigated above, was altered by damage location and severity, the target mode shapes and the other data required (mass and stiffness matrices) were evaluated for 10 damaged configurations of the beam with 4 different damage severities. The damaged configurations investigated were obtained decreasing the thickness of one element per time, starting from the 9th element, and selecting one every 9. This means that in the first damaged configuration, the damaged element is the 9th, in the second is the 18th and so on up to the 10th configuration with the 90th element damaged. For each damaged configuration four scenarios were analysed, obtained by decreasing the undamaged element thickness respectively of 5%, 10%, 15%, and 20%.

A.3.1 Statistic OSP techniques

As observed by the results of the first comparison criterion the two sub-classes of the statistic OSP techniques tend to behave differently. The Fisher information matrix based methods were affected by both the location and the severity of the defect introduced, although, the EFI (Figure A. 10) and KEM (Figure A. 11) sensor locations presented small variations compared to those of the EFI-DPR technique.

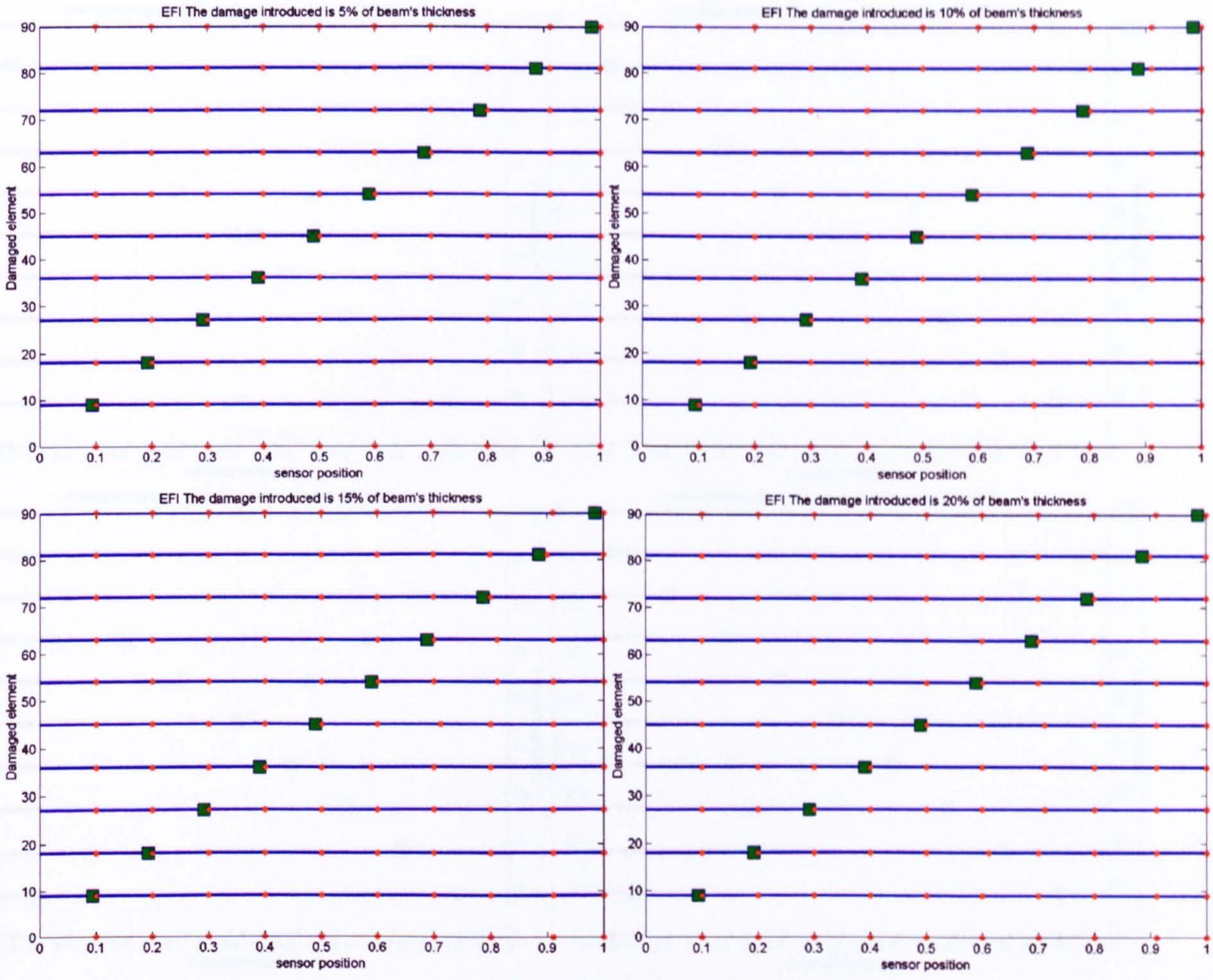

Figure A. 10– EFI: Effect of damage location and severity.

If for KEM (Figure A. 11) and EFI-DPR (Figure A. 12) method no particular remarks can be made except for the increase of changes recorded with the defect severity, for the EFI (Figure A. 10) can be observed also that the nearest sensor position to the defect location, for the undamaged configuration, shifted closing the gap between them. This phenomenon had become clearer with the increase of the damage severity.

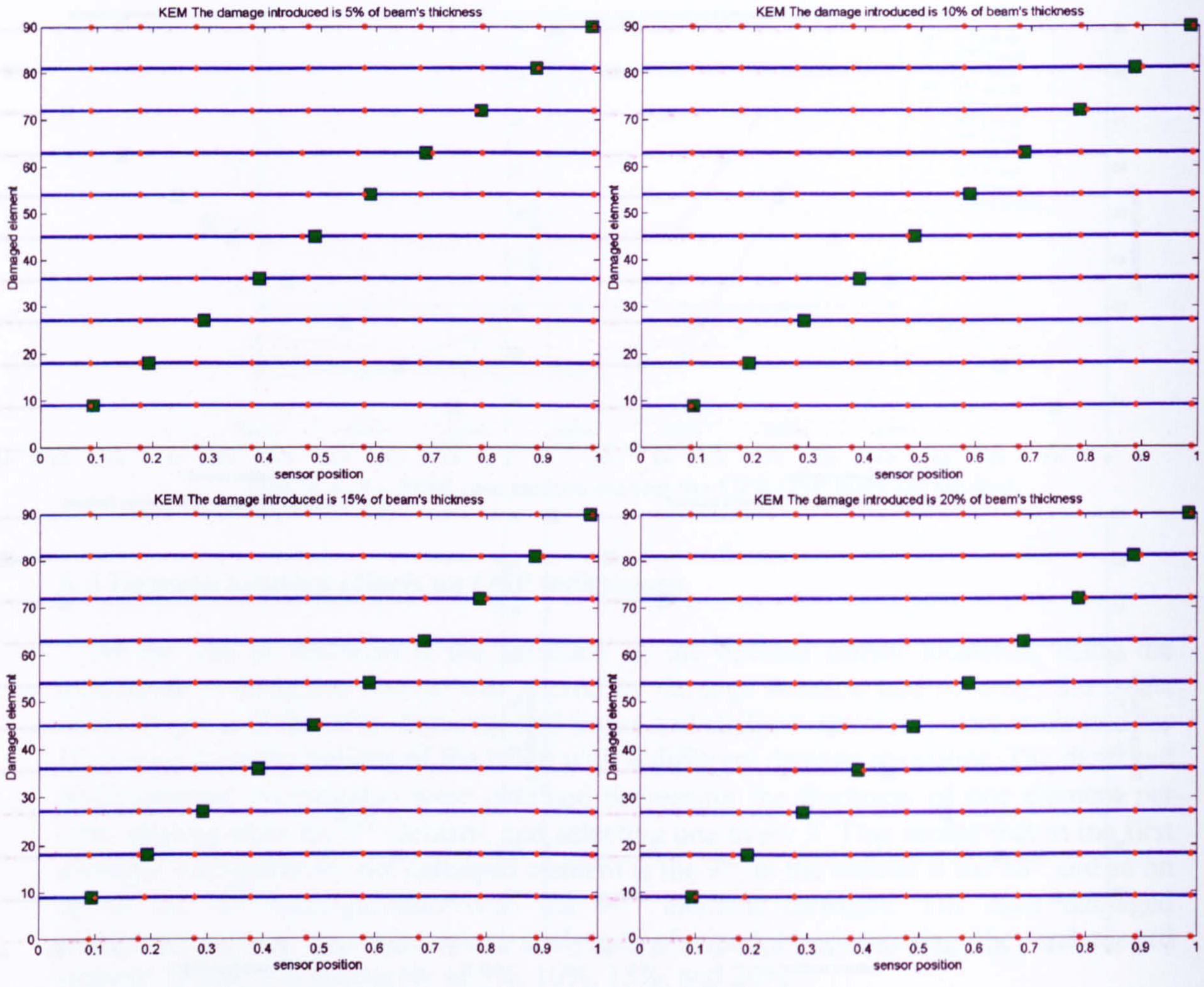

Figure A. 11– KEM: Effect of damage location and severity.

In contrast with the sensitivity to the damage presence showed by the Fisher information matrix techniques, the variance based methods resulted completely insensitive as, for instance, the PCA sensor locations in two of the four evaluated damage severity scenarios studied (Figure A. 13, the least and the most severe, 5% and 20%).

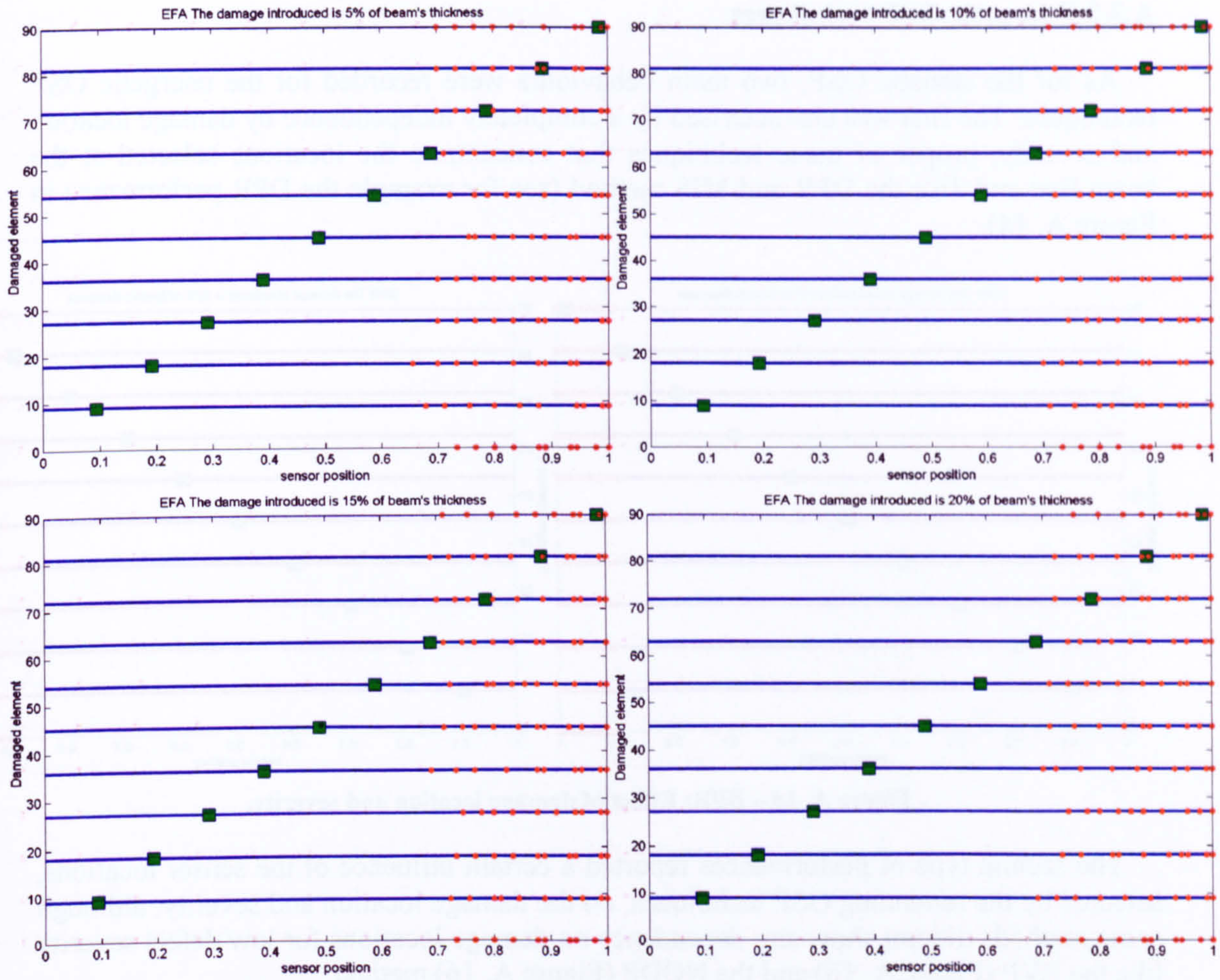

Figure A. 12 – EFI-DPR (EFA): Effect of damage location and severity.

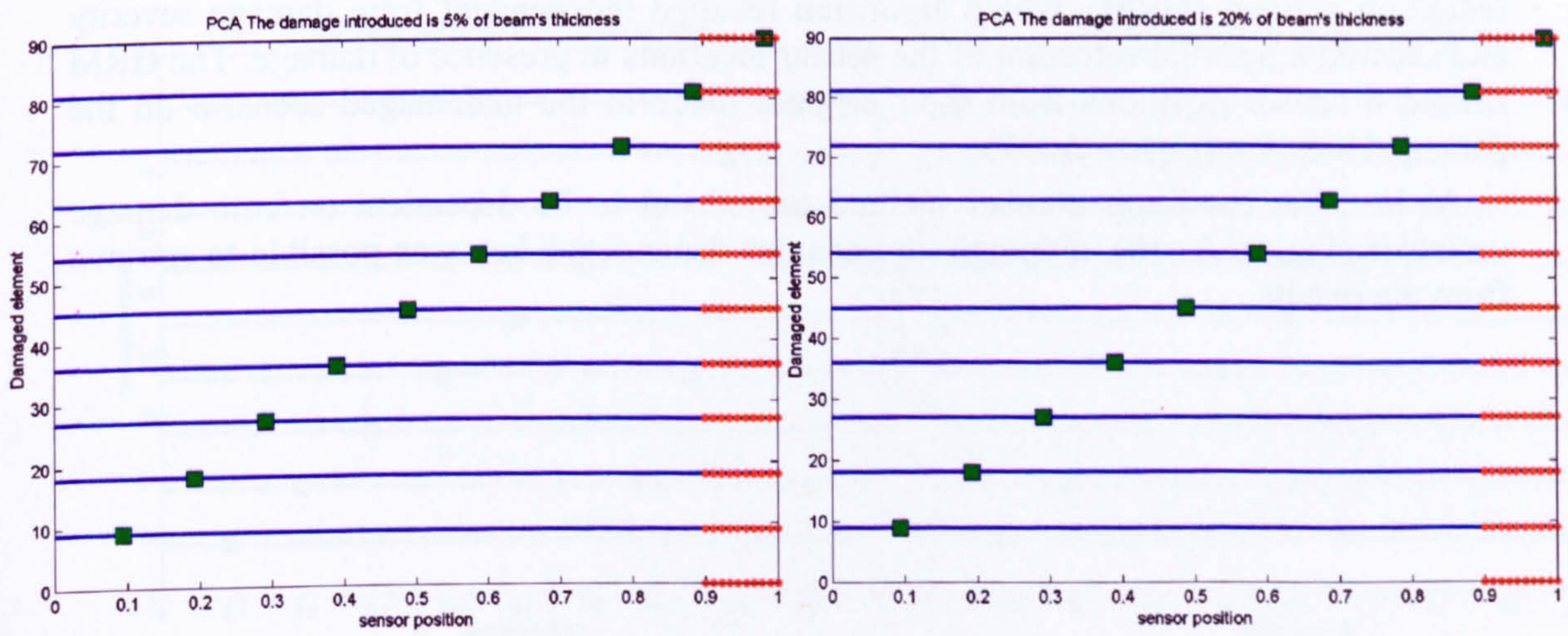

Figure A. 13 – PCA: Effect of damage location and severity.

A.3.2 Energetic OSP techniques

As for the statistic OSP, two main behaviours were recorded for the energetic OSP techniques. The first was characterised by a completely independence by damage location and severity, proper of those techniques that concentrate the locations selected at the beam free end, like the DPR and MIS method (see for example the DPR performance in Figure A. 14).

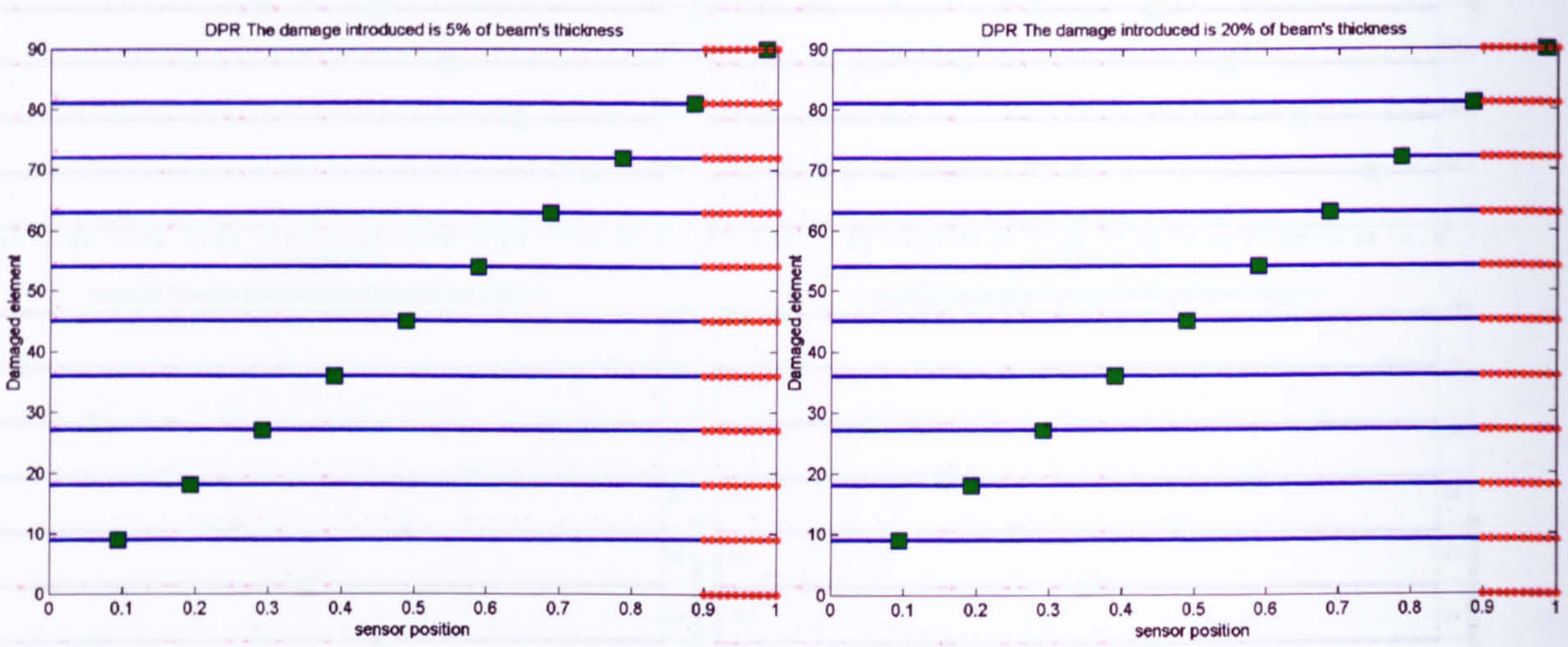

Figure A. 14 – DPR: Effect of damage location and severity.

The second type of performances reported a certain influence of the sensor locations, selected by the remaining OSP techniques, on the damage location and severity, although some methods did not show any dependence on damage locations for low defect severity like the EVP (Figure A. 15) and the NODP (Figure A. 16) method.

A completely different behaviour to those seen previously was given by the Guyan reduction method (GRM), which algorithm resulted independent from damage severity and showed a peculiar selection of the sensor locations in presence of damage. The GRM shifted 6 sensor positions from their original place in the undamaged scenario on the damaged location (Figure A. 17).

At last, the condition number method turned out to be dependent on both damage variables (Figure A. 18), although no apparent dependence law was possible to retrieve from the results.

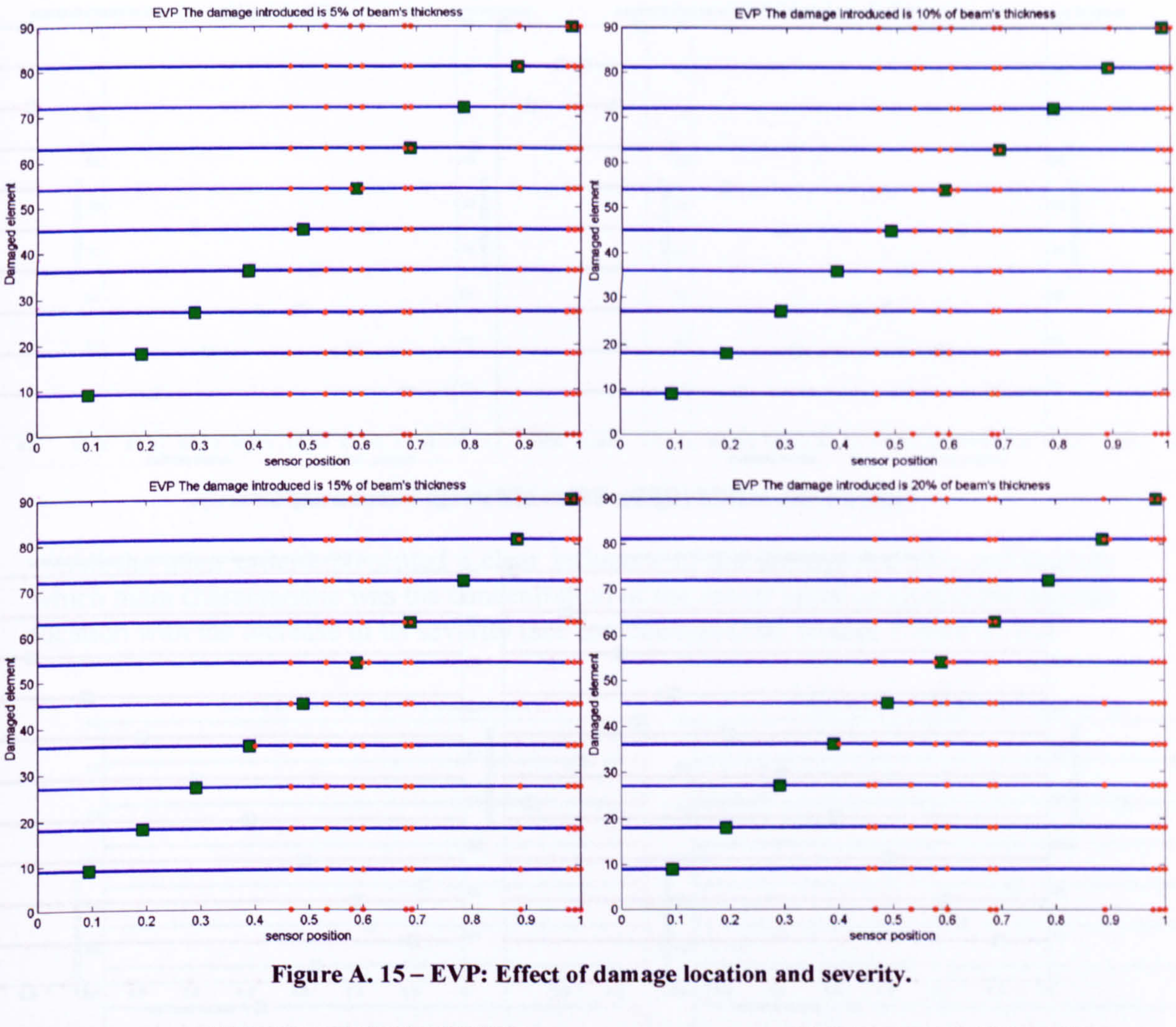

Figure A. 15 – EVP: Effect of damage location and severity.

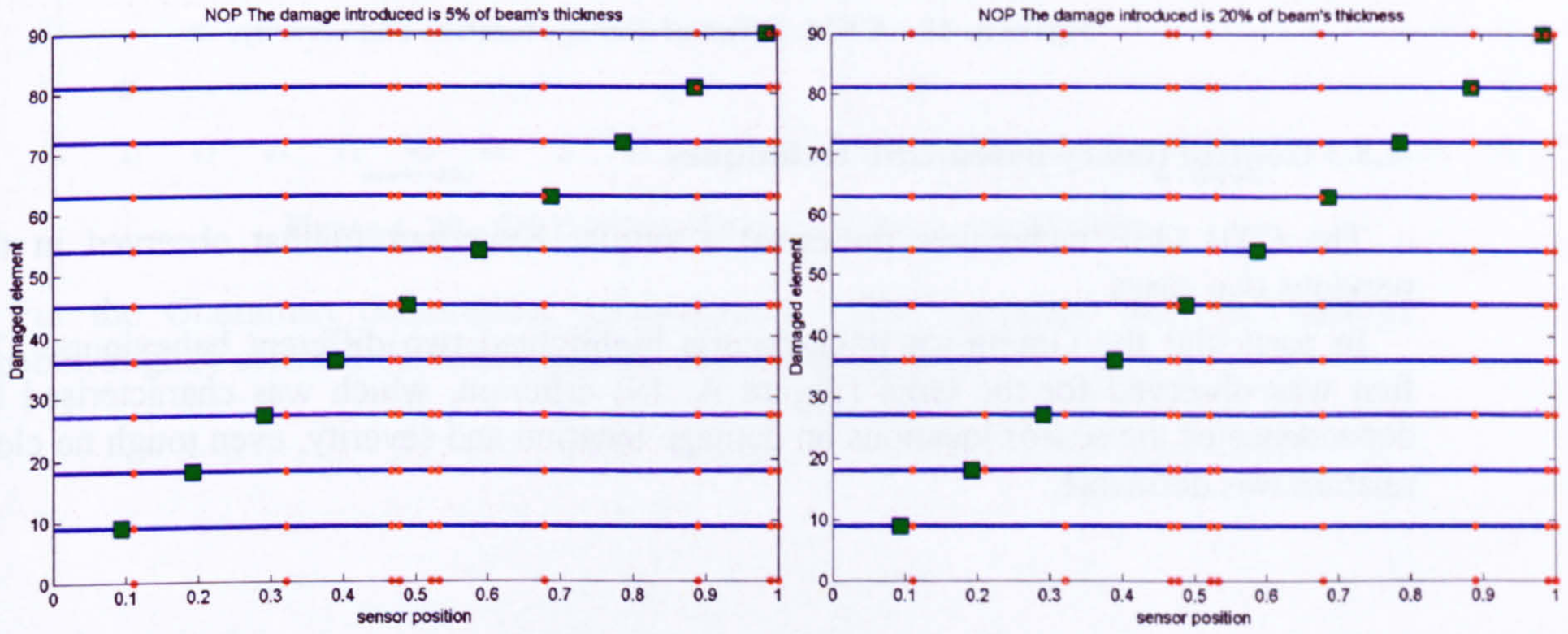

Figure A. 16 – NODP (NOP): Effect of damage location and severity.

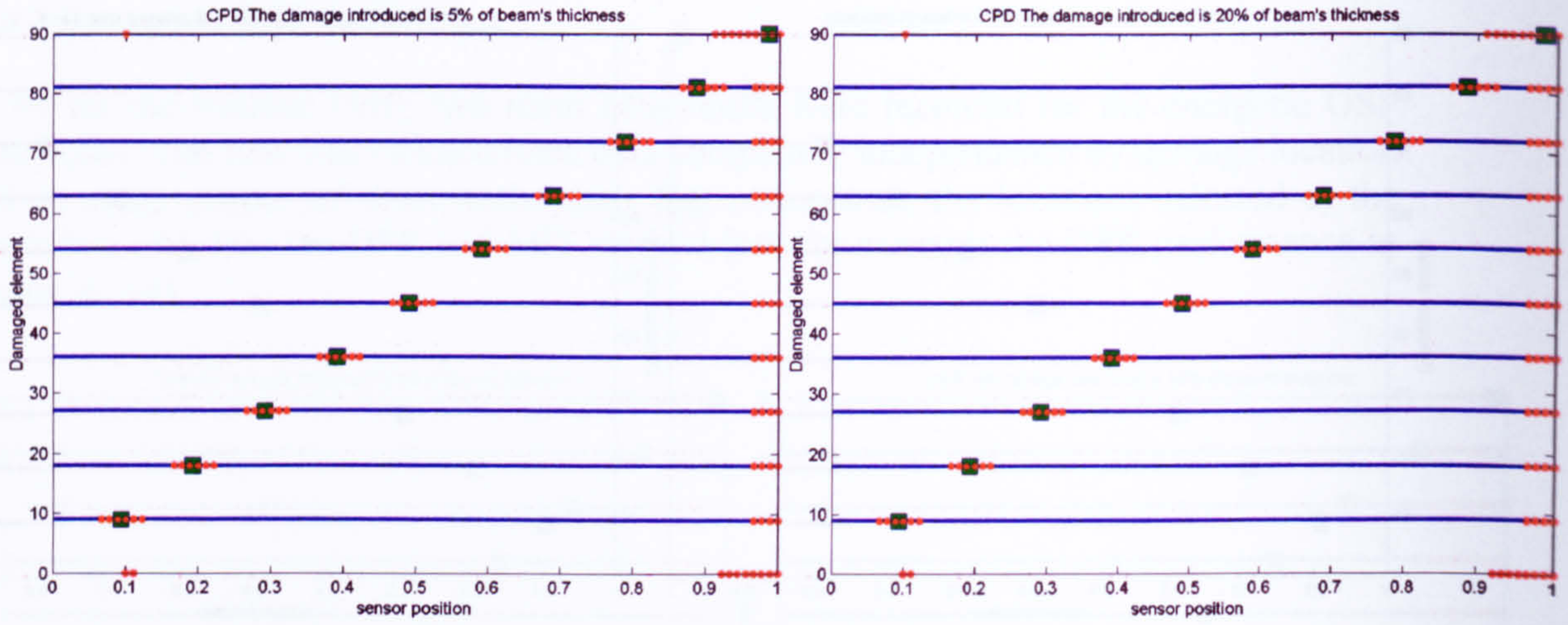

Figure A. 17 – GRM (CPD): Effect of damage location and severity.

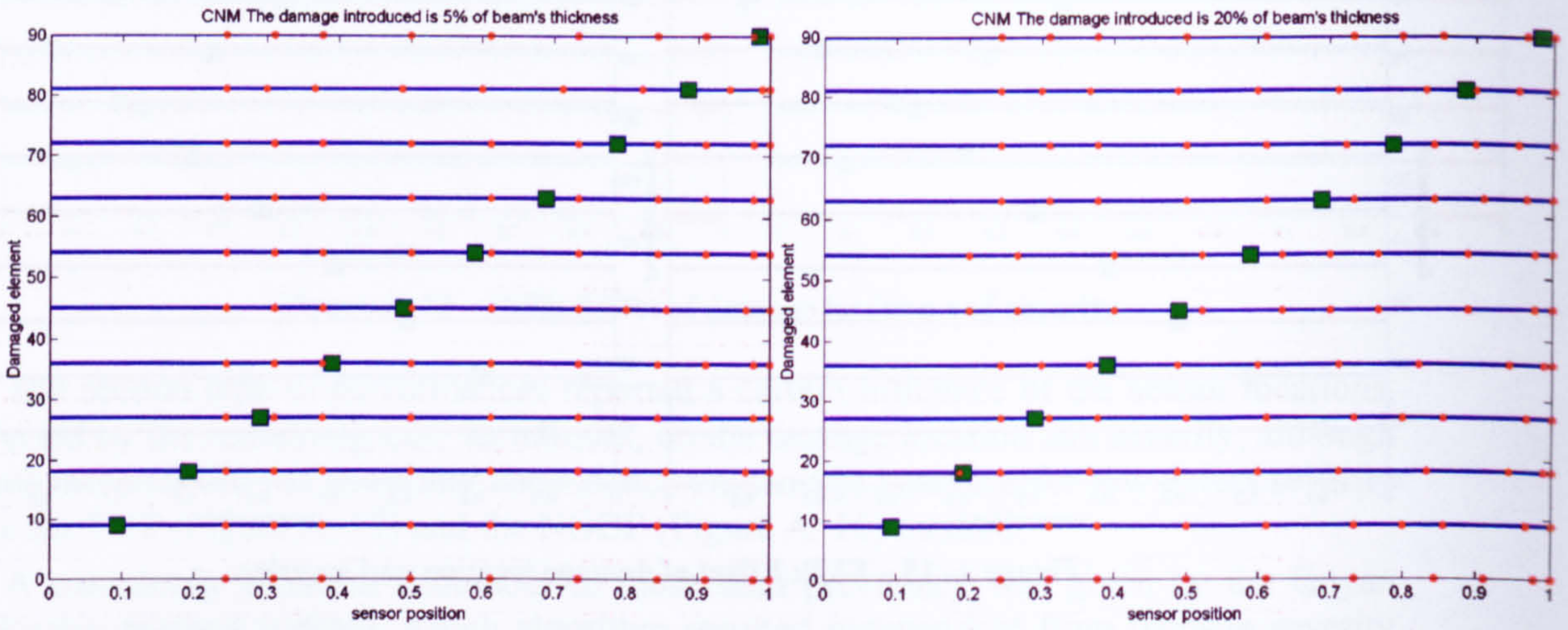

Figure A. 18 – CNM: Effect of damage location and severity.

A.3.3 Control theory based OSP techniques

The CTB OSP techniques presented a similar behaviour to that observed in the previous two cases.

In particular the Grammian trace criteria highlighted two different behaviours. The first was observed for the Gm4 (Figure A. 19) criterion, which was characterised by dependence of the sensor locations on damage location and severity, even tough no clear relation was definable.

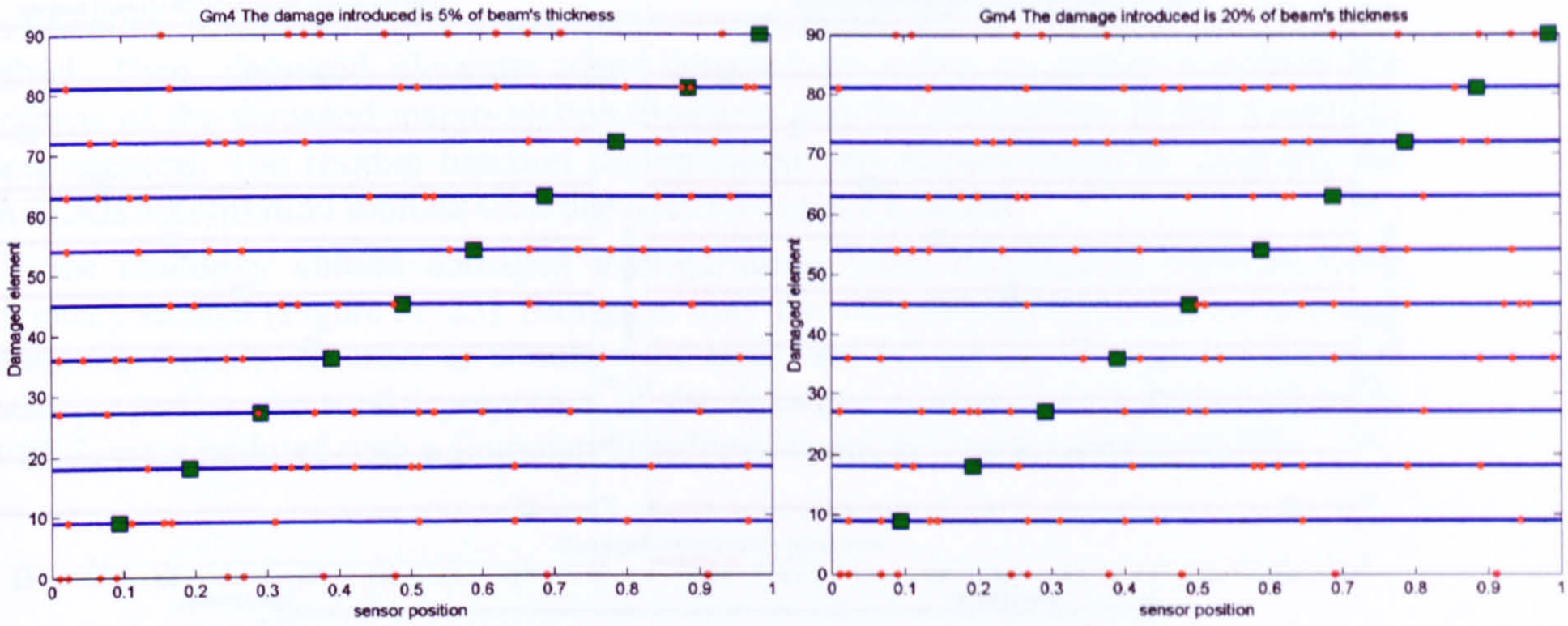

Figure A. 19 – Gm4: Effect of damage location and severity.

All the other criteria presented a clear influence of the damage location and severity which main characteristic was the concentration of the sensor location around the damage location with the increase of its severity (see for example Gm1 results, Figure A. 20).

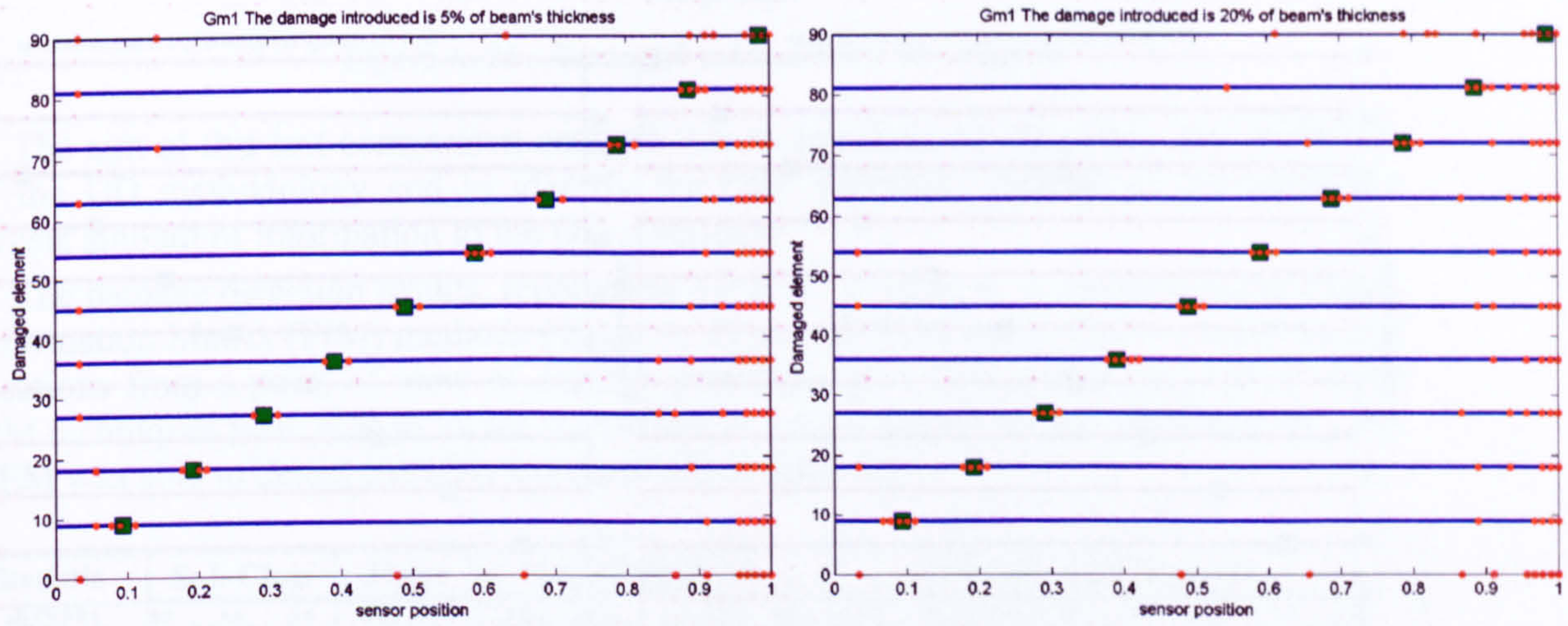

Figure A. 20 – Gm1: Effect of damage location and severity.

For the Grammian determinant maximisation (GDM) criterion only the damage location slightly affected the sensor placements (Figure A. 21)

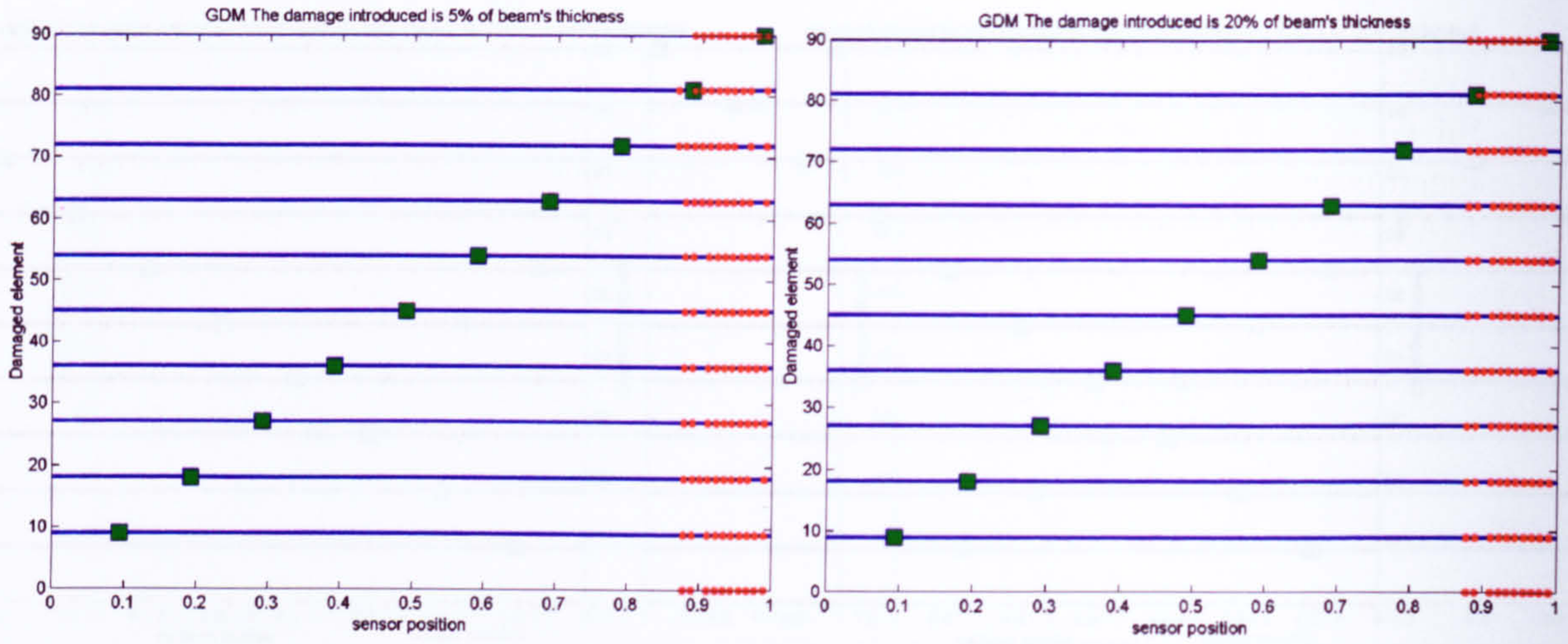

Figure A. 21 – GDM: Effect of damage location and severity.

The last CBT criterion (GCN) investigated did not show any variation to the damage location and severity (Figure A. 22), confirming the imperturbability to damage presence of those OSP techniques that concentrate the sensor positions on high energy structure sectors.

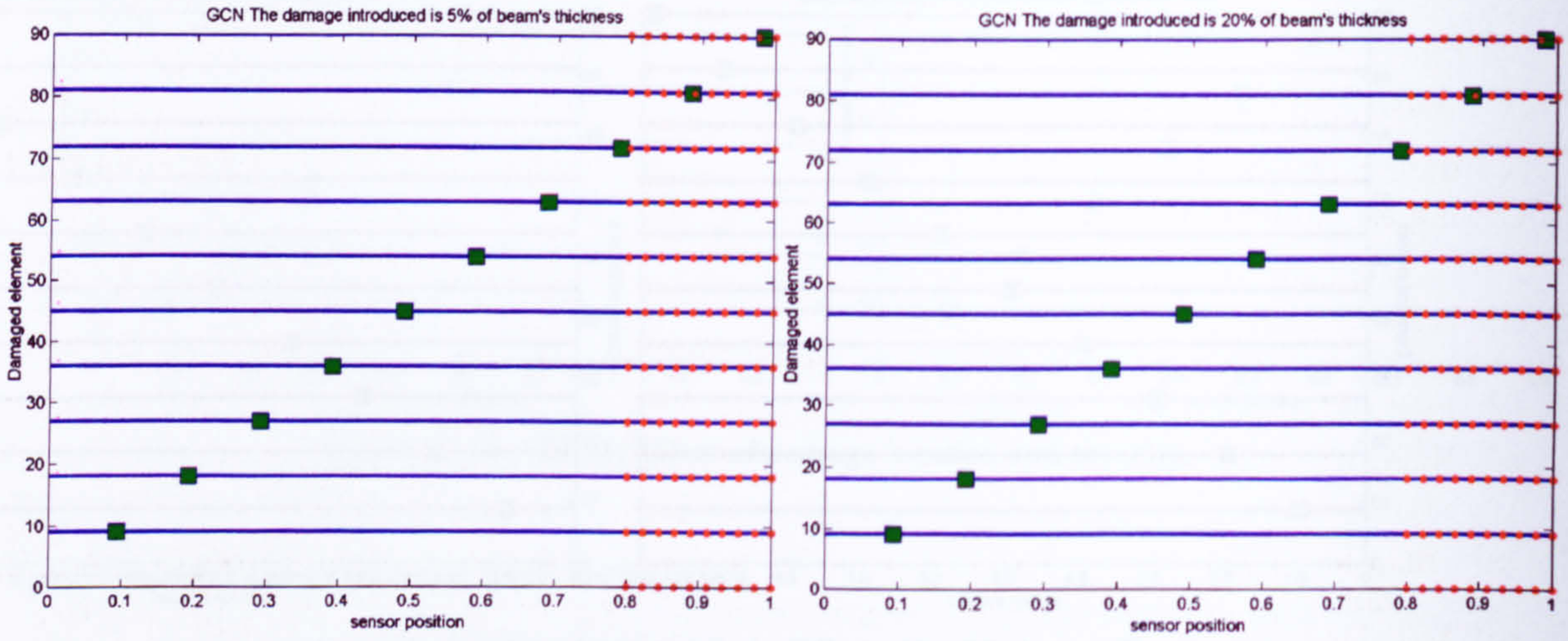

Figure A. 22 – GCN: Effect of damage location and severity.

A.4 Damage detection comparison criterion

The damage detection comparison criterion was based on the capability of the OSP to provide the necessary information for correct damage detection. The OSP techniques were calculate by using data relative to the undamaged structure.

The damage detection was carried out by using the Global-Local Damage Detection Optimisation (GLDDO) approach and by employing the COMAC MAC residue function (see chapter 2). The beam structure was divided into 9 macro-sections of 10 consecutive finite elements each, starting from the clamped beam edge to the free one. The

identification of the damaged macro-section constituted the first step of the GLDDO method. Then, damaged elements were detected by using as design variables the thickness of the damaged macro-section elements and the thicknesses of the remaining macro-sections. The residue function minimisation was accomplished by coupling the MATLAB optimisation toolbox with the ANSYS beam FE model.

Three randomly chosen damaged configurations were investigated between those previously studied (Figure A. 23). Moreover only the 10% damage severity scenario was considered. Finally, in order to simulate the error that affects experimentally extracted modal properties, the modal properties of the damaged configurations, estimated using ANSYS, were polluted with a Gaussian distributed noise, having a variance of 10%.

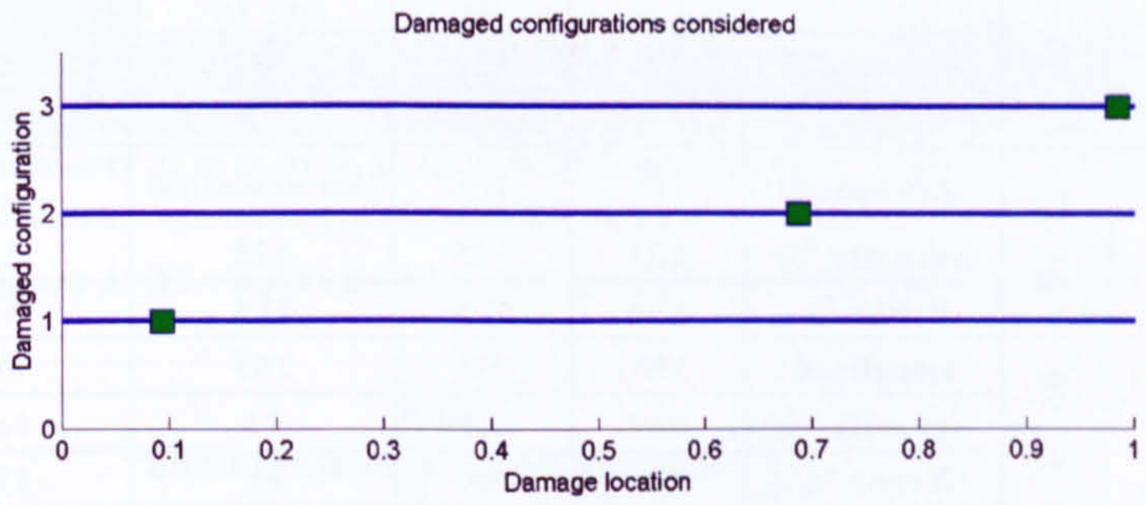

Figure A. 23 – Damaged configuration investigated

The aim of this last comparison analysis was to establish the efficiency and reliability of the DD methodology and to identify the OSP technique capable of providing the largest amount of information to the DD algorithm.

The damage detection results, reported in Table A. 1-Table A. 3, showed as the Fisher Information Matrix (FIM) methods (Table A. 1) provided the most effective set of sensor locations from a point of view of damage detection. Two (EFI and KEM) out of three FIM techniques were able to locate the correct damaged macro-section, although only the KEM was able to detect correctly every damaged location.

Statistic OSP Techniques		Sub-Class	*Fisher Inf. Mat. Methods*			*Variance based Methods*				
		Method	***EFI***	***EFI-DPR***	***KEM***	***PCA***	***MIS***	***VrM***	***Gr1***	***Gr2***
Damaged Configurations	***1st El. 9***	***Localised***	*Next Element (10)*	*Next Element (10)*	*YES*	*Next Element (10)*	*Next Element (10)*	*Next Element (10)*	*NO*	*Next Macro-section (El. 11)*
		Severity %	5.22	2.94	3.87	3.5	3.5	3.5	1.65	1.05
		Error %	47.8	70.6	61.3	65	65	65	83.5	89.5
	2nd El. 63	***Localised***	*YES*	*YES*	*YES*	*YES*	*YES*	*YES*	*YES*	*YES*
		Severity %	4.95	4.76	4.42	3.25	3.25	3.25	5.5	4.25
		Error %	50.5	52.4	55.8	67.5	67.5	67.5	45	57.5
	3rd El. 90	***Localised***	*YES*	*NO*	*YES*	*NO*	*NO*	*NO*	*NO*	*NO*
		Severity %	5.79	0.96	8.75	0.4	0.4	0.4	0.35	0.3
		Error %	42.1	90.4	12.5	96	96	96	96.5	97

Table A. 1– Statistic OSP techniques: damage detection results.

The variance based OSP techniques (Table A. 1) failed to identify the defect location of the third damaged configuration investigated, despite of the fact that the sensor locations selected by them were mostly concentrated on the damaged position.

Between the energetic OSP techniques (Table A. 2), only the EVP method was capable of identifying correctly all damaged macro-sections, even though, for the first damaged scenario explored, the most damaged element resulted to be the element number 10, next to the real one (9^{th}).

Energetic OSP Methods		Method	*EVP*	*DPR*	*NODP*	*CNM*	*GRM*
Damaged Configurations	*1st El. 9*	*Localised*	*Next Element (10)*	*Next Element (10)*	*Next Macro-section (El. 11)*	*Next Macro-section (El. 11)*	*NO*
		Severity %	1.21	3.52	0.81	1.39	1.42
		Error %	87.9	64.8	91.9	86.1	85.8
	2nd El. 63	*Localised*	*YES*	*YES*	*Next element (64)*	*Previous Element (62)*	*YES*
		Severity %	5.21	3.25	4.25	3.9	5.65
		Error %	47.9	67.5	57.5	61	43.5
	3rd El. 90	Localised	*YES*	*NO*	*YES*	*NO*	*NO*
		Severity %	4.49	0.4	5.5	1.65	4.12
		Error %	55.1	96	45	83.5	58.8

Table A. 2 - Energetic OSP techniques: damage detection results.

CTB OSP Techniques		Sub-Class	*Grammian Trace Matrix Methods*					*GDM*	*GCN*
		Method	*Gm1*	*Gm2*	*Gm3*	*Gm4*	*Gm5*		
Damaged Configurations	*1st El. 9*	*Localised*	*Next Element (10)*	*YES*	*Next Element (10)*	*NO*	*YES*	*Macro-section (El.7)*	*Previous Element (8)*
		Severity %	4.72	4.56	4.72	1.62	5.99	0.8	2.42
		Error %	52.8	54.4	52.8	83.8	40.1	92	75.8
	2nd El. 63	*Localised*	*YES*	*YES*	*YES*	*Next Element (64)*	*Next Element (64)*	*YES*	*YES*
		Severity %	4.22	4.41	4.22	4.95	4.75	1.78	1.56
		Error %	57.8	55.9	57.8	50.5	52.5	82.2	84.4
	3rd El. 90	Localised	*NO*	*NO*	*NO*	*NO*	*NO*	*NO*	*NO*
		Severity %	1.04	0.41	1.04	0.7	1.74	0.72	1.23
		Error %	89.6	95.9	89.6	93	82.6	92.8	87.7

Table A. 3 – Control Theory Based OSP techniques: damage detection results.

Finally, none of the CTB OSP methods (Table A. 3) was able to provide enough information to the DD algorithm in order to detect the third damage location. However, only the kinetic energy maximisation criterion (Gm2) was able to detect correctly the remaining damage locations.

Finally, although the damage location identification was carried out successfully using several sensor configurations, the damage severity was poorly predicted. Except for rare cases (for instance KEM for 3^{rd} damaged configuration, see Table A. 1), the error was over 50%. Moreover, the damage seemed being smeared around the damaged locations as can be seen by the element thickness distribution estimated using KEM optimal sensor

placements (Figure A. 24-Figure A. 26). Further analysis of these results were reported in §6.2.

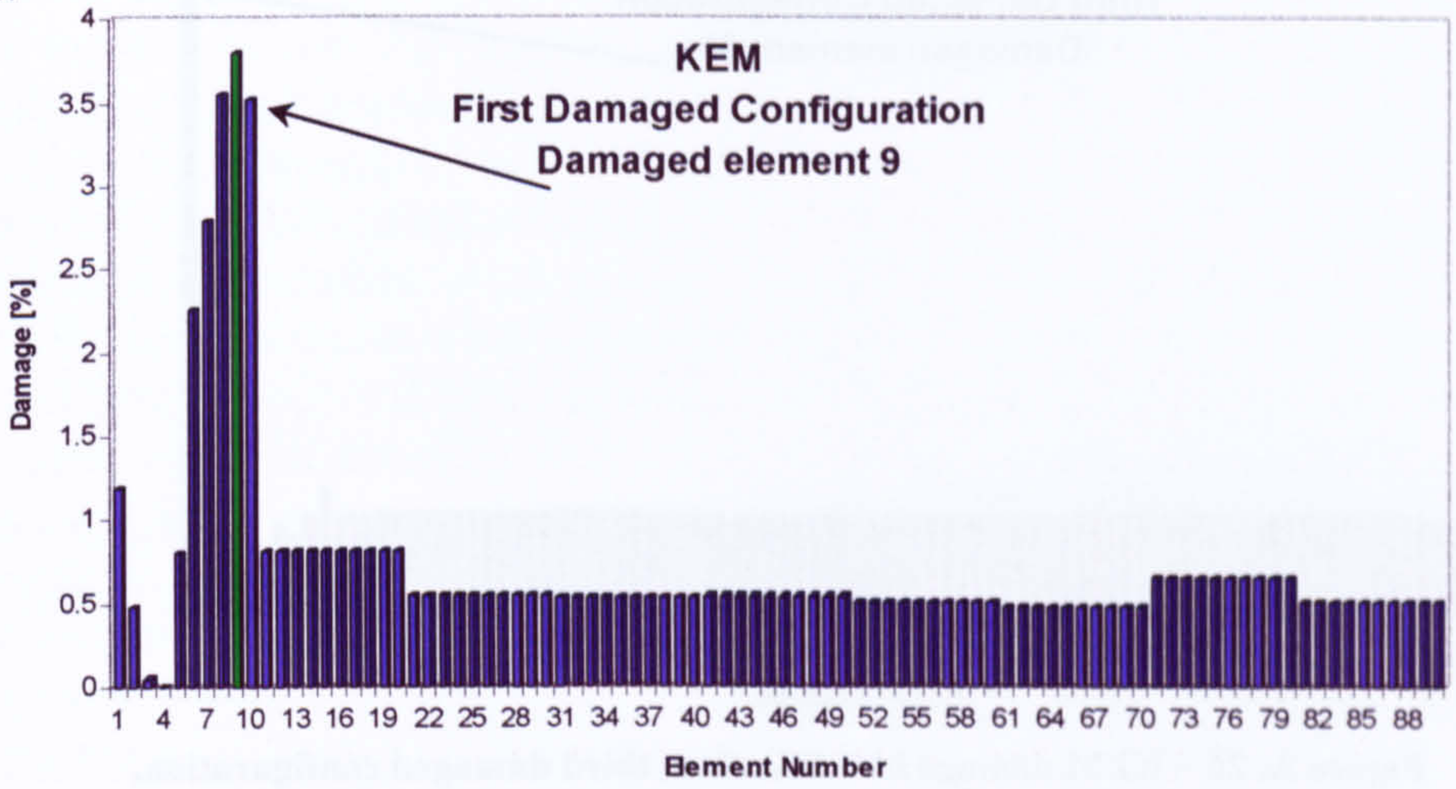

Figure A. 24 – KEM damage detection for the first fault investigated.

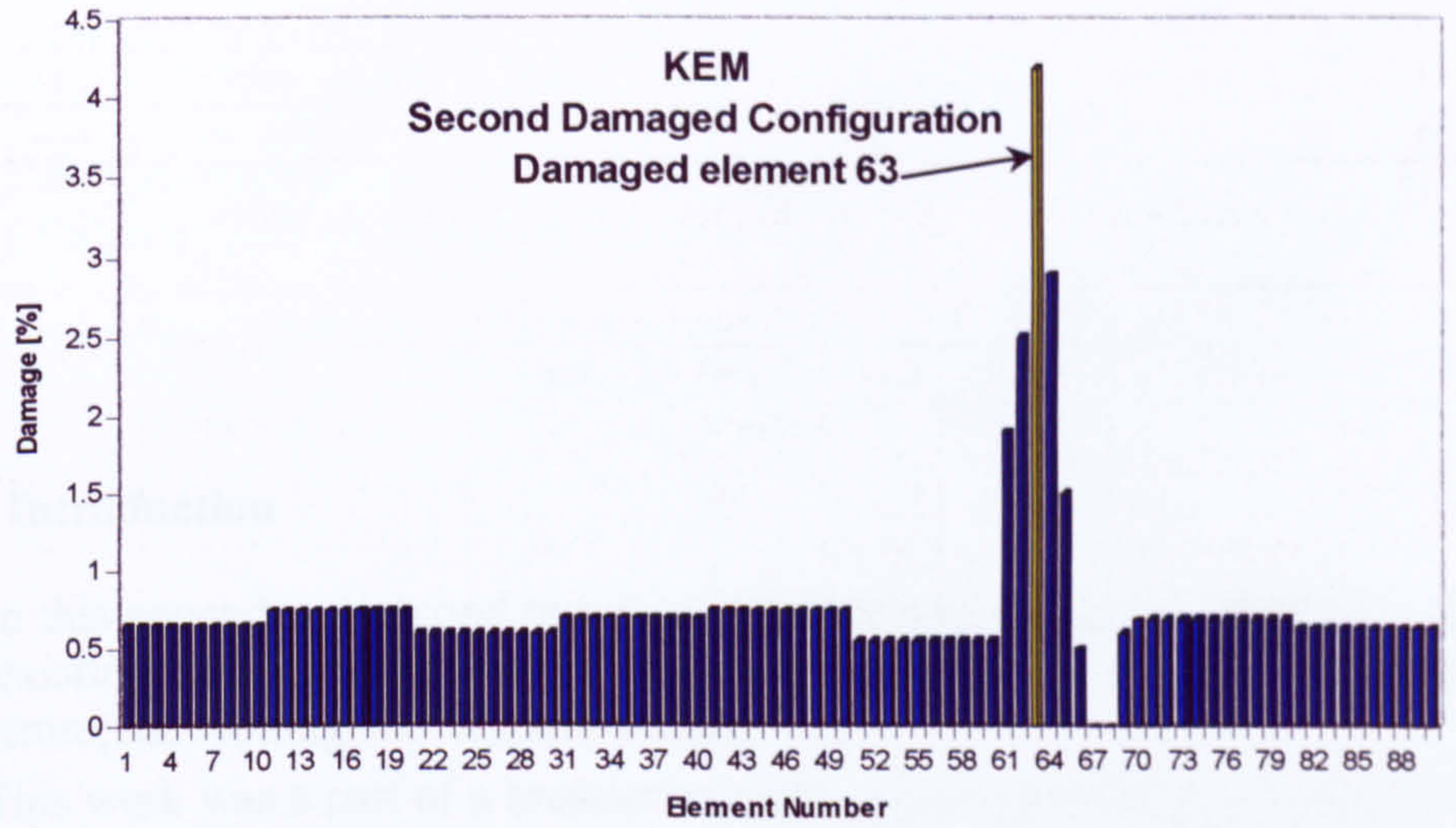

Figure A. 25 – KEM damage identification, second damaged configuration.

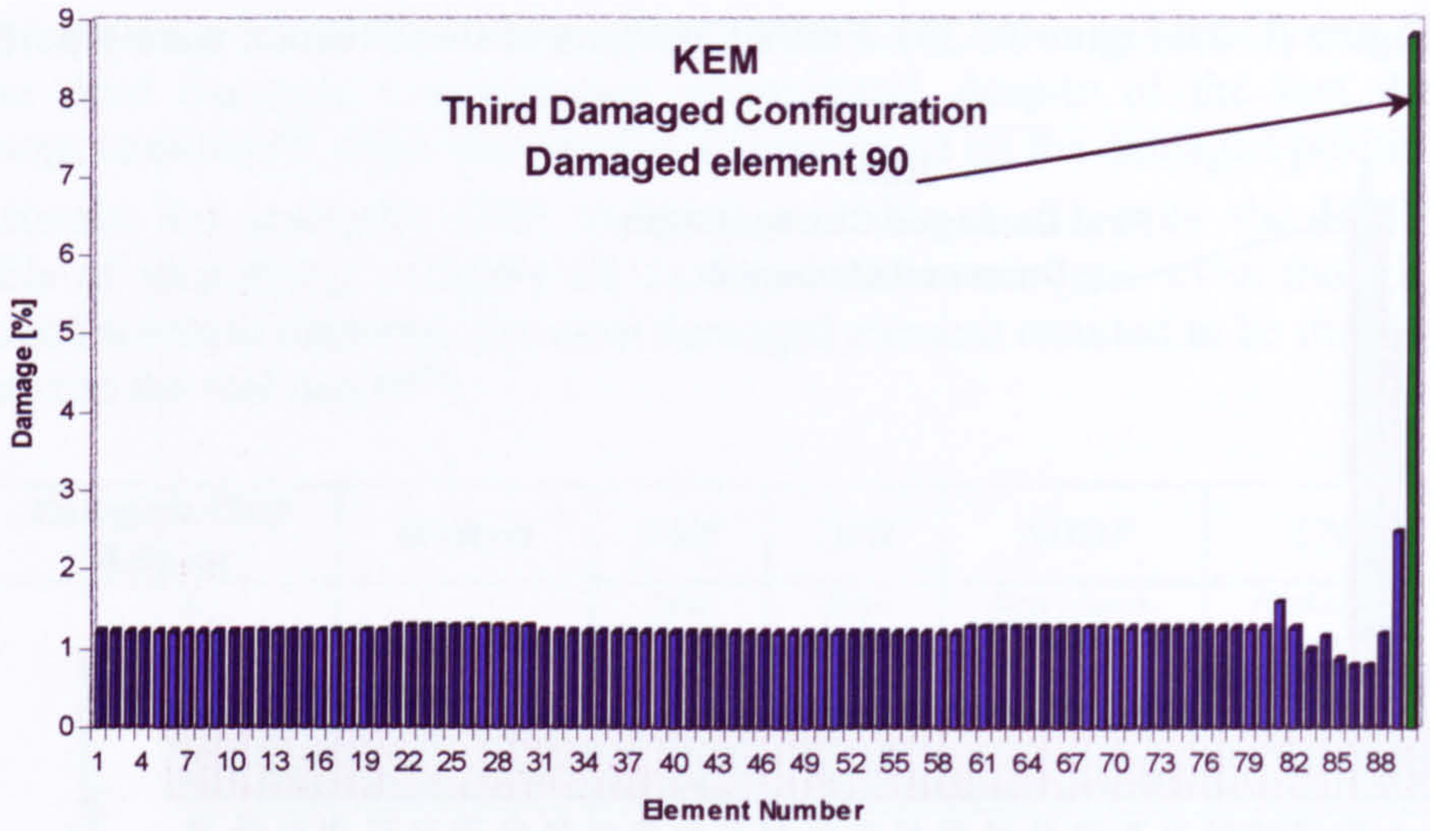

Figure A. 26 – KEM damage identification, third damaged configuration.

APPENDIX B: THE NOTTINGHAM WILFORD BRIDGE

B.1 Introduction

In this appendix, a second test case structure was studied. In particular, the capability of existing and developed OSP and modal extraction were investigated on a real structure, the Nottingham Wilford Bridge.

This work was a part of a broader research project [180-181] aimed at undertaking the research necessary to set up a basic remote health monitoring system, using GPS sensors placed on an operational bridge, linked to a new finite element/optimisation based health assessment software.

The project was organised in three phases. The first task aim was to locate the optimal sensor placements and was undertaken by Cranfield. The second phase consisted in the placements of the GPS sensors in the location indicated by Cranfield and the acquisition of the data necessary (Nottingham University) for the extraction of the bridge modal properties (third task - Cranfield University).

For the OSP investigation task, six different optimal sensor placement techniques have been investigated, three based on the maximisation of the Fisher Information Matrix (FIM), one on the properties of the covariance matrix coefficients, and two on energetic approaches. Mode shape displacements were taken as the "measured" data set and two comparison criteria were employed. The first criterion was based on the mean square error between the FE model and the cubic spline interpolated mode shapes. The second

criterion measured the information content of each sensor location to investigate on the strength of the acquired signals and their ability to withstand noise pollution keeping intact the information relative to structure properties.

The results showed that the Effective Independence Driving-Point Residue (EFI-DPR) method provides an effective method for optimal sensor placement to identify the vibration characteristics of the studied bridge. The Variance Method (VM) developed by the author resulted very close to the EFI-DPR technique, in terms of its capability to capture the vibration mode shape and signal strength. However, the VM presented a unique characteristic in the world of the OSP techniques, which is the indication of the Optimal Number of Sensors (ONS).

The last phase of the project consisted in the application of the modal extraction methodologies investigated in chapter 4 to test the capabilities of the real-time kinematic (RTK) global positioning network system (GPS) to measure low frequency vibrations of a medium span suspension bridge. In particular, the identification of modal parameters, including natural frequencies, damping coefficients and mode shapes of a suspension bridge using ambient excitation loads, was carried out.

B.2 Bridge Structure

The Nottingham Wilford suspension bridge (Figure B. 1) was chosen as a test bed because it experiences deflection in the decimetre range under normal environmental loading.

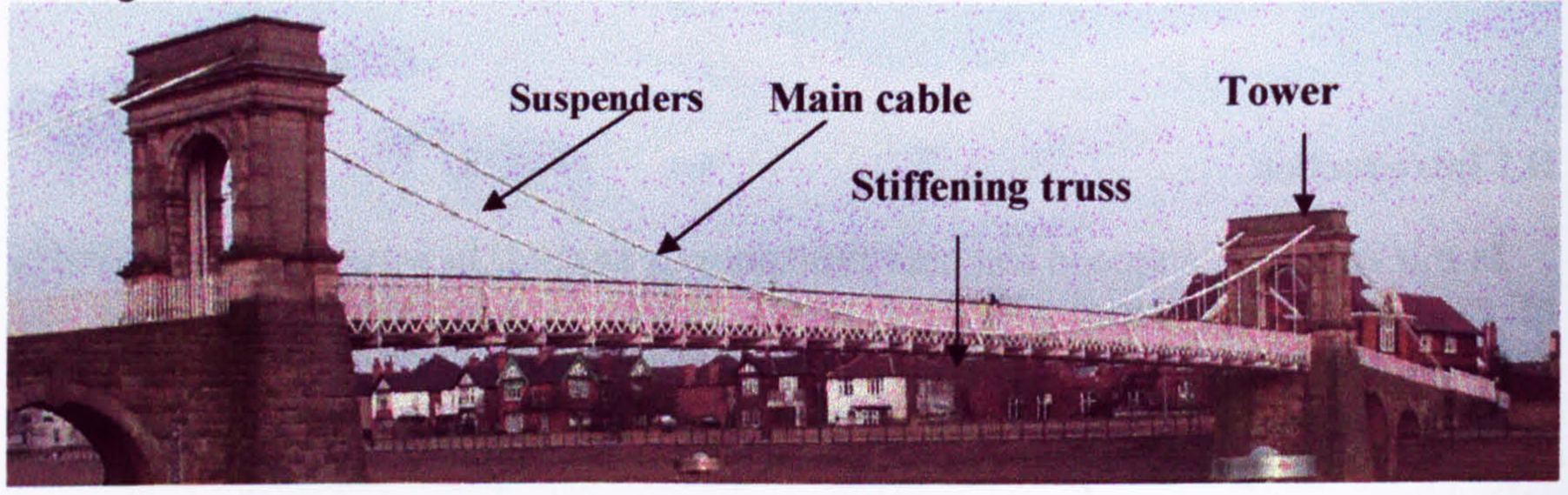

Figure B. 1 - Nottingham Suspension Bridge.

The suspension bridge studied is a footbridge composed of two sets of suspension cables restrained by massive masonry anchorage. The span sidewalk is 3.65 m wide and 68.58 m long, and it is composed of a steel deck covered by a floor of wooden slats.

A suspension bridge is a complex structural system in which each member plays a different role. It is inherently a flexible structure and with some form of stiffness incorporated in the design. The stiffness is usually obtained with a properly designed cable system or with a stiffening truss. Stringers and floor beams transfer the weight of the deck to the suspenders and trusses and, then, to the suspension cables. Suspension cables then transfer the loads to the anchorage and the towers.

Suspension rods pull down on the chain causing it to sag and to pull inwards at its ends. As the main span is loaded, the load causes the cables to pull on the support tower

and hence pull the other span up. The tension in the main cables and the consequent movement of the towers gives rise to uplift in the main span.

In order to provide input data for the OSP methods a three-dimensional finite element model of the bridge was built. The construction of a finite element model, capable of accurately replicating the behaviour of the real world structure, was undertaken using the SAFESA™ Method [225]. The three-dimensional finite element model developed is shown in Figure B. 2. The vibration properties were calculated by performing a modal analysis using the finite element analysis code and pre/post processor system ANSYS. The reference frame has X axis across the bridge width, Y axis along the bridge span and Z axis orthogonal to the plane XY.

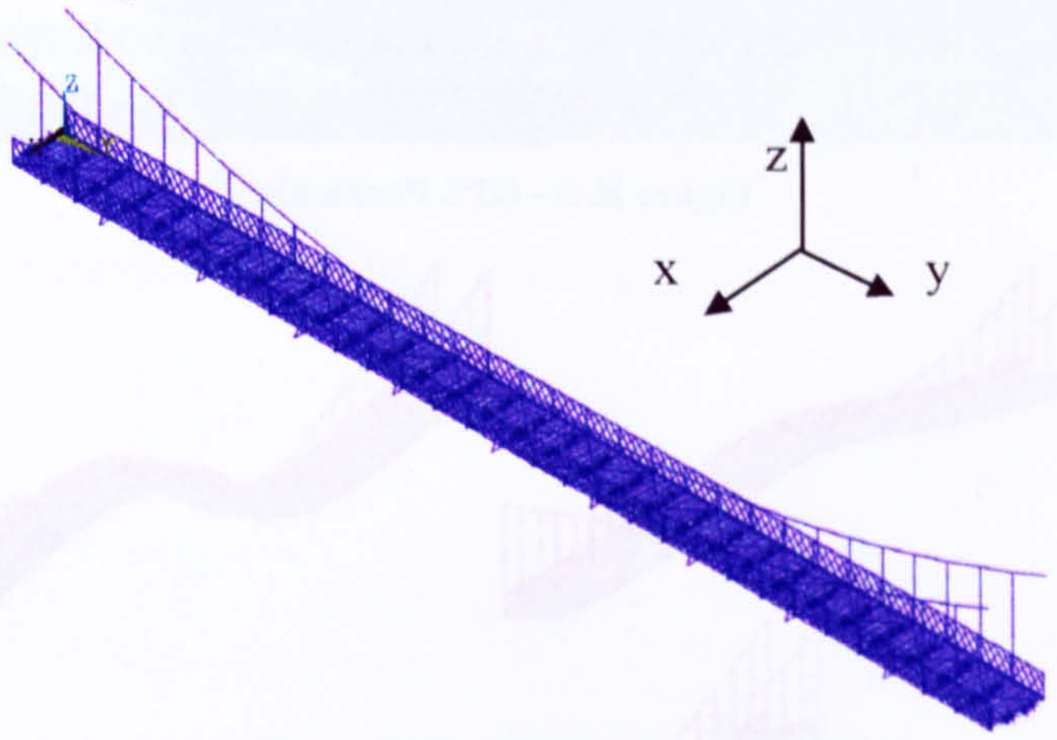

Figure B. 2 - Bridge Finite Element Model

The GPS sensors were used to measure the vibration properties of the bridge. Recent advances in GPS receiver technology and data-processing software have made GPS a much more cost-effective tool to monitor structural movements of large scale civil structures, such as bridges, tall buildings and offshore platforms. Experimental results highlighted GPS as a viable mean of measuring thermally induced displacements, shorter-term transient motion and long-term settlements of the foundations of large civil structures with an accuracy of the order of a few millimetres [180-181]. The Global Positioning System provided by Leica Corporation was capable of acquiring the real time absolute three-dimensional positions at the rate of 10 Hz. GPS dimensions and allocation requirements were such that the only suitable locations were the bridge handrails (Figure B. 3). The possibility of disturbances due to the handrail modal characteristics during the acquisition of bridge global mode shapes (less than 10 Hz), was checked out by comparing their respective frequencies. The modal analysis results confirmed that the handrail eigenfrequencies were by far higher than those of interest (larger than 60 Hz).

The sampling theory (Nyquist theorem) states that the maximum measurable frequency has to be less than half of the GPS sampling rate (5 Hz). Therefore, according to the modal frequencies estimated with the FE analysis, the first 3 global modal properties (Table B. 1, Figure B. 4) were used as input data to find the optimal sensor locations. Hence, the OSP methodologies considered, in the next paragraph, employed only the first 3 mode shapes and the candidate sensor positions were those defined by the bridge handrails. The objective of the OSP selection was to identify the best locations of

the available sensors (10 GPSs) in such a way to capture the dynamic response of the structure.

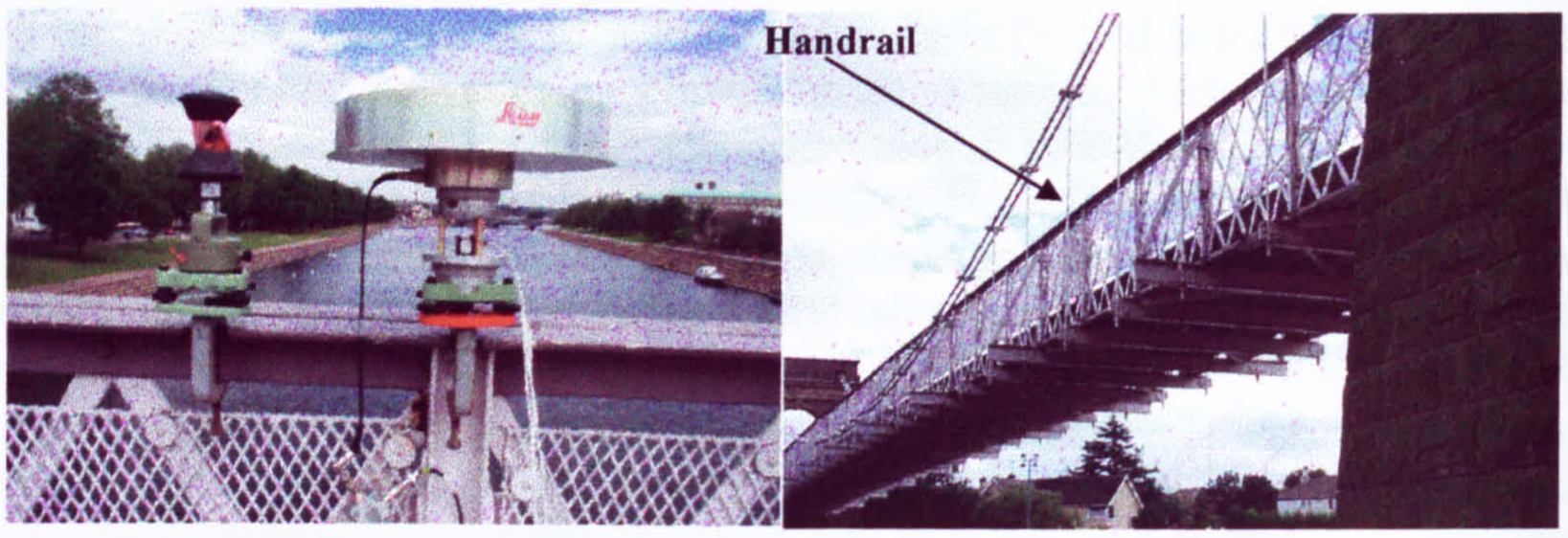

Figure B. 3 - GPS Positioning

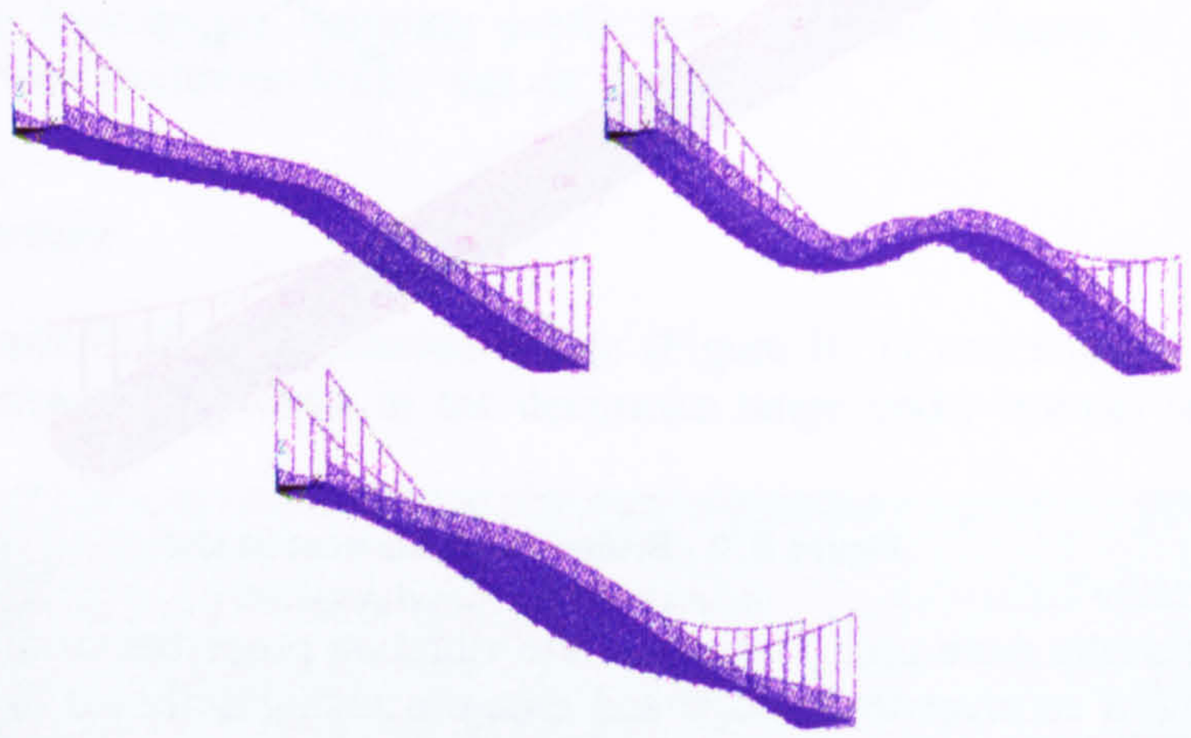

Figure B. 4 – First three mode shape

N.	Freq. [Hz]
1	1.44
2	2.79
3	4.66
4	6.75
5	8.9

Table B. 1 – Modal frequencies calculated using FE model

B.3 Optimal Sensor Placements

The problem being addressed is that of placing 10 sensors on a structure at locations which will allow the computational software to give the best fit to a set of 3 targeted mode shapes. Six OSP algorithms were investigated, the EFI, the EFI-DPR, the KE, the EVP, the NODP and the Variance method (VM).

The OSP techniques investigated (except for the VM) on the bridge were selected because they resulted to be the best performing on the cantilever beam as reported in APPENDIX A and in chapter 6.

Instead, the VM was investigated, since a new sensor selection algorithm was employed that allowed to select well-spaced sensor on the structure and capable of indicating the optimal number of sensor to use (see section 3.5.6).

The EFI sensor placement method (§3.5.1) was developed to maximise both the spatial independence and signal strength of the N targeted mode shapes by maximising the determinant of the associated Fisher Information Matrix. The results obtained from this OSP technique defined a fairly uniformly distributed sensor locations along the length of the beam as shown in Figure B. 5.

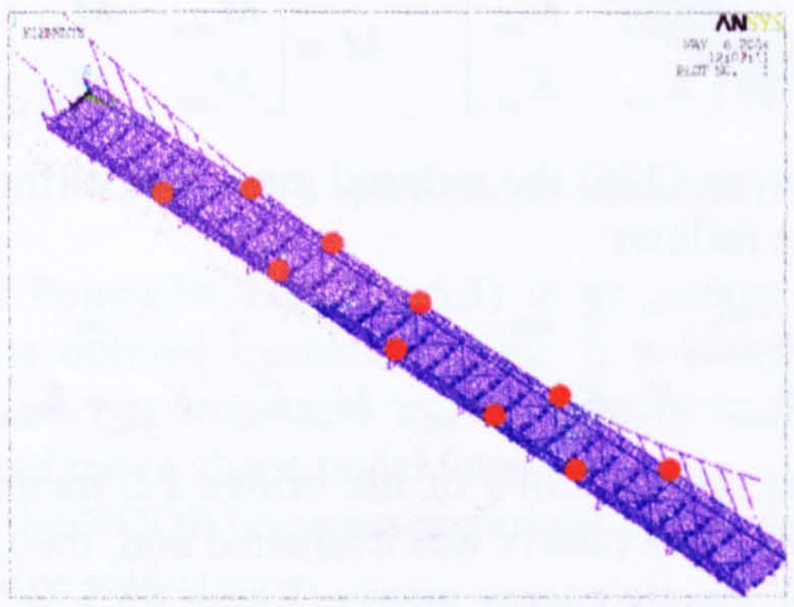

Figure B. 5 – EFI Sensor Location.

A limitation of the EFI method is that sensor locations with low energy content can be selected with a consequent possible loss of information. The EFI-DPR (Driving-Point Residue - §3.6.2) method (§3.5.2) eliminates this problem by multiplying the candidate sensor contribution of the EFI by the corresponding Driving Point Residue (DPR) coefficient. This methodology concentrates sensor positions in the high energy content regions resulting in sensors quasi-uniformly spaced and symmetrically deployed as shown in Figure B. 6.

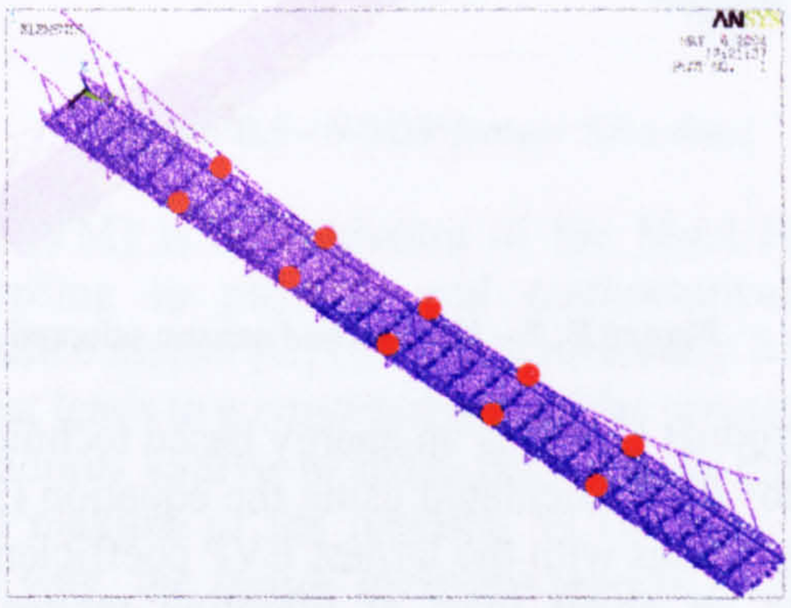

Figure B. 6 - EFI-DPR Sensor Selection

The Kinetic Energy Method (KEM - §3.5.3) sensor location procedure is similar to the EFI method. The main difference is that the KEM objective is to find a reduced configuration of sensor placements, which maximizes a measure of the kinetic energy of the structure rather than the determinant of the FIM.

Differently from Heo et al. [93], the FE model used for the bridge is very accurate and the candidate sensor locations are restricted to the bridge handrails. In order to calculate the mass matrix reflecting the global mass distribution of the bridge, a dynamic reduction of the bridge FE model was undertaken. This was accomplished using substructuring [79], which partitioned the FE model DoFs in master (m, retained DoFs) and slaves (s, removed DoFs). The mass and the stiffness matrices where partitioned in four submatrices as described below:

$$K = \begin{bmatrix} K_{mm} & K_{ms} \\ K_{sm} & K_{ss} \end{bmatrix} \quad M = \begin{bmatrix} M_{mm} & M_{ms} \\ M_{sm} & M_{ss} \end{bmatrix} \tag{B.1}$$

In accordance with Guyan [226] the reduced mass and stiffness matrices at the master DOFs where computed as follows:

$$\hat{K} = K_{mm} - K_{ms} K_{ss}^{-1} K_{sm} \tag{B.2}$$

$$\hat{M} = M_{mm} - K_{ms}K_{ss}^{-1}M_{sm} - M_{ms}K_{ss}^{-1}K_{sm} + K_{ms}K_{ss}^{-1}M_{ss}K_{ss}^{-1}K_{sm} \tag{B.3}$$

Finally, considering as master DoFs of the bridge FE model those belonging to the bridge banisters, a reduced mass matrix was evaluated and, then, equation (B.3) was used for the computation of the kinetic energy matrix (Kem - §3.5.3).

The sensor locations identified by the KE method tend to be concentrated only on one side of the bridge handrails, as shown in Figure B. 7 in contrast with the EFI and the EFI-DPR that distributed an equal number of sensors on both sides of the bridge.

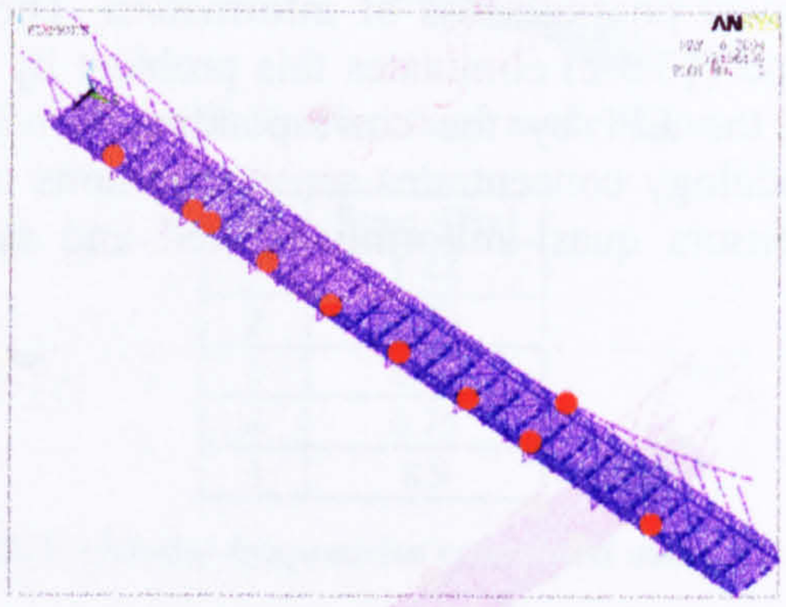

Figure B. 7 – KE method sensor selected

The Eigenvalue Vector Product (EVP) is an energy based technique (§3.6.1) consisting in the evaluation of the vector EVP calculated using the equation (3.25) and the selection of the 10 sensor candidate locations with the largest EVP coefficients in order to prevent the choice of sensors placed on nodal lines of vibration modes and to maximise their vibration energy.

As it can be seen in Figure B. 8, the sensor distribution estimated by the EVP method is mainly concentrated in a small area of the bridge. It is clear that this method will not be able to capture accurately the bridge vibration mode shapes.

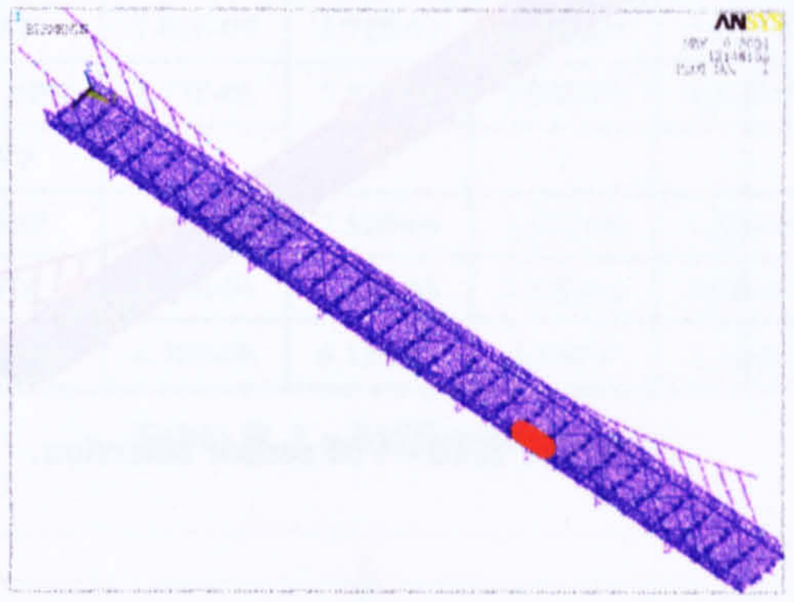

Figure B. 8 - EVP Sensor Selection

The Non-Optimal Drive Point (NODP) (§3.6.3) is an energy based method and it is generally used to find the optimal excitation point. It is based on the concept that the amount of the vibration energy measured by the sensors is a function of the relative positions of the sensors and mode shape nodal lines.
As shown in Figure B.9, the NODP selection technique places the sensors asymmetrically and mainly located at bridge mid-span.

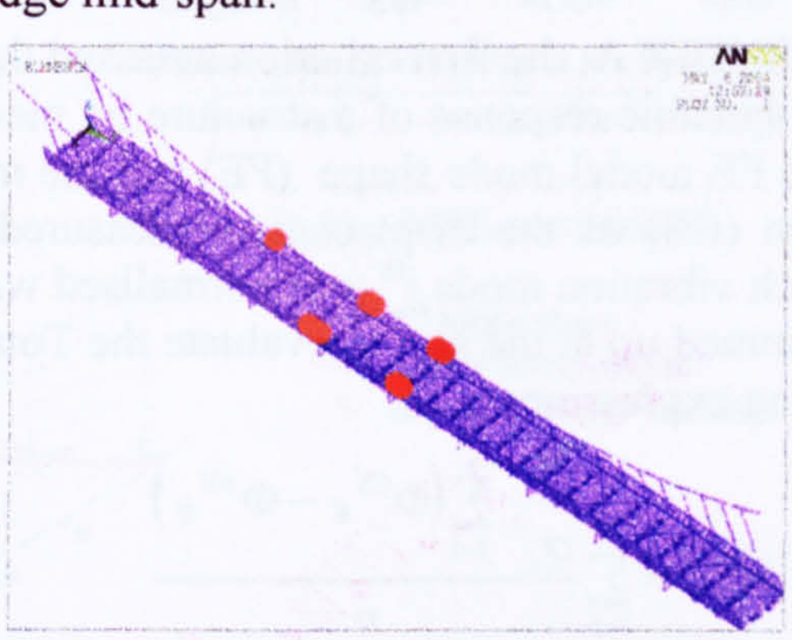

Figure B.9 - NODP Sensor Selection.

The variance method (VM) is an evolution of the Most Informative Subset (MIS) technique (§3.5.5) according to physical and mathematical considerations on the coefficients of the covariance matrix [C] (§3.5.6). Differently from the selection criterion used in APPENDIX A that leads to a concentration of the sensor locations selected in few regions of the bridge handrails similar to those provided by the EVP technique, sensors were placed on the local maxima of the function Vr (§3.5.6 – equation 3.23) sorted in decreasing order. In this way, the sensor locations selected resulted scattered along the bridge handrail as reproduced in Figure B.10. The sensor locations selected did not respect the bridge symmetry, since the covariance matrix coefficients are sensible to the signs of the mode shape displacements. Therefore, in some extent, the VM matches more closely the energy distribution along the structure due to mode shapes.

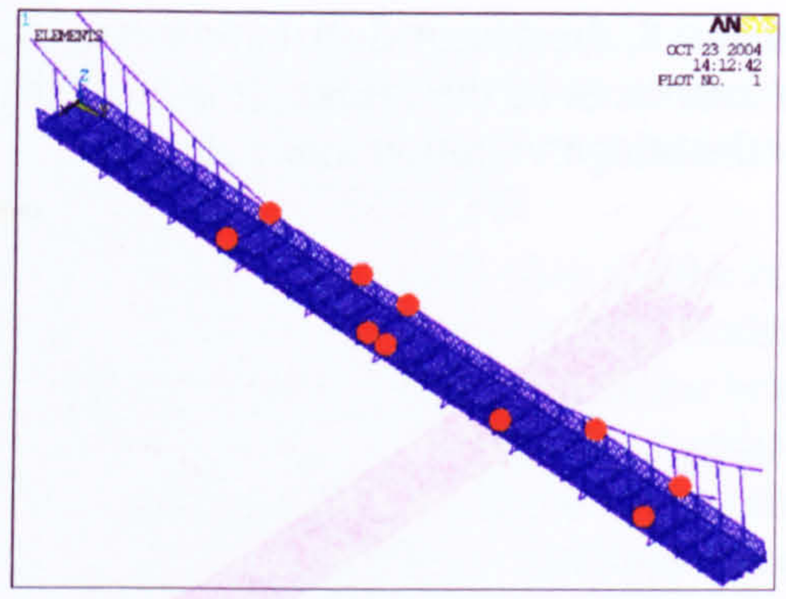

Figure B.10 - VM sensor selection.

B.4 OSP comparison

In order to compare the capability of the different OSP techniques analysed to capture the vibration behaviour of the bridge two different criteria were used. Conceptually, a criterion of optimality should also be related to maximum damage information, i.e. sensor locations should be chosen in such a way that they produce reliable and sensitive information on the potential damages of the structural system. However, this aspect was not considered in this study, since no a priori information on damages occurring on the bridge was available.

As mentioned in APPENDIX A, the first criterion assessed the capability of each OSP technique to capture the dynamic response of a structure by measuring the Mean Square Error (MSE) between the FE model mode shape (FE) and the mode shape obtained by a cubic spline interpolation (CS) of the displacement measured at the sensor locations selected. The MSE of each vibration mode i^{th} was normalised with respect to its standard deviation σ_i and, then summed up at the aim to evaluate the Total MSE (TMSE, eq. B.4) as showed by the following expression:

$$MSE = \sum_{i=1}^{N} \frac{\frac{1}{\sigma_i^{\,2}} \sum_{j=1}^{n} \left(\Phi^{CS}{}_{ij} - \Phi^{FE}{}_{ij} \right)^2}{n} \tag{B.4}$$

A cubic spline interpolation was carried out, using a MATLAB coded function, separately for each handrail. The MSE criterion results were summarized in Table B. 2 and showed in Figure B. 11. As expected the MSE of the EVP method was the highest due to the concentration of sensors only on the left banister of the bridge (Figure B. 8). In contrast, the MSE for the EFI-DPR method resulted slightly better than, respectively, VM and the EFI method and about 3 and 5 size order lower than the NODP and KE method, respectively.

The comparison between the FE and the spline interpolated mode shapes using the EFI-DPR technique for all three vibration modes investigated was shown in Figure B. 12.

OSP Method	Mean Square Error			
	Mode Shape			TMSE
	1st	2nd	3rd	
EFI	7.66E-09	1.31E-07	2.68E-09	1.42E-07
EFI_DPR	1.57E-08	5.57E-08	1.09E-08	8.23E-08
EVP	1	1	1	3
NODP	3.03E-06	7.51E-06	1.63E-06	1.22E-05
KEM	5.30E-04	4.25E-03	2.52E-04	5.03E-03
VM	4.50E-08	6.12E-08	1.18E-8	1.18e-07

Table B. 2 – MSE comparison.

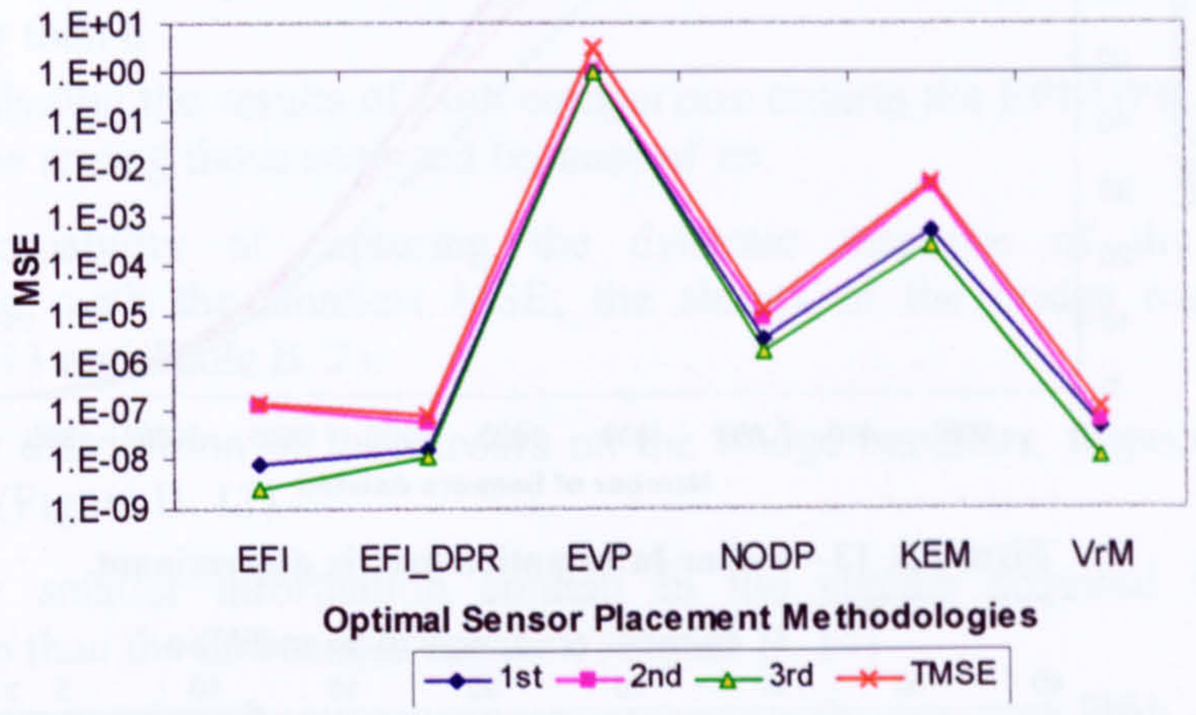

Figure B. 11 – MSE comparison.

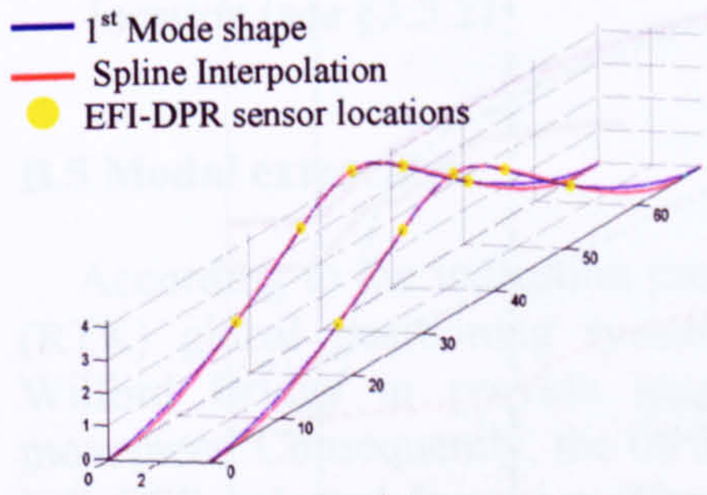

(a)

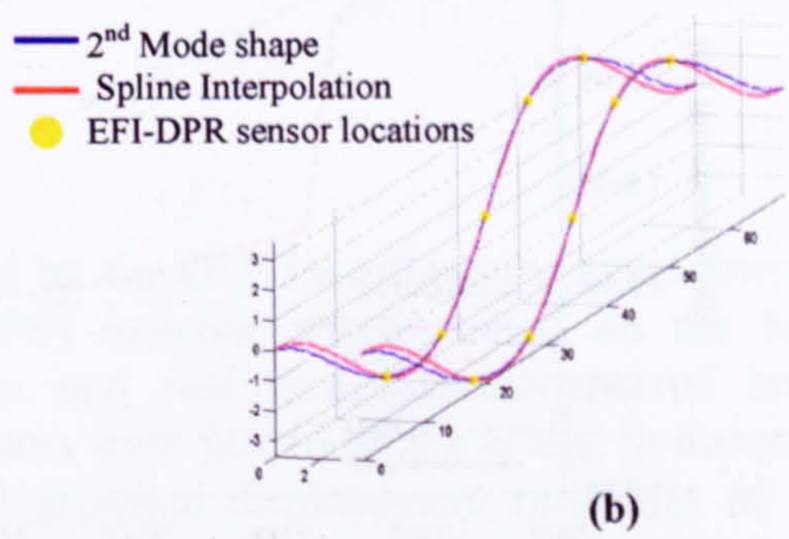

(b)

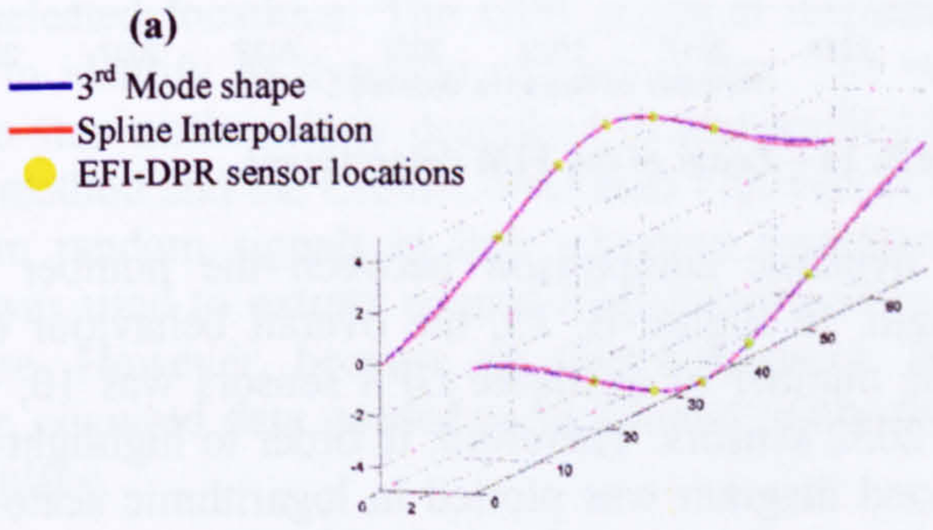

(c)

Figure B. 12 – EFI–DPR: (a) 1st mode shape; (b) 2nd mode shape; (c) 3rd mode shape.

The second comparison criterion was based on the concept that the strength of the signals acquired associated with modal characteristics should be as high as possible in order to reduce the noise. In order to comply with this important aspect, the Fisher Information matrix (FIM) determinant behaviour was recorded during the sensor selection and displayed in terms of percentages of its initial value against the progressive number of the dropped candidate sensors (Figure B. 13 and Figure B. 14). The number of the initial possible locations was 2042.

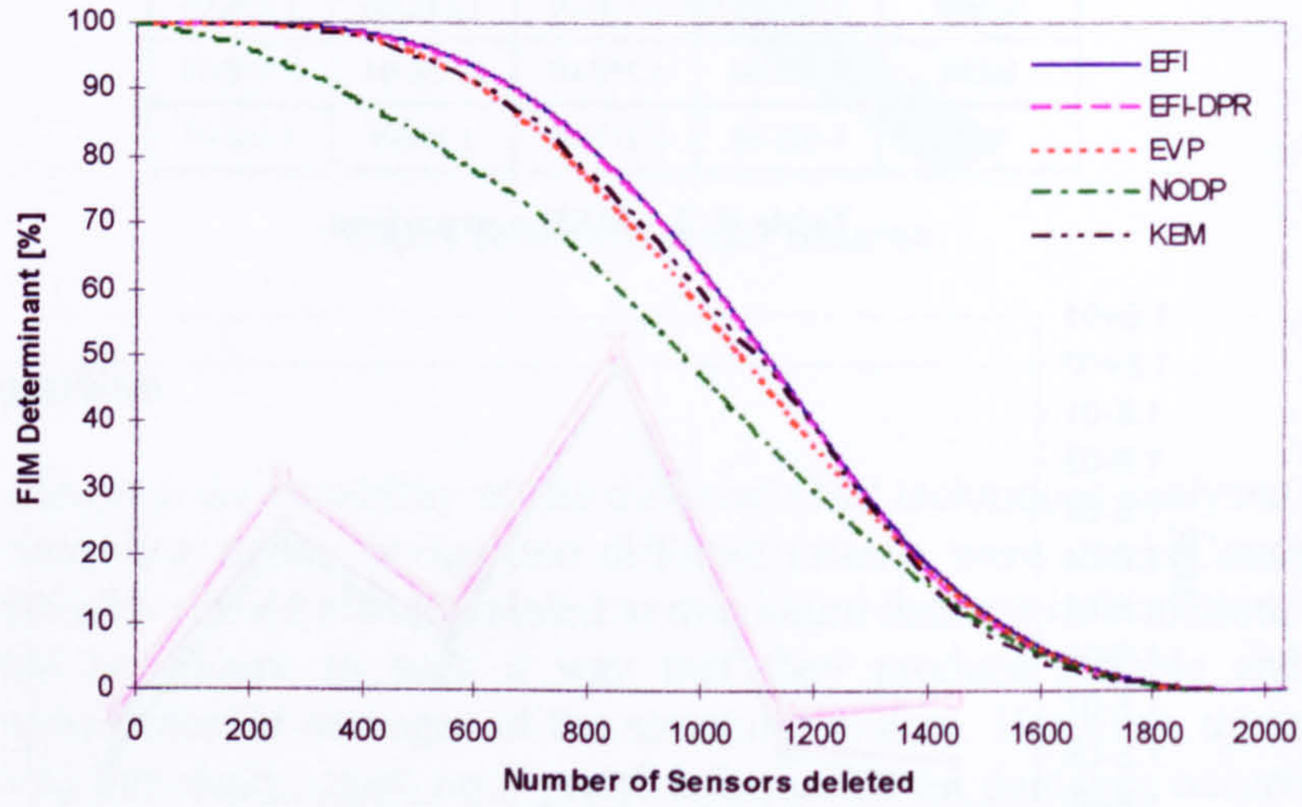

Figure B. 13 – Fisher Information matrix determinant.

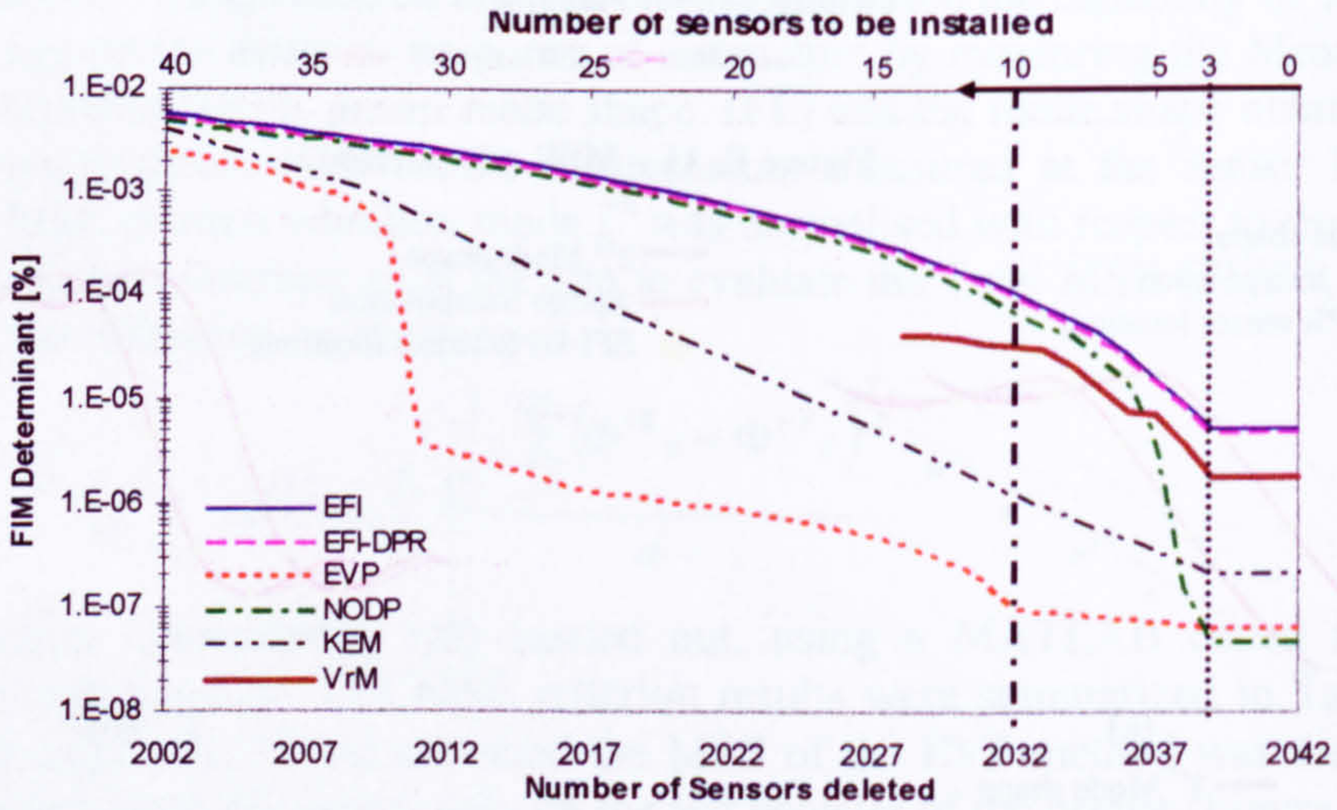

Figure B. 14 – Zoom of the FIM determinant.

This procedure allowed a dynamic comparison between the number of sensors employed and the signal strength. In Figure B. 13, the overall behaviour of the FIM determinant is shown. Since the number of available GPS sensors was 10, the area of interest was between 2042 and 2032 sensors. Therefore, in order to highlight the area of concern in Figure B. 13, a second diagram was plotted in logarithmic scale (Figure B. 14). Two vertical lines were drawn; the first (the dash dot line) highlights the FIM determinant value using a network of sensor made of 10 GPS, while, the dotted line

represents a 3 sensor monitoring network, which is the smallest number of sensor that can be used according to the FIM based techniques and KEM (§3.5), since the FIM would be singular for a smaller number of sensors. Therefore, beyond this line the FIM determinant was kept constant. Moreover, in this diagram, the VM is also reported, but only for a number of sensors installed smaller than the optimal sensor number (the number of local maxima of the Vr - §3.5.6 eq. 3.23 - function was 14).

The diagram showed that the trend and the values of the signal strength of the EFI, EFI-DPR and NODP method were very close, while the signal strength of the EVP and KEM were very small. The VM underperformed the FIM and NODP techniques, even though it had the signal strength of the same order for 10 sensors installed. Decreasing the number of the sensors of the sensing network, the VM behaviour improves with respect to the FIM techniques and become better than the NODP method for a number of sensors smaller than 8.

Finally, analyzing the results of both comparison criteria the EFI-DPR proved to be a better technique among those analyzed because of its:

- Superior capability of capturing the dynamic response of the structure by reproducing, with the smallest MSE, the shapes of the bridge modal properties (Figure B. 11 and Table B. 2).
- Symmetric distribution of the sensors on the bridge banisters, respecting the bridge symmetry (Figure B. 12).
- Marginally smaller information content in the signals acquired by its sensors distribution than the EFI sensor network (Figure B. 14).
- A better vibration energy content in the signals acquired than the EFI technique since the EFI-DPR selection procedure tended to select higher vibration energy sensor location (see §3.5.2).

B.5 Modal extraction

According to the indication provided by the OSP investigation, a real-time kinematic (RTK) global positioning system (GPS) network was installed on the Nottingham Wilford Bridge to provide long-term and real-time measurement of bridge deck movement. Consequently, the GPS sensors were placed on the bridge in accordance with EFI-DPR selected locations. The GPS acquired displacement responses of the bridge were used to identify its dynamic characteristics. The modal properties were extracted using a two-step methodology described in paragraph 4.4. In the first step, the random decrement method and the Cross-Correlation Function (CCF) based technique were used to transform random signals in free vibration responses. Secondly, a wavelets based technique was used to extract natural frequencies and to determine the mode shapes of the structure. However, because of electro-magnetic interferences affecting the GPS functioning, acquired data needed to be filtered out before the modal extraction process could take place.

B.5.1 Signal filtering

As mentioned above, the bridge ambient vibrations were acquired using a network of GPS sensors installed on the bridge handrails in locations determined by an OSP technique (EFI-DPR). The number of the GPS sensor employed was 10 and the acquisition lasted for 24000 seconds with a sampling rate of 10Hz. In Figure B. 15, the GPS time signals of some of the sensors were reported. The loss of lock to the satellite signals and electromagnetic interferences on the GPS sensors generate sudden jumps in the time signals and low frequency noise called multipath. This noise was caused by indirect signal transmission from satellites to the antennas of GPS receivers. This was the major factor affecting positioning accuracy. To address this problem two different filtering techniques were used, adaptive filtering and wavelet filtering.

Adaptive filtering techniques were employed to reduce the multipath signature [227]. Since satellite constellation repeat at a period of 23 hours and 56 minute, the multipath at specific location with relative fixed observation environment repeats at the same period. In Figure B. 16, the first row is the vertical mean movement at mid span of the Wilford Bridge and second row is the time series at the same location but collected on previous day. These two time series are input into the adaptive filter and the relative clean data are produced (row 3 in Figure B. 16). Multipaths were extracted and expressed in the fourth row. Included in row 3 are real bridge movements and thermal noise caused by the GPS receivers [227].

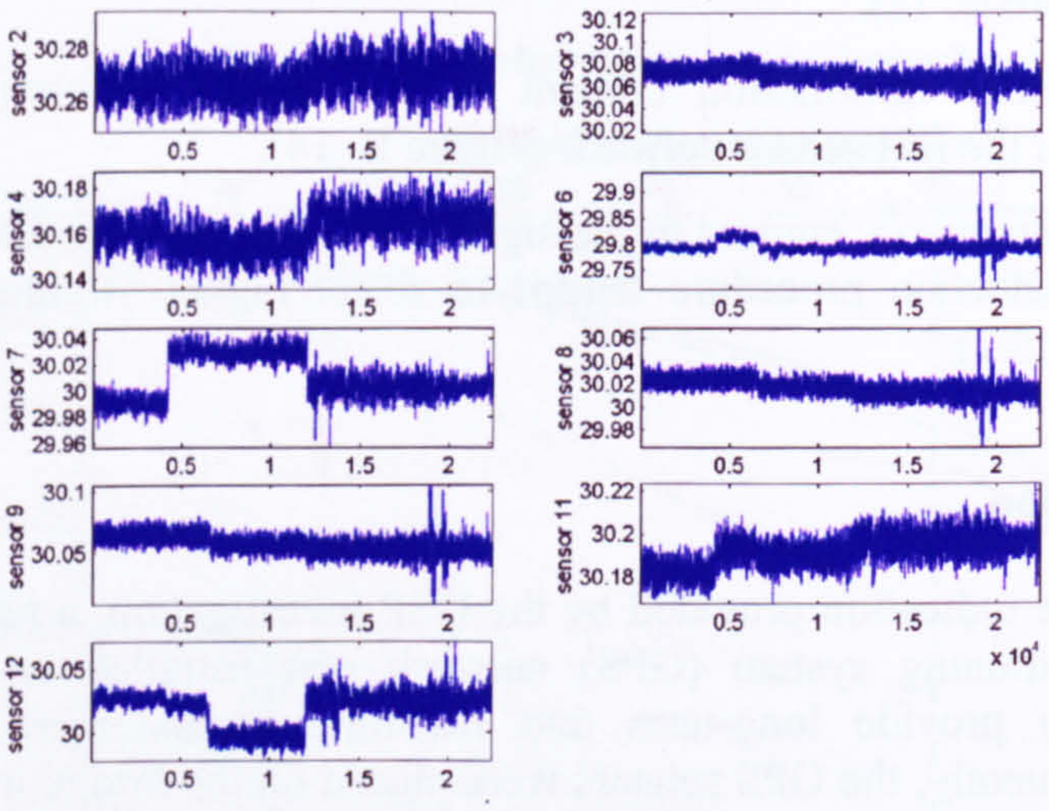

Figure B. 15 - GPS sensor time signal.

In the second procedure a pass-band filter [0.3, 5] Hz, with a 5 level Daubechies (db5) wavelet decomposition scheme, was employed [128] to get rid of this non zero mean noise, uncorrelated with the structure dynamic response.
The portions of signals filtered out were plotted in Figure B. 17-a, while the remaining part is shown in Figure B. 17-b. In the filtered signals (filtered -b), there were still some sudden peaks due to in-service loading. The extraction of the modal properties using the two different filtering techniques produced the same results. Below the modal properties calculated by using the band-pass filtering techniques were presented.

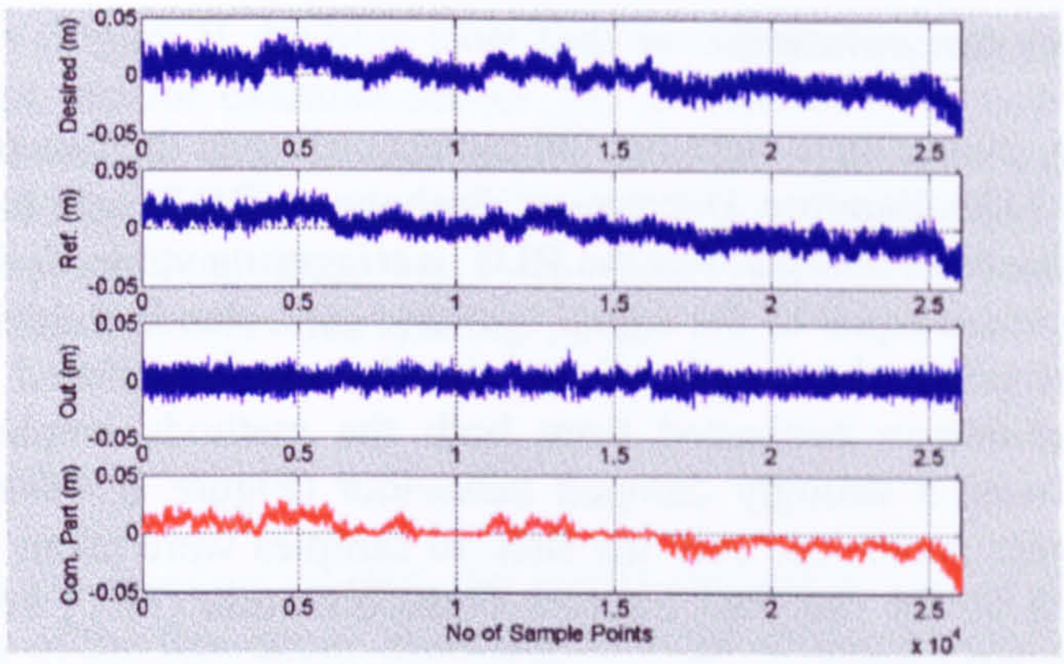

Figure B. 16 – Multipath and its mitigation (Nottingham University)

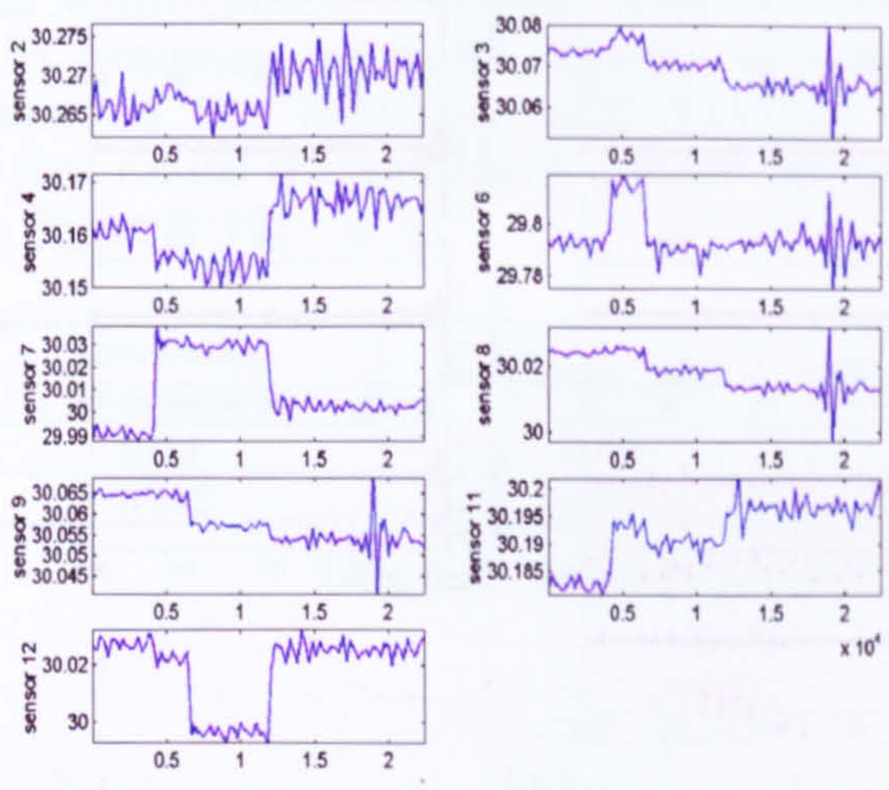

(a)

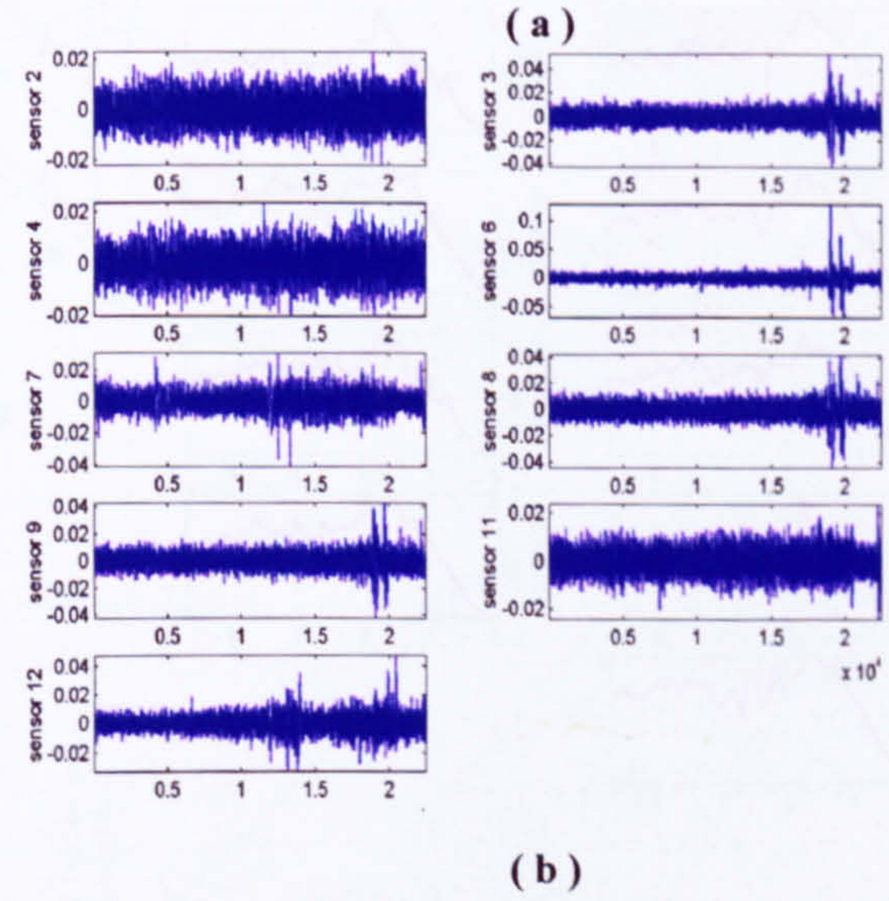

(b)

Figure B. 17 – Wavelet filtering: (a) portion of the signals erased; (b) cleaned signals.

B.5.2 Free-decays computation

The free-decay evaluations were carried out according to the two procedures described in paragraph 4.5, The Random Decrement Technique (RDT) and the Cross-Correlation Function (CCF) based technique. For the RDT, a triggering value X_0 for the time segment selection was assumed equal to the signal variance (one standard deviation). For both the techniques investigated, the length of the signals was established to be 200 samples (20sec). The free-decays evaluated from both the methods employed resulted to be identical and showed a strongly damped behaviour (Figure B. 18-a). Consequently, in order to avoid noise problems, only the first 50 samples were taken into account for the extraction as well as for the Fast Fourier Transformation (FFT) evaluation showed in Figure B. 18-b.

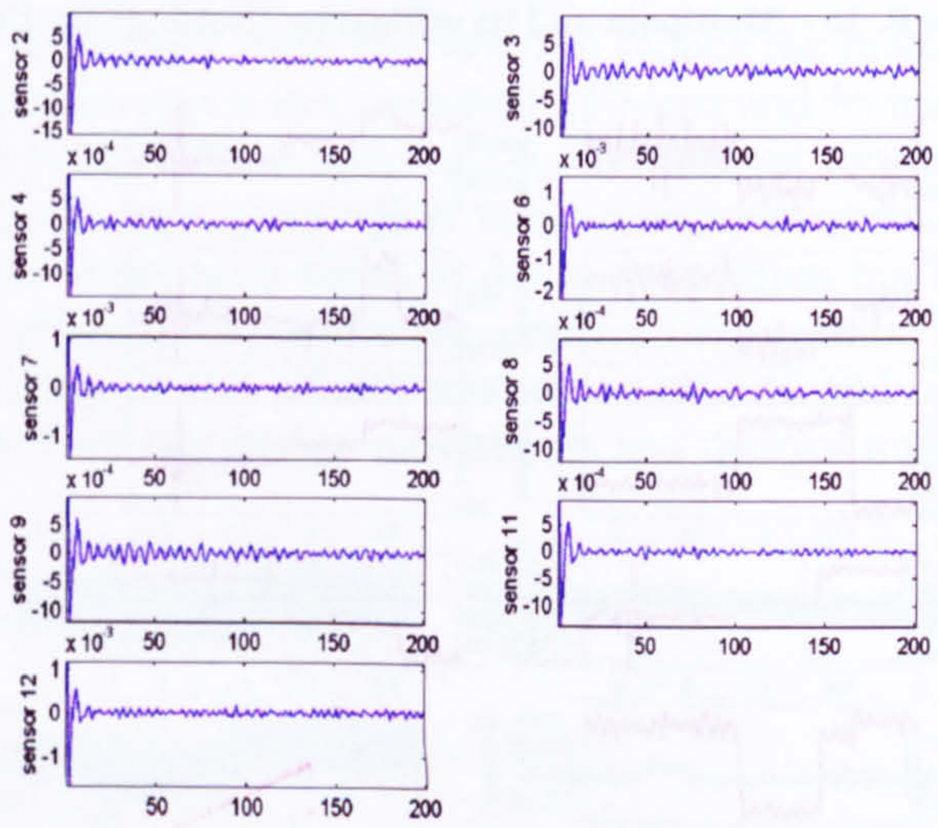

(a)

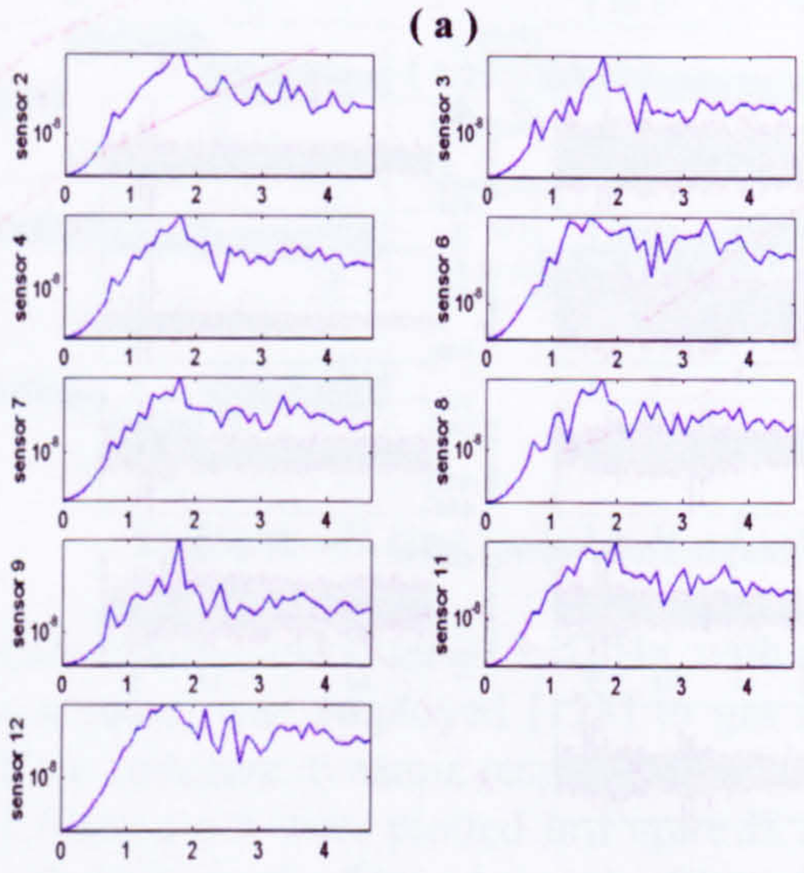

(b)

Figure B. 18 – RDT free-decays: (a) time histories; (b) FFT (the magnitude is in logarithmic scale)

By the FFT plots (Figure B. 18-b) is clear that not all the random noise was taken out by the RDT process, see for example sensor 12. Moreover, there was only one clearly identifiable peak around 2 Hz. All this could be due to short acquisition time. This concern is confirmed by the occurrence of isolated burst in the sensor time histories (Figure B. 18-b), which lead to a not fully satisfaction of the zero mean random distribution assumption for in-service loading §4.5).

B.5.3 Modal extraction

As mentioned in the previous section, the modal extraction was carried out using only the first 50 samples of the free-decay evaluated in order to avoid possible noise pollution in the results. Two techniques were used to extract the modal properties of the bridge, the ERA (§4.6.1) and WME (§4.6.2) technique. Both the techniques extracted only one vibration mode, its frequency and modal damping were reported in Table B. 3. The results showed that the two techniques used provided very similar results in the estimation of the first natural frequency with a difference of 1%. The calculated mode shape is shown in Figure B. 19.

Extraction Technique	Frequency [H z]	Modal Damping
ERA	1.74	0.025
WME	1.72	0.019

Table B. 3 – Modal properties.

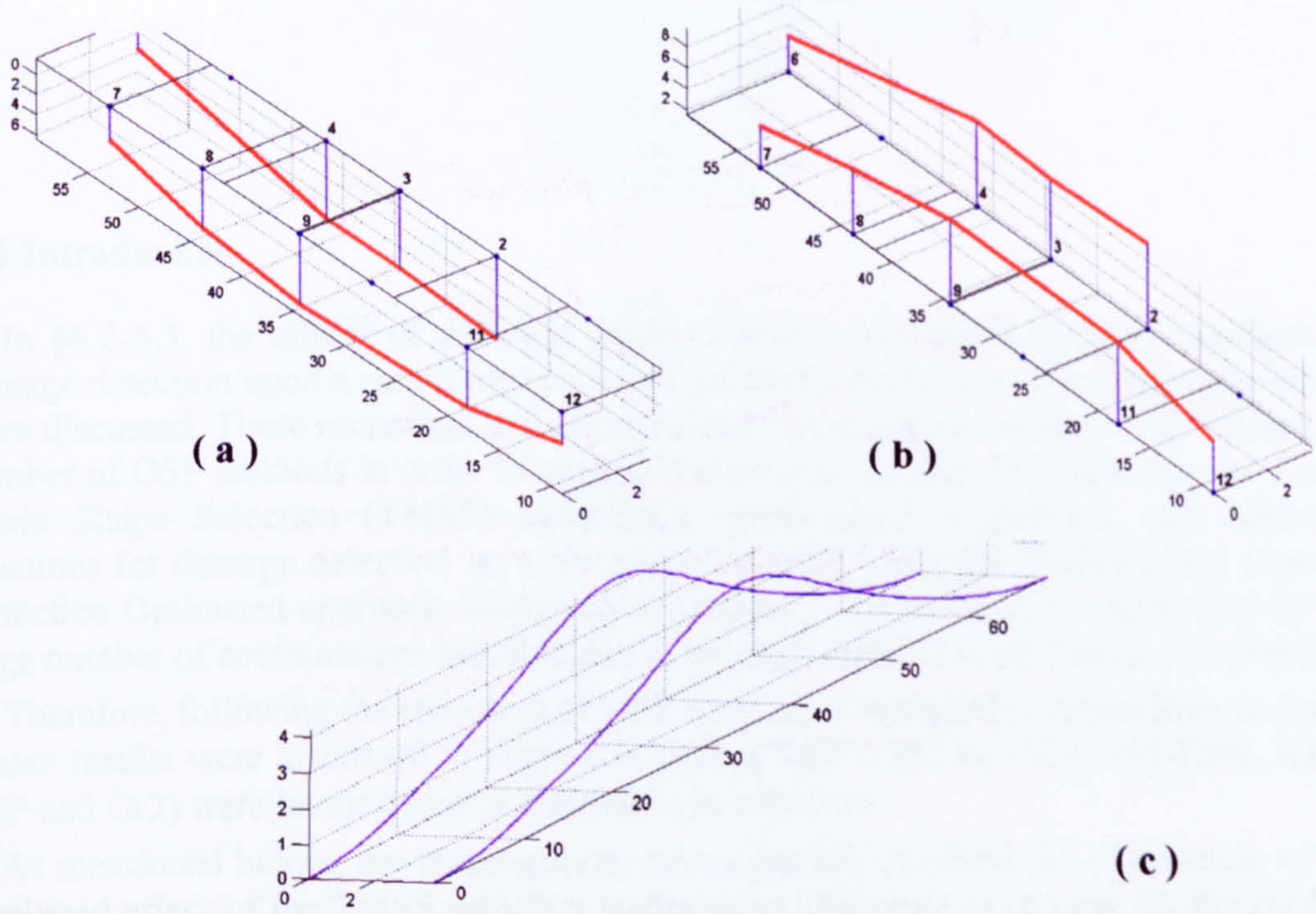

Figure B. 19 – First Mode Shape: (a) ERA; (b) WME; (c) FE model.

The results produced by the two techniques seemed to be consistent, although, for the mode shape evaluated using the ERA methodology Figure B. 19-a, the Modal Assurance Criterion (MAC) [73], evaluated using the FE model shape, Figure B. 19-c was 0.90 against 0.75 for the shape extracted by the WME technique (Figure B. 19-a).

Further discussion and analysis of the results were presented in §6.3-6.4.

APPENDIX C: DAMAGE DETECTION ON A PLATE: OSP, TMS AND MODEL UPDATING INVESTIGATIONS

C.1 Introduction

In §6.2-6.3, the effects of different Optimal Sensor Placement (OSP) techniques on damage detection upon a cantilever beam and on modal extraction of a suspension bridge were discussed. These numerical and experimental investigations helped to size down the number of OSP methods in order to analyse the optimal combination between the Target Mode Shape Selection (TMSS) techniques, optimisation algorithms, and objective functions for damage detection on a plate-like structure using the Global-Local Damage Detection Optimised approach illustrated in chapter 2. This was made necessary by the large number of combinations possible due to the high number of parameters involved.

Therefore, following the reduction of OSP techniques operated in appendices A and B, whose results were discussed in chapter 6, only 5 OSP methods (EFI, EFI-DPR, KEM, EVP and Gr2) were investigated on the plate like structure.

As mentioned before, the investigation, here reported, involved the exploration of the combined effect of the TMSS selection techniques (illustrated in chapter 3), the Global-Local approach and the several optimisation algorithms (described in chapter 2) on the damage detection compared to sensitivity approach used in literature.

C.2 Plate like structure

The plate like structure used as test case for the damage detection investigations carried out in this appendix was a 30 by 20 cm rectangular aluminium plate constrained at the edges (Figure C. 1). A 2000 finite element model was built in the commercial FE code ANSYS and used for the evaluation of mode shapes and FRF needed by the damage detection techniques for their investigation.

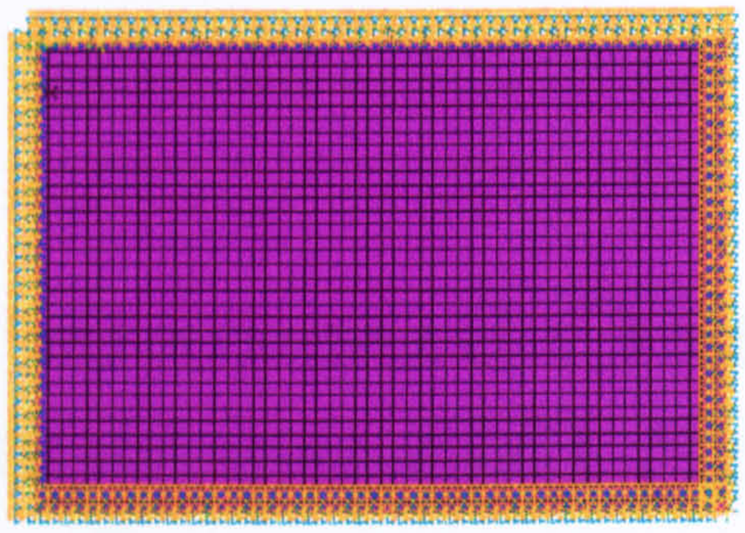

Figure C. 1 – Plate FE model.

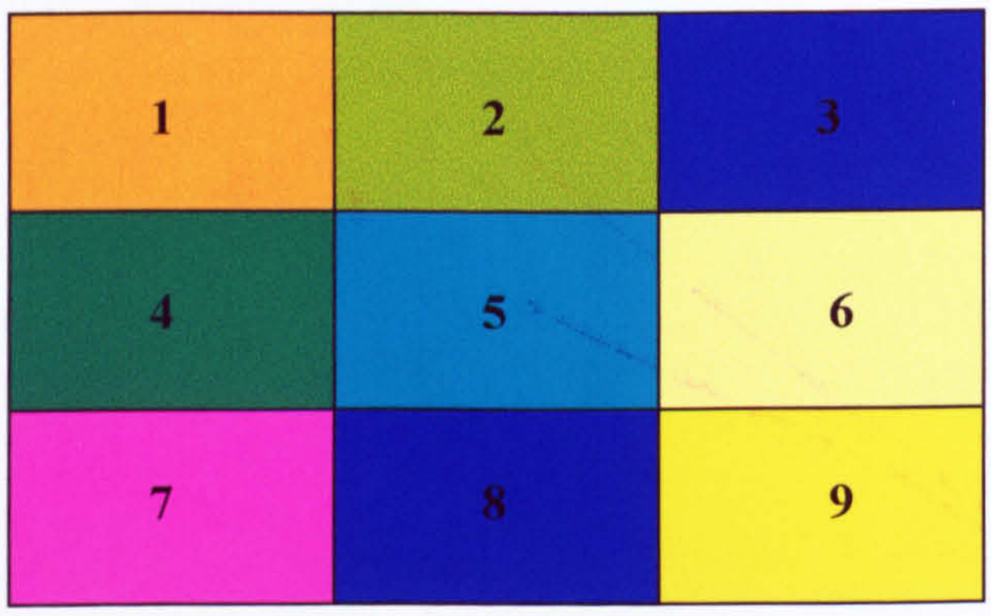

Figure C. 2 – Plate Macro-Areas.

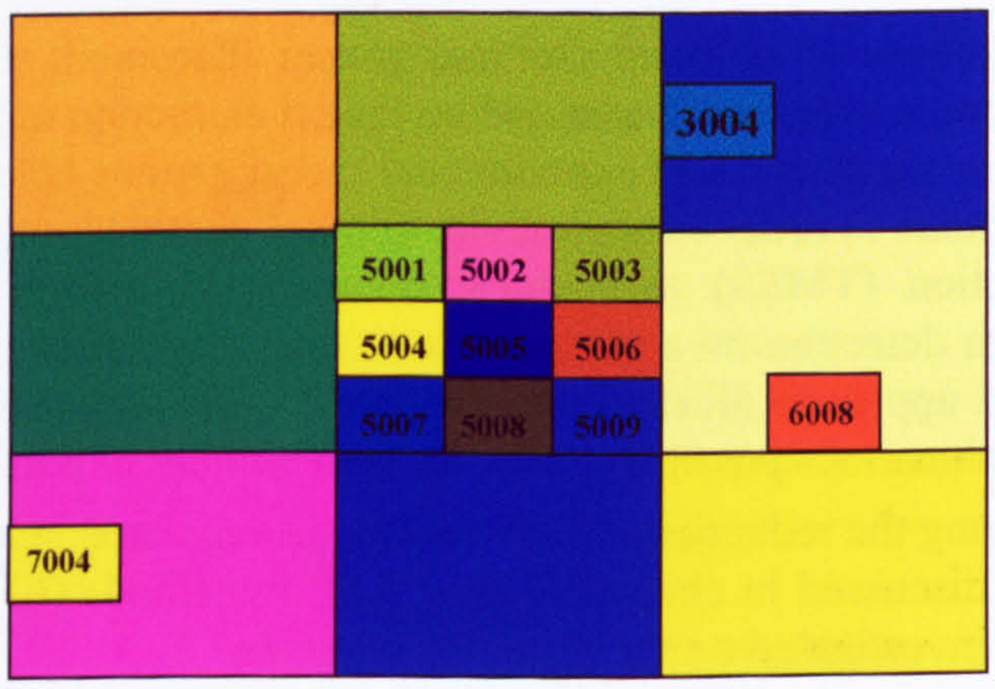

Figure C. 3 – Macro-Area division.

The plate surface was reorganised in 9 macro-areas, which at their time were divided in 9 areas (see Figure C. 2-Figure C. 3). This partition in macro-areas and areas was used for the global-local approach and to identify univocally were the damage was introduced.

Once the initial (undamaged) model was built, the plate was progressively damaged in a number (three) of damage scenarios. Damage was introduced numerically in the FE model by reducing of 20% the thickness of the elements included in the areas 7004, 6008 and 3004 (Figure C. 3). The dynamic properties of the plate structure were measured before and after each damaged scenario. Gaussian noise (10% standard deviation) was added to the numerical modal properties and FRF to simulate the real environment noisy effect on the damage detection procedure under investigation.

C.3 Noise effects on the MAC and COMAC functions

A first estimate of the advantage derived by the adoption as objective function of MAC and COMAC based functions was carried out by adding noise with zero mean and variance from 0% up to 16% to a set of 10 mode shapes evaluated using the plate FE model described in the previous paragraph. The results (Figure C. 4) proved that the MAC and the COMAC functions tended to downsize the effect of the noise, since they have a mean error smaller than the noise introduced exemplified in the plot by the 45 degree line.

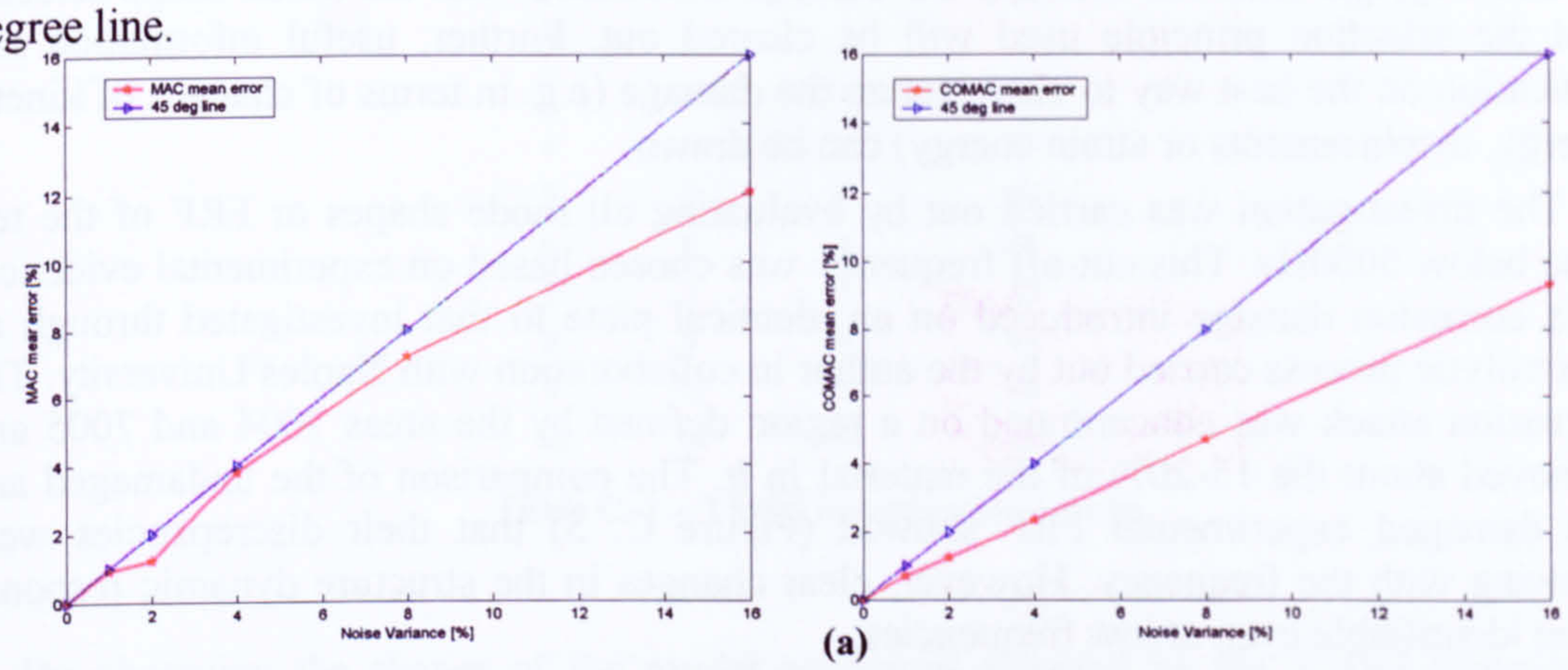

(a)

Figure C. 4 - Noise effect: (a) MAC mean error (b) COMAC mean error.

C.4 Damage detection investigation configuration

In order to perform a comprehensive investigation on the efficiency and reliability of the GLDDO approach, a series of tasks were carried out to compare the detection capability of the technique developed and to identify the most suitable objective function.

The first task was targeted to the understanding of the efficiency and reliability of the global-local approach on the global one, common to most of the updating techniques existing in literature.

A second task was tailored on the analysis of the combined effect of different TMSS techniques and of different OSP methods on the damage detection capability of the GLDDO approach.

A last task was designed to explore the efficiency of the developed DD methodology in comparison to a model updating technique very well known in literature.

It has to be mentioned that only the subproblem approximation method was an internal feature of the ANSYS code, while the other optimization algorithms were implemented in MATLAB, so as ANSYS became a special function of the MATLAB scripts written by the author and executed when requested by the optimization processes.

Before proceeding to a detailed description and result analysis of the tasks mentioned above, the results of the TMSS and the OSP investigation carried out on the plate were presented.

C.4.1 Target Mode Shape Selection

As described in chapter 3, four TMSS techniques were identified and analyzed, Minimum Modal Frequency (MMF) criterion, the Root-Sum-Square displacement (RSS) method, the Modal Kinetic Energy (MKE) approach and the Maximum Strain Energy (MSE) criterion. Of this four techniques, only the first (MMF) and the last (MSE) criterion have been used in literature for damage detection purposes. Then, it is clear the reason why a fully enquire on the effect on the different TMSS techniques is necessary. In this way, the relations between the damage introduced with the mode shape selected and the selection principle used will be cleared out. Further, useful information and indication on the best way to characterize the damage (e.g. in terms of changes of kinetic energy, displacements or strain energy) can be drawn.

The investigation was carried out by evaluating all mode shapes or FRF of the test case below 5000Hz. This cut-off frequency was chosen based on experimental evidences of a corrosion damage introduced on an identical plate to that investigated through an electrolytic process carried out by the author in collaboration with Naples University. The corrosion attack was concentrated on a region defined by the areas 7004 and 7005 and removed about the 15-20% of the material in it. The comparison of the undamaged and the damaged experimental FRF showed (Figure C. 5) that their discrepancies were growing with the frequency. However, clear changes in the structure dynamic response were identifiable even at low frequencies.

This remarks suggested that in order to identify this type of damage, the 5000 Hz threshold seemed to be a right compromise between the need to raise the frequency of the investigation in order to have large damaged/undamaged structure response changes and the rising computational time with the frequency increase. In this way 50 mode shapes were computed and used for TMSS investigation. The results showed (Table C. 1) that the RSS and the MKE yielded to the same target mode shapes, whose 8/10 were coincident to the MMF's. On the other hand, the MSE criterion selected high order mode shapes next to the cut-off frequency.

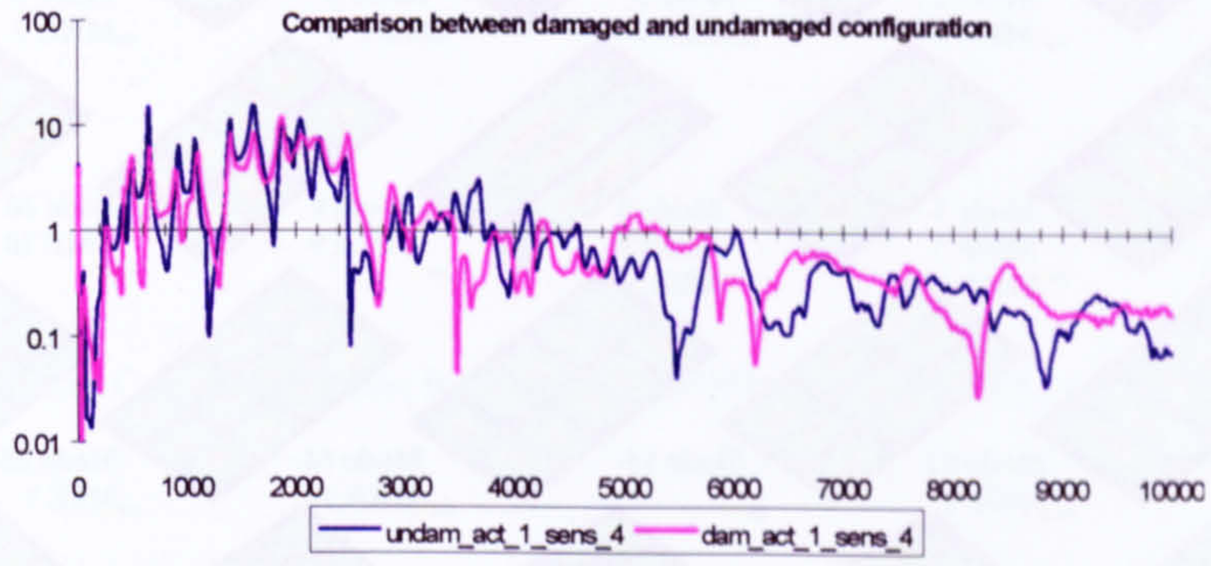

Figure C. 5 – Corroded plate: comparison between the undamaged and the undamaged FRF acquired at the centre of the plate.

MMF	RSS	MKE	MSE
1	1	1	35
2	2	2	37
3	3	3	41
4	4	4	43
5	5	5	44
6	6	6	45
7	7	7	47
8	9	9	48
9	12	12	49
10	14	14	50

Table C. 1 – TMSS investigation results.

By observing the shapes of the modal properties selected by the TMSS techniques employed, the RSS/MKE and the MSE criteria tended to unselect those modes that had fewer domes than the modes nearby (e.g. modes 8, 10 11 and 13 for the RSS and MKE criteria and mode 42 and 46 for the MSE method, see Figure C. 5).

Then, the target mode shapes selected were used to feed the OSP MATLAB codes (written by the author) in order to identify the optimal locations for damage detection purposes.

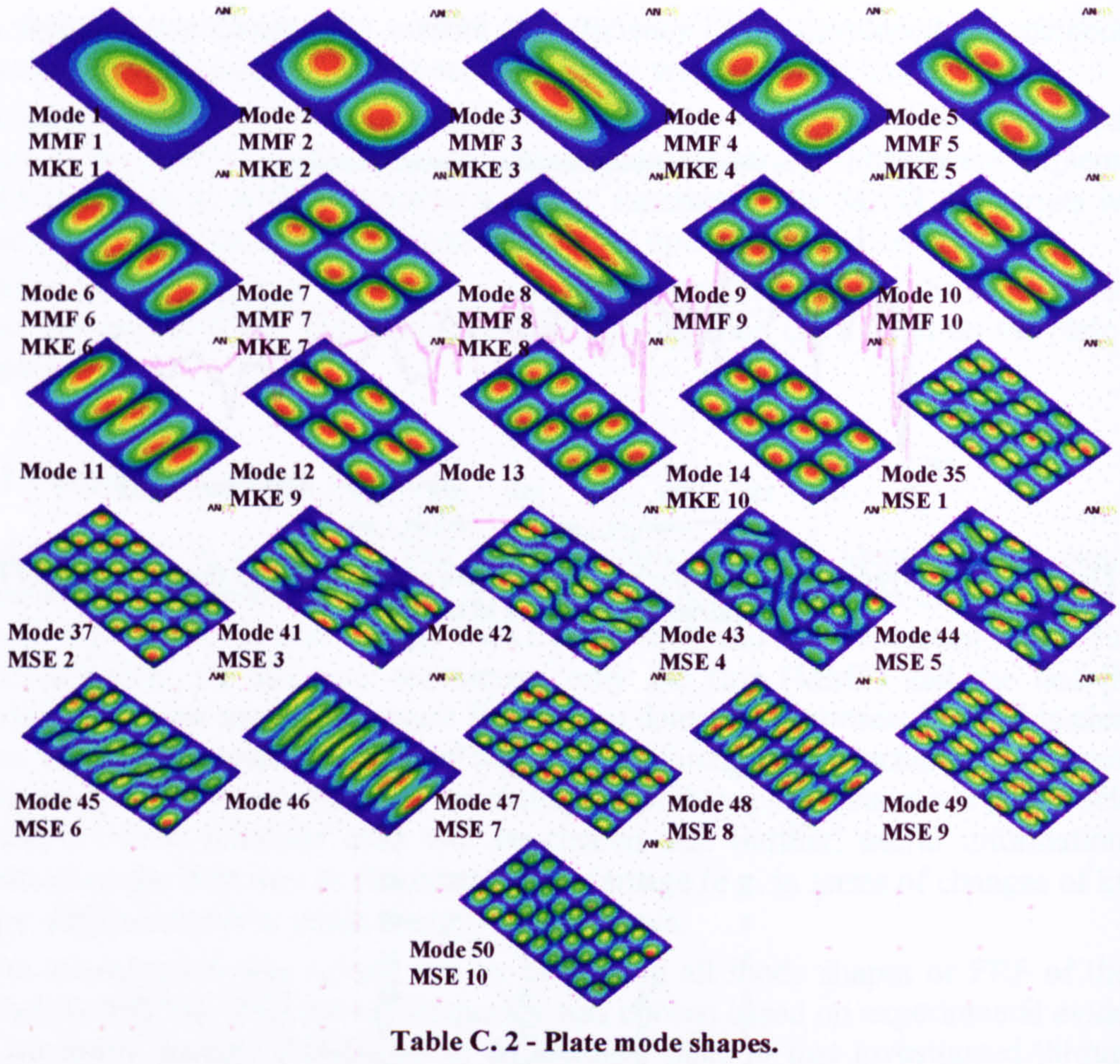

Table C. 2 - Plate mode shapes.

C.4.2 Optimal Sensor Placements

Many researchers think that the optimal sensor placements for damage detection purposes should be carried out using damaged target mode shapes in order to maximize the damage information content identifiable by the sensor network. This idea is surely right if damages occurring on the structure under investigation are known a priori in terms of their types, locations and severities. In any other case, this approach cannot be pursued and the target mode shapes to use have to be evaluated for the structure in pristine conditions, as in the case here investigated.

Therefore, following the selection of the target mode shapes (§C.4.1) and the selection of the most reliable and efficient OSP techniques (appendix A and B, chapter 6), between those investigated in chapter 3, the optimal sensor locations were evaluated according to the criteria identified by EFI, EFI-DPR, KEM, EVP and Gm2 methods.

The locations chosen by the EFI method were fairly spaced on the plate surface as well as the locations selected by the KEM and EVP methods, in contrast with the EFI-DPR and the Gm2, which concentrated the picked sensor positions either around the mid of the plate (EFI-DPR) or along two lines (Gm2). The optimal locations selected using MSE target mode shapes were deployed in proximity of the plate borders, except for

those selected by the Gm2 method, which was independent by the target mode shape set used, since was based on the Grammian matrix, related directly to the mass and stiffness matrices defining the structure FE model.

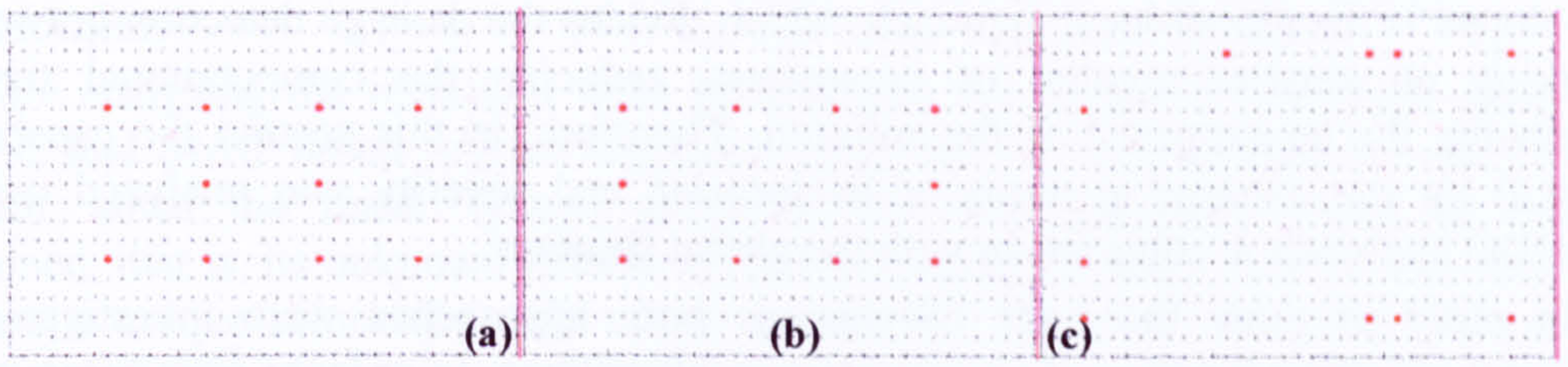

Figure C. 6 – EFI sensor locations: (a) MMF; (b) RSS/MKE; (c) MSE.

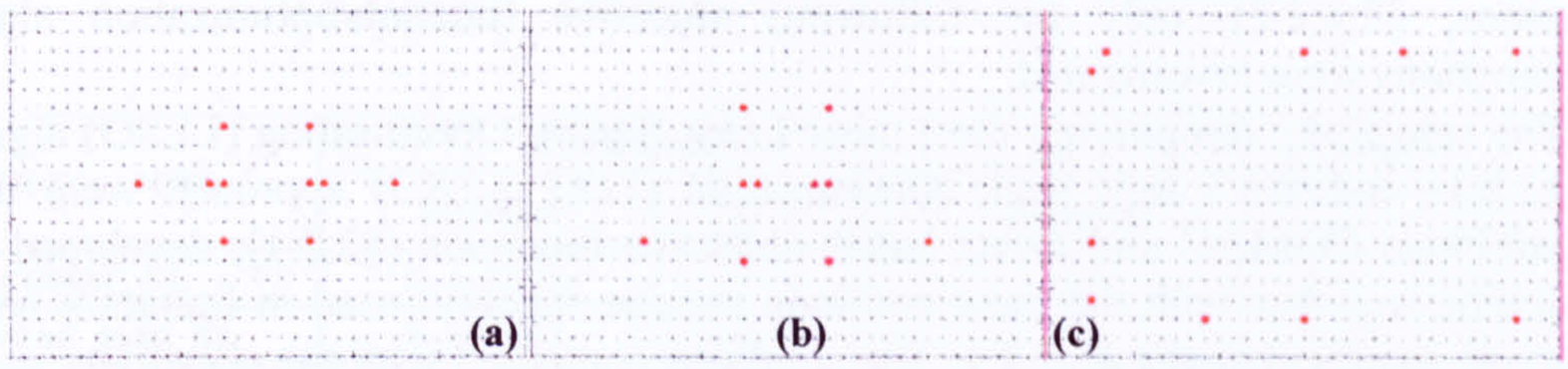

Figure C. 7 – EFI-DPR sensor locations: (a) MMF; (b) RSS/MKE; (c) MSE.

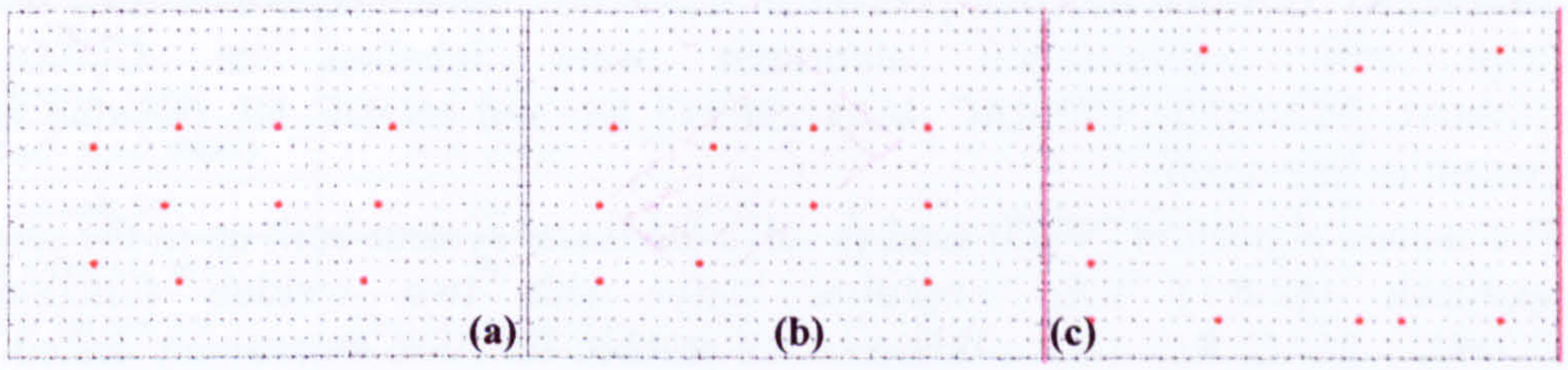

Figure C. 8 – KEM sensor locations: (a) MMF; (b) RSS/MKE; (c) MSE.

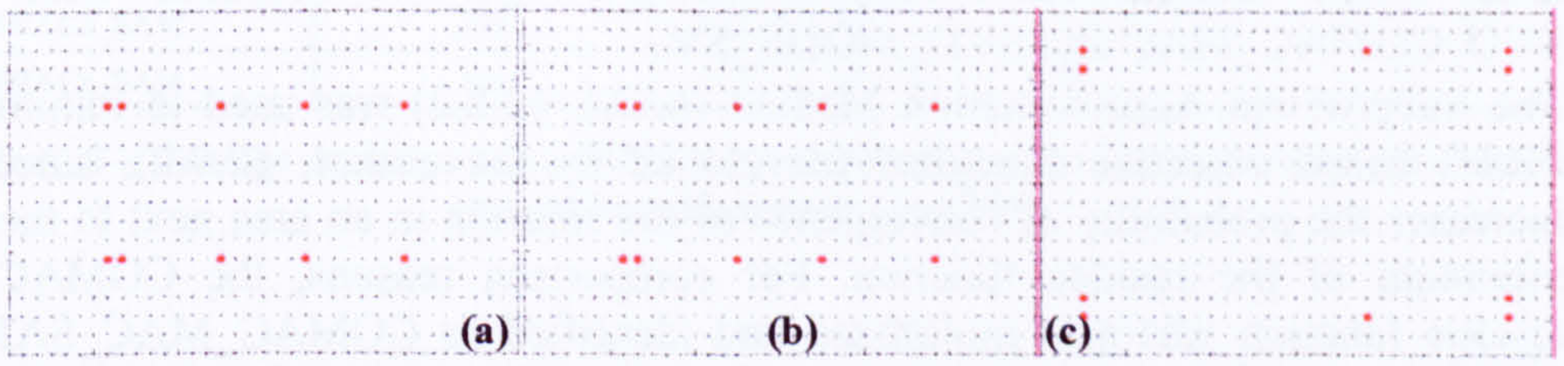

Figure C. 9 – EVP sensor locations: (a) MMF; (b) RSS/MKE; (c) MSE.

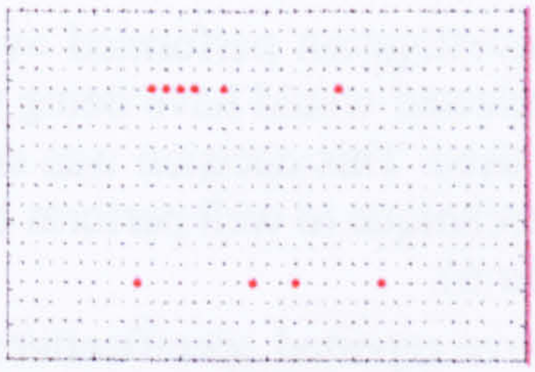

Figure C. 10 – Gm2 sensor locations.

C.4.3 Global Vs Global-Local approach

As mentioned before, the main feature of the damage detection methodology developed is the global-local approach, which divides the damage detection in two steps, working on smaller number of parameters, reducing the computational time and enhancing the convergence of the solution. Therefore, in this section the capability of identifying the damage in terms of its location and severity was analyzed using the GLDDO approach in comparison with the global solution.

In order to draw the right conclusions both approaches were investigated with different objective functions and optimization algorithms. In order to save computational time and to limit the danger of not converging solutions (as for FRF based residue functions, §2.4.2.2), only the following objective function/optimization algorithm combinations were investigated:

- The sensitivity (employing the Linear Least Square Optimisation (LLSO) algorithm, §2.8.1) and the Large Scale Optimisation (LSO, §2.8.3) approach were used to minimize COMAC and MAC based objective functions (§2.7.1), developed by the author, together with the most common residue function used in literature based on mode shapes changes §2.4.2.1. The solutions computed with the sensitivity approach were identified as COMAC, COMAC_MAC, COMAC_MAC_FREQ and MODE_SV (residue function present in literature), while those evaluated using the large scale optimization algorithm were labelled as COMAC_NL, COMAC_MAC_NL, COMAC_MAC_FREQ_NL and MODE_NL (residue function present in literature).
- The second algorithm (SVD) used to solve the linear system built up in the sensitivity approach (§2.8.1) was employed only with two residue functions the COMAC_MAC_ReF (since this was the residue function extensively tested on the cantilever beam, where did not showed any convergence problem §2.7.1) and the mode shape changes based residue function. The two solutions were named SVD_COMAC_MAC and SVD_MODE_SV.
- The Subproblem Approximation Method (SAM, §2.8.2) was used to minimize the FRAC based objective functions (developed by the author, §2.7.2), since SAM increases the probability of convergence of the solution in an area next to the global minimum of the residue function. For comparison reasons, the COMAC_MAC residue function was also minimized and identified as COMAC_MAC_SAM. The FRAC based solution were labeled, respectively, FRACm_SAM, FRACr_SAM and FRACc_SAM.

Moreover, since a similar investigation performed over all the five OSP techniques and the three TMSS methods selected would have being too computationally expensive, only the EFI OSP method was used. This decision was corroborated by the fact that the EFI method was the only OSP technique to well perform both on the cantilever beam and on the suspension bridge (chapter 6).

Finally, according to the above reported specifications, the results of the Global Vs Global-Local approach were reported in table format (Table C. 3-Table C. 11), where two sections can be identified, one for each approach investigated. Both table sections had a first column where was specified if the damage location was identified. The error of the predicted severity in terms of the plate thickness was input in the second column (0%

perfect damage identification, 20% damage unidentified). In the third column of each section was reported the computational time needed for such prediction. In the fourth column of the Global section was also reported the mean error in percentage points of the plate thickness.

Before analysing the results, it must be said that the sensitivity approach using the COMAC and MAC based residue functions could not be implemented for the Global approach, since the linear system generated by such approach would be under-determined, that is, its unknown number (columns) would be larger than its row number, therefore, a unique solutions would not be guaranteed. However, since the SVD solver was quicker than the linear least square optimization algorithm, this was used as proof of the impossibility of the sensitivity approach to deliver any solution for a problem so defined.

7004 EFI – MMF	Global-Local			Global			
	Identified	Error (%)	time (min)	Identified	Error (%)	time (min)	Mean error (%)
COMAC_NL	N. A. (7001)	16.40	62	No	9.72	656	8.44
COMAC_MAC_NL	N. A. (7007)	15.64	75	No	5.92	571	8.46
COMAC_MAC_FREQ_NL	N. A. (7001)	16.40	91	Second peak of 2	14.88	574	0.24
MODE_NL	No	20.00	18	Yes	0.00	431	0.37
COMAC	No	20.00	17	Not Implementable	20.00		
COMAC_MAC	N. A. (7001)	17.87	11	Not Implementable	20.00		
COMAC_MAC_FREQ	N. A. (7007)	13.93	29	Not Implementable	20.00		
MODE_SV	No	20.00	21	No convergence	20.00	33	
SVD_COMAC_MAC	No	20.00	18	No convergence	20.00	65	
SVD_MODE_SV	Next Macro_area (4)	20.00	16	Yes	-20.09	233	1.27
COMAC_MAC_SAM	Yes	7.52	183	Yes	7.70	285	3.52
FRACm_SAM	Yes	4.02	552	Yes	4.52	1354	2.32
FRACr_SAM	Yes	8.32	345	Yes	8.68	902	3.52
FRACc_SAM	Yes	14.3	345	No			

Table C. 3 – Damage detection using MMF target mode shape set: Global-Local/Global approach comparison (Damaged area 7004).

6008 EFI - MMF	Global-Local			Global			
	Identified	Error (%)	time (min)	Identified	Error (%)	time (min)	Mean error (%)
COMAC_NL	No	20.00	63	Yes	11.69	652	4.35
COMAC_MAC_NL	Yes	6.04	98	N. A. (6007)	10.29	567	7.10
COMAC_MAC_FREQ_NL	Next Macro_area (9)	20.00	82	Second peak of 3	17.00	589	0.28
MODE_NL	Macro_area	20.00	41	Third peak of 4	19.78	425	0.29
COMAC	No	20.00	17	Not Implementable	20.00		
COMAC_MAC	Next Macro_area (9)	20.00	18	Not Implementable	20.00		
COMAC_MAC_FREQ	Next Macro_area (9)	19.54	22	Not Implementable	20.00		
MODE_SV	Macro_area	12.77	22	No convergence	20.00	33	
SVD_COMAC_MAC	Yes	0.35	13	No convergence	20.00	66	
SVD_MODE_SV	Macro_area	9.54	17	Yes	-1.13	228	1.21
COMAC_MAC_SAM	Yes	5.83	76	Yes	7.55	213	1.00
FRACm_SAM	Yes	4.22	840	Yes	7.55	1882	1.03
FRACr_SAM	Yes	5.81	180	Yes	5.68	598	1.25
FRACc_SAM	Yes	5.04	120	Yes	5.25	498	1.38

Table C. 4 - Damage detection using MMF target mode shape set: Global-Local/Global approach comparison (Damaged area 6008).

3004 EFI - MMF	Global-Local			Global			
	Identified	Error (%)	time (min)	Identified	Error (%)	time (min)	Mean error (%)
COMAC_NL	No	20.00	65	Yes	3.91	636	9.36
COMAC_MAC_NL	Next Macro_area (6)	20.00	100	No	17.75	577	3.32
COMAC_MAC_FREQ_NL	No	20.00	91	Yes	1.98	568	0.09
MODE_NL	Next Macro_area (6)	20.00	55	No	20.00	443	0.24
COMAC	N. A. (2006)	20.00	17	Not Implementable	20.00		
COMAC_MAC	Next Macro_area (6)	20.00	7	Not Implementable	20.00		
COMAC_MAC_FREQ	No	20.00	30	Not Implementable	20.00		
MODE_SV	No	20.00	21	No convergence	20.00	42	
SVD_COMAC_MAC	No	20.00	17	No convergence	20.00	66	
SVD_MODE_SV	Next Macro_area (6)	20.00	17	Yes	-1.69	230	0.98
COMAC_MAC_SAM	Yes	5.79	142	Yes	8.78	251	1.94
FRACm_SAM	Yes	2.26	642	Yes	2.57	1702	2.05
FRACr_SAM	Yes	5.01	352	Yes	4.57	868	3.95
FRACc_SAM	Yes	1.67	451	No	19.15	652	9.45

Table C. 5 - Damage detection using MMF target mode shape set: Global-Local/Global approach comparison (Damaged area 3004).

7004 EFI - MKE	GLOBAL-LOCAL			GLOBAL			
	Identified	Error (%)	time (min)	Identified	Error (%)	time (min)	Mean error (%)
COMAC_NL	Macro_area	17.34	40	No	9.72	656	8.44
COMAC_MAC_NL	N. A. (7007)	15.34	46	No	6	571	8.46
COMAC_MAC_FREQ_NL	N. A. (7007)	14.05	79	Second peak of 2	14.88	574	0.24
MODE_NL	N. A. (7001)	20.00	73	Yes	0.00	431	0.00
COMAC	Yes	14.83	35	Not Implementable	20.00		
COMAC_MAC	Yes	9.75	38	Not Implementable	20.00		
COMAC_MAC_FREQ	Yes	8.17	41	Not Implementable	20.00		
MODE_SV	No	20.00	7	No convergence	20.00	35	
SVD_COMAC_MAC	Next Macro_area (8)	20.00	38	No convergence	20.00		
SVD_MODE_SV	Yes	4.40	20	No	20.00	212	4.52
COMAC_MAC_SAM	Yes	5.26	81	Yes	6.89	247	0.95
FRACm_SAM	Yes	3.54	793	Yes	6.84	1724	1.27
FRACr_SAM	Yes	5.57	194	Yes	6.04	607	1.67
FRACc_SAM	Yes	4.97	107	Yes	5.98	478	1.09

Table C. 6 - Damage detection using MKE target mode shape set: Global-Local/Global approach comparison (Damaged area 7004).

6008 EFI - MKE	GLOBAL-LOCAL			GLOBAL			
	Identified	Error (%)	time (min)	Identified	Error (%)	time (min)	Mean error (%)
COMAC_NL	Next Macro_area (9)	20.00	71	Yes	12	652	4.35
COMAC_MAC_NL	Next Macro_area (9)	20.00	71	N. A. (6007)	10	567	7.10
COMAC_MAC_FREQ_NL	Next Macro_area (9)	20.00	74	Second peak of 3	17	589	0.28
MODE_NL	Next Macro_area (5)	20.00	36	Third peak of 4	20	425	0.29
COMAC	No	20.00	34	Not Implementable	20.00		
COMAC_MAC	Yes	1.07	35	Not Implementable	20.00		
COMAC_MAC_FREQ	Next Macro_area (9)	20.00	39	Not Implementable	20.00		
MODE_SV	Yes	2.72	22	No convergence	20	36	
SVD_COMAC_MAC	Next Macro_area (5)	20.00	38	No convergence	20	49	
SVD_MODE_SV	No	20.00	20	No convergence	20	53	
COMAC_MAC_SAM	Yes	6.57	97	Yes	8.01	284	1.54
FRACm_SAM	Yes	4.21	824	Yes	7.18	1823	1.47
FRACr_SAM	Yes	5.24	206	Second peak of 3	9.21	729	4.33
FRACc_SAM	No	18.54	193	No	17.97	494	3.87

Table C. 7 - Damage detection using MKE target mode shape set: Global-Local/Global approach comparison (Damaged area 6008).

3004 EFI - MKE	GLOBAL-LOCAL			GLOBAL			
	Identified	Error (%)	time (min)	Identified	Error (%)	time (min)	Mean error (%)
COMAC_NL	No	20.00	69	Yes	3.91	636	9.36
COMAC_MAC_NL	Next Macro_area (6)	20.00	74	No	17.75	577	3.32
COMAC_MAC_FREQ_NL	No	20.00	82	Yes	1.98	568	0.09
MODE_NL	No	20.00	74	No	20.00	443	0.24
COMAC	No	20.00	34	Not Implementable	20.00		
COMAC_MAC	No	20.00	40	Not Implementable	20.00		
COMAC_MAC_FREQ	No	20.00	38	Not Implementable	20.00		
MODE_SV	Next Macro_area (6)	20.00	7	No convergence	20.00	40	
SVD_COMAC_MAC	No	20.00	14	No convergence	20.00	64	
SVD_MODE_SV	No	20.00	19	No convergence	20.00	73	
COMAC_MAC_SAM	Yes	5.96	87	Yes	8.57	257	2.08
FRACm_SAM	Yes	5.84	893	Yes	6.84	1742	2.54
FRACr_SAM	Yes	6.15	218	No	17.59	635	9.45
FRACc_SAM	No	17.87	223	No	19.27	566	8.39

Table C. 8 - Damage detection using MKE target mode shape set: Global-Local/Global approach comparison (Damaged area 3004).

7004 EFI - MSE	GLOBAL-LOCAL			GLOBAL			
	Identified	Error (%)	time (min)	Identified	Error (%)	time (min)	Mean error (%)
COMAC_NL	Yes	6.28	96	N. A. (7007)	9.74	815	6.19
COMAC_MAC_NL	Yes	3.93	102	N. A. (7007)	15.40	592	1.71
COMAC_MAC_FREQ_NL	Yes	0.71	109	N. A. (7007)	11.73	574	4.69
MODE_NL	No	20.00	95	No	20.00	43	0.25
COMAC	Yes	0.69	42	Not Implementable	20.00		
COMAC_MAC	Yes	0.50	47	Not Implementable	20.00		
COMAC_MAC_FREQ	Yes	0.28	54	Not Implementable	20.00		
MODE_SV	No	20.00	44	No	20.00	34	0.52
SVD_COMAC_MAC	Yes	4.40	20	No convergence	20.00		
SVD_MODE_SV	Yes	3.98	24	No convergence	21.00		
COMAC_MAC_SAM	Yes	4.51	78	Yes	7.87	276	3.52
FRACm_SAM	Yes	4.16	763	Yes	7.35	1821	3.05
FRACr_SAM	Yes	5.24	235	No	17.82	624	7.52
FRACc_SAM	Yes	7.43	267	No	16.53	561	6.46

Table C. 9 - Damage detection using MSE target mode shape set: Global-Local/Global approach comparison (Damaged area 7004).

6008 EFI - MSE	GLOBAL-LOCAL			GLOBAL			
	Identified	Error (%)	time (min)	Identified	Error (%)	time (min)	Mean error (%)
COMAC_NL	Next Macro_area (9)	20.00	96	N. A. (9002)	12	838	5.52
COMAC_MAC_NL	Yes	0.59	106	Yes	15	589	3.01
COMAC_MAC_FREQ_NL	Yes	0.22	103	Yes	13	576	4.84
MODE_NL	Next Macro_area (5)	20.00	95	No	20.00	56	0.38
COMAC	Yes	0.26	42	Not Implementable	20.00		
COMAC_MAC	Yes	0.15	49	Not Implementable	20.00		
COMAC_MAC_FREQ	Yes	0.10	54	Not Implementable	20.00		
MODE_SV	No	20.00	52	No	20.00	34	0.58
SVD_COMAC_MAC	No	20.00	20	No convergence	20.00		
SVD_MODE_SV	No	20.00	20	No convergence	20.00		
COMAC_MAC_SAM	Yes	5.24	92	Yes	8.61	316	4.57
FRACm_SAM	Yes	3.72	751	Yes	6.37	1867	3.92
FRACr_SAM	Yes	4.95	264	No	16.24	631	7.63
FRACc_SAM	No	15.43	227	No	17.96	572	7.82

Table C. 10 - Damage detection using MSE target mode shape set: Global-Local/Global approach comparison (Damaged area 6008).

3004 EFI - MSE	GLOBAL-LOCAL			GLOBAL			
	Identified	Error (%)	time (min)	Identified	Error (%)	time (min)	Mean error (%)
COMAC_NL	No	20.00	96	Second peak	10.06	814	6.00
COMAC_MAC_NL	Yes	2.32	106	No	13.45	588	3.05
COMAC_MAC_FREQ_NL	Yes	0.59	100	No	9.02	579	6.27
MODE_NL	No	20.00	95	No	20.00	49	0.26
COMAC	Yes	0.30	43	Not Implementable	20.00		
COMAC_MAC	N. A. (2006)	20.00	53	Not Implementable	20.00		
COMAC_MAC_FREQ	Yes	0.13	53	Not Implementable	20.00		
MODE_SV	Next Macro-area (2)	20.00	52	No	20.00	38	0.36
SVD_COMAC_MAC	No	20.00	19	No convergence	20.00		
SVD_MODE_SV	No	20.00	20	No convergence	20.00		
COMAC_MAC_SAM	Yes	4.67	73	Yes	8.34	364	4.67
FRACm_SAM	Yes	3.54	726	Yes	7.57	1794	4.16
FRACr_SAM	Yes	4.27	254	No	17.94	735	9.57
FRACc_SAM	Yes	6.14	217	No	17.41	537	8.54

Table C. 11 - Damage detection using MSE target mode shape set: Global-Local/Global approach comparison (Damaged area 3004).

C.4.3.1 Global Vs Global-Local approach: Results analysis.

The tables (Table C. 3-Table C. 11), showed in the previous section, gave every information about the damage detection processes carried out in the investigation delineated in section C.4.3. These data could be organized differently in order to highlight separately the detection of the presence, the location and the severity of the

damage introduced with the different residue functions, optimization algorithms and target mode shape sets employed.

The first two features (the damage presence and location) can be evinced by grouping the "identified" columns of the above mentioned tables in a single table (Table C. 12). Except for the COMAC and MAC derived residue functions (Global approach) minimized using a sensitivity approach, all the detection processes performed pointed out the damage presence, though not all identification procedures were able to localize correctly the actual location of the introduced flaw. In order to guide the reader in a quick visualization of the information on the predicted location of the damage, the table cells were shaded according a defined colour scale.

In accordance with this colour scale, a cell was shaded with yellow if and only if the absolute local maximum of the thickness changes, predicted by either the Global or the Global-Local approach, was localized correctly. A green shaded cell corresponded to the absolute local maximum of thickness changes predicted on an area next to the actual damaged. Then, an orange depicted cell meant that either the macro-area, where actually the damage was located, was identified or a local maximum of the predicted thickness changes identified the real location of the introduced defect. Following, a red cell indicated the identification of a macro area next to that actually containing the damage. Finally, the colour scale ends with a sky blue cell, which designated a completely faulted damage localization.

Moreover, the table was divided in three sections, one for each target mode shape set used (MMF, MKE and MSE). Each section was partitioned in four parts, identifying the different optimization algorithm used, Large Scale Optimization (LSO) algorithm, Linear Least Square Optimisation algorithm (LLSO, sensitivity approach), SVD (sensitivity approach) and the Subproblem Approximation Method.

METHODOLOGY		MMF			MKE			MSE		
		7004	6008	3004	7004	6008	3004	7004	6008	3004
COMAC_NL	GLOBAL	No	Yes	Yes	No	Yes	Yes	N. A. (7007)	N. A. (9002)	2nd peak of 2
	GLOB.-LOCAL	N. A. (7001)	No	No	Macro_area	N. M._A.(9)	No	Yes	N. M._A.(9)	No
COMAC_MAC_NL	GLOBAL	No	N. A. (6007)	No	No	N. A. (6007)	No	N. A. (7007)	Yes	No
	GLOB.-LOCAL	N. A. (7007)	Yes	N. M._A.(6)	N. A. (7007)	N. M._A.(9)	N. M._A.(6)	Yes	Yes	Yes
COMAC_MAC_FREQ_NL	GLOBAL	2nd peak of 2	2nd peak of 3	Yes	2nd peak of 2	2nd peak of 3	Yes	N. A. (7007)	Yes	No
	GLOB.-LOCAL	N. A. (7001)	N. M._A.(9)	No	N. A. (7007)	N. M._A.(9)	No	Yes	Yes	Yes
MODE_NL	GLOBAL	Yes	3rd peak of 4	No	Yes	3rd peak of 4	No	No	No	No
	GLOB.-LOCAL	No	Macro_area	N. M._A.(6)	N. A. (7001)	N. M._A.(5)	No	No	N. M._A.(5)	No
COMAC	GLOBAL	Not Impl.	Not Impl.	Not Impl.	Not Impl.	Not Impl.	Not Impl.	Not Impl.	Not Impl.	Not Impl.
	GLOB.-LOCAL	No	No	N. A. (2006)	Yes	No	No	Yes	Yes	Yes
COMAC_MAC	GLOBAL	Not Impl.	Not Impl.	Not Impl.	Not Impl.	Not Impl.	Not Impl.	Not Impl.	Not Impl.	Not Impl.
	GLOB.-LOCAL	N. A. (7001)	N. M._A.(9)	N. M._A.(6)	Yes	Yes	No	Yes	Yes	N. A. (2006)
COMAC_MAC_FREQ	GLOBAL	Not Impl.	Not Impl.	Not Impl.	Not Impl.	Not Impl.	Not Impl.	Not Impl.	Not Impl.	Not Impl.
	GLOB.-LOCAL	N. A. (7007)	N. M._A.(9)	No	Yes	N. M._A.(9)	No	Yes	Yes	Yes
MODE_SV	GLOBAL	No conv.	No conv.	No conv.	No conv.	No conv.	No conv.	No	No	No
	GLOB.-LOCAL	No	Macro_area	No	No	Yes	N. M._A.(6)	No	No	N. M._A. (2)
SVD_COMAC_MAC	GLOBAL	No conv.	No conv.	No conv.	No conv.	No conv.	No conv.	No conv.	No conv.	No conv.
	GLOB.-LOCAL	No	Yes	No	N. M._A.(8)	N. M._A.(5)	No	Yes	No	No
SVD_MODE_SV	GLOBAL	Yes	Yes	Yes	No	No conv.	No conv.	No conv.	No conv.	No conv.
	GLOB.-LOCAL	N. M._A.(4)	Macro_area	N. M._A.(6)	Yes	No	No	Yes	No	No
COMAC_MAC_SAM	GLOBAL	Yes	Yes	Yes	Yes	Yes	Yes	Yes	Yes	Yes
	GLOB.-LOCAL	Yes	Yes	Yes	Yes	Yes	Yes	Yes	Yes	Yes
FRACm_SAM	GLOBAL	Yes	Yes	Yes	Yes	Yes	Yes	Yes	Yes	Yes
	GLOB.-LOCAL	Yes	Yes	Yes	Yes	Yes	Yes	Yes	Yes	Yes
FRACr_SAM	GLOBAL	Yes	Yes	Yes	Yes	2nd peak of 3	No	No	No	No
	GLOB.-LOCAL	Yes	Yes	Yes	Yes	2nd peak of 3	No	No	No	No
FRACc_SAM	GLOBAL	No	Yes	No	Yes	No	No	No	No	No
	GLOB.-LOCAL	Yes	Yes	Yes	Yes	No	No	Yes	No	Yes

N. A. : Next Area; Not Imp. : Not Implementable; N. M._A : Next Macro_area; No conv. : No convergence;

Table C. 12 – Global-Local Vs Global approach: Damage presence and location predicted.

Following the above indications, it is clear that minimizing the residue functions using a large scale optimization algorithm provided a series of contrasting behaviours of the two investigated approaches (Global vs Global-Local) with the change of the target mode shape set employed.

First, for a MMF selected set of target mode shapes, the best performance was recorded by the Global approach, which was able to give information on the location of the damage introduced for all the three cases studied (COMAC_MAC_FREQ_NL), even though in two cases out of three, the damage location was identified by the second peak of the thickness change distribution predicted.

Only another prediction (COMAC_MAC_NL for the Global-Local approach) was capable of supplying, in some extent, information on the damage location for all the damage configurations investigated.

Changing the target mode shape set selected (MKE), a decrease of the number of completely faulted damage localization (number of blue cells) is observed, although the best performances were recorded at the same places as for the MMF predictions.

A radical improvement into the damage localization was obtained by employing MSE target mode shapes. In this case 100% damage localization was scored by the Global-Local approach for two residue functions, the COMAC_MAC_NL and the COMAC_MAC_FREQ_NL. The Global approach was not able to match these performances, even if it was able to provide information on the three damage sites investigated (COMAC_NL). In contrast with this tendency, the MODE_NL (residue function used in literature) did not identify correctly any damage location with the Global approach.

Then, analyzing the results of the residue function minimization carried out using a LLSO algorithm (sensitivity solution methodology), the completely failure of the Global approach blunted to the eyes. Not even the MODE_SV residue function (used in literature with an identical minimization process) was able to provide any information on the defect site.

Conversely, the Global-Local approach using the LLSO algorithm predicted correctly the location of the damages introduced for the MSE case and for all the residue functions developed by the author.

In contrast with the results so far discussed, the SVD minimization (for the MODE_SV residue function used in literature with an identical minimization methodology) process provided a perfect localization of the damage sites for the Global approach using a MMF target mode shape set.

At last, the SAM minimization of the COMAC_MAC_SAM and the FRACm_SAM (author's residue functions) was able to identify correctly, the damage location independently from the target mode shape set and the approach (Global, Global-Local) used. The other two FRAC based residue function (FRACr and FRACc) were capable of identifying all the three damage sites investigated only for the MMF case.

In order to complete the comparison between the Global and the Global-Local approach other two characteristics have to be analyzed, the damage severity and the run time of the damage detections. This could be readily obtained by plotting the errors of the estimated severities and the run times against the residue functions (Figure C. 11-Figure C. 12).

In terms of severity the best estimation (error smaller than 1%) was provided by the COMAC and MAC based residue functions (Global-Local) minimized by the LLSO algorithm (sensitivity methodology) for the MSE target mode shape set. A comparable estimate of the damage severity, but slightly larger, was supplied by the COMAC_MAC_FREQ_NL function (Global-Local).

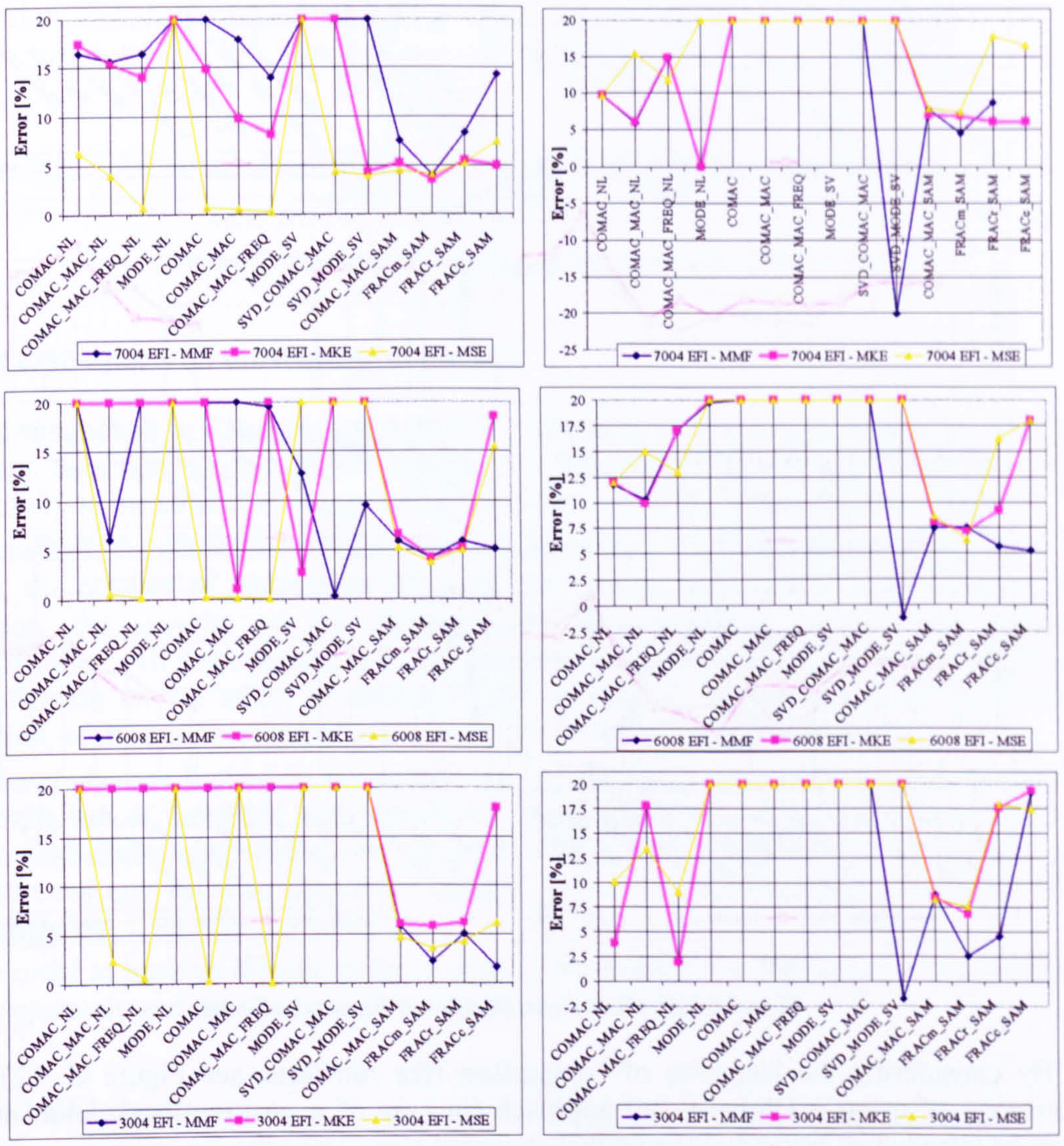

Figure C. 11 – Severity prediction: (a) Global-Local; (b) Global.

As mentioned before, for the Global approach only the SVD_MODE_SV function was capable of identifying correctly the damage locations, but overestimated its severity in all cases studied (Figure C. 11) from about 1% (for the areas 6008 and 3004) to 20% (the double of its real severity) for the area 7004.

The severity estimated minimizing the residue functions investigated using the SAM was predicted with an error between the 3 and 5% for the Global-Local against the 5÷7% of the Global approach.

Figure C. 12 – Run time: (a) Global-Local; (b) Global.

By considering the last term of comparison (the run time, see Figure C. 12), the advantage of using a Global-Local approach (in case of a positive localization of the damage introduced) instead of the Global appeared clear, since the run times ranged from 10min (sensitivity approach) to the 800min of the FRACm_SAM residue function (Global-Local) against 200min of the Global SVD_MODE_SV residue function and the 1800min of the FRACm_SAM residue function.

Therefore, the time savings obtained ranged from about the 90% for large scale approach to the 50% of the SAM optimization (Figure C. 13).

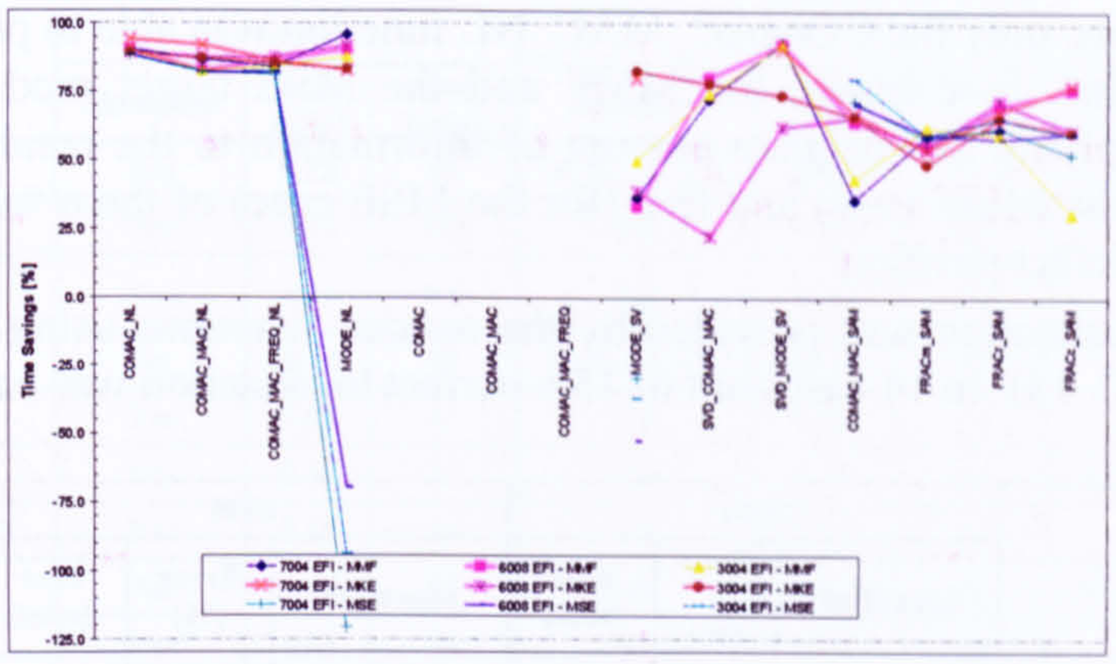

Figure C. 13 – Global-Local Vs Global approach: Time savings.

C.4.4 OSP effects on the damage detection

As mentioned in Chapter 2, the OSP is a central piece of a reliable and an efficient damage detection, since a clever choice of the sensor locations would lead to greater sensitivity to the structural changes and, therefore, a stronger noise withstanding.

However, the choice of the best OSP techniques is not easy, because of the number of them, the number of parameters affecting the damage detection such as the type, the location, the severity of the damage, and the algorithms used for the damage identification. All these factors and their complex interactions led to the set-up of a broad investigation on the effect of different OSP techniques, on the choice of the residue function, of the minimisation algorithm and the set of target mode shapes to select.

The study was limited to the sensitivity and the large scale minimisation approach, since the use of the SAM with the FRAC and COMAC functions was considered too much time consuming. Moreover, since the SVD_COMAC_MAC residue function did not sort out any valuable detection (Table C. 12) this was not considered for the OSP investigation.

In order to have an organic point of view of the results, the OSP results were analysed first separately and, then, an overall analysis was carried out.

C.4.4.1 EFI results

As pointed out in Chapter 3 (§3.5.1) the EFI technique places sensors on a structure maximising both the spatial independence and signal strength of N target mode shapes. Because three different sets of target mode shapes were investigated, one for each TMSS technique studied, the damage detection results were organized in three different tables (Table C. 13-Table C. 15), one for each sets.

Moreover, in order to highlight the residue functions that provided correct information on the damage site, the relative table row was yellow shaded.

In this way, it was immediate that MKE target mode shape selection technique did not provided sufficient information for most of the residue functions during the damage

detection process, only the COMAC_MAC_NL function was able to provide clues on the damage locations. In contrast, the MMF and the MSE target mode shape sets were capable of supplying an adequate amount of information to the residue functions, such that three (for the MMF case) and five (for the MSE case) of them were able to provide insight on the defect position.

The best localization was provided by the residue functions using MSE target mode shapes (Table C. 15). In 14 cases out of 15 a perfect localization was achieved.

MMF_EFI	7004			6008			3004		
	Identified	Error (%)	time (min)	Identified	Error (%)	time (min)	Identified	Error (%)	time (min)
COMAC_NL	N. A. (7001)	16.40	62	No	20.00	63	No	20.00	65
COMAC_MAC_NL	N. A. (7007)	15.64	75	Yes	6.04	98	N. M._A. (6)	20.00	100
COMAC_MAC_FREQ_NL	N. A. (7001)	16.40	91	N. M._A. (9)	20.00	82	No	20.00	91
MODE_NL	No	20.00	18	Macro_area	20.00	41	N. M._A. (6)	20.00	55
COMAC	No	20.00	17	No	20.00	17	N. A. (2006)	20.00	17
COMAC_MAC	N. A. (7001)	17.87	11	N. M._A. (9)	20.00	18	N. M._A. (6)	20.00	7
COMAC_MAC_FREQ	N. A. (7007)	13.93	29	N. M._A. (9)	19.54	22	No	20.00	30
MODE_SV	No	20.00	21	Macro_area	12.77	22	No	20.00	21
SVD_MODE_SV	N. M._A. (4)	20.00	16	Macro_area	9.54	17	N. M._A. (6)	20.00	17

Table C. 13 – OSP investigation: EFI technique – MMF target mode shapes.

MKE_EFI	7004			6008			3004		
	Identified	Error (%)	time (min)	Identified	Error (%)	time (min)	Identified	Error (%)	time (min)
COMAC_NL	Macro_area	17.34	40	N. M._A. (9)	20.00	71	No	20.00	69
COMAC_MAC_NL	N. A. (7007)	15.34	46	N. M._A. (9)	20.00	71	N. M._A. (6)	20.00	74
COMAC_MAC_FREQ_NL	N. A. (7007)	14.05	79	N. M._A. (9)	20.00	74	No	20.00	82
MODE_NL	N. A. (7001)	20.00	73	N. M._A. (5)	20.00	36	No	20.00	74
COMAC	Yes	14.83	35	No	20.00	34	No	20.00	34
COMAC_MAC	Yes	9.75	38	Yes	1.07	35	No	20.00	40
COMAC_MAC_FREQ	Yes	8.17	41	N. M._A. (9)	20.00	39	No	20.00	38
MODE_SV	No	20.00	7	Yes	2.72	22	N. M._A. (6)	20.00	7
SVD_MODE_SV	Yes	4.40	20	No	20.00	20	No	20.00	19

Table C. 14 – OSP investigation: EFI technique – MKE target mode shapes.

MSE_EFI	7004			6008			3004		
	Identified	Error (%)	time (min)	Identified	Error (%)	Time (min)	Identified	Error (%)	time (min)
COMAC_NL	Yes	6.28	96	N. M._A. (9)	20.00	96	No	20.00	96
COMAC_MAC_NL	Yes	3.93	102	Yes	0.59	106	Yes	2.32	106
COMAC_MAC_FREQ_NL	Yes	0.71	109	Yes	0.22	103	Yes	0.59	100
MODE_NL	No	20.00	95	N. M._A. (5)	20.00	95	No	20.00	95
COMAC	Yes	0.69	42	Yes	0.26	42	Yes	0.30	43
COMAC_MAC	Yes	0.50	47	Yes	0.15	49	N. A. (2006)	20.00	53
COMAC_MAC_FREQ	Yes	0.28	54	Yes	0.10	54	Yes	0.13	53
MODE_SV	No	20.00	44	No	20.00	52	N. M._A. (2)	20.00	52
SVD_MODE_SV	Yes	4.40	20	No	20.00	20	No	20.00	19

Table C. 15 – OSP investigation: EFI technique – MSE target mode shapes.

By plotting the error of the damage severity predicted of only the shaded cells (Figure C. 14), the enhancements in the severity prediction, due to the change of the target mode shape set employed during the damage detection process, could be observed. For example, the error of the COMAC_MAC_NL damage severity prediction decreased from 15-20% range (MKE) to 1-4% range (MSE), via a 6-20% range for the MMF case. However, the best damage detection prediction was carried out by the sensitivity minimisation (LLSO algorithm). Three out of four residue functions had an error smaller than 1% for each damage location investigated. Among these three functions the COMAC – MSE resulted to be the quickest (Figure C. 15) among those capable of identifying correctly the damage in term of its severity and location.

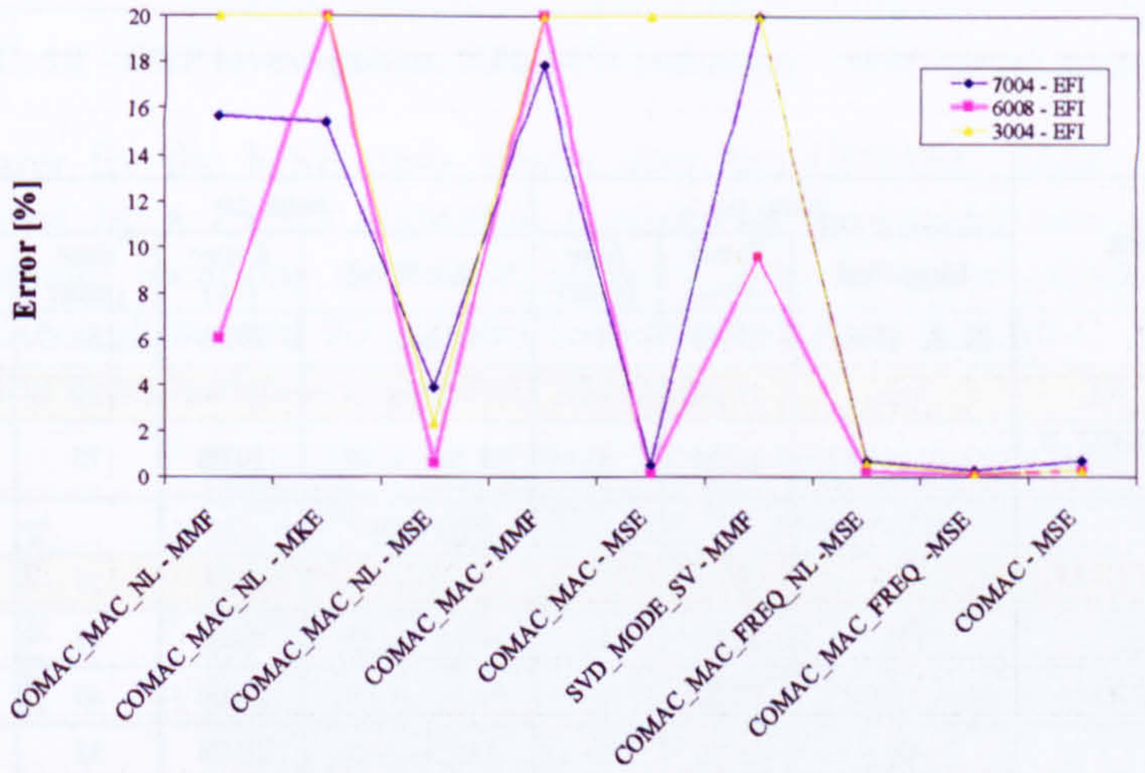

Figure C. 14 - OSP investigation (EFI technique): Error in the severity predicted.

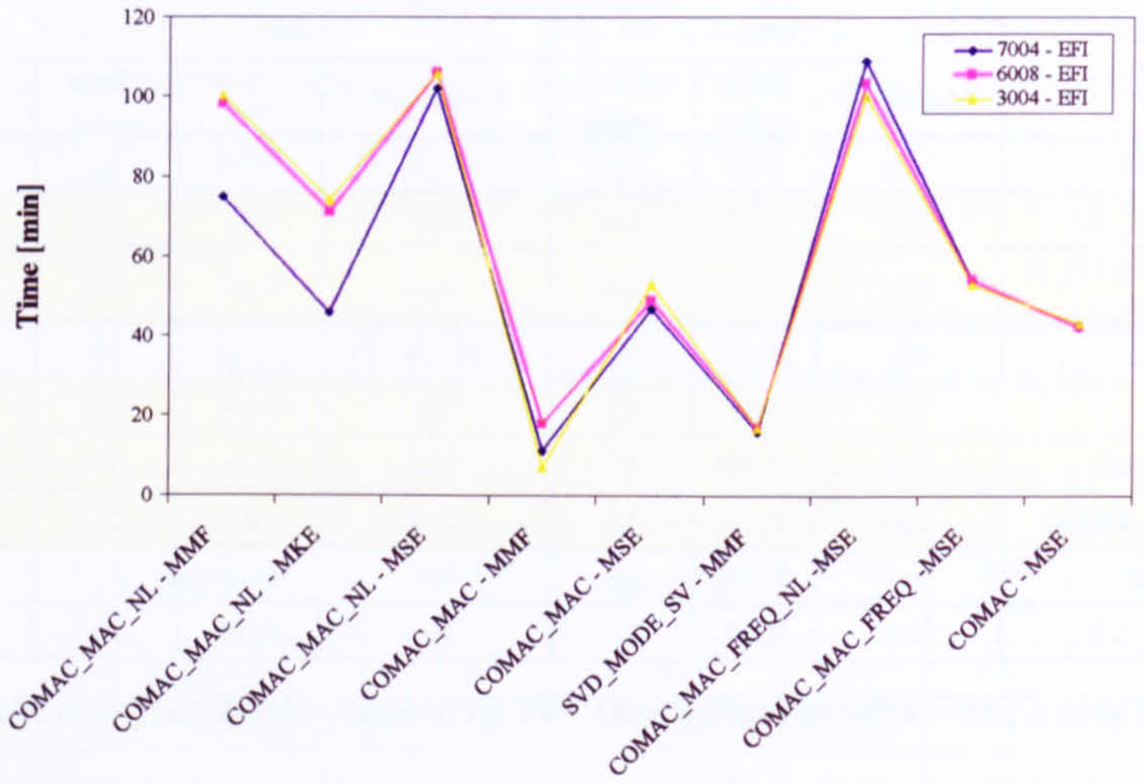

Figure C. 15 – OSP investigation (EFI technique): Run time.

C.4.4.2 EFI-DPR results

The EFI-DPR technique was developed to avert the selection of low energy locations from the EFI algorithm, which would result in a loss of information for the damage detection process.

The damage prediction carried out with the EFI-DPR designed sensor network (Table C. 16-Table C. 18) showed a loss of capability of the damage process to locate and estimate the damage thickness changes compared to that recorded using an EFI selected sensor network.

MMF_EFI-DPR	7004_20			6008_20			3004_20		
	Identified	Error (%)	time (min)	Identified	Error (%)	time (min)	Identified	Error (%)	time (min)
COMAC_NL	N. A. (7001)	17.13	45	No	20.00	64	N. M._A. (6)	20.00	72
COMAC_MAC_NL	Yes	15.30	76	Yes	7.71	78	N. M._A. (6)	20.00	81
COMAC_MAC_FREQ_NL	N. A. (7007)	13.22	81	N. M._A. (9)	20.00	75	No	20.00	78
MODE_NL	Not conv.			Not conv.			Not conv.		
COMAC	N. M._A. (4)	20.00	34	Yes	3.52	27	N. M._A. (6)	20.00	23
COMAC_MAC	No	20.00	41	N. M._A. (5)	20.00	41	No	20.00	41
COMAC_MAC_FREQ	N. A. (7007)	12.29	40	N. M._A. (9)	20.00	40	No	20.00	40
MODE_SV	No	20.00	35	Macro-Area	10.99	35	No	20.00	37
SVD_MODE_SV	N. M._A. (4)	20.00	18	Macro-Area	9.76	18	N. M._A. (6)	20.00	18

Table C. 16 – OSP investigation: EFI-DPR technique – MMF target mode shapes.

MKE_EFI-DPR	7004_20			6008_20			3004_20		
	Identified	Error (%)	time (min)	Identified	Error (%)	time (min)	Identified	Error (%)	time (min)
COMAC_NL	No	20.00	74	No	20.00	67	N. M._A. (6)	20.00	74
COMAC_MAC_NL	N. A. (7007)	13.65	80	N. M._A. (9)	20.00	78	No	20.00	81
COMAC_MAC_FREQ_NL	N. A. (7007)	13.14	83	N. A. (9002)	20.00	78	No	20.00	81
MODE_NL	Macro-Area	20.00	74	Not conv.			No	20.00	74
COMAC	N. A. (7007)	13.32	33	Yes	1.35	30	N. M._A. (6)	20.00	35
COMAC_MAC	No	20.00	42	Yes	1.02	37	No	20.00	43
COMAC_MAC_FREQ	Yes	10.28	42	N. A. (9002)	20.00	41	No	20.00	42
MODE_SV	Yes	0.08	38	N. M._A. (5)	20.00	39	No	20.00	36
SVD_MODE_SV	N. M._A. (4)	20.00	19	NO	20.00	19	No	20.00	19

Table C. 17 – OSP investigation: EFI-DPR technique – MKE target mode shapes

MSE_EFI-DPR	7004_20			6008_20			3004_20		
	Identified	Error (%)	time (min)	Identified	Error (%)	time (min)	Identified	Error (%)	time (min)
COMAC_NL	Yes	3.50	108	N. M._A. (5)	20.00	109	No	20.00	108
COMAC_MAC_NL	Yes	1.02	114	N. M._A. (5)	20.00	114	Yes	0.85	112
COMAC_MAC_FREQ_NL	Yes	1.35	84	Yes	0.09	89	Yes	0.76	95
MODE_NL	No	20.00	103	N. M._A. (5)	20.00	98	No	20.00	97
COMAC	Yes	0.82	47	N. M._A. (5)	20.00	51	N. M._A. (6)	20.00	52
COMAC_MAC	N. M._A. (4)	20.00	58	N. M._A. (6)	20.00	58	No	20.00	58
COMAC_MAC_FREQ	Yes	0.33	52	Yes	0.02	53	No	20.00	57
MODE_SV	No	20.00	51	N. M._A. (5)	20.00	55	Yes	0.06	55
SVD_MODE_SV	No	20.00	24	N. M._A. (5)	20.00	27	No	20.00	25

Table C. 18 – OSP investigation: EFI-DPR technique – MSE target mode shapes.

This was clearer for the MSE case, where only the COMAC_MAC_FREQ residue function minimised by a LLSO algorithm (sensitivity approach) was able to predict correctly the damage locations and their severity with an error smaller than 1.35% (Figure C. 16), although needed 90 minutes for each detection (Figure C. 17), the second largest between the detection process yellow shaded.

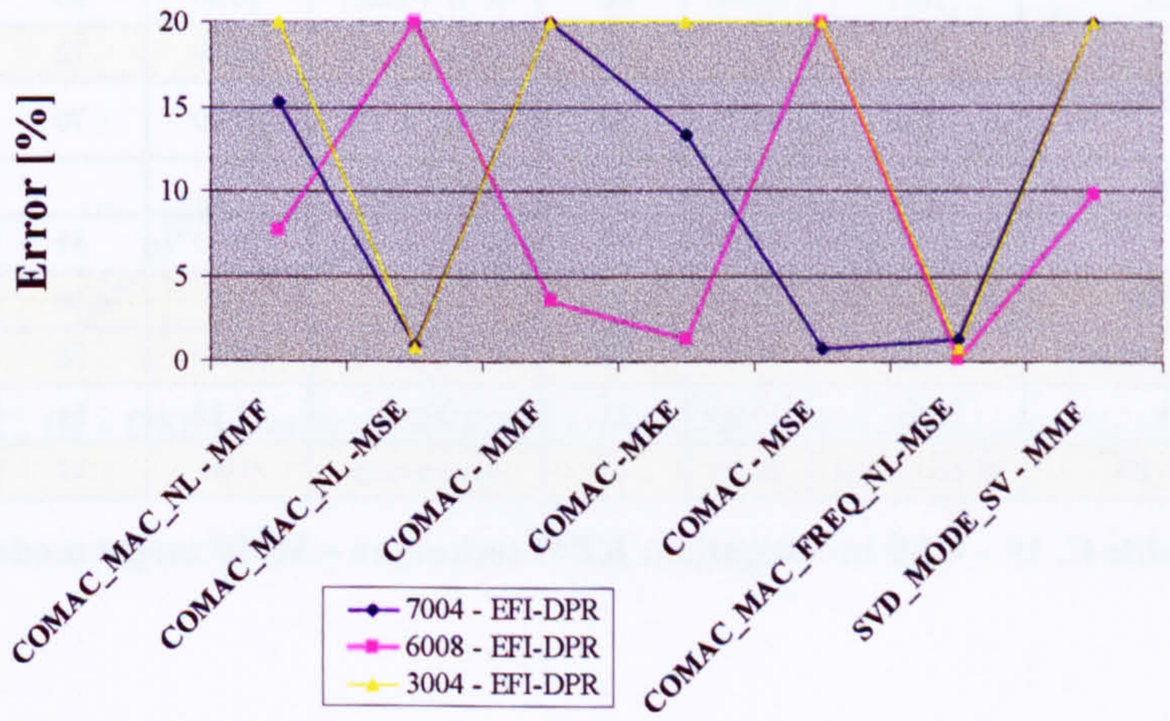

Figure C. 16 - OSP investigation (EFI-DPR technique): Error in the severity predicted.

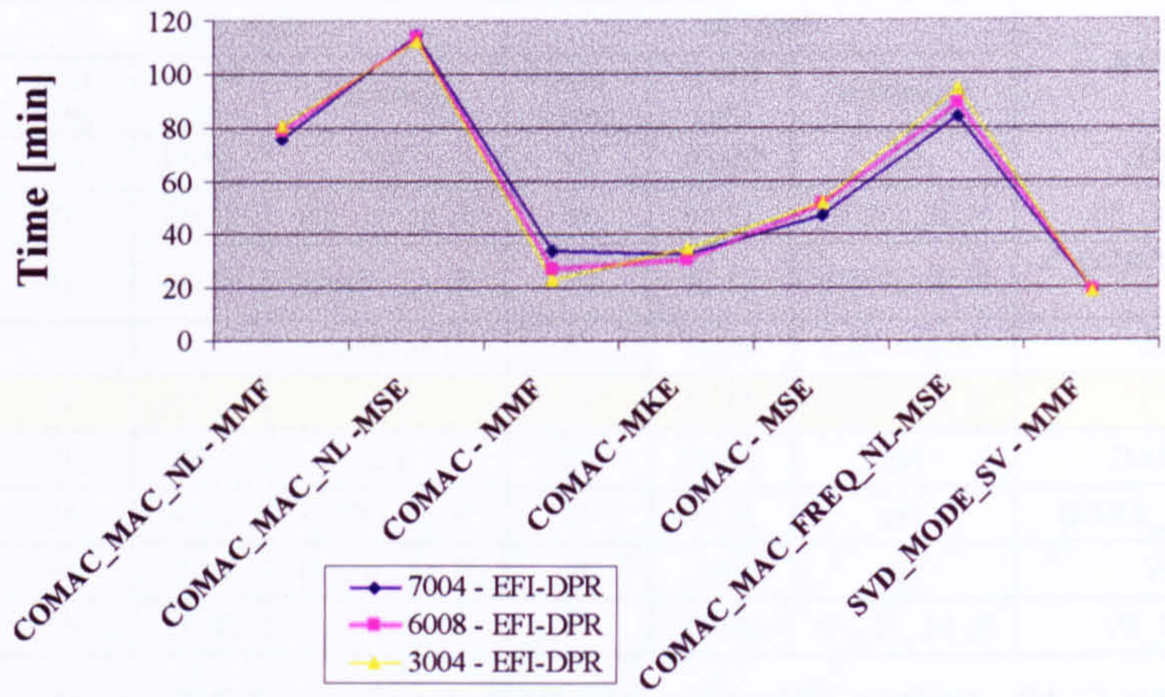

Figure C. 17 – OSP investigation (EFI-DPR technique): Run time.

C.4.4.3 KEM results

The KEM OSP technique consisted in the maximisation of the kinetic energy acquired by the sensor network using the same selection algorithm of the EFI technique, which maximised the Fisher Information matrix determinant.

Once all the detection results were assembled in tables (Table C. 19-Table C. 21), it was clear that the KEM sensor network was capable of supplying more detailed information for MMF selected target mode shape set than for MSE set. However, the best detection was supplied by the COMAC_MAC_FREQ residue function for a MSE target mode shape set, even though the damage detection process failed to identify the defect introduced on the area 6008, where a macro-area (the 9th) next to the actual damaged (the 6th) was identified (Table C. 21, Figure C. 18-Figure C. 19).

MMF_KEM	7004			6008			3004		
	Identified	Error (%)	time (min)	Identified	Error (%)	time (min)	Identified	Error (%)	time (min)
COMAC_NL	Yes	15.60	60	N. A. (9002)	20.00	60	No	20.00	68.77
COMAC_MAC_NL	Yes	15.61	49	N. M._A. (9)	20.00	72	N. M._A. (6)	20.00	69.55
COMAC_MAC_FREQ_NL	Yes	13.79	67	N. M._A. (9)	20.00	70	No	20.00	73.97
MODE_NL	No	20.00	68	Not conv.			No	20.00	67.80
COMAC	N. A. (7001)	15.69	30	N. M._A. (9)	20.00	32	No	20.00	32.27
COMAC_MAC	N. M._A. (4)	20.00	37	Yes	1.15	30	N. M._A. (6)	20.00	37.17
COMAC_MAC_FREQ	Yes	9.37	36	N. M._A. (9)	20.00	36	N. M._A. (6)	20.00	36.00
MODE_SV	No	20.00	31	Yes	12.13	54	No	20.00	36.45
SVD_MODE_SV	N. M._A. (4)	20.00	17	Macro-area	9.98	17	N. M._A. (6)	20.00	17.28

Table C. 19 – OSP investigation: KEM technique – MMF target mode shapes.

MKE_KEM	7004_20			6008_20			3004_20		
	Identified	Error (%)	time (min)	Identified	Error (%)	time (min)	Identified	Error (%)	time (min)
COMAC_NL	No	20.00	64	N. M._A. (9)	20.00	59	No	20.00	63.60
COMAC_MAC_NL	Yes	16.20	73	N. M._A. (9)	20.00	70	No	20.00	72.45
COMAC_MAC_FREQ_NL	N. A. (7007)	12.63	74	N. M._A. (9)	20.00	69	No	20.00	73.93
MODE_NL	No	20.00	68	Not conv.			No	20.00	67.80
COMAC	Yes	12.15	32	No	20.00	32	No	20.00	32.45
COMAC_MAC	No	20.00	38	Yes	1.30	31	No	20.00	37.68
COMAC_MAC_FREQ	Yes	10.29	37	N. A. (9002)	20.00	38	No	20.00	37.77
MODE_SV	Yes	0.32	36	N. M._A. (5)	20.00	36	No	20.00	35.93
SVD_MODE_SV	N. M._A. (4)	20.00	17	No	20.00	18	No	20.00	18.22

Table C. 20 – OSP investigation: KEM technique – MKE target mode shapes

MSE_KEM	7004_20			6008_20			3004_20		
	Identified	Error (%)	time (min)	Identified	Error (%)	time (min)	Identified	Error (%)	time (min)
COMAC_NL	N. A. (7007)	7.35	78	No	20.00	78	No	20.00	78.08
COMAC_MAC_NL	Yes	4.90	85	No	0.25	69	No	0.37	84.72
COMAC_MAC_FREQ_NL	Yes	2.07	85	No	20.00	85	Yes	0.48	55.65
MODE_NL	No	20.00	77	N. M._A. (5)	20.00	77	No	20.00	77.10
COMAC	Yes	0.96	32	N. M._A. (9)	20.00	37	No	20.00	36.80
COMAC_MAC	Macro Area	16.92	43	N. M._A. (9)	20.00	43	No	20.00	43.40
COMAC_MAC_FREQ	Yes	0.09	42	N. M._A. (9)	20.00	43	Yes	0.11	43.00
MODE_SV	No	20.00	35	No	20.00	40	No	20.00	40.05
SVD_MODE_SV	No	20.00	19	No	20.00	19	No	20.00	19.20

Table C. 21 – OSP investigation: KEM technique – MSE target mode shapes

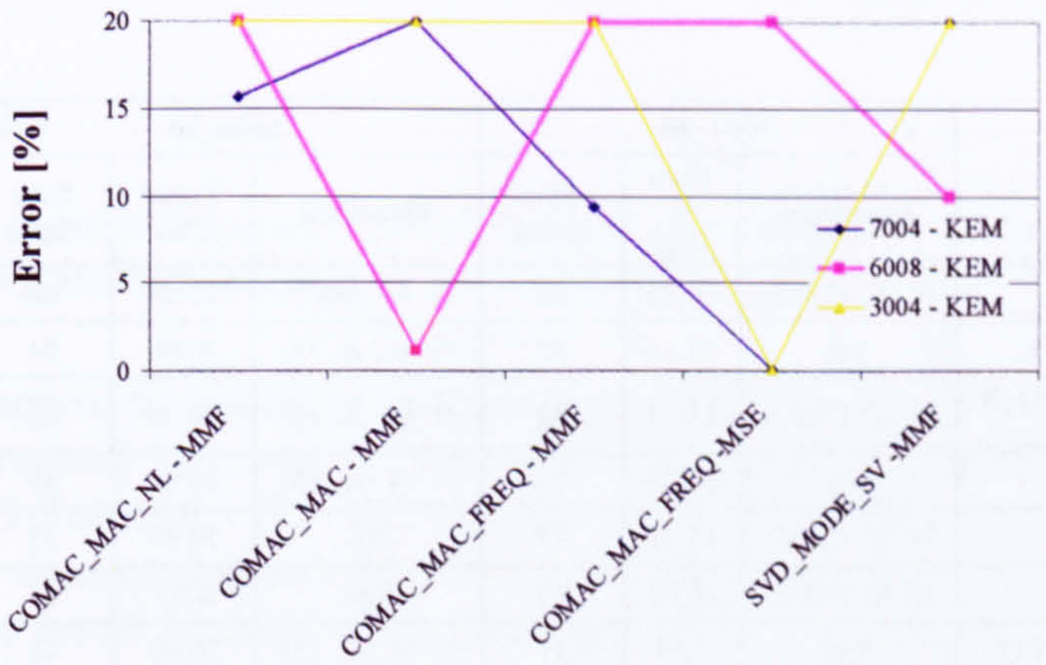

Figure C. 18 - OSP investigation (KEM technique): Error in the severity predicted.

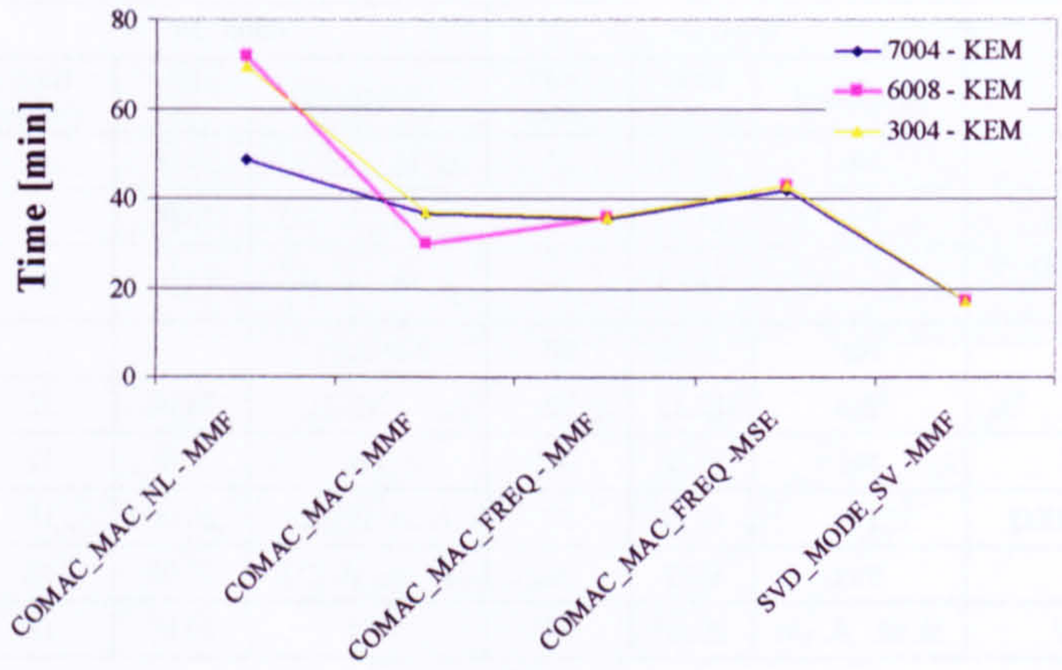

Figure C. 19 - OSP investigation (KEM technique): Run time.

C.4.4.4 EVP results

The EVP sensor selection was designed in order to prevent the placement of sensors on nodal lines of a vibration mode and to maximise the vibration energy measured by the sensors.

This selection philosophy proved to be quite inconsistent for the damage detection processes (Table C. 22-Table C. 24) using MMF and MKE target mode shape sets, since none of the residue functions investigated was capable of identifying correctly all the three damages investigated. On the other hand, the EVP sensor network was able to identify the damaged scenarios studied with the COMAC_MAC function using a MSE selected target mode shape set with a maximum error in the estimate of the severity of 10% (Table C. 24).

MMF_EVP	7004_20			6008_20			3004_20		
	Identified	Error (%)	time (min)	Identified	Error (%)	time (min)	Identified	Error (%)	time (min)
COMAC_NL	N. A. (7007)	16.76	44	N. A. (9002)	20.00	68	No	20.00	75
COMAC_MAC_NL	Yes	16.16	52	N. M._A. (5)	20.00	84	No	20.00	61
COMAC_MAC_FREQ_NL	N. A. (7007)	13.22	84	N. M._A. (5)	20.00	82	No	20.00	61
MODE_NL	No	20.00	86	N. M._A. (5)	20.00	89	No	20.00	65
COMAC	N. A. (7001)	15.71	33	No	20.00	35	No	20.00	35
COMAC_MAC	N. A. (7001)	16.09	40	Yes	0.83	42	No	20.00	37
COMAC_MAC_FREQ	Yes	9.39	41	N. M._A. (9)	20.00	41	No	20.00	41
MODE_SV	No	20.00	34	Second Pick	11.68	39	Yes	0.03	38
SVD_MODE_SV	No	20.00	24	Second Pick	9.63	27	N. M._A. (6)	20.00	25

Table C. 22 – OSP investigation: EVP technique – MMF target mode shapes.

MKE_EVP	7004_20			6008_20			3004_20		
	Identified	Error (%)	time (min)	Identified	Error (%)	time (min)	Identified	Error (%)	time (min)
COMAC_NL	N. A. (7007)	16.10	43	N. A. (9002)	20.00	66	No	20.00	76
COMAC_MAC_NL	Yes	17.55	54	N. M._A. (5)	20.00	84	No	20.00	59
COMAC_MAC_FREQ_NL	N. A. (7007)	12.88	86	N. M._A. (5)	20.00	83	No	20.00	57
MODE_NL	No	20.00	85	N. M._A. (5)	20.00	83	No	20.00	65
COMAC	N. A. (7001)	15.71	33	No	20.00	35	No	20.00	35
COMAC_MAC	N. A. (7001)	15.09	38	Yes	0.34	42	No	20.00	37
COMAC_MAC_FREQ	Yes	7.59	38	N. M._A. (9)	20.00	42	No	20.00	43
MODE_SV	No	20.00	34	Second Pick	10.53	41	Yes	0.03	46
SVD_MODE_SV	No	20.00	21	Second Pick	7.63	21	N. M._A. (6)	20.00	24

Table C. 23 – OSP investigation: EVP technique – MKE target mode shapes.

MSE_EVP	7004_20			6008_20			3004_20		
	Identified	Error (%)	time (min)	Identified	Error (%)	time (min)	Identified	Error (%)	time (min)
COMAC_NL	N. A. (7007)	17.04	40	N. A. (9002)	20.00	72	No	20.00	75
COMAC_MAC_NL	N. A. (7007)	15.54	61	N. M._A. (9)	20.00	81	No	20.00	87
COMAC_MAC_FREQ_NL	Yes	15.98	89	N. M._A. (9)	20.00	81	No	20.00	89
MODE_NL	No	20.00	90	No	20.00	87	No	20.00	69
COMAC	N. A. (7001)	16.00	35	N. M._A. (9)	20.00	38	No	20.00	38
COMAC_MAC	Yes	10.28	43	Yes	1.07	40	Yes	0.53	46
COMAC_MAC_FREQ	Yes	8.84	44	N. M._A. (9)	20.00	45	No	20.00	45
MODE_SV	Yes	0.49	39	N. M._A. (5)	20.00	41	N. A. (3001)	20.00	42
SVD_MODE_SV	N. M._A. (4)	20.00	20	No	20.00	20	No	20.00	20

Table C. 24 – OSP investigation: EVP technique – MSE target mode shapes.

C.4.4.5 Gm2 results

The Gm2 was a control based OSP technique that exploited the concept of robust observability and Grammian aiming at the maximisation of the kinetic energy acquired by the sensors.

This selective approach leaded to damage detections that failed to localise correctly damages with increasing rate with the increase of the order of the target mode shapes used (Table C. 25-Table C. 27). As matter of fact, the MMF set provided enough information to the damage detection process so that three residue functions were able to supply clues on the actual location of the damages studied. In contrast, the MSE selected target mode set did not provided any evidence of the location of the damage.

MMF_Gm2	7004_20			6008_20			3004_20		
	Identified	Error (%)	time (min)	Identified	Error (%)	time (min)	Identified	Error (%)	time (min)
COMAC_NL	N. A. (7007)	16.71	47	Yes	16.20	74	N. M._A. (6)	20.00	76
COMAC_MAC_NL	N. A. (7007)	16.40	42	N. M._A. (9)	20.00	85	No	20.00	85
COMAC_MAC_FREQ_NL	Yes	14.90	82	N. M._A. (9)	20.00	85	No	20.00	83
MODE_NL	No	20.00	87	No	20.00	86	No	20.00	85
COMAC	N. A. (7001)	16.45	36	No	20.00	36	Yes	-13.21	36
COMAC_MAC	N. A. (7001)	14.40	43	N. M._A. (9)	20.00	43	No	20.00	43
COMAC_MAC_FREQ	Yes	10.55	43	N. M._A. (9)	20.00	42	N. M._A. (6)	20.00	42
MODE_SV	No	20.00	39	Second Pick	12.79	39	No	20.00	39
SVD_MODE_SV	N. M._A. (4)	20.00	19	Second Pick	8.23	19	N. M._A. (6)	20.00	19

Table C. 25 - OSP investigation: Gm2 technique – MMF target mode shapes.

MKE_Gm2	7004_20			6008_20			3004_20		
	Identified	Error (%)	time (min)	Identified	Error (%)	time (min)	Identified	Error (%)	time (min)
COMAC_NL	No	20.00	75	Yes	14.30	80	N. M._A. (2)	20.00	113
COMAC_MAC_NL	Yes	16.46	86	Yes	9.83	87	No	20.00	87
COMAC_MAC_FREQ_NL	N. A. (7007)	15.47	90	N. M._A. (9)	20.00	90	No	20.00	87
MODE_NL	No	20.00	79	No	20.00	79	No	20.00	85
COMAC	N. A. (7001)	19.98	20	Yes	-0.68	38	No	20.00	23
COMAC_MAC	Yes	14.95	45	N. M._A. (9)	20.00	45	Yes	-0.42	42
COMAC_MAC_FREQ	Yes	5.67	44	N. M._A. (9)	20.00	45	No	20.00	45
MODE_SV	Yes	0.19	34	N. M._A. (5)	20.00	41	No	20.00	41
SVD_MODE_SV	N. M._A. (4)	20.00	20	No	20.00	20	No	20.00	20

Table C. 26 - OSP investigation: Gm2 technique – MKE target mode shapes.

MSE_Gm2	7004_20			6008_20			3004_20		
	Identified	Error (%)	time (min)	Identified	Error (%)	time (min)	Identified	Error (%)	time (min)
COMAC_NL	No	20.00	89	N. M._A. (5)	20.00	90	Yes	5.85	89
COMAC_MAC_NL	No	20.00	97	Yes	0.22	97	Yes	1.22	97
COMAC_MAC_FREQ_NL	No	20.00	97	No	20.00	91	Yes	19.99	97
MODE_NL	No	20.00	92	No	20.00	95	No	20.00	89
COMAC	Yes	1.32	43	No	20.00	43	Yes	1.41	43
COMAC_MAC	No	20.00	50	No	20.00	50	Yes	0.64	50
COMAC_MAC_FREQ	No	20.00	50	No	20.00	50	Yes	0.57	50
MODE_SV	Yes	0.01	43	N. M._A. (5)	20.00	39	No	20.00	46
SVD_MODE_SV	No	20.00	22	Second Pick	11.19	22	No	20.00	22

Table C. 27 - OSP investigation: Gm2 technique – MSE target mode shapes.

C.4.4.6 Overall results analysis

In the previous sections, OSP techniques were analysed in terms of their capability to supply information to the damage detection process to detect the presence, the location and estimate the severity of the damages introduced.

This analysis led to the observation that the MSE selected target mode shapes improved considerably the damage detection performances for all the OSP techniques investigated, except for the kinetic energy based OSP methods (KEM and Gm2). This behaviour did not come unexpected. Since, the damage investigated entailed a loss of mass (corrosion) and the kinetic energy is proportional to the mass distribution, therefore a so based methodology (OSP or TMSS techniques) was linearly dependent on the structure thickness changes against a cubic dependence (see flexural rigidity §5.3) of methodologies based on only the structural response (e.g. mode shape displacements) and so dependent mainly on stiffness changes. This meant that for a 20% decrease of the FE thickness, there is a loss of the 20% in mass and so in kinetic energy, but also a stiffness reduction of 48.8%.

By considering only those damage detection results that correctly located the three damages introduced (Table C. 28, Figure C. 20-Figure C. 21), further considerations can be done on the different damage detection processes implemented.

1. Only the MSE target_mode_shape_set was able to supply sufficient information for a correct localisation of the defects investigated (Table C. 28).
2. The EFI sensor network resulted to be the best, since three residue functions (COMAC, COMAC_MAC and COMAC_MAC_FREQ) were able to identify the damage locations studied using it (Table C. 28).
3. The Large Scale Optimisation (LSO) resulted to be more time consuming than the LSSO (sensitivity approach), see Figure C. 21. This was owed to the linearization carried out into the building up of the sensitivity matrix determining a consistent time saving compared to the non linear approach pursued by the LSO algorithm in the construction of the trust region (§2.8).
4. In terms of severity estimate (Figure C. 20), the three best performances were given by the COMAC_MAC_FREQ, minimised by a LLSO algorithm using an EFI sensor network, followed by the COMAC residue functions using the same sensor network and minimisation algorithm. At the third place, there was the COMAC_MAC_FREQ, once again, but this time, minimised by the LSO algorithm.
5. The COMAC_MAC residue function recorded an increasing severity error passing from a LSO to a LLSO minimisation and, then, for changing the EFI sensor network with EVP's (Figure C. 20).
6. An opposite behaviour to that recorded by the COMAC_MAC residue function was recorded by the COMAC_MAC_FREQ residue function (Figure C. 20), which severity error decreased by switching from a LSO to a LLSO minimisation.

TMSS	OSP	Residue Function	Algorithm	7004			6008			3004		
				Loc.	error [%]	time [min]	Loc.	error [%]	time [min]	Loc.	error [%]	time [min]
MSE	EFI	COMAC	LLSO	Yes	0.69	42	Yes	0.26	42	Yes	0.3	43
		COMAC_MAC	LSO	Yes	3.93	102	Yes	0.59	106	Yes	2.32	106
			LLSO	Yes	0.50	47	Yes	0.15	49	N. A. 2006	9.15	53
		COMAC_MAC_FREQ	LSO	Yes	0.71	109	Yes	0.22	103	Yes	0.59	100
			LLSO	Yes	0.28	54	Yes	0.1	54	Yes	0.13	53
	EFI-DPR		LSO	Yes	1.35	84	Yes	0.09	89	Yes	0.76	95
	EVP	COMAC_MAC	LLSO	Yes	10.28	43	Yes	1.07	40	Yes	0.53	46

Table C. 28 - OSP investigation: Overall comparison

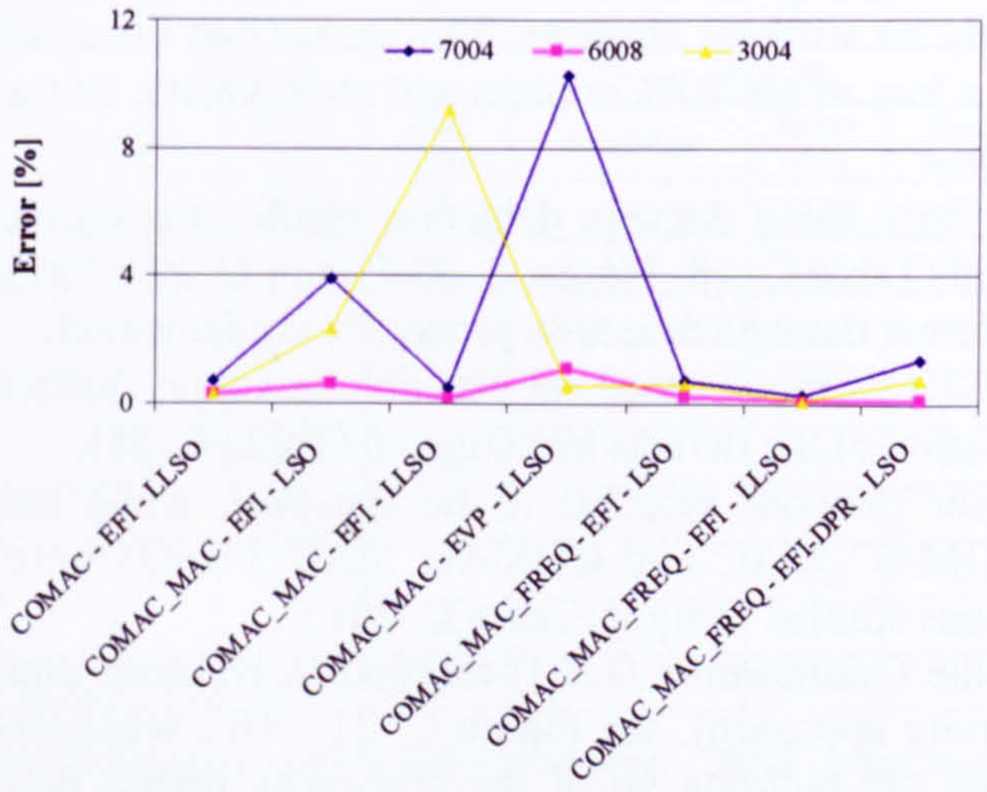

Figure C. 20 - OSP investigation: Overall severity error comparison

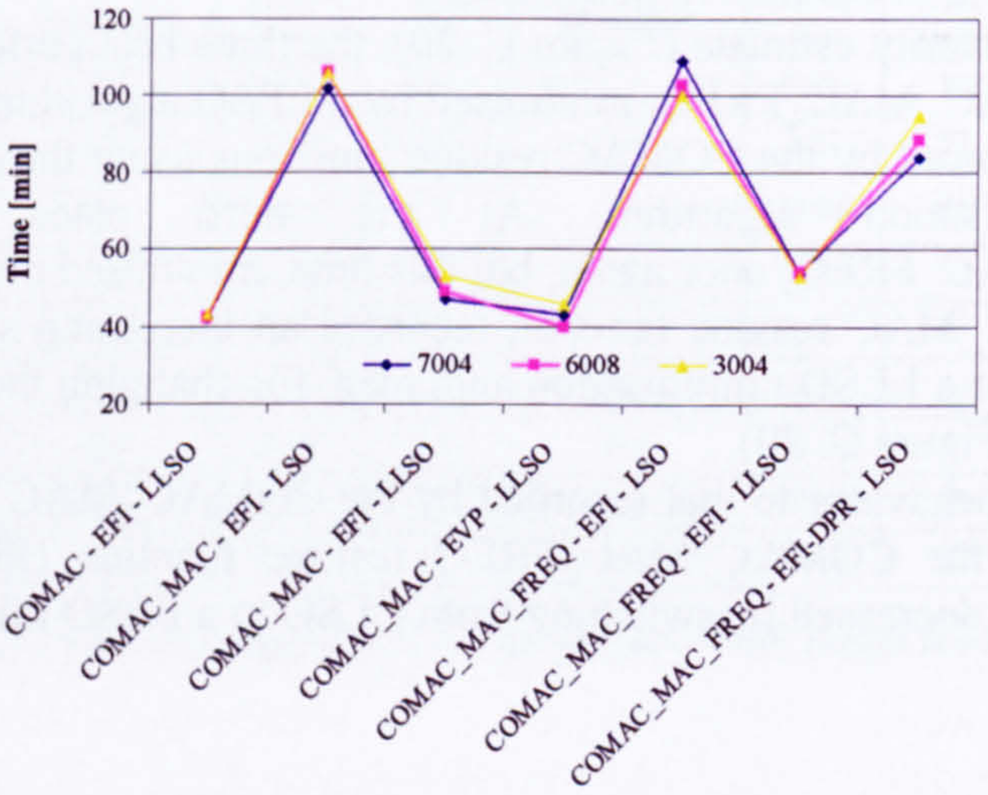

Figure C. 21 - OSP investigation: Overall run time comparison.

APPENDIX D: DIRECT APPROACH RESULTS

D.1 Introduction

A central piece of the damage detection methods based on Model Updating (MU) technique explored in chapter 2, tested and discussed in appendices A, B and C, was the FE modelling of a real structure. However, the reduction of a continuous system (real structure) in a discrete system (structure FE model) constitutes a big drawback, because the FE model is able to represent only limited number of characteristics of the structures within a reasonable approximation. Therefore, a damage detection technique using a FE model is able to detect damages if and only if the structure response changes due to their presence affect the structure features reproduced by the FE model. This reason together with considerable run time, needed for the updating of the model to the damaged configuration, have brought to analyse alternative structure models, which can be described by analytical functions, giving a continuous representation of the structures.

The existence of an analytical model for plate-like structures made possible the development of a direct approach for damage detection purposes as described in chapter 5. A series of test were carried out in order to understand the reliability and efficiency of the direct damage detection method for plate-like structures. Three different damaged configurations, two single sites and one multi-site, were investigated using three different solvers for a linear algebraic system.

D.2 Plate-like structure

The direct damage detection approach for plate-like structures was tested on a plate identical to that used in the GLDDO approach investigations (Appendix C), a 30 by 20 cm rectangular aluminium plate constrained at its edges.

In order to reduce the number of unknowns and increasing the well-conditioning of the algebraic system, a global-local approach as described in chapter 2 (§2.6) was adopted. So, a plate partition as that described in paragraph C.2 was made necessary for a correct identification of the damaged locations (Figure D.1- Figure D. 2)

Therefore, the damage detection process was articulated in two steps as explained in section 2.5.2.

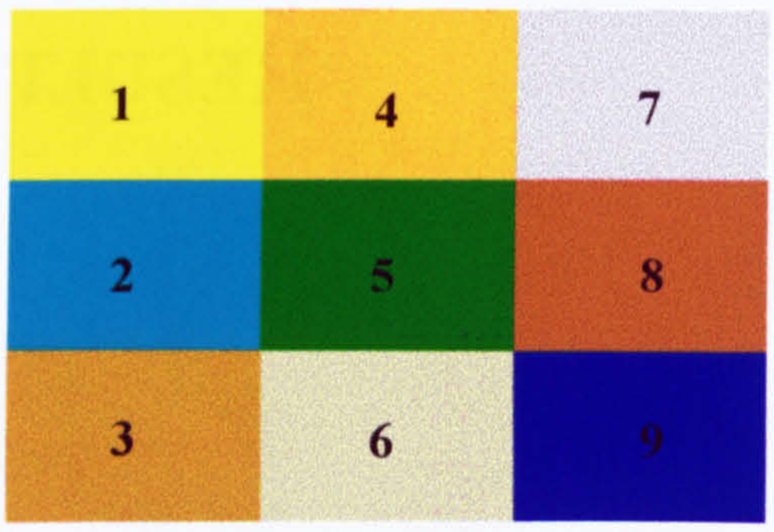

Figure D.1 - Macro-areas display

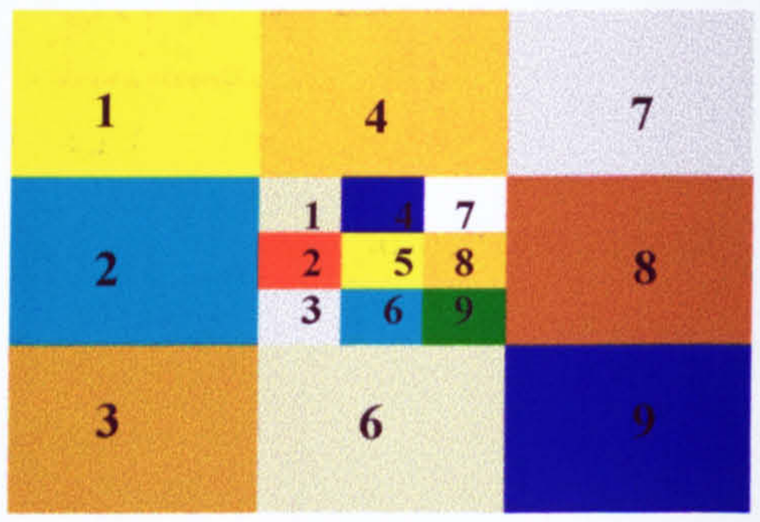

Figure D. 2- Example about the macro area partition.

Three damaged scenarios were introduced on the plate. The first two defects introduced were single site damages obtained by decreasing of 10% the undamaged elastic module of the forth area of the third macro-area (3004) and of the 8th area of the sixth macro-area (6008) (Figure D. 3). A further damage detection was performed on the 3004 area with a reduced damage severity (5%) with the purpose to probe the methodology sensitivity.

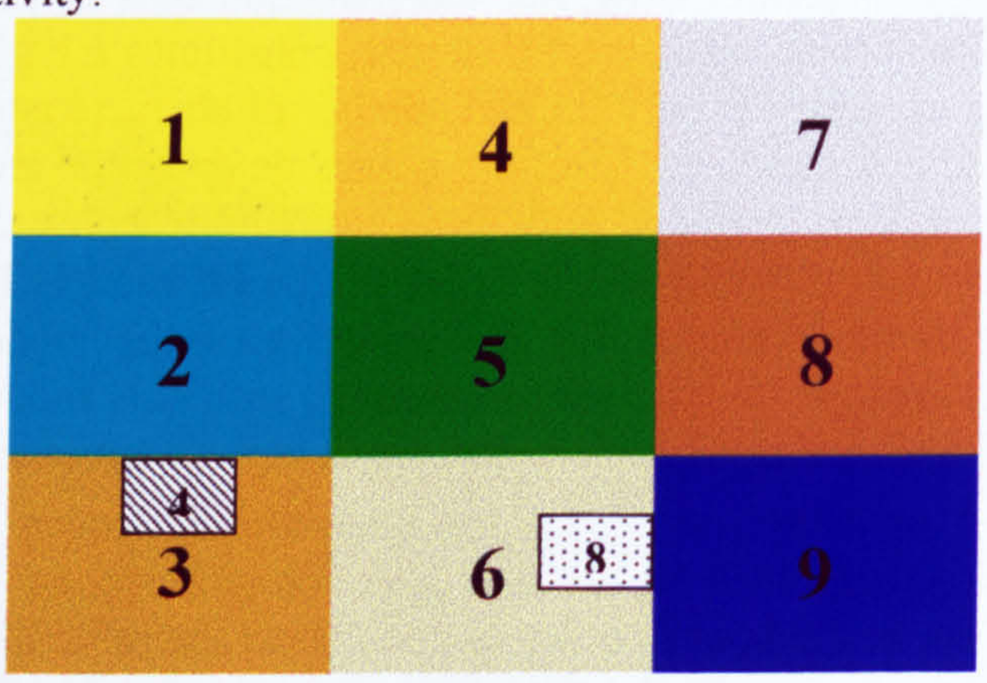

Figure D. 3 – Single-site damages.

The last defect introduced was a multi-site damage as displayed in Figure D.4. The damaged areas 1009, 7005 and 3002 were faulted by decreasing their elastic modules, respectively, of 5%, 8% and 6%.

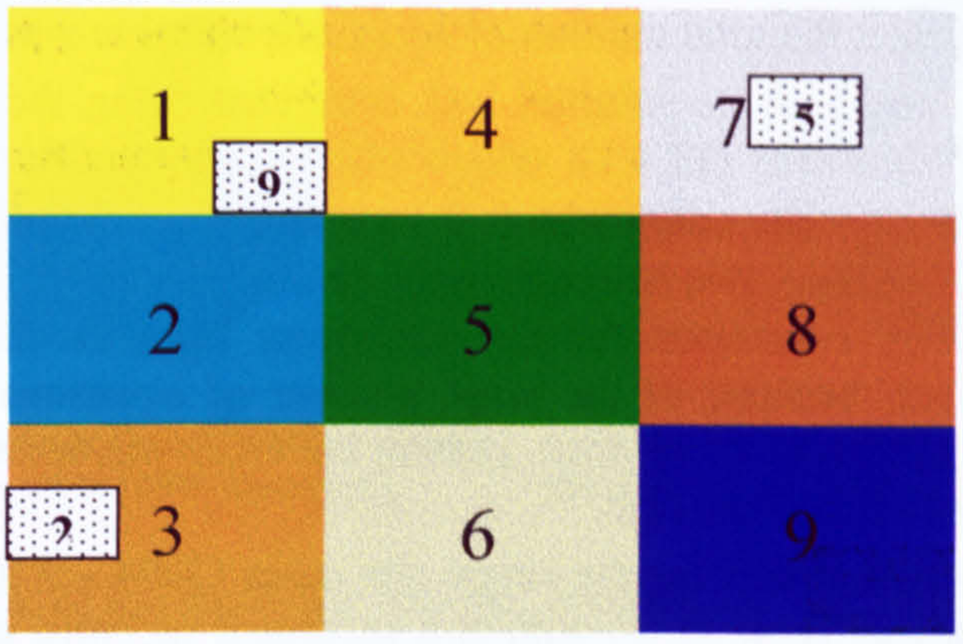

Figure D.4 - Multi-site damage.

Finally, the sensor locations were selected by the EFI method as Figure D.5 shows.

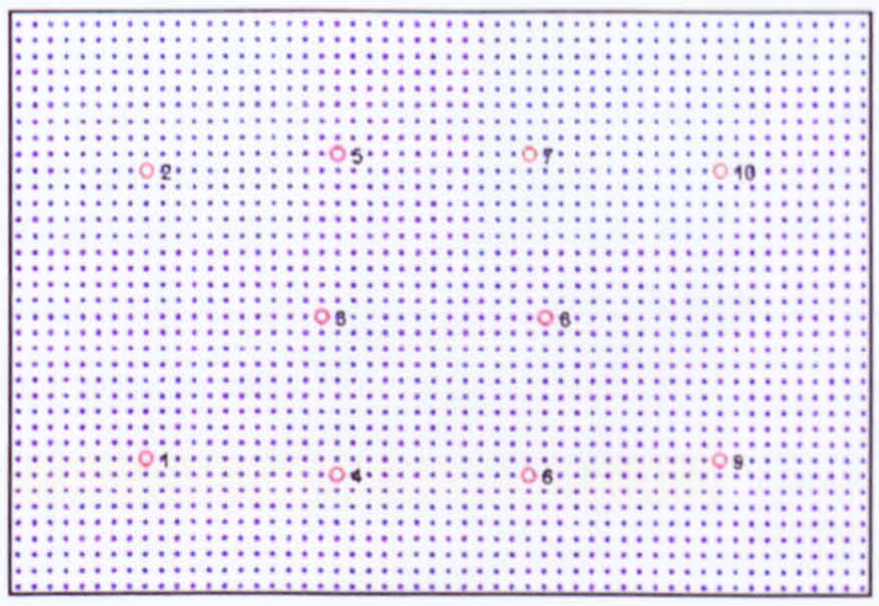

Figure D.5 – EFI's optimal sensor locations.

D.3 Damage detection results

As described in chapter 5, for the solution estimate of the algebraic system derived by the direct approach, three different approaches were proposed and, therefore, investigated in terms of their capability to determine the presence, the location and the severity of the defects described in the damaged configurations illustrated in the previous paragraph.

Consequently, the damage detection results were, first, analysed approach by approach (over-determined system, determined system, singular value decomposition) and, then, all together.

D.3.1 Over-determined system results

For over-determined system is meant a system having a number of equations larger than its unknown number. In the case analysed, the maximum number of equations that could be written is given by the product of the sensor number times the excitation

location number times the number of excitation frequencies. Therefore, since the FRF was acquired in, alternatively, 9 sensors out of the 10 selected by the EFI technique and exciting in the remaining 10^{th} sensor location, using 200 frequency points within the 0-5000 Hz frequency range, the total number of equations writable was 9*10*200=18000.

Once the system was built its solution was computed using the linear Least Square Optimisation (LSO) algorithm (§2.8.1), which offered the opportunity to fix the upper and lower end of the system unknowns ($\bar{d}_j$ expressed in terms of Young modulus percentage points). Therefore, two solutions were evaluated with ($0 \leq \bar{d}_j \leq 1$) or without ($-\infty \leq \bar{d}_j \leq +\infty$) boundary conditions for the unknowns for each damage configuration investigated. Moreover, because of the large number of equations used, the run time turned to be significant (order of 10 min). Hence, the ODS was tested only for FRF data corrupted with a noise of 2% variance.

The damage detection results for the single site cases (3004 – 5 and 10% - and 6008) were organised in tables (Table D. 1) with two separated sections, one for each damage detection step.

The damage detection results showed that the single site damages investigated (Table D. 1) were all located correctly using the LSO unbounded solver, although the damaged introduced in the area 6008 was identified in the area nearby (6009). In contrast, the bounded version of the LSO solver was not capable of locating the macro-area for the damage introduced in area 6008 and presented at the second step, an estimation error on the damage severity larger than that evaluated by the LSO unbounded solver (Table D. 1).

First Step						
Damage	**5% of the area 3004**		**10% of the area 3004**		**10% of the area 6008**	
Bounds	No	0<DJ<1	No	0<DJ<1	No	0<DJ<1
Macro - Area identified	Yes	Yes	Yes	Yes	Yes	No
Macro - Area Damage	1.52	0.85	3.07	1.76	1.42	0.23
Second Step						
Damage	**5% of the area 3004**		**10% of the area 3004**		**10% of the area 6008**	
Bounds	No	0<DJ<1	No	0<DJ<1	No	0<DJ<1
Area identified	Yes	Yes	Yes	Yes	Area 9	Area 9
Damage Error [%]	0.53	1.93	0.60	1.09	2.81	3.41

Table D. 1 - ODS: Single site damage detection.

An indication of the distribution of the elastic module changes, predicted by the unbounded LSO solver for damage introduced in area 3004, is given in Figure D.6 and Figure D.7 (the actual damaged location were depicted in sky blue).

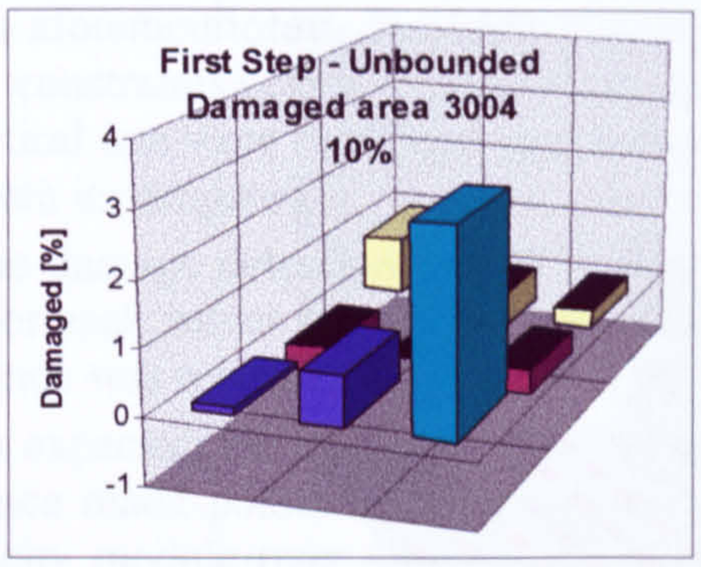

Figure D.6 - First step in the evaluation of the damage on the area 3004 (10% damaged).

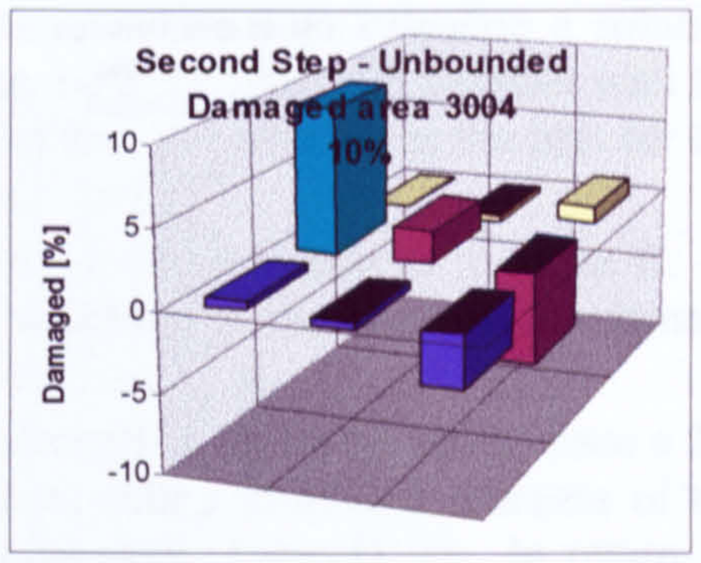

Figure D.7 - Second step in the evaluation of the damage on the area 3004 (10% damaged).

For the assessment of the multi-site damage investigated, the ODS was able to identify correctly the damaged macro-areas only with the unbounded solution (Figure D.8), since the bounded algorithm identified properly only two damaged macro-areas (the third and the seventh) out of three.

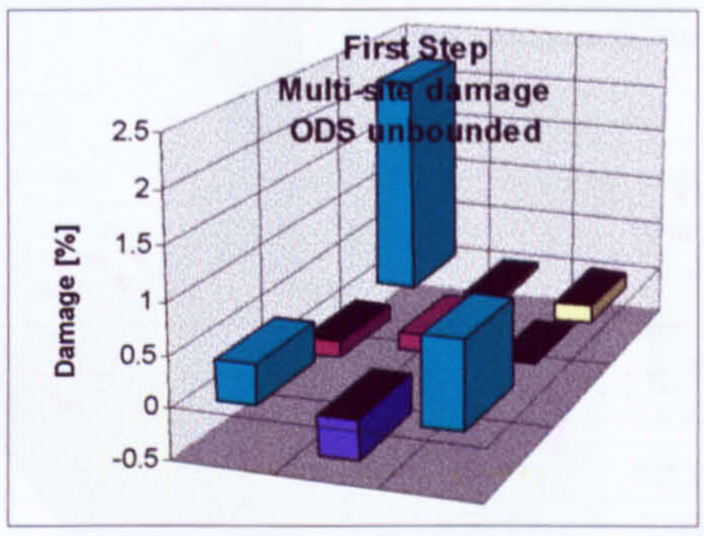

Figure D.8 - First Step, ODS detection of a multi-site damage.

In the second detection step (Figure D.9-Figure D.10), only the damage in the first macro-area was detected correctly (the 9th) with an error of 1% for the bounded solution and 0.2% for the unbounded. While, in the macro-areas three and seven, the bounded LSO recognised, as most damaged areas, regions next to the real faulted (Figure D.9-Figure D.10). Moreover, the bounded LSO solution had the smallest mean error 0.8% against the 1.2% of the unbounded one.

Concluding, the ODS approach showed that the unbounded solver was the best in detecting the single site damages inspected, although resulted less efficient than the LSO bounded solver in the second damage detection step of the multi-site damage.

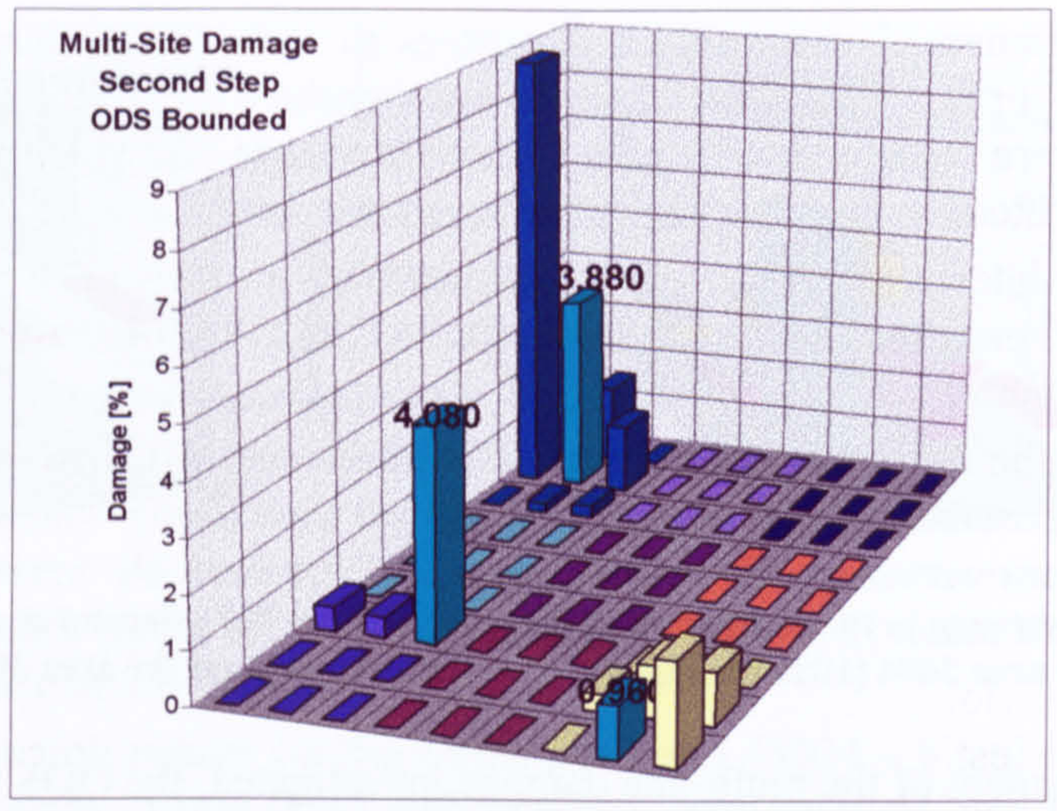

Figure D.9 – Multi-site damage scenario: bounded ODS solution.

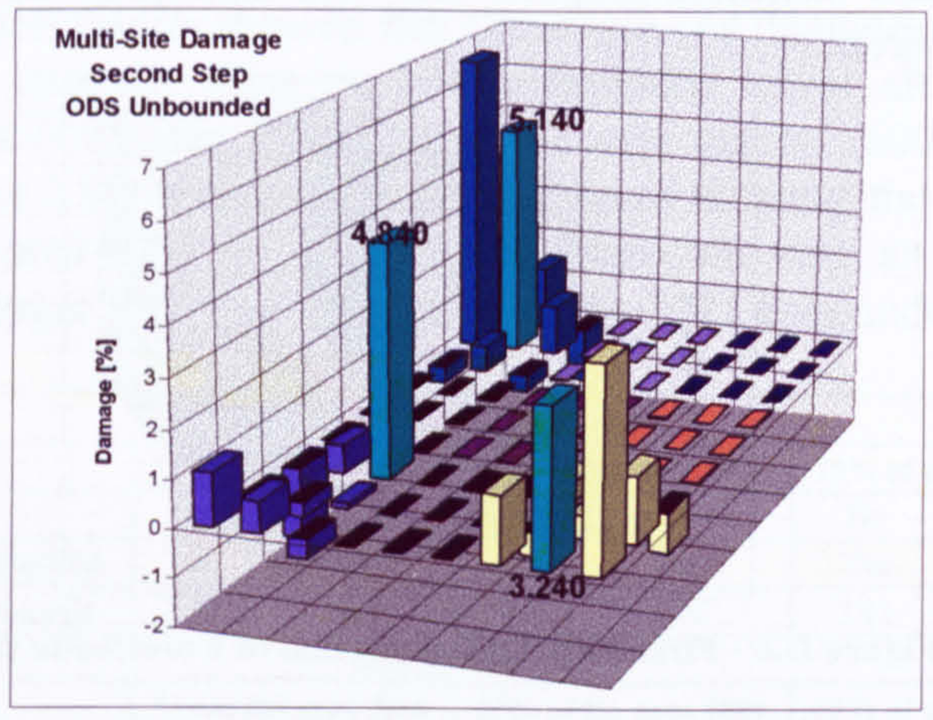

Figure D.10 – Multi-site damage scenario: unbounded ODS solution.

D.3.2 Determined System results

The Determined System (DS) approach offers the possibility to evaluate the structural changes using an "analytical" inversion, since its number of unknowns is equal to its equation number. The DS equations were selected among those of the ODS minimising the coefficient matrix [Xij] condition number (§5.6.3) and maximising the vibration energy acquired by the sensors. However, because the acquired FRFs might be heavily corrupted by noise, the inversion of the coefficient matrix could lead to unphysical results. Therefore, in order to increase the robustness of the DS approach, a least square optimisation algorithm that minimises the error between the experimental and the analytical FRFs was used as well.

The efficiency of the technique was checked polluting the FRFs numerically estimated using a normal distributed noise with a variance from 2% to 50%, which means a Signal Noise Ratio, respectively, from 34 to 4dB.

As aforementioned, the LSO algorithm gives the possibility to calculate a solution using constraints or not. Therefore, even in this case, both the solutions together with the analytical one were evaluated and, then, compared to find out which was the best for the problem investigated.

The damage detection results were grouped in three tables (Table D. 2-Table D. 4), one for each solver employed. In these tables, the influence of the noise on the damage detection was reported.

As expected, the Analytical Inversion (AI) was strongly affected by noise, since a 2% variance made possible an explosion of the solution, with a predicted decrease of the elasticity module over 40% (area 3004 -10% damage case, Table D. 2). In return, in absence of noise, the AI solver gave the exact solution (Table D. 2).

A similar behaviour was recorded by the Unbounded LSO (ULSO) solver, but with a larger error in the estimate of the damage severity (Table D. 3). In contrast, the Bounded LSO (BLSO) solver (Table D. 4) showed larger stability to the noise pollution and identified all the single site damages studied with a maximum error of the predicted severity of 5% (of the elastic module), even though for the damaged introduced in the area 6008, the next area, 6009, resulted to be the most damaged.

AI	AREA 3004 damaged of 10%				AREA 3004 damaged of 10%				AREA 6008 damaged of 10%			
	First Step		Second _step		First Step		Second _step		First Step		Second _step	
Noise	M_A Ident.	Damage [%]	M_A Ident.	Damage [%]	M_A Ident.	Damage [%]	M_A Ident.	Damage [%]	M_A Ident.	Damage [%]	M_A Ident.	Damage [%]
0%	Yes	1.42	Yes	5.00	Yes	2.84	Yes	10.00	Yes	1.09	Yes	10.00
2%	Yes	1.54	Area 5	8.69	Yes	2.85	No	43.96	Yes	1.68	Area 9	5.10
5%	Yes	1.17	No	2.89	Yes	2.91	No	55.31	Yes	1.98	Area 9	19.34
10%	No	0.95	No	10.33	Yes	3.60	No	165.42	Yes	1.90	Area 9	15.82
15%	No	1.29	Area 5	33.60	Yes	3.73	No	12.42	Yes	1.68	Area 9	90.23
20%	No	0.00	No	0.00	No		No	32.64	Yes	1.68	Area 9	81.12

Table D. 2 – DS approach: Analytic Inversion – Single site damage detection.

ULSO	AREA 3004 damaged of 10%				AREA 3004 damaged of 10%				AREA 6008 damaged of 10%			
	First Step		Second _step		First Step		Second _step		First Step		Second _step	
Noise	M_A Ident.	Damage [%]	M_A Ident.	Damage [%]	M_A Ident.	Damage [%]	M_A Ident.	Damage [%]	M_A Ident.	Damage [%]	M_A Ident.	Damage [%]
0%	Yes	0.84	Yes	4.83	Yes	1.68	Yes	9.66	Yes	1.11	Area 9	7.56
2%	Yes	0.86	No	3.23	Yes	1.68	No	11.17	No	1.03	Area 9	8.51
5%	Yes	0.92	No	4.75	Yes	1.98	No	6.69	Yes	1.04	Area 9	2.24
10%	No	0.74	No	11.40	Yes	1.90	No	15.59	Yes	1.48	Area 9	14.53
15%	No	0.47	No	0.45	Yes	1.68	No	21.85	No	1.57	Area 9	23.53
20%	No	0.00	No	0.00	Yes	1.68	No	2.09	No	0.80	Area 9	13.04

Table D. 3 - DS approach: Unbounded LSO – Single site damage detection.

BLSO	AREA 3004 damaged of 10%				AREA 3004 damaged of 10%				AREA 6008 damaged of 10%			
	First Step		Second _step		First Step		Second _step		First Step		Second _step	
Noise	M_A Ident.	Damage [%]	M_A Ident.	Damage [%]	M_A Ident.	Damage [%]	M_A Ident.	Damage [%]	M_A Ident.	Damage [%]	M_A Ident.	Damage [%]
0%	Yes	0.94	Yes	3.51	Yes	2.97	Yes	6.47	Yes	0.80	Area 9	6.41
2%	Yes	1.50	Yes	3.34	Yes	2.85	Yes	6.26	Yes	0.79	Area 9	6.09
5%	Yes	1.61	Yes	3.52	Yes	3.43	Yes	5.94	Yes	0.64	Area 9	6.42
10%	No	0.89	Area 1	2.62	Yes	3.07	No	5.62	Yes	0.86	Area 9	6.43
15%	No	0.01	No	2.84	Yes	2.47	Yes	5.19	No	0.61	Area 9	6.16
20%	No	0.00	No	0.00	Yes	2.47	Yes	6.34	No	0.74	Yes	5.98

Table D. 4 - DS approach: Bounded LSO – Single site damage detection.

Finally, the multi-site damage detection results identified (damaged areas 1009, 3002 and 7005), in the first step, as damaged only two out of the three damaged macro-areas (the 3rd and 4th), leaving undetected the fault introduced in the first (Table D. 5).

Multi Site Damage - First Step						
Solver	Analytical Inversion		LSO Bounded		LSO Unbounded	
Noise	M_A Ident.	M_A Dam	M_A Ident.	M_A Dam	M_A Ident.	M_A Dam
0%	No	3rd 7th	No	3rd 7th	No	3rd 7th
2%	No	3rd 7th	No	3rd 7th	No	3rd 7th
5%	No	3rd 7th	No	3rd 7th	No	3rd 7th
10%	No	3rd 7th	No	3rd 7th	No	3rd 7th
15%	No	7th	No	7th	No	7th

Table D. 5 - DS approach: Multi-site damage (first damage detection step).

The second detection step confirmed the relationship between the noise and the solution quality and only the BLSO produced physical solutions as displayed in Figure D. 11 for the 5% noise case investigated.

By the results illustrated above, the DS approach presented a limited stability to the noise effects, since it was capable of proper identification of single damaged locations for noise variance smaller than 10%. Moreover, the DS approach did not detect all the damaged areas in the multi-site case inspected. Due to this issue this technique, nonetheless, its fastness (1-2 minutes) compared with the over-determined approach, cannot be taken into consideration for damage identification on structure where the likelihood of multi-site damages is high.

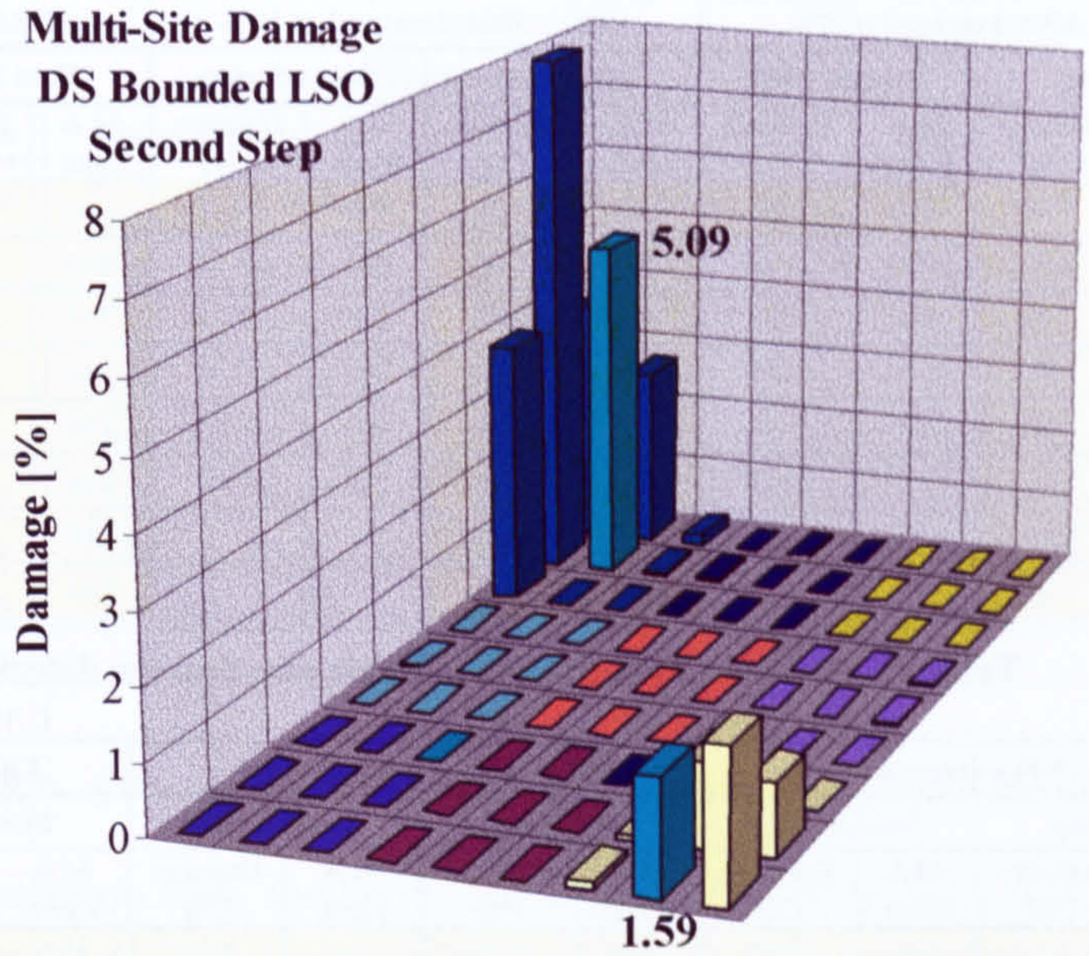

Figure D. 11 – DS BLSO: 2nd detection step for the multi-site damage scenario (5% noise variance)

D.3.3 Singular Value Decomposition approach results

The aim of the introduction of the Singular Value Decomposition (SVD) was to increase the speed of the detection evaluation together with its efficiency. The efficiency enhancement was obtained by using all information available on the structure. Instead, the speed was improved (order of 2-3 minutes) by reducing the number of equations to the unknown number by the use of SVD.

In this way, the damage identification produced was less affected by the noise than the case discusses previously, as can be seen by the results illustrated below.

Three different cases were studied. The first case computed the system solution by inverting the coefficient matrix [Xij], while the second and the third used the LSO algorithm (bounded and unbounded version).

The analytical inversion of the SVD algebraic system exhibited a particular weakness with the noise increase in the second step detection, where only the unpolluted FRFs leaded to a localisation and perfect severity estimate of the damages investigated (Table D. 6). In contrast, a stronger noise withstanding was obtained using the ULSO solver (Table D. 7), which provided a correct detection of the damages inspected as long as the noise variance was smaller than 10%. A further improvement in the detection of the damages investigated was obtained employing as solver the BLSO (Table D. 8), which compared to the ULSO had a larger error in the prediction of the damage severity, but endured data pollution up to 50% of variance.

AI	AREA 3004 damaged of 5%				AREA 3004 damaged of 10%				AREA 6008 damaged of 10%			
	First Step		Second step		First Step		Second step		First Step		Second step	
Noise	M A Ident.	Damage [%]	M A Ident.	Damage [%]	M A Ident.	Damage [%]	M A Ident.	Damage [%]	M A Ident.	Damage [%]	M A Ident.	Damage [%]
0%	Yes	1.46	Yes	5.00	Yes	2.93	Yes	10.00	Yes	1.65	Yes	10.00
2%	Yes	1.43	No	5.53	Yes	2.85	No	11.10	Yes	1.65	Yes	10.47
5%	Yes	1.48	No	4.87	Yes	2.88	No	10.36	Yes	1.64	No	11.26
10%	Yes	1.56	No	3.80	Yes	2.94	No	23.31	Yes	1.64	No	5.22
15%	Yes	1.49	No	5.20	Yes	3.13	No	28.62	Yes	1.72	No	24.19
20%	Yes	1.24	No	10.28	Yes	2.49	No	9.06	Yes	1.73	No	20.31
30%	Yes	1.53			Yes	2.70			Yes	1.43		
50%	Yes	1.24			Yes	3.92			Yes	1.29		

Table D. 6 - SVD approach: AI – Single site damage detection.

ULSO	AREA 3004 damaged of 5%				AREA 3004 damaged of 10%				AREA 6008 damaged of 10%			
	First Step		Second step		First Step		Second step		First Step		Second step	
Noise	M A Ident.	Damage [%]	M A Ident.	Damage [%]	M A Ident.	Damage [%]	M A Ident.	Damage [%]	M A Ident.	Damage [%]	M A Ident.	Damage [%]
0%	Yes	1.40	Yes	4.81	Yes	2.93	Yes	9.62	Yes	1.63	Yes	8.35
2%	Yes	1.38	Yes	4.78	Yes	2.85	Yes	9.46	Yes	1.62	Yes	8.28
5%	Yes	1.40	Yes	5.14	Yes	2.88	Yes	10.11	Yes	1.61	Area 9	8.17
10%	Yes	1.49	No	5.35	Yes	2.94	Yes	11.97	Yes	1.70	Yes	8.24
15%	Yes	1.49	No	3.91	Yes	3.13	No	9.70	Yes	1.70	Yes	12.36
20%	No	1.35	No	5.53	Yes	2.49	No	9.25	Yes	1.42	Area 9	9.30
30%	Yes	1.51			Yes	2.70	No	6.98	Yes	1.96	Yes	9.27
50%	Yes	1.18			Yes	3.92	No	16.96	Yes	1.29	Area 9	2.49

Table D. 7 - SVD approach: ULSO – Single site damage detection.

BLSO	AREA 3004 damaged of 5%				AREA 3004 damaged of 10%				AREA 6008 damaged of 10%			
	First Step		Second step		First Step		Second step		First Step		Second step	
Noise	M A Ident.	Damage [%]	M A Ident.	Damage [%]	M A Ident.	Damage [%]	M A Ident.	Damage [%]	M A Ident.	Damage [%]	M A Ident.	Damage [%]
0%	Yes	0.95	Yes	4.20	Yes	1.83	Yes	6.96	Yes	0.82	Area 9	7.22
2%	Yes	0.96	Yes	3.56	Yes	1.90	Yes	6.96	Yes	0.88	Area 9	7.28
5%	Yes	0.95	Yes	4.44	Yes	1.76	Yes	6.93	Yes	0.87	Area 9	7.32
10%	Yes	0.99	Yes	4.14	Yes	1.82	Yes	8.90	Yes	0.68	Area 9	7.12
15%	Yes	0.98	Yes	3.45	Yes	1.88	Yes	6.36	Yes	0.57	Area 9	7.21
20%	Yes	0.98	Yes	4.50	Yes	1.92	Yes	6.79	Yes	0.55	Area 9	6.43
30%	Yes	1.02	Yes	3.38	Yes	1.71	Yes	5.54	Yes	0.63	Area 9	7.07
50%	Yes	0.88	Yes	3.17	Yes	1.99	Yes	7.69	Yes	0.80	Yes	8.20

Table D. 8 - SVD approach: BLSO – Single site damage detection.

The multi-site damage detection using the SVD approach had its best performances using the analytical and the ULSO solver, which identified correctly all the damaged macro-areas, in contradiction with the bounded LSO results, which identified only the third and the seventh macro-area (Table D. 9).

Multi-site damage						
Solver	**Analytical Inversion**		**BLSO**		**ULSO**	
Noise	M. A. Ident.	M. A. Dam.	M A Ident.	M. A. Dam.	MA Ident.	M. A. Dam.
0%	Yes	1st 3rd 7th	No	3rd 7th	Yes	1st 3rd 7th
2%	Yes	1st 3rd 7th	No	3rd 7th	Yes	1st 3rd 7th
5%	Yes	1st 3rd 7th	No	3rd 7th	Yes	1st 3rd 7th
10%	Yes	1st 3rd 7th	No	3rd 7th	Yes	1st 3rd 7th
15%	Yes	1st 3rd 7th	No	3rd 7th	Yes	1st 3rd 7th
20%	Yes	1st 3rd 7th	No	3rd 7th	Yes	1st 3rd 7th
30%	No	7th	No	3rd 7th	No	3rd 7th
40%			No	3rd 7th	No	
50%			No	3rd 7th	No	

Table D. 9 - SVD approach: Multi-site damage (first damage detection step).

In the second detection step, the analytical (Figure D. 14) and the unbounded solution (Figure D. 13) were not able to give a reliable detection with corrupted experimental data. Fortunately, this tendency was confuted by the BLSO solutions that exhibited a correct detection up to 10% noise variance, even if the actual damaged areas were not always predicted as the most damaged (Figure D. 12, Figure D. 14). With the increase of the noise intensity, in some cases, the damage was located in areas next to the actual damaged (yellow, red and blue strips in Figure D. 12).

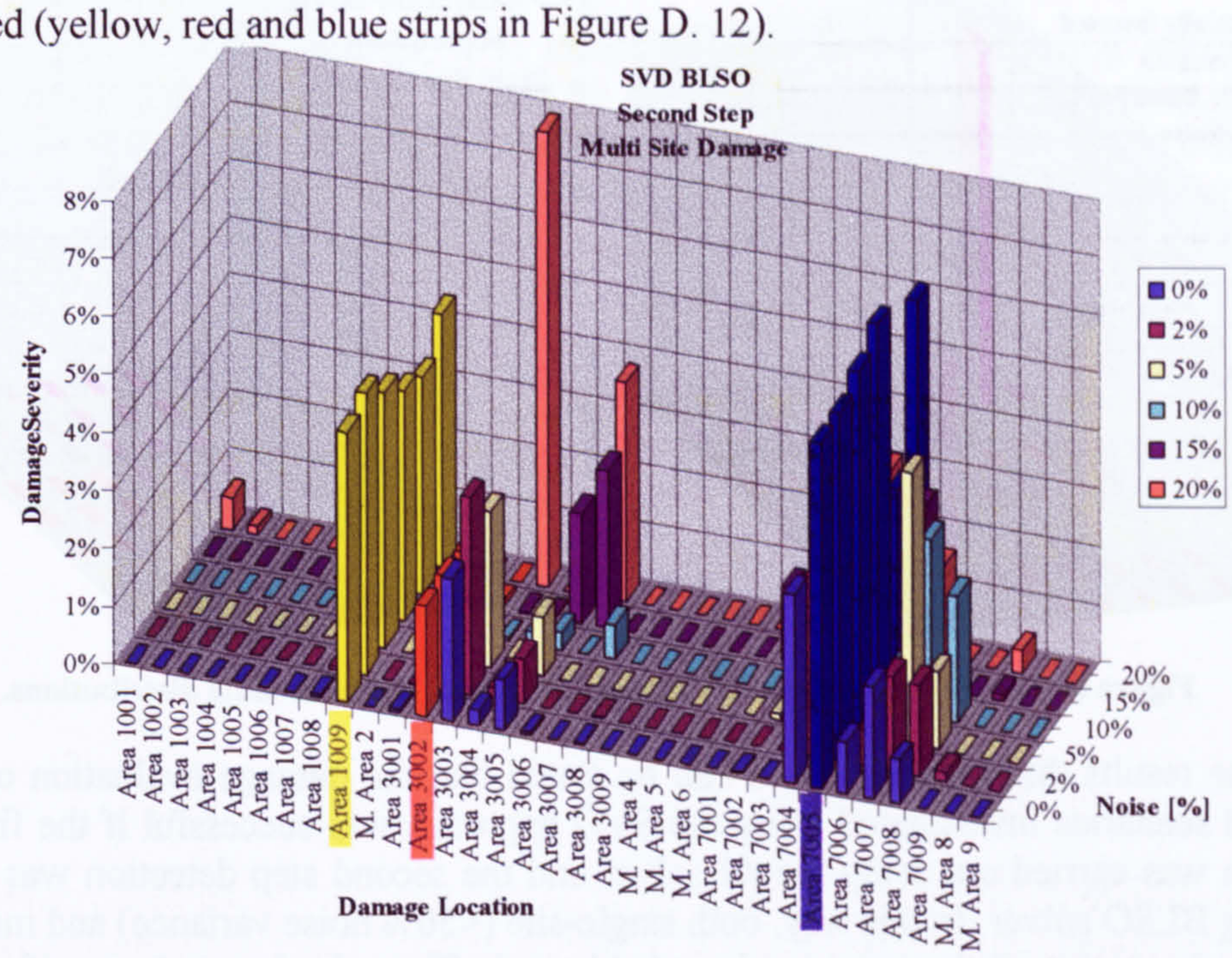

Figure D. 12 – SVD approach: BLSO solver - Second detection step for the multi-site damage scenario.

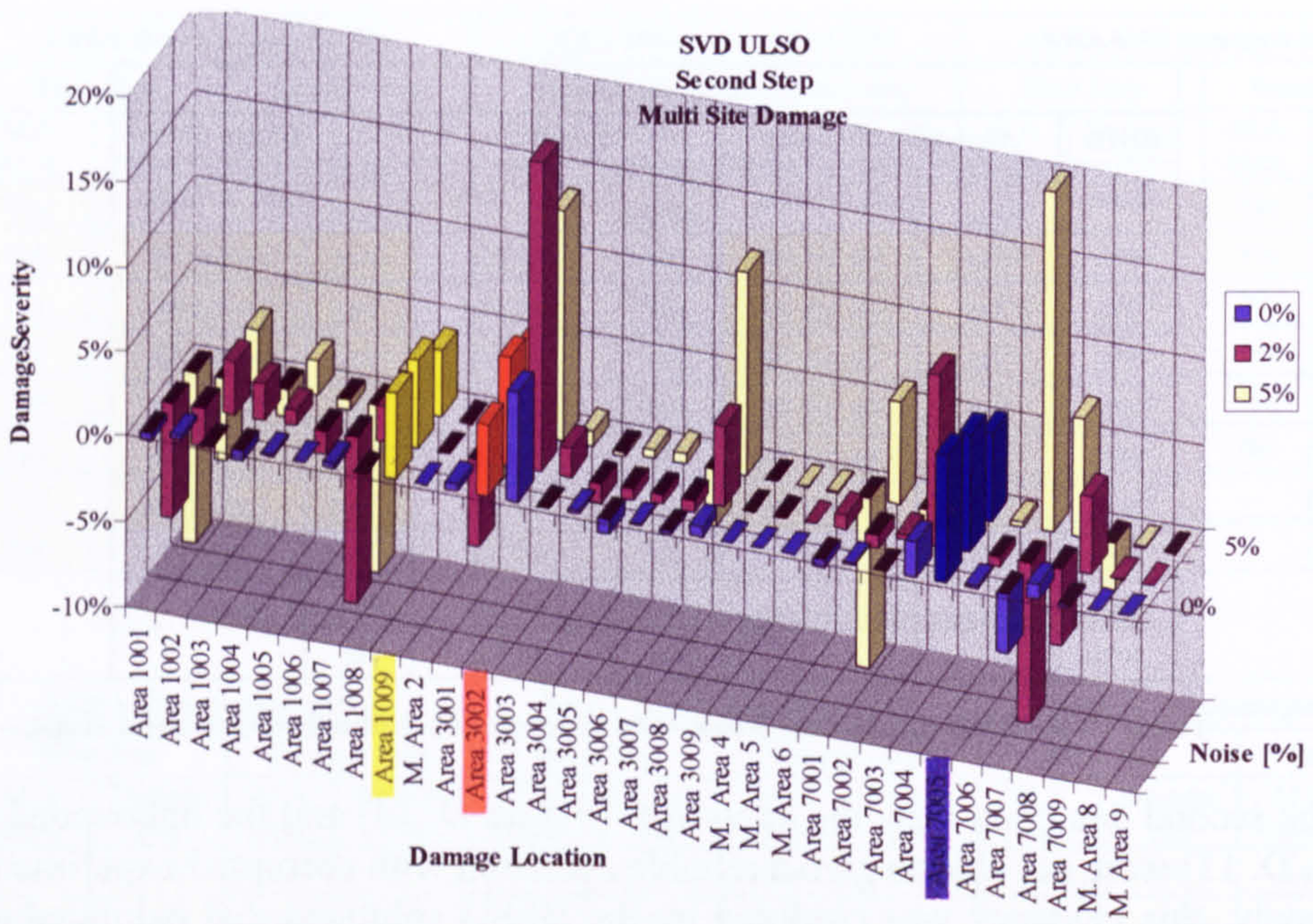

Figure D. 13 - SVD approach: ULSO solver - 2nd detection step for the multi-site damage scenario (2% noise variance).

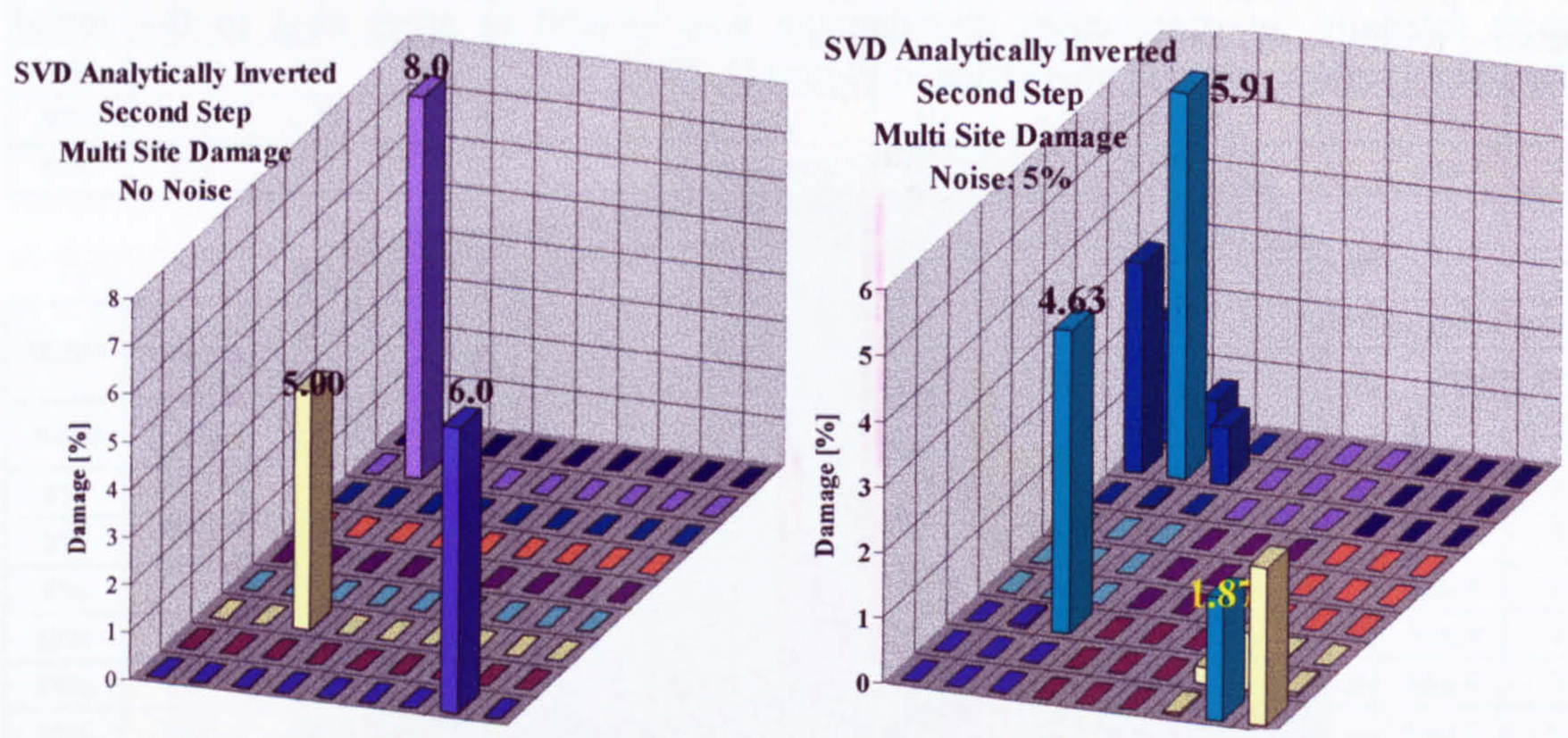

Figure D. 14 - SVD approach: 2nd damage detection, elastic module distributions.

By the results discussed above, it can be stated that the damage evaluation over the damaged scenarios investigated using the SVD approach was successful if the first step detection was carried out using the AI solver and the second step detection was carried out using BLSO solver. In this way, both single-site (<50% noise variance) and multi-site (<10% noise variance) damages can be reliably and efficiently detected even if strongly polluted.

D.3.4 Approach comparison

From the results above presented, the main results of the direct approach in damage detection is the possibility to have an exact identification of the structure changes occurring on a structure, in absence of noise (DS and SVD approach using the AI solver). This result is almost impossible to obtain using structure FE model, since the inversion of the problem involving linearization and optimisation determines a certain amount of approximation.

However, because a clean signal (FRFs) cannot be obtained in nature, an analysis of the influence of noise pollution on the damage detection capabilities of the direct approach was necessary.

This investigation brought to light that the DS approach could not provide reliable multi-site damage detection in presence of noise, and for single site fault identification its withstanding of noise pollution stopped to 10% variance.

An improved behaviour was highlighted by the ODS approach, which could detect correctly both single and multi site damages but its run time limited is application to a 2% noise variance. A quicker damage detection and noise resistant was provided by the SVD approach, which proved to be capable of identifying any type of damage inspected, in any noisy condition evaluated, with errors in the severity prediction 3-4% for the 6008 case. These performances were obtained by solving the first step with the AI solver and the second with the BLSO solver.

According to these findings, it is clear the considerable stabilising effect on the solution of the algebraic system brought by the Singular Value Decomposition (SVD) in presence of noise. This is due to the fact that the SVD approach uses all the information available, as the ODS approach, but has a better noise withstanding and smaller error in the damage severity estimation.